Woodhead Publishing Series in Composites Science and Engineering

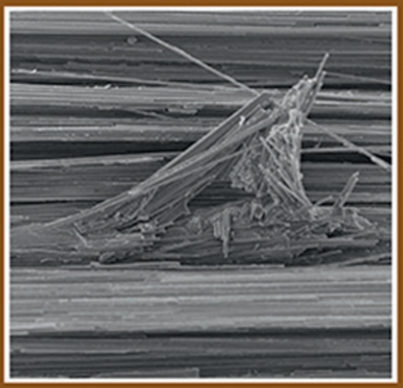

Toughening Mechanisms in Composite Materials

Edited by
Qinghua Qin and
Jianqiao Ye

WP
WOODHEAD PUBLISHING

Toughening Mechanisms in Composite Materials

Related titles

Composite joints and connections
(ISBN 978-1-84569-990-1)

Composite reinforcements for optimum performance
(ISBN 978-1-84569-965-9)

Non-crimp fabric composites
(ISBN 978-1-84569-762-4)

Woodhead Publishing Series in Composites Science and Engineering: Number 55

Toughening Mechanisms in Composite Materials

Edited by

Qinghua Qin and Jianqiao Ye

AMSTERDAM • BOSTON • CAMBRIDGE • HEIDELBERG
LONDON • NEW YORK • OXFORD • PARIS • SAN DIEGO
SAN FRANCISCO • SINGAPORE • SYDNEY • TOKYO
Woodhead Publishing is an imprint of Elsevier

Woodhead Publishing is an imprint of Elsevier
80 High Street, Sawston, Cambridge, CB22 3HJ, UK
225 Wyman Street, Waltham, MA 02451, USA
Langford Lane, Kidlington, OX5 1GB, UK

British Library Cataloguing in Publication Data
A catalogue record for this book is available from the British Library.

Library of Congress Control Number: 2015931787

ISBN 978-1-78242-279-2 (print)
ISBN 978-1-78242-291-4 (online)

Contents

List of contributors

G. Allegri Imperial College London, London, UK

S. Araby School of Engineering, University of South Australia (UniSA), Salisbury, SA, Australia

C. B. Emrullahoglu Abi Afyon Kocatepe University, Afyonkarahisar, Turkey

K. Bilge Sabanci University, Istanbul, Turkey

M. Esmkhani Iran University of Science and Technology, Tehran, Iran

S.M. Ghoreishi Iran University of Science and Technology, Tehran, Iran

M. Kašiarová Slovak Academy of Sciences, Košice, Slovak Republic

V. Kompiš University of Žilina, Žilina, Slovakia

T. Kusaka Ritsumeikan University, Kusatsu, Japan

J.K. Lander Rolls-Royce Plc, Derby, UK

X. Lin University of New South Wales, Canberra, ACT, Australia

X. Liu Beijing University of Technology, Beijing, China

J. Ma School of Engineering, University of South Australia (UniSA), Salisbury, SA, Australia

Q. Meng School of Engineering, University of South Australia (UniSA), Salisbury, SA, Australia

Z. Mouti Eaton, West Midlands, UK

Z. Murčinková Technical University, Košice, Slovakia

J. Njuguna Robert Gordon University, Aberdeen, UK

M. Papila Sabanci University, Istanbul, Turkey

I.K. Partridge University of Bristol, Bristol, UK

Q.H. Qin Australian National University, Acton, ACT, Australia

M. Quaresimin University of Padova, Vicenza, Italy

M. Salviato University of Padova, Vicenza, Italy, and Northwestern University, Evanston, IL, USA

M.M. Shokrieh Iran University of Science and Technology, Tehran, Iran

P. Tatarko Slovak Academy of Sciences, Košice, Slovak Republic, and Queen Mary University of London, London, UK

H. Tian The University of New South Wales, Canberra, ACT, Australia

K. Westwood Eaton, West Midlands, UK

Q.-S. Yang Beijing University of Technology, Beijing, China

M. Yasaee University of Bristol, Bristol, UK

M. Zappalorto University of Padova, Vicenza, Italy

Y.X. Zhang The University of New South Wales, Canberra, ACT, Australia

M. Žmindák University of Žilina, Žilina, Slovakia

Woodhead Publishing Series in Composites Science and Engineering

1 **Thermoplastic aromatic polymer composites**
F. N. Cogswell
2 **Design and manufacture of composite structures**
G. C. Eckold
3 **Handbook of polymer composites for engineers**
Edited by L. C. Hollaway
4 **Optimisation of composite structures design**
A. Miravete
5 **Short-fibre polymer composites**
Edited by S. K. De and J. R. White
6 **Flow-induced alignment in composite materials**
Edited by T. D. Papthanasiou and D. C. Guell
7 **Thermoset resins for composites**
Compiled by Technolex
8 **Microstructural characterisation of fibre-reinforced composites**
Edited by J. Summerscales
9 **Composite materials**
F. L. Matthews and R. D. Rawlings
10 **3-D textile reinforcements in composite materials**
Edited by A. Miravete
11 **Pultrusion for engineers**
Edited by T. Starr
12 **Impact behaviour of fibre-reinforced composite materials and structures**
Edited by S. R. Reid and G. Zhou
13 **Finite element modelling of composite materials and structures**
F. L. Matthews, G. A. O. Davies, D. Hitchings and C. Soutis
14 **Mechanical testing of advanced fibre composites**
Edited by G. M. Hodgkinson
15 **Integrated design and manufacture using fibre-reinforced polymeric composites**
Edited by M. J. Owen and I. A. Jones
16 **Fatigue in composites**
Edited by B. Harris
17 **Green composites**
Edited by C. Baillie

18 **Multi-scale modelling of composite material systems**
Edited by C. Soutis and P. W. R. Beaumont
19 **Lightweight ballistic composites**
Edited by A. Bhatnagar
20 **Polymer nanocomposites**
Y-W. Mai and Z-Z. Yu
21 **Properties and performance of natural-fibre composite**
Edited by K. Pickering
22 **Ageing of composites**
Edited by R. Martin
23 **Tribology of natural fiber polymer composites**
N. Chand and M. Fahim
24 **Wood-polymer composites**
Edited by K. O. Niska and M. Sain
25 **Delamination behaviour of composites**
Edited by S. Sridharan
26 **Science and engineering of short fibre reinforced polymer composites**
S-Y. Fu, B. Lauke and Y-M. Mai
27 **Failure analysis and fractography of polymer composites**
E. S. Greenhalgh
28 **Management, recycling and reuse of waste composites**
Edited by V. Goodship
29 **Materials, design and manufacturing for lightweight vehicles**
Edited by P. K. Mallick
30 **Fatigue life prediction of composites and composite structures**
Edited by A. P. Vassilopoulos
31 **Physical properties and applications of polymer nanocomposites**
Edited by S. C. Tjong and Y-W. Mai
32 **Creep and fatigue in polymer matrix composites**
Edited by R. M. Guedes
33 **Interface engineering of natural fibre composites for maximum performance**
Edited by N. E. Zafeiropoulos
34 **Polymer-carbon nanotube composites**
Edited by T. McNally and P. Pötschke
35 **Non-crimp fabric composites: Manufacturing, properties and applications**
Edited by S. V. Lomov
36 **Composite reinforcements for optimum performance**
Edited by P. Boisse
37 **Polymer matrix composites and technology**
R. Wang, S. Zeng and Y. Zeng
38 **Composite joints and connections**
Edited by P. Camanho and L. Tong
39 **Machining technology for composite materials**
Edited by H. Hocheng
40 **Failure mechanisms in polymer matrix composites**
Edited by P. Robinson, E. S. Greenhalgh and S. Pinho
41 **Advances in polymer nanocomposites: Types and applications**
Edited by F. Gao

42 **Manufacturing techniques for polymer matrix composites (PMCs)**
Edited by S. Advani and K-T. Hsiao
43 **Non-destructive evaluation (NDE) of polymer matrix composites: Techniques and applications**
Edited by V. M. Karbhari
44 **Environmentally friendly polymer nanocomposites: Types, processing and properties**
S. S. Ray
45 **Advances in ceramic matrix composites**
Edited by I. M. Low
46 **Ceramic nanocomposites**
Edited by R. Banerjee and I. Manna
47 **Natural fibre composites: Materials, processes and properties**
Edited by A. Hodzic and R. Shanks
48 **Residual stresses in composite materials**
Edited by M. Shokrieh
49 **Health and environmental safety of nanomaterials: Polymer nanocomposites and other materials containing nanoparticles**
Edited by J. Njuguna, K. Pielichowski and H. Zhu
50 **Polymer composites in the aerospace industry**
Edited by P. E. Irving and C. Soutis
51 **Biofiber reinforcement in composite materials**
Edited by O. Faruk and M. Sain
52 **Fatigue and fracture of adhesively-bonded composite joints: Behaviour, simulation and modelling**
Edited by A. P. Vassilopoulos
53 **Fatigue of Textile Composites**
Edited by V. Carvelli and S. V. Lomov
54 **Wood Composites – From Nanocellulose to Superstructures**
Edited by M. Ansell
55 **Toughening Mechanisms in Composite Materials**
Edited by Q. Qin and J. Ye

This page intentionally left blank

Introduction to the composite and its toughening mechanisms

1

Q.H. Qin
Australian National University, Acton, ACT, Australia

1.1 Basic concepts

The word "composite" usually signifies that two or more separate materials are combined on a macroscopic scale to form a structural unit for various engineering applications. Each of the material components may have distinct thermal, mechanical, electrical, magnetic, optical, and chemical properties. It is noted that a composite composed of an assemblage of these different materials gives us a useful new material whose performance characteristics are superior to those of the constituent materials acting independently (Ye, 2003; Qin and Yang, 2008). One or more of the material components is usually discontinuous, stiffer, and stronger and known as the reinforcement; the less stiff and weaker material is continuous and called the matrix. Sometimes, because of chemical interactions or other processing effects, an additional distinct phase, called an interphase, exists between the reinforcement and the matrix (Damiel and Ishai, 2006). Composite materials have some advantages when compared to their components or metal parts. Some material properties that can be improved by forming a composite material are (Jones, 1999):

- Strength
- Stiffness
- Wear resistance
- Weight
- Fatigue life
- Extreme temperature response
- Thermal insulation or conduction
- Electrical insulation or conduction
- Acoustical insulation or conduction
- Response to nuclear, X-ray, or magnetic radiation
- Chemical response or inertness to an environment (corrosion resistance)
- Electromagnetic and radar insulation or conduction
- Crack (fracture) resistance and arrest
- Cost
- Fabrication
- Temperature-dependent behavior
- Attractiveness.

Further, composite materials have the following advantages: (1) composites can have unique properties (e.g., specific strength and modulus) that are significantly better

Toughening Mechanisms in Composite Materials. http://dx.doi.org/10.1016/B978-1-78242-279-2.00001-9

than their metal, polymer, and ceramic counterparts; (2) composites offer a greater flexiblity in designing and manufacturing a specific engineering structure; (3) composites can be fabricated to a final product from raw materials; and (4) composites can be tailored to have given properties required by the end users.

1.1.1 Matrix materials

Polymers, metals, and ceramics are all used as matrix materials in composites. They are the constituents that are continuously distributed in a composite. Examples of matrix materials are (1) polymers: epoxies, polyesters, phenolics, silicone, polyimide, nylon, polyethelene, polystyrene, and polycarbonate. The first five belong to the category of thermoset plastic, which is the material that can be melted and shaped only once (if it is heated a second time, it tends to crack or disintegrate); whereas the last four are categorized as thermoplastic, which is, in contrast, a material that can be melted and shaped over and over again; (2) metals: steel, iron, aluminum, zinc, carbon, copper, nickel, silver, titanium, and magnesium; and (3) ceramics: alumina, silicon carbide, aluminum nitride, silicon nitride, zirconia, and mullite. The functions of the matrix are to transmit forces between fibers, hold fibers in proper orientations, protect fibers from the environment, and stop cracks from spreading between fibers. To effectively realize those functions, a desired matrix material should have good ductility, high toughness and interlaminar shear strength, stable temperature properties, and high moisture/environmental resistance. In addition, a strong interface bond between the fiber and matrix materials is desirable, so the matrix must be capable of developing a mechanical or chemical bond with the fiber (Gibson, 2012).

1.1.2 Reinforcement materials

Reinforcement materials usually add rigidity and greatly impede crack propagation. In particular, they enforce the mechanical properties of the matrix and, in most cases, are harder, stronger, and stiffer than the matrix. The reinforcement can be divided into four basic categories: fibers, particulates, fillers, and flakes.

Flakes are in flat platelet form and have a primarily two-dimensional geometry with strength and stiffness in two directions. They can form an effective composite material when suspended in a glass or plastic. Ordinarily, flakes are packed parallel to one another with a resulting higher density than fiber-packing concepts. Typical flake materials are mica, aluminum, and silver. Mica flakes embedded in a glassy matrix provide composites that can be machined easily and are used in electrical applications. Aluminum flakes are commonly used in paints and other coatings in which they orient themselves parallel to the surface of the coating. Silver flakes are used where good conductivity is required.

Fillers are particles or powders added to material to change and improve the physical and mechanical properties of composites. They are also used to lower the consumption of a more expensive binder material. In particular, fillers are used to modify or enhance properties such as thermal conductivity, electrical resistivity, friction, wear resistance, and flame resistance. Typical fillers are calcium carbonate,

aluminum oxide, lime (also known as calcium oxide), fumed silica, treated clays, and hollow glass beads.

Particulates used in composites can be small particles (<0.25 μm), hollow spheres, cubes, platelets, or carbon nanotubes. In each case, the particulates provide desirable material properties, and the matrix acts as a binding medium necessary for structural applications. The arrangement of particulate materials may be random or with a preferred orientation. In general, particles are not very effective in improving strength and fracture resistance. Typical particle materials are lead, copper, tungsten, molybdenum, and chromium.

Finally, a fiber is a rope or string used as a component of composite materials whose aspect ratio (length/diameter) is usually very large (>100). The cross-section can be circular, square, or hexagonal. Commonly used fibers in the composite include the following: (1) glass fiber, which consists primarily of silicon dioxide and metallic oxide modifying elements and are generally produced by mechanical drawing of molten glass through a small orifice. They are widely used due to low cost and high corrosion resistance. Glass fibers can be used in fishing rods, storage tanks, and aircraft parts; (2) aramid fiber, which has higher specific strength and is lighter than glass, is more ductile than carbon. Examples of industrial application are armor, protective clothing, and sporting goods; (3) carbon fiber, which is often produced from an oxidized polyacrylonitrile or via pyrolysis carbonized polymers. The carbon fiber can have a modulus as high as 950 GPa with low density. Its diameter is usually between 5 and 8 μm, smaller than a human hair (50 μm); (4) boron fiber, which usually has high stiffness, good compressive strength, and large diameters (0.05–0.2 mm) compared to other types of fibers. Composites with boron fibers are widely used in aerospace structures where high stiffness is needed; and (5) silicon carbide fiber, which is usually used in high-temperature metal and ceramic matrix composites (CMC) because of its excellent oxidation resistance, high modulus, and strength in high-temperature atmosphere.

1.2 Historical developments

Although it is difficult to say when or where people first learned about composites, nature and literature provide us with numerous examples. About 3000 BC, people used brick made of straw and mud for construction. Mud reinforced with bamboo shoots and glued laminated wood were used in houses built by the Egyptians in 1500 BC. Mongols invented the first composite bow in 1200 AD. Glass–polyester radomes were introduced in 1938 for application in aerospace structures: here, the fiberglass was combined for the first time with good unsaturated polyester resins. The first molded fiberglass boat was built in 1942. The U.S. government patented the first filament winding process in 1946, followed by missile applications in the 1950s. In 1952, Herring and Galt (1952) described the mechanical properties of thin whiskers of Sn, and inferred that whiskers were single crystals. Boeing 727 started to employ reinforced plastic components in 1960. The first boron and high-strength

carbon fibers were introduced in the early 1960s. It was not until 1969 that carbon/epoxy materials were applied to operational fighter aircraft structures. Metal matrix composites (MMC) such as boron/aluminum were introduced in 1970. DuPont developed Kevlar fibers in early 1970s (Greenwoo and Rose, 1974). Starting in the late 1970s, the application of composites has greatly increased and expended to tennis rackets, large-diameter thin-walled pipes, civilian structural members, golf clubs, automobile and truck components, skis, fiber-reinforced concrete, epoxy-impregnated concrete, composite-pressure vessels, armor, space vehicles, boats, and airplanes, due to the development of new fibers such as carbon, boron, and nanotube and new composite systems with matrix made of polymers and metals.

1.3 Classification and applications

There are two classification systems of composite materials. One is based on the type of matrix material (metal, ceramic, polymer, carbon/graphite) and the second is based on the geometry of reinforcing material (fiber, whisker, flake, and particulate).

1.3.1 Classification based on matrix materials

Based on matrix materials, four commonly accepted composites are:

- MMC are composite materials with at least two constituent parts, one being a metal (aluminum, magnesium, iron, cobalt, copper), which is considered as the matrix phase. The other material may be a different metal (lead, tungsten, molybdenum) or another material (oxides, carbides, organic compound). Typical engineering structures containing MMC include carbide drills, tank armor, automotive disc brakes, automotive engines, and the F-16 Fighting Falcon.
- CMC are composed of a ceramic matrix and embedded fibers of other ceramic material (dispersed phase). Advantages of CMC include high strength and hardness at very high temperature, high service temperature limits for ceramics, low density, and chemical inertness. The applications of CMCs are in fields requiring reliability at high temperatures (beyond the capability of metals) and resistance to corrosion and wear (e.g., heat shield systems for space vehicles; components for high-temperature gas turbines; components for burners, flame holders, and hot gas ducts; and components for slide bearings under heavy loads requiring high corrosion and wear resistance).
- Polymer matrix composites (PMC) are composed of a matrix from thermoset (epoxies, phenolics) or thermoplastic (polycarbonate, polyvinylchloride, nylon, acrylics) and embedded glass, carbon, steel, or Kevlar fibers. Unlike a CMC, in which the reinforcement is used primarily to improve the fracture toughness, the reinforcement in a PMC provides high strength and stiffness. The advantages of PMC are attributed to its light weight, high stiffness and strength along the direction of the reinforcement, and superior corrosion and fatigue resistance compared to metals. Examples of PMC application are secondary load-bearing aerospace structures, boat bodies, canoes, kayaks, automotive parts, radio-controlled vehicles,

sporting goods (golf clubs, skis, tennis racquets, fishing rods), bullet-proof vests and other armor parts, and brake and clutch linings.

- Carbon–carbon composites (C/C) consist of carbon fibers embedded in a carbonaceous matrix. Carbon is a very versatile material that can exist in a variety of forms: amorphous, graphite, diamond, pyrolytic graphite, carbon black, carbon nanotube, fullerenes, and grapheme. Carbon is an excellent high-temperature material used in an inert or nonoxidizing atmosphere. The working temperature can be as high as 2000 °C. Typical high-temperature applications involve breaks for aircraft and automobiles, dies for use in hot-pressing, high-temperature fasteners, heating elements in furnaces and protection tubes, and space shuttle nose cones.

1.3.2 Classification based on the geometry of reinforcement

There are four typical types of composites based on the geometry of reinforcement:

- Fiber-reinforced composites (FRC) consist of three components: (1) the fibers as the discontinuous or dispersed phase; (2) the matrix as the continuous phase; and (3) the fine interphase region, also known as the interface. The fiber may be of short (discontinuous) or long (continuous) fiber. As indicated in Gibson (2012), in a fiber composite, commonly used matrix materials are epoxy, aluminum, calcium-alumino silicate, polymer, and carbon. Examples of FRP application are bridges and columns, prestressing tendons, reinforcing bars, grid reinforcement, and dowels. In addition, FRC is also used in outdoor deck floors, railings, fences, cladding and siding, park benches, and window and door frames.
- Whisker composites are composed of a matrix material and embedded reinforcing whisker materials (e.g., potassium titanate whisker, graphite, aluminum oxide, silicon carbide, silicon oxide, boron carbide, and beryllium oxide). A whisker is the nearly perfect, single-crystal material produced synthetically under controlled conditions. It is a very thin, short filament with large length/diameter ratio and is smaller than chopped fibers. Owing to its small diameter, the whisker is nearly free of internal defects and yields strength close to the maximum theoretical value. For example, whiskers of silicon nitride are being made as fine as 0.2–0.5 μm in diameter. Tjong and Meng (1999) found that whiskers could have much higher specific strength than short glass or carbon fibers and could reinforce polymers more effectively.
- Flake composites consist of flat reinforcements of matrices. Typical flake materials are glass, mica, aluminum, and silver. As indicated in Kaw (2006), flake composites provide advantages such as high out-of-plane flexural modulus, high strength, and low cost. However, flakes cannot be oriented easily and only a limited number of materials are available for use.
- Particulate composites consist of particles of various sizes and shapes randomly dispersed within the matrix. Because of the usual randomness of particle distribution, these composites can be regarded as quasi-homogeneous and quasi-isotropic on a scale much larger than the particle size and spacing. Particulate composites have advantages such as improved strength, increased operating temperature, oxidation resistance, high creep resistance, and high strength to weight ratio (Kaw, 2006). Typical examples of application are appliances, toys, cell phone casings, helmets, body panels of automotive cars, breaks, bumpers, and intake manifolds.

1.4 Effective mechanical behavior of composites

As indicated in Section 1.1, a composite is composed of two or more separate materials. Each of the material components may have distinct material properties. It is important to determine the effective material properties if we replace the composite with a homogeneous material. In classical mechanics, at a macrolevel, the material properties are always assumed to be homogeneous on an average basis, whereas at a microlevel, i.e., inside the composite, the material properties are heterogeneous. At a microlevel, the heterogeneous microstructure and physical laws are usually known. The task is to find homogeneous material properties at a macrolevel based on the information of microstructure. These properties are often called overall material properties or effective material properties, and the process is often known as homogenization. Recently, some investigations have been made into the composite array using methods such as the homogenization method (Qin and Yang, 2008). Grassi et al. (2002) numerically examined the effect of fiber volume fraction of the through thickness Young's modulus. Qin (2004a,b, 2005) and Yang and Qin (2004) presented several boundary elements–micromechanics models for predicting effective properties of materials with defects or inclusions. Antoniou et al. (2009) developed a FE model to predict mechanical behavior of glass/epoxy tubes under static loading. Xu et al. (2008) conducted an experiment on the plate size in determining the effective modulus. Yang and Qin (2001, 2003) used the finite element method (FEM) to predict effective elasto-plastic properties of composites. To determine the ranges of effective properties using various micromechanics models, the Voigt and Reuss rule (Gasik, 1998) presented a method to find the upper and lower bounds, respectively, of the stiffness for a composite material with arbitrary fiber-matrix geometry. Micromechanic models were also used to determine effective properties of piezoelectric materials with cracks (Qin et al., 1998; Yu and Qin, 1996; Qin and Yu, 1997), microvoids (Qin and Yu, 1998), and of human dentine materials (Wang and Qin, 2007, 2011; Qin and Swain, 2004). Several other research studies have used representative unit cell models to investigate the dependence of component properties on composite materials (Tvergaard, 1990; Bao et al., 1991; Zahl and McMeeking, 1991; Levy and Papazian, 1990; Li et al., 1995; Feng et al., 2003). This section briefly describes major micromechanics models commonly used to determine effective material properties and to analyze the corresponding mechanical behavior of composite materials. It includes the mechanics of materials approach (MMA), finite element modeling, direct and indirect homogenization, and boundary element approach.

1.4.1 Mechanics of materials approach

MMA provides an analytical technique to calculate effective material properties of the fiber-reinforced composites. These overall material properties can be used to predict the material behavior with various interfaces. MMA is used to determine the overall material properties due to their respective fiber and matrix volume fractions and constituent material properties. It assumes an average of stresses and strains to examine the global response.

1.4.1.1 Determination of longitudinal modulus E_1

We begin with determining the Young's modulus E_1 (Young's modulus in the fiber direction) of a fiber-reinforced composite. To this end, consider a representative volume element (RVE) in Figure 1.1. It is subjected to a longitudinal normal stress σ_1, as shown in Figure 1.1. Static equilibrium requires that the total resultant force F on the RVE must equal the sum of the forces acting on the fiber and matrix:

$$F = \sigma_1 A = \overline{\sigma}_{m1} A_m + \overline{\sigma}_{f1} A_f \tag{1.1}$$

where subscripts "m" and "f" refer to matrix and fiber, A, A_m, and A_f stand for cross areas of composite, matrix, and fiber respectively, and

$$\overline{\sigma}_{m1} = \frac{1}{V}\int \sigma_{m1} dV = \frac{1}{A}\int \sigma_{m1} dA, \quad \overline{\sigma}_{f1} = \frac{1}{V}\int \sigma_{f1} dV = \frac{1}{A}\int \sigma_{f1} dA \tag{1.2}$$

Since the length of matrix and fiber are the same (Figure 1.1), area fractions are equal to the corresponding volume fractions. As such, Eq. (1.1) can be rearranged to give a "rule of mixtures" for longitudinal stress:

$$\sigma_1 = \overline{\sigma}_{m1}\frac{A_m}{A} + \overline{\sigma}_{f1}\frac{A_f}{A} = \overline{\sigma}_{m1} v_m + \overline{\sigma}_{f1} v_f \tag{1.3}$$

where v_m and v_f are area fraction of matrix and fiber, respectively.

If both the matrix and fiber are linear elastic and isotropic, we have from Hooke's law

$$\sigma_1 = E_1 \overline{\varepsilon}_1, \quad \sigma_{m1} = E_m \overline{\varepsilon}_{m1}, \quad \sigma_{f1} = E_f \overline{\varepsilon}_{f1} \tag{1.4}$$

where

$$\overline{\varepsilon}_1 = \frac{1}{A}\int \varepsilon_1 dA, \quad \overline{\varepsilon}_{m1} = \frac{1}{A}\int \varepsilon_{m1} dA, \quad \overline{\sigma}_{f1} = \frac{1}{A}\int \varepsilon_{f1} dA \tag{1.5}$$

and Eq. (1.3) becomes

$$E_1 \overline{\varepsilon}_1 = E_m \overline{\varepsilon}_m v_m + E_f \overline{\varepsilon}_f v_f \tag{1.6}$$

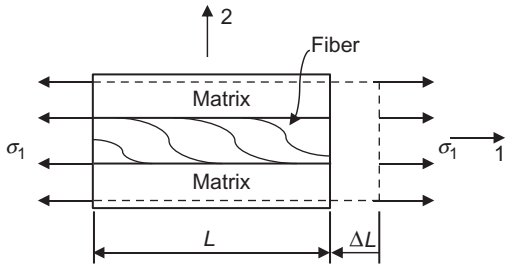

Figure 1.1 Composite loaded in fiber direction.

If the matrix and fiber are perfectly bonded, the average strains in the composite, matrix, and fiber along the one direction are all equal:

$$\overline{\varepsilon}_1 = \overline{\varepsilon}_{m1} = \overline{\varepsilon}_{f1} \tag{1.7}$$

Combination of Eqs. (1.6) and (1.7) yields the rule of mixtures for the longitudinal modulus:

$$E_1 = E_f v_f + E_m v_m \tag{1.8}$$

1.4.1.2 Determination of transverse modulus E_2

The Young's modulus of the composite material in the transverse direction can be determined by considering the loading case shown in Figure 1.2.

With the loading case in Figure 1.2, the normal strains in the fiber and matrix are found to be

$$\varepsilon_{f2} = \frac{\sigma_2}{E_f}, \quad \varepsilon_{m2} = \frac{\sigma_2}{E_m} \tag{1.9}$$

The total elongation in the transverse direction is $\Delta W = \varepsilon_2 W$ on average. It should be equal to the sum of the corresponding transverse elongation in the fiber, $W_f \varepsilon_{f2}$, and the matrix, $W_m \varepsilon_{m2}$:

$$\Delta W = \varepsilon_2 W = \frac{W}{E_2}\sigma_2 = \varepsilon_{f2} W_f + \varepsilon_{m2} W_m = \left(\frac{W_f}{E_f} + \frac{W_m}{E_m}\right)\sigma_2 \tag{1.10}$$

where W, W_f, and W_m are, respectively, the width of composite, fiber, and matrix. Equation (1.10) can be reduced to the "inverse rule of mixtures" for E_2 by dividing W on both sides of the equation:

$$\frac{1}{E_2} = \frac{v_f}{E_f} + \frac{v_m}{E_m} \tag{1.11}$$

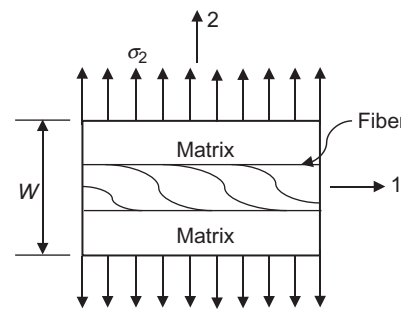

Figure 1.2 Composite loaded in transverse direction.

1.4.1.3 Determination of major Poisson's ratio μ_{12}

The major Poisson's ratio μ_{12}, is obtained by an approach similar to the derivation for E_1. For the loading case shown in Figure 1.1, the major Poisson's ratio is defined as:

$$\mu_{12} = -\frac{\varepsilon_2}{\varepsilon_1} \tag{1.12}$$

The transverse deformation ΔW is then equal to $\varepsilon_2 W = -W\mu_{12}\varepsilon_1$. In a manner of the derivation for E_2, the transverse deformation in the fiber, ΔW_f, and the matrix, ΔW_m, are given as

$$\Delta W_m = W v_m \mu_m \varepsilon_1, \quad \Delta W_f = W v_f \mu_f \varepsilon_1 \tag{1.13}$$

Since geometric compatibility requires that $\Delta W = \Delta W_f + \Delta W_m$, we have

$$\mu_{12} = \mu_m v_m + \mu_f v_f \tag{1.14}$$

This gives the rule of mixtures for the major Poisson's ratio.

1.4.1.4 Determination of in-plane shear modulus G_{12}

Consider the loading case shown in Figure 1.3a. The in-plane shear modulus of a lamina, G_{12}, is determined in the mechanics of materials method by assuming that the shearing stresses on the fiber and on the matrix are the same. From this assumption, we obtain:

$$\gamma = \frac{\tau}{G_{12}}, \quad \gamma_m = \frac{\tau}{G_m}, \quad \gamma_f = \frac{\tau}{G_f} \tag{1.15}$$

The shear deformations in matrix and fiber are then given as (Figure 1.3b):

$$\Delta_m = \gamma_m W_m = \gamma_m v_m W, \quad \Delta_f = \gamma_f W_f = \gamma_f v_f W \tag{1.16}$$

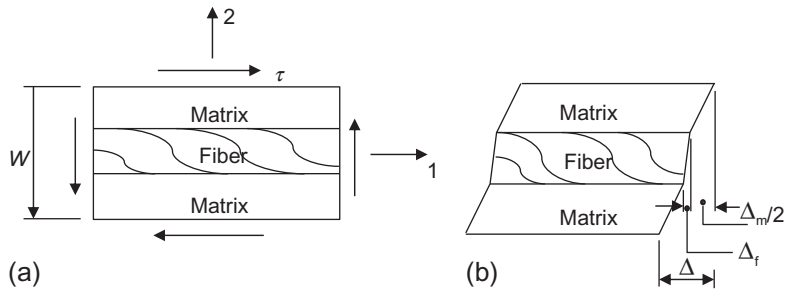

Figure 1.3 Composite loaded with shear stress.

The total shear deformation is $\Delta = \gamma W$, which is made up of approximate microscopic deformations (Figure 1.3). Again, geometric compatibility requires that $\Delta = \Delta_f + \Delta_m$ (Figure 1.3b), which yields by dividing W:

$$\gamma = \gamma_m v_m + \gamma_f v_f \tag{1.17}$$

Substituting Eq. (1.15) into Eq. (1.17), we have

$$\frac{1}{G_{12}} = \frac{v_m}{G_m} + \frac{v_f}{G_f} \tag{1.18}$$

1.4.2 Finite element approach

In order to obtain values for the material properties of fiber-reinforced composites using an FEM, the basic formulations are briefly described in this section. These differ to MMA in that they relate to the basic understanding of stress/strain relations and are not directly related to the volume fractions as stated in Section 1.4.1.

1.4.2.1 Calculation of E_1 and μ_{12}

E_1 and μ_{12} can be determined by considering the loading case shown in Figure 1.1, where a stress σ_1 is applied in the fiber direction of the composite. The effective Young's modulus and major Poisson ratio are, then, evaluated by

$$E_1 = \frac{\overline{\sigma}_1}{\overline{\varepsilon}_1} = \frac{\int_V \sigma_1 \, dV/V}{\int_V \varepsilon_1 \, dV/V} = \frac{\int_V \sigma_1 \, dV}{\int_V \varepsilon_1 \, dV}, \quad v_{12} = -\frac{\overline{\varepsilon}_2}{\overline{\varepsilon}_1} = -\frac{\int_V \varepsilon_2 \, dV/V}{\int_V \varepsilon_1 \, dV/V} = -\frac{\int_V \varepsilon_2 \, dV}{\int_V \varepsilon_1 \, dV} \tag{1.19}$$

If the left end is fixed and $\Delta\overline{L}$ represents the average displacement at the right end, the average strain can be defined as

$$\overline{\varepsilon} = \frac{\Delta\overline{L}}{L} \tag{1.20}$$

Therefore, the major task for FE calculation is to determine $\Delta\overline{L}$ and the average stress $\overline{\sigma}_1$. Further, the calculation of major Poisson ratio requires the information of $\varepsilon_2 = \Delta W/W$. As a result, the major issue for FE calculation is to calculate average transverse displacement ΔW. This has been implemented into our FE program.

1.4.2.2 Calculation of E_2

Considering the loading case as shown in Figure 1.2, the effective transverse Young's modulus E_2 is defined as

$$E_2 = \frac{\overline{\sigma}_2}{\overline{\varepsilon}_2} = \frac{\int_V \sigma_2 \mathrm{d}V/V}{\int_V \varepsilon_2 \mathrm{d}V/V} = \frac{\int_V \sigma_2 \mathrm{d}V}{\int_V \varepsilon_2 \mathrm{d}V} \tag{1.21}$$

where $\overline{\varepsilon}_2 = \Delta\overline{W}/W$. The major task for FE calculation is, then, to determine $\Delta\overline{W}$ and the average stress $\overline{\sigma}_2$.

1.4.2.3 Calculation of G_{12}

The in-plane shear modulus of a fiber-reinforced composite can be determined by considering the loading case shown in Figure 1.3, a shear stress is applied over the boundary of the composite.

$$G_{12} = \frac{\overline{\tau}}{\overline{\gamma}} = \frac{\int_V \tau \mathrm{d}V/V}{\int_V \gamma \mathrm{d}V/V} = \frac{\int_V \tau \mathrm{d}V}{\int_V \gamma \mathrm{d}V} \tag{1.22}$$

Considering the fact that the shear strain can be defined as u/y, where u is displacement in fiber direction and y stands for the vertical coordinate originated at the bottom of the composite, the task of FE calculation, in this case, is to evaluate shear stress and the displacement u.

From these equations, we can determine E_1, E_2, and G_{12}, noting that all other stresses and strains are taken as zero except for the stress and strain along the direction for the material property being determined.

1.4.2.4 A numerical example

As a numerical illustration, consider a composite composted of carbon fiber and epoxy resin matrix. Table 1.1 lists the mechanical properties of materials used in finite element approach (FEA).

To study effects of fiber's geometry on the overall properties of the composite, the following six combinations of geometry are considered: (a) rectangular matrix with circular fibers (RMCF); (b) rectangular matrix with hexagonal fibers (RMHF); (c) rectangular matrix with triangular fibers (RMTF); (d) square matrix with circular fibers (SMCF); (e) square matrix with hexagonal fibers (SMHF); and (f) square matrix with triangular fibers (SMTF). The corresponding fiber volume fraction for each of these is:

Table 1.1 Material properties

Material	Carbon fiber	Epoxy resin
Young's modulus	294 GPa	2.415 GPa
Poisson's ratio	0.3	0.35

RMCF = 0.13089; RMHF = 0.14433; RMTF = 0.08333;
SMCF = 0.08726; SMHF = 0.09622; SMTF = 0.05555.

Figure 1.4 shows the geometrical configuration of the unit cell used. It is obvious from Figure 1.4 that: (a) total area is 6 for RM and 9 for SM; and (b) the fiber's area is $\pi r^2 = 0.78539$ for circular fiber, $3^{3/2}t^2/2 = 3^{3/2} \times 0.57735^2/2 = 0.86602$ for hexagonal fiber, and 0.5 for triangular fiber. The fiber volume fraction listed above is obtained based on these data. The finite element meshes used in the calculation are shown in Figure 1.5.

The FE results obtained are listed in Table 1.2 and also shown in Figures 1.6–1.8. A comparison of the results between FEA and MMA for E_1 yield quite similar results. The average error between these results is within 3%, for all results, in determination of E_1. It indicates that MMA can provide acceptable accurate results for E_1. Figure 1.6 shows a comparison between the result E_1 of varying fiber and matrix geometries. Figures 1.7 and 1.8 list the comparison in results between E_2 and G_{12}, respectively,

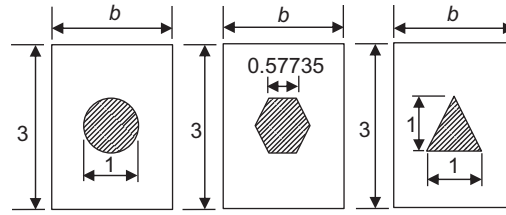

Figure 1.4 Geometrical configurations of matrix and fiber ($b = 2$ for RM and $b = 3$ for SM).

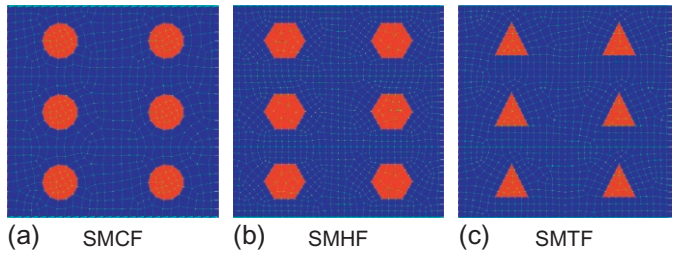

Figure 1.5 Finite element meshes for square matrix with different fiber geometries. (a) SMCF, (b) SMHF, and (c) SMTF.

Table 1.2 Composite's properties for carbon fiber with epoxy resin

Properties	E_1 (GPa)		E_2 (GPa)		G_{12} (GPa)	
Approach	MMA	FEA	MMA	FEA	MMA	FEA
RMCF	40.583	38.923	2.775	3.021	1.028	1.034
RMHF	44.502	43.743	2.818	3.145	1.044	1.062
RMTF	26.714	23.764	2.633	2.846	0.975	0.991
SMCF	27.861	26.351	2.644	2.774	0.979	0.991
SMHF	30.473	29.640	2.670	2.845	0.989	1.021
SMTF	18.614	18.710	2.556	2.736	0.947	0.994

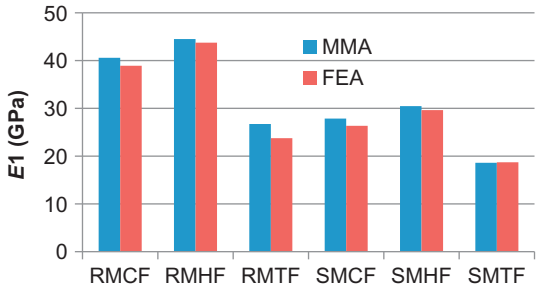

Figure 1.6 Comparison of E_1 results from FEA with those from MMA in the case of carbon fiber/epoxy resin.

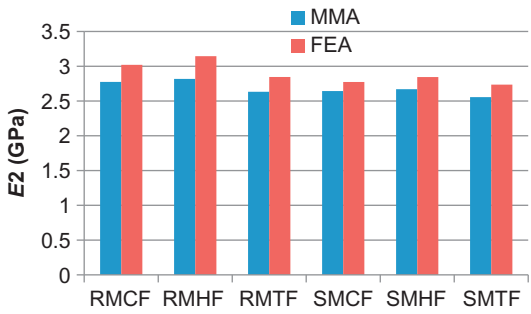

Figure 1.7 Comparison of E_2 results from FEA with those from MMA in the case of carbon fiber/epoxy resin.

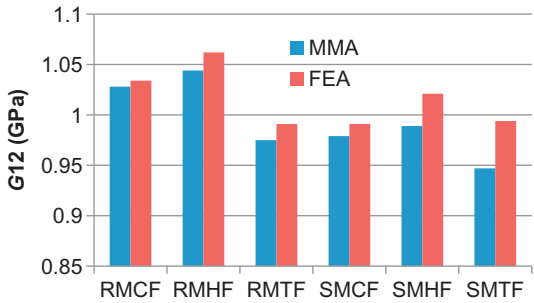

Figure 1.8 Comparison of G_{12} results from FEA with those from MMA in the case of carbon fiber/epoxy resin.

derived through MMA and FEA. The difference of these results is within 8%, between all the results collected for E_2 and G_{12}. As revealed by the graph, the difference in results is not always constant. The square matrix with circular fibers, for example, has a smaller difference than the other models between MMA and FEA results. This highlights the nonlinear nature of FEA modeling software. Another point to note is that the values obtained for E_1 using FEA are lower than those from MMA, while the values obtained for E_2 and G_{12} using FEA are higher than those from MMA. This is a result of the model thickness or the length in the fiber direction.

1.4.3 Direct homogenization

Direct homogenization is based on the average of local fields to calculate effective material properties. For instance, a uniform strain is applied to a fiber-reinforced composite and the average of the elastic displacement is calculated. Then one can calculate the effective material coefficients of the composite. In general, the local fields can be calculated by a numerical method, such as boundary element method (BEM) (Qin, 2004b) or FEM (Qin and Yang, 2008; Qin, 2000).

The constitutive equation used in direct method can be written as

$$\boldsymbol{\sigma} = \mathbf{E}\boldsymbol{\varepsilon} \tag{1.23}$$

where $\boldsymbol{\sigma}$, $\mathbf{E}$, and $\boldsymbol{\varepsilon}$ are, respectively, generalized stress, stiffness, and strain tensors. In direct method, $\boldsymbol{\varepsilon}$ and $\boldsymbol{\sigma}$ are averaged first, then the effective stiffness properties are obtained. In detail, for a heterogeneous medium, consider an RVE subjected to a specific boundary condition and calculate the local fields, $\boldsymbol{\varepsilon}$ and $\boldsymbol{\sigma}$, by a numerical method, such as FEM. Then a volume averaging is carried out and homogenized fields, $\overline{\boldsymbol{\varepsilon}}$ and $\overline{\boldsymbol{\sigma}}$, are obtained by

$$\overline{\boldsymbol{\varepsilon}} = \frac{1}{V}\int_{\Omega} \boldsymbol{\varepsilon} \mathrm{d}\Omega, \quad \overline{\boldsymbol{\sigma}} = \frac{1}{V}\int_{\Omega} \boldsymbol{\sigma} \mathrm{d}\Omega \tag{1.24}$$

The effective stiffness $\bar{\mathbf{E}}$ can be determined by

$$\overline{\boldsymbol{\sigma}} = \overline{\mathbf{E}}\overline{\boldsymbol{\varepsilon}} \tag{1.25}$$

Expanding Eq. (1.25), one can obtain

$$\overline{\sigma}_i = \overline{E}_{ij}\overline{\varepsilon}_j \tag{1.26}$$

Applying uniaxial $\overline{\varepsilon}_1 = 1$ and other $\overline{\varepsilon}_i = 0$ on the right-hand-side vector $\overline{\boldsymbol{\varepsilon}}$ and calculating all $\overline{\varepsilon}_i$ of the left-hand-side vector $\overline{\boldsymbol{\sigma}}$, one can obtain the effective stiffness coefficients $\bar{E}_{i1}$. The remaining $\bar{E}_{ij}$ can be obtained similarly.

1.4.4 Indirect homogenization

Indirect homogenization here refers to various homogenization methods derived from the generalized Eshelby's inclusion theory in which an elastic solution has been obtained for a single inclusion embedded in infinite elastic medium (Qin and Yang, 2008; Qin et al., 1998). Such a method is not involved in the calculation of average fields. A self-consistent scheme, a generalized self-consistent scheme, the Mori–Tanaka method, and a differential method are developed along this routine. The indirect methods have been widely used to predict the effective properties of composites (Yu and Qin, 1996; Qin and Yu, 1997, 1998). This section, however, is based on the developments in Qin and Yang (2008).

The effective properties that are represented by the effective stiffness $\bar{\mathbf{E}}$ or compliance $\overline{\mathbf{F}}$ of the composites, according to the average stress and strain, can be defined by Eq. (1.25) or

$$\overline{\boldsymbol{\varepsilon}} = \overline{\mathbf{F}}\overline{\boldsymbol{\sigma}} \tag{1.27}$$

The homogeneous boundary conditions are usually used to determine the overall material properties. For homogeneous traction $\boldsymbol{\sigma}^{\infty}$ on the boundary of an RVE, we have

$$\overline{\boldsymbol{\sigma}} = \boldsymbol{\sigma}^{\infty} \tag{1.28}$$

and

$$\overline{\boldsymbol{\varepsilon}} = \overline{\mathbf{F}}\boldsymbol{\sigma}^{\infty} \tag{1.29}$$

Thus, to find the effective compliance $\overline{\mathbf{F}}$, the average strain $\overline{\boldsymbol{\varepsilon}}$ must be computed for a composite subjected to a homogeneous traction boundary condition.

For homogeneous strain condition $\boldsymbol{\varepsilon}^{\infty}$ on the boundary of the RVE, one has

$$\overline{\boldsymbol{\varepsilon}} = \boldsymbol{\varepsilon}^{\infty}, \quad \overline{\boldsymbol{\sigma}} = \overline{\mathbf{E}}\boldsymbol{\varepsilon}^{\infty} \tag{1.30}$$

Accordingly, to determine $\bar{\mathbf{E}}$, the average stress $\overline{\boldsymbol{\sigma}}$ must be computed for a heterogeneous material subjected to a homogeneous strain boundary condition.

It is worthwhile to note that the volume average of stress and strain can be expressed in terms of phase volume fractions. For a general function G, the volume average can be written as

$$\begin{aligned} \overline{G} &= \frac{1}{V}\int_{\Omega} G\mathrm{d}\Omega = \frac{1}{V}\left[\int_{\Omega_1} G\mathrm{d}\Omega + \int_{\Omega_2} G\mathrm{d}\Omega + \cdots\right] \\ &= \frac{V_1}{V}\overline{G}^{(1)} + \frac{V_2}{V}\overline{G}^{(2)} + \cdots = v_1\overline{G}^{(1)} + v_2\overline{G}^{(2)} + \cdots \end{aligned} \tag{1.31}$$

where $\Omega_1, \Omega_2, \ldots (\Omega_1 + \Omega_2 + \cdots = \Omega)$ are subdomains that represent the domains occupied by phase $1, 2, \ldots$ of the composite material, and $V_1, V_2, \ldots$ are their volumes, while

$$v_1 = \frac{V_1}{V}, v_2 = \frac{V_2}{V}, \ldots \tag{1.32}$$

are referred to as volume fractions of the corresponding phases and $v_0 + v_1 + v_2 + \cdots = 1$. For an n-phase composite, the stress and strain can be expressed by

$$\overline{\boldsymbol{\sigma}} = \sum_{i=0}^{n-1} v_i \overline{\boldsymbol{\sigma}}^{(i)} \tag{1.33a}$$

$$\overline{\boldsymbol{\varepsilon}} = \sum_{i=0}^{n-1} v_i \overline{\boldsymbol{\varepsilon}}^{(i)} \tag{1.33b}$$

where the superscript (i) corresponds with phase i, and phase 0 ($i = 0$) refers to matrix.

The stress or strain in an inclusion is uniform when the inclusion shape is ellipsoidal. In this case, the effective properties can be expressed by so-called concentration factor of the stress or strain. It is assumed that the Hooke's law holds in each elastic phase

$$\boldsymbol{\sigma}^{(r)} = \mathbf{E}^{(r)} \boldsymbol{\varepsilon}^{(r)}, \quad (r = 0, 1, \ldots, n-1) \tag{1.34a}$$

$$\boldsymbol{\varepsilon}^{(r)} = \mathbf{F}^{(r)} \boldsymbol{\sigma}^{(r)}, \quad (r = 0, 1, \ldots, n-1) \tag{1.34b}$$

Substituting Eq. (1.34a) into Eq. (1.33a), and using Eq. (1.25), yields

$$\overline{\mathbf{E}} = \mathbf{E}^0 + \sum_{r=1}^{n} v_r \left(\mathbf{E}^{(r)} - \mathbf{E}^0 \right) \boldsymbol{\varepsilon}^{(r)} \overline{\boldsymbol{\varepsilon}}^{-1} \tag{1.35}$$

Substituting Eq. (1.34b) into Eq. (1.33b), and using Eq. (1.27), we have

$$\overline{\mathbf{F}} = \mathbf{F}^0 + \sum_{r=1}^{n} v_r \left(\mathbf{F}^{(r)} - \mathbf{F}^0 \right) \boldsymbol{\sigma}^{(r)} \overline{\boldsymbol{\sigma}}^{-1} \tag{1.36}$$

It is assumed that there are relations between average strain and local strain

$$\boldsymbol{\varepsilon}^{(r)} = \mathbf{A}^r \overline{\boldsymbol{\varepsilon}} \tag{1.37}$$

Similarly, the average stress and local stress have the relation

$$\boldsymbol{\sigma}^{(r)} = \mathbf{B}^r \overline{\boldsymbol{\sigma}} \tag{1.38}$$

Thus, the effective stiffness $\overline{\mathbf{c}}$ and compliance $\overline{\mathbf{f}}$ of the composite can be written as

$$\overline{\mathbf{E}} = \mathbf{E}^0 + \sum_{r=1}^{n} v_r \left(\mathbf{E}^{(r)} - \mathbf{E}^0 \right) \mathbf{A}^r \tag{1.39}$$

$$\overline{\mathbf{F}} = \mathbf{F}^0 + \sum_{r=1}^{n} v_r \left(\mathbf{F}^r - \mathbf{F}^0 \right) \mathbf{B}^r \tag{1.40}$$

where $\mathbf{A}^r$ and $\mathbf{B}^r$ are referred to as concentration factors of stress and strain, respectively. They are functions in terms of the properties of the constituents and the shape of inclusions.

1.4.4.1 Self-consistent scheme

In the self-consistent scheme, the effect of inclusion interaction is taken into account approximately by embedding each inclusion directly in the effective medium. In other words, it is assumed that a typical inclusion (fiber, particle, or microvoid) is embedded in an infinite effective medium subjected to a uniform strain $\boldsymbol{\varepsilon}^{\infty}$ at infinite boundary. The corresponding effective stress is then written as

$$\overline{\boldsymbol{\sigma}} = \overline{\mathbf{E}} \boldsymbol{\varepsilon}^{\infty} \tag{1.41}$$

The strain in the inclusion consists of two parts, uniform strain $\boldsymbol{\varepsilon}^{\infty}$ and a perturbing strain $\boldsymbol{\varepsilon}^{\mathrm{pt}}$, and the corresponding stress in the inclusion is $\overline{\boldsymbol{\sigma}} + \boldsymbol{\sigma}^{\mathrm{pt}}$, that is

$$\boldsymbol{\varepsilon}^{(1)} = \overline{\boldsymbol{\varepsilon}} + \boldsymbol{\varepsilon}^{\mathrm{pt}} \tag{1.42}$$

$$\boldsymbol{\sigma}^{(1)} = \overline{\boldsymbol{\sigma}} + \boldsymbol{\sigma}^{\mathrm{pt}} \tag{1.43}$$

where superscript (1) refers to the inclusion.

Using equivalent inclusion principle and the assumption of self-consistent method, yields

$$\overline{\boldsymbol{\sigma}} + \boldsymbol{\sigma}^{\mathrm{pt}} = \mathbf{E}^{(1)} \left(\overline{\boldsymbol{\varepsilon}} + \boldsymbol{\varepsilon}^{\mathrm{pt}} \right) = \overline{\mathbf{E}} \left(\overline{\boldsymbol{\varepsilon}} + \boldsymbol{\varepsilon}^{\mathrm{pt}} - \boldsymbol{\varepsilon}^{*} \right) \tag{1.44}$$

and

$$\boldsymbol{\varepsilon}^{\mathrm{pt}} = \mathbf{S} \boldsymbol{\varepsilon}^{*} \tag{1.45}$$

where $\mathbf{S}$ is Eshelby tensor and $\boldsymbol{\varepsilon}^{*}$ is equivalent to eigenstrain.

Solving Eqs. (1.42)–(1.44), yields

$$\boldsymbol{\varepsilon}^{(1)} = \left[\mathbf{I} + \mathbf{S}\overline{\mathbf{E}}^{-1}\left(\mathbf{E}^{(1)} - \overline{\mathbf{E}}\right)\right]^{-1}\overline{\boldsymbol{\varepsilon}} \tag{1.46}$$

where $\mathbf{I}$ is unit tensor. A comparison of Eq. (1.46) with Eq. (1.37) yields the strain concentration factor as

$$\mathbf{A}^{(1)} = \left[\mathbf{I} + \mathbf{S}\overline{\mathbf{E}}^{-1}\left(\mathbf{E}^{(1)} - \overline{\mathbf{E}}\right)\right]^{-1} \tag{1.47}$$

The effective properties can be found by substituting Eq. (1.47) in Eq. (1.39). It should be mentioned that the strain concentration factor is a function of unknown effective stiffness $\bar{\mathbf{E}}$. An iteration procedure is required to solve Eq. (1.39) for the effective properties.

1.4.4.2 Mori–Tanaka method

Consider a finite-fraction inclusion problem with eigenstrain $\boldsymbol{\varepsilon}^*$. With the Mori–Tanaka method, the average stress can be expressed as

$$\langle\boldsymbol{\sigma}\rangle_m = \mathbf{E}^{(0)}\langle\boldsymbol{\varepsilon}\rangle_m = -v_1\mathbf{E}^{(0)}(\mathbf{S}\boldsymbol{\varepsilon}^* - \boldsymbol{\varepsilon}^*) \tag{1.48}$$

where $\langle\boldsymbol{\varepsilon}\rangle_m$ is average strain in the matrix, and v_1 is volume fraction of inclusion.

For a binary composite subjected to homogeneous boundary condition (1.28), denoting $r=0$ matrix and $r=1$ inclusion, the effective stress is $\boldsymbol{\sigma}^\infty$. For the same shaped pure matrix applied to the same boundary condition, the corresponding strain $\boldsymbol{\varepsilon}^\infty$ can be expressed by

$$\boldsymbol{\sigma}^\infty = \mathbf{E}^0\boldsymbol{\varepsilon}^\infty \tag{1.49}$$

where $\mathbf{E}^0$ is the stiffness of the matrix. Due to the presence of inclusion, the strain in real matrix of the composite differs from one in pure matrix. Denote $\widetilde{\boldsymbol{\varepsilon}}$ as the perturbing strain and $\widetilde{\boldsymbol{\sigma}}$ as the corresponding perturbing stress. Thus, $\boldsymbol{\varepsilon}^\infty + \widetilde{\boldsymbol{\varepsilon}}$ and $\boldsymbol{\sigma}^\infty + \widetilde{\boldsymbol{\sigma}}$ are strain and stress in real matrix with

$$\boldsymbol{\sigma}^\infty + \widetilde{\boldsymbol{\sigma}} = \mathbf{E}^0(\boldsymbol{\varepsilon}^\infty + \widetilde{\boldsymbol{\varepsilon}}) \tag{1.50}$$

The strain and stress in the inclusion are different from ones in the matrix. The differences are $\boldsymbol{\varepsilon}'$ and $\boldsymbol{\sigma}'$, respectively. Thus $\boldsymbol{\varepsilon}^\infty + \widetilde{\boldsymbol{\varepsilon}} + \boldsymbol{\varepsilon}'$ and $\boldsymbol{\sigma}^\infty + \widetilde{\boldsymbol{\sigma}} + \boldsymbol{\sigma}'$ are the strain and stress in the inclusion. The equivalent inclusion principle yields:

$$\boldsymbol{\sigma}^{(1)} = \boldsymbol{\sigma}^\infty + \widetilde{\boldsymbol{\sigma}} + \boldsymbol{\sigma}' = \mathbf{E}^1(\boldsymbol{\varepsilon}^\infty + \widetilde{\boldsymbol{\varepsilon}} + \boldsymbol{\varepsilon}') = \mathbf{E}^0(\boldsymbol{\varepsilon}^\infty + \widetilde{\boldsymbol{\varepsilon}} + \varepsilon' - \boldsymbol{\varepsilon}^*) \tag{1.51}$$

$$\boldsymbol{\varepsilon}' = \mathbf{S}\boldsymbol{\varepsilon}^* \tag{1.52a}$$

$$\widetilde{\boldsymbol{\varepsilon}} = -v_1(\mathbf{S} - \mathbf{I})\boldsymbol{\varepsilon}^* \tag{1.52b}$$

Equation (1.52b) is obtained based on the Mori–Tanaka's concept of average stress, in Eq. (1.48). Solving Eq. (1.51) yields

$$\boldsymbol{\varepsilon}^{*} = \mathbf{H}\boldsymbol{\varepsilon}^{\infty} \tag{1.53}$$

where $\mathbf{H} = \left[\mathbf{E}^{0} + \Delta\mathbf{E}(v_1\mathbf{I} - v_0\mathbf{S})\right]^{-1}\Delta\mathbf{E}$, $\Delta\mathbf{E} = \mathbf{E}^{1} - \mathbf{E}^{0}$, and $v_0 = 1 - v_1$ is the volume fraction of matrix.

Accordingly, the effective strain $\overline{\boldsymbol{\varepsilon}}$ is

$$\begin{aligned}\overline{\boldsymbol{\varepsilon}} = (1-v_1)\boldsymbol{\varepsilon}^{(0)} + v_1\boldsymbol{\varepsilon}^{(1)} &= (1-v_1)(\boldsymbol{\varepsilon}^{\infty} + \widetilde{\boldsymbol{\varepsilon}}) + v_1(\boldsymbol{\varepsilon}^{\infty} + \widetilde{\boldsymbol{\varepsilon}} + \boldsymbol{\varepsilon}') \\ &= \boldsymbol{\varepsilon}^{\infty} + v_1\boldsymbol{\varepsilon}^{*} = (\mathbf{I} + v_1\mathbf{H})\boldsymbol{\varepsilon}^{\infty}\end{aligned} \tag{1.54}$$

The effective stiffness of the composite is then given by

$$\overline{\mathbf{E}} = \mathbf{E}^{0}(\mathbf{I} + v_1\mathbf{H})^{-1} \tag{1.55}$$

1.4.4.3 Differential method

The essence of the differential scheme, an incremental form of the self-consistent method, is the construction of the final defected medium from the intact material through successive replacement of an incremental area of the current defected material with that of the inclusions. Denote $\bar{\mathbf{E}}$ as the effective stiffness of composite with volume V_0 and inclusion volume fraction v_1. Add volume δV of inclusion to the composite so that inclusion volume fraction is $v_1 + \delta v_1$ and the effective stiffness is $\overline{\mathbf{E}} + \delta\overline{\mathbf{E}}$. To keep a constant volume V_0 of the composite, the volume of composite is detracted by δV before adding the inclusion. Thus concentration of the inclusion is

$$v_1 V_0 + \delta V - v_1\delta V = (v_1 + \delta v_1)V_0 \tag{1.56}$$

It is rearranged as

$$\frac{\delta V}{V} = \frac{\delta v_1}{1 - v_1} \tag{1.57}$$

The average stress is

$$\overline{\boldsymbol{\sigma}} = \left(\overline{\mathbf{E}} + \delta\overline{\mathbf{E}}\right)\overline{\boldsymbol{\varepsilon}} \tag{1.58}$$

Then one has

$$\overline{\boldsymbol{\varepsilon}} = \frac{V_0 - \delta V}{V_0}\boldsymbol{\varepsilon} + \frac{\delta V}{V_0}\boldsymbol{\varepsilon}^{(1)}, \quad \overline{\boldsymbol{\sigma}} = \frac{V_0 - \delta V}{V_0}\boldsymbol{\sigma} + \frac{\delta V}{V_0}\boldsymbol{\sigma}^{(1)} \tag{1.59}$$

where $\boldsymbol{\sigma}$ and $\boldsymbol{\varepsilon}$ denote the average stress and strain in instantaneous composite, respectively. $\boldsymbol{\sigma}^{(1)}$ and $\boldsymbol{\varepsilon}^{(1)}$ represent the average stress and strain of the added inclusion, respectively. Because the added inclusion is very small, the strain concentration factor can be calculated by Eshelby's solution of a dilute inclusion problem

$$\boldsymbol{\varepsilon}^{(1)} = \mathbf{A}\overline{\boldsymbol{\varepsilon}} \tag{1.60}$$

where $\mathbf{A} = \left[\mathbf{I} + \mathbf{S}\overline{\mathbf{E}}^{-1}\left(\mathbf{E}^1 - \overline{\mathbf{E}}\right)\right]^{-1}$.

Substituting Eqs. (1.59) and (1.60) into Eq. (1.58), yields

$$\delta\overline{\mathbf{E}} = \left(\mathbf{E}^1 - \overline{\mathbf{E}}\right)\mathbf{A}\frac{\delta V}{V_0} \tag{1.61}$$

Using Eq. (1.57), and setting $\delta v_1 \to 0$, we can obtain

$$\frac{\mathrm{d}\mathbf{E}}{\mathrm{d}v_1} = \frac{1}{1 - v_1}\left(\mathbf{E}^1 - \mathbf{E}\right)\mathbf{A} \tag{1.62}$$

This is a differential equation about effective stiffness. Its initial condition is

$$\overline{\mathbf{E}}\big|_{v_1 = 0} = \mathbf{E}^0 \tag{1.63}$$

Equation (1.62) is a nonlinear equation that can be solved by a numerical procedure.

1.4.5 Micromechanics-boundary element mixed approach

It is noted that common to each of the micromechanics theories described in Section 1.4.4 is the use of the well-known stress and strain concentration factors obtained through an analytical solution of a single crack, void, or inclusion embedded in an infinite medium. However, for a problem with complexity in the aspects of geometry and mechanical deformation, a combination of these micromechanics approaches and numerical methods such as the FEM and BEM presents a powerful computational tool for estimating effective material properties. It is also noted from Section 1.4.4 that the estimation of the average strain (or stress), which may be expressed in terms of integral equations contains unknown variables on the boundary only, is the key to predicting the concentration factor $\mathbf{A}_2$ (or $\mathbf{B}_2$). Therefore, BEM is very suitable for performing this type of calculation. In this section, a micromechanics-BE mixed algorithm reported in Qin (2004a,b) for analyzing the effective behavior of piezoelectric composites is described. The algorithm is based on a typical micromechanics model (self-consistent) and a two-phase BE formulation. An iteration scheme is designated for the self-consistent-BE mixed method.

1.4.5.1 BE formulation for two-phase composites

In this section, a two-phase BE model is introduced for displacements and stresses on the boundary of the subdomain of each phase (Qin and Yang, 2008; Qin, 2004a; Yang and Qin, 2004). The two subdomains are separated by the interfaces between inclusion

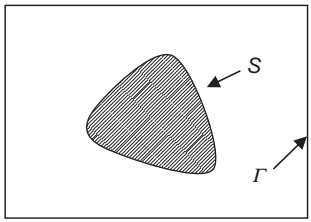

Figure 1.9 RAE used in BE analysis.

and matrix (see Figure 1.9). Each subdomain can be separately modeled by direct BEM. Global assembly of the BE subdomains is then performed by enforcing continuity of the displacements and stresses at the subdomain interface.

In two-dimensional linear elasticity, the BE formulation takes the form (Qin, 1993, 1998, 2009):

$$c^{(\alpha)}(\boldsymbol{\xi})u_i^{(\alpha)}(\boldsymbol{\xi}) = \int_{S^{(\alpha)}} \left[U_{ij}^{(\alpha)}(\mathbf{x},\boldsymbol{\xi})T_j^{(\alpha)}(\mathbf{x}) - F_{ji}^{(\alpha)}(\mathbf{x},\boldsymbol{\xi})u_j^{(\alpha)}(\mathbf{x})\right] \mathrm{d}S(\mathbf{x}) \tag{1.64}$$

where u_i and $T_i = \sigma_{ij}n_j$ are, respectively, the displacement and boundary traction in i direction with n_j being the component of the unit outward normal to the boundary, superscript (α) stands for the quantity associated with the αth phase ($\alpha = 1$ being matrix and $\alpha = 2$ being inclusion) and

$$S^{(\alpha)} = \begin{cases} S+\Gamma & \alpha = 1 \\ S & \alpha = 2 \end{cases}, \quad c^{(\alpha)}(\boldsymbol{\xi}) = \begin{cases} 1 & \text{if } \boldsymbol{\xi} \in \Omega^{(\alpha)} \\ 0.5 & \text{if } \boldsymbol{\xi} \in S^{(\alpha)} \left(S^{(\alpha)} \text{ smooth}\right) \\ 0 & \text{if } \boldsymbol{\xi} \notin \Omega^{(\alpha)} \cup S^{(\alpha)} \end{cases} \tag{1.65}$$

For plane strain, the integral kernels G_{ij} and F_{ij} are given by Qin (1998) and Qin and Huang (1990)

$$U_{ij}^{(\alpha)}(\mathbf{x},\boldsymbol{\xi}) = \frac{1}{8\pi G^{(\alpha)}(1-\mu^{(\alpha)})}\left[\left(3-4\mu^{(\alpha)}\right)\ln\left(\frac{1}{r}\right)\delta_{ij} + \frac{r_i r_j}{r^2}\right] \tag{1.66}$$

$$F_{ji}^{(\alpha)}(\mathbf{x},\boldsymbol{\xi}) = -\frac{1}{4\pi(1-\mu^{(\alpha)})r}\left(1-2\mu^{(\alpha)}\right)\left(n_j\frac{r_i}{r} - n_i\frac{r_j}{r}\right) + \left[\left(1-2\mu^{(\alpha)}\right)\delta_{ij} + \frac{2r_i r_j}{r^2}\right]\frac{r_n}{r} \tag{1.67}$$

with

$$r_i = x_i - \xi_i, \quad r_n = r_i n_i, \quad r = \sqrt{r_i r_i} \tag{1.68}$$

Equations (1.66) and (1.67) can be used for plane stress if $\mu^{(\alpha)}$ is replaced by $\mu^{(\alpha)}\left(1-\mu^{(\alpha)}\right)$.

To obtain a weak solution of Eq. (1.64) as in the conventional BEM, the boundary $S^{(\alpha)}$ is divided into a series of boundary elements. After performing discretization

using various kinds of boundary elements (e.g., constant element, linear element, higher-order element) and collecting the unknown terms to the left-hand side and the known terms to the right-hand side as well as using continuity conditions at the interface S (Figure 1.9), the boundary integral Eq. (1.64) becomes a set of linear algebraic equations:

$$\mathbf{KY} = \mathbf{P} \tag{1.69}$$

where $\mathbf{Y}$ and $\mathbf{P}$ are the total unknown and known vectors, respectively, and $\mathbf{K}$ is the known coefficient matrix.

1.4.5.2 Algorithm for self-consistent approach

As stated in Section 1.4.4.1, in the self-consistent method, for each inclusion, the effect of inclusion interaction is taken into account approximately by embedding each inclusion in the effective medium whose properties are unknown. In this case, the material constants appearing in the boundary element formulation (1.64) are unknown. Consequently a set of initial trial values of the effective properties is needed and an iteration algorithm is required. In detail, for the algorithm:

(a) Assume initial values of material constants $\bar{\mathbf{E}}_{(0)}$.
(b) Solve Eq. (1.69) for the displacement u_j using the values of $\overline{\mathbf{E}}_{(i-1)}$, where the subscript (i) stands for the variable associated with the ith iterative cycle. Calculate the average strains using the current values of u_j.
(c) Calculate $\mathbf{A}_i^{(1)}$ in Eq. (1.47) by way of Eq. (1.37) using the current values of average strain, and then determine $\bar{\mathbf{E}}_{(i)}$ by way of Eq. (1.47).
(d) If $\delta_{(i)} = \left\|\overline{\mathbf{E}}_{(i)} - \overline{\mathbf{E}}_{(i-1)}\right\| / \left\|\overline{\mathbf{E}}_{(0)}\right\| \leq \delta$, where δ is a convergent tolerance, terminate the iteration; otherwise take $\bar{\mathbf{E}}_{(i)}$ as the initial value and go to step (b).

1.4.6 Periodic boundary conditions in unit cell scheme

From a practical point of view, it is regarded that the composite material is an assembly of periodic unit cells (Figure 1.10). A unit cell is an RVE, as shown in Figure 1.10.

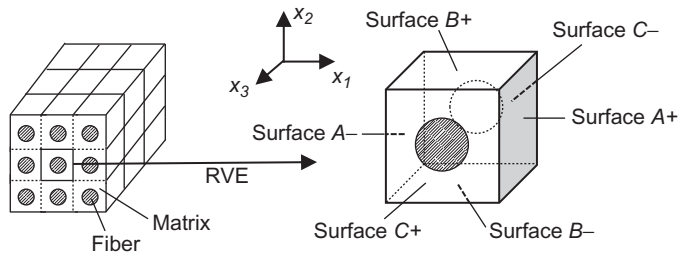

Figure 1.10 Schematic diagrams of periodic 1–3 composite laminate (a) and unit cell (b) (the fiber laminates are poled in x_3 direction) (Berger et al., 2005).

1.4.6.1 Periodic boundary condition

For the statistically homogeneous medium consisting of periodic unit cells (Figure 1.10), periodic boundary conditions are required to apply on the boundaries of the RVE. The general periodic conditions expressed by Havner (1971) can be applied to ensure periodic displacement and subsequent stress field.

$$\begin{aligned} u_i(y) &= u_i(y+Y) \\ \sigma_{ij}(y) &= \sigma_{ij}(y+Y) \end{aligned} \quad (i,j=1,2,3) \tag{1.70}$$

where σ_{ij} denotes the stress components in three-dimensions respectively, y represents any point in the periodic domain and Y, the periodicity. Applying this displacement condition to the boundary of the unit cell in Figure 1.10 yields

$$u_i^{j+} = u_i^{j-} \quad (i,j=1,2,3) \tag{1.71}$$

which means that the three-dimensional displacement vector for any pair of corresponding locations on areas $A-/A+$, $B-/B+$, and $C-/C+$ should be the same. A more explicit periodic boundary condition is then given as (Qin and Yang, 2008)

$$u_i = \overline{S}_{ij}x_j + v_i \tag{1.72}$$

where the average strain $\overline{S}_{ij}$ is included as an arbitrarily imposed constant strain; v_i denotes the periodic part of displacement component, which depends on the global loadings.

Based on the boundary condition (Eq. 1.72), Xia et al. (2003) and Berger et al. (2005) developed a unified periodic boundary condition:

$$u_i^{j+}(x,y,z) - u_i^{j-}(x,y,z) = c_i^j \quad (i,j=1,2,3) \tag{1.73}$$

where the constant terms c_1^1, c_2^2, and c_3^3 represent the normal loads that are either traction or compression; while, $c_1^2 = c_2^1$, $c_1^3 = c_3^1$, and $c_2^3 = c_3^2$ represent the in-plane shear load.

1.4.6.2 FE modeling

Element type and material property

To show the application of the periodic boundary condition in FE modeling, the SOLID226 in ANSYS element library is used in the following analysis, which is a 20-node hexagonal shaped element type with 3D displacement degree-of-freedom (DoF) and additional voltage DoF. This element type is easy for the implementation of periodic boundary conditions.

The material properties inputs are based on Berger et al. (2005) and listed in Table 1.3 for the reader's convenience.

Table 1.3 **Composite constituent's properties (Berger et al., 2005)**

	c_{11} (10^{10})	c_{12} (10^{10})	c_{13} (10^{10})	c_{33} (10^{10})	c_{44} (10^{10})	c_{66} (10^{10})	e_{15}	e_{31}	e_{33}	κ_{11} (10^{-9})	κ_{33} (10^{-9})
PZT-5	12.1	7.54	7.52	11.1	2.11	2.28	12.3	5.4	15.8	8.11	7.35
Polymer	0.386	0.257	0.257	0.386	0.064	0.064	—	—	—	0.07965	0.07965

Element mesh

For meshing, the area geometry is generated first and then sweep mesh is used to further generate the volume. In this way, the meshing result on $C+/C-$ is the same. In addition, with the setting of the RVE edge line divisions, meshing results on $A+/A-$ and $B+/B-$ are also the same. Ultimately, this provides explicit convenience to imposing periodic boundary conditions. As illustrated, when dealing with the situation when volume fraction is specified, say 0.666, the outline of the fiber circle is much closer to the RVE edge; in this case, a lower density of element as shown in Figure 1.11a is not sufficient for accurate analysis since the elements between the boundary of the RVE and the fiber have been lessened and shown distortion. When the edge division is 40 indicated in Figure 1.11b, the meshing quality is significantly improved.

As for periodic boundary condition, specific boundary conditions will be assigned to the exact opposite positions, namely $A+/A-$, $B+/B-$, and $C+/C-$. For example, in x-direction

$$u_i\left(x^{A+}, y_j, z_j\right) - u_i\left(x^{A-}, y_k, z_k\right) = c \quad (i = 1,2,3) \tag{1.74}$$

where subscripts j and k are the nodal number of any pair of nodes on opposite locations, $A+$ and $A-$ area, respectively.

The boundary conditions are shown in Figure 1.12.

Since the meshing scheme has ensured that there exists a pair of corresponding nodes at the opposite positions, the problem lies in developing a method to apply constraint equations on each pair of node for overcoming the problem of time-consuming over the node pair selection by graphical users' interface. An internal program has thus been designed for accomplishing the task. The procedures for the implementation are described as follows:

(a) Define the area $A+$, $B+$, and $C+$ as master areas, while $A-$, $B-$, and $C-$ as slave areas. Establish two arrays containing the node number (j, k) and coordinates ($y_{j,k}$, $z_{j,k}$) of each node (the x coordinate is not necessary, because the nodes are located on $A+$ and $A-$ areas where the x coordinate is a constant).

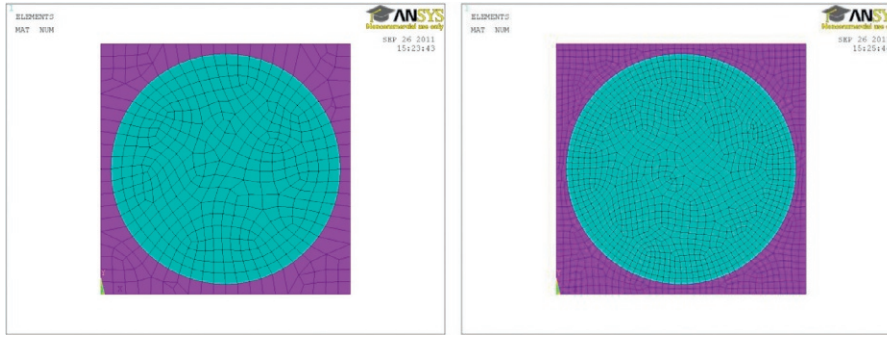

Figure 1.11 Different meshing density when volume fraction is 0.666. The RVE edge line is set into (a) 20 and (b) 40 divisions.

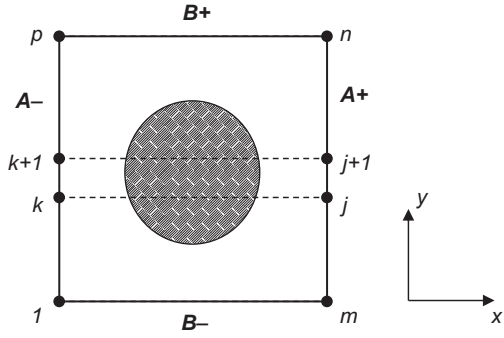

Figure 1.12 Application of periodic boundary conditions from a coordinate's view.

(b) Start from the first node in master array; get the node number j;
(c) Use the coordinates (y_j, z_j) of the node j to find the node at the exact opposite location, $y_j = y_k$; $z_j = z_k$; and select the node k from the slave array.
(d) Given the node number of the nodes on opposite location, constraint equations could be established.

The same procedures are applied on $B+/B-$ and $C+/C-$ areas, while the coordinates obtained and stored will be X/Z and X/Y, respectively.

When integrating the constraint equations in three directions, special care has been taken to avoid over-constraint over the edges that connect areas $A+/A-$, $B+/B-$, and $C+/C-$. Over-constraint may occur when the DoF of one node is specified more than once. For example, when applying $x-y$ in-plane shear load via constraint equations as shown in Figure 1.13, based on the periodic boundary conditions for $A+/A-$, the DoF relations between node 1 and 2 are $u_2 = u_1$ and $v_2 = v_1 + c$ while as to areas $B+/B-$, there will be relations between nodes 2 and 3 that $u_2 = u_3 + c$ and $v_2 = v_3$; the same situation will also occur in node 3. In this case, when applying constraint equations over $B+/B-$, the corner nodes of the RVE will be excluded to avoid over-constraint.

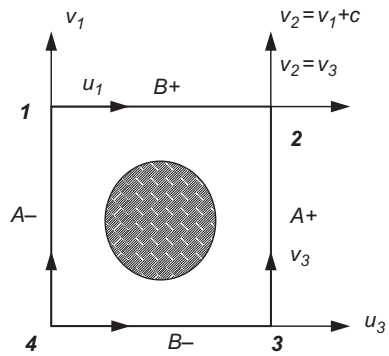

Figure 1.13 Over-constraint situations for a 2D model.

Numerical results

After applying appropriate boundary conditions to the RVE, the element stiffness matrix is integrated to form a global matrix, and the constitutive equations are solved to obtain the strain and stress field by ANSYS. To further clarify, for the arbitrary term in the periodic boundary conditions, when required, the imposed nodal displacement difference c is prescribed to be 0.1 mm and the imposed electric potential V is controlled to be 10 V. It is noted that when calculating the dielectric tensors, the relative permittivity factor of the free-space is constrained to be zero, rather than the default value, which is 8.85E−12 F/m. To maintain consistency, the units of the results listed in Tables 1.3 and 1.4 are N/m^2, C/m^2, and F/m, for elastic, piezoelectric, and dielectric tensors, respectively.

The effective coefficients for different fiber volume fraction are calculated using the same algorithm with the variation to the fiber radius. The results are listed in Table 1.4.

1.5 Toughening mechanisms of composites

Composite toughening could be made in many ways, such as transformation toughening, toughening by particle-induced shear bending, crack-deflection toughening, and crack bridging toughening. This section, however, focuses on matrix toughened by particulate materials. When a particulate second phase is introduced in a matrix, there are several toughening mechanisms, including crack front pinning, particle bridging, crack-path deflection, matrix cracking. Each of these mechanisms is briefly reviewed below.

1.5.1 Crack front pinning

As indicated in Pearson and Yee (1993), in this mechanism, the particles (rigid thermoplastic particles in particular) could act as impenetrable objectives that cause the crack to bow out, which consumes extra energy, if the difference in toughness between the brittle matrix and the ductile particles is large enough. Indirect evidence for the occurrence of this mechanism is the observation of "tails" near the particles on the fracture surface when viewed using SEM. The toughening effect due to this mechanism is evaluated by (Pearson and Yee, 1993; Lange, 1970)

$$\frac{G_{\mathrm{Ic}}}{G_0} = 1 + \frac{T}{d_{\mathrm{s}} G_0} \tag{1.75}$$

where G_{Ic} is the fracture toughness of the matrix modified by the particles, G_0 is the fracture toughness of the matrix unmodified by the particles, T is the line energy per unit crack front, and d_{s} is the center-to-center distance between particles:

$$d_{\mathrm{s}} = \frac{2d_{\mathrm{p}}(1-f)}{3f} \tag{1.76}$$

with d_{p} being the diameter of the particles and f the volume fraction of particles.

Table 1.4 Effective properties versus different volume fractions

	Fiber volume fraction					
	0.111	**0.222**	**0.333**	**0.444**	**0.555**	**0.666**
c_{11}	4.459E+09	5.301E+09	6.572E+09	8.399E+09	1.108E+10	1.632E+10
c_{12}	2.874E+09	3.222E+09	3.652E+09	4.135E+09	4.680E+09	5.883E+09
c_{13}	2.920E+09	3.367E+09	3.958E+09	4.780E+09	6.071E+09	8.493E+09
c_{33}	9.725E+09	1.584E+10	2.189E+10	2.851E+10	3.661E+10	4.327E+10
c_{44}	7.974E+08	9.925E+08	1.242E+09	1.600E+09	2.339E+09	3.298E+09
c_{66}	7.533E+08	8.781E+08	1.026E+09	1.230E+09	1.540E+09	2.163E+09
e_{13}	−2.903E−02	−6.643E−02	−1.166E−01	−1.878E−01	−2.986E−01	5.075E−01
e_{33}	2.410E+00	4.801E+00	7.199E+00	9.643E+00	1.198E+01	1.418E+01
e_{15}	9.465E−02	2.120E−01	3.620E−01	5.774E−01	1.021E+00	1.597E+00
κ_{11}	7.965E−11	7.965E−11	7.965E−11	7.965E−11	7.965E−11	7.965E−11
κ_{33}	1.066E−09	1.920E−09	2.844E−09	3.789E−09	4.703E−09	5.559E−09

1.5.2 Particle bridging or crack bridging

The mechanism of particle bridging is effective if the particles are perfectly bonded to the matrix and if the advancing crack tip is drawn to particles so that bridges are left behind. An explanation of toughening via crack bridging considers the energy consumed when the particles are plastically deformed and then torn. To evaluate the amount of toughness one can expect from the crack bridging, Ahmad et al. (1986) proposed a model for rubber-modified matrix based on the idea that improvements in toughness may be attributed solely to the stretching and tearing of rubber particles in the crack wake. Thus increase in toughness can be rationalized by considering the shielding effect, which is the reduction of the stress intensity factor K at the crack tip (Pearson and Yee, 1993):

$$\frac{K_c}{K_0} = \phi(1-f) + \frac{fE^*\Gamma_t}{2\phi(1-f)K_0^2} \tag{1.77}$$

where K_c is the fracture toughness of the rubber-modified matrix, K_0 is the fracture toughness of the unmodified matrix, ϕ is a correction factor that accounts for crack bowing, f is the volume fraction of rubber particles, E^* is the stiffness of the particle, and Γ_t is the tearing energy of the rubber particles. The model shows that improvements in toughness should be greater when larger particles are used.

Besides, crack bridging may occur by frictional interlocking of opposing fracture surfaces and by the formation of ligamentary bridges between them. Whiskers or fibers can also act as crack bridging sites like coarse grains (Bengisu and Inal, 1994).

1.5.3 Crack path deflection

Theoretically, crack-deflection toughening occurs whenever interactions between the crack front and a second-phase inclusion, such as particles, cause the crack to propagate out of plane, reducing the stress intensity factor at the crack tip, compared to self-similar planar crack growth. In other words, the energy required to propagate such a crack increases. The toughening mechanism for different inclusions was analyzed by Faber and Evans (1983) who proposed the following model:

$$\frac{K_c}{K_0} = \left(\frac{E_c}{E_0}(1+0.87f)\right)^{1/2} \tag{1.78}$$

where E_c is the Young's modulus of the modified matrix, and E_0 is the Young's modulus of the unmodified matrix. As indicated in Bengisu and Inal (1994), two conditions can lead to crack deflection: residual strain in the composite and weak matrix/second-phase interfaces. Residual strain can be generated by elastic modulus and/or thermal expansion mismatch between the matrix and second-phase anisotropy of thermal expansion in a monolithic or composite material.

1.5.4 Microcrack toughening

The idea behind the mechanism of microcrack toughening is that stable grain boundary microcracks are nucleated by the high stresses in the vicinity of the macroscopic crack tip. These microcracks then lower the stress experienced by the tip. This shielding effect has been studied from two vantage points: one involving a smearing out of the effects of the microcracks appropriate to a zone of profuse microcracking and the other treating the interaction of the macrotip with discrete microcracks (Hutchinson, 1989). Generally, microcrack toughening involves two types of crack shielding phenomena (Bengisu and Inal, 1994; Evans and Fu, 1985): one type is due to the reduced elastic modulus of the material upon microcracking; another and more important type is due to dilatation caused by microcracking. Hutchinson (1987) defined the elastic modulus contribution as

$$\frac{dK_c}{K_c} = \frac{\left(k_1 - \frac{5}{8}\right)\left(\frac{G}{G^*} - 1\right)\left(k_2 + \frac{3}{4}\right)\left(\frac{\mu^* G}{G^*} - \mu\right)}{1 - \mu} \tag{1.79}$$

where K_c is the toughness in the absence of microcracking, k_1 and k_2 are constants depending on the microcracking zone shape (Bengisu and Inal, 1994), G and G^* are shear moduli of the material before and after microcracking, respectively, and μ and μ^* represent Poisson's ratios before and after microcracking, respectively.

The dilatational contribution is given by (Bengisu and Inal, 1994):

$$dK_c = k_3 E \theta_T h^{1/2} \tag{1.80}$$

where k_3 is a constant that depends on the microcrack zone shape and size, E is the Young's modulus of the material before microcracking, θ_T is the dilatational strain caused by microcracking, and h is the process zone width.

References

Ahmad, Z.B., Ashby, M.F., Beaumont, P.W.R., 1986. The contribution of particle-stretching to the fracture-toughness of rubber modified polymers. Scr. Metall. 20, 843–848.

Antoniou, A.E., Kensche, C., Philippidis, T.P., 2009. Mechanical behavior of glass/epoxy tubes under combined static loading. Part II: validation of FEA progressive damage model. Compos. Sci. Technol. 69, 2248–2255.

Bao, G., Hutchinson, J.W., McMeeking, R.M., 1991. Particle reinforcement of ductile matrices against plastic-flow and creep. Acta Metall. Mater. 39, 1871–1882.

Bengisu, M., Inal, O.T., 1994. Whisker toughening of ceramics—toughening mechanisms, fabrication, and composite properties. Annu. Rev. Mater. Sci. 24, 83–124.

Berger, H., Kari, S., Gabbert, U., Rodriguez-Ramos, R., Guinovart, R., Otero, J.A., Bravo-Castillero, J., 2005. An analytical and numerical approach for calculating effective material coefficients of piezoelectric fiber composites. Int. J. Solids Struct. 42, 5692–5714.

Damiel, I.M., Ishai, O., 2006. Engineering Mechanics of Composite Materials. Oxford University Press, New York.
Evans, A.G., Fu, Y., 1985. Some effects of microcracks on the mechanical-properties of brittle solids. 2. Microcrack toughening. Acta Metall. 33, 1525–1531.
Faber, K.T., Evans, A.G., 1983. Crack deflection processes. 1. Theory. Acta Metall. 31, 565–576.
Feng, X.Q., Mai, Y.W., Qin, Q.H., 2003. A micromechanical model for interpenetrating multiphase composites. Comput. Mater. Sci. 28, 486–493.
Gasik, M.M., 1998. Micromechanical modelling of functionally graded materials. Comput. Mater. Sci. 13, 42–55.
Gibson, R.F., 2012. Principles of Composite Material Mechanics. CRC Press, New York.
Grassi, M., Zhang, X., Meo, M., 2002. Prediction of stiffness and stresses in z-fibre reinforced composite laminates. Compos. Part A Appl. Sci. Manuf. 33, 1653–1664.
Greenwoo, J.H., Rose, P.G., 1974. Compressive behavior of kevlar-49 fibers and composites. J. Mater. Sci. 9, 1809–1814.
Havner, K.S., 1971. A discrete model for the prediction of subsequent yield surfaces in polycrystalline plasticity. Solid Struct. 7, 719–730.
Herring, C., Galt, J.K., 1952. Elastic and plastic properties of very small metal specimens. Phys. Rev. 85, 1060–1061.
Hutchinson, J.W., 1987. Crack tip shielding by microcracking in brittle solids. Acta Metall. 35, 1605–1619.
Hutchinson, J.W., 1989. Mechanisms of toughening in ceramics. In: Germain, P., Piau, M., Caillerie, D. (Eds.), Theoretical and Applied Mechanics. Elsevier, North-Holland.
Jones, R.M., 1999. Mechanics of Composite Materials. Taylor & Francis, New York.
Kaw, A.K., 2006. Mechanics of Composite Materials. Taylor & Francis, Boca Raton.
Lange, F.F., 1970. Interaction of a crack front with a second-phase dispersion. Philos. Mag. 22, 983–992.
Levy, A., Papazian, J.M., 1990. Tensile properties of short fiber-reinforced sic/al composites. 2. Finite-element analysis. Metall. Trans. A 21, 411–420.
Li, Z.H., Schmauder, S., Wanner, A., Dong, M., 1995. Expressions to characterize the flow behavior of particle-reinforced composites based on axisymmetrical unit-cell models. Scr. Metall. Mater. 33, 1289–1294.
Pearson, R.A., Yee, A.F., 1993. Toughening mechanisms in thermoplastic-modified epoxies. 1. Modification using poly(phenylene oxide). Polymer 34, 3658–3670.
Qin, Q.H., 1993. Nonlinear analysis of Reissner plates on an elastic foundation by the BEM. Int. J. Solids Struct. 30, 3101–3111.
Qin, Q.H., 1998. Nonlinear analysis of plate bending by BEM. In: Aliabadi, M.H. (Ed.), BEM Formulation for Plate Bending Analysis. Computational Mechanics Publications, Southampton, pp. 249–274.
Qin, Q.H., 2000. The Trefftz Finite and Boundary Element Method. WIT Press, Southampton.
Qin, Q.H., 2004a. Material properties of piezoelectric composites by BEM and homogenization method. Compos. Struct. 66, 295–299.
Qin, Q.H., 2004b. Micromechanics-BE solution for properties of piezoelectric materials with defects. Eng. Anal. Boundary Elem. 28, 809–814.
Qin, Q.H., 2005. Micromechanics-BEM analysis for piezoelectric composites. Tsinghua Sci. Technol. 10, 30–34.
Qin, Q.H., 2009. Boundary element method. In: Yang, J.S. (Ed.), Special Topics in the Theory of Piezoelectricity. Springer, Cambridge, MA, pp. 137–168.

Qin, Q.H., Huang, Y.Y., 1990. BEM of postbuckling analysis of thin plates. Appl. Math. Model. 14, 544–548.
Qin, Q.H., Swain, M.V., 2004. A micro-mechanics model of dentin mechanical properties. Biomaterials 25, 5081–5090.
Qin, Q.H., Yang, Q.S., 2008. Macro-micro Theory on Multifield Coupling Behaivor of Heterogenous Materials. Higher Education Press and Springer, Beijing.
Qin, Q.H., Yu, S.W., 1997. Using Mori-Tanaka method for effective moduli of cracked thermopiezoelectric materials. In: ICF 9-Sydney, Australia-1997, pp. 2211–2218.
Qin, Q.H., Yu, S.W., 1998. Effective moduli of piezoelectric material with microcavities. Int. J. Solids Struct. 35, 5085–5095.
Qin, Q.H., Mai, Y.W., Yu, S.W., 1998. Effective moduli for thermopiezoelectric materials with microcracks. Int. J. Fract. 91, 359–371.
Tjong, S.C., Meng, Y.Z., 1999. Microstructural and mechanical characteristics of compatibilized polypropylene hybrid composites containing potassium titanate whisker and liquid crystalline copolyester. Polymer 40, 7275–7283.
Tvergaard, V., 1990. Analysis of tensile properties for a whisker-reinforced metal matrix composite. Acta Metall. Mater. 38, 185–194.
Wang, Y., Qin, Q.H., 2007. A generalized self consistent model for effective elastic moduli of human dentine. Compos. Sci. Technol. 67, 1553–1560.
Wang, Y., Qin, Q.H., 2011. Micromechanics for determining effective material properties of dentine composites. In: Qin, Q.H., Sun, B. (Eds.), Advances in Engineering Mechanics. Nova Science Publishers, New York, pp. 319–358.
Xia, Z.H., Zhang, Y.F., Ellyin, F., 2003. A unified periodical boundary conditions for representative volume elements of composites and applications. Int. J. Solids Struct. 40, 1907–1921.
Xu, L.M., Li, C., Fan, H., Wang, B., 2008. Elastic property prediction by finite element analysis with random distribution of materials for tungsten/silver composite. J. Mater. Sci. 43, 5804–5808.
Yang, Q.S., Qin, Q.H., 2001. Fiber interactions and effective elasto-plastic properties of short-fiber composites. Compos. Struct. 54, 523–528.
Yang, Q.S., Qin, Q.H., 2003. Modelling the effective elasto-plastic properties of unidirectional composites reinforced by fibre bundles under transverse tension and shear loading. Mater. Sci. Eng. A 344, 140–145.
Yang, Q.S., Qin, Q.H., 2004. Micro-mechanical analysis of composite materials by BEM. Eng. Anal. Boundary Elem. 28, 919–926.
Ye, J., 2003. Laminated Composite Plates and Shells: 3D Modelling. Springer, London.
Yu, S.W., Qin, Q.H., 1996. Damage analysis of thermopiezoelectric properties: part II. Effective crack model. Theor. Appl. Fract. Mech. 25, 279–288.
Zahl, D.B., McMeeking, R.M., 1991. The influence of residual-stress on the yielding of metal matrix composites. Acta Metall. Mater. 39, 1117–1122.

Part One

Toughening mechanisms for particle-reinforced composites

This page intentionally left blank

Silicon nitride based ceramic composites toughened by rare-earth oxide additives

2

P. Tatarko[1,2], *M. Kašiarová*[1]
[1]Slovak Academy of Sciences, Košice, Slovak Republic; [2]Queen Mary University of London, London, UK

2.1 Introduction

Silicon nitride (Si_3N_4) is an attractive material for designers and manufacturers of various components. Silicon nitride-based ceramics are prime candidates for such diverse high-temperature products like rotors and stator vanes for advanced gas turbines as well as valves and cam roller followers for petrol and diesel engines. In addition, silicon nitride is used for a variety of structural applications, such as cutting tools of nonferrous metal materials and ball bearings. All these applications take advantage of the superior wear resistance, high hardness and strength, reasonable fracture toughness, good corrosion resistance, and very good creep resistance of silicon nitride.

However, the applications of silicon nitride-based ceramics still require the improvement of their mechanical properties and long-term reliability. This improvement can be achieved through the control of factors, such as phase composition of the starting powders, type and amount of sintering additives, and processing parameters. Therefore, there is still a challenge for material researchers to improve the mechanical properties of silicon nitride by changing some of these parameters or by developing new kinds of composite materials.

In order to exploit all the outstanding properties of Si_3N_4-based ceramics, the structural application of silicon nitride requires a fully dense material, as porosity deteriorates the properties of a sintered material. However, it is usually very difficult to achieve a theoretical density of silicon nitride due to a highly covalent Si—N bond and a very low coefficient of self-diffusion. The silicon nitride is thus usually densified with the sintering additives that help its densification via liquid phase sintering mechanisms and form a residual grain boundary glassy phase in the sintered Si_3N_4. Therefore, the mechanical properties of Si_3N_4-based ceramics strongly depend on the oxide additives used for the densification. At the temperature of densification, the sintering aids form a low-melting point eutectic liquid with the silica layer present on the surface of starting Si_3N_4 powder particles. A resulting amorphous phase present at the multi-grain junctions and the boundaries of Si_3N_4 grains determines the fracture behavior of ceramics and high-temperature mechanical properties because the amorphous phase softens at elevated temperatures. Numerous studies have been done in

Toughening Mechanisms in Composite Materials. http://dx.doi.org/10.1016/B978-1-78242-279-2.00002-0

order to find the best combination of sintering additives with respect to the mechanical behavior of silicon nitride-based ceramics.

There are essentially two approaches to improving the mechanical properties of Si_3N_4. The mechanical properties of Si_3N_4 can be improved using suitable sintering additives and microstructure design, resulting in acicular grains that grow *in situ* when sintering conditions and composition are appropriate (Becher et al., 2010; Belmonte et al., 2009). In such a microstructure, the intergranular crack and crack deflection at the boundaries of elongated Si_3N_4 grains followed by bridging mechanisms were reported to increase the fracture toughness ("self-toughened" microstructure). During recent years, it has been reported that the chemical composition of the intergranular phases directly influences the interfacial strength and the ability of a crack to propagate intergranularly (Satet and Hoffmann, 2000, 2005; Becher et al., 2008).

Rare-earth (RE) oxide sintering additives are considered ideal additives for Si_3N_4 due to their high melting point and the fact that they control the $\alpha \rightarrow \beta$ phase transformation rate, the grain growth anisotropy, and the aspect ratio (AR) of the β-Si_3N_4 grains (Satet and Hoffmann, 2000, 2005; Becher et al., 2008; Lojanová et al., 2010; Tatarko et al., 2010a,b, 2013a,b; Hyuga et al., 2004). RE elements with a larger ionic radius (i.e., with a smaller atomic number) result in delayed phase transformation and weaker interfacial bonding (Becher et al., 2010; Satet and Hoffmann, 2005; Kitayama et al., 2006). The physical properties of the RE disilicate glasses, such as glass transformation, softening temperatures, and thermal expansion coefficient vary linearly with the ionic radius of the RE elements. This trend was attributed to the field strength of the ion, which varies with the reciprocal of cationic radius (Cinibulk et al., 1992a,b).

An overall chemical composition of the grain boundary phases rather than the sole effect of RE oxides determines the properties of Si_3N_4 ceramics, leading to ambiguous results reported in the literature. It was reported that the fracture toughness of silicon nitrides sintered with RE_2O_3–MgO–SiO_2 additives and containing the amorphous intergranular phase increased with the increasing ionic radius of RE^{3+}, while the bending strength decreased with the increasing radius of RE^{3+} (Satet and Hoffmann, 2005). It was found that a weaker grain boundary interface connected with the addition of La^{3+} resulted in a higher toughness but a lower strength of the bulk Si_3N_4 material. On the other hand, when a crystalline secondary phase was present in the Si_3N_4 with bimodal microstructures, no significant influence of RE oxides (La_2O_3, Gd_2O_3, Lu_2O_3) on the fracture toughness of Si_3N_4 was observed by Becher et al. (2008). On the contrary, Lojanová et al. (2010) and Tatarko et al. (2010a,b) reported that the AR of β-Si_3N_4 grains increased with a decreasing ionic radius of RE^{3+} in the Si_3N_4-based ceramics with the grain boundary composition of RE_2O_3–SiO_2 (RE = La, Nd, Sm, Y, Yb, and Lu). The increased fracture toughness then resulted in the improved fracture toughness and bending strength for the materials with a smaller ionic radius of RE^{3+}. Apart from their ambiguous influence on the mechanical properties of Si_3N_4 at room temperature, it was undoubtedly observed that the mechanical properties of Si_3N_4 at high temperatures can be significantly improved when the RE oxides with a larger ionic radius are replaced with the smaller ones (Tatarko et al., 2013a,b; Lojanová et al., 2010; Choi et al., 1997, 1999; Cinibulk et al., 1992a,b; Hong et al., 2002). Despite a discrepancy in the reported data on the effect of RE on the mechanical properties

at room temperature, it is obvious that they play an important role in the microstructural evolution and mechanical properties of Si_3N_4. Their effect depends on the cation size of RE elements (RE^{3+}), e.g., La (the largest ionic radius) versus Lu (the smallest ionic radius among the RE elements).

The intent of the second approach is to improve the properties by incorporating second-phase ceramic reinforcing elements into the microstructure of silicon nitride, thereby forming the Si_3N_4-based composite materials. Among them, Si_3N_4-SiC composites are one of the most widely used and investigated. Si_3N_4–SiC nanocomposites have been prepared by doping of Si_3N_4 powder with amorphous SiNC precursor (Šajgalík et al., 2000) or using a carbothermal reaction (SiO_2+C) (Hnatko et al., 2004) in order to improve the mechanical properties of Si_3N_4 ceramics. However, the results of the influence of the SiC nanoparticles on the fracture toughness are ambiguous. No additional toughening effect of the SiC addition on the fracture toughness of Si_3N_4–SiC nanocomposite was observed by Herrmann et al. (1998). Moreover, even a lower fracture toughness and a lower strength of the Si_3N_4–SiC nanocomposite compared to the Si_3N_4 monolith were observed by Kašiarová et al. (2006). Tian et al. (1998) reported a 5 vol.% of SiC to be an optimum content of SiC nanoparticles in the Si_3N_4–SiC composite. For this SiC loading, they found the highest flexural strength and fracture toughness as well as the highest thermal shock resistance of the materials.

To summarise, it has been clearly demonstrated that both the incorporation of SiC nanoinclusion to the Si_3N_4 matrix and design of the grain boundary phase composition can be effective tools to improve the mechanical properties of Si_3N_4 materials. More recently, several studies have shown that both these approaches can be used together and a beneficial mutual effect of the SiC nanoparticles and RE oxide additives with a smaller ionic radius on the mechanical properties at room (Lojanová et al., 2010; Tatarko et al., 2010a,b) as well as high temperatures (Lojanová et al., 2010; Tatarko et al., 2013a,b) has been reported. In these works, it was discovered that RE oxide additives strongly affect the formation and the distribution of the SiC nanoparticles in the microstructure of Si_3N_4.

According to the literature, it is obvious that a type of the sintering additives significantly influences the microstructure evolution and the final mechanical properties of the Si_3N_4 ceramics and Si_3N_4–SiC composites. The literature survey indicates that a role of the RE additives in the Si_3N_4 materials is mainly related to their influence on the densification process and the properties of the residual secondary grain boundary phases. Since a final microstructure significantly affects the final mechanical properties, this chapter provides a brief overview of the microstructure development of Si_3N_4 and the role of the RE elements in the processing and the microstructure evolution of these materials. A relationship between the microstructure and the fracture toughness of Si_3N_4-based materials is then clearly defined. The chapter also summarises the effect of RE_2O_3 additives on the fracture toughness of Si_3N_4 materials via a microstructure design as well as the properties of the residual glassy phases at the Si_3N_4 grain boundaries. Moreover, their significant effect on the *in situ* formation and the distribution of the SiC nanoparticles within the Si_3N_4 matrix is also reported. It is shown that different RE oxides result in a different location of the SiC particles due to the different properties of the liquid phase during the sintering. Such a different location of the SiC nanoparticles (inside the Si_3N_4 grains vs. at

the grain boundaries of Si_3N_4) significantly affects the mechanical properties of the Si_3N_4-based materials.

2.2 Preparing Si_3N_4-based ceramics and the role of RE oxide additives

2.2.1 Densification mechanism of Si_3N_4

Si_3N_4 ceramic-based materials are usually made by sintering of powders and therefore their mechanical properties strongly depend on the quality of the starting powders and the processing parameters. Densification of Si_3N_4 is only possible when the following parameters are applied: (1) ultrafine powders, (2) external pressure, (3) increase of the sintering temperature (simultaneously an increase of nitrogen pressure is necessary), (4) establishment of the equilibrium partial pressures of the various silicon compounds by using Si_3N_4 powder bed, and (5) addition of sintering additives to form a liquid phase. The addition of sintering aids, which results in a formation of a suitable liquid, is the most important step in the densification of Si_3N_4 (Ziegler et al., 1987).

Except hot isostatic pressing (HIP) and spark plasma sintering (SPS) methods, all attempts to densify Si_3N_4 powder without additives have not been successful. Silicon nitride is therefore very often densified with the sintering additives because of a highly covalent Si—N bonding and a very low coefficient of self-diffusion. The sintering additives react with the phases containing oxygen, such as SiO_2, or oxynitride, which is always present on the particle surfaces of commercially available Si_3N_4 powder. This reaction takes place at high temperatures during the sintering and produces a liquid phase, which allows mass transport through solution–reprecipitation process (Petzow and Herrmann, 2002; Ziegler et al., 1987). Impurities in the starting powders are often incorporated in this silicate melt. Most of the additives do not form a solid solution with Si_3N_4, and therefore they remain in the microstructure as the amorphous or crystalline grain boundary phases after cooling from the sintering temperature.

The last stage of the liquid phase sintering process is a coalescence of the grains; however, this process does not further contribute to the densification. In this stage, a grain coarsening takes place, which is in many cases accompanied by an unfavorable change in morphology from the idiomorphic rod-like to a more equiaxed grain structure due to the effort to minimize the surface energy (Ziegler et al., 1987).

Usually, densification starts at 1200–1300 °C when the eutectic melt begins to form. The sintering behavior is promoted with an increasing amount of additives; however, gas bubbling can occur when the amount is above 15–20% because of the increased formation of gaseous SiO. After cooling, the stable β-phase is embedded in an amorphous phase, from which an oxynitride can precipitate during a devitrification heat treatment. This heat treatment is performed just below the eutectic temperature. A certain amount of the amorphous phase (in the form of thin grain boundary films) always remains even after very long annealing times (Petzow and Herrmann, 2002).

It is well known that the densification process is enhanced by increasing both the sintering temperature and time; however, they cause undesirable changes of the microstructure above the optimum values. Similarly, increasing pressure during the HP (hot pressing), HIP, or SPS processes results in the increased densification rate, refinement, and, for HP, an anisotropic orientation of the microstructure as well (Petzow and Herrmann, 2002).

It can be concluded that Si_3N_4 is a multiphased material consisting of mainly β- and α-phases of Si_3N_4, secondary grain boundary phases (mainly oxynitrides), and an amorphous film at the grain boundaries. All these phases have characteristic morphologies and can be arranged in all kinds of microstructures.

2.2.2 Microstructure evolution of Si_3N_4

Microstructure of any material has a significant influence on the characteristic properties of the material. The factors, such as type, amount, arrangement, size, shape, and orientation of the various phases contribute to the resultant microstructure of the material.

Silicon nitride is mostly produced from α-Si_3N_4 powder that is transformed to β-solid solution during the sintering via the solution–reprecipitation process. The microstructural evolution is controlled mainly by Si_3N_4 starting powder, additives, and sintering parameters.

From theoretical consideration, it is assumed that prism planes of the hexagonal-shaped grains have a higher stability compared to basal planes (Figure 2.1). However, the growth rate of basal planes (*c*-axis) is much higher than that of prism planes (*a*-axis), resulting in needle-like grain morphology. This difference is related to the

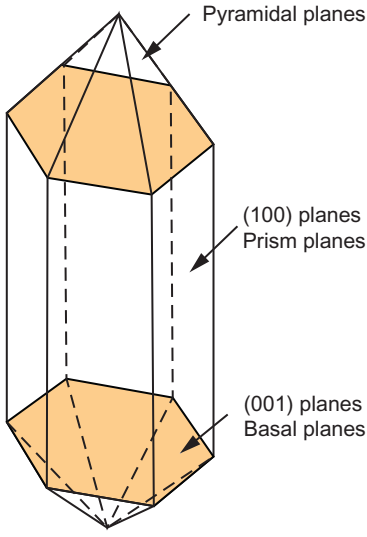

Figure 2.1 Theoretical shape of β-Si_3N_4 (Satet and Hoffmann, 2000).

Si_3N_4 crystal structure and is attributed to an energetically more favorable attachment of a surface nucleus on a basal plane. The basal planes (001) are "atomically rough" and the growth mechanism is diffusion controlled and much faster. The prism planes (100) are "automatically flat" and the growth rate is determined by the formation of surface nuclei (Petzow and Herrmann, 2002; Becher et al., 2006; Satet and Hoffmann, 2000). Attachment of Si (and N), which controls the growth rate, is determined by the population of surface ledges/steps. The adsorption of the additives on the surface of Si_3N_4 impedes the attachment of Si and N to the prismatic plane and therefore decreases the grain growth along *a*-axis (Satet and Hoffmann, 2000).

As has been already mentioned, the sintering parameters have a significant influence on the microstructural evolution. A faster heating rate leads to a coarser microstructure due to the dissolution of fine β-Si_3N_4 particles during the heating in the oxynitride melt. On the other hand, it is important to point out that a slow heating rate in the interval 1500–1700 °C also intensively increases the grain growth. After complete phase transformation and partial devitrification, the grain growth starts through a dissolution of smaller β-Si_3N_4 grains.

In addition, in the case of compositions that form low eutectic temperature liquids, the phase transformation initiates when densification is essentially completed. On the other hand, when high-viscosity liquids are formed, densification and phase transformation can occur simultaneously (Becher et al., 2008).

Observations by HR-TEM (high-resolution transmission electron microscopy) revealed that a residual glassy phase remains at the tip of each triple junction as well as at two-grain junctions in the form of a stable amorphous film either between two Si_3N_4 grains or between Si_3N_4 and a crystalline secondary phase. Its thickness depends on the temperature, additive composition, and impurities of the starting powder (Petzow and Herrmann, 2002). Moreover, using HR-TEM Liu and Nemat-Nasser (1998) found that the crystalline boundary phase is often seen at two-grain boundaries near the multi-grain pockets, whereas the boundary phase located at the middle portion of a two-grain boundary is often, if not always, amorphous. Their observation suggested that the crystallization of the boundary phase most probably initiates at the grain pockets where the majority of the sintering aids are accumulated. They also showed that the thickness of the crystalline phases at the two-grain boundaries is relatively stable, varying from 1.5 to 1.9 nm, whereas the thickness of the amorphous phases at the two-grain boundaries varies over a wide range (from 0.7 to 3.0 nm).

Two factors are considered to be the reasons why complete crystallization of boundary phase is hard to achieve (Liu and Nemat-Nasser, 1998). It was found that nucleation of the boundary phase in silicon nitride is heterogeneous and takes place in some discrete places at the interface between the boundary phase and the Si_3N_4 grains. Once created, nuclei grow into the boundary phase by a displacement of well-faceted crystallization fronts. For initiation of the crystallization, the nucleation needs a local composition fluctuation with respect to the average composition, in order to reach locally the composition of a crystalline phase, and probably a suitable orientation with respect to the neighboring silicon nitride grains to promote an "epitaxial" nucleation and growth. In addition, it was reported that complete crystallization of small amounts of the glassy phase segregated at the grain boundaries is much more

difficult than crystallization of a bulk material of the same composition (Liu and Nemat-Nasser, 1998). This is a result of the fact that the glassy phase segregated at the grain boundaries is constrained from flowing over distances larger than the grain size, because the channels through which the liquid must move are quite small (only a few nanometers). Therefore, the initial glassy phases are essentially confined within the rigid ceramic grains. As a result, the glassy phase has to sustain hydrostatic stress since shear stresses would relax by the fluid flow within the intergranular region. In general, volume change during the phase transformation increases the strain energy, which would oppose the transformation. Such an increase in the strain energy causes a barrier to the crystallization.

2.2.3 RE elements and their role in Si_3N_4 ceramics

Silicon nitrides sintered with various RE oxides (RE_2O_3) as the additive, having a bimodal character of microstructure, are commercially used because it was recognized that *in situ* reinforced microstructures yield a higher fracture toughness; the more refractory RE oxides yield better high-temperature mechanical properties.

RE elements are a set of 17 chemical elements in the periodic table, specifically the 15 lanthanoids (with atomic number from 57 (La) to 71 (Lu)) plus scandium (Sc) and yttrium (Y). Sc and Y are considered to be RE elements since they tend to occur in the same ore deposits as the lanthanoids and exhibit similar chemical properties. RE elements have a common ionic valence z of 3^+ and are known to be the most electropositive elements, but Sm and Yb can also occur as Sm^{2+} and Yb^{2+} (Lofaj et al., 2003). Lanthanide elements exhibit decrease in their ionic radii with increasing atomic number, and this fact is known as "lanthanide contraction." However, ionic radius at the given valence state depends also upon the coordination number, whose typical value for lanthanides in oxides with $z = 3^+$ is 6 (Lofaj et al., 2003).

A cation of the RE oxides, RE^{3+}, acts as a glass modifier in the SiO_4^{4-} tetrahedron because its size is larger than that of the Si ion (0.026 nm). The RE—O bond is the weakest bond in the glass structure because the cationic radius of the RE additive is the largest and the ionic charge (3^+) is lower than that of silicon cation (4^+). Glass properties, such as glass transition temperature, softening temperature, and Young's modulus depend on the weakest bond strength. The bond strength is characterized as a cation field strength (CFS) and is proportional to the ionic charge (Z) and the reciprocal of the ionic radius (r_i) (Hong et al., 2002; Lofaj et al., 2003, 2004; Hampshire and Pomeroy, 2004):

$$\mathrm{CFS} = \frac{Z}{r_i^2}\left(\text{Å}^{-2}\right) \tag{2.1}$$

This relationship indicates that the CFS increases with a decreasing ionic radius of RE element (with assumption that ionic charge is the same, 3^+). For example, the values of CFS for the largest cation of RE (La—1.05 Å) and the smallest one (Lu—0.848 Å) are 2.72 and 4.17 Å^{-2}, respectively (Becher and Ferber, 2004).

Similarly, "field strength" can also be estimated using another equation (Choi et al., 1997):

$$F_c = \frac{Z_a e \cdot Z_c e}{a_i^2} \left(\text{Å}^{-2} \right) \tag{2.2}$$

where F_c is the field strength, Z_a is the charge of the anion, Z_c is the charge of the cation, e is the elementary electric charge, and a_i is the distance between the centers of two ions.

The influence of the various RE oxides on the properties of intergranular phase in Si_3N_4 has been investigated by measuring the physical and mechanical properties of bulk glasses containing different RE elements (Lofaj et al., 2003, 2004; Hampshire and Pomeroy, 2004; Becher and Ferber, 2004). The softening as well as the glass transition temperature of intergranular phase in Si_3N_4 decreased with an increasing ionic radius of RE^{3+}. The coefficient of thermal expansion (CTE) is also dependent on the size of RE^{3+} and its value increases with an increasing ionic radius (Becher et al., 2002; Sun et al., 1999) and with a decreasing nitrogen content (Becher et al., 2002; Lofaj et al., 2004). It was also reported that a thickness of the intergranular glass films decreases as RE ion radius decreases (from ~1.6 nm for La to ~1.0 nm for Yb) and the film thickness is determined by the composition rather than by the volume fraction of the glassy phase (Wang et al., 1996). This result implies that RE^{3+} cations are localized at the glassy film, thereby changing intergranular forces to determine the film thickness.

Moreover, smaller RE cations prefer to bond to O with the result that N atom is concentrated in the intergranular films (IGFs) and smaller RE cations diffuse out to the triple points. On the contrary, larger RE ions have a preference for bonding to N, and thus remain concentrated in the intergranular glass film, resulting in their smaller amounts in the triple points (Becher et al., 2010; Hampshire and Pomeroy, 2004).

Initial theoretical efforts to understand the differences in the behavior of RE elements addressed their preference for nitrogen versus oxygen against that of silicon within a differential binding energy (DBE) model. The DBE model considers segregation of a RE relative to a competing cation (Si) in a compositionally graded anion environment (O and N). The DBE, $\delta_{Si,RE}$, gives a measure of the relative strength of segregation and is defined as a second difference of total energies (Shibata et al., 2004, 2005; Painter et al., 2008):

$$\delta_{Si,RE} = \Delta E_{Si-O} - \Delta E_{Si-N} - (\Delta E_{RE-O} - \Delta E_{RE-N})\,(\text{eV}) \tag{2.3}$$

where ΔE_{IJ} is the binding energy of a cation I (Si or RE) in an anion environment J (the oxygen-rich or nitrogen-rich host sites) in the ceramics.

Thus, the DBE gives a qualitative measure of the expected relative amount of a selected rare earth at the grain surfaces. The increasing values of $\delta > 0$ signify an increasing preference to bond in O-rich regions (oxynitride glass), whereas the increasing negative δ indicates a higher preference to bond in N-rich interfacial region (surfaces of β-Si_3N_4), all relative to Si. Therefore, these atomic cluster results indicate

a driving force for each RE to segregate to either N-rich (grain surfaces) or O-bearing (the surrounding oxynitride phase) regions in the microstructure (Becher et al., 2010; Shibata et al., 2005; Painter et al., 2008).

It was reported that Young's modulus and microhardness of rare-earth containing SiREAl glasses are primarily a function of the bond strength within the glass network as well as the strength of cross-linking bonds. Both the Young's modulus and the hardness increase as nitrogen replaces oxygen in the glass network. Both properties are also improved when the smaller REs are incorporated into the Si_3N_4 matrix, which is consistent with a strengthening in the network bonds resulting from the increases in the field strength of the RE—O bond (Becher et al., 2002). Moreover, the fracture toughness of the glasses was also reported to increase with a decreasing ionic radius of RE^{3+} (Lofaj et al., 2003). Similarly, viscosity of SiREAl glasses can be tailored by controlling the glass composition. The viscosity of glasses shifts to higher temperatures by increasing the N:O and RE:Al ratios in the glass compositions as well as by incorporating progressively smaller RE elements (Becher and Ferber, 2004). Nitrogen forms strong bridging links between three silicon tetrahedron as opposed to only two for oxygen, and appears to prefer bridging rather than nonbridging sites. Thus, replacing oxygen with nitrogen will strengthen the network and increase the viscosity. On the other hand, RE elements coordinate with a larger number of anions apparently promoting the generation of nonbridging oxygen, particularly in the case of larger RE^{3+}. This leads to a lower viscosity of the intergranular phase consisting of the RE elements with the larger RE^{3+} cations compared to the smaller ones. It was concluded that nitrogen as a network former is more effective than the lanthanide modifiers (Lofaj et al., 2003; Becher et al., 2002).

2.2.4 Effect of RE oxides on the microstructure development of Si_3N_4

As mentioned above, the grain growth occurs in the presence of a glassy phase derived from the native surface oxide on the Si_3N_4 powder and the additives used to enhance the densification of Si_3N_4. The sintering additives affect the glass viscosity by altering the glass composition. When growth of β-grains is controlled by a diffusion through the glassy phase, changes in the glass composition modify the diffusion rates of silicon and nitrogen and, thereby, a rate of the grain growth. Alteration in the RE elements being used as a sintering additive has a significant effect on the growth rates of β-Si_3N_4 grains. It was reported that the growth-limiting step shifts from an interface control to control by a diffusion within the glass phase as the size of RE cation decreases (Becher et al., 1998).

A formation of the elongated hexagonal cross-sectioned grains with curved end caps is typically observed in β-Si_3N_4 and β-SiAlON ceramics. The shape of the end caps is believed to represent a diffusion-controlled *c*-axis growth process. Diffusion coefficient is inversely proportional to the compositional dependent viscosity of the intergranular amorphous phase. In the range of 800–1000 °C, the viscosity of bulk Si–RE–Al and Si–RE–Mg oxynitride glasses of fixed compositions increases with a

decreasing size of RE cations. At the same time, nitrogen solubility in the bulk Si–Me–RE oxynitride glasses slightly increases with increasing RE ions, which leads to an increase in the viscosity. In other words, a presence of nitrogen slightly compensates for decrease in viscosity due to the larger RE ions in the glass network. However, it is well known that the viscosities of glasses significantly decrease with an increasing temperature (Becher et al., 2006).

The growth rate in the *c*-axis direction of the grains is not affected by the RE elements used as the additive. On the other hand, RE cation has a significant influence on the *a*-axis growth rate of β-Si_3N_4 grains (Becher et al., 2006).

Several works reported that the RE oxide additives control the $\alpha \rightarrow \beta$ phase transformation rates of Si_3N_4, the grain growth anisotropy, and the AR of β-Si_3N_4 (Satet and Hoffmann, 2005; Kitayama et al., 2006; Park et al., 1997; Lojanová et al., 2010; Tatarko et al., 2010). RE elements with a larger ionic radius (i.e. with a smaller atomic number) delay the phase transformation and weaken the interfacial bonding (Kitayama et al., 2006; Park et al., 1997).

The microstructures of the hot-pressed monolithic Si_3N_4 ceramics sintered with the different RE oxides (La_2O_3, Nd_2O_3, Yb_2O_3, and Lu_2O_3) are shown in Figure 2.2. It is obvious that these materials possess a typical bimodal microstructure that consists of the large elongated β-Si_3N_4 grains distributed in a fine β-Si_3N_4 matrix. It should be pointed out that the presence of different RE elements in the Si_3N_4 grain boundary glassy phase led to the differences in a grain growth anisotropy (Figure 2.2). The materials with the smaller RE^{3+} cations (Yb and Lu) contained the elongated β-Si_3N_4 grains with a larger diameter, embedded in a finer β-Si_3N_4 matrix. This constitutes a typical bimodal distribution of the grains in the microstructure (Figure 2.2c and d). On the other hand, the Si_3N_4 sintered with the larger RE^{3+} cations (mainly La, but partially also Nd) did not exhibit this bimodal distribution so significantly (Figure 2.2a and b). It was reported that a higher number of the β-Si_3N_4 grains with a small diameter ($d \leq 0.08$ μm) was observed for the monolithic Si_3N_4 doped with Y, Yb, and Lu, when compared to the Si_3N_4 doped with La, Nd, and Sm cations (Lojanová et al., 2010). Moreover, a small number of the robust Si_3N_4 grains with a diameter of approximately 1 μm was also observed for the materials containing Yb_2O_3 and Lu_2O_3 as the additives. Although the apparent AR as a function of RE^{3+} radius did not change significantly (Figure 2.3), the average value of AR increased slightly when La^{3+} cation was replaced by Lu^{3+} (Lojanová et al., 2010). This observation is in keeping with the fact that the larger RE ions delay the phase transformation (Kitayama et al., 2006) and that the RE ions impact the temperature at which the phase transformation initiates (Becher et al., 2010). It was reported by Becher et al. (2008) that the early onset of the transformation gives β-grains more time for growth if Lu_2O_3 is used, less time for Gd_2O_3, and the least for La_2O_3. They also observed that more of the larger β-grains at early stages of the transformation were present when Lu_2O_3 was used, compared to La_2O_3 additive.

The reason for different microstructural evolutions of Si_3N_4 with various types of the RE oxide additives can be related to the different viscosities of the liquid phases at the sintering temperature. It was reported that the viscosity of the oxynitride glasses increases with an increasing CFS, and thus a decreasing ionic radius of RE^{3+}

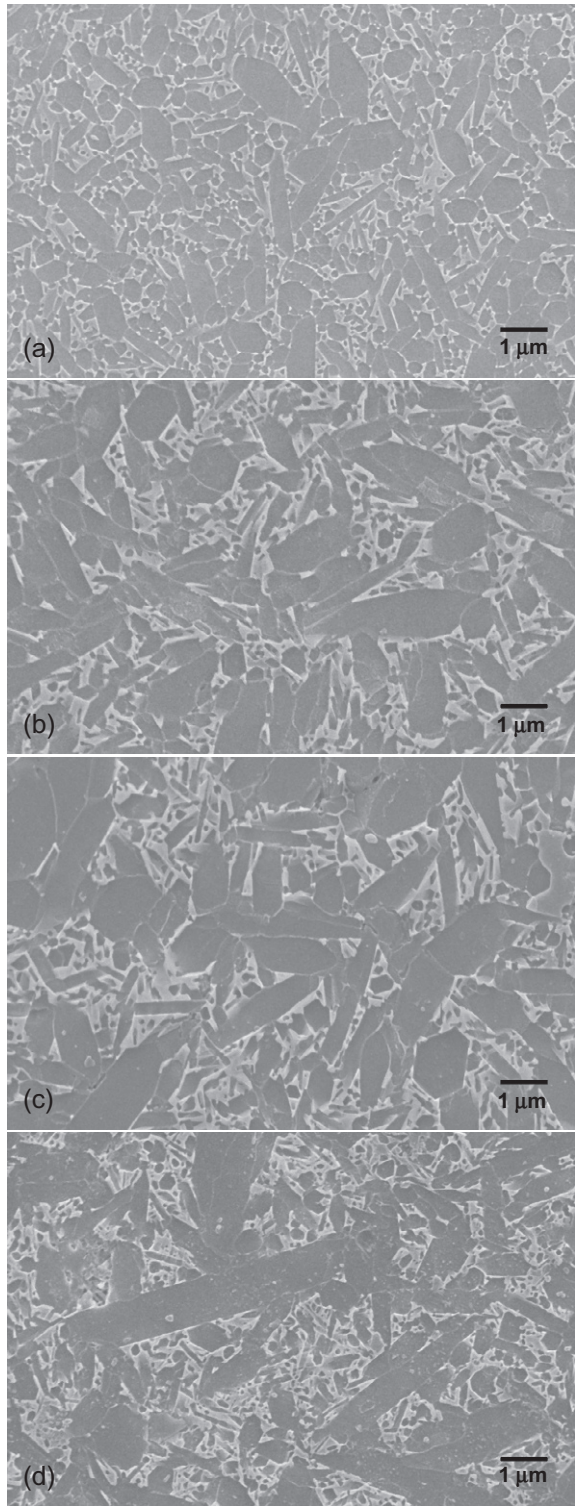

Figure 2.2 Microstructures of Si_3N_4 monoliths sintered with SiO_2 and various RE_2O_3: (a) La_2O_3, (b) Nd_2O_3, (c) Yb_2O_3, and (d) Lu_2O_3.

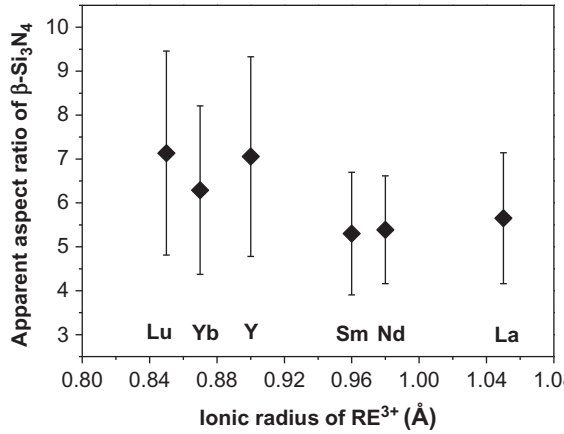

Figure 2.3 Apparent aspect ratio of β-Si_3N_4 grains in the Si_3N_4 monoliths with various RE_2O_3 additives (Lojanová et al., 2010).

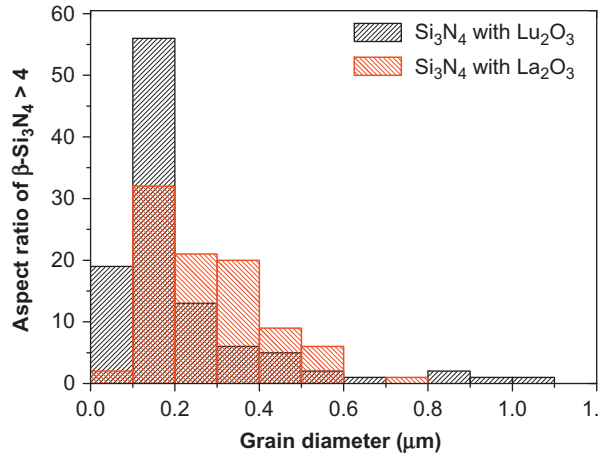

Figure 2.4 Volume fraction of β-Si_3N_4 grains with AR > 4 in La- and Lu-doped Si_3N_4 monoliths (Tatarko et al., 2010a).

(Lofaj et al., 2004; Becher and Ferber, 2004; Hampshire and Pomeroy, 2004). The volume fraction of β-Si_3N_4 grains with AR >4 (needle-like grains) as the function of the grain diameter in the monolithic Si_3N_4 ceramics sintered with La (the largest RE^{3+}) and Lu (the smallest RE^{3+}) is shown in Figure 2.4 (Tatarko et al., 2010a,b). This graph reveals that the Si_3N_4 sintered with Lu exhibited a remarkably higher volume fraction of the thin needle-like β-Si_3N_4 grains (mean grain diameter <0.2 μm) and a slightly higher volume fraction of the thick needle-like grains (mean grain diameter >0.8 μm) than the Si_3N_4 with La. The increased number of small diameter grains was observed for the material having a higher AR of β-Si_3N_4 (sintered with Lu_2O_3) due to a higher viscosity of the liquid phase at the sintering temperature. A higher viscosity restrains dissolution of silicon nitride grains in the melt with a consequence of a lower concentration of ions needed for the precipitation. Moreover, a high melt viscosity hinders the material transport by means of diffusion through the liquid.

Such a different growth behaviour of the diameter of preexisting β-Si_3N_4 grains was attributed to the different propensity of RE elements to segregate on the

crystallographic surfaces of silicon nitride grains. Shibata et al. (2004, 2005) reported that La has an increasing preference for the adsorption on the prismatic grain surfaces (preferred bonding to N), which impedes the attachment of Si to the growing interface, thereby hindering the grain growth in this direction. Therefore, a larger diameter of the needle-like β-Si_3N_4 grains for the Lu sample can be explained by a higher stability of Lu in the glass (preferred bonding to O). Thus, the Lu atoms do not impede the attachment of Si and N to the prismatic plane.

Kitayama et al. (2006) studied the influence of RE oxides on the phase transformation of Si_3N_4. They observed a larger activation energy for α–β transformation when a larger ionic radius of RE was used and hence, the slower phase transformation proceeds at the same annealing temperature for different RE oxide additives. Becher et al. (2006, 2010) found that RE additions have a strong effect on the temperatures of the initiation and finishing of the phase transformation, both of which decrease with a decreasing ionic radius of RE. At the same time, the anisotropy of the grains decreased with a decreasing ionic radius of RE. If the transformation is initiated at lower temperatures, the forming β-Si_3N_4 grains have a larger final diameter as they have more time to grow.

However, there is a discrepancy between the studies on the influence of RE oxide additives on the microstructural development of Si_3N_4 ceramics reported in the literature. While the AR of β-Si_3N_4 grains increased with a decreasing ionic radius of RE^{3+} in the Si_3N_4 sintered with RE_2O_3 and SiO_2 in the works of Lojanová et al. (2010) and Tatarko et al. (2010a,b), insignificant influence of the various RE oxide additives on the microstructural evolution was observed by Hyuga et al. (2004) and Hong et al. (2002). On the contrary, Satet and Hoffmann (2005) showed that the AR of Si_3N_4 grains and anisotropy of the grain growth increased with an increasing ionic radius of RE in the Si_3N_4 with RE_2O_3 and MgO. These discrepant results indicate that the size of the cations of RE oxide additives may not be the only dominant parameter in the microstructural evolution of Si_3N_4. A different chemistry of the grain boundary phases as well as different processing routes can be considered to be the main reasons for this contradiction.

In order to understand the influence of RE elements on the growth of Si_3N_4 grains, several works have been done with the aim of detecting an adsorption of the RE ions on prism and/or basal planes of β-Si_3N_4 grains (Shibata et al., 2004, 2005; Ziegler et al., 2004; Painter et al., 2008). A high-angle annular dark field (HAADF) scanning transmission electron microscopy (STEM) for imaging and electron energy loss spectroscopy for chemical analyses were used for this investigation. The immediate interface between the Si_3N_4 grains and the amorphous IGF was examined. However, an agreement between the individual studies was again not obtained.

Shibata et al. (2004, 2005) and Painter et al. (2008) reported that La atoms were observed more frequently at the grain surfaces and within the nanometer-thick amorphous films between the Si_3N_4 grains, when compared to Lu atoms. Since the chemical composition of the grain boundaries plays an important role, it is important to note that the investigated Si_3N_4 materials were sintered with a mixture of RE_2O_3 and MgO. The calculated values of DBE ($\delta_{Si,RE}$) was reported to be 2.50 eV for Lu compared to −0.98 eV for La. The positive value for Lu indicates a higher stability in the glass, whereas a negative value for La corresponds to the increasing preferences for the

adsorption at the nitride surface (see Section 2.2.3). Thus, while Lu can adsorb at the preferred grain surface sites, it would be expected to desorb more easily into the glass compared to La. The attachment of Si to the growing interface is predicated by a desorption of those RE adsorbed on the prismatic plane, which should occur easier for Lu than La.

It was therefore concluded that the transformation of Si_3N_4 occurs at the lowest temperature when Lu is used, as it has the least surface adsorption. On the other hand, the highest adsorption ability of La leads to a delay in the transformation to much higher temperatures. The early onset of transformation provides more time for the growth of β-Si_3N_4 grains when Lu_2O_3 is used, less for Gd_2O_3, and the least for La_2O_3. It was observed that more of the larger β-grains were present with Lu_2O_3 in the early stages of the transformation. At the same time, the final AR of the β-grains increased with the same dependence on the RE cations. Microstructures of the materials showed that the reinforcing grains produced with Lu_2O_3 exhibited the largest diameters, while La_2O_3 produced long, thinner reinforcing grains (Painter et al., 2008). This is in keeping with the work of Lojanová et al. (2010) and Tatarko et al. (2010a,b).

On the other hand, Ziegler et al. (2004) obtained direct atomic resolution images that illustrate how a range of RE atoms bind to the interface between a grain and the intergranular phase. Contrary to the previous results, La showed no specific or periodic bonding at the interface (Figure 2.5). The La atoms were present in the intergranular phase but were not arranged into any atomic columns. In contrast, the

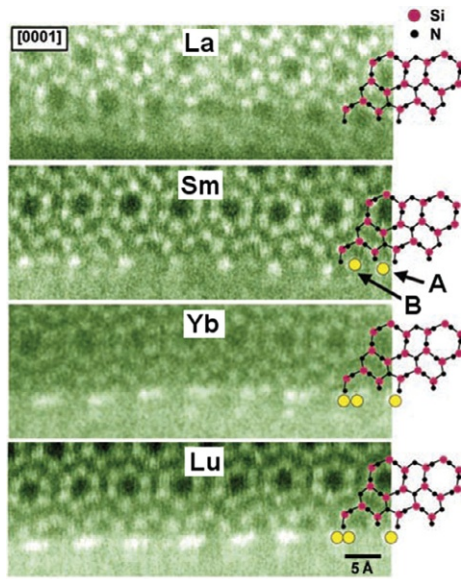

Figure 2.5 STEM images of the Si_3N_4 ceramics doped with La, Sm, Yb, and Lu showing the attachment of RE elements at the Si_3N_4 interface. The matrix grain is oriented along the [0001] zone.
Adapted from Ziegler et al. (2004).

examination of other three compositions (Sm, Yb, and Lu) showed that these atoms were arranged into the columns at the interface. Ziegler concluded that the segregation tendency of RE ions at the interface increases with an increasing atomic number, i.e., with a decreasing ionic radius of RE^{3+}. The adsorption of RE ions results in a decreasing interfacial energy of the prism plane of β-Si_3N_4 and the equilibrium shape of the β-Si_3N_4 grains would be more elongated toward the [001] direction. This contradicts the fact that the morphology of the β-Si_3N_4 grains is more elongated in the La system (less adsorption) than in the Yb or Lu system (more adsorption), as it was reported in Satet and Hoffmann (2005), Shibata et al. (2005), and Painter et al. (2008). On the other hand, the results are in good accordance with the work of Kitayama et al. (2006). They reported that the adsorption of RE atoms at the prism and/or basal interfaces decreases the activation energy for nucleation, and hence, decreases the activation energy for the phase transformation. The activation energy was reported in their work to decrease with a decreasing ionic radius of RE^{3+} due to a higher number of the atoms attached to the interface.

Taking into account these different results reported on the effect of RE oxides on the microstructure of Si_3N_4, Becher et al. (2010) concluded that the role of RE_2O_3 additives during liquid phase densification of Si_3N_4 may be changed by the addition of other oxide additives. They reported that the effect of RE_2O_3 on the microstructure evolution might be different in a system with low viscosity (using the addition of MgO, Al_2O_3 in combination with RE_2O_3) compared to a system with high-viscosity liquid phase (combination of RE_2O_3 with SiO_2):

(1) *System with low-viscosity liquid phases*: The Mg (or Al)-bearing Si–RE oxynitride glasses are low-viscosity systems, but the viscosity–temperature profiles are shifted to higher temperatures when RE changes from La to Lu. These viscosity changes indicate the faster diffusion with increasing size of RE ion; therefore, the onset of densification and the phase transformation would be initiated at lower temperatures with La rather than with Lu, along with the promotion of the grain growth. On the other hand, the transformation with RE_2O_3 + MgO additions, which is initiated after densification is completed, is initiated at increasing temperatures as the RE shifts from Lu to La. The grain AR also increases in the same trend, but the amount of larger diameter elongated β-grains increases when RE shifts from La to Lu. In this case, the phase transformation and the elongated growth behaviour are controlled by the RE adsorption/desorption processes. When RE_2O_3 additives are combined with Al_2O_3, densification is promoted; however, grain growth is inhibited in comparison with that of RE_2O_3 + MgO. If only RE additives are used, the rate of the phase transformation increases as the activation energy decreases with a decreasing size of RE (in the range of 1700–1850 °C).

(2) *System with high-viscosity liquid phases ($RE_2O_3 + SiO_2$)*: The increased viscosity clearly impacts densification process because increase in processing temperature of some 125–150 °C is required to achieve full density in 1 h over that with combination of RE_2O_3 and MgO. Moreover, the viscosity of Si–RE–Me oxynitride glasses increases with a decreasing size of RE. The phase transformation initiates before samples reach full density; in this case, the transformation is initiated and completed with La before than that with Lu. It means that effect of La_2O_3 versus Lu_2O_3 combined with SiO_2 is just the opposite of that observed for combination of RE_2O_3 with MgO and for RE_2O_3 as the only additive. Now, La serves to enhance the microstructure evolution resulting in the formation of larger elongated reinforcing grains at temperature up to 1800 °C in comparison with Lu.

All these facts imply that the dominant mechanisms controlling the phase transformation with RE_2O_3 alone or in combination with MgO or Al_2O_3 differ from that when the RE_2O_3 is combined with SiO_2. This actually explains the differences between the microstructure evolution of Si_3N_4 reported by Satet and Hoffmann, (2005) (where a low-viscosity liquid phase is considered as MgO was used besides RE_2O_3) and that reported by Lojanová et al. (2010) and Tatarko et al. (2010a,b) (with a high-viscosity liquid phase, as RE_2O_3 with original SiO_2 were used as the only additives).

A dominating mechanism for the first case is difference in the affinity of each RE atom to adsorb at the prism plane of β-Si_3N_4 grains. Since the La atoms showed a higher tendency to segregate at the surface of Si_3N_4 rather than Lu atoms, the attachment of Si on the β-grains was hindered more significantly in the case of Si_3N_4 containing La at the grain boundaries. Increased temperature is required to promote desorption of the RE and allow the transformation to proceed. It is important to note that the RE adsorption behavior remains basically the same, regardless of the addition of other additives. To answer the question of why Lu delays the transformation compared to La when combined with silica, two factors are needed to be considered: (1) transport through the liquid phase and (2) solubility of Si_3N_4 in the liquid phase (Becher et al., 2010). Transport of Si and N through the liquid can be determined by the viscosity of the liquid phases. It is well known that viscosity of oxynitride glasses increases with decreasing size of RE (Becher and Ferber, 2004). Although the temperature shifts in the viscosity curves are relatively small (<100 °C) between La- and Lu-containing glasses of the same composition, a significant slope of the viscosity curves leads to a difference in the viscosity from two to four orders of magnitude for La versus Lu at the same temperature. This fact results in a decrease in diffusion rates with Lu in the glass compared to La. It is therefore necessary to raise the temperature in order to initiate the phase transformation in the case of Lu_2O_3 with SiO_2 additive. With regard to the solubility of Si_3N_4 in the liquid phase, it was reported that solubility of nitrogen in the Si–RE–Me glasses (where Me = Al or Mg) consistently increases with an increasing size of RE. Therefore, a higher solubility of Si_3N_4 grains is expected in the surrounding La-bearing liquid phase than that with Lu. This leads to a higher rate of the phase transformation for material sintered with La (Becher et al., 2010).

2.2.5 Processing of Si_3N_4–SiC composites

To improve the mechanical or functional properties of Si_3N_4-based ceramic materials, various types of composite materials have been developed. Among them, Si_3N_4–SiC composites are the most extensively investigated. Si_3N_4 ceramics containing two different fractions of Si_3N_4 grains (β-Si_3N_4 whiskers or large β-Si_3N_4 seeds) might also be considered as a special composite system, i.e., Si_3N_4–Si_3N_4 composites.

As a possible way to improve the mechanical properties of Si_3N_4 ceramics, particularly the high-temperature ones, the Si_3N_4–SiC nanocomposites have been developed (Niihara, 1991; Hnatko et al., 2004; Kašiarová et al., 2009; Dusza et al.,

2005; Lojanová et al., 2010; Tatarko et al., 2010a,b, 2013a,b; Herrmann et al., 1998; Park et al., 1998a,b). These materials consist of a submicrometer-sized Si_3N_4 matrix that contains a dispersion of nano-sized SiC particles of essentially globular shape. The particles are located both at the grain boundaries of Si_3N_4 (with a size of approximately 150–170 nm) and within the Si_3N_4 grains (with a size of 30–40 nm) (Kašiarová et al., 2006). Si_3N_4–SiC nanocomposites exhibit excellent mechanical properties at both ambient and elevated temperatures. It has been suggested that the particles located at the grain boundaries are directly bonded with the adjacent Si_3N_4 grains and develop a direct Si_3N_4–SiC interface without any interfacial amorphous phase (Niihara, 1991). Thus, the particles are thought to act as the effective obstacles to grain boundary sliding and subcritical crack growth at high temperatures. Therefore, these particles are responsible for the superior high-temperature properties.

Thermo-mechanical data show that the lower bound of the stability ranges of the two solid phases Si_3N_4 and SiC (as a function of temperature, nitrogen pressure, and SiO_2 activity) is defined by the decomposition of Si_3N_4 at a low nitrogen pressure, according to the reaction (Herrmann et al., 1998):

$$Si_3N_4(s) \rightarrow 3Si(l) + 2N_2(g) \tag{2.4}$$

The upper bound of the stability range of composite is given by decomposition of SiC at a high nitrogen pressure (Herrmann et al., 1998):

$$3SiC(s) + 2N_2(g) \rightarrow Si_3N_4(s) + 3C(s) \tag{2.5}$$

A variety of processes have been reported to produce Si_3N_4–SiC nanocomposites:

(1) HP or gas pressure sintering of a mechanical mixture of crystalline Si_3N_4 and SiC powders (Tian et al., 1998; Koh et al., 2001).
(2) HP of a SiCN amorphous powder (Šajgalík et al., 2000) which was prepared via a chemical vapor deposition process.
(3) HP of Si_3N_4 powder by *in situ* carbothermal reduction of SiO_2 (Hnatko et al., 2004).

The preparation of Si_3N_4–SiC nanocomposites by *in situ* carbothermal reduction of silica is a suitable and low-cost processing way, because the cheaper powders (with a higher amount of oxygen) can be used as an initial mixture. The oxygen (in the form of SiO_2) is considered to be the impurity in other cases, but for this method, is used for a reaction with carbon (in the form of soot) to produce the SiC nanoparticles during sintering. Typical technological regime of such an approach to produce Si_3N_4–SiC nanocomposites is shown in Figure 2.6.

Reduction of SiO_2 to form SiC in the SiO_2–RE_2O_3 system is possible when activity of carbon is high:

$$SiO_2(s,l) + 3C(s) \rightarrow SiC(s) + 2CO(g) \tag{2.6}$$

Formation of CO (g) by this reaction within the bulk composite is problematic. Evolved gas can be entrapped in the closed pores and hinder densification, and can

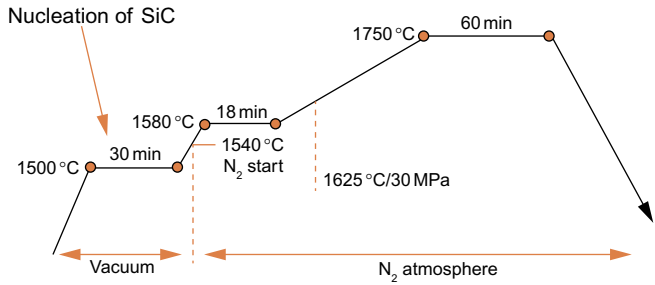

Figure 2.6 Schematic sketch of the technological process of Si_3N_4–SiC micro–nano composites.

cause the formation of cracks when the pressure within the pores exceeds locally the strength of the material (Hnatko et al., 2004).

Another source of SiC is the reaction of Si_3N_4 with carbon, which at normal pressure of nitrogen proceeds at temperatures exceeding 1440 °C:

$$\alpha - Si_3N_4(s) + 3C(s) \rightarrow 3\beta - SiC(s) + 2N_2(g) \tag{2.7}$$

There are two possible ways by which the SiC nanoparticles influence the microstructural evolution of Si_3N_4 (Park et al., 1998a,b). The SiC may act as nucleation sites for the β-Si_3N_4 grains and in this case, all the SiC particles would be enclosed in the grains. It is expected that the average size of Si_3N_4 decreases with an increasing number of nucleation sites. Another possibility is that the SiC may act as a grain growth inhibitor. The dissolution–reprecipitation process and the grain boundary migration of Si_3N_4 are hindered by the presence of the inert SiC particles. However, this effect depends on the relative size of the SiC particles. When the size of SiC is much smaller than that of Si_3N_4, the Si_3N_4 grain grows around the SiC easily, trapping the SiC inside the Si_3N_4 grains. On the other hand, if the size of SiC is comparable to that of Si_3N_4 grains, the inhibition effect is stronger, resulting in the reduction of the average grain size and leaving the SiC at the grain boundaries.

It was reported that the best mechanical properties can be achieved when the amount of SiC varies between 5 and 15 wt.% (Petzow and Herrmann, 2002; Hnatko et al., 2004; Sasaki et al., 1992).

2.2.6 Effect of RE_2O_3 on the microstructure development of Si_3N_4–SiC composites

Microstructures of the Si_3N_4/SiC composites sintered with different RE oxides (La_2O_3, Nd_2O_3, Yb_2O_3, and Lu_2O_3) are shown in Figure 2.7. The microstructures exhibit a typical bimodal character with the elongated β-Si_3N_4 micrograins and randomly distributed SiC nanoinclusions in the Si_3N_4 matrix. The globular nano (∼30 nm) SiC inclusions are located intragranularly within the Si_3N_4 grains while

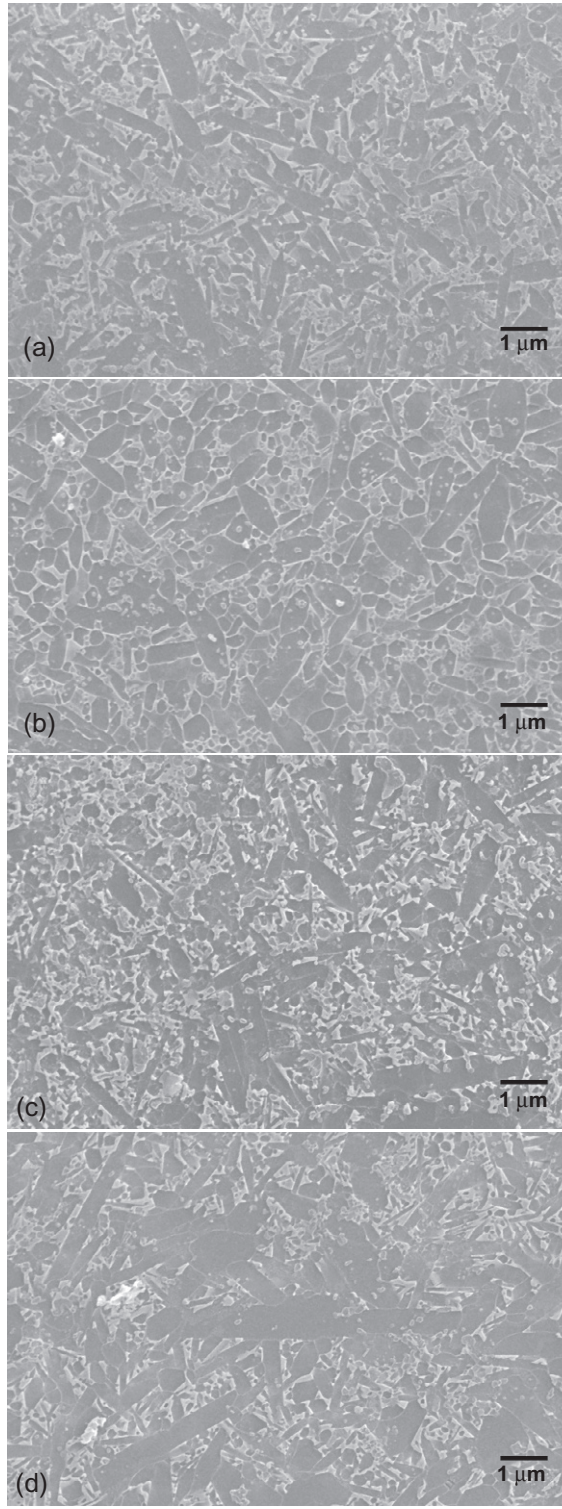

Figure 2.7 Microstructures of Si_3N_4–SiC composites sintered with SiO_2 and various RE_2O_3: (a) La_2O_3, (b) Nd_2O_3, (c) Yb_2O_3, and (d) Lu_2O_3.

the submicron-sized (~150 nm) SiC inclusions are located intergranularly between the Si_3N_4 grains (Tatarko et al., 2010a,b).

Evolution of the microstructure of the Si_3N_4/SiC composites (Figure 2.7) is comparable to the reference monolithic Si_3N_4 materials (compare with Figure 2.2, Section 2.2.4); however, the microstructures of the composites are generally finer (Lojanová et al., 2010; Tatarko et al., 2010a,b). This result is in keeping with the assumption that SiC inclusions hinder the grain growth of silicon nitride by a grain boundary pinning. Taking into account the fact that β-Si_3N_4 grain growth is preferential in the *c*-direction (Krämer et al., 1993, 1994), the presence of SiC grains hinders the silicon nitride grain growth, particularly in this direction. Therefore, this has an impact on the average values of the apparent AR of β-Si_3N_4 that was reported to be slightly lower for the Si_3N_4–SiC composites sintered with RE_2O_3 (Figure 2.8), when compared to the Si_3N_4 monoliths with the same RE additives (see Figure 2.3).

It was reported that there is a difference in the preferential location of SiC nanoparticles in the Si_3N_4 matrix when different RE additives are used (Lojanová et al., 2010; Tatarko et al., 2010a,b). The Si_3N_4–SiC composite sintered with La_2O_3 exhibited a preferential location of SiC particles inside the silicon nitride grains (Figure 2.9a), while the SiC particles located at the grain boundaries were observed more frequently in the Lu-doped composite (Figure 2.9c). On the other hand, the composite sintered with Y_2O_3 exhibited a mixture of both location, and no preferential location was observed (Figure 2.9b). It can therefore be concluded that a liquid phase with a lower viscosity (larger ion of RE^{3+}–La) tends to form intragranular SiC particles, whereas a higher viscosity of a liquid phase (smaller ion of RE^{3+}–Lu) promotes the formation of the intergranular particles of SiC. The lower viscosity liquid phase promotes the solution–reprecipitation process and the growth of β-Si_3N_4 grains and also diminishes the interfacial energy, which is beneficial for the entrapping of the smallest SiC inclusions inside the β-Si_3N_4 host grain.

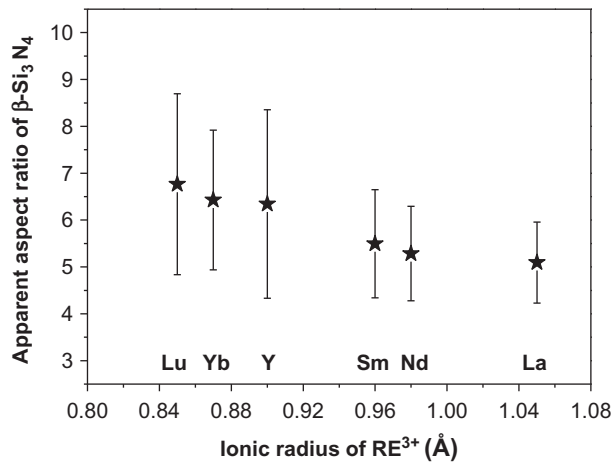

Figure 2.8 Apparent aspect ratio of β-Si_3N_4 grains in the Si_3N_4–SiC composites with various RE_2O_3 additives (Lojanová et al., 2010).

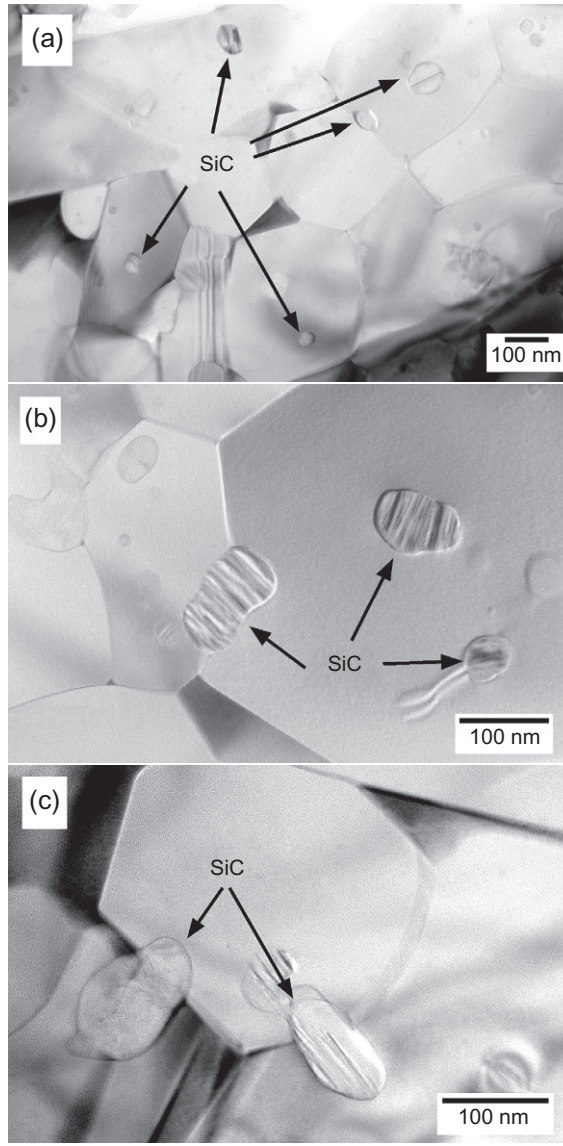

Figure 2.9 TEM micrographs of the Si_3N_4–SiC sintered with (a) La_2O_3, (b) Y_2O_3, and (c) Lu_2O_3, showing the location of the SiC particles (Kašiarová et al., 2014).

The interface between the intragranularly located SiC nanoparticles and the Si_3N_4 grains was observed to be either clear (Figure 2.10a) or with an additional glassy film. On the other hand, an intergranular glassy phase was very often found between the intergranularly located SiC and the Si_3N_4 grains (Figure 2.10b).

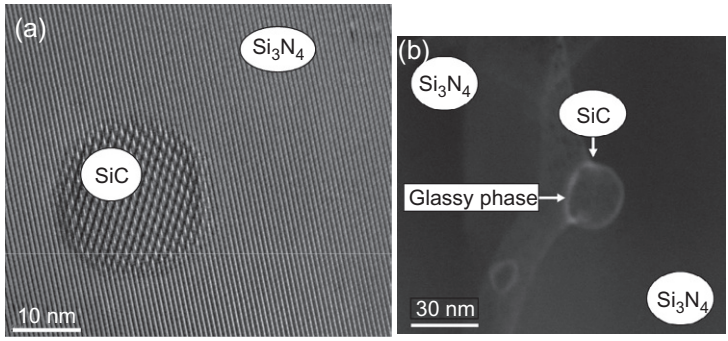

Figure 2.10 Intragranularly located SiC grain, HREM, lattice fringe image (a); back scattered HAADF image of the intergranularly located SiC particles (b) (Kašiarová et al., 2014).

2.3 Toughening of Si_3N_4-based ceramics

2.3.1 Fracture toughness of Si_3N_4 monoliths

Fracture toughness of Si_3N_4 varies in a wide range from 3 to 12 MPa $m^{1/2}$, which is related to variations in the microstructure of the materials. Another reason is that different methods of determination of fracture toughness provide slightly different values. Generally, the fracture toughness of silicon nitride depends on the microstructural parameters, chemistry of the grain boundary phases, and the amount of the sintering additives. The fracture toughness of Si_3N_4 increases with the increasing values of the microstructural parameters, such as grain diameter and AR of β-Si_3N_4 grains, or volume fraction of the elongated β-Si_3N_4 grains. The chemical composition of the grain boundary phase is also very important, as it determines the residual stresses at the grain/secondary phase interface (due to the different thermal expansion coefficients compared to Si_3N_4) as well as the interfacial debonding. A higher amount of the sintering additives usually leads to the increased fracture toughness due to the promoted grains evolution, resulting in the coarser microstructure of Si_3N_4.

The presence of a microstructure similar to whisker-reinforced ceramic composites, containing the elongated β-Si_3N_4 grains as a reinforcing agent, is a necessary but not sufficient condition to improve the fracture toughness of Si_3N_4 ceramic materials. Crack bridging, crack deflection, and pull-out were determined as dominant toughening mechanisms in composite-like microstructures. The materials with such a microstructure are also well known as "self-reinforced" Si_3N_4 ceramics.

Silicon nitrides prepared with different sintering additives and processing routes exhibiting self-reinforced microstructures can have very different fracture toughness. One of the critical issues in the microstructural design of Si_3N_4 is to control the debonding at the interface between the β-Si_3N_4 and the intergranular glassy phase, in such a way, the elongated β-Si_3N_4 grains can contribute to the toughening mechanisms, such as crack deflection and crack bridging. Several studies indicated that the interfacial debonding in silicon nitrides could be influenced by the composition of the sintering additives, which ultimately altered the composition of the intergranular

amorphous phase. However, there are some experimental difficulties regarding a systematic investigation of the effect of the sintering additives on the fracture behavior of silicon nitrides. The reason is that different additives generally induce different grain growth rates during densification and result in the microstructures with different grain morphologies and sizes (Becher et al., 1998). It should be noted that a weak interface between the grains and the intergranular phases is generally required for the toughening mechanisms (Kleebe et al., 1999).

Kleebe et al. (1999) showed that chemistry of a secondary phase plays a key role in the toughening behavior of Si_3N_4 ceramics, due to a threefold effect: (1) influence on the Si_3N_4 grain morphology, (2) the effect on the secondary phase crystallization at triple pockets, and (3) the influence on the development of residual stresses in addition to the change of the atomic glass structure.

Similarly, Peterson and Tien (1995) reported that thermal expansion coefficient, elastic properties, and fracture toughness of the grain boundary phase, along with the bonding strength between the Si_3N_4 matrix and the grain boundary, are expected to affect the crack propagation. When the thermal expansion coefficient of the grain boundary phase is larger than that of the silicon nitride, both the tensile stresses in the grain boundary and the compressive stresses in the silicon nitride grains increase as the thermal expansion coefficient of the grain boundary phase increases. Tensile stresses at the grain boundaries and compressive stresses in silicon nitride grains promote crack deflection and the formation of bridging grains. The fracture of grains that become bridges depends on the fracture of grains that intersect the crack at an angle favorable for the crack deflection (Peterson and Tien, 1995). On the other hand, Sun et al. (1999) showed that differences in the residual stresses have only a marginal effect on the first crack deflection event. The CTE measured on nitrogen-saturated bulk glasses varied from $6.44 \times 10^{-6}\ K^{-1}$ in the Lu-based glass to $7.09 \times 10^{-6}\ K^{-1}$ for the La-based glass. Since the CTE of the Si–Mg–RE–O–N glasses increased only insignificantly when La was replaced for Lu, the increased radial residual stresses will not affect the toughening mechanism significantly, but might contribute marginally to an increase in debonding length (Satet and Hoffmann, 2005).

It was found that high fracture resistance (>10 MPa $m^{1/2}$) combined with a steeply rising R-curve and high fracture strength (>1 GPa) can be developed in the self-reinforced silicon nitrides by carefully controlling the size and amount of well-dispersed large elongated grains in a fine-grained matrix (Becher et al., 1998). On the other hand, when a fine equiaxed microstructure was generated, the fracture toughness was significantly lower ($\sim$3.5 MPa $m^{1/2}$).

Šajgalík et al. (1995) examined the influence of microstructural characteristics of Si_3N_4 sintered with Y_2O_3 and Al_2O_3 additives on the fracture toughness values and toughening mechanisms. The material with the highest volume fraction of the grains with the AR >4 exhibited the highest fracture toughness of >8 MPa $m^{1/2}$. On the other hand, the materials without such grains possessed the lowest fracture toughness of 6 MPa $m^{1/2}$. Moreover, a dominant toughening mechanism changed with respect to the diameter of the elongated grains. Elastic bridging and pull-out were observed only for thin, needle-like grains with diameters <1 μm, whereas frictional bridges were independent of the thickness of the toughening ligament. The crack deflection was mainly associated with thick needle-like grains (>1 μm).

2.3.2 Fracture toughness of Si_3N_4–SiC composites

Influence of the presence of SiC particles on the fracture toughness is attributed to the residual stresses that lead to a nanophase toughening effect (Kašiarová et al., 2006). During the cooling of nanocomposites from sintering temperature, the differences in the elastic moduli and the linear thermal expansion coefficients generally result in residual stresses in the matrix as well as in the particles. A thermal expansion mismatch in the Si_3N_4–SiC nanocomposite caused the formation of the tensile radial stresses at the Si_3N_4/SiC grain boundaries. The radial residual stresses between the SiC particles and the Si_3N_4 matrix have tensile character, but a tangential component of the residual stress is compressive. In the case of the intergranularly located SiC, these compressive stresses positively influence the Si_3N_4/SiC grain boundary strength. However, the presence of a glassy film at the grain boundaries caused the internal stress relaxation, leading to lower residual stresses in the Si_3N_4–SiC nanocomposite compared to Al_2O_3 with nano SiC composite (Kašiarová et al., 2006). However, taking these facts into account, a significant discrepancy can be found in the fracture toughness data reported in the literature for Si_3N_4–SiC nanocomposites. It was reported that fracture toughness increased as the SiC content increased and reached a maximum in the range of 5–25 vol.% SiC (Niihara, 1991; Sasaki et al., 1992). However, Herrmann et al. (1998) found that the fracture toughness was not affected by the increasing volume fraction of SiC nanoparticles. Moreover, Kašiarová et al. (2006) and Poorteman et al. (2003) even observed a decrease in fracture toughness of the Si_3N_4–SiC nanocomposites compared to the monolithic Si_3N_4 sintered with Y_2O_3. They also found that the microstructural characteristics (grain diameter and AR) had a significantly stronger effect on the fracture toughness than a presence of the residual stresses. In the monolithic Si_3N_4 with coarser grains and higher AR, the pull-out and a crack deflection were observed as the toughening mechanisms, whereas they were not found in the finer microstructures of the nanocomposites. Tian et al. (1998) observed that after the addition of 5 vol.% SiC, the fracture toughness increased from 5.7 (monolithic Si_3N_4) to 7.7 MPa $m^{1/2}$. However, the fracture toughness decreased with a further increasing amount of SiC and reached 4.3 MPa $m^{1/2}$ at 25 vol.%. A higher amount of SiC resulted in the finer microstructure and more equiaxed grains, which led to a reduction in toughening mechanisms in the microstructure.

2.4 The influence of RE oxide additives on the toughening of Si_3N_4-based materials

2.4.1 Fracture toughness of the monolithic Si_3N_4 ceramics sintered with RE_2O_3

Several works have focused on the study of the influence of RE elements on the fracture toughness of Si_3N_4 materials (Satet and Hoffmann, 2005; Hyuga et al., 2004; Becher et al., 2010; Lojanová et al., 2010; Tatarko et al., 2010a,b). Generally, their effect on the fracture toughness was recognized to be either direct, as the size of their cations determines the interfacial bonding strength (between the Si_3N_4 grains and the

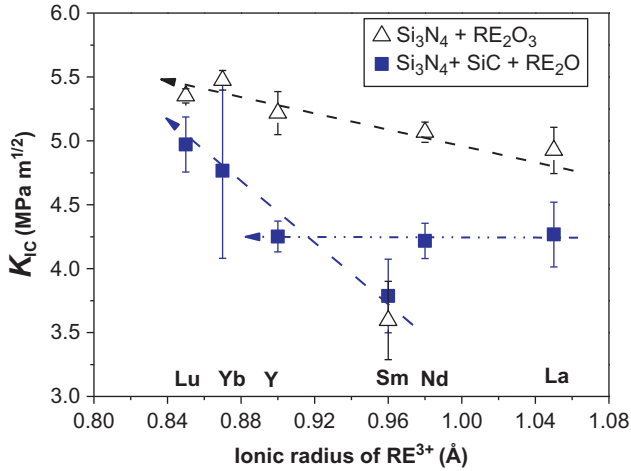

Figure 2.11 Fracture toughness of Si_3N_4 monoliths and Si_3N_4–SiC composites sintered with SiO_2 and various RE_2O_3, measured by chevron notch beam method.
Adapted from Lojanová et al. (2010).

grain boundary glassy phase) as well as the residual tensile stresses, or indirect, via alteration of the microstructural parameters.

Microstructural parameters play an important role in the assessment of the fracture toughness of Si_3N_4 ceramic materials. Lojanová et al. (2010) and Tatarko et al. (2010a,b) reported that the fracture toughness of the monolithic Si_3N_4 almost linearly increased with a decreasing ionic radius of RE^{3+} (Figure 2.11). This is in keeping with the results of the AR of β-Si_3N_4 grains that also slightly increased with a decreasing ionic radius of RE^{3+} (Figure 2.3). A higher fracture toughness of the samples with the smaller RE elements (Lu, Yb, Y) resulted from the reinforcing effect of the microstructure. The material with Lu_2O_3 contained a large amount of the elongated grains with a small grain diameter and it also contained a small amount of "robust" elongated grains with a large diameter, around 1 μm (see Section 2.2.4). A higher volume fraction of both the thin and the thick elongated β-Si_3N_4 grains in the Si_3N_4 sintered with Lu_2O_3 resulted in a higher frequency of the pull-out events and the frictional bridges. This results in a larger dissipation of the crack energy by the toughening mechanisms. Figure 2.12 shows the increasing amount of the toughening mechanisms in the case of sample doped by Lu (many crack deflections) compared to the material with La^{3+}, where a straight path of the crack can be observed. Šajgalík et al. (1995) reported that the microstructures containing both the fine and the coarse elongated β-grains (with AR ≥4) possessed the maximum fracture toughness, whereas the microstructures with a moderate diameter of the elongated β-grains exhibited a lower facture toughness. This can be attributed to the fact that pull-out and elastic bridging are the dominant toughening mechanisms for the elongated grains with a small diameter. On the other hand, crack deflection is a dominant mechanism for the coarser elongated grains (Šajgalík et al., 1995).

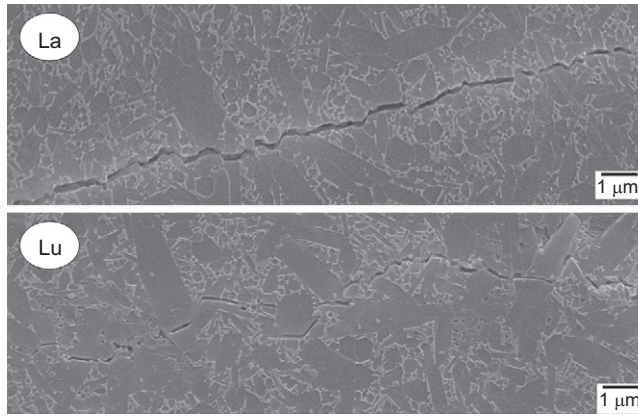

Figure 2.12 Crack propagation in the monolithic Si_3N_4 sintered with SiO_2 and La_2O_3 and Lu_2O_3.

Guo et al. (2003) investigated the influence of various amounts of Lu_2O_3 sintering additive (in the range from 1.68 to 12.51 wt.%) on the fracture toughness of Si_3N_4. They found that the fracture toughness increased steeply with the increasing amount of Lu_2O_3 up to 6.52 wt.% and then increased slowly with the further increasing amount of Lu_2O_3. The fracture toughness was in keeping with the microstructure parameters, such as the grain diameter (compare the Figure 2.13a and b). It was confirmed that the K_{IC} values increased with the increasing amount of the Lu_2O_3 sintering additive due to the larger diameters of the β-Si_3N_4 grains. The dependence of fracture toughness of Si_3N_4 on the grain diameter is shown in Figure 2.14. An approximately linear relationship is seen between the fracture toughness and the grain diameter, leading to a higher fracture toughness when the grain diameter is larger. This suggests that the fracture toughness of Si_3N_4 is mainly dominated by the grain diameter; the elongated grains are particularly effective for increasing fracture toughness. This is in a good accordance with the results reported by Lojanová et al. (2010) and Tatarko et al. (2010a,b).

On the other hand, the influence of the chemical composition of the grain boundary phases on the fracture toughness of the Si_3N_4 ceramics was also investigated by the same authors (Guo et al., 2004). The Si_3N_4 containing $Lu_4Si_2O_7N_2$ as the grain boundary phase exhibited a higher fracture toughness compared to the Si_3N_4 with $Lu_2Si_2O_7$ at the grain boundaries. However, only an indirect effect of the chemical composition of the grain boundary phase was reported, as the higher fracture toughness of Si_3N_4–$Lu_4Si_2O_7N_2$ (from 5.63 to 6.21 MPa $m^{1/2}$ compared to 4.81 MPa $m^{1/2}$ for Si_3N_4–$Lu_2Si_2O_7$) was attributed to the larger grain size (0.48 μm vs. 0.27 μm), the increased volume fraction of the needle-like grains and the enhanced interfacial debonding.

An important role of the grain boundary chemistry was also reported by Lojanová et al. (2010): they observed a deviation from the linear increase in the fracture toughness

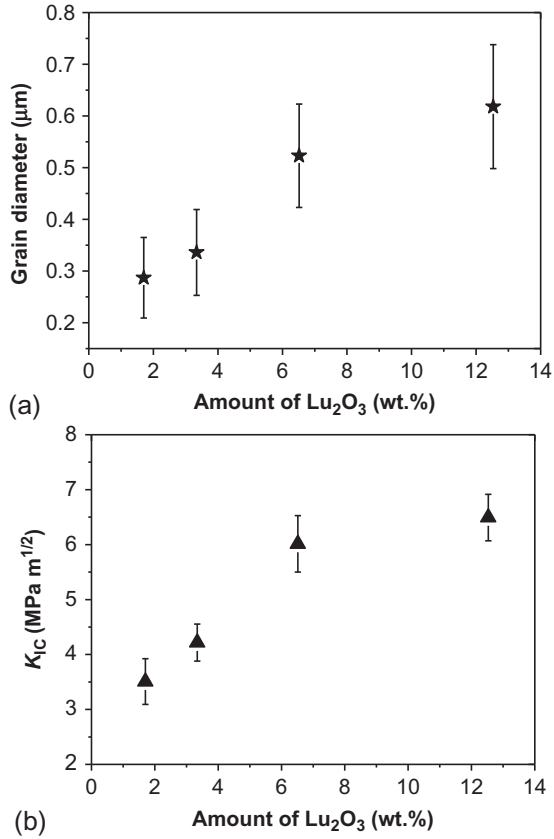

Figure 2.13 Influence of the amount of Lu_2O_3 additive on the (a) grain size and (b) fracture toughness of the Si_3N_4 ceramics.
Adapted from Guo et al. (2003).

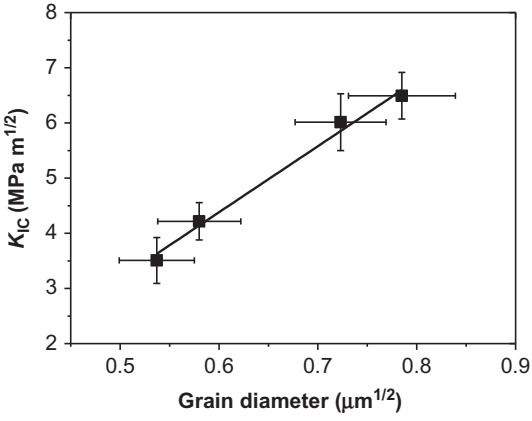

Figure 2.14 Relationship between the fracture toughness and the grain size of the Si_3N_4 ceramics sintered with Lu_2O_3 additive.
Adapted from Guo et al. (2003).

of Si_3N_4 with a decreasing ionic radius (from La to Lu) in the case of the Si_3N_4 sintered with Sm_2O_3 (see Figure 2.11). The lowest value of fracture toughness for this material was reported to be 3.6 ± 0.31 MPa $m^{1/2}$. They found that an apatite type of secondary crystalline phase with the formula of $Sm_{10}(SiO_4)_6N_2$ caused this deterioration in the fracture toughness. Such an apatite phase usually possesses a CTE of 1×10^{-5} K^{-1} (Sun et al., 2008; Mitomo et al., 1982), which is much higher in comparison with Si_3N_4 (3×10^{-6} K^{-1}) or $RE_2Si_2O_7$ (4×10^{-6} K^{-1}) (Lojanová et al., 2010). Therefore, the presence of the apatite phase located at the multi-grain junctions with approximately three times higher thermal expansion coefficient compared to the major silicon nitride phase resulted in the formation of significant residual tensile stresses. Such tensile stresses significantly deteriorated the fracture behavior of the Si_3N_4 ceramics sintered with Sm_2O_3 when compared to the other Si_3N_4 ceramics with the $RE_2Si_2O_7$ type of the grain boundary phases. This result proves the conclusion of many authors: in addition to the microstructural factors, the phase composition and the chemistry of the secondary phases significantly affect the fracture behavior of Si_3N_4 at room temperature.

In order to confirm a direct influence of the RE-containing grain boundary glassy phase on the fracture behaviour of Si_3N_4, many studies have been conducted on the bulk glass compositions simulating the grain boundary composition of the Si_3N_4 ceramics (Lofaj et al., 2004; Hampshire and Pomeroy, 2004; Becher and Ferber, 2004). These results confirmed that the fracture toughness of the glasses doped with RE elements increased with the increasing CFS, which increases with a decreasing radius of RE^{3+}. In other words, the size of the ionic radius of RE^{3+} has a significant influence on the grain boundary glassy phase in the Si_3N_4 ceramics due to its influence on the bonding strength within the glass network.

As mentioned above, there is a discrepancy between the reported results on the influence of RE oxide additives on the fracture toughness of Si_3N_4. The additional additives modifying the final compositions and properties of the grain boundary phase are believed to be responsible for this contradiction. Contrary to the work of Lojanová et al. (2010) and Tatarko et al. (2010a,b) ($RE_2O_3 + SiO_2$), different RE oxide additives (La_2O_3, Gd_2O_3, Lu_2O_3) added in combination with MgO did not influence significantly the fracture toughness of Si_3N_4 with bimodal microstructures and the crystalline secondary phases at the grain boundaries (Becher et al., 2008). Moreover, Hyuga et al. (2004) showed that despite the similar microstructures, the fracture toughness of Si_3N_4 sintered with $Lu_2O_3 + SiO_2$ (4.3 MPa $m^{1/2}$) was significantly lower than that of Si_3N_4 doped with $Y_2O_3 + SiO_2$ (6.0 MPa $m^{1/2}$) or $Yb_2O_3 + SiO_2$ (6.4 MPa $m^{1/2}$). In the case of the Lu-containing Si_3N_4, the interfacial bonding is considered to be stronger than in the other two cases; therefore, the crack deflection at the grain boundaries did not occur. A weaker interfacial bonding in the case of Y–Si_3N_4 and Yb–Si_3N_4 led to a crack deflection and the improved toughness due to the crack bridging mechanism. Similarly, Satet and Hoffmann (2005) reported that the fracture toughness of bulk silicon nitride sintered with $RE_2O_3 + MgO$ increased with an increasing ionic radius of RE^{3+} from 5.5 MPa $m^{1/2}$ (Lu-doped Si_3N_4) to 7.2 MPa $m^{1/2}$ (Sm-doped Si_3N_4) (Figure 2.15). However, it must be pointed out that their investigated materials exhibited a fully amorphous grain boundary phase

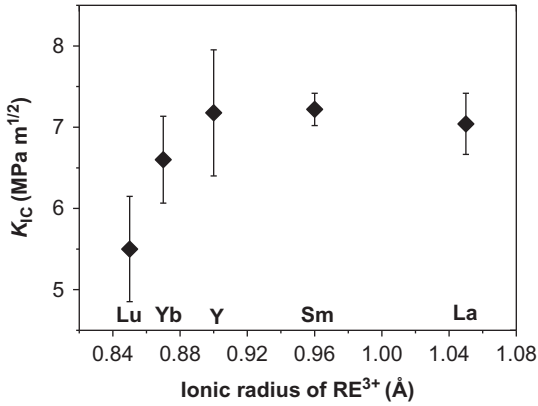

Figure 2.15 Fracture toughness of Si_3N_4 monoliths sintered with MgO, SiO_2, and various RE_2O_3, measured by single-edge V-notch beam method.
Adapted from Satet and Hoffmann (2005).

after the sintering. They also observed that debonding and pull-out events occurred more frequently in the materials with a larger RE^{3+}. The explanation for this behavior was given by the higher frequency of pull-out events and the frictional bridges as the consequence of the lower interfacial strength when the size of the RE^{3+} cation present in the grain boundary phase increased.

Such an observation is contrary to the results reported by Lojanová et al. (2010) and Tatarko et al. (2010a,b), where the fracture toughness increased with a decreasing ionic radius of RE^{3+} (Figure 2.11). There are two possible explanations for this discrepancy. The first one is a microstructural aspect, while the second is related to a compositional aspect. In Lojanová's and Tatarko's works, the microstructures varied with the addition of different RE oxides, i.e., the AR of the β-Si_3N_4 grains increased when La^{3+} was replaced with Lu^{3+} addition (Figure 2.3). However, Satet and Hoffmann (2005) made an effort to develop the materials with similar bimodal microstructures for all Si_3N_4 sintered with different RE elements. They changed the sintering conditions accordingly (mainly the temperature) in order to obtain the same/similar microstructural parameters (grain diameters, AR, and a number of the elongated β-Si_3N_4 grains) for all of the materials sintered with various RE oxide additives. Nevertheless, their Lu oxide containing Si_3N_4 material exhibited a higher AR compared to the materials doped with the other RE oxides. However, although the Si_3N_4 sintered with Lu_2O_3 additive exhibited the highest AR, the fracture toughness measured for this composition was the lowest among all investigated materials. This indicates that the compositional aspect was in their case more important than the microstructural one. It is important to note that in addition to SiO_2 and RE_2O_3, MgO was used as a sintering additive in their work (Satet and Hoffmann, 2005). As was already discussed above, the adsorption sites of RE elements on the surface of Si_3N_4 grains were studied, and it is believed that their location is known (see Section 2.2.4). On the other hand, a location of Mg in the nanometer-thick IGF (intergranular film) and/or grain–IGF interface has not yet been investigated. An understanding of the nature of the bonding within the IGF and along the interface between the Si_3N_4 grain and the IGF in ceramics with different chemical

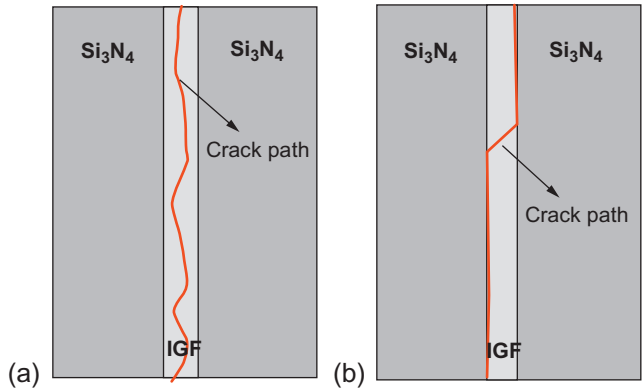

Figure 2.16 Possible crack path in the Si_3N_4-based materials doped by various RE_2O_3 additives; IGF - intergranular film (Lojanová et al., 2010).

compositions of the additives is required to provide an appropriate explanation for the crack propagation. For example, Becher et al. (2005) observed that an increase of Y/Al ratio in the self-reinforced silicon nitride sintered with Si–Al–Y oxynitride glass promotes debonding within the IGF due to the weakening of the glassy phase. Figure 2.16 shows a schematic picture of hypothetically possible ways of a crack path: (a) a crack propagates within the IGF and (b) a crack propagates through the interface between Si_3N_4 grain and IGF (interfacial debonding). It can be deduced that in the first case (a), when the crack path runs through the IGF, the fracture behavior of ceramics should be determined by the properties of the residual glass. When the fracture toughness of the Si_3N_4 with various RE additives increases with a decreasing ionic radius of RE^{3+} in the residual intergranular glassy phase (as reported by Lojanová et al. and Tatarko et al.), a trend is consistent with a dependence of the fracture toughness of glasses doped by the RE elements (Lofaj et al., 2003). Taking this similarity into account, it can be concluded that the crack most likely propagated within the IGF in the Si_3N_4 materials sintered with RE_2O_3 and SiO_2 sintering additives investigated by Lojanová et al. (2010) and Tatarko et al. (2010a,b). Therefore, the fracture toughness of the bulk Si_3N_4 materials is determined by the properties of the glassy phase and not by the strength of the bond between the Si_3N_4 grains and the IGF. A different crack path, which depends strongly on the glassy phase composition, can be one of the reasons for the dissimilarities in the fracture behavior of the Si_3N_4 materials with RE_2O_3 and MgO prepared by Satet and Hoffmann (2005). Knowledge of the chemical composition and the structure of the IGF is therefore crucial for this idea. A thorough research of IGF with the thickness of less than 1 nm is necessary. This investigation is rather problematic not only because of technical difficulties but also because of a questionable reliability of the data obtained from a limited number of HR-TEM micrographs. The first principle calculations coupled with HR-TEM analysis could shed more light on this problem (Shibata et al., 2005).

2.4.2 Fracture toughness of the Si_3N_4–SiC composites sintered with RE_2O_3

Generally, the fracture toughness of the Si_3N_4–SiC micro-/nanocomposites is slightly lower compared to the reference monolithic Si_3N_4 materials when both are sintered with the same RE oxide additives (see Figure 2.11). One plausible explanation of this observation is related to the finer microstructures of the Si_3N_4–SiC composites that which exhibit a lower average AR of the elongated Si_3N_4 grains (see the influence of RE on the microstructural evolution in Section 2.2.6). It is well known that in the finer microstructure of Si_3N_4, there is a lower possibility for the toughening mechanisms to take place in comparison with a coarser microstructure of Si_3N_4 ceramics.

More importantly, a relationship between the fracture toughness of Si_3N_4–SiC composites and the size of the RE cations showed a different dependence compared to that of the monolithic Si_3N_4 (Figure 2.11). The fracture toughness of the Si_3N_4–SiC micro-/nanocomposites containing Lu^{3+}, Yb^{3+}, and Y^{3+} linearly decreased from 5.0 MPa $m^{1/2}$ for the Si_3N_4–SiC with Lu_2O_3 to 4.2 MPa $m^{1/2}$ for the composite with Y_2O_3 additive. It is interesting to note that even the Si_3N_4–SiC composite with Sm_2O_3 additive apparently followed this tendency. As was discussed above (see Section 2.4.1), the Sm^{3+}-containing material clearly showed a deviation from the linear trend observed for the monolithic Si_3N_4 materials due to the different chemical composition (apatite phase vs. $RE_2Si_2O_7$). The same apatite phase was detected for the composite material; however, this did not lead to a deviation from the trend of the fracture toughness of the composites, as it did for the monoliths. On the other hand, the fracture toughness of the Si_3N_4–SiC composites sintered with Nd_2O_3 and La_2O_3 additives exhibited a different tendency. The values of fracture toughness were similar and almost constant as that measured for the composite sintered with Y_2O_3 additive (Lojanová et al., 2010).

These different trends observed when the RE additives are changed can be related to the different location of the SiC nanoparticles in the individual material compositions. It was already shown (see Section 2.2.6) that the distribution of the SiC nanoparticles in the RE oxide-doped micro-/nanocomposites changes with the changing of the RE elements. It was concluded that a lower viscosity of the liquid phase (larger RE elements) predominantly leads to the formation of *intra*-SiC inclusions (inside Si_3N_4 grains) and a higher viscosity (smaller RE elements) leads to the formation of *inter*-SiC (at the grain boundaries of Si_3N_4), as it is documented on the TEM micrographs in Figure 2.9. Therefore, a higher fraction of the intragranular SiC particles was observed for La- and Nd-doped materials than for the Lu- and Yb-doped Si_3N_4–SiC materials. A higher concentration of the SiC particles located inside the Si_3N_4 grains restrains the microstructural and/or compositional effect on the fracture toughness and consequently stops a tendency of decreasing toughness for the La- and Nd oxide-doped composites. It was reported that the SiC inclusions distributed in the Si_3N_4 matrix have a positive effect on the fracture toughness because of the formation of significant residual stresses in the silicon nitride matrix (Rouxel et al., 1993; Niihara, 1991). These stresses are formed due to different thermal expansion coefficients of these

two phases. Therefore, a lower fracture toughness of the composite materials with La_2O_3 and Nd_2O_3 indicates that intra-SiC nanoinclusions with an oxygen-rich surface layer helped the stresses around the SiC inclusions to be relaxed, and hence decreased the positive influence of SiC nanoinclusions on the fracture toughness. This oxygen-rich surface layer is formed by the carbothermal reduction of SiO_2 with carbon during sintering process (Hnatko et al., 2004). Moreover, if the fracture toughness of the Si_3N_4 monoliths is compared to the fracture toughness of the Si_3N_4–SiC composites for the individual RE_2O_3 additives, the lowest difference between these two values for one additives was observed for the Lu_2O_3 (Figure 2.11). A higher frequency of the SiC nanoparticles at the grain boundaries of Si_3N_4 in the Lu oxide-doped composite has a positive effect on the fracture toughness because of a higher incidence of the crack impediment events. A crack can be deflected by the intergranular SiC inclusions.

2.5 Future trends

Nowadays, some grades of silicon nitride have already been proven to be a cost-effective alternative to metal components in several commercial diesel engine applications (roller cam follower and fuel pump applications), when the life cycle cost of the system is taken into account. However, the cost of the product is a major factor in successful automotive applications even after a technical benefit has been demonstrated. Silicon nitride component costs generally depend on the raw material costs, material processing route, and product finishing costs.

This chapter has summarized that RE oxide additives are very useful for the processing of Si_3N_4 materials and the mechanical properties can be improved if RE oxides with a smaller cation size are used. However, one can see that the improvement in fracture toughness is just moderate, reaching ~10% of improvement when La is replaced by Lu for the monolithic Si_3N_4 and ~15% for the Si_3N_4–SiC composites. Similarly, RE oxides with a lower cation size have also been demonstrated to improve other mechanical properties of Si_3N_4 at room temperature, such as hardness, strength, and wear resistance, at the similar level (Tatarko et al., 2010a,b; Satet and Hoffmann, 2005; Lojanová et al., 2010). Despite this moderate improvement in the mechanical properties at room temperature, RE oxides have been found to improve significantly the mechanical properties at high temperatures by several orders of magnitude when La is replaced by Lu (Tatarko et al., 2013a,b; Lojanová et al., 2010).

Since RE oxide powders are considered expensive, particularly those with a smaller cation size (such as Lu_2O_3), there is an increased attention towards replacing them with other types of additives to densify Si_3N_4 ceramics for applications performing at room or moderate temperatures. On the other hand, RE oxides with a small ionic size are considered as the ideal candidates (thereby irreplaceable) for densification of Si_3N_4 ceramics for high-temperature applications, such as rotor and stator vanes for advanced gas turbines, valves, and cam roller followers for petrol and diesel engines. Therefore, the future trends and research on the use of RE elements in silicon nitride based materials are being focused on the materials for high-temperature applications.

More importantly, the superior effect of RE elements with a small cation size is even multifold when they are used in the Si_3N_4–SiC composite system (Tatarko et al., 2013a,b; Lojanová et al., 2010). A possibility of controlling the formation and distribution of SiC nanoparticles by changing the RE elements has also been reported in this chapter. Moreover, a technological process via *in situ* carbothermal reduction of silica could represent a suitable and cost-effective method of processing, as cheaper powders can be used as the initial mixture. The oxygen (in the form of SiO_2), which is considered to be an impurity for other technological processes, is used for the reaction with carbon to produce SiC nanoparticles during the sintering. The RE additives with a smaller cation size have been proven to promote the formation of SiC nanoparticles at the grain boundaries of Si_3N_4, leading to a significant improvement in the mechanical properties, particularly at high temperatures.

Therefore, it is reasonable to expect that future research will be carried out with the aim of amplifying the mutual effect of suitable RE additives and SiC nanoparticles in order to develop the Si_3N_4-based materials for high-temperature applications, such as rotor and stator vanes for advanced gas turbines, valves, and cam roller followers for petrol and diesel engines.

2.6 Sources of further information

One of the most authoritative sources of information, which provides an overview on silicon nitride ceramics, is a chapter on silicon nitride ceramics published in High Performance Non-oxide Ceramics II by G. Petzow and M. Herrmann, ISBN-10: 3540431322, 2002, pp. 46–166.

Among all the references mentioned in this chapter, the following are the most related to the study of the effect of RE oxide additives on the properties of microstructure and room temperature:

1. Lojanová, Š., Tatarko, P., Chlup, Z., Hnatko, M., Dusza, J., Lenčéš, Z., Šajgalík, P., 2010. Rare-earth element doped Si_3N_4/SiC micro/nano-composites-RT and HT mechanical properties. J. Eur. Ceram. Soc. 30, 1931–1944.
2. Tatarko, P., Lojanová, Š., Dusza, J., Šajgalík, P., 2010. Influence of various rare-earth oxide additives on microstructure and mechanical properties of silicon nitride based nanocomposites. Mater. Sci. Eng. A 527, 4771–4778.
3. Tatarko, P., Kašiarová, M., Dusza, J., Morgiel, J., Šajgalík, P., Hvizdoš, P., 2010. Wear resistance of hot-pressed Si_3N_4/SiC micro/nanocomposites sintered with rare-earth oxide additives. Wear 269, 867–874.
4. Becher, P.F., Shibata, N., Painter, G.S., Averill, F., van Benthem, K., Lin, H.-T., Waters, S. B., 2010. Observations on the influence of secondary Me oxide additives (Me = Si, Al, Mg) on the microstructural evolution and mechanical behavior of silicon nitride ceramics containing RE_2O_3 (RE = La, Gd, Lu). J. Am. Ceram. Soc. 93, 570–580.
5. Satet, R.L., Hoffmann, M.J., 2005. Influence of the rare-earth element on the mechanical properties of RE-Mg-bearing silicon nitride. J. Am. Ceram. Soc. 88, 2485–2490.

With regard to the influence of RE elements on the high-temperature properties, the following sources are recommended for detail study:

1. Lojanová, Š., Tatarko, P., Chlup, Z., Hnatko, M., Dusza, J., Lenčéš, Z., Šajgalík, P., 2010. Rare-earth element doped Si_3N_4/SiC micro/nano-composites-RT and HT mechanical properties. J. Eur. Ceram. Soc. 30, 1931–1944.
2. Tatarko, P., Kašiarová, M., Chlup, Z., Dusza, J., Šajgalík, P., Vávra, I., 2013. Influence of rare-earth oxide additives and SiC nanoparticles on the wear behavior of Si_3N_4-based composites at temperature up to 900 °C. Wear 300, 155–162.
3. Tatarko, P., Kašiarová, M., Dusza, J., Šajgalík, P., 2013. Influence of rare-earth oxide additives on the oxidation resistance of Si_3N_4-SiC nanocomposites. J. Eur. Ceram. Soc. 33, 2259–2268.
4. Park, H., Kim, H.W., Kim, H.E., 1998. Oxidation and strength retention of monolithic Si_3N_4 and nanocomposite Si_3N_4-SiC with Yb_2O_3 as a sintering aid. J. Am. Ceram. Soc. 81, 2130–2134.
5. Choi, H.J., Lee, J.G., Kim, Y.W., 1997. High temperature strength and oxidation behaviour of hot-pressed silicon nitride-disilicate ceramics. J. Mater. Sci. 1997, 1937–1942.
6. Šajgalík, P., Hnatko, M., Lofaj, F., et al., 2000. SiC/Si_3N_4 nano/micro-composite—processing, RT and HT mechanical properties. J. Eur. Ceram. Soc. 20, 453–462.
7. Dusza, J., Kovalčík, J., Hvizdoš, P., Šajgalík, P., Hnatko, M., Reece, M.J., 2005. Enhanced creep resistant silicon-nitride-based nanocomposite. J. Am. Ceram. Soc. 86, 1500–1503.
8. Kašiarová, M., Shollock, B., Boccaccini, A., Dusza, J., 2009. Microstructure and creep behavior of a Si_3N_4-SiC micronanocomposite. J. Am. Ceram. Soc. 92, 439–444.

Acknowledgments

The authors gratefully acknowledge the financial support of projects APVV-0161-11, APVV-0500-10, VEGA 2/0156/10, and VEGA 2/0057/14. Part of the work was realized within the frame of the projects NanoCEXmat II: ITMS No: 26220120035, NanoCEXmat I: ITMS No: 26220120019, and Centre of Excellence SAS CLTP-MREC.

References

Becher, P.F., Ferber, M.K., 2004. Temperature-dependent viscosity of SiREAl-based glasses as a function of N:O and RE:Al ratios (RE = La, Gd, Y, and Lu). J. Am. Ceram. Soc. 87, 1274–1279.

Becher, P.F., Sun, E.Y., Plucknett, K.P., Alexander, K.B., Hsueh, C.H., et al., 1998. Microstructural design of silicon nitride with improved fracture toughness: I, effects of grain shape and size. J. Am. Ceram. Soc. 81, 2821–2830.

Becher, P.F., Waters, S.B., Westmoreland, C.G., Riester, L., 2002. Compositional effects on the properties of Si-Al-RE-based oxynitride glasses (RE = La, Nd, Gd, Y, or Lu). J. Am. Ceram. Soc. 85, 897–902.

Becher, P.F., Painter, G.S., Lance, M.J., Li, S., Ikuhara, Y., 2005. Direct observations of debonding of reinforcing grains in silicon nitride ceramics sintered with yttria plus alumina additives. J. Am. Ceram. Soc. 88, 1222–1226.

Becher, P.F., Painter, G.S., Shibata, N., Satet, R.L., Hoffmann, M.J., Pennycook, S.J., 2006. Influence of additives on anisotropic grain growth in silicon nitride ceramics. Mater. Sci. Eng. A 422, 85–91.

Becher, P.F., Painter, G.S., Shibata, N., Waters, S.B., Lin, H.T., 2008. Effects of rare-earth (RE) intergranular adsorption on the phase transformation, microstructure evolution, and mechanical properties in silicon nitride with RE_2O_3 + MgO additives: RE = La, Gd, and Lu. J. Am. Ceram. Soc. 91, 2328–2336.

Becher, P.F., Shibata, N., Painter, G.S., Averill, F., van Benthem, K., Lin, H.-T., Waters, S.B., 2010. Observations on the influence of secondary Me oxide additives (Me = Si, Al, Mg) on the microstructural evolution and mechanical behavior of silicon nitride ceramics containing RE_2O_3 (RE = La, Gd, Lu). J. Am. Ceram. Soc. 93, 570–580.

Belmonte, M., Miranzo, P., Osendi, M.I., Gomes, J.R., 2009. Wear of aligned silicon nitride under dry sliding conditions. Wear 266, 6–12.

Choi, H.J., Lee, J.G., Kim, Y.W., 1997. High temperature strength and oxidation behaviour of hot-pressed silicon nitride-disilicate ceramics. J. Mater. Sci. 1997, 1937–1942.

Choi, H.J., Lee, J.G., Kim, Y.W., 1999. Oxidation behavior of hot-pressed Si_3N_4 with Re_2O_3 (RE = Y, Yb, Er, La). J. Eur. Ceram. Soc. 19, 2757–2762.

Cinibulk, M.K., Thomas, G., Johnson, S.M., 1992a. Fabrication and secondary-phase crystallization of rare-earth disilicate-silicon nitride ceramics. J. Am. Ceram. Soc. 75, 2037–2043.

Cinibulk, M.K., Thomas, G., Johnson, S.M., 1992b. Strength and creep behavior of rare-earth disilicate-silicon nitride ceramics. J. Am. Ceram. Soc. 75, 2050–2055.

Dusza, J., Kovalčík, J., Hvizdoš, P., Šajgalík, P., Hnatko, M., Reece, M.J., 2005. Enhanced creep resistant silicon-nitride-based nanocomposite. J. Am. Ceram. Soc. 86, 1500–1503.

Guo, S., Hiroskai, N., Yamamoto, Y., Nishimura, T., Mitomo, M., 2003. Hot-pressed silicon nitride ceramics with Lu_2O_3 additives: elastic moduli and fracture toughness. J. Eur. Ceram. Soc. 23, 537–545.

Guo, S., Hiroskai, N., Yamamoto, Y., Nishimura, T., Mitomo, M., 2004. Fracture toughness of hot-pressed $Lu_2Si_2O_7$-Si_3N_4 and $Lu_4Si_2O_7N_2$-Si_3N_4 ceramics and correlation to microstructure and grain-boundary phases. Ceram. Int. 30, 635–641.

Hampshire, S., Pomeroy, M.J., 2004. Effect of composition on viscosities of rare earth oxynitride glasses. J. Non-Cryst. Solids 344, 1–7.

Herrmann, M., Schuber, C., Rendtel, A., Hübner, H., 1998. Silicon nitride/silicon carbide nanocomposite materials: I, fabrication and mechanical properties at room temperature. J. Am. Ceram. Soc. 81, 1095–1108.

Hnatko, M., Galusek, D., Šajgalík, P., 2004. Low-cost preparation of Si_3N_4-SiC micro/nano composites by in-situ carbothermal reduction of silica in silicon nitride matrix. J. Eur. Ceram. Soc. 24, 189–195.

Hong, Z.L., Yoshida, H., Ikuhara, Y., Sakuma, T., Nishimura, T., Mitomo, M., 2002. The effect of additives on sintering behavior and strength retention in silicon nitride with RE-disilicate. J. Eur. Ceram. Soc. 22, 527–534.

Hyuga, H., Jones, M.I., Hirao, K., Yamauchi, Y., 2004. Influence of rare-earth additives on wear properties of hot-pressed silicon nitride ceramics under dry sliding conditions. J. Am. Ceram. Soc. 87, 1683–1686.

Kašiarová, M., Dusza, J., Hnatko, M., Šajgalík, P., 2006. Microstructure and fracture-mechanical properties of carbon derived Si_3N_4 + SiC nanomaterials. Mater. Sci. Eng. C 26, 862–866.

Kašiarová, M., Shollock, B., Boccaccini, A., Dusza, J., 2009. Microstructure and creep behavior of a Si_3N_4-SiC micronanocomposite. J. Am. Ceram. Soc. 92, 439–444.

Kašiarová, M., Tatarko, P., Burik, P., Dusza, J., Šajgalík, P., 2014. Thermal shock resistance of Si_3N_4 and Si_3N_4-SiC ceramics with rare-earth oxide sintering additives. J. Eur. Ceram. Soc. 34, 3301–3308.

Kitayama, M., Hirao, K., Kanzaki, S., 2006. Effect of rare-earth oxide additives on the phase transformation rates of Si_3N_4. J. Am. Ceram. Soc. 89, 2612–2618.

Kleebe, H.J., Pezzotti, G., Ziegler, G., 1999. Microstructure and fracture toughness of Si_3N_4 ceramics: combined roles of grain morphology and secondary phase chemistry. J. Am. Ceram. Soc. 82, 1857–1867.

Koh, Y.H., Kim, H.W., Kim, H.E., 2001. Mechanical properties and oxidation resistance of Si_3N_4-SiC nanocomposites. Scr. Mater. 44, 2069–2073.

Krämer, M., Hoffmann, M.J., Petzow, G., 1993. Grain growth studies of silicon nitride dispersed in an oxynitride glass. J. Am. Ceram. Soc. 76, 2778–2784.

Krämer, M., Wittmuss, D., Kuppers, H., Hoffmann, M.J., Petzow, G., Lofaj, F., 1994. Relations between crystal structure and growth morphology of β-Si_3N_4. J. Cryst. Growth 140, 157–166.

Liu, M., Nemat-Nasser, S., 1998. The microstructure and boundary phases of in-situ reinforced silicon nitride. Mater. Sci. Eng. A 254, 242–252.

Lofaj, F., Hvizdoš, P., Dorčáková, F., Satet, R.L., Hoffmann, M.J., de Arellano López, A.R., 2003. Indentation moduli and microhardness of RE-Si-Mg-O-N glasses (RE = Sc, Y, Sm, Yb and Lu) with different nitrogen content. Mater. Sci. Eng. A 357, 181–187.

Lofaj, F., Satet, R.L., Hoffmann, M.J., de Arellano López, A.R., 2004. Thermal expansion and glass transition temperature of the rare-earth doped oxynitride glasses. J. Eur. Ceram. Soc. 24, 3377–3385.

Lojanová, Š., Tatarko, P., Chlup, Z., Hnatko, M., Dusza, J., Lenčéš, Z., Šajgalík, P., 2010. Rare-earth element doped Si_3N_4/SiC micro/nano-composites-RT and HT mechanical properties. J. Eur. Ceram. Soc. 30, 1931–1944.

Mitomo, M., Izumi, F., Horiuchi, S., Matsui, Y., 1982. Phase relationships in the system Si_3N_4–SiO_2–La_2O_3. J. Mater. Sci. 17, 2359–2366.

Niihara, K., 1991. New design concept of structural ceramics-ceramic nanocomposites. J. Ceram. Soc. Jpn. 99, 974–982.

Painter, G.S., Averill, F.W., Becher, P.F., Shibata, N., van Benthem, K., Pennycook, S.J., 2008. First-principles study of rare earth adsorption at β-Si_3N_4 interfaces. Phys. Rev. B 78, 214206-1–214206-9.

Park, H., Kim, H.E., Niihara, K., 1997. Microstructural evolution and mechanical properties of Si3N4 with Yb2O3 as a sintering additive. J. Am. Ceram. Soc. 80, 750–756.

Park, H., Kim, H.W., Kim, H.E., 1998a. Oxidation and strength retention of monolithic Si_3N_4 and nanocomposite Si_3N_4-SiC with Yb_2O_3 as a sintering aid. J. Am. Ceram. Soc. 81, 2130–2134.

Park, H., Kim, H.E., Niihara, K., 1998b. Microstructure and high-temperature strength of Si_3N_4-SiC nanocomposite. J. Eur. Ceram. Soc. 18, 907–914.

Peterson, I.M., Tien, T.Y., 1995. Effect of the grain boundary thermal expansion coefficient on the fracture toughness in silicon nitride. J. Am. Ceram. Soc. 78, 2345–2352.

Petzow, G., Herrmann, M., 2002. Silicon nitride ceramics. In: High Performance Non-oxide Ceramics II. Springer, Berlin, Heidelberg, ISBN: 978-3-540-43132-9, pp. 46–166.

Poorteman, M., Descamps, P., Cambier, F., Plisner, M., Canonne, V., Descamps, J.C., 2003. Silicon nitride/silicon carbide nanocomposite obtained by nitridation of SiC: fabrication and high temperature mechanical properties. J. Eur. Ceram. Soc. 23, 2361–2366.

Rouxel, T., Wakai, F., Brito, M.E., Iwamoto, A., Izaki, K., 1993. Intragranular crack deflection and crystallographic slip in Si_3N_4/SiC nano-composites. J. Eur. Ceram. Soc. 11, 431–438.

Šajgalík, P., Dusza, J., Hoffmann, M.J., 1995. Relationship between microstructure, toughening mechanism, and fracture toughness of reinforced silicon nitride ceramics. J. Am. Ceram. Soc. 78, 2619–2624.

Šajgalík, P., Hnatko, M., Lofaj, F., et al., 2000. SiC/Si_3N_4 nano/micro-composite—processing, RT and HT mechanical properties. J. Eur. Ceram. Soc. 20, 453–462.

Sasaki, G., Nakase, H., Suganuma, K., Fujita, T., Niihara, K., 1992. Mechanical properties and microstructure of Si_3N_4 matrix composite with nano-meter scale SiC particles. J. Ceram. Soc. Jpn. 100, 536–540.

Satet, R.L., Hoffmann, M.J., 2000. Experimental evidence of the impact of rare-earth elements on particle growth and mechanical behaviour of silicon nitride. J. Am. Ceram. Soc. 88, 2485–2490.

Satet, R.L., Hoffmann, M.J., 2005. Influence of the rare-earth element on the mechanical properties of RE-Mg-bearing silicon nitride. J. Am. Ceram. Soc. 88, 2485–2490.

Shibata, N., Pennycook, S.J., Gosnell, T.R., Painter, G.S., Shelton, W.A., Becher, P.F., 2004. Observation of rare-earth segregation in silicon nitride ceramics at subnanometre dimensions. Nature 428, 730–732.

Shibata, N., Painter, G.S., Satet, R.L., Hoffmann, M.J., Pennycook, S.J., Becher, P.F., 2005. Rare-earth adsorption at intergranular interfaces in silicon nitride ceramics: subnanometer observations and theory. Phys. Rev. B 72, 140101-1–140101-4.

Sun, E.Y., Becher, P.F., Hsueh, C.H., Painter, G.S., Waters, S.B., Hwang, S.L., Hoffmann, M.J., 1999. Debonding behavior between β-Si_3N_4 whiskers and oxynitride glasses with or without an epitaxial β-SiAlON interfacial layer. Acta Mater. 47, 2777–2785.

Sun, Z., Li, M., Li, Z., Zhou, Y., 2008. Hot corrosion of γ-$Y_2Si_2O_7$ in strongly basic Na_2CO_3 molten salt environment. J. Eur. Ceram. Soc. 28, 259–265.

Tatarko, P., Lojanová, Š., Dusza, J., Šajgalík, P., 2010a. Influence of various rare-earth oxide additives on microstructure and mechanical properties of silicon nitride based nanocomposites. Mater. Sci. Eng. A 527, 4771–4778.

Tatarko, P., Kašiarová, M., Dusza, J., Morgiel, J., Šajgalík, P., Hvizdoš, P., 2010b. Wear resistance of hot-pressed Si_3N_4/SiC micro/nanocomposites sintered with rare-earth oxide additives. Wear 269, 867–874.

Tatarko, P., Kašiarová, M., Chlup, Z., Dusza, J., Šajgalík, P., Vávra, I., 2013a. Influence of rare-earth oxide additives and SiC nanoparticles on the wear behavior of Si_3N_4-based composites at temperature up to 900 °C. Wear 300, 155–162.

Tatarko, P., Kašiarová, M., Dusza, J., Šajgalík, P., 2013b. Influence of rare-earth oxide additives on the oxidation resistance of Si_3N_4-SiC nanocomposites. J. Eur. Ceram. Soc. 33, 2259–2268.

Tian, L., Zhou, Y., Zhou, W.L., 1998. SiC nanoparticle-reinforced Si_3N_4 matrix composites. J. Mater. Sci. 33, 797–802.

Wang, C.M., Pan, X., Hoffmann, M.J., Cannon, R.M., Rühle, M., 1996. Grain boundary films in rare-earth-glass-based silicon nitride. J. Am. Ceram. Soc. 79, 788–792.

Ziegler, G., Heinrich, J., Wötting, G., 1987. Relationships between processing, microstructure and properties of dense and reaction-bonded silicon nitride. J. Mater. Sci. 22, 3041–3086.

Ziegler, A., Idrobo, J.C., Cinibulk, M.K., Kisielowski, C., Browning, N.D., Ritchie, R.O., 2004. Interface structure and atomic bonding characteristics in silicon nitride ceramics. Science 306, 1768–1770.

This page intentionally left blank

Toughening mechanisms in epoxy/graphene platelets composites

3

Q. Meng, S. Araby, J. Ma
School of Engineering, University of South Australia (UniSA), Salisbury, SA, Australia

3.1 Introduction

This chapter mainly reviews the toughening mechanism of epoxy/graphene platelets (GnPs) composites. Epoxy resins are one of the thermoset materials most commonly used in industry due to their unique properties, including high chemical resistance to severe corrosive conditions; good adhesion to a wide range of materials; good physical properties, such as high strength, hardness, and abrasion resistance; and ease of processing that needs no specific facilities or high temperatures (Zubeldia et al., 2004). Nevertheless, most epoxy resins are inherently brittle, implying poor resistance to crack initiation and growth (Kanga et al., 2001; Mark et al., 1995); this is caused by their highly cross-linked structure with aromatic rings in the backbone, making polymer chains difficult to slide past each other. Therefore, toughening epoxy is one of the most important research topics over the past decades. Extensive studies have thus been conducted on toughening epoxy by adding either micron-sized fillers or nanoscale fillers.

The development of nanotechnology has led to reduction in the filler size of composites from micron-scale to nanoscale. This reduction conceptually produces an increase in the total particle surface area per unit volume and a reduction in the interparticle distance. Therefore, nanocomposites produce superior performance compared to their peer micron-composites, creating bright prospects with regard to industrial applications. Figure 3.1 shows the effect of filler size on the surface–surface interparticle distance and total particle surface area in a 5 vol% polymer composite. The surface–surface interparticle distance in the composite increases linearly with the filler size, while the interparticle total surface area demonstrates a significant reduction. Within nanoscale (from 1 to 100 nm as shown in a rectangle in Figure 3.1), the total surface area of nanoparticles enhances more significantly than micron particles. Therefore, nanoparticles are able to contribute more interface area with matrices to restrain the matrix molecular deformation under loading.

Conventional toughening is achieved by the incorporation of elastomers into epoxy, leading to loss of rigidity and decrease of thermal properties. In addition to elastomers, rigid fillers including silica and clay have been employed for improving

Toughening Mechanisms in Composite Materials. http://dx.doi.org/10.1016/B978-1-78242-279-2.00003-2

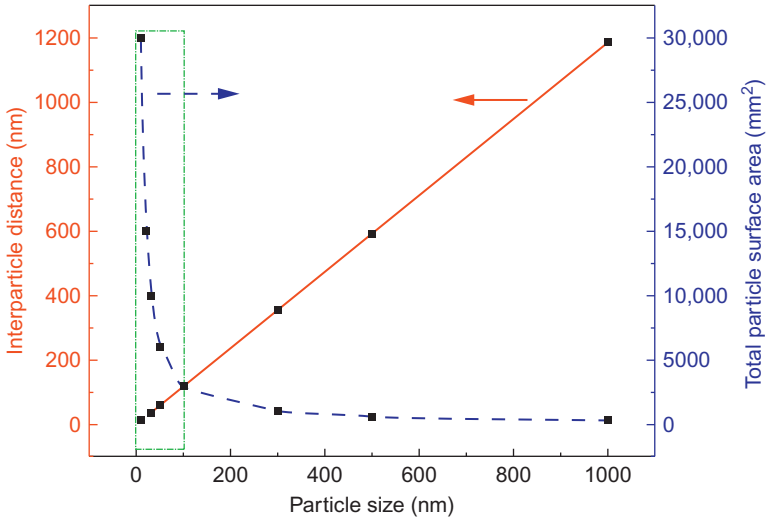

Figure 3.1 Effect of particle size on surface–surface interparticle distance and total particle surface area in 1 mm^3 of a 5 vol% composite.

toughness without sacrificing rigidity (Ma et al., 2008; Zaman et al., 2011a,b). However, rigid additives cannot effectively stabilize and stop crack propagation (Buchman et al., 2009).

Over the past two decades, carbon nanomaterials have been extensively studied, including fullerenes, nanofibers, and nanotubes. Atomically thin graphene is now hailed as the latest rising star in material science after its isolation by Novoselov et al. (2004). Graphene has attracted enormous interest due to its exceptional properties—Young's modulus 1 TPa, fracture strength 130 GPa, and enormous electron mobility and thermal conductivity values (Balandin, 2011). Therefore, graphene could potentially produce superior toughening effects and other functional properties compared to previous studies (Rafiee et al., 2009; Ramanathan et al., 2008).

3.2 Graphene and its derivatives

3.2.1 From graphene to graphene oxide

Pristine graphene is not very compatible with polymers due to its inert surface and lack of edge defects (Banhart et al., 2011). Hence, graphene oxide (GnO) (Zhu et al., 2010) has been widely studied by taking advantage of its rich functional groups that can be used for surface modification to improve its compatibility with polymer matrix (Potts et al., 2011). However, all these efforts start with highly oxidized graphite and short-chain surfactants, and this implies the necessity for reduction, which is inappropriate

for the mass production of functional graphene-based materials (Singh et al., 2011; Zhu et al., 2010). In addition, even the reduced GnO is limited by low structural integrity, implying unsatisfactory electrical and thermal conductivities (Zaman et al., 2012b). As a result, GnPs (also called graphene nanoplatelets) consisting of a few layers of graphene have been developed, which feature cost-effectiveness, high structural integrity, and modified surface for compounding with other materials (Zaman et al., 2012a).

3.2.2 Characteristic of GnPs

A GnP refers to a nanosheet consisting of a few stacked layers of graphene, most often below ~10 nm in thickness. GnPs, a very recently developed graphene derivative used mainly for polymer composites, are different to graphite nanosheets and nanoplatelets; the latter are far thicker than 10 nm. The thickness determines whether these platelets can take the maximum advantages of the unique structure and striking functional and mechanical performance of graphene. It is of great importance to keep the GnP as thin as possible, because (i) the total number of GnPs and their total surface area in a given volume of a composite abruptly increase with the reduction in thickness, and (ii) low thickness reduces the negative effect of the poor through-plane functional and mechanical properties of graphene. Through the use of a model, the total number and surface area of graphene sheets in a 10 μm^3 composite at 1 vol% GnPs are illustrated in Figure 3.2a and b, respectively. Both the number and total surface area are dramatically reduced when GnP thickness increases from 1 to 10 nm; the reduction become far less obvious when the thickness is greater than 10 nm. Therefore, we propose 10 nm as the upper limit of the thickness.

We herein introduce two approaches to the fabrication of GnPs: (i) ultrasonication method and (ii) the combination of thermal shock with ultrasonication. These methods obviously play major roles in producing highly toughened composites with other desirably functional properties.

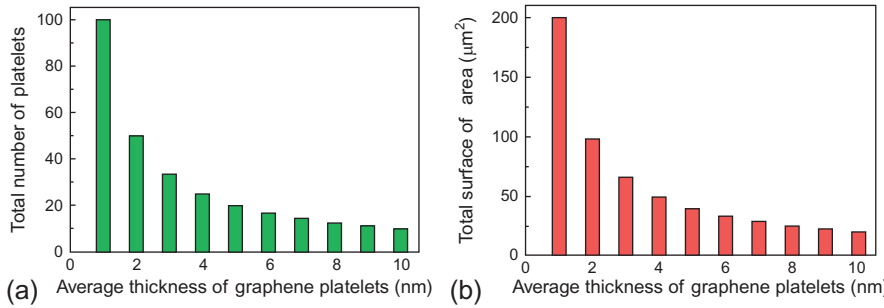

Figure 3.2 Number of graphene platelets (GnPs) and their total surface area in a given volume of matrix.

3.3 Fabrication, structure, properties, and toughening mechanisms of epoxy composites containing GnPs of ~10 nm in thickness

This section presents a study of epoxy/GnP nanocomposites with different interface strength and thus different morphology and properties, in particular focusing on fracture toughening mechanisms. The GnPs selected were fabricated by ultrasonicating a graphite intercalation compound (GIC) without any thermal or chemical treatment. Two types of epoxy-based nanocomposites were synthesized using unmodified GnPs and modified GnPs (m-GnPs).

3.3.1 Fabrication of GnPs by sonication

Figure 3.3 shows a schematic of GnP fabrication by ultrasonicating GIC without any other treatment. Specifically, 4 g of GIC was crushed in a mortar and pestle, and then immersed in acetone using a 400-ml metal container. The container was then covered and treated in an ultrasonication bath for 30 min to obtain a uniform suspension. (During sonication, graphite was able to split into GnPs (Zaman et al., 2011a,b).) With great care taken to leave the precipitate in the container, the suspension was removed to a glass beaker following the sonication process. Afterward, the beaker was covered and stored at room temperature for 2 h, during which the suspended GnPs precipitated. The precipitate was collected and dried. These steps were repeated until a required amount of GnPs was produced. When at least ten GnPs were randomly

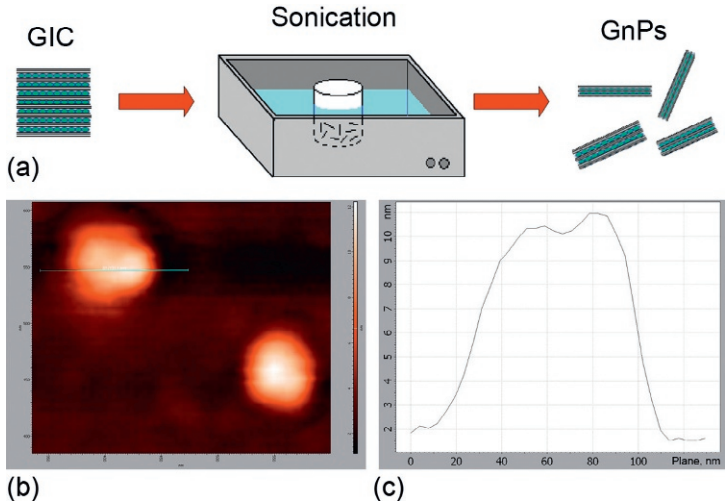

Figure 3.3 (a) Schematic of fabrication of GnPs by sonicating a graphite intercalation compound and (b–c) characterization of graphene platelets using atomic force microscopy. GnPs were dispersed in *N*-methyl-2-pyrrolidone (NMP).

selected and measured for thickness by atomic force microscopy (AFM), an average thickness 10.5 ± 0.4 nm was obtained. Figure 3.3b and c shows a representative measurement.

3.3.2 Interface modification of GnPs

3.3.2.1 Fabrication of m-GnPs

GnPs were suspended in tetrahydrofuran (THF) by sonication. The suspension was then transferred to a round-bottom flask equipped with a condenser. At a weight ratio 0.5 of 4,4′-methylene diphenyl diisocyanate (MDI) to graphite, MDI was dropped into the suspension within 3 min during mixing, followed by mixing for 6 h at 70–80 °C by a magnetic stirrer. The modified graphite is denoted as m-GnPs.

3.3.2.2 Fourier transform infrared spectroscopy (FT-IR) analysis

Figure 3.4 contains the FT-IR spectra of GIC, GnPs, and m-GnPs. A number of obvious absorption bands were found for GIC: (i) an absorption at 2327 cm^{-1} and a band between 3304 and 3500 cm^{-1}, corresponding to the presence of —OH group; (ii) two absorption at 1043 and 1144 cm^{-1} relating to the presence of —S═O group; (iii) absorptions at 1655 and 873 cm^{-1} caused by the stretching vibration of —C═O and —C—O—, implying the existence of carboxyl group. Regarding GnPs, the intensity of all absorption bands reduces dramatically, and this indicates the removal of intercalates via purification. Two absorption bands at 2348 cm^{-1} and at 3304–3500 cm^{-1} can be distinguished, implying the presence of —OH groups. After

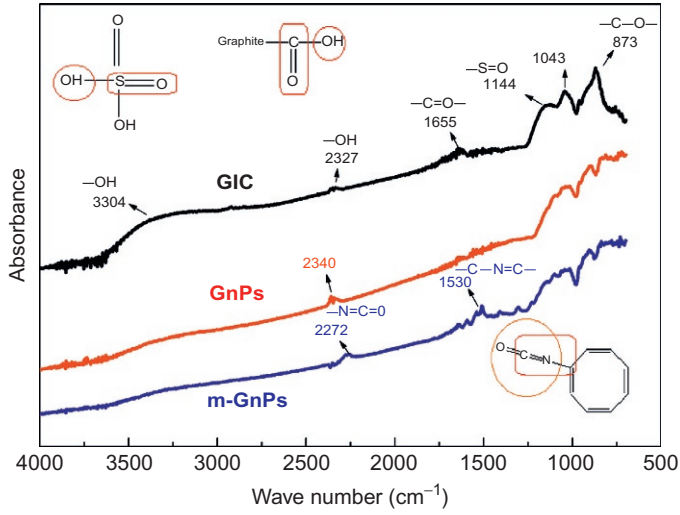

Figure 3.4 FT-IR spectra of GIC, GnPs, and m-GnPs.
Zaman et al. (2011b). Copyright © Elsevier Ltd. With permission.

modification by MDI, the absorption intensity at 3304 and 3500 cm^{-1} was further reduced and the absorption at 2348 cm^{-1} was shifted to low wave number—this means that the —OH groups were involved in and consumed by the modification—two new absorption peaks appear: one at 2272 cm^{-1} corresponding to the isocyanate —N═C═O stretching and another at 1530 cm^{-1} relating to the vibration of CNH groups (Kim et al., 2010; Kuan et al., 2005). In conclusion, MDI was grafted to GnPs through the modification.

3.3.2.3 X-ray diffractometry

Figure 3.5 contains the X-ray diffractometry (XRD) patterns of GIC, GnPs, m-GnPs, and their 1.99 vol% nanocomposite. GIC shows a twin-diffraction pattern, which indicates that the layer spacing of graphite was increased by intercalates during manufacturing by supplier. A sharp diffraction at $2\theta = 26.38°$ was observed for GnPs, corresponding to a d-spacing of 0.34 nm; this is caused by the removal of intercalates during purification. Upon modification, the diffraction broadens. Since great care was taken to ensure that the same amount was tested using an identical procedure for all the samples, the broadening phenomenon suggests that the modification changes the layer spacing. Actually, the —OH— groups of GnPs reacted with MDI during modification as analyzed in FT-IR section, which reduced the regularity of the stacked layers, thus broadening the diffraction of GnPs. When these two types of GnPs compound with epoxy, the nanocomposites with m-GnPs show a more broadened peak with a small

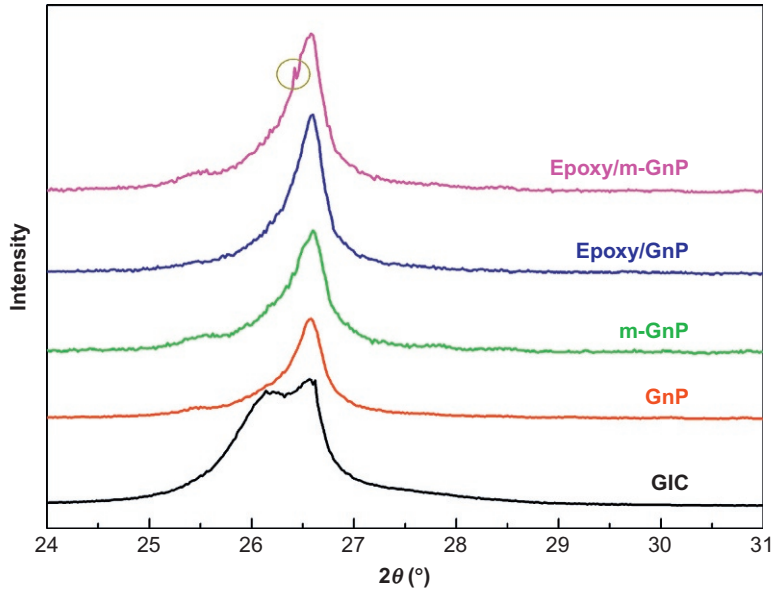

Figure 3.5 XRD patterns of GIC, GP, m-GP, and their nanocomposites.
Zaman et al. (2011b). Copyright © Elsevier Ltd. With permission.

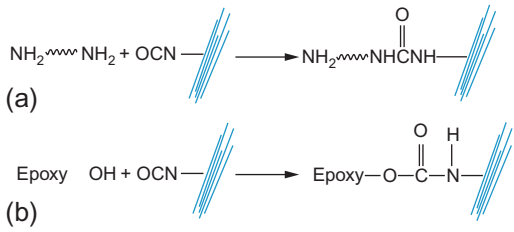

Figure 3.6 Reactions between grafted MDI and (a) molecules of J230, and (b) DGEBA.
Zaman et al. (2011b). Copyright © Elsevier Ltd. With permission.

shoulder as circled in Figure 3.5; this implies that the modification facilitates the interaction of matrix molecules into the layer spacing of GnPs. The intercalated matrix molecules—epoxy resin and hardener J230—reacted with the grafted MDI in Figure 3.6. Since these reactions are well known, no characterization is made herein. These reactions certainly build up a strong interface, supposedly leading to improved morphology and fracture toughness.

3.3.3 Fabrication of epoxy/GnP composites

A calculated amount (1–3 g) of GnPs (or m-GnPs) was added to 100 g THF in a metal container. The container was then covered and put through a sonication process for 30 min below 30 °C. Diglycidyl ether of bisphenol A (DGEBA) was added and mixed with a mechanical mixer at 100 °C for 60 min for two purposes: achieving a homogeneous dispersion of GnPs in epoxy matrix, and vaporizing THF. When hardener J230 was added, the temperature was controlled at 40–50 °C for 1 min to avoid premature curing, followed by a vacuum oven-degassing process to remove bubbles. The final mixture was poured into a rubber mold and heated by a programmed curing procedure.

3.3.4 Morphology of composites

The dispersion of GnPs in epoxy was investigated by TEM. Figure 3.7 contains a series of micrographs of the 1.99 vol% epoxy/GnP nanocomposite. In Figure 3.7a, a number of micron-sized clusters are observed. When magnified in Figure 3.7b, a typical cluster was found consisting of GnPs with a few exfoliated graphene layers as indicated by black arrows; this proved that graphite existed in the form of GnPs in the nanocomposites fabricated. Figure 3.7c provides the following information: coexistence of intercalation, as shown by white arrows; exfoliation, shown by black arrows; and the wrinkling of graphene layers, as circled. The coexistence is confirmed in Figure 3.7d, which also indicates a rolled structure of grapheme, as shown in a circle. The rolled structure may be caused by curing. The curing of epoxy is the formation of a highly cross-linked network by the reaction of epoxy molecules with hardener molecules, which is accompanied by a phase transition from liquid state to solid state. The platelets are scrolled or folded during curing to reduce configurational entropy. The thinner the platelets are, the more scrolls (resembling small-diameter single-walled carbon nanotubes (Gass et al., 2008; Meyer et al., 2007)) they create on the nanosheets' edges. This can be seen clearly in Figure 3.7c.

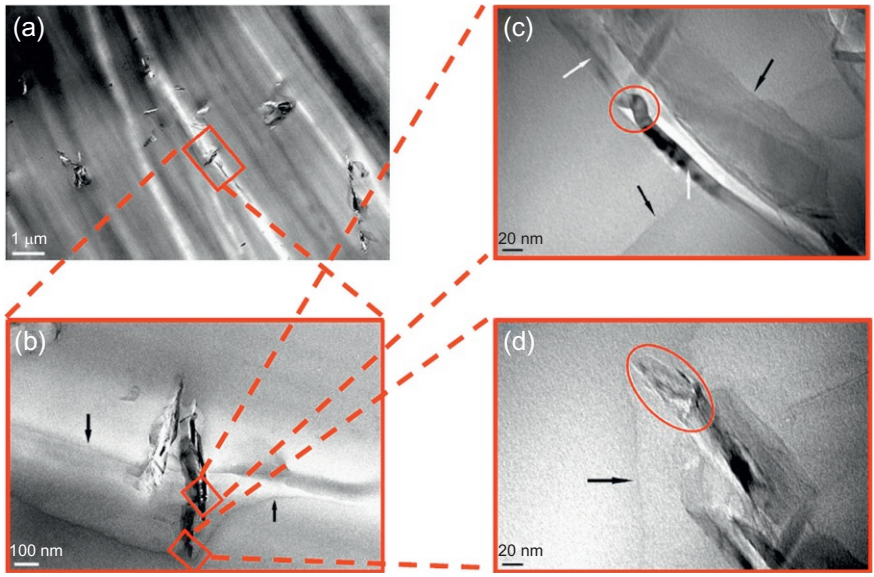

Figure 3.7 TEM micrographs of 1.99 vol% epoxy/GnP nanocomposite at different magnification levels of (a) 1 μm, (b) 100 nm, and (c, d) 20 nm.
Zaman et al. (2011b). Copyright © Elsevier Ltd. With permission.

Generally, a monolayer graphene has a tendency to scroll because it is thermodynamically unstable in a nanosize. When phase transition occurs in curing, (i) GnPs would form clusters, although they may disperse uniformly prior to curing; and/or (ii) the density and size of clusters would increase if the platelets had dispersed as clusters at the time of curing, because aggregation can reduce configurational entropy; this phenomenon is somewhat similar to the phase separation in liquid-rubber-toughened epoxy.

The morphology of the 1.99 vol% epoxy/m-GnP nanocomposite is shown in Figure 3.8. In comparison with epoxy/GnP nanocomposite, clusters appear less in quantity but larger in size, as demonstrated by a typical cluster in Figure 3.8a. When they are observed at higher magnification in Figure 3.8b and c, rolling is found to be predominant, as shown in the circles. Rolling is further confirmed in Figure 3.8d, which indicates the dispersion of graphene layers.

Comparing Figures 3.7 and 3.8 leads to a conclusion that more mono- or multi-graphene layers were found for epoxy/m-GnP nanocomposite, and that these platelets just scrolled. This is explained in light of modification and phase separation. Upon modification by MDI, platelets reacted with hardener J230 during curing; the reaction separated the platelets into thinner ones, as indicated by the increased number of graphene layers in Figure 3.8. Because these platelets have ultra-thin layered structures, they are more readily scrolled to reduce configurational entropy during curing, leading to more scrolls in Figure 3.8.

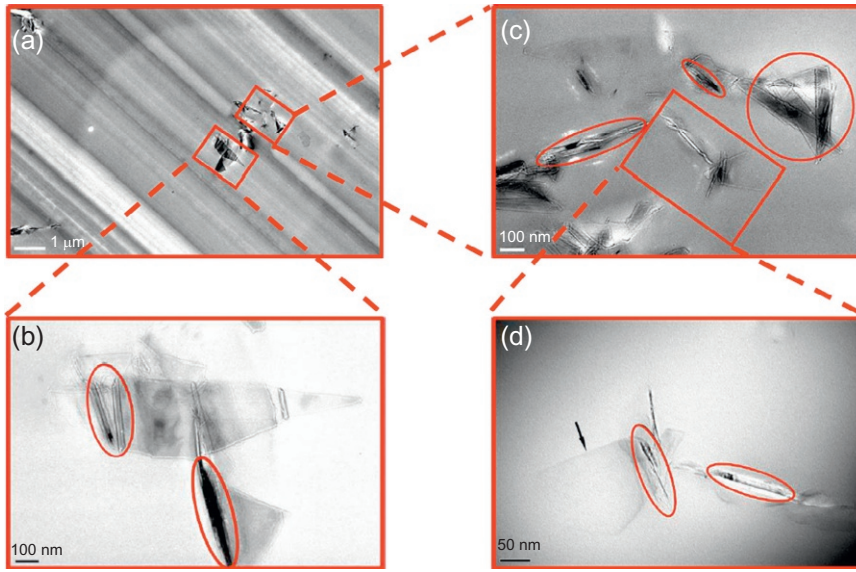

Figure 3.8 TEM micrographs of 1.99 vol% epoxy/m-GnP nanocomposite at different magnification levels of (a) 1 μm, (b and c) 100 nm, and (d) 50 nm.
Zaman et al. (2011b). Copyright © Elsevier Ltd. With permission.

3.3.5 Toughening mechanisms

Of all types of fillers, silicate layers have shown the greatest reinforcing effect for many polymers; the fillers' high specific total surface area, functionality, and cost-effective fabrication have attracted the most extensive research and development (Ma et al., 2003, 2004, 2005; Podsiadlo et al., 2007). However, silicate layers cannot toughen epoxy effectively; this is probably caused by its silicon-based composition and low density of grafting sites on surface. By contrast, GnPs consist of carbon—which is compatible with most polymers.

3.3.5.1 Fracture toughness and mechanical property

The plane-strain fracture toughness K_{1c} and critical strain energy release rate G_{1c} of all the composites are graphically shown in Figure 3.9. Epoxy/GnP nanocomposites show a greater increase in both properties at low filler content only, while a steady increase of toughness is observed for the epoxy/m-GnP before it dropped slightly at a high fraction of 2.76 vol%. At 1.99 vol% m-GnPs, the G_{1c} of neat epoxy increases from 157.3 to 472.3 J/m^2, by an increment of 200%; by contrast, the same fraction of GnPs improves the G_{1c} to 320.9 J/m^2, by an increment of merely 104%.

It is worth noting that GnPs increase Young's modulus and fracture toughness at low content 0.49–1.23 vol% and then these properties dramatically reduce

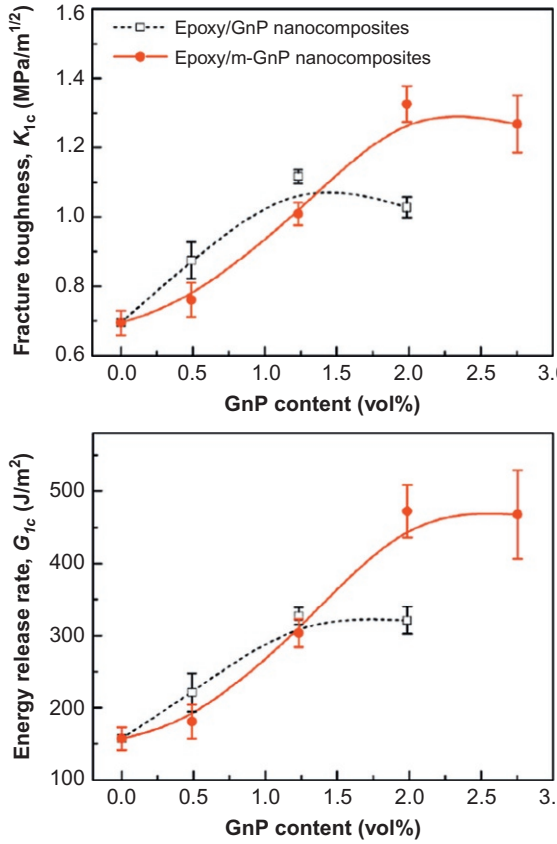

Figure 3.9 Fracture toughness and energy release rate of epoxy/GnP and epoxy/m-GnP nanocomposites. Zaman et al. (2011b). Copyright © Elsevier Ltd. With permission.

(Zaman et al., 2011a,b). This is explained in light of GnP modification. As shown in Figure 3.6, m-GnPs were modified by MDI; after modification, the unreacted MDI molecules were not removed for the simplicity of processing. These molecules bridged with epoxy molecules, locking GnPs inside clusters; this increased the cluster size while reducing the quantity of clusters, as supported by the comparison of Figures 3.7 and 3.8. The modification results in the following: (i) bridging the platelets with matrix molecules for high interface strength, (ii) promoting exfoliation, and (iii) increasing the cluster size and reducing the quantity of clusters. Hence, there are not as many clusters of m-GnPs as those of GnPs in the matrix. It means that GnPs create a higher stiffening and toughening effect at low content 0–1.23 vol% due to their higher cluster numbers than m-GnPs; at 1.99 vol%, the effect diminishes because their surface was not modified and more clusters mean more regions of weak interface. By contrast, 1.99 vol% m-GnPs provide a significant toughening effect due to their high interface strength and optimum dispersion capability.

The toughness improvement of GnPs and m-GnPs surpasses previous efforts in toughening epoxy using silicate layers (Dean et al., 2007; Frohlich et al., 2004;

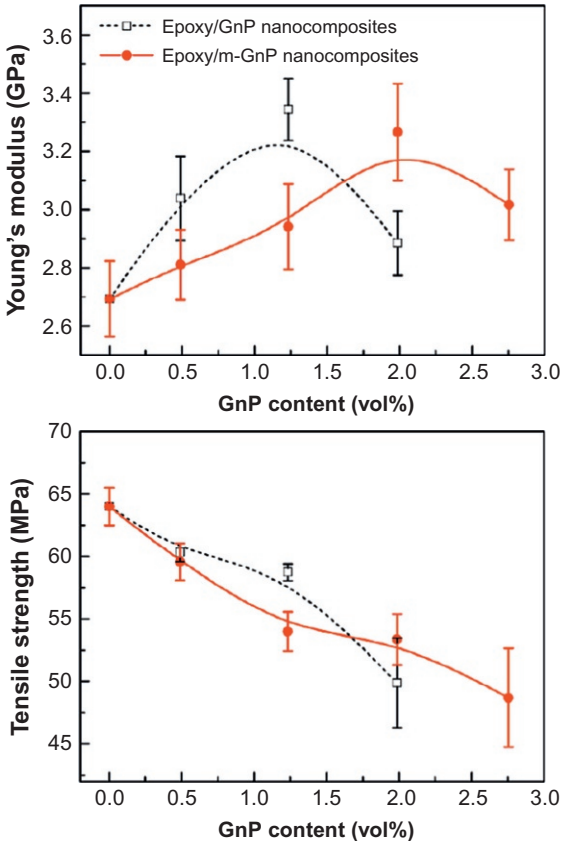

Figure 3.10 Young's modulus and tensile strength of epoxy/GnP and epoxy/m-GnP nanocomposites. Zaman et al. (2011b). Copyright © Elsevier Ltd. With permission.

Wang et al., 2005). Although GnPs have layered structures that are similar to silicate layers, they are highly effective in achieving prominent reinforcing or toughening effects, because the platelets that consist of graphene of 0.34 nm in thickness and ~1 μm in the lateral dimension are more compatible with hydrophobic polymer matrix than silicate layers.

Figure 3.10 shows the Young's modulus and tensile strength of neat epoxy and its nanocomposites at 0.49–2.76 vol%. Epoxy/GnP nanocomposites show a more prominent increase in modulus at 0.49–1.23 vol% but the stiffening effect nearly diminishes at 1.99 vol%, while the epoxy/m-GnP modulus steadily increases up to 1.99 vol% and drops at 2.76 vol%. The 1.99 vol% m-GnPs increase the modulus of neat epoxy from 2.69 to 3.27 GPa, by an increment of 21.6%, while the same fraction of GnPs increases the modulus to 2.89 GPa, by an increment of 7.4%. Although both nanocomposites show a reduction of tensile strength, epoxy/m-GnP indicates less reduction at 1.99 vol%. Overall, it can be concluded that interface strength of epoxy/GnP and epoxy/m-GnP makes less impact on tensile properties than toughness of the nanocomposites.

3.3.5.2 *Fractography analysis*

The fracture surface of compact tension (CT) specimen provides critical information in identifying fracture and toughening mechanisms for polymer nanocomposites. Since neat epoxy shows a smooth, featureless fracture surface (Le et al., 2010), its SEM micrographs are not shown in this study. Figure 3.11 contains the CT fracture surface of the 1.99 vol% epoxy/GnP nanocomposite. A stress-whitened zone of ~5 mm in height was observed in front of the crack tip in Figure 3.11a; a randomly selected region is magnified in Figure 3.11b, which indicates a few clusters as shown by white arrows, corresponding to the clusters observed in Figure 3.8a; fracture phenomena shown in Figure 3.11c includes voids and layer breakage as indicated by circles; Figure 3.11d demonstrates a few cracks.

In Figure 3.12a, the stress-whitened zone for epoxy/m-GnP nanocomposite is as high as ~11 mm, over 50% increment of the zone for the epoxy/GnP; this may indicate that the size-increased zone is able to consume more energy when a fracture occurs, corresponding to a higher degree of fracture toughness in Figure 3.9. Two features are shown in Figure 3.12b: a trench and clusters, as indicated by black arrows and white arrows, respectively. Trenches are more popular for epoxy/m-GnP nanocomposite in Figure 3.12 than for the epoxy/GnP in Figure 3.11; the appearance of tranches indicates a high degree of surface deformation, which consumes more fracture energy. The clusters in Figure 3.12b appear larger than those of the epoxy/GnP in Figure 3.11b, corresponding to TEM analysis (Figures 3.7 and 3.8). A typical region of the clusters is magnified in Figure 3.12c, showing a number of white dots. Since

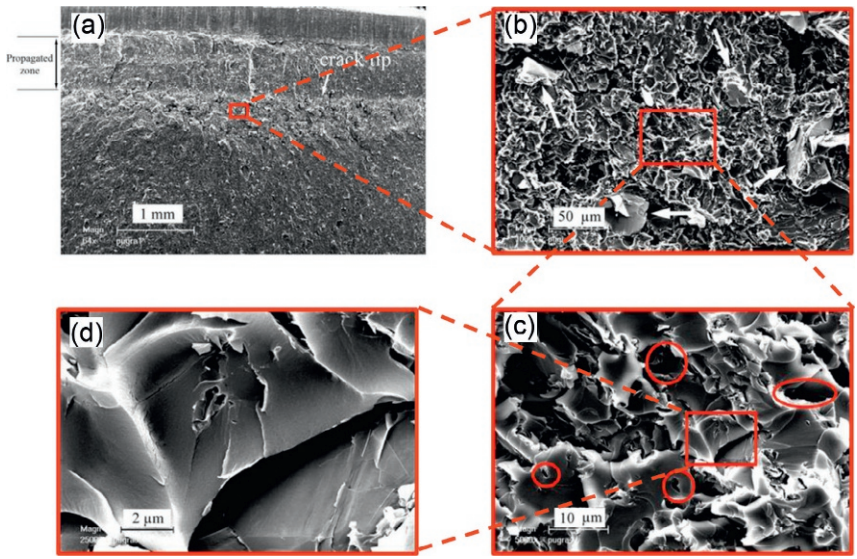

Figure 3.11 SEM micrograph of fracture surface of CT of the 1.99 vol% epoxy/GnP nanocomposite with crack propagating from top to bottom (b, c, d are the magnified images of the boxes of a). Note the white arrows in (b), indicating clusters.
Zaman et al. (2011b). Copyright © Elsevier Ltd. With permission.

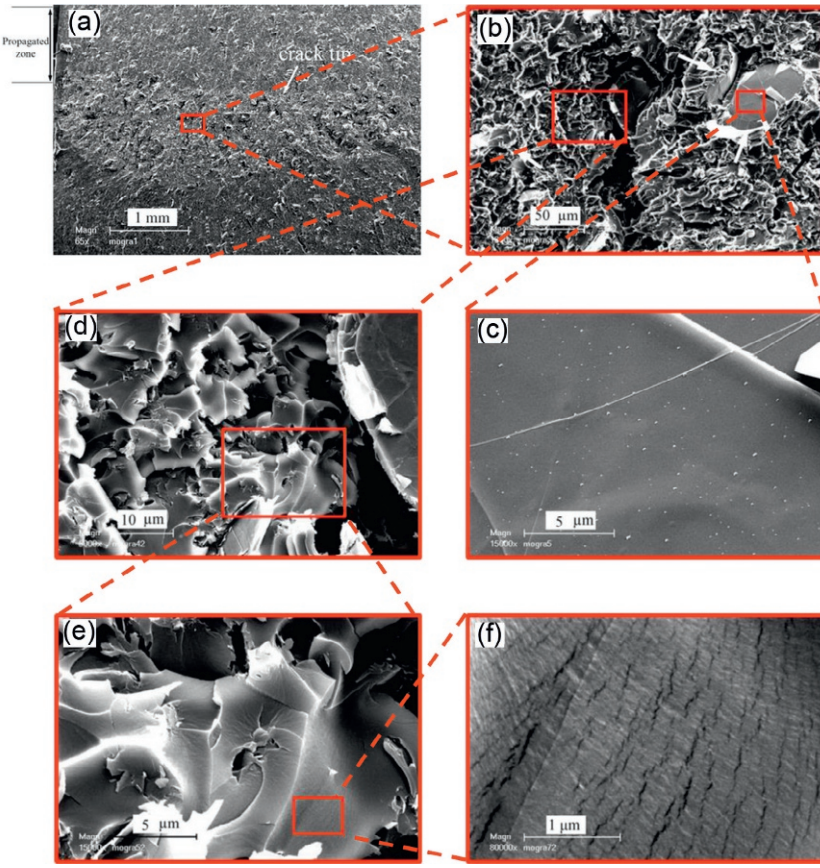

Figure 3.12 SEM micrograph of fracture surface of CT of the 1.99 vol% epoxy/m-GnP nanocomposite with crack propagating from top to bottom.
Zaman et al. (2011b). Copyright © Elsevier Ltd. With permission.

these dots were not found in the clusters in Figure 3.11, the dots must be organic molecules produced by the reaction of MDI with the hardener J230 during modification. Epoxy/m-GnP nanocomposite in Figure 3.12d shows a higher quantity of fracture phenomena—voids and layer breakage—than the epoxy/GnP in Figure 3.10c. A region randomly selected in Figure 3.12d is magnified in Figure 3.12e where much more tiny cracks are found; Figure 3.12f shows a clear image of the cracks which grow in the direction of crack propagation. While it is clear that all the voids and layer breakage occurred in GnPs, a new technique is needed to identify where microcracks start: matrix or GnPs. Elemental analysis of SEM to determine the carbon–oxygen atom ratio is conducted on neat graphite, neat epoxy, and the microcrack zone of epoxy/m-GnP fracture surface. At least five different locations were measured for each sample. Table 3.1 shows the comparison of the ratios of these samples. Since the C—O atom ratio of the microcrack zone is similar to that of neat graphite, these microcracks must initiate from GnPs and then grow under loading.

Table 3.1 Elemental analysis of neat graphite, neat epoxy, and microcracks of the nanocomposite

Materials	Neat graphite	Neat epoxy	Zone of microcrack of epoxy/m-GnP nanocomposite, 1.99 vol%
The atomic ratio of carbon to oxygen	10.0 ± 1.4	5.53 ± 0.19	10.8 ± 1.7

A proposed toughening mechanism for epoxy/GnP nanocomposites is crack deflection (Rafiee et al., 2009), which is the process by which an initial crack tilts and twists when it encounters a rigid inclusion. This generates an increase in the total fracture surface area and results in greater energy absorption as compared to the unfilled polymer material. The tilting and twisting of the crack front as it is forced to move out of the initial propagation plane also forces the crack to grow locally under mixed-mode (tensile/in-plane shear and tensile/antiplane shear) conditions. Crack propagation under mixed-mode conditions requires a higher driving force than in mode I (tension), which also results in higher fracture toughness of the material. However, neither SEM micrographs of fractured CT nor in-depth fractography analysis has shown to support this claim.

Based on observation and analysis in Figures 3.11 and 3.12, the toughening mechanisms of these two types of epoxy/GnPs nanocomposites are proposed as below: (1) when subjected to loading, a high level of stress concentration occurs at the sharp crack tip, which induces local dilation, since J230-cured epoxy is relatively ductile (see Figure 12 in Agarwal and Broutman, 1990). Stress concentrates around each GnP due to the difference in modulus and Poisson ratio between epoxy and GnPs. (2) With continued loading, fracture initiates (i) at the interface between GnPs and matrix, which is difficult to observe using SEM; and (ii) on the plane of a GnP where voids, layer breakage, and microcracks are formed as shown in Figures 3.10 and 3.11. (3) Upon further loading, the voids, layer breakage, and microcracks develop, causing catastrophic fracture. Since m-GnPs produced a stronger interface with matrix than GnPs, m-GnPs were able to carry a higher level of loading upon fracture, as indicated by the increased quantity of fracture features in Figure 3.12.

3.4 Fracture mechanisms of epoxy/GnPs nanocomposites—fabricated by a thermal-sonication approach

Studies on fabrication of expanded graphite and GnPs of over 10 nm in thickness have been well documented in reviews (Li and Zhong, 2011; Sengupta et al., 2011) as well as in Section 3.3. As discussed in Section 3.2.2, it is of great importance to keep the GnP thickness below 10 nm (Figure 3.2). In this section, GIC will be expanded using a common furnace, and the expanded product will be dispersed in a solvent by sonication to produce a new type of GnPs, each of which is thinner than 10 nm.

3.4.1 Fabrication of GnPs and its epoxy nanocomposite

1 g of GIC was carefully transferred into a crucible that had been preheated in a furnace at 700 °C. After 1 min of heat treatment, the crucible was moved out to sit on a ceramic for 30 s. The expanded product was then transferred into a container. The operator must wear a respirator, safety glasses, heat-resistant gloves, and closed shoes; the furnace should be placed in a fume cupboard to prevent inhaling hazard. 1 g of expanded product was dispersed in 100 g THF using a metal container. The container was covered and treated in an ultrasonic bath (200 W and 42 kHz) for 2 h to obtain a uniform suspension of GnPs; the temperature was controlled at ~10 °C by connecting the bath to a freezer, since low-temperature ultrasonication produced a better nanofiller dispersion than high temperature ultrasonication (Zaman et al., 2011a,b). As shown in Figure 3.13, the fabrication of epoxy/GnP nanocomposites is similar to the previous section. The hardeners used are J230 and 4,4′-diaminodiphenyl sulfone (DDS).

3.4.2 Analysis of GnPs

3.4.2.1 Atomic force microscopy

GnPs were first dispersed in THF at 1 wt% by ultrasonication, and then their suspension was dropped on a silicon wafer and dried. By randomly selecting and measuring 10 GnPs by AFM, we obtained an average thickness of 3.57 ± 0.50 nm. Figure 3.14a and b shows a typical measurement. Since previous research has shown that corrugation of graphene can increase its thickness to ~1 nm (Nemes-Incze et al., 2008), each of these GnPs may comprise three to four layers of graphene when dispersed in THF.

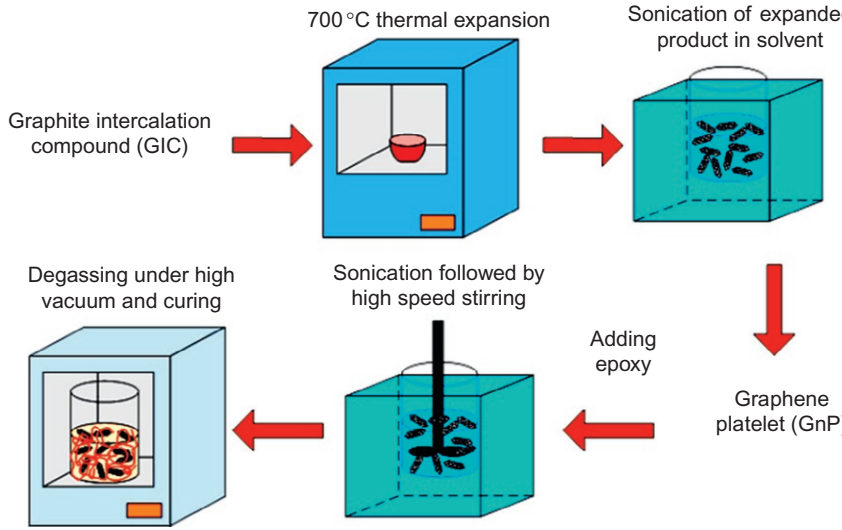

Figure 3.13 Fabrication of epoxy/graphene platelet and its nanocomposites.
Zaman et al. (2012a). Copyright © The Royal Society of Chemistry. With permission.

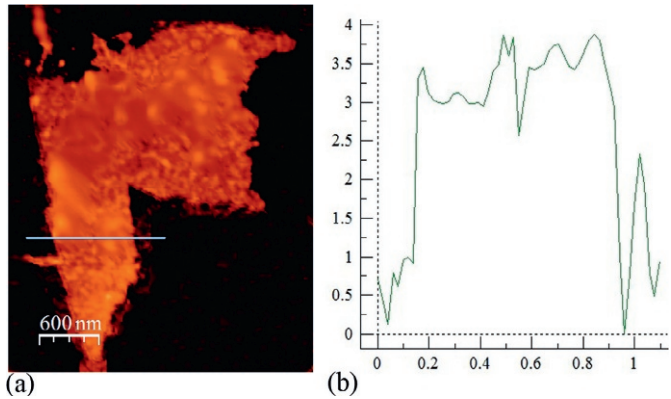

Figure 3.14 Characterization of graphene platelets using atomic force microscopy. Zaman et al. (2012a). Copyright © The Royal Society of Chemistry. With permission.

When GnPs were dispersed in a solvent *N*-methyl-2-pyrrolidone (NMP), their thickness was measured to be 2.51 ± 0.39 nm. It was observed that GnPs could suspend longer in NMP than in THF, implying that NMP is a better solvent to produce thinner GnPs although NMP is inconvenient for solution compounding due to its high-boiling point. By increasing the number of graphene layers from one to three, stiffness does not change and fracture strength reduces 23% from 130 to 101 GPa (Lee et al., 2009). Given that the fracture strength of most polymers ranges from 1 to 80 MPa, these GnPs are indeed sufficiently robust to toughen or reinforce polymers.

3.4.2.2 Raman spectrum

GIC and GnPs were examined as powders by Raman spectrometer regarding their hybridized carbon structure. In Figure 3.15, both samples show absorption at D, G, and 2D bands at around 1340, 1585, and 2690 cm^{-1}, respectively. The D band intensity corresponds to in-plane vibration of sp^3-hybridized carbon atoms, while the G band intensity refers to that of sp^2-hybridized carbon atoms (Gu et al., 2009; Shen et al., 2009). The I_D/I_G of GIC is merely 0.25, much lower than those of graphite oxide originated from the oxidation method (Hsiao et al., 2010; Wang et al., 2009a,b; Wang and Hu, 2011), implying that the starting GIC possesses far lower oxidation degree and thus sound structural integrity for high functionality and mechanical performance. Through thermal treatment using a common furnace, I_D/I_G reduces to 0.06 and this means an increase in quantity of sp^2-hybridized carbon atoms through thermal treatment using a common furnace. No virtual difference in the 2D band intensity between GIC and GnPs is seen, because both testings were conducted on powder samples. The high sp^2–sp^3-hybridized carbon atoms of GIC and the increased quantity of sp^2-hybridized carbon through thermal treatment are further confirmed by elemental analysis in Table 3.2, where the high C—O ratio observed for GIC is further enhanced through thermal treatment.

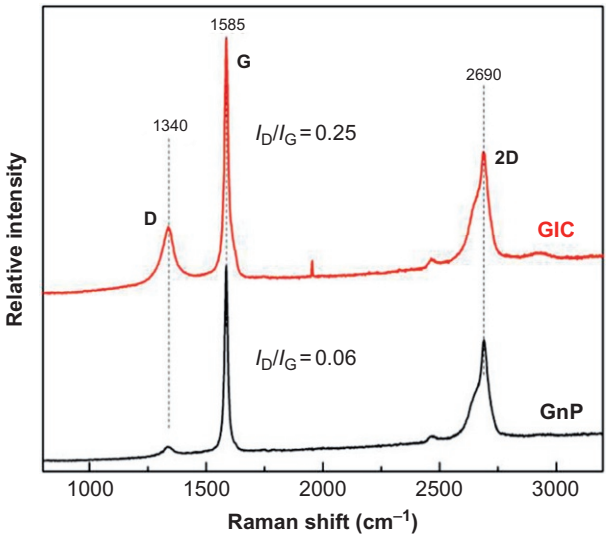

Figure 3.15 Characterization of graphene platelets using Raman spectrometer. Zaman et al. (2012a). Copyright © The Royal Society of Chemistry. With permission.

Table 3.2 Elemental analysis of GIC and GnPs

Name	C atomic ratio (%)	O atomic ratio (%)
GIC	83.8	16.2
GnPs	90.3	9.73

3.4.3 X-ray diffraction patterns of composites

Figure 3.16 contains the XRD patterns of two sets of epoxy/GnP nanocomposites: one was cured by polyoxypropylene (J230) and another by DDS. A wide diffraction from 11° to 28° observed for both sets are caused by the scattering of cured epoxy molecules, and a sharp diffraction at 26.7° is associated with layered crystalline GnPs. This diffraction angle corresponds to an interlayer spacing of $d_{002} = 3.35$ Å, determined from Bragg's law ($n\lambda = 2d \sin\theta$, where $\lambda = 1.5406$ Å). The appearance of this diffraction means that part or all of layered structure of GnPs are retained in the nanocomposites, which needs further investigation by TEM.

The diffraction intensity at 26.7° in both systems enhances with increase in GnPs content, and this implies that more platelets are stacked at higher fractions. In spite of the similarity between XRD patterns of these two groups of nanocomposites, analysis using the area under the diffraction shows difference. In Table 3.2, the area values for J230-cured system, nearly at all fractions, are larger than those for DDS-cured nanocomposites, indicating that GnPs disperse and exfoliate better in DDS-cured system. In Table 3.3, DDS features benzene groups. Benzene group-based molecules are well known for their affinity by π–π interaction with graphene (Rochefort and Wuest,

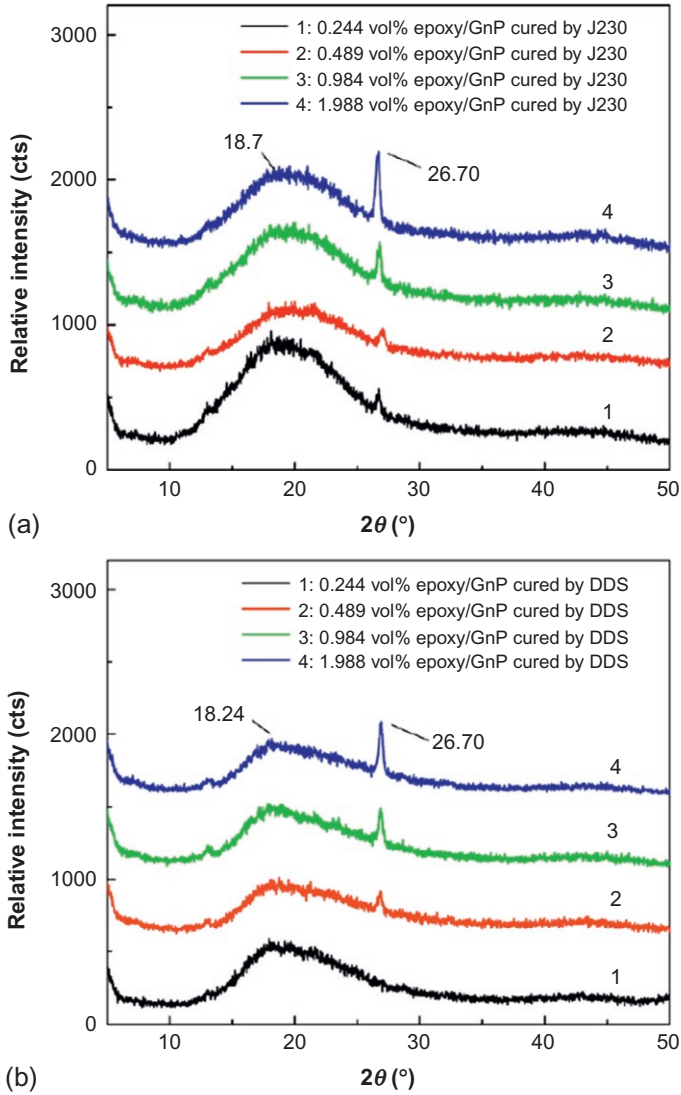

Figure 3.16 XRD plots of epoxy/GnP nanocomposites cured by (a) J230 and (b) DDS. All graphs were vertically shifted for clarity.
Zaman et al. (2012a). Copyright © The Royal Society of Chemistry. With permission.

Table 3.3 Integration area under diffraction at 26°

Materials	Area under diffraction at 26°	
	J230 cured system	DDS-cured system
0.244 vol%	47.7	Nil
0.489 vol%	45.7	50.1
0.984 vol%	89.8	82.9
1.988 vol%	177.2	140.0

2009; Su et al., 2011). When DDS was mixed with epoxy and GnPs, it was more readily to intercalate into the layer spacing of GnPs than J230; during curing, the intercalated DDS molecules reacted with epoxy molecules promoting the separation of platelets. Thus, DDS-cured nanocomposites show a higher degree of dispersion and exfoliation.

3.4.4 Morphology of composites

Figure 3.17 presents TEM micrographs of the 0.984 vol% epoxy/GnP nanocomposites cured by DDS. Two types of dispersion phase are observed in Figure 3.17a: uniformly dispersed GnPs of lateral dimension smaller than 1 μm and GnP clusters which are over a few microns in lateral size. The light horizontal band across the image would be a defect produced during microtoming. As marked by white arrows, cracks were initiated by microtoming within each cluster, indicating that clusters would act as defects posing a negative effect on the mechanical performance. When a part of a typical cluster was examined at a higher magnification in Figure 3.17b, it was found consisting of thin layers of graphene, a void, and thick aggregates.

In Figure 3.17c, these thin layers of graphene show rolled and corrugated structure, as pointed out by white arrows; these features would be produced by curing, as they are similar to what have been observed in epoxy/GnPs nanocomposites fabricated by ultrasonication and chemical modification (see Figure 3.8b in Section 3.3.5.2). When

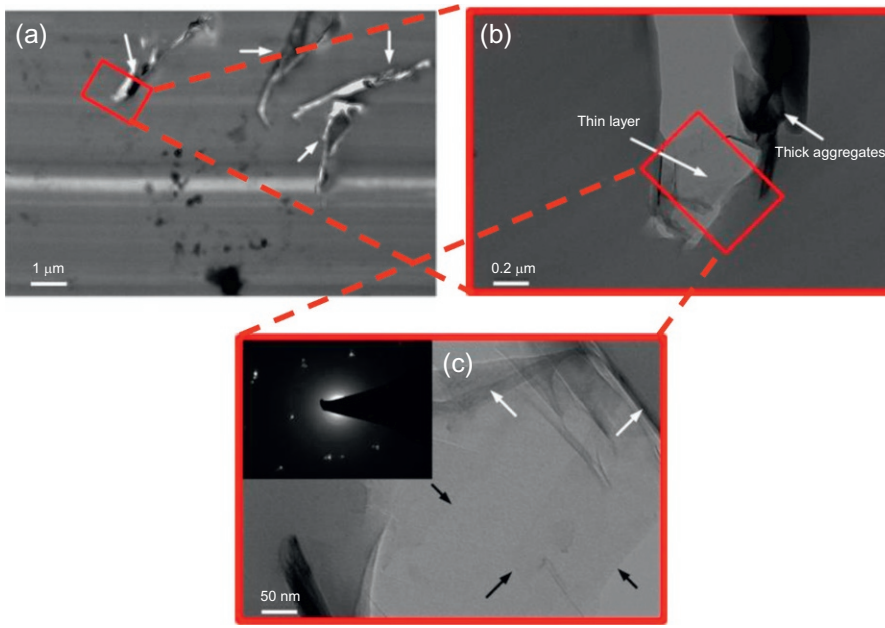

Figure 3.17 TEM micrograph of epoxy/GnP nanocomposites (0.984 vol%) cured by DDS. Zaman et al. (2012a). Copyright © The Royal Society of Chemistry. With permission.

the black arrow-pointed region was observed under diffraction mode, clear crystalline diffraction was found. In comparison with the diffraction image of single layer graphene (Park and Ruoff, 2009), this diffraction pattern implies that the total number of graphene layers would be lower than 5; this number is in agreement with previous AFM analysis in Figure 3.14a. It means that GnPs without interface modification are able to disperse in polymer matrix separately, although they do form clusters.

3.4.5 Toughening mechanism

3.4.5.1 Fracture toughness and mechanical properties

Figure 3.18 illustrates fracture toughness K_{1c} and critical strain energy release rate G_{1c} of neat epoxy and its nanocomposites. Both K_{1c} and G_{1c} increase steadily with increase in GnP fractions, reaching a maximum at 0.984 vol%, and then start to decline. The justification for such increase could be described as: (i) GnPs acting as stress concentrators to absorb fracture energy, (ii) GnPs acting as obstacles, preventing cracks from propagating and thus consuming energy, and (iii) crack tip blunting due to debonding of particle/matrix interface (Caprino et al., 1980; Liu et al., 2005).

With 0.984 vol% GnPs, G_{1c} increases from 178.1 to 462.9 J/m^2 for J230-cured system, 160% improvement, and from 67.4 to 453.6 J/m^2 for DDS-cured system, 573% improvement. Although the absolute G_{1c} values nearly at all volume fractions are higher for J230-cured nanocomposites, the G_{1c} improvements in DDS-cured nanocomposites are much higher. Toughening is usually difficult for a more brittle resin. Since DDS-cured epoxy is more brittle than J230-cured epoxy, toughening the former is more challenging. For example, 8.3 vol% silica particles of ~25 nm in diameter produced G_{1c} improvement of 110.3% for J230-cured epoxy and only 49.3% for DDS-cured one (Ramanathan et al., 2008); and 2.7 vol% rubber particles of ~55 nm in diameter produced G_{1c} improvement of 877.1% for J230-cured epoxy and merely 378.1% for DDS-cured one (Le et al., 2010). However, these GnPs have achieved 573% improvement in G_{1c} for DDS-cured system in comparison with 160% for J230-cured system. This far higher improvement in DDS-cured system is explained by the better dispersion and exfoliation of GnPs in epoxy when cured by DDS. Due to its affinity via π–π interaction with graphene, DDS during fabrication intercalates between GnPs more effectively than J230, promoting a higher degree of dispersion and exfoliation of GnPs. This corresponds to XRD analysis.

Figure 3.19a and b shows mechanical performance of neat epoxy and its nanocomposites cured by J230 and DDS, respectively. DDS-cured system shows higher modulus than J230-cured system because DDS backbone contains benzene and sulphone groups providing the network with more rigidity. The Young's modulus of epoxy is obviously improved with increasing GnPs fractions due to the exceptional stiffness of 1 TPa of graphene. At all fractions, J230-cured system demonstrates more modulus increases than DDS-cured system, which is explained by the stiffening effect of graphene being less pronounced in a stiff matrix.

By contrast, tensile strength reduces with an increase in GnP content, similar to what has been observed in nanoclay-toughened epoxy (Zaman et al., 2011a,b). The matrix stiffness plays a key role in the effect of layered additive on the tensile strength

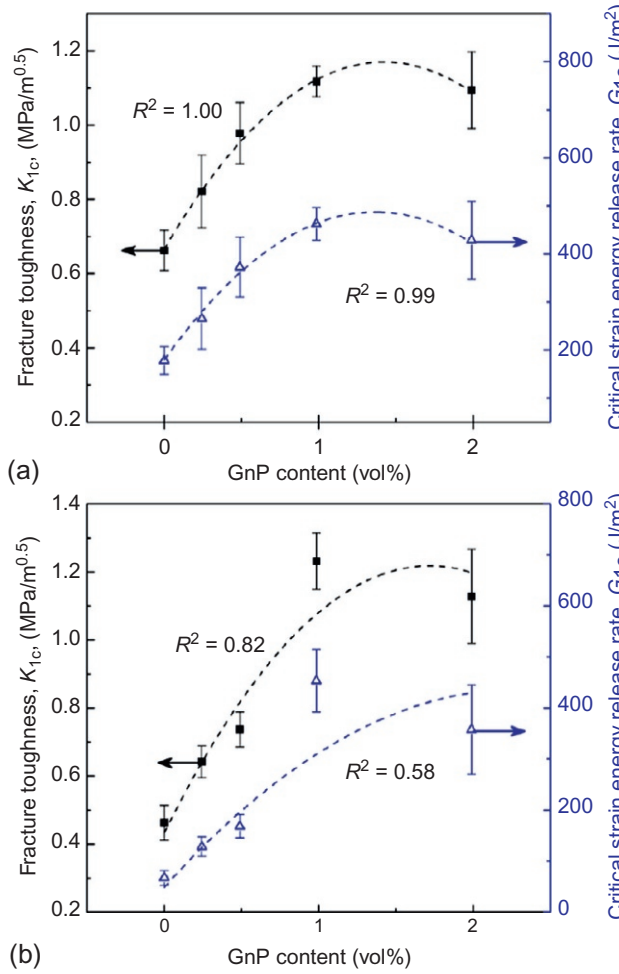

Figure 3.18 Fracture toughness K_{1c} and energy release rate G_{1c} of epoxy and its nanocomposites cured by (a) J230 and (b) DDS.
Zaman et al. (2012a). Copyright © The Royal Society of Chemistry. With permission.

of nanocomposites: tensile strength is often improved by layered additive in an elastomeric matrix (Ma et al., 2004, 2005), while it would be reduced in a stiff matrix such as brittle epoxy resins. Hence, it is reasonable that DDS-cured system shows more reduction in tensile strength than J230-cured system.

3.4.5.2 *Fractography analysis by SEM*

Figure 3.20a–f contains SEM micrographs of the fractured CT surface of the 0.984 vol% epoxy/GnP nanocomposite cured by DDS. Since neat epoxy fracture surface is well known for being relatively smooth and mirror-like (Le et al., 2010; Ma et al., 2011), it was not included in this study. By contrast, the nanocomposite shows a typically rough

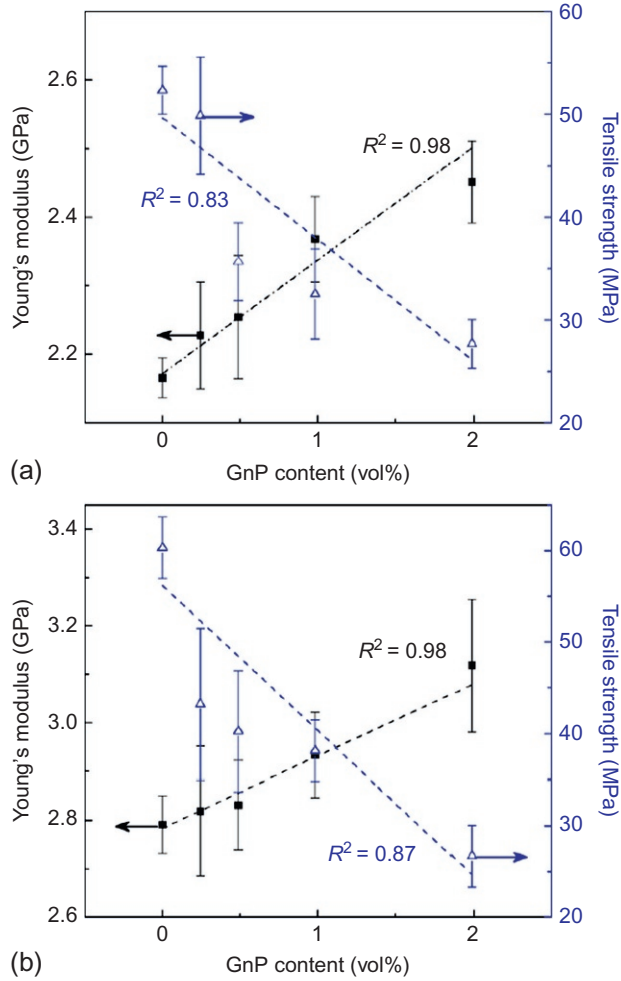

Figure 3.19 Young's modulus and tensile strength of epoxy/graphene platelets nanocomposites cured by (a) J230 and (b) DDS. The closer a correlation coefficient R^2 is to 1, the better the regression line fits into the data. Zaman et al. (2012a). Copyright © The Royal Society of Chemistry. With permission.

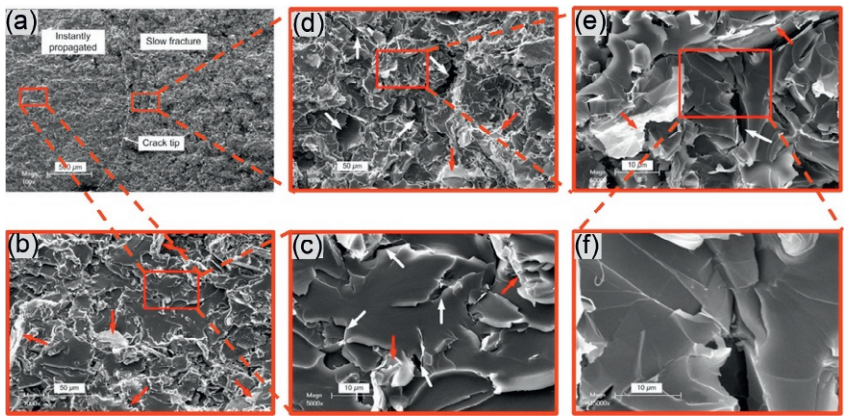

Figure 3.20 SEM fractographs of the 0.984 vol% epoxy/GnP nanocomposites cured by DDS. Zaman et al. (2012a). Copyright © The Royal Society of Chemistry. With permission.

fracture surface (Figure 3.20a) which implies a large amount of energy was consumed during crack propagation, resulting in high fracture toughness K_{1c} and energy release rate G_{1c} (see Figure 3.18). Figure 3.20b shows a magnified region in the instantly propagated crack zone made by a razor blade rather than loading. A few clusters were observed as indicated by red arrows, consistent with what was seen in Figure 3.16a. When a typical fracture zone is magnified in Figure 3.20c, it clearly shows GnPs pulled-out as indicated by red arrows, explaining that interfacial debonding has occurred between GnPs and matrix. The GnP breakages are also observed as indicated by white arrows. Figure 3.20d shows a magnified representative region from the slow fracture zone (also known as stress-whitening zone), where two features are observed: voids and cluster indicated by white and red arrows, respectively. It is noted that most crack propagation occurred near clusters, in alignment with TEM analysis. When the image is magnified in Figure 3.20e, more layer breakages (as pointed out by a white arrow) and GnP pull-outs (red arrows) can be found. This can be explained by a crack undergoing a tilt and twisting under a mixed mode when encountering a rigid obstacle of GnPs. Owing to no modification made on GnP surface, the crack could propagate readily along the interface between matrix and GnPs, therefore leading to debonding. A clear image of crack growth is seen in Figure 3.20f.

3.5 Toughening mechanism of epoxy composites containing long-chain modified GnPs of ~3 nm in thickness

In Section 3.4, a facile method of fabricating GnPs of ~2.5 nm in thickness was presented. In this section, GnPs will be further covalently modified by a long-chain surfactant; each surfactant molecule has only one end-amine group. The interface–morphology–property relations and toughening mechanism of these novel materials will be investigated.

3.5.1 Graphene modification by a long-chain surfactant

0.1 g of GnPs was dispersed in 20 g of NMP in a metal container at 0.5 wt% by mechanically mixing for 10 min and ultrasonicating for 60 min. Since low-temperature sonication expands GnPs more effectively (Zaman et al., 2011a,b), the temperature was set under 20 °C for this study. 1.6 g of surfactant B200 and 1.38 g of catalyst triisopropanolamine were added to the suspension, followed by mixing for 5 min by a mechanical mixer and ultrasonicating for 2 h. The mixture was then transferred into a round-bottom flask equipped with a condenser and magnetically stirred for 4 h at 150 °C. The mixture was finally washed and filtered thrice using acetone to remove NMP and excessive surfactant and catalyst. The B200-modified GnPs are abbreviated as m-GnPs. Figure 3.21 shows the reaction mechanism.

The modification markedly improved the suspension of GnPs in solvent, since m-GnPs were able to suspend in THF at 0.1 wt% for 7 days while GnPs only remained

Figure 3.21 Mechanism of surface modification of graphene platelets (GnPs).

suspended for a few hours. When m-GnPs were dispersed in NMP, no precipitation was observed for at least 5 months of storage. This stable colloidal suspension of m-GnPs will provide a platform for a wide range of research and development of graphene-related products.

3.5.2 Analysis of long-chain m-GnPs

Transmission electron microscopy and electron diffraction (ED) (Figure 3.22) were used to characterize the m-GnPs. In comparison with those diffraction patterns of previous single graphene (Li et al., 2008; Meyer et al., 2007), the pattern suggests a well-crystallized, two to three layered graphene structure, in agreement with the thickness of unmodified GnPs.

Through covalent functionalization, the C:O ratio reduces to 90:10 (Figure 3.23a) due to the high C:O ratio 2.9 of the grafted modifier. Figure 3.15b shows Raman spectra of thoroughly washed samples of GnPs and chemically modified graphene platelets (m-GnPs). All samples show absorption at 1340 and 1585 cm^{-1} corresponding to D band and G band, respectively. However, the broadness and intensity of these absorption patterns were different. The ratio increases markedly from 0.07 to 0.13 through the chemical modification, indicating the existence of B200 molecules on graphene surface produced by the grafting, corresponding to the XPS and FT-IR analysis (Figure 3.24).

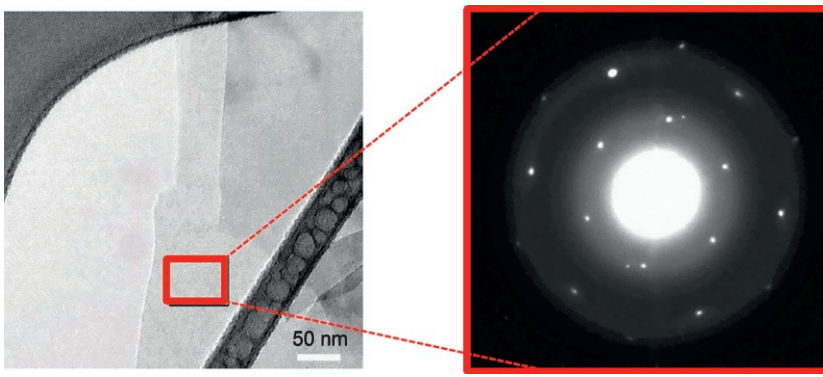

Figure 3.22 TEM micrograph of a typical modified graphene platelet.
Zaman et al. (2012a). Copyright © The Royal Society of Chemistry. With permission.

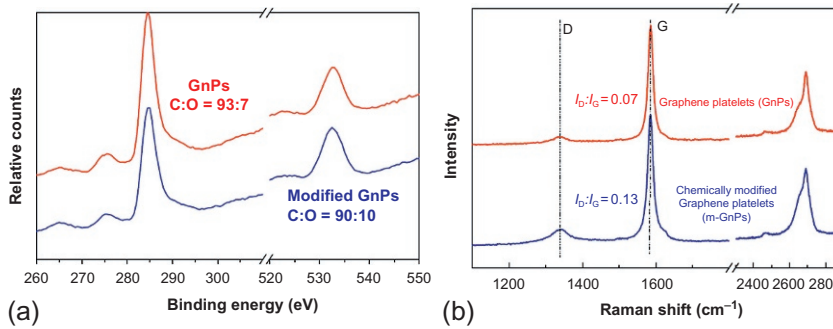

Figure 3.23 XPS and Raman spectra of unmodified and modified graphene platelets. Zaman et al. (2012a). Copyright © The Royal Society of Chemistry. With permission.

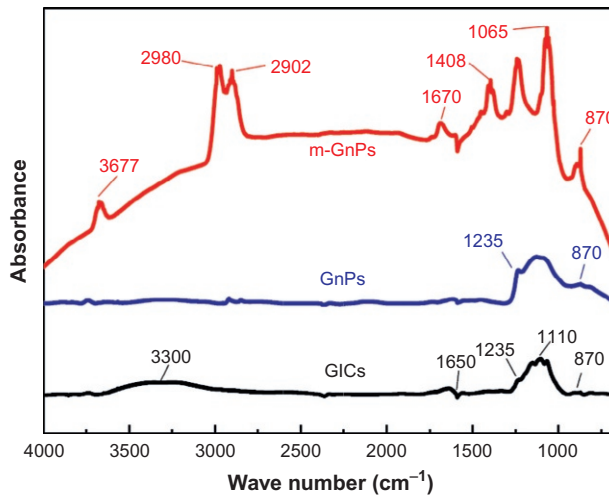

Figure 3.24 FT-IR of GIC, GnPs, and m-GnPs.
Zaman et al. (2012b). Copyright © WILEY-VCH Verlag GmbH & Co. KGaA, Weinheim. With permission.

Figure 3.24 contains FT-IR spectra of the washed GIC, GnPs, and chemically modified m-GnPs. GIC shows absorptions at 3400, 1650, and 1235 cm^{-1}, corresponding to —OH groups, —COOH groups and epoxide groups, respectively. Through the thermal treatment, the absorption bands of oxygenated functionalities, in particular at 3400 cm^{-1} for —OH groups, are considerably reduced and the absorptions for ether or epoxide groups at 1235 and 870 cm^{-1} are noticeably increased. This result reveals

that certain oxygen-containing groups of GnPs were removed during the rapid heating. After covalent modification by surfactant B-200, new absorptions are found at 3677 and 1065 cm^{-1}, corresponding to N—H and C—N groups, respectively. Absorption bands at 2980 and 2902 cm^{-1} correspond to the stretching vibration of the CH_2 groups of B200. This indicates that B-200 was indeed grafted onto graphene layers.

3.5.3 Toughening mechanism of epoxy/m-GnP composites

It is a daunting challenge to prevent graphene from stacking in polymer matrixes, which in our perspective can be addressed only by interface modification. Interface modification promotes the exfoliation and dispersion of GnPs in the matrix leading to the improvement of the GnPs' compatibility with the matrix, so the role of interface is crucial for toughening mechanism of polymer/graphene composites.

3.5.3.1 Fracture toughness and mechanical properties

Figure 3.25 shows fracture toughness K_{1c} and critical strain energy release rate G_{1c} of neat epoxy and its epoxy/m-GnP nanocomposites. Both fracture toughness and energy release rate improve steadily with increase in GnP content. By introducing merely 0.489 vol% GnPs, K_{1c} in Figure 3.25a increases from 0.657 ± 0.034 to 1.472 ± 0.023 MPa/m^2, 124% improvement, while G_{1c} increases from 140.7 ± 7.9 J/m^2 for neat epoxy to 557.3 ± 2.7 J/m^2, 297% improvement (Figure 3.25b). The unmodified nanocomposites discussed in Section 3.4 demonstrate relatively low degree of toughness in comparison with modified nanocomposites. This means that m-GnPs may exfoliate better and disperse more uniformly in matrix than the unmodified platelets. The long-chain surfactants used for GnP modification are based on propylene oxide compatible with epoxy resin and its hardener. Thus the compatibility between m-GnPs and epoxy was improved, preventing GnPs stacking and aggregating.

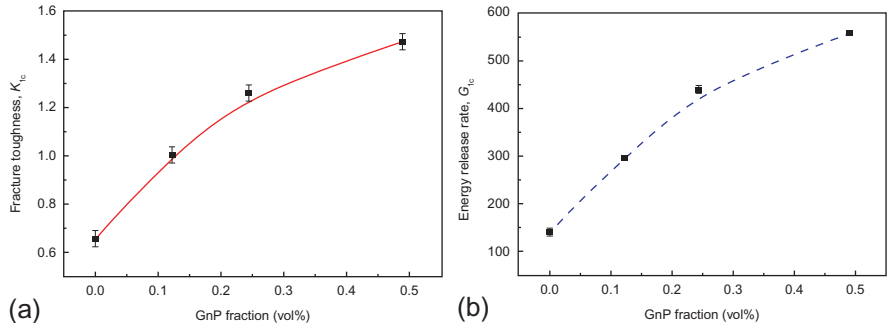

Figure 3.25 Fracture toughness and energy release rate of epoxy/m-GnP nanocomposites.

Table 3.4 Mechanical properties of neat epoxy and its nanocomposites cured by J230

Materials	Young's modulus (GPa)	Tensile strength (MPa)
Neat epoxy	2.692 ± 0.129	63.98 ± 2.14
0.122 vol% epoxy/GnPs	2.992 ± 0.234	61.51 ± 1.49
0.244 vol% epoxy/GnPs	3.158 ± 0.089	51.44 ± 0.12
0.489 vol% epoxy/GnPs	3.412 ± 0.173	49.21 ± 2.94

Table 3.4 shows the mechanical properties of neat epoxy and its nanocomposites. The improvement of mechanical properties surpasses the unmodified system in Section 3.4 as well as previous reported efforts in improving Young's modulus (Li et al., 2007; Yasmin and Daniel, 2004; Zhao et al., 2007).

3.5.3.2 *Effect of GnP dispersion on toughening mechanism for nanocomposites*

Figure 3.26 shows the TEM micrographs of 0.244 vol% long-chain modified nanocomposite. Figure 3.26a demonstrates very different features than unmodified nanocomposites shown in Figure 3.17. No obvious GnP aggregates and overlapping platelets are observed, implying that the interface modification markedly improved the dispersion of GnPs in the matrix. A higher degree of dispersion and exfoliation of GnPs through interface modification may build up a relatively balanced filler–filler network to promote both stress transferring and energy absorption under loading, leading to the highly improved performance shown in Figure 3.25 and Table 3.4.

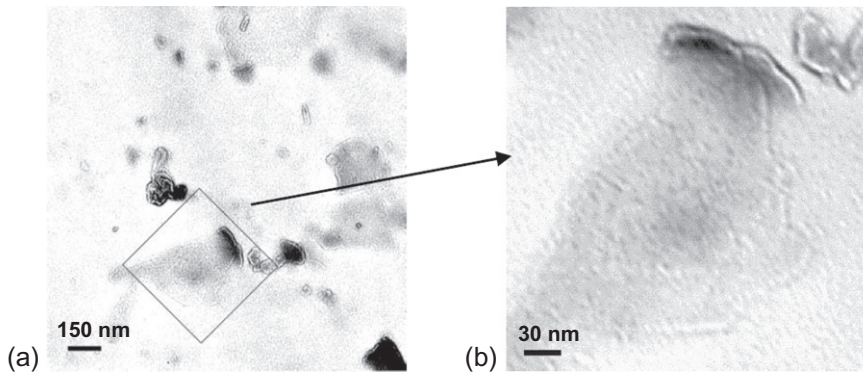

Figure 3.26 (a, b) TEM micrographs of long-chain modified graphene/epoxy nanocomposites (0.244 vol%).
Zaman et al. (2012b). Copyright © WILEY-VCH Verlag GmbH & Co. KGaA, Weinheim. With permission.

3.6 Fabrication, structure, property, and toughening mechanism of epoxy composites containing GnPs, which are reactively modified

An interface for a composite can be described as the boundary between the matrix and the dispersion phase, and theoretically it is the link that bonds the constituting entities. The interface has a central part in the overall mechanical and functional performance of polymer nanocomposites and as a result a great deal of effort is being placed on the interface bonding. Upon interface modification, GnPs should show a more uniform dispersion and a higher degree of stress transfer across interface, leading to greater increments in fracture toughness and mechanical properties. In this section, we will design and fabricate a covalently bonded interface for epoxy/graphene nanocomposites, investigate their fracture and toughening mechanism, and identify the structure–property relations of these nanocomposites.

3.6.1 Modification of GnPs by molecules with two end-amine groups

In this section, DDS and Jeffamine D 2000 (J2000) were chosen to react with the epoxied groups of GnPs (Ma et al., 2013). Each molecule of either DDS or J2000 contains two end-amine groups: one grafting with GnPs and another with the matrix in an ideal situation.

0.1 g GnPs were suspended in 20–60 g NMP through 30-min sonication, followed by addition of 1.6 g DDS or J2000 and 1.38 g catalyst TIPA (see Section 3.5). The mixture was sonicated again for 1 h under 20 °C to promote the intercalation of surfactants and catalyst molecules into the spacing between adjacent GnPs. It was then transferred into a round-bottom flask equipped with a condenser and a magnetic stirrer, followed by mixing and heating at 150 °C for 8 h with an oil bath, to produce surfactant-functionalized GnPs (DDS-m-GnPs or J2000-m-GnPs). The mixture was then washed by acetone at least thrice to remove excessive surfactant and any remaining catalyst.

Further modification of J2000 or DDS m-GnPs was carried out by suspending them in NMP (~0.1 wt%) using a metal container followed by sonication for 30 min below 20 °C. After adding 1.6 g DGEBA, the mixture was subjected to mechanical stirring and sonication for 30 min. The mixture then was transferred into a round-bottom flask with a condenser and kept reacting at 150 °C overnight with an oil bath. Finally, the products were washed again using acetone to remove excessive DGEBA. This furnishes the two-step process for modifying GnPs; the resultant product was denoted as m-GnPs.

3.6.1.1 FT-IR analysis

Figure 3.27 contains FT-IR spectra of unmodified GnPs and DDS modified GnPs (DDS-m-GnPs) and further modified platelets (m-GnPs). Upon modification by DDS, two medium-intensity absorptions at 1606 and 1670 cm^{-1} are due to complex

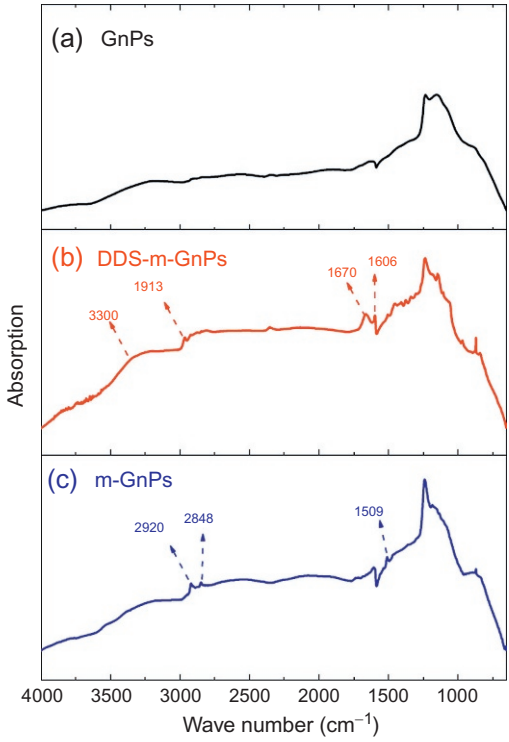

Figure 3.27 FT-IR spectra of GnPs, DDS-m-GnPs, and m-GnPs. Ma et al. (2013). Copyright © The Royal Society of Chemistry. With permission.

molecular motions of the entire rings of DDS; 1 weak absorption at 2913 cm^{-1} corresponds to C—H stretching; and a broad and intense absorption at 3300 cm^{-1} would be caused by the end-amine groups of DDS (Ma et al., 2013). These provide a solid evidence for the grafting between the GnPs' epoxide groups and the DDS's end-amine groups.

After a thorough washing process, DDS-m-GnPs were mixed and reacted with a superfluous amount of DGEBA (monomer of epoxy), which was thoroughly washed again to remove nonreacted DGEBA molecules; In this process, the end-amine groups of DDS-m-GnPs would react with the epoxide groups of DGEBA, to produce m-GnPs. Figure 3.27c contains spectra of m-GnPs. The following absorption evolution is observed for m-GnPs: (i) two absorptions at 2920 and 2848 cm^{-1} correspond to C—H and CH_2—O bonds, (ii) one at 1660 cm^{-1} disappeared, implying the reaction of the grafted end-amine groups with DGEBA, and (iii) one at 1509 cm^{-1} may be caused by C—H_3 asymmetric stretching or C—H_2 stretching (Pretsch et al., 2009). All these point toward the reaction of DGEBA with DDS-m-GnPs. This two-step modification can create a covalently bonded interface for epoxy/GnP composites, as schematically shown in Figure 3.28. The FT-IR graph of the GnPs modified by J2000 is similar to this DDS system, and thus omitted.

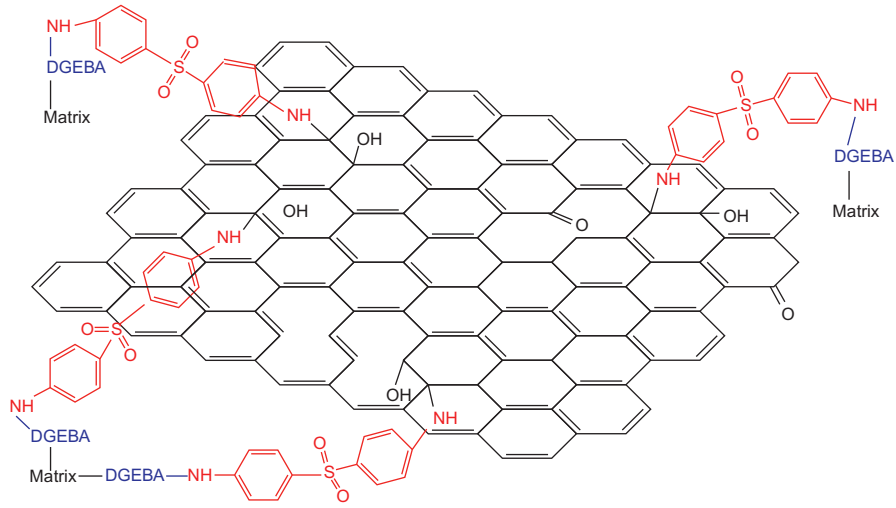

Figure 3.28 Atomic structures of covalently bonded interface between GnPs and matrix. Ma et al. (2013). Copyright © The Royal Society of Chemistry. With permission.

3.6.1.2 Raman spectrum

Raman spectrometer is employed to measure the structural integrity of GnPs—a high structural integrity of graphene always leads to an excellent toughening effect and mechanical performance. We chose J2000 as a reprehensive in this section. Both GnPs and J2000-m-GnPs show two absorptions at around 1350 and 1575 cm^{-1} in Figure 3.29, where D band refers to the absorption at 1350 cm^{-1}, and its intensity indicates the quantity of disordered structure such as voids caused by oxidation and reduction; the G band intensity at 1575 cm^{-1} corresponds to ordered structure of sp^2-hybridized carbon. Hence, the I_D/I_G ratio indicates a disorder degree. Both thermally and chemically reduced GnO produced an I_D/I_G ratio of ~1.0; by contrast, our GnPs demonstrate a significantly lower I_D/I_G ratio of 0.07 in Figure 3.29, aligning with Section 3.5. The ratio decreases to 0.03 after the modification, because GnPs were heated in NMP at 150 °C for 8 h and this reduced GnPs. The comparison demonstrates the much higher structural integrity of m-GnPs. In previous graphene studies, dozens of sonication hours produced a lot of defects in the product, leading to a reduction in the lateral size of GnPs and an increase in the I_D/I_G ratio. In comparison, the sonication time in this study is no longer than 2 h in total; thus, its effect on the lateral dimension is trivial. It is worth to note that GnPs show D and G bands at 1359.2 and 1584.3 cm^{-1}, while these two bands shift to 1351.3 and 1581.7 cm^{-1} for m-GnPs, respectively. These red shifts must be caused by the surface modification of GnPs. No obvious change is seen on the 2D absorption.

The two-step surface modification grafted organic molecules on GnPs, lead to an increase in the GnP thickness and their structural integrity. This may also produce some difference in the GnP layer spacing, which needs investigation by XRD.

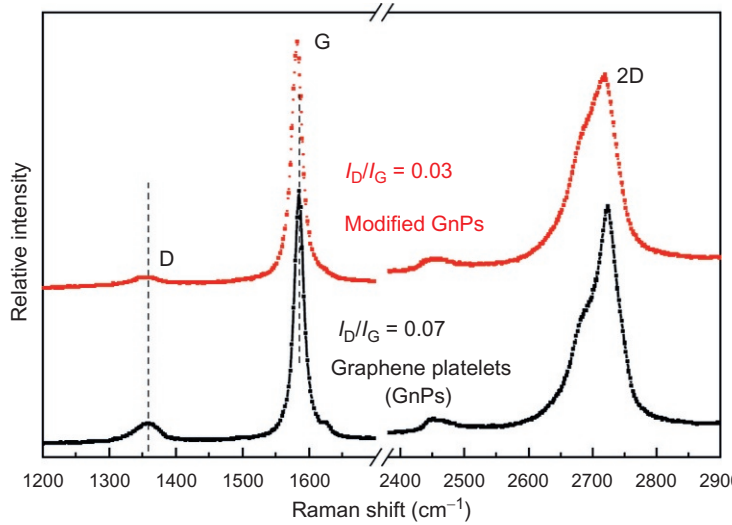

Figure 3.29 Raman spectra of graphene platelets (GnPs) and m-GnPs.
Ma et al. (2013). Copyright © The Royal Society of Chemistry. With permission.

3.6.1.3 TGA analysis

The fraction of organic molecules grafted (2-step surface modification by J2000 and epoxy) with GnPs was identified by TGA analysis. Both GnPs and m-GnPs show an obvious mass loss at 100 to 200 °C, attributed to the deintercalation of H_2O. While GnPs demonstrate a little further loss until 600 °C, an obvious loss is observed for m-GnPs, which must be caused by the grafted DDS and DGEBA. From room temperature to 600 °C, the loss values of GnPs and m-GnPs are 2.69 and 7.53 wt%, respectively. The difference in these two values yields 4.84 wt%—the least weight fraction of the grafted molecules (Figure 3.30).

3.6.2 Structure and properties of composites

3.6.2.1 X-ray diffraction spectra

Compounding polymers with additives to produce composites is one of the major ways of utilizing polymer in industries (Jun et al., 2000; Kang et al., 2013; Li et al., 2006, 2012, 2013; Yu et al., 2008; Zhu et al., 2013). Figure 3.31 shows XRD patterns of neat epoxy and its composites with modified and unmodified GnPs. A wide diffraction from 11° to 28° is observed in all curves, which represents the scattering of cured epoxy molecules. The composites containing 0.5–1 vol% m-GnPs show diffractions at 26.5° in Figure 3.31a, corresponding to an interlayer distance of 3.35 Å associated with the graphitic plane, since the layered structure in each GnP would retain throughout the functionalization and

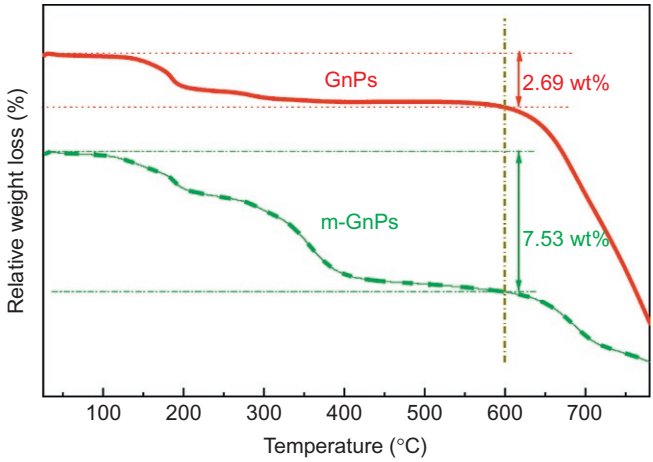

Figure 3.30 Weight loss of GnPs and m-GnPs in air.
Meng et al. (2014). Copyright © IOP Publishing. With permission.

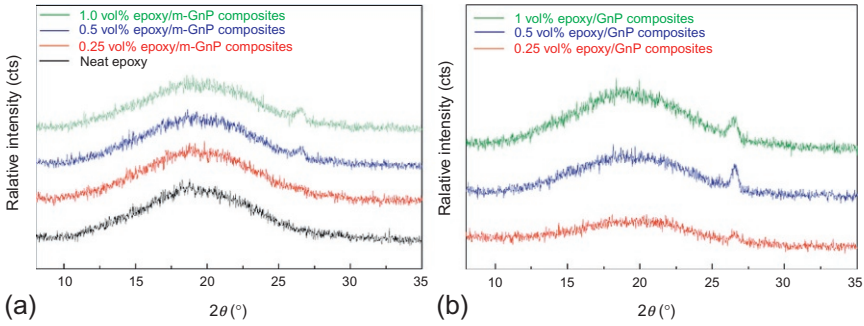

Figure 3.31 XRD spectra of (a) epoxy/m-GnP composites at various fractions and (b) unmodified composites.
Meng et al. (2014). Copyright © IOP Publishing. With permission.

compounding processes. The significant diffraction of epoxy molecules may cover some of the m-GnP diffraction pattern at 26.5° in the 0.25 vol% composite. By contrast, all the unmodified composites demonstrate higher diffraction intensity at 26.5° in Figure 3.31b than the epoxy/m-GnP composites, implying a higher degree of dispersion and exfoliation of GnPs through interface modification. Therefore, the surface modification of GnPs by long-chain molecules builds up a covalently bonded interface with the matrix, promoting the dispersion and delamination of GnPs.

3.6.2.2 Transmission electron microscopy

As discussed in previous section, the exfoliation and dispersion of GnPs are two critical factors determining the mechanical and functional performance of their polymer composites. Since the morphology of an unmodified epoxy/GnP composite has been reported in Section 3.4 and previous research (Zaman et al., 2012a), it is not mentioned here. In general, the unmodified GnPs appear as obviously aggregated or clustered structures with over a few microns in size in the matrix. Figure 3.32 presents TEM micrographs of the 0.25 vol% epoxy/m-GnP composite. The dispersion of m-GnPs in the matrix appears to be relatively uniform as indicated in Figure 3.32a, where inconspicuous light bands from right top to left bottom are the defects produced by microtoming. We randomly selected two platelets, as indicated by red rectangles in Figure 3.32a, and observed these at higher magnifications in Figure 3.32b and c, respectively. The platelet in Figure 3.32b appears to contain at least two graphene

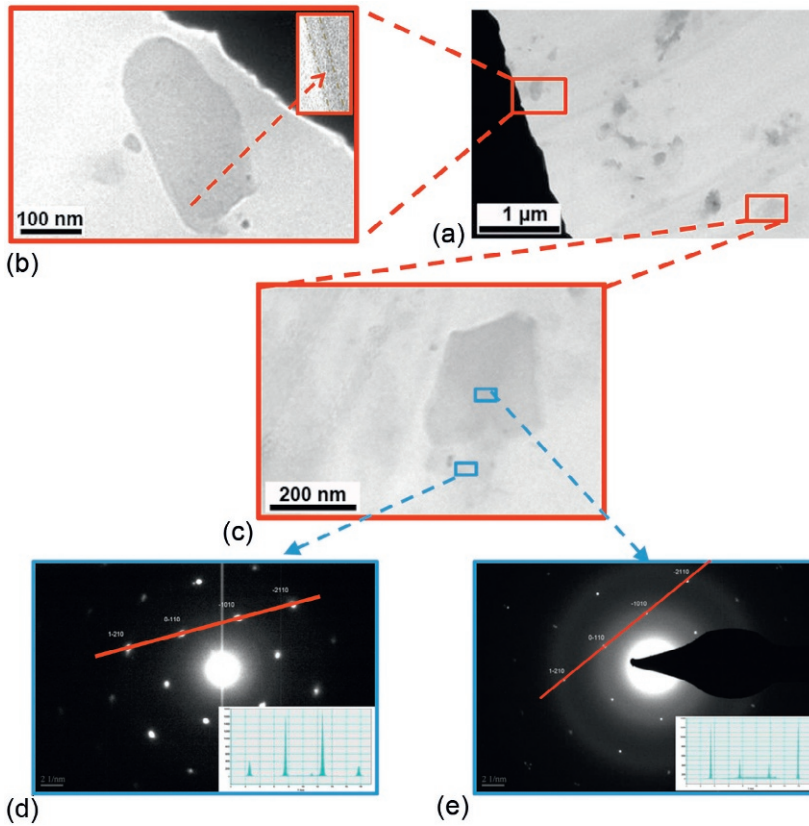

Figure 3.32 TEM micrographs of the 0.25 vol% epoxy/m-GnP composite. Meng et al. (2014). Copyright © IOP Publishing. With permission.

sheets, as indicated at the edge area of flake (see the enlarged region at the right top corner of Figure 3.32b). Many platelets in Figure 3.32a appear semitransparent, implying a low thickness. When a randomly selected platelet is magnified in Figure 3.32c, its lower part appears lighter than the upper area. It is known that the numbers of graphene layers can be roughly estimated by the distinguishable edges of exfoliated graphene in TEM images (Khan et al., 2010). But in this study, we adopted ED to identify the exact number of graphene layers in a platelet. First, the lower area as indicated by the blue rectangle in Figure 3.32c was examined. Its ED pattern shows a typical sixfold symmetry expected for graphene in Figure 3.32d, and its diffraction illustrates a stronger inner intensity than outer ($I_{(0–110)}/I_{(1–210)}$ is greater than 1), confirming this area contains graphene (Hernandez et al., 2008; Vallés et al., 2008). The middle area of the platelet was then examined; its ED pattern (Figure 3.32e) illustrates a well-crystallized structure containing two layers of graphene. These measurements are in agreement with the AFM results discussed in previous section.

3.6.3 Toughening mechanism of nanocomposites

Fracture toughness represents the resistance of a material to the propagation of a sufficiently sharp crack. Since obvious toughness improvements were reported in previous nanofiller-toughened epoxy, we herein investigate the effect of interface on toughness and other mechanical properties.

3.6.3.1 Fracture toughness and mechanical properties

Figure 3.33a and b shows fracture toughness K_{1c} and critical strain energy release rate G_{1c} of neat epoxy and its composites. Both fracture toughness and energy release rate steadily increase with GnP content until reaching peak values at 0.25–0.50 vol% and then start to decline gradually, likely due to the filler–filler network reaching a saturation point where GnPs may start to stack themselves or form agglomeration. The toughening effect at low graphene fraction can be generally explained as: (i) under loading, rigid GnPs promoting stress concentrations in epoxy matrix and effectively absorbing fracture energy by debonding with the matrix or fracturing themselves, (ii) GnPs acting as obstacles, preventing crack growth and propagation to release energy under critical loading and post-critical loading conditions, and (iii) the fracture of GnPs absorbing fracture energy.

By introducing merely 0.25 vol% GnPs, K_{1c} in Figure 3.33a increases from 0.77 ± 0.07 to 1.82 ± 0.19 MPa/m^2 for the unmodified system, while in the modified system it increases to 2.22 ± 0.12 MPa/m^2. G_{1c} increases from 0.204 ± 0.03 kJ/m^2 for neat epoxy to 1.01 ± 0.24 kJ/m^2 for the 0.25 vol% unmodified composites. In Figure 3.33b, m-GnPs at 0.25 vol% increases G_{1c} to 1.422 ± 0.24 kJ/m^2. The highest toughness reported by using GnPs is only 0.557 ± 0.02 kJ/m^2 at 0.489 vol% (Zaman et al., 2012b). More details for the toughening mechanisms were discussed in the Section 3.7 of Meng et al., (2014).

Young's moduli and tensile strengths of neat epoxy and its composites are demonstrated in Figure 3.34. It is noticeable that the modulus increases with rigid-additive

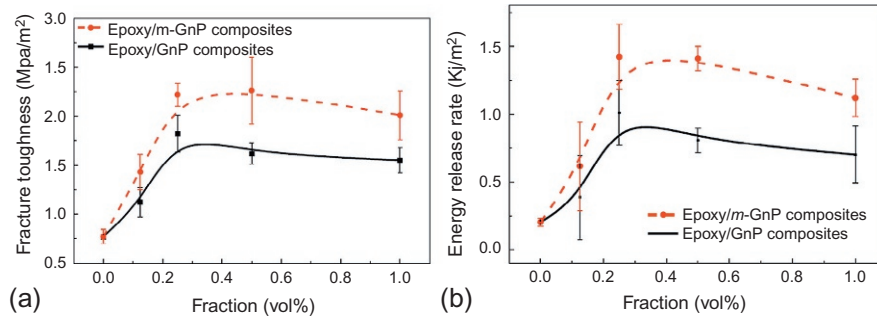

Figure 3.33 Fracture toughness (a) and energy release rate (b) of epoxy and its interface-modified and unmodified composites.
Meng et al. (2014). Copyright © IOP Publishing. With permission.

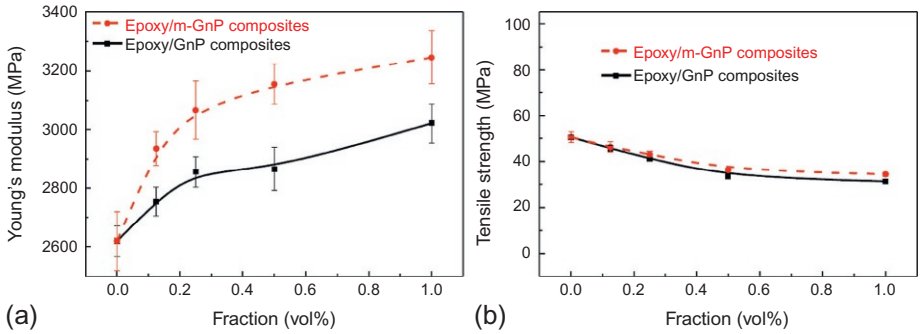

Figure 3.34 Mechanical properties of epoxy/m-GnP and unmodified GnP composites.
Meng et al. (2014). Copyright © IOP Publishing. With permission.

fraction (Figure 3.34a) in both modified and unmodified systems, but it is far more substantial in the interface-modified system. At 1 vol% m-GnPs, Young's modulus of epoxy increases from 2620 ± 100 to 3246 ± 91 MPa, a 23.9% improvement, which is 8.6% higher than its peer unmodified composite. This may be caused by (i) improved dispersion of m-GnPs in epoxy matrix, producing more total specific surface area in a unit volume, which can prevent stress concentrations and facilitate stress transfer across interface under loading; and (ii) the strong interface formed by covalent bonding transfers stress more efficiently between matrix and GnPs rather than interface debonding for an unmodified composite. These obvious modulus improvements align with our previous study on the interface modification of nanolayer-based composites (Ma et al., 2013; Zaman et al., 2011a,b).

Figure 3.34b shows that tensile strength slightly reduces with increase in GnPs content in both systems. The matrix stiffness plays a crucial role in determining the effect

of layered additives on the tensile strength of composites (Dai et al., 2009): tensile strength is often improved by introducing nano-layer additives in a relative ductile matrix (Araby et al., 2013a,b), but it is usually reduced in a rigid matrix such as brittle epoxy resin (Ma et al., 2002, 2013; Zaman et al., 2012a). On account of interface modification, tensile strength demonstrates a smaller reduction in comparison with the unmodified system. At 0.25 vol% GnPs, the modified system shows 14.5% reduction in tensile strength compared to 18.2% for the unmodified one. This obvious difference in the stiffness and strength between these two systems confirms that the formation of interfacial bonding may enhance the mechanical properties of polymer matrix.

3.7 Conclusions and challenges

3.7.1 Further applications

As a cost-effective derivative (10–20 US$/kg) of graphene, GnPs feature high structural integrity while their surface can be covalently modified. These platelets may have a wide range of applications not only in composites and energy storage, but in sensors, catalysis, drug/gene delivery, biological sensing and imaging, antibacterial materials, and biocompatible scaffold for cell culture.

3.7.2 Future challenges for GnPs

A number of key challenges confronting GnPs are as follows.

(1) More surface functional groups are desired for GnPs. After surface functionalization by a long-chain surfactant J2000 ($M_w = 2000$), the grafting ratio is only at about 5–6 wt%, and this ratio needs further improvement to promote the suspension of GnPs in solvent and their complete exfoliation and uniform dispersion in polymer matrixes. A higher grafting ratio also means that when used as an electrode, GnPs have more surface area to facilitate ionic and electric transportation. More surface functional groups should be produced with no sacrifice of high structural integrity.

(2) GnPs need to be thinner. As discussed in Figure 3.1, the specific surface area of platelets in a given fraction and volume of a composite reduces significantly with an increase in thickness for platelets thinner than 10 nm. The low thickness also obviously alleviates the negative effect of poor through-plane conductivities of graphene.

References

Agarwal, B.D., Broutman, L.J., 1990. Analysis and Performance of Fiber Composites. John Wiley & Sons, New York.

Araby, S., Zaman, I., Meng, Q., Kawashima, N., Michelmore, A., Kuan, H.C., Majewski, P., Ma, J., Zhang, L., 2013a. Melt compounding with graphene to develop functional, high-performance elastomers. Nanotechnology 26 (16), 165601.

Araby, S., Zhang, L.Q., Kuan, H.C., Dai, J.B., Majewski, P., Ma, J., 2013b. A novel approach to electrically and thermally conductive elastomers using graphene. Polymer 54 (14), 3663–3670.

Balandin, A.A., 2011. Thermal properties of graphene and nanostructured carbon materials. Nat. Mater. 10 (8), 569–581.
Banhart, F., Kotakoski, J., Krasheninnikov, A.V., 2011. Structural defects in graphene. ACS Nano 5 (1), 26–41.
Buchman, A., Dodiuk-Kenig, H., Dotan, A., Tenne, R., Kenig, S., 2009. Toughening of epoxy adhesives by nanoparticles. J. Adhes. Sci. Technol. 23 (5), 753–768.
Caprino, G., Halpin, J.C., Nicolais, S., 1980. Fracture toughness of graphite/epoxy laminates. Composites 11 (2), 105–107.
Dai, J.-B., Kuan, H.-C., Du, X.-S., Dai, S.-C., Ma, J., 2009. Development of a novel toughener for epoxy resins. Polym. Int. 58 (7), 838–845.
Dean, K., Krstina, J., Tian, W., Varley, R.J., 2007. Effect of ultrasonic dispersion methods on thermal and mechanical properties of organoclay epoxy nanocomposites. Macromol. Mater. Eng. 292, 415–427.
Frohlich, J., Golombowski, D., Thomann, R., Mulhaupt, R., 2004. Synthesis and characterisation of anhydride-cured epoxy nanocomposites containing layered silicates modified with phenolic alkylimidazolineamide cations. Macromol. Mater. Eng. 289, 13–19.
Gass, M.H., Bangert, U., Bleloch, A.L., Wang, P., Nair, R.R., Geim, A.K., 2008. Free-standing graphene at atomic resolution. Nat. Nanotechnol. 3, 676–681.
Gu, W., Zhang, W., Li, X., Zhu, H., Wei, J., Li, Z., Shu, Q., Wang, C., Wang, K., Shen, W., Kang, F., Wua, D., 2009. Graphene sheets from worm-like exfoliated graphite. J. Mater. Chem. 19, 3367–3369.
Hernandez, Y., Nicolosi, V., Lotya, M., Blighe, F.M., Sun, Z., De, S., McGovern, I.T., Holland, B., Byrne, M., Gun'Ko, Y.K., Boland, J.J., Niraj, P., Duesberg, G., Krishnamurthy, S., Goodhue, R., Hutchison, J., Scardaci, V., Ferrari, A.C., Coleman, J.N., 2008. High-yield production of graphene by liquid-phase exfoliation of graphite. Nat. Nanotechnol. 3 (9), 563–568.
Hsiao, M.-C., Liao, S.-H., Yen, M.-Y., Liu, P.-I., Pu, N.-W., Wang, C.-A., Ma, C.-C.M., 2010. Preparation of covalently functionalized graphene using residual oxygen-containing functional groups. ACS Appl. Mater. Interfaces 2, 3092–3099.
Jun, M., Changchun, L., Yuxing, F., Yujun, Z., 2000. Advance in study on EPDM blend system. China Synth. Rubber Ind. 23 (3), 186–191.
Kang, H.L., Qiao, B., Wang, R.G., Wang, Z., Zhang, L.Q., Ma, J., Coates, P., 2013. Employing a novel bioelastomer to toughen polylactide. Polymer 54 (9), 2450–2458.
Kanga, S., Honga, S.I., Choe, C.R., Park, M., Rimb, S., Kim, J., 2001. Preparation and characterization of epoxy composites filled with functionalized nanosilica particles obtained via sol-gel process. Polymer 42 (3), 879–887.
Khan, U., O'Neill, A., Lotya, M., De, S., Coleman, J.N., 2010. High-concentration solvent exfoliation of graphene. Small 6 (7), 864–871.
Kim, H., Miura, Y., Macosko, C.W., 2010. Graphene/polyurethane nanocomposites for improved gas barrier and electrical conductivity. Chem. Mater. 22, 3441–3450.
Kuan, H.C., Chuang, W.P., Ma, C.C.M., Chiang, C.L., Wu, H.L., 2005. Synthesis and characterization of a clay/waterborne polyurethane nanocomposite. J. Mater. Sci. 40, 179–185.
Le, Q.H., Kuan, H.-C., Dai, J.-B., Zaman, I., Luong, L., Ma, J., 2010. Structure-property relations of 55 nm particle-toughened epoxy. Polymer 51, 4867–4879.
Lee, C., Wei, X.D., Li, Q.Y., Carpick, R., Kysar, J.W., Hone, J., 2009. Elastic and frictional properties of graphene. Phys. Status Solidi B 246 (2562–2567), 2562.
Li, B., Zhong, W.-H., 2011. Review on polymer/graphite nanoplatelet nanocomposites. J. Mater. Sci. 46, 5595–5614.

Li, B.Y., Ma, J., Liu, H.Y., Guo, X.L., Zhang, X.L., Xu, J., 2006. Siloxane surfactant-modified clay and its effect in reinforcing the laminate of polymethylsilsesquioxane. J. Appl. Polym. Sci. 100 (5), 3974–3980.

Li, J., Sham, M.L., Kim, J.K., Marom, G., 2007. Morphology and properties of uv/ozone treated graphite nanoplatelet/epoxy nanocomposites. Compos. Sci. Technol. 67, 296–305.

Li, X., Zhang, G., Bai, X., Sun, X., Wang, X., Wang, E., Dai, H., 2008. Highly conducting graphene sheets and Langmuir–Blodgett films. Nat. Nanotechnol. 3 (9), 538–542.

Li, Y., Zhu, C., Lu, T., Guo, Z., Zhang, D., Ma, J., Zhu, S., 2012. Simple fabrication of a Fe_2O_3/carbon composite for use in a high-performance lithium ion battery. Carbon 52, 565.

Li, F., Lu, Y.L., Liu, L., Zhang, L.Q., Dai, J.B., Ma, J., 2013. Relations between carbon nanotubes' length and their composites' mechanical and functional performance. Polymer 54 (8), 2158–2165.

Liu, W., Hoa, S.V., Pugh, M., 2005. Organoclay-modified high performance epoxy nanocomposites. Compos. Sci. Technol. 65, 307–316.

Ma, J., Shi, L., Yang, M., Li, B., Liu, H., Xu, J., 2002. Synthesis and structure of polymethylsilsesquioxane–clay nanocomposite via in situ intercalative polymerization. J. Appl. Polym. Sci. 86 (14), 3708–3711.

Ma, J., Xu, J., Ren, J.H., Yu, Z.Z., Mai, Y.W., 2003. A new approach to polymer/montmorillonite nanocomposites. Polymer 44, 4619–4624.

Ma, J., Xiang, P., Mai, Y.W., Zhang, L.Q., 2004. A novel approach to high performance elastomer by using clay. Macromol. Rapid Commun. 25, 1692–1696.

Ma, J., Yu, Z.-Z., Kuan, H.-C., Dasari, A., Mai, Y.-W., 2005. A new strategy to exfoliate silicone rubber/clay nanocomposite. Macromol. Rapid Commun. 26, 830–833.

Ma, J., Mo, M.S., Du, X.S., Rosso, P., Friedrich, K., Kuan, H.C., 2008. Effect of inorganic nanoparticles on mechanical property, fracture toughness and toughening mechanism of two epoxy systems. Polymer 49 (16), 3510–3523.

Ma, J., La, L.T.B., Zaman, I., Meng, Q., Luong, L., Ogilvie, D., Kuan, H.-C., 2011. Fabrication structure and properties of epoxy/metal nanocomposites. Macromol. Mater. Eng. 296, 465–474.

Ma, J., Meng, Q., Michelmore, A., Kawashima, N., Izzuddin, Z., Bengtsson, C., Kuan, H.-C., 2013. Covalently bonded interfaces for polymer/graphene composites. J. Mater. Chem. A 1 (13), 4255–4264.

Mark, E., Lee, C.Y.-C., Bianconi, P.A., 1995. Hybrid Organic-Inorganic Composites. American Chemical Society, Washington.

Meng, Q., Jin, J., Ma, J., Wang, R., Kuan, H.C., Kawashima, N., Michelmore, A., Zhu, S., Wang, C.H., 2014. Processable 3-nm thick graphene platelets of high electrical conductivity and their epoxy composites. Nanotechnology 25 (12), 125707.

Meyer, J.C., Geim, A.K., Katsnelson, M.I., Novoselov, K.S., Booth, T.J., Roth, S., 2007. The structure of suspended graphene sheets. Nature 446 (7131), 60–63.

Nemes-Incze, P., Osváth, Z., Kamarás, K., Biró, L.P., 2008. Anomalies in thickness measurements of graphene and few layer graphite crystals by tapping mode atomic force microscopy. Carbon 46, 1435–1442.

Novoselov, K.S., Geim, A.K., Morozov, S.V., Jiang, D., Zhang, Y., Dubonos, S.V., Grigorieva, I.V., Firsov, A.A., 2004. Electric field effect in atomically thin carbon films. Science 306 (5696), 666–669.

Park, S., Ruoff, R.S., 2009. Chemical methods for the production of graphenes. Nat. Nanotechnol. 4, 217–224.

Podsiadlo, P., Kaushik, A.K., Arruda, E.M., Waas, A.M., Shim, B.S., Xu, J., Nandivada, H., Pumplin, B.G., Lahann, J., Ramamoorthy, A., Kotov, N.A., 2007. Ultrastrong and stiff layered polymer nanocomposites. Science 318, 80–83.

Potts, J.R., Dreyer, D.R., Bielawski, C.W., Ruoff, R.S., 2011. Graphene-based polymer nanocomposites. Polymer 52 (1), 5–25.

Pretsch, E., Bèuhlmann, P., Buhlmann, P., Badertscher, M., 2009. Structure Determination of Organic Compounds: Tables of Spectral Data, fourth ed. Springer-Verlag, Berlin Heidelberg, pp. 269–355.

Rafiee, M.A., Rafiee, J., Wang, Z., Song, H., Yu, Z.-Z., Koratkar, N., 2009. Enhanced mechanical properties of nanocomposites at low graphene content. ACS Nano 3 (12), 3884–3890.

Ramanathan, T., Abdala, A.A., Stankovich, S., Dikin, D.A., Herrera-Alonso, M., Piner, R.D., Adamson, D.H., Schniepp, H.C., Chen, X., Ruoff, R.S., Nguyen, S.T., Aksay, I.A., Prud'homme, R.K., Brinson, L.C., 2008. Functionalized graphene sheets for polymer nanocomposites. Nat. Nanotechnol. 3 (6), 327–331.

Rochefort, A., Wuest, J.D., 2009. Interaction of substituted aromatic compounds with graphene. Langmuir 25, 210–215.

Sengupta, R., Bhattacharya, M., Bandyopadhyay, S., Bhowmick, A.K., 2011. A review on the mechanical and electrical properties of graphite and modified graphite reinforced polymer composites. Prog. Polym. Sci. 36 (5), 638–670.

Shen, J., Yizhe, H., Shi, M., Lu, X., Qin, C., Ye, M., 2009. Fast and facile preparation of graphene oxide and reduced graphene oxide nanoplatelets. Chem. Mater. 21, 3514–3520.

Singh, V., Joung, D., Zhai, L., Das, S., Khondaker, S.I., Seal, S., 2011. Graphene based materials: past, present and future. Prog. Mater. Sci. 56 (8), 1178–1271.

Su, Y.H., Wu, Y.K., Tu, S.-L., Chang, S.J., 2011. Electrostatic studies of π–π interaction for benzene stacking on a graphene layer. Appl. Phys. Lett. 99 (16), 163102.

Vallés, C., Drummond, C., Saadaoui, H., Furtado, C.A., He, M., Roubeau, O., Ortolani, L., Monthioux, M., Pénicaud, A., 2008. Solutions of negatively charged graphene sheets and ribbons. J. Am. Chem. Soc. 130 (47), 15802–15804.

Wang, H., Hu, Y.H., 2011. Effect of oxygen content on structures of graphite oxides. Ind. Eng. Chem. Res. 50, 6132–6137.

Wang, K., Chen, L., Wu, J., Toh, M.L., He, C., Yee, A.F., 2005. Epoxy nanocomposites with highly exfoliated clay: mechanical properties and fracture mechanism. Macromolecules 38, 788–800.

Wang, G., Shen, X., Wang, B., Yao, J., Park, J., 2009a. Synthesis and characterization of hydrophilic and organophilic graphene nanosheets. Carbon 47, 1359–1364.

Wang, H., Robinson, J.T., Li, X., Dai, H., 2009b. Solvothermal reduction of chemically exfoliated graphene sheets. J. Am. Chem. Soc. 131, 9910–9911.

Yasmin, A., Daniel, I.M., 2004. Mechanical and thermal properties of graphite platelet/epoxy composites. Polymer 45, 8211–8219.

Yu, S., Hu, H., Ma, J., Yin, J., 2008. Tribological properties of epoxy/rubber nanocomposites. Tribol. Int. 41 (12), 1205–1211.

Zaman, I., Le, Q.H., Kuan, H.C., Kawashima, N., Luong, L., Gerson, A., Ma, J., 2011a. Interface-tuned epoxy/clay nanocomposites. Polymer 52 (2), 497–504.

Zaman, I., Phan, T.T., Ma, J., Kuan, H.-C., Meng, Q., La, L.T.B., Luong, L., Youssf, O., 2011b. Epoxy/graphene platelets nanocomposites with two levels of interface strength. Polymer 52 (7), 1603–1611.

Zaman, I., Kuan, H.-C., Ma, J., Dai, J., Kawashima, N., Michelmore, A., Sovi, A., Dong, S., Luong, L., 2012a. From carbon nanotubes and silicate layers to graphene platelets for polymer nanocomposites. Nanoscale 4 (15), 4578–4586.

Zaman, I., Kuan, H.-C., Ma, J., Meng, Q., Michelmore, A., Kawashima, N., Pitt, T., Zhang, L., Gouda, S., Luong, L., 2012b. A facile approach to chemically modified graphene and its polymer nanocomposites. Adv. Funct. Mater. 22 (13), 2735–2743.

Zhao, Y.F., Xiao, M., Wang, S.J., Ge, X.C., Meng, Y.Z., 2007. Preparation and properties of electrically conductive PPS/expanded graphite nanocomposites. Compos. Sci. Technol. 67, 2528–2534.

Zhu, Y., Murali, S., Cai, W., Li, X., Suk, J.W., Potts, J.R., Ruoff, R.S., 2010. Graphene and graphene oxide: synthesis, properties, and applications. Adv. Mater. 22 (35), 3906–3924.

Zhu, S., Zhu, C., Ma, J., Meng, Q., Guo, Z., Yu, Z., Lu, T., Li, Y., Zhang, D., Lau, W.M., 2013. Controlled fabrication of Si nanoparticles on graphene sheets for Li-ion batteries. RSC Adv. 3 (17), 6141–6146.

Zubeldia, A., Larranaga, M., Remiro, P., Mondragon, I., 2004. Fracture toughening of epoxy matrices with blends of resins of different molecular weights and other modifiers. J. Polym. Sci. Polym. Phys. 42, 3920–3933.

Toughening mechanisms in nanoparticle polymer composites: experimental evidences and modeling

4

M. Quaresimin[1], *M. Salviato*[1,2], *M. Zappalorto*[1]
[1]University of Padova, Vicenza, Italy; [2]Northwestern University, Evanston, IL, USA

4.1 Introduction

Nanotechnology has recently emerged as a promising tool to optimize properties of materials by designing their structure at the nanoscale, assisting in the achievement of desirable mechanical properties (Ajayan et al., 2003; Thostenson et al., 2005; Sumfleth et al., 2010).

Nanocomposites offer exceptional improvements at very low filler concentrations, providing high-level performances across various engineering applications. In particular, nanomodification of polymers with nanosized fillers allow an increase, among other things, in the stiffness, strength, wear resistance, and fracture toughness of the unmodified polymers.

Because the weak out-of-plane interlaminar properties of composite laminates are definitely those with the greatest potential and need to be improved, matrix toughness improvement itself is the most interesting and promising result, the interlaminar fracture behavior of traditional composites being a weak-matrix dominated property.

The full exploitation of the potential benefits of nanomodification requires appropriate models able to soundly predict the macroscale mechanical properties, from material structure to nanodesign the best material solution for a specific application. These formulations should be able to account for the large amount of energy dissipated by the different damaging mechanisms taking place at the nanoscale, which is the main source for the high fracture toughness improvements exhibited by nanofilled polymers. However, modeling the effects of nanoscale damaging mechanisms on macroscale properties is far from easy, essentially because at that scale, classical micromechanics is no longer valid. Instead, the adoption of a multiscale strategy is necessary in order to describe the nanocomposite material behavior, physically and mathematically, in each individual scale of interest.

As a basic step toward this challenging goal, it is essential to identify the dominant nanoscale damaging mechanisms in nanoparticle-reinforced polymers. A significant contribution to this end is the work by Hsieh et al. (2010a,b), who studied the fracture toughness improvements resulting from nanomodification of epoxy resins with silica nanoparticles. On the basis of accurate experimental observations, they identified two

Toughening Mechanisms in Composite Materials. http://dx.doi.org/10.1016/B978-1-78242-279-2.00004-4

dominant mechanisms responsible for toughening improvements, namely localized shear banding of the polymer and particle debonding followed by subsequent plastic void growth.

Starting from these bases, in the recent literature, several authors have dealt with the analysis of toughening mechanisms in polymer/particle nanocomposites. An initial study on the energy dissipation due to the interfacial debonding of nanoparticles was done by Chen et al. (2007). By means of an energy analysis of the process, these authors derived a simple size-dependent formulation for the debonding stress, which was later used to compute the energy dissipation due to this mechanism. The size distribution of particles was thought of as obeying a logarithmic normal distribution, and the Weibull distribution function was used to describe the probability of debonding at the interface. The analysis carried out by Chen et al. (2007) was later extended by Zappalorto et al. (2011), who developed a closed form expression for the critical debonding stress, accounting for the existence of an interphase zone embedding the nanoparticle. Salviato et al. further analyzed this topic, also including the effects of surface elasticity (Salviato et al., 2013a).

In the above-mentioned works, the interphase zone between the polymer and the nanofiller is characterized by chemical and physical properties different from those of the matrix, due to the inter- and supramolecular interactions taking place at the nanoscale.

Other theoretical analyses on nanocomposite damaging were presented by Lauke (2008), who considered voiding and subsequent yielding of the polymer in addition to particle debonding. Later, Williams (2010) reanalyzed in detail the toughening of particle-filled polymers, assuming that plastic void growth around debonded or cavitated particles is the dominant mechanism for energy dissipation. Williams (2010) further noted that, even if the debonding process is generally considered to absorb little energy, it is essential to reduce the constraint at the crack tip and, in turn, allow the epoxy polymer to deform plastically via a void-growth mechanism.

A multiscale and multimechanism model to assess the fracture toughness enhancement in nanoparticle-reinforced polymers were recently developed by the present authors (Quaresimin et al., 2014). The model accounts for the main damaging mechanisms, i.e., nanoparticle debonding, plastic yielding of nanovoids, and plastic shear banding of the polymer. Furthermore, the proposed analytical framework considers the influence of an interphase around nanoparticles, a particular feature of nanocomposites.

The investigations in Hsieh et al. (2010a,b), Lauke (2008), Williams (2010), and Quaresimin et al. (2014) support the idea that the most effective approach to predict the nanocomposite toughness is a "multimechanism" modeling strategy, in which the contribution of each mechanism is appropriately determined and weighted according to the specific case (accounting for the type, morphology, and the functionalization of the nanofiller).

The present chapter aims to review the contributions reported in the literature dealing with the damage mechanisms of nanoparticle-reinforced polymers, with the

further aim of including new insights and discussing predictive models incorporating these mechanisms.

4.2 Discussion on the effect of the "scale": micro mechanisms and nano mechanisms

The issue of damaging and energy absorption in nanocomposites is very complicated, especially in the perspective of obtaining a clear understanding of the active toughening mechanisms.

In the previous literature, several energy absorption mechanisms have been detected from experimental observations, when possible.

The scenario being very widespread, it is the authors' opinion that a first differentiation should be made based on the scale at which damaging occurs, the latter being strictly correlated to the morphology of the material, which, in turn, is affected by several parameters linked to the manufacturing process, and, in particular to the nanofiller size, dispersion, and distribution. Indeed, the same reinforcing material might act, by a mechanical and physical point of view, in a different way depending on the actual filler size (such as the nanoparticle radius) and the level of dispersion within the polymer matrix.

When the filler size belongs to the nanometer scale, toughening mechanisms like crack deflection or crack pinning are likely to occur only in the presence of micrometer-sized filler aggregates, since a single nanosized reinforcement cannot mechanically act to pin or deflect the crack front. *Ceteris paribus*, a completely different scenario is present when nanofillers are uniformly dispersed within the matrix. The last mentioned morphology allows, indeed, to maximize the "nano-effect," i.e., the enormous interfacial area per unit volume (SSA) (Fiedler et al., 2006; Wichmann et al., 2006a), and promotes the formation of an interphase "layer" with properties different from those of the constituents. Such an interphase is ascribable to the chemical interactions between the polymer chains and the nanofiller surface features (such as functionalizers) and might substantially contribute to the energy absorption and polymer toughening.

According to these simple concepts, it is clear that the "key brick" of the whole problem addressed in this chapter is not merely limited to a simple "mechanical size effect." Indeed as the filler size reduces, the contribution to energy dissipation due to "nano-phenomena" is considerably emphasized. A proof of this effect is given in Figure 4.1, where with reference to rigid nanoparticle-filled polymers, the normalized strain energy absorbed within the matrix, u_m, the interphase, u_a, and the total energy absorbed, u_{tot}, are plotted versus the nanoparticle radius (Salviato et al., 2013b).

It is evident that in the range of radiuses characterizing nanoparticles, the fraction of energy dissipated within the interphase, u_a, is very high; conversely, the contribution of the interphase becomes lower than 10% for nanoparticle diameters larger than 120 nm.

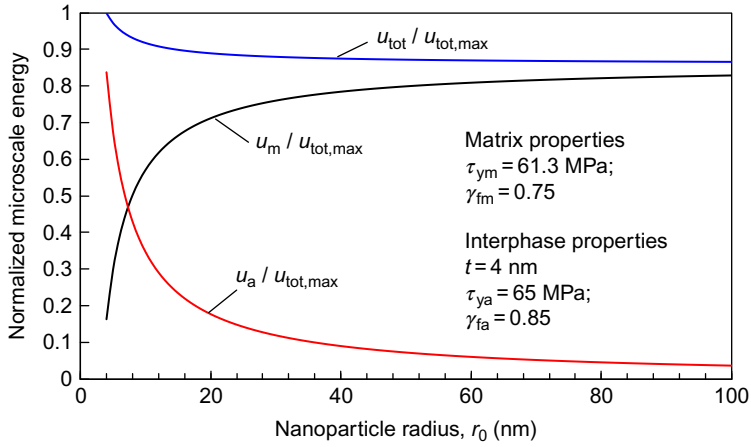

Figure 4.1 Normalized microscale energy dissipated by shear banding within the matrix, u_m, and the interphase, u_a, as a function of the nanoparticle radius.

The natural conclusion of this initial discussion is that a first distinction between damaging mechanisms should be based on the filler morphology and, in turn, on the actual scale at which the mechanisms take place. For this reason, in the following sections a clear distinction is made between "micro" mechanisms (in the presence of agglomerates, or larger particles) and "nano" mechanisms, in the presence of well-dispersed and distributed nanofillers.

4.3 "Micro" mechanisms: crack deflection, crack pinning, and matrix deformation

4.3.1 Crack deflection

The mechanical interaction between the advancing crack front and one or more hard inclusions, such as microsized filler clusters, might give rise to a perturbation of the crack path, with the final result of a non planar crack propagation. In its most general meaning, this toughening mechanism is known in the literature as crack deflection, which might appear essentially in two forms:

- Crack tilting, often referred to as in-plane crack deflection, and giving rise to an in-plane mixed-mode crack tip stress state (opening and sliding);.
- Crack twisting, often referred to as out-of-plane crack deflection, and giving rise to an out-of-plane mixed-mode crack tip stress state (opening and tearing);.

A schematic of these mechanisms is presented in Figure 4.2. As is well known, a mixed-mode crack propagation requires a higher energy, and this provokes, as a consequence, an enhancement of the polymer fracture toughness. The energy

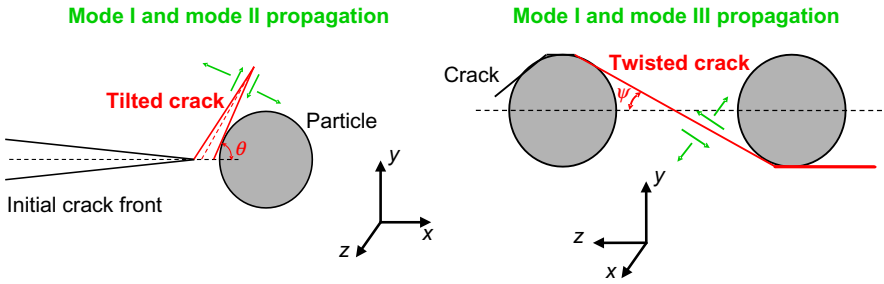

Figure 4.2 Schematic of crack deflection.

dissipation caused by this mechanism is often evident from the increase of the total fracture surface and of the fracture surface roughness (Arakawa and Takahashi, 1991).

As mentioned, crack deflection is due to a mechanical interaction between the heterogeneity and the propagating flaw, so that an effective deflection is possible only whenever the filler size is, at least, comparable to the crack tip opening displacement (CTOD).

The occurrence of this mechanisms in nanoparticle-modified epoxy resins was highlighted by Wetzel et al. (2006), who analyzed the fracture surfaces through AFM scans and noted an explicit correlation between G_{Ic} and the average roughness, thought of as due to crack deflection.

Notwithstanding this, the same authors, comparing experimental results to predictions based on the model by Faber and Evans (1983a,b), stated that crack deflection was not the main damaging mechanism for such a case. The same conclusion was drawn by Zhao et al. (2008), while Johnsen et al. (2007) even excluded a direct correlation between G_{Ic} and the surface roughness.

4.3.2 Crack pinning

The existence of the crack-pinning mechanism in microsized hard particle-reinforced polymers was discussed for the first time in a very illuminating work by Lange (1970). The basic idea introduced by Lange is that an advancing crack front does not possess enough energy to penetrate or cut hard and well-bonded particles; however, instead, when encountering rigid inclusions, the flaw tends to pin and to bow out between the particles, resulting in many secondary crack paths (Lange, 1970; see the schematic in Figure 4.3a). After passing a particle, secondary cracks tend to unify forming fracture steps, appearing as a tail. Experimental evidence of this mechanism in nanocomposites was provided by Wetztel et al. (2006) in the fracture surfaces from specimens made of epoxy modified through TiO_2 particles (with diameters in the range of 200–500 nm), where they noted the appearance of the characteristic features of crack pinning (Figure 4.3b). The same authors also analyzed aluminium oxide/epoxy nanocomposites with particles size of

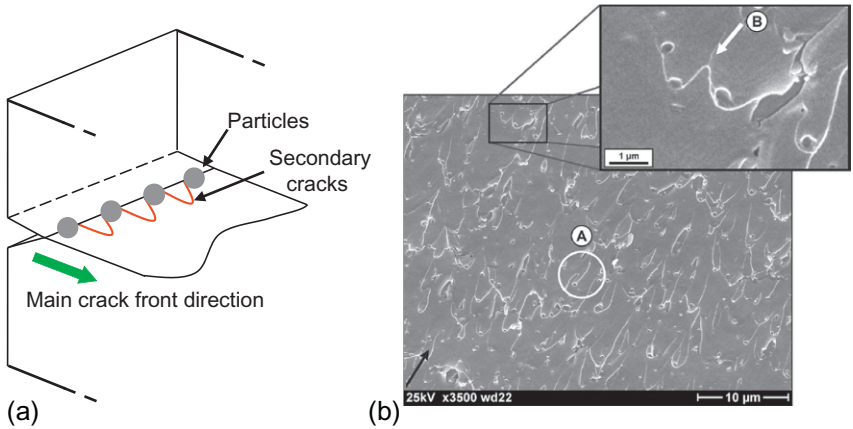

Figure 4.3 (a) Schematic of crack pinning in a particulate reinforced polymer. (b) Crack pinning and crack front bowing in EP/TiO_2 (300 nm) nanocomposites (Wetzel et al., 2006).

about 13 nm; however, in this case, the bowing of the crack front was excluded, probably due to the reduced filler size.

Some year later, Jajam and Tippur (2012) pointed out that the crack front bowing and pinning on the fracture surfaces of nanoparticle-filled epoxy specimens were much less prominent than those exhibited by microfiller-modified epoxy specimens.

Supporting the ideas exposed in Section 4.2, many authors agree that, within reason, nanometric sized particles are inadequate to pin the crack front, so that the pinning mechanism is unlike to take place in nanoparticle-filled polymers with well-dispersed nanoparticles (Wetzel et al., 2006; Johnsen et al., 2007; Jajam and Tippur, 2012; Zhang et al., 2006; Liang and Pearson, 2009).

4.3.3 Other microsized mechanisms

The fracture behavior of epoxy nanocomposites with reduced interparticle distance was discussed by Zhang et al. (2006), who noted that the presence of material regions where several individual nanoparticles were very close, resulting in noncured weak sites triggering the formation of "dimples." They further noted rough, river-like lines on crack initiation and propagation regions thought of as associated with crack tip blunting. The emergence of this damaging mechanism was confirmed by CTOD measurements, especially at high alumina contents.

4.4 "Nano" mechanisms: debonding, plastic void growth, and shear banding

Focusing the attention on nanoscale toughening mechanisms arising in nanoparticle-filled polymers, the contribution of particle debonding is acknowledged to be essential. Indeed, even if its contribution to energy absorption can be regarded as negligible,

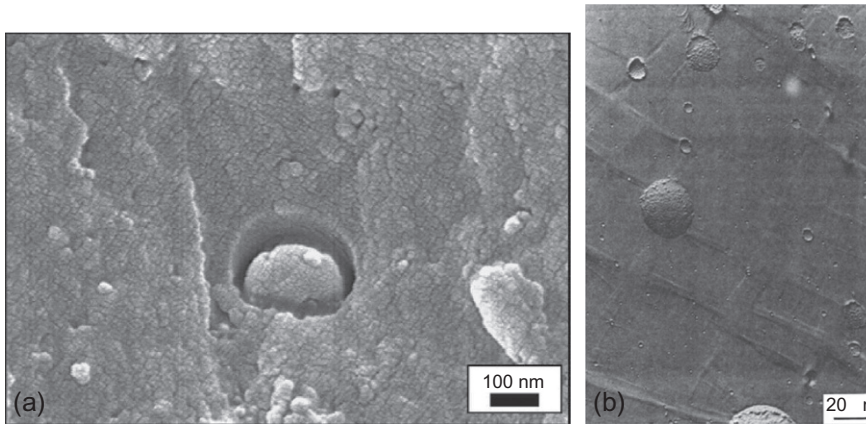

Figure 4.4 (a) Debonding/formation of a cavity in EP/Al_2O_3 (2 vol.%) (Wetzel et al., 2006). (b) Shear bands around microsized particles (Pearson and Yee, 1993; Akbari and Bagheri, 2007).

it might work as a trigger for other, more substantial, mechanisms such as plastic yielding or expansion of voids (caused by debonded particles) (Hsieh et al., 2010a, b; Williams, 2010; Quaresimin et al., 2014; Zappalorto et al., 2012a). The high hydrostatic stress concentration around a nanoparticle located within the crack process zone might induce the detachment of the particle from the polymer matrix. One of the clearest images of this phenomenon can be found in Wetzel et al. (2006) (Figure 4.4a). Other evidence supporting the appearance of this mechanism can be found in Hsieh et al. (2010a,b). In the latter works, the fracture behavior of silica nanoparticle-filled epoxies was analyzed and several high-resolution scanning electron microscopy (FEG-SEM) analyses were taken from the fracture surfaces of broken specimens. These analyses made evident the presence of a large bulk of voids around nanoparticles, which indicates the occurrence of nanoparticle detachment followed by the plastic yielding and growth of voids. Because the fracture process was characterized by a statistical nature, not all of the nanoparticles within the process zone were seen to undergo debonding; this was also due to the fact that the plastic yielding of voids, around already detached particles, relieves the triaxial stress in the adjacent regions, thus making debonding of further particles more difficult.

This behavior is further documented in many other papers on this topic published in the recent literature (see, among others, Johnsen et al., 2007; Liang and Pearson, 2009; Dittanet and Pearson, 2012; Zamanian et al., 2013).

In addition to nanoparticle debonding and void yielding, Hsieh et al. (2010a,b) noted the appearance of localized shear bands in the polymer matrix, attributed to the stress concentrations around the periphery of the silica nanoparticles.

The mechanism of "microshear banding" was initially proposed as an evident toughening mechanisms for rubber-modified epoxies (see Figure 4.4b) and later recognized to be of primary concern also in microsized silica-filled epoxy resins (Pearson and Yee, 1993; Akbari and Bagheri, 2007).

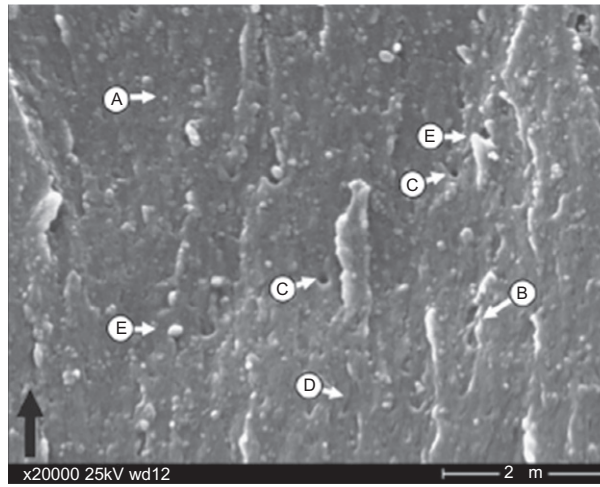

Figure 4.5 Fracture surface of epoxy/Al_2O_3 (2 vol.%) taken in the "plastic zone" close to the initial crack. Features (cautiously) indicate: A—an apparent agglomerate, B—plastic deformation, C—formation of cavities/debonding, D—shear banding, and E—crack bridging (Wetzel et al., 2006).

However, different from microsized particles, the emergence of shear banding around nanoparticles at the nanoscale is more difficult to be identified (see Figure 4.5). More commonly, it is inferred on the basis of indirect observations such as transmission optical micrographs taken between crossed polarizers, where the birefringence of the plastically deformed regions close to the crack tip can be observed (Hsieh et al., 2010a,b; Jajam and Tippur, 2012; Liang and Pearson, 2009; Dittanet and Pearson, 2012; Rosso et al., 2006).

4.5 Modeling the toughening improvements in nanoparticle-filled polymers

4.5.1 Preliminary remarks

The successful application of nanocomposites requires the availability of predictive models able to include their *hierarchical structure*.

To this end, a different way of thinking is necessary with respect to that adopted for conventional composites, where micromechanics is used to address problems concerning two different characteristic lengths (microscale and macroscale) both described, within reason, by continuum mechanics.

This task is made even more difficult by the reduced filler size that is, on one hand, the source of the extraordinary properties of nanocomposites, but is, on the other hand, responsible for their very complex behavior in terms of damaging and the main cause of

tangling phenomena such as agglomeration, limiting their performances (Fiedler et al., 2006; Wichmann et al., 2006a,b). A proper nanofiller distribution and dispersion is, indeed, essential to obtain high SSA, which would be compromised by the emergence of clusters that are potentially accountable for brittle response (Becker et al., 2003). Furthermore, a large particle density reduces the load transfer from the matrix to the nanofillers by strain shielding (Chen et al., 2008), affecting the overall mechanical response.

Another issue to be carefully accounted for is the interfacial region surrounding the nanofiller, a zone of altered chemistry, chain mobility, degree of cure, and crystallinity, whose properties are not just a synergistic combination of those of each bulk constituent (Zax et al., 2000; VanderHart et al., 2001; Ng et al., 2001; Odegard et al., 2005; Yu et al., 2009). The emergence of large regions of nonbulk polymer might lower the energy barrier for some toughening mechanisms (Zappalorto et al., 2012a). Within this scenario, the analytical description of the interface and the assessment of the overall properties accounting for the interphase region is of utmost importance.

To capture the influence of the interphase on the overall behavior of nanocomposites, an insightful study at the molecular level must be carried out (Odegard et al., 2005; Yu et al., 2009; Toth et al., 2004, 2006; Qian et al., 2003; Lordi and Yao, 2000; Liao and Li, 2001; Wong et al., 2003; Fermeglia et al., 2003; Gou et al., 2004, 2005).

All these above-mentioned inherent difficulties may explain the fact that in the recent literature, considerable efforts have been devoted to model the elastic properties of nanocomposites while comparatively less work has been done regarding the modeling of toughening mechanisms, despite their importance in view of developing ternary namomodified laminates. Moreover, while a model for elastic property prediction can be directly validated by means of macroscopic experimental data when dealing with energy absorption mechanisms, the processes at the nanoscale are not only difficult to identify, but also require observation and validation at the same length scale.

To correctly face the modeling of nanocomposite mechanical properties, it is essential to first acknowledge that in the most general case, three main stages should be addressed and tackled with the aid of dedicated models, with the aim of ranging from the nanoscale to the macroscale. In particular:

- *Molecular models*. The chemical–physical interactions arising at the nanoscale can be accounted for by means of discrete methodologies, predicting the time evolution of a system of interacting items (e.g., atoms, molecules, granules, etc.). The most common of these methodologies is molecular dynamics (MD) (see, among the others, Odegard et al., 2005; Yu et al., 2009).
- *Nanostructural models*. In addition to chemical interactions, mechanical interactions must obviously be accounted for regarding the filler size and morphology. This can be achieved by nanostructural models, usually developed within a Cauchy, or more sophisticated (Cosserat), continuum mechanics-based frame, to effectively describe the stress transfer with the matrix.
- *Micromechanical models*. Eventually, nanoscale-related properties must be scaled up to the macroscale. This problem can be tackled by means of conventional micromechanics, often exploiting the concept of representative volume element (RVE), with a number of DOFs much smaller than that required by MD.

Once having identified the main stages, the related basic models can be assembled to build a multiscale modeling strategy; its nature and efficacy will depend on how many and which of the above-mentioned models are used, thus inherently defining the scale from which the problem is addressed (micro, nano, and molecular).

Accordingly, the possible multiscale modeling strategies can be divided into three main groups: "*micromechanical modeling strategies*," "*nanostructural modeling strategies*," and "*molecular modeling strategies*"

- *Micromechanical modeling strategies* are the simplest, but unfortunately, least effective way to address the problem. Since they make use of only micromechanical models, the nanoscale structure as well as the nanofiller and matrix molecular interactions are neglected. Accordingly they fail in capturing the "nano-effect." For these reasons, micromechanical strategies proved to be incapable of predicting the reported high increments in dissipated energy at low nanofiller volume fractions (Wetzel et al., 2006; Zhao et al., 2008).
- *Nanostructural modeling strategies* use both micromechanical models and nanostructural models, and in this way, account for the effects of the inherent nanostructure on the overall macroscopic properties but not for the chemical–physical interactions. An inherent advantage of nanostructural modeling strategies, when compared to micromechanical ones, is that they offer a more insightful analysis of the nanofiller-matrix mechanical interactions without compromising simplicity.
- *Molecular modeling strategies* combine all three above-mentioned models. The scope of the analysis is taken to the actual nanoscale level to account for intermolecular and supramolecular interactions by means of discrete methodologies. Obviously, this complicates the scaling-up process from nano- to macrolength scales and requires an effective multiscale approach.

The concept of assembling basic models to build a multiscale modeling strategy is referred to as the "three-stage strategy" (TSS) in the literature (Quaresimin et al., 2012). A schematic representation of this concept is shown in Figure 4.6.

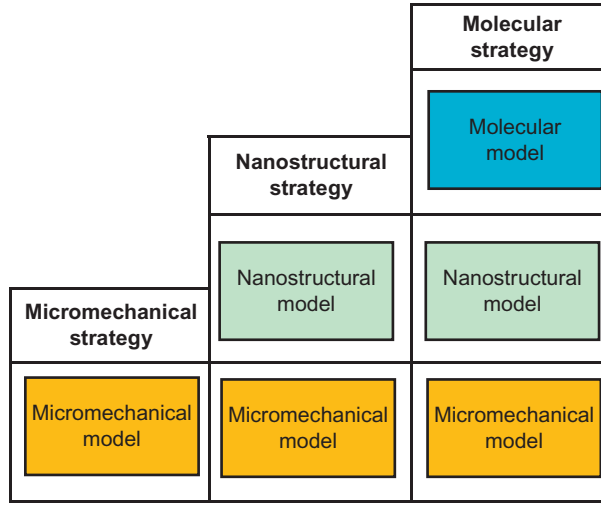

Figure 4.6 The concept of the "three-stage strategy" (TSS): building of modeling strategies from basic models (Quaresimin et al., 2012).

4.5.2 Multiscale modeling of the toughness improvements in nanoparticle-filled polymers

4.5.2.1 Basic concepts

In agreement with the concepts introduced in Section 4.5.1, it is evident that three stages should be addressed in nanocomposite modeling; each stage refers to a specific length scale and is characterized by mechanical quantities that are, by a conceptual point of view, very different.

In the following, the **macroscale system** is meant as an amount of material over which all the mechanical quantities are averaged values representative of the overall material behavior (Bishop and Hill, 1951). This requires the assumption that the material is homogeneously and continuously distributed over its volume "*so that the smallest element cut from the body possesses the same specific physical properties as the body*" (Timoshenko and Goodier, 1970). In addition, if the nanofiller is randomly oriented and uniformly distributed, the material can also be treated as isotropic.

The **microscale system** is instead thought of as sufficiently small to be regarded, mathematically, as an infinitesimal volume of the macroscale, one, where all the mechanical properties are supposed to be pointwise values (Bishop and Hill, 1951). However, at the same time, it has to be large enough to be statistically representative of the properties of the material system, according to the classical definition of RVE, this being valid as far as the nanofiller is uniformly distributed and dispersed over the volume.

Eventually, the **nanoscale system** is simply a single unit cell of those compounding the microscale system and accounts for the material morphology.

Given the definition of the involved scales, it is also necessary to formulate the relevant relationships between stresses and strains in the different systems. In a general boundary value problem of statics, the macroscale stresses or strains, σ or ε, are often regarded as functions of material coordinates $\sigma, \varepsilon = \{f_1(X_1, X_2, X_3), f_2(X_1, X_2, X_3)\}$. Within this definition, functions f_i, can be regarded as an average value over an RVE $\{\sigma, \varepsilon\} = \{\overline{\sigma}, \overline{\varepsilon}\} = \left\{\frac{1}{V}\int_V \hat{\sigma}\mathrm{d}V,\ \frac{1}{V}\int_V \hat{\varepsilon}\mathrm{d}V\right\}$, where $\hat{\sigma}$ and $\hat{\varepsilon}$ are the microscale stress and strain distributions and V is the volume of the RVE (Bishop and Hill, 1951; Hutchinson, 1964; Gurson, 1977).

However, things are made easier by the Mori–Tanaka theorem, which allows an approximation of the stress or the strain acting on the boundary of a single nanoinhomogeneity (nanoscale), thus disregarding the actual microscale fields. This can be achieved by invoking the global concentration tensors of Eshelby dilute solution and the mean value for the stress/strain fields over the RVE, which, in turn, equates the macroscale one.

4.5.2.2 A multiscale strategy to the modeling of the toughness improvements in nanoparticle-filled polymers

As exhaustively argued in the previous sections, the modeling of nanocomposites requires that interfacial effects are included (Ajayan et al., 2003; Wichmann et al., 2006a; Tian and Rajapakse, 2007). Accordingly, particular attention must be paid to the interphase zone surrounding the nanoparticle, which is usually characterized

by the chemical and physical properties different from those of the constituents. Unfortunately, the data available so far in the literature about the interphase zone are not enough to precisely formulate the law of variation of its properties across the thickness as well as its size (Sevostianov and Kachanov, 2007), so that a through-the-thickness average of the needed properties is often used (Zappalorto et al., 2011; Odegard et al., 2005; Yu et al., 2009). According to these preliminary remarks, the system under investigation at the nanoscale, shown in Figure 4.7, can be thought of as constituted by:

- a spherical nanoparticle of radius r_0, which creates a nanovoid of the same diameter;
- a shell-shaped interphase of external radius a and uniform properties; and
- a loaded matrix of radius b, b being much greater than a and r_0.

The properties required by the analysis can be computed by means of numerical simulations carried out within the frame of MD as done, for example, by Odergard et al. (2005) and Yu et al. (2009). Alternatively, for a specific system, they could be fitted *a posteriori* on the basis of some experimental results, as better explained in the following.

A cracked nanocomposite is considered, instead, at the macroscale (see again Figure 4.7), where the crack stress fields give rise to a process zone containing all the sites of nanoscale damage.

As discussed before, the two dominant mechanisms responsible for toughening improvements for polymers reinforced by rigid nanoparticles (such as silica or alumina nanoparticles) are the localized shear banding of the polymer and particle debonding followed by subsequent plastic yielding of nanovoids (Hsieh et al., 2010a,b; Quaresimin et al., 2014; Salviato et al., 2013b; Zappalorto et al., 2012a).

Accordingly, the nanocomposite toughness can be written as

$$G_{\mathrm{Ic}} = G_{\mathrm{Im}} + \sum_i \Delta G_i \tag{4.1}$$

where G_{Im} is the toughness of the unloaded matrix and ΔG_i is the toughness improvement due to the ith damaging mechanism. Denoting with U_i the energy produced at the

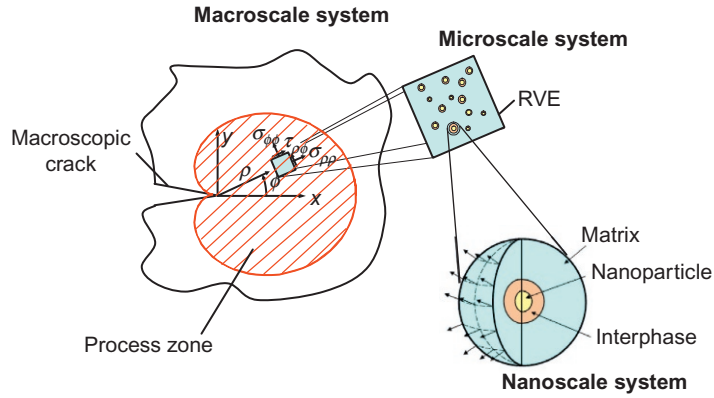

Figure 4.7 Description of the multiscale system under analysis.

nanoscale by a particular mechanism, the corresponding microscale strain energy density is:

$$u_i = U_i \times \frac{3f_{p0}}{4\pi r_0^3} \tag{4.2}$$

where f_{p0} is the volume fraction of nanoparticles. Finally, the fracture toughness enhancement due to the single damage mechanism, to be inserted in Eq. (4.1), can be determined as (Quaresimin et al., 2014; Salviato et al., 2013b; Zappalorto et al., 2012a; Freund and Hutchinson, 1985; Huang and Kinloch, 1992):

$$\Delta G_i = 2 \times \int_0^{\rho_i} u_i \mathrm{d}\rho \tag{4.3}$$

where ρ_i denotes the extension of the damaged zone ahead of the crack tip.

The following sections present closed form expressions useful in evaluating the fracture toughness improvements, ΔG_i, due to the above-mentioned mechanisms. Finally, a unified expression for the overall nanocomposite fracture toughness is presented.

4.5.2.3 Particle debonding

The high level of the crack-induced hydrostatic stress promotes debonding of nanoparticles, resulting in the following dissipated microscale strain energy:

$$u_{db} = 3\frac{\gamma_{db}}{r_0} f_{p0} \tag{4.4}$$

where f_{p0} is the nanofiller volume fraction and γ_{db} is the interfacial fracture energy. The associated macroscale increment in terms of strain energy release rate is:

$$\Delta G_{db} = f_{p0} \times \psi_{db} \times G_{Ic} \tag{4.5}$$

where G_{Ic} is the fracture toughness of the nanocomposite and ψ_{db} is a term accounting for energy dissipation (Zappalorto et al., 2012a):

$$\psi_{db} = \frac{2}{3\pi} \times \frac{\gamma_{db}}{r_0} \times \frac{1+\nu_o}{1-\nu_o} \times \frac{E_o}{\sigma_{cr}^2 (C_h)^2} \tag{4.6}$$

In Eq. (4.6), E_o and ν_o are the elastic properties of the nanocomposite, σ_{cr} is the critical debonding stress (Zappalorto et al., 2011):

$$\sigma_{cr} \cong \sqrt{\frac{4\gamma_{db}}{r_0}\frac{E_m}{1+\nu_m}} \sqrt{\frac{\chi(4+\xi) - \xi(\chi-1)(r_0/a)^3}{4+\xi+4(\chi-1)(r_0/a)^3}} \tag{4.7}$$

and C_h is the reciprocal of the hydrostatic part of the global stress concentration tensor (Zappalorto et al., 2011)

$$C_h = \frac{K_m}{K_p}\frac{(\xi+4)\ (3K_p/G_m+4\chi)}{(\xi+4\chi)\ (3K_m/G_m+4)} + \frac{(4\xi-12K_p/G_m)\ (1-\chi)}{(\xi+4\chi)\ (3K_m/G_m+4)}\left(\frac{r_0}{a}\right)^3 \tag{4.8}$$

where E_m and v_m the elastic modulus and Poisson's ratio of the matrix, K_m, K_a, and K_p the bulk moduli of the matrix, the interphase and the nanoparticle, G_m and G_a are the shear elastic moduli of the matrix and the interphase, $\chi = G_a/G_m$ and $\xi = 3K_a/G_m$.

4.5.2.4 Plastic yielding of nanovoids

Debonding of nanoparticles creates a number of nanovoids of the same diameter of the initial nanoparticles. Whenever the stress field around a nanovoid is high enough, it might cause local yielding of the nanovoids. The associated fracture toughness enhancement can be estimated as (Zappalorto et al., 2012a):

$$\Delta G_{py} = f_{p0} \times \psi_p \times G_{Ic} \tag{4.9}$$

where G_{Ic} is the fracture toughness of the nanocomposite and ψ_p is a term accounting for energy dissipation:

$$\psi_p = \frac{4}{9\pi C_h}\frac{E_o}{E_m}\frac{(1+v_o)(1+v_m)}{1-v_o}\frac{\sigma_{Ym}}{\sigma_{cr}}\left(\frac{a}{r_0}\right)^{3\times\left(1-\frac{\sigma_{Ya}}{\sigma_{Ym}}\right)} e^{\left(3C_h\frac{\sigma_{cr}}{\sigma_{Ym}}-1\right)} \tag{4.10a}$$

for an elastic perfectly plastic behavior of the matrix and the interphase:

$$\psi_p = \left\{\frac{2}{9\pi C_h}\times\frac{1+v_o}{1-v_o}\frac{E_o}{G_m}\frac{\sigma_{Ym}}{\sigma_{cr}}\times\left(\frac{a}{r_0}\right)^3 \times \left[\frac{3C_h\frac{\sigma_{cr}}{\sigma_{Ym}}-(1-n_m)}{n_a\frac{\sigma_{Ya}}{\sigma_{Ym}}\left(\frac{\varepsilon_{Ym}}{\varepsilon_{Ya}}\right)^{1/n_a}\left[\left(\frac{a}{r_0}\right)^{3/n_a}-1\right]+n_m}\right]^{n_m}\right\} \tag{4.10b}$$

for a hardening behavior of the matrix and the interphase, where σ_{Ym} and $\sigma_{Ya,}$ the yield stress of the matrix and the interphase, n_m and n_a, are the hardening exponents of the matrix and the interphase, respectively.

4.5.2.5 Localized shear banding

In a damaged region close to the crack tip (shear- banding region, or SBR) the stress concentrations around nanoparticles might promote local shear yielding, with the formation of plastic shear bands. The overall fracture toughness enhancement related to this mechanism can be determined as (Salviato et al., 2013b):

$$\Delta G_{SB} = f_{p0} \times \psi_{SB} \times G_{Ic} \tag{4.11}$$

where ψ_{SB} accounts for the energy dissipation at the nanoscale:

$$\psi_{SB} = \frac{I_{SB}}{4\pi\sigma_{yca}^2\left(1-\mu/\sqrt{3}\right)^2}\frac{E_o}{1-\nu_o^2}\times\Gamma \tag{4.12}$$

In Eq. (4.12), μ is a dimensionless pressure coefficient, σ_{yca} is the interphase yielding stress under compression, whereas function Γ quantifies the energy produced at the nanoscale, and I_{SB} accounts for the stress concentration around nanoparticles (Salviato et al., 2013b):

$$\Gamma = \tau_{ym}\gamma_{fm}\left\{\left(\frac{\pi}{6f_{p0}}\right)^{1/3} - \frac{52}{63}\frac{\tau_{ya}\gamma_{fa}}{\tau_{ym}\gamma_{fm}} - \left(1-\frac{\tau_{ya}\gamma_{fa}}{\tau_{ym}\gamma_{fm}}\right)\left[\frac{32}{21}Q\left(\frac{1}{3}+\frac{\overline{a}^4}{5}\right) + \frac{\overline{a}^2}{315}\left(4S - 32\overline{a}^4 Z + 128\overline{a}^6 M\right)\right]\right\} \tag{4.13a}$$

$$I_{SB} = \frac{1}{2\pi}\left(pH_{vM}^2 + k\mu H_h H_{vM} + j\mu^2 H_h^2\right) \tag{4.13b}$$

$$\overline{a} = \frac{a}{r_0};\quad Q = \sqrt{\overline{a}^2-1};\quad M = \overline{a} - Q;\quad S = 105\overline{a} - 88Q;\quad Z = 9\overline{a} - 7Q \tag{4.13c}$$

In Eq. (4.13a), τ_{ym} and τ_{ya} are the shear yielding stress of the matrix and of the interphase, whereas γ_{fm} and γ_{fa} are the shear fracture strains.

In Eq. (4.13b), the parameters p, k, and j are functions of the Poisson's ratio, $H_h = 1/C_h$ and H_{vM} are the deviatoric component of the global stress concentration tensor. It can be evaluated numerically or analytically (Salviato et al., 2013b; Zappalorto et al., 2012b).

4.5.2.6 Estimation of interphase size and properties

As evident, the use of the solutions proposed in the previous sections requires the properties and size of the interphase to be determined.

The elastic properties and the thickness of the interphase can be computed by means of numerical simulations carried out within the frame of MD, as carried out for example, by Odergard et al. (2005) and Yu et al. (2009), which provide, as outputs, the radial extension of the interphase as well as the elastic properties averaged through the thickness.

Alternatively, for a specific system, they could be determined *a posteriori* by fitting the experimental values for the elastic properties of the nanocomposite by a multiphase, micromechanical model. As far as the previous approach is concerned, a two-step analytical model based on the Hashin–Shtrikman solution (Hashin and Shtrikman, 1963) developed by the authors (Pontefisso et al., 2013) can be used. In Pontefisso et al. (2013) the three-phase nanocomposite material showed in Figure 4.7 is considered, and each particle and the surrounding interphase are changed for an "equivalent homogeneous particle (EHP)" of total radius $a = r_0 + t$ with bulk and shear elastic moduli, K' and G', given by:

$$K' = K_a \left\{ 1 + \frac{\left(\frac{r_0}{a}\right)^3 \left(\frac{K_p}{K_a} - 1\right)}{1 + \left[1 - \left(\frac{r_0}{a}\right)^3\right] \frac{1 + v_a}{3(1 - v_a)} \left(\frac{K_p}{K_a} - 1\right)} \right\} \tag{4.14}$$

$$G' = G_a \left\{ 1 + \frac{\left(\frac{r_0}{a}\right)^3 \left(\frac{G_p}{G_a} - 1\right)}{1 + \left[1 - \left(\frac{r_0}{a}\right)^3\right] \frac{8 - 10v_a}{15(1 - v_a)} \left(\frac{G_p}{G_a} - 1\right)} \right\} \tag{4.15}$$

where $(r_0/a)^3$ is the volume fraction of the nanoparticle within the EHP. As a second step, the elastic properties of the nanocomposite, K_o and G_o, can be assessed as:

$$K_o = K_m \left\{ 1 + \frac{f_{p0} \left(\frac{a}{r_0}\right)^3 \left(\frac{K'}{K_m} - 1\right)}{1 + \left[1 - f_{p0} \left(\frac{a}{r_0}\right)^3\right] \frac{1 + v_m}{3(1 - v_m)} \left(\frac{K'}{K_m} - 1\right)} \right\} \tag{4.16}$$

$$G_o = G_m \left\{ 1 + \frac{f_{p0} \left(\frac{a}{r_0}\right)^3 \left(\frac{G'}{G_m} - 1\right)}{1 + \left[1 - f_{p0} \left(\frac{a}{r_0}\right)^3\right] \frac{8 - 10v_m}{15(1 - v_m)} \left(\frac{G'}{G_m} - 1\right)} \right\} \tag{4.17}$$

where $f_{p0}(a/r_0)^3$ is the volume fraction of the EHPs (Pontefisso et al., 2013). Finally, the modulus of elasticity in tension of the nanocomposite is $E_o = 9K_oG_o/(3K_o + G_o)$. Using Eqs. (4.14)–(4.17) in combination with the experimental data for the elastic modulus allows the best fitting for the elastic properties and size of the interphase zone (Quaresimin et al., 2014).

It is finally worth mentioning that, as highlighted by Eqs. (4.10) and (4.13), the estimated value of the overall fracture toughness of the nanocomposite depends also on the strength and yield properties of the interphase. However, precise information on these interphase properties are unavailable thus far and, for the sake of simplicity, can be considered as identical to those of the matrix.

4.5.2.7 *Overall fracture toughness of the nanocomposites*

As far as the fracture toughness improvements due to each relevant damaging mechanism, ΔG_i, are known, the overall nanocomposite fracture toughness can be estimated substituting Eqs. (4.5), (4.9), and (4.11) into Eq. (4.1):

$$G_{Ic} = \frac{G_{Im}}{1 - f_{p0}\left(\psi_{db} + \psi_p + \psi_{SB}\right)} \tag{4.18}$$

As a final note, it is necessary to point out that as a basic assumption of the proposed model, the nanofiller is supposed to be uniformly dispersed and distributed, neglecting the high tendency to agglomerate exhibited by nanoparticles beyond a certain value of the weight fraction. It is clear that this approximation limits the application of the model to low nanofiller contents.

In Quaresimin et al. (2014), Eq. (4.18) has been validated versus several experimental results, taken from the literature, showing a very satisfactory agreement for low nanofiller contents. Two examples are shown in Figures 4.8 and 4.9. It is evident that, while increasing the filler content, Eq. (4.18) results in an overestimation of the fracture toughness of the nanocomposite, according to the explanations given before.

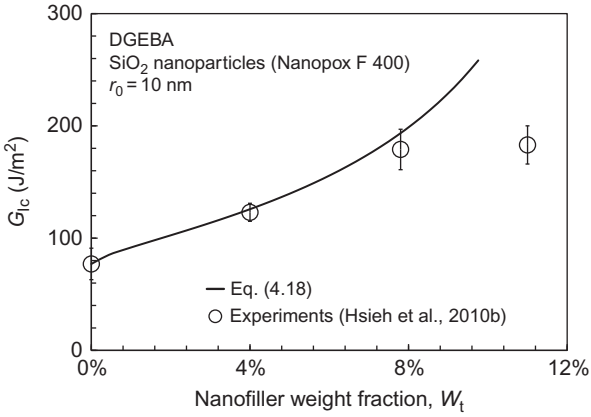

Figure 4.8 Comparison between Eq. (4.18) (solid line) and the experimental data from DGEBA/Nanopox system reported in Hsieh et al. (2010b).

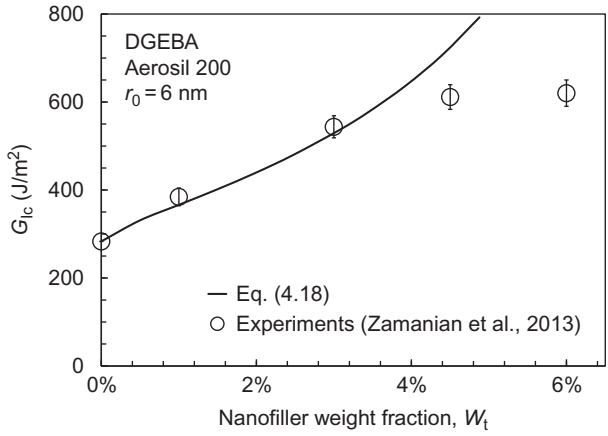

Figure 4.9 Comparison between Eq. (4.18) (solid line) and the experimental data from DGEBA/Aerosil 200 system (Zamanian et al., 2013).

4.6 Conclusions

This chapter has reviewed the main contributions reported in the literature dealing with the damage mechanisms of nanoparticle-reinforced polymers. The energy absorption mechanisms detected from experimental observations have been classified and described. Insights in predictive models incorporating these mechanisms have been given, along with examples of applications.

References

Ajayan, P.M., Schadler, L.S., Braun, P.V., 2003. Nanocomposite Science and Technology. Wiley-VCH, Weinheim, ISBN: 3527303596.

Akbari, B., Bagheri, R., 2007. Deformation mechanism of epoxy/clay nanocomposite. Eur. Polym. J. 43, 782–788.

Arakawa, K., Takahashi, K., 1991. Relationships between fracture parameters and fracture surface roughness of brittle polymers. Int. J. Fract. 48, 103–114.

Becker, O., Cheng, Y.B., Varley, R., Simon, G., 2003. Layered silicate nanocomposites based on various high-functionality epoxy resins: the influence of cure temperature on morphology, mechanical properties and free volume. Macromolecules 36, 1616–1625.

Bishop, J.F.W., Hill, R., 1951. A theory of the plastic distortion of a polycrystalline aggregate under combined stresses. Philos. Mag. 42, 414–427.

Chen, J.K., Huang, Z.P., Zhu, J., 2007. Size effect of particles on the damage dissipation in nanocomposites. Compos. Sci. Technol. 14, 2990–2996.

Chen, Q., Chasiotis, I., Chen, C., Roy, A., 2008. Nanoscale and effective mechanical behavior and fracture of silica nanocomposites. Compos. Sci. Technol. 68, 3137–3144.

Dittanet, P., Pearson, R.A., 2012. Effect of silica nanoparticle size on toughening mechanisms of filled epoxy. Polymer 53, 1890–1905.

Faber, K.T., Evans, A.G., 1983a. Crack deflection process—I. Theory. Acta Metall. 31, 565–576.

Faber, K.T., Evans, A.G., 1983b. Crack deflection process—II. Experiment. Acta Metall. 31, 577–584.

Fermeglia, M., Ferrone, M., Pricl, S., 2003. Computer simulation of nylon-6/organoclay nanocomposites: prediction of the binding energy. Fluid Phase Equilib. 212, 315–329.

Fiedler, B., Gojny, F.H., Wichmann, M.H.G., Nolte, M.C.M., Schulte, K., 2006. Fundamental aspects of nano-reinforced composites. Compos. Sci. Technol. 66, 3115–3131.

Freund, L.B., Hutchinson, J.W., 1985. High-strain-rate crack growth in rate dependent plastic solids. J. Mech. Phys. Solids 33, 169–191.

Gou, J.H., Minaie, B., Wang, B., Liang, Z.Y., Zhang, C., 2004. Computational and experimental study of interfacial bonding of single-walled nanotube reinforced composites. Comput. Mater. Sci. 31, 225–236.

Gou, J.H., Liang, Z.Y., Zhang, C., Wang, B., 2005. Computational analysis of effect of single-walled carbon nanotube rope on molecular interaction and load transfer of nanocomposites. Composites 36, 524–533.

Gurson, A.L., 1977. Continuum theory of ductile rupture by void nucleation and growth: part I—yield criteria and flow rules for porous ductile media. J. Eng. Mater. Technol. 99, 2–15.

Hashin, Z., Shtrikman, S., 1963. A variational approach to the theory of the elastic behaviour of multiphase materials. J. Mech. Phys. Solids 11, 127–140.
Hsieh, T.H., Kinloch, A.J., Masania, K., Taylor, A.C., Sprenger, S., 2010a. The mechanisms and mechanics of the toughening of epoxy polymers modified with silica nanoparticles. Polymer 51, 6284–6294.
Hsieh, T.H., Kinloch, A.J., Masania, K., Sohn Lee, J., Taylor, A.C., Sprenger, S., 2010b. The toughness of epoxy polymers and fibre composites modified with rubber microparticles and silica nanoparticles. J. Mater. Sci. 45, 1193–1210.
Huang, Y., Kinloch, A.J., 1992. Modelling of the toughening mechanisms in rubber-modified epoxy polymers. Part II: a quantitative description of the microstructure–fracture property relationships. J. Mater. Sci. 27, 2763–2769.
Hutchinson, J.W., 1964. Plastic stress–strain relation of F.C.C polycrystalline metals hardening according to Taylor's rule. J. Mech. Phys. Solids 12, 11–24.
Jajam, K.C., Tippur, H.V., 2012. Quasi-static and dynamic fracture behavior of particulate polymer composites: a study of nano- vs. micro-size filler and loading-rate effects. Composites 43, 3467–3481.
Johnsen, B.B., Kinloch, A.J., Mohammed, R.D., Taylor, A.C., Sprenger, S., 2007. Toughening mechanisms of nanoparticle-modified epoxy polymers. Polymer 48, 530–541.
Lange, F.F., 1970. The interaction of a crack front with a second-phase dispersion. Philos. Mag. 22, 983–992.
Lauke, B., 2008. On the effect of particle size on fracture toughness of polymer composites. Compos. Sci. Technol. 68, 3365–3372.
Liang, Y.L., Pearson, R.A., 2009. Toughening mechanisms in epoxy–silica nanocomposites (ESNs). Polymer 50, 4895–4905.
Liao, K., Li, S., 2001. Interfacial characteristics of a carbon nanotube-polystyrene composite system. Appl. Phys. Lett. 79, 4225–4227.
Lordi, V., Yao, N., 2000. Molecular mechanics of binding in carbon-nanotube–polymer composites. J. Mater. Res. 15, 2770–2779.
Ng, C.B., Ash, B.J., Schadler, L.S., Siegel, R.W., 2001. A study of the mechanical and permeability properties of nano- and micron-TiO_2 filled epoxy composites. Adv. Compos. Lett. 10, 101–111.
Odegard, G.M., Clancy, T.C., Gates, T.S., 2005. Modeling of mechanical properties of nanoparticle/polymer composites. Polymer 46, 553–562.
Pearson, R.A., Yee, A.F., 1993. Toughening mechanisms in thermoplastic-modified epoxies: 1. Modification using poly(phenylene oxide). Polymer 34 (17), 3658–3670.
Pontefisso, A., Zappalorto, M., Quaresimin, M., 2013. Influence of interphase and filler distribution on the elastic properties of nanoparticle filled polymers. Mech. Res. Commun. 52, 92–94.
Qian, D., Liu, W.K., Ruoff, R.S., 2003. Load transfer mechanism in carbon nanotube ropes. Compos. Sci. Technol. 63, 1561–1569.
Quaresimin, M., Salviato, M., Zappalorto, M., 2012. Strategies for the assessment of nanocomposite mechanical properties. Composites 43, 2290–2297.
Quaresimin, M., Salviato, M., Zappalorto, M., 2014. A multi-scale and multi-mechanism approach for the fracture toughness assessment of polymer nanocomposites. Compos. Sci. Technol. 91, 16–21.
Rosso, P., Ye, L., Friedrich, K., Sprenger, S., 2006. A toughened epoxy resin by silica nanoparticle reinforcement. J. Appl. Polym. Sci. 100, 1849–1855.
Salviato, M., Zappalorto, M., Quaresimin, M., 2013a. Nanoparticle debonding strength: a comprehensive study on interfacial effects. Int. J. Solids Struct. 50, 3225–3232.

Salviato, M., Zappalorto, M., Quaresimin, M., 2013b. Plastic shear bands and fracture toughness improvements of nanoparticle filled polymers: a multiscale analytical model. Compos. A: Appl. Sci. Manuf. 48, 144–152.

Sevostianov, I., Kachanov, M., 2007. Effect of interphase layers on the overall elastic and conductive properties of matrix composites. Applications to nanosize inclusion. Int. J. Solids Struct. 44, 1304–1315.

Sumfleth, J., Prehn, K., Wichmann, M.H.G., Wedekind, S., Schulte, K., 2010. A comparative study of the electrical and mechanical properties of epoxy nanocomposites reinforced by CVD- and arc-grown multi-wall carbon nanotubes. Compos. Sci. Technol. 70, 173–180.

Thostenson, E.T., Li, C., Chou, T.W., 2005. Nanocomposites in context. Compos. Sci. Technol. 65, 491–516.

Tian, L., Rajapakse, R.K.N.D., 2007. Elastic field of an isotropic matrix with a nanoscale elliptical inhomogeneity. Int. J. Solids Struct. 44, 7988–8005.

Timoshenko, S.P., Goodier, J.N., 1970. Theory of Elasticity, third ed. McGraw-Hill, New York.

Toth, R., Coslanich, A., Ferrone, M., Fermeglia, M., Pricl, S., Miertus, S., Chiellini, E., 2004. Computer simulation of polypropylene/organoclay nanocomposites: characterization of atomic scale structure and prediction of binding energy. Polymer 45, 8075–8083.

Toth, R., Ferrone, M., Miertus, S., Chiellini, E., Fermeglia, M., Pricl, S., 2006. Structure and energetics of biocompatible polymer nanocomposite systems: a molecular dynamics study. Biomacromolecules 7, 1714–1719.

VanderHart, D.L., Asano, A., Gilman, J.W., 2001. Solid state NMR. Investigation of paramagnetic nylon-6 clay nanocomposites. 1. Crystallinity, morphology, and the direct influence of Fe^{3+} on nuclear spins. Chem. Mater. 131, 3796–3809.

Wetzel, B., Rosso, P., Haupert, F., Friedrich, K., 2006. Epoxy nanocomposites—fracture and toughening mechanisms. Eng. Fract. Mech. 73, 2375–2398.

Wichmann, M.H.G., Cascione, M., Fiedler, B., Quaresimin, M., Schulte, K., 2006a. Influence of surface treatment on mechanical behaviour of fumed silica/epoxy resin nano-composites. Compos. Interface 13, 699–715.

Wichmann, M.H.G., Sumfleth, J., Gojny, F.H., Quaresimin, M., Fiedler, B., Schulte, K., 2006b. Glass fibre-reinforced composites with enhanced mechanical and electrical properties—benefits and limitations of a nanoparticle-modified matrix. Eng. Fract. Mech. 73, 2346–2359.

Williams, J.G., 2010. Particle toughening of polymers by plastic void growth. Compos. Sci. Technol. 70, 885–891.

Wong, M., Paramsothy, M., Xu, X.J., Ren, Y., Li, S., Liao, K., 2003. Physical interactions at carbon nanotube–polymer interface. Polymer 44, 7757–7764.

Yu, S., Yang, S., Cho, M., 2009. Multi-scale modeling of cross-linked epoxy nanocomposites. Polymer 50, 945–952.

Zamanian, M., Mortezaei, M., Salehnia, B., Jam, J.E., 2013. Fracture toughness of epoxy polymer modified with nanosilica particles: particle size effect. Eng. Fract. Mech. 97, 193–206.

Zappalorto, M., Salviato, M., Quaresimin, M., 2011. Influence of the interphase zone on the nanoparticle debonding stress. Compos. Sci. Technol. 72, 49–55.

Zappalorto, M., Salviato, M., Quaresimin, M., 2012a. A multiscale model to describe nanocomposite fracture toughness enhancement by the plastic yielding of nanovoids. Compos. Sci. Technol. 72, 1683–1691.

Zappalorto, M., Salviato, M., Quaresimin, M., 2012b. Stress distributions around rigid nanoparticles. Int. J. Fract. 176, 105–112.

Zax, D.B., Yang, D.K., Santos, R.A., Hegemann, H., Giannelis, E.P., Manias, E., 2000. Dynamical heterogeneity in nanoconfined polystyrene chains. J. Chem. Phys. 112, 2945–2951.

Zhang, H., Zhang, Z., Friedrich, K., Eger, C., 2006. Property improvements of in situ epoxy nanocomposites with reduced interparticle distance at high nanosilica content. Acta Mater. 54, 1833–1842.

Zhao, S., Schadler, L.S., Hillborg, H., Auletta, T., 2008. Improvements and mechanisms of fracture and fatigue properties of well-dispersed alumina/epoxy nanocomposites. Compos. Sci. Technol. 68, 2976–2982.

This page intentionally left blank

Part Two

Toughening mechanisms for fiber-reinforced composites

This page intentionally left blank

Toughening mechanisms for the fiber of middle-large-aspect-ratio-reinforced composites

5

V. Kompiš[1], *Z. Murčinková*[2], *M. Žmindák*[1]
[1]University of Žilina, Žilina, Slovakia; [2]Technical University, Košice, Slovakia

5.1 Introduction

In past decades, fiber-reinforced composites have been widely used in practical engineering due to the superiority of their electro-thermo-mechanical properties over the single matrix (Agarwal et al., 2006; Peters, 1998). Particularly, composite materials reinforced by fibers such as carbon nanotubes (CNT) are often defined as materials of the future (Shonaike and Advani, 2003; Tang and Sheng, 2003; Legrand and Sénémand, 2003). In this application, the aspect ratio of fibers is often very large. CNT with a typical diameter of 1 nm and length of 1 cm would have an aspect ratio of 10^7:1. For reference, a tube of 1 in. in diameter would need to be 160 mile long to have the same aspect ratio.

CNTs are the stiffest and strongest of the existing fibers. They have a measured Young's modulus equal to 1400 GPa, compared to steel, which is only about 200 GPa. The projected tensile strength of a single CNT is greater than 100 GPa, with the stranded strength being many times higher. Again, for comparison, steel is usually about 1–2 GPa. Additionally, a single-wall-nanotube can be bent completely in half; when released, it will return to its original state with no dislocations or other defects. By orienting the CNT in a nanocomposite properly, the material can be made into a thermal conductor or insulator. Scientists discovered that if all the nanotubes are lined up parallel to each other and a heat flux is applied parallel to the direction of the nanotubes, the material is an excellent thermal conductor. However, for the same material, if the heat is applied perpendicular to the direction of the nanotubes, then the material reflects the heat and is an insulator.

Understanding the physical behavior of these fiber-reinforced composites is essential for structural design. The aim of this chapter is to show the method of continuous source functions (MCSF) developed by the first author (Kompiš et al., 2007, 2008) for composite materials reinforced by finite fibers. We will present the mathematical basis of the MCSF, some results, and a discussion of the toughening mechanism conductivity of composite materials reinforced by straight fibers of finite length.

Toughening Mechanisms in Composite Materials. http://dx.doi.org/10.1016/B978-1-78242-279-2.00005-6

5.2 Computational models for materials reinforced by parallel fibers of finite length

We assume all matrix materials and fibers are homogeneous and isotropic, the dimensions of the matrix are infinite (i.e., we will deal with the infinite matrix of material with homogeneous material properties), and models are restricted to linear behavior. Primary variables can be scalar, such as the temperature field in heat conduction; or vector, such as the displacement field in deformation of elastic bodies by forces. All fields are split into two parts: the homogeneous part corresponding to the homogeneous problem of the matrix without fibers, and the local (complementary) part simulating the influence of interactions of fibers with the matrix. We will particularly investigate the local fields in the matrix of the composite material.

The MCSF is a meshless method that satisfies the inter-domain compatibility in discrete collocation points (Figure 5.1) on the fiber–matrix interface.

Due to large aspect ratio of fibers, the toughening in elasticity and increase of conductivity in heat conduction of the composite material are realized particularly by a corresponding effect in the fiber axis direction. Because of this, the inter-domain compatibility between the fiber and matrix can be simplified and to assume that the temperature, displacement, strain, stress, etc., constant in all points of the cross-section are equal to each other. This property of the model is equivalent to the assumption of zero bending stiffness of fiber, which is important to the reduction of the computational model and to the correct simulation of composite materials reinforced by fibers with large aspect ratio as the nanotubes and similar fibers.

The interaction of fibers with matrix is simulated in the MCSF by source functions, which are 1D-continuously distributed along the fiber axis. The source functions are a fundamental solution of the corresponding problem (heat sources in heat conduction and forces in elasticity) and their derivatives. The forces are directed in the fiber axis direction. These source functions, however, are not able to simulate correctly the interaction of fibers with the matrix. In addition to the derivatives of the source functions, heat dipoles, force dipoles, and force couples are included along the fiber axes in order to correctly simulate the large axial stiffness of fibers to negligible bending stiffness and also the interaction among fibers.

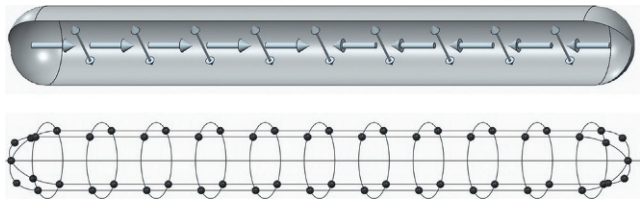

Figure 5.1 Distribution of source functions and collocation points.

Temperature field induced by a unit heat source acting in the arbitrary point of infinite domain is the fundamental solution for heat problems and is given by:

$$T = \frac{1}{4\pi r} \tag{5.1}$$

r is the distance of the field point t and source point s, where the heat source is acting at, i.e.,

$$r = \sqrt{r_i r_i}, \quad r_i = x_i(t) - x_i(s) \tag{5.2}$$

with the summation convention over repeated indices.

Temperature field induced by a unit heat dipole in x_i direction is

$$T = \frac{1}{4\pi}\left(\frac{1}{r}\right)_{,i} = -\frac{1}{4\pi}\frac{1}{r^2}r_{,i} = -\frac{1}{4\pi}\frac{x_i}{r^3} \tag{5.3}$$

where

$$r_{,i} = \frac{\partial r}{\partial x_i(t)} = \frac{r_i}{r} \tag{5.4}$$

Similarly, the displacement field in an elastic continuum caused by a unit force (upper index F denotes force) acting in the direction of the axis x_p is given by the Kelvin solution as it is known from boundary element method (BEM) (Kachanov et al., 2003; Brebbia et al., 1984):

$$U^F_{pi} = \frac{1}{16\pi G(1-v)r}\left[(3-4v)\delta_{ip} + r_{,i}r_{,p}\right] \tag{5.5}$$

where G and v are shear modulus and Poisson's ratio of the material of the matrix. δ_{ij} is the Kronecker's delta.

Gradients of the displacement fields are corresponding derivatives of the field (5.5) at the point t:

$$U^F_{pi,j} = -\frac{1}{16\pi G(1-v)r^2}\left[(3-4v)\delta_{pi}r_{,j} - \delta_{pj}r_{,i} - \delta_{ij}r_{,p} + 3r_{,i}r_{,j}r_{,p}\right] \tag{5.6}$$

The strains are:

$$\begin{aligned} E^F_{pij} &= \frac{1}{2}\left(U^F_{pi,j} + U^F_{pj,i}\right) \\ &= -\frac{1}{16\pi G(1-v)r^2}\left[(1-2v)\left(\delta_{pi}r_{,j} + \delta_{pj}r_{,i}\right) - \delta_{ij}r_{,p} + 3r_{,i}r_{,j}r_{,p}\right] \end{aligned} \tag{5.7}$$

and the stress components ij of this field are given by:

$$S^F_{pij} = 2GE^F_{pij} + \frac{2Gv}{1-2v}\delta_{ij}E^F_{pkk} = \frac{1}{8\pi(1-v)r^2}\left[(1-2v)\left(\delta_{ij}r_{,p} - \delta_{jp}r_{,i} - \delta_{ip}r_{,j}\right) - 3r_{,i}r_{,j}r_{,p}\right] \tag{5.8}$$

Displacement field of a dipole (upper index D denotes dipole) can be obtained from the displacement field of a force by differentiating it in the direction of the acting force, i.e.:

$$U^F_{pi,p} = U^D_{pi} = -\frac{1}{16\pi G(1-v)r^2}\left[3r_{,i}r^2_{,p} - r_{,i} + 2(1-2v)r_{,p}\delta_{ip}\right] \tag{5.9}$$

The summation convention does not apply over the repeated indices p here and in the following relations, as well.

Gradients of a dipole displacement field (5.9) obtained from the force fields by differentiating it in the direction of the acting force are:

$$U^D_{pi,j} = -\frac{1}{16\pi G(1-v)r^3} \left[\left(3 - 15r^2_{,p}\right)r_{,i}r_{,j} + 2(1-2v)\delta_{ip}\left(\delta_{jp} - 3r_{,j}r_{,p}\right) + 6r_{,i}r_{,p}\delta_{jp} + \delta_{ij}\left(3r^2_{,p} - 1\right)\right] \tag{5.10}$$

and from this field, corresponding strain and stress fields are obtained in the form:

$$E^D_{pij} = \frac{1}{2}\left(U^D_{pi,j} + U^D_{pj,i}\right) = -\frac{1}{16\pi G(1-v)r^3}\left[\left(3 - 15r^2_{,p}\right)r_{,i}r_{,j} + 2(1-2v)\delta_{ip}\delta_{jp} + 6v\left(\delta_{ip}r_{,j}r_{,p} + \delta_{jp}r_{,i}r_{,p}\right) + \delta_{ij}\left(3r^2_{,p} - 1\right)\right] \tag{5.11}$$

$$S^D_{pij} = 2GE^D_{pij} + \frac{2Gv}{1-2v}\delta_{ij}E^D_{pkk} = -\frac{1}{8\pi(1-v)r^3}\left[(1-2v)\left(2\delta_{ip}\delta_{jp} + 3r^2_{,p}\delta_{ij} - \delta_{ij}\right) + 6vr_{,p}\left(r_{,i}\delta_{jp} + r_{,j}\delta_{ip}\right) + 3\left(1 - 5r^2_{,p}\right)r_{,i}r_{,j}\right] \tag{5.12}$$

Gradients of the displacement field of a couple (upper index C denotes the couple) are obtained from the displacement field by differentiating it in the direction perpendicular to the acting force. It is also used in the model in order to satisfy the continuity conditions and bending flexibility of the fiber (defined by the difference of strains in the points of the fiber cross-section) as:

$$U^C_{pqi} = -\frac{1}{16\pi G(1-v)r^2}\left[(3-4v)\delta_{ip}r_{,q} + 3r_{,p}r_{,q}r_{,i} - \delta_{iq}r_{,p}\right] \tag{5.13}$$

Corresponding strain and stress fields are

$$E^C_{pqij} = -\frac{1}{16\pi G(1-\nu)r^3}\left[(1-2\nu)\left(\delta_{ip}\delta_{jq}+\delta_{jp}\delta_{iq}\right) - 3(1-2\nu)\left(\delta_{ip}r_{,j}+\delta_{jp}r_{,i}\right)r_{,q} + 3r_{,p}\left(\delta_{jq}r_{,i}+\delta_{iq}r_{,j}\right) + 3\delta_{ij}r_{,p}r_{,q} - 15r_{,p}r_{,q}r_{,i}r_{,j}\right] \tag{5.14}$$

$$S^C_{pij} = -\frac{1}{8\pi(1-\nu)r^3}\left[3(1-2\nu)\left(\delta_{ij}r_{,p}-\delta_{jp}r_{,i}-\delta_{ip}r_{,j}\right)r_{,q} + 3\left(\delta_{iq}r_{,j}r_{,p}+\delta_{jq}r_{,i}r_{,p}\right) + (1-2\nu)\left(\delta_{jp}\delta_{iq}+\delta_{ip}\delta_{jq}\right) - 15r_{,p}r_{,q}r_{,i}r_{,j}\right] \tag{5.15}$$

In order to find the unknown intensities of the source functions, we have to solve the 1D quasi-singular integral equations of the form:

$$\int_r K(s,t)f(t)\mathrm{d}\Gamma = g(s) \tag{5.16}$$

where $K(s,t)$ is kernel function, which is the corresponding source function in our case, $f(t)$ is the unknown intensity of the source function, $g(s)$ is the function containing boundary conditions (BC), and Γ is the 1D integration curve along axes of fibers.

Note that in the present model, the solution of the integral equation (5.16) is made in the discrete points, s, of the fiber–matrix interface and the integration path and integration points, t, are outside of the domain (the domain of the solution is the matrix material), i.e., inside the fiber. Because of this, we can call this method a quasi-meshless method, as the mesh is used for the integration of source functions along the axes of fibers only.

In the numerical evaluation of the integral equation (5.16), the intensity of source functions is approximated by 1D quadratic nonuniform rational basis splines (NURBS) (Piegl and Tiller, 1997; Rogers, 2001) which enable a definition of shape functions to have continuous first derivative over the whole integration path and nonequal distribution of nodal points. Because of large gradients in the source functions close to the end parts of the fibers, this is a good choice for numerical stability of the model (Kompiš et al., 2007, 2008).

Basic variables are temperature in heat and displacement in elasticity problems. Basic source functions are defined by the unit heat source in heat and unit force in elasticity. Note that corresponding source functions for these variables are weak singular, i.e. integrable in normal sense, for both problems (see Eqs. 5.1 and 5.5).

The computations are performed on the homogeneous field of matrix material, and BCs are prescribed along fiber boundaries. Fields of variables in the fibers are computed in the iteration process in the next steps. In the present models, fibers are considered to be straight and parallel. As the BCs are not known *a priori*, the problem is solved iteratively, and it is assumed that the fibers are superconductors in heat and rigid in elasticity problems in the first iteration step. This is equivalent to the assumption of a constant gradient of temperature and displacement in the fiber axes direction, if the fibers are straight. This corresponds to constant heat flow in heat problem and constant strain in elasticity along a fiber.

As the temperature and displacement are not known in the composite, the BC for the local problem can be specified as follows:

- temperature difference between corresponding collocation point and the center of the fiber (it is opposite to the temperature difference in the homogeneous material),
- temperature difference between pairs of points on opposite sides of the fiber cross-section (assumed equal to zero) in order to simulate the interaction between fibers, for heat transfer,
- displacement difference between corresponding collocation point and the center of the fiber (it is opposite to the displacement difference in the homogeneous material),
- displacement difference between pairs of points on opposite sides of the fiber cross-section (assumed equal to zero) in order to simulate the interaction between fibers, and
- strain difference between pairs of points on opposite sides of the fiber cross-section (assumed equal to zero) to simulate the stiffness of fibers with good numerical stability/accuracy, for elasticity.

The inter-domain continuity is satisfied using heat sources and vectors of heat dipoles with vector direction perpendicular to each other and also to the fiber axis in heat transfer problems and by unit forces in fiber axis direction and two force dipoles perpendicular to each other and also to the fiber axis direction and two couples with torque effect perpendicular to the fiber axis. All these sources are 1D-continuously distributed along the fiber axes.

The temperature/displacement change of the center of each fiber by the interaction is not known *a priori* in both the heat and elasticity problem. It is obtained by the energy-balance/equilibrium condition in each fiber. This is realized by including further r.h.s. (right-hand side) terms by prescribing temperature/displacement in corresponding fiber center equal to one and zero for the other fibers. In this way, we have as many additional r.h.s. terms as there are fibers in the problem. Thus, we have to solve after discretization and integration the following system of linear equations

$$\mathbf{AC} = \mathbf{B} \tag{5.17}$$

where **A** is the matrix in which rows express the temperatures in collocation points along fiber–matrix interface and columns correspond to the NURBS shape functions of the intensities of heat sources along the fiber axes. **B** is the matrix with rows corresponding to the rows of the matrix **A** and n_f+1 columns for problem with n_f fibers in the patch of fibers in the matrix of the composite. The first n_f columns contain units in collocation points of corresponding fiber and zeros in collocation points of all other fibers. The last column is negative values of the temperatures corresponding to the gradient of temperature in the matrix material and equal to zero in the center of the fiber. The matrix **C** is the intensities of heat sources in the fibers corresponding to all n_f+1 columns of **B**.

Integrating the heat sources along each fiber for the given gradient of temperature, c_{ti}, (from the last column in the matrix **C**) and also for the unit and zero temperatures in fibers, c_{ij}, we can find the state of equilibrium of energy in all fibers, which defines the temperature in the center of each fiber, t_{Cj}:

$$c_{ij}t_{Cj} = c_{ti} \tag{5.18}$$

Having computed the source functions (i.e., the heat sources and heat dipoles) one can compute temperatures and temperature gradients in each direction in arbitrary point of the matrix as well as along fibers.

Because of the fiber dimensions, the constant heat flow in the cross-section of fibers is a good approximation. The heat flow in fibers is obtained from the heat sources in corresponding fiber.

For the finite conductivity of fibers, the temperature change along fiber is computed by the iteration process, with the starting assumption of the fiber material to be superconducting. The heat flow in fibers is obtained in the next iteration steps. From the heat flow and fiber material conductivity one can obtain temperature distribution in the fibers and correct the r.h.s. terms for the next iteration step. Note that compatibility of both temperature and heat flow in the collocation points along fibers is satisfied in each iteration step in this way. The matrix **A** is computed only once, as the problem is linear, i.e., material properties of the matrix material do not change.

There are more equations (usually much more equations) than the unknown parameters defining the source functions and the problem is solved in the least squares sense (Kaukič, 1998). The formulation using differences of temperature (and not the temperature) in corresponding collocation points results in good numerical stability of the models.

The problem is very similar in the elasticity. The iteration starts with assuming stiff fibers and prescribing displacement along a fiber without a corresponding rigid body displacement in its center. Displacements, strains, and stresses in the matrix are obtained directly, and total forces, strains, and displacements in the cross-sections of fibers are again computed from the source functions.

The systems of Eqs. (5.17) and (5.18) are similar also in elasticity, but there are more source functions in this case. We have forces in fiber direction and dipoles and couples in two perpendicular directions to the fiber axis. Also, there are displacements in the fiber direction and displacement and strain differences in opposite points of the fiber cross-section in the fiber axis direction. However, the system (5.18) has only as many rows and columns as we have fibers in the patch, because only equilibrium in fiber axis direction is used in the present model.

Recall that the deformation of fiber is obtained assuming constant strains in fiber direction for finite stiffness of fibers, and it is used to correct the r.h.s. terms in the next iteration step. Compatibility of displacement and strains in fiber axis direction is satisfied in collocation points.

5.3 Computational results, toughening mechanism, and homogenization

As the models are linear, all variables are considered to be dimensionless; so, it is supposed that material constants of the matrix, conductivity k_m, and modulus of elasticity E_m, are equal to one. Behavior of the composite will be shown in similar problems for both the heat conduction and elasticity. In examples, the radius of fibers $R = 1$, length of fibers $L = 100$, resp. $L = 1000$, i.e. AR = 50:1, resp. AR = 500:1. The fibers are regularly

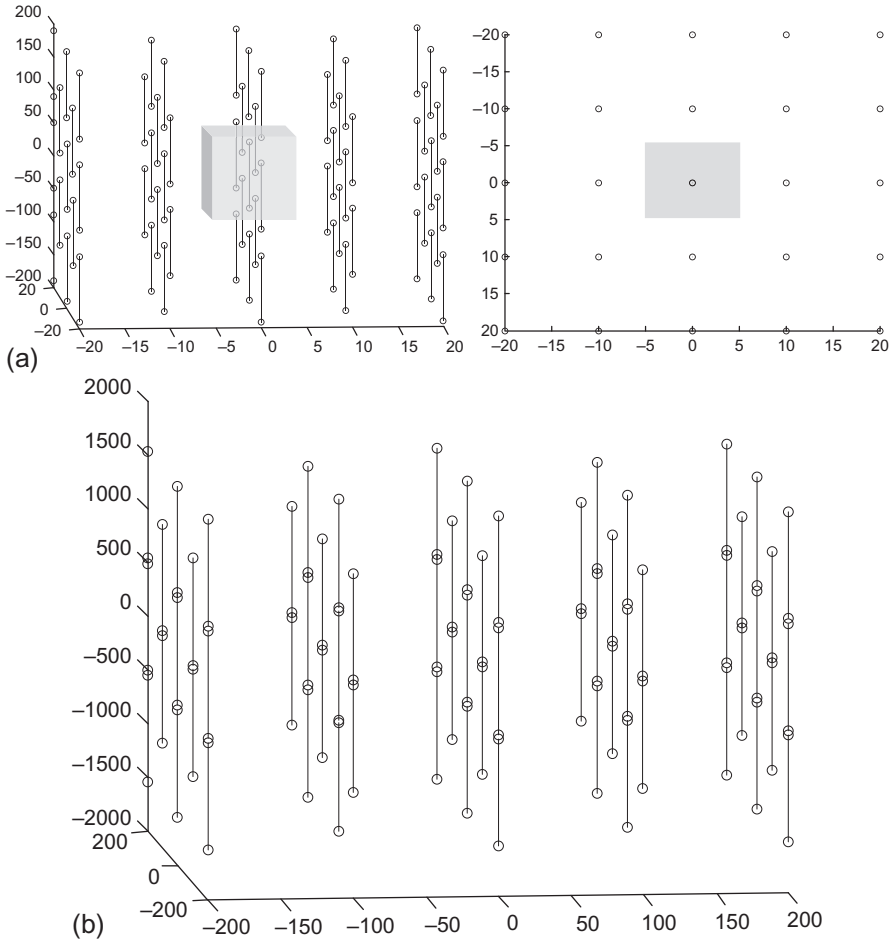

Figure 5.2 (a) Fiber alignment in the matrix, model Nos. A–D. (b) Fiber alignment in the matrix, model No. E.

distributed, parallel to each other with overlay in fibers' direction x_3. Two different gaps in fiber direction x_3 are considered: in the first case, the gap $g = 40$ and in the second $g = 5$ and the distance between fibers in perpendicular direction will be $d = 10$ in the first and $d = 4$ in the second case (in Figure 5.2a shown the first case). The gap between fibers $g = 40$ and $d = 100$ for the examples with aspect ratio AR = 500:1 (Figure 5.2b).

Heat flow in corresponding homogeneous cases will be $q_3 = 1$ and strain $\varepsilon_{33} = 1$. The material of fibers is chosen close to superconductive material with a coefficient of conductivity $k_f = 50{,}000$ in one case, and in another problem $k_f = 500$, and the modulus of elasticity for very stiff fibers $E_f = 50{,}000$ and 500 for another problem. The characteristics of all models are summarized in Table 5.1. The fibers are arranged symmetrically in all directions.

Table 5.1 Model characteristics

	Model No.				
	A	**B**	**C**	**D**	**E**
k_f, resp. E_f	50,000	50,000	1000	1000	50,000
AR	50:1	50:1	50:1	50:1	500:1
g, d	40, 10	5, 4	40, 10	5, 4	40, 100

As we model the finite number of fibers in infinite matrix, we will show change of the fields in five layers of fibers (63 fibers, Figure 5.2). Heat flow and temperature along fibers relative to the temperature in the fiber center are shown in Figures 5.3 and 5.4; strains and displacements in fiber axes direction of points along fiber (also related the displacement in the center of corresponding fiber) are presented in Figures 5.5 and 5.6. The results of previous iteration steps are shown by dashed lines, those of the last iteration step by a solid line.

Maximum heat flow in fibers and temperatures in the centers of fibers, respectively, maximal axial stresses in fibers and displacements in the centers of fibers are given in Tables 5.2–5.5.

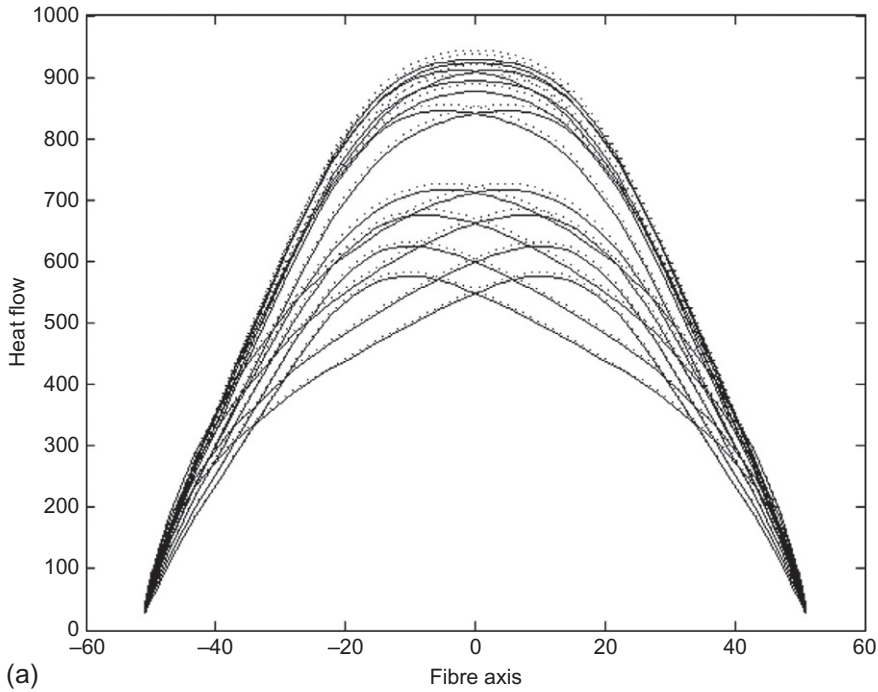

Figure 5.3 Heat flow along fibers.

(Continued)

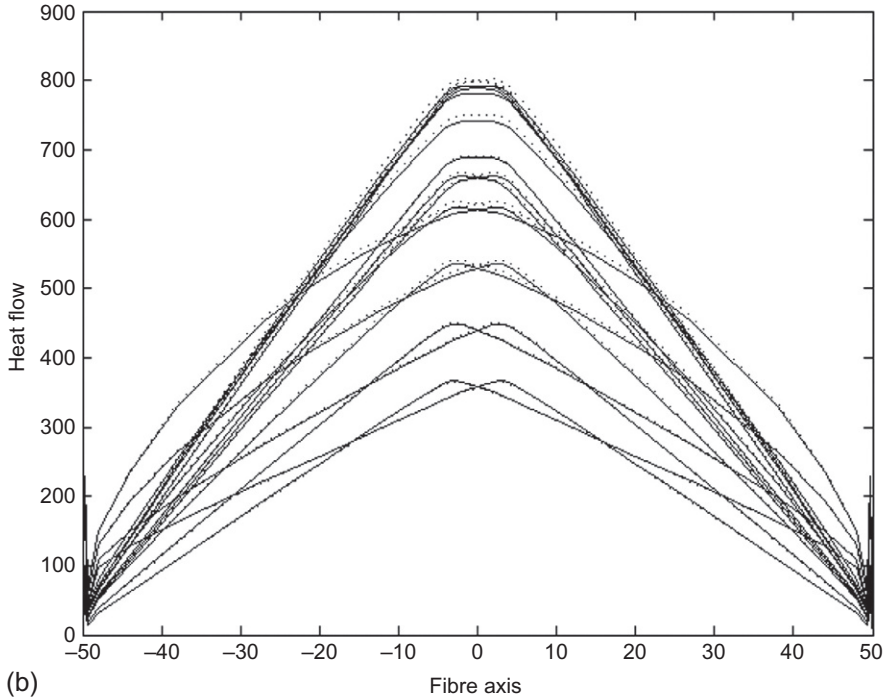

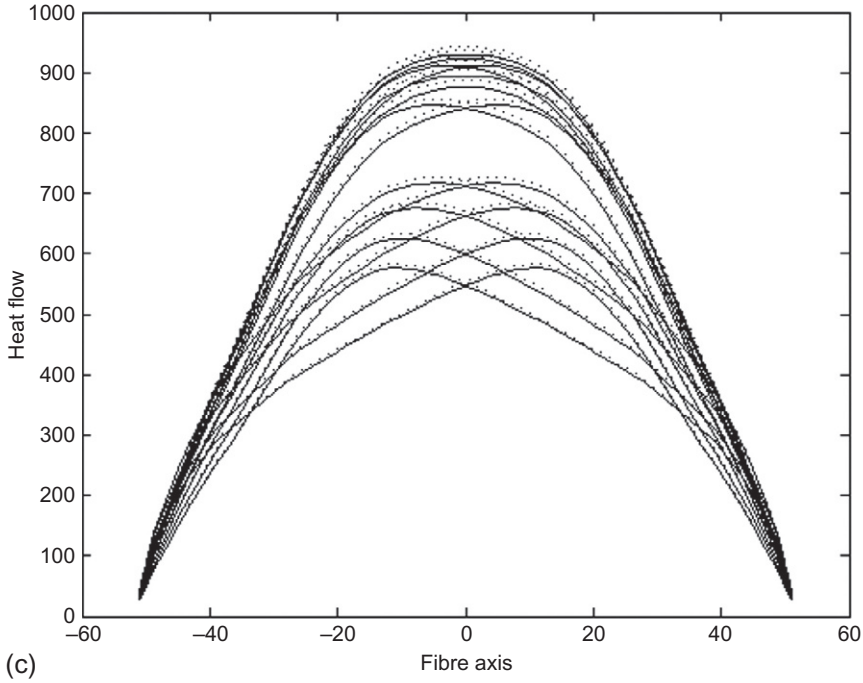

Figure 5.3. continued

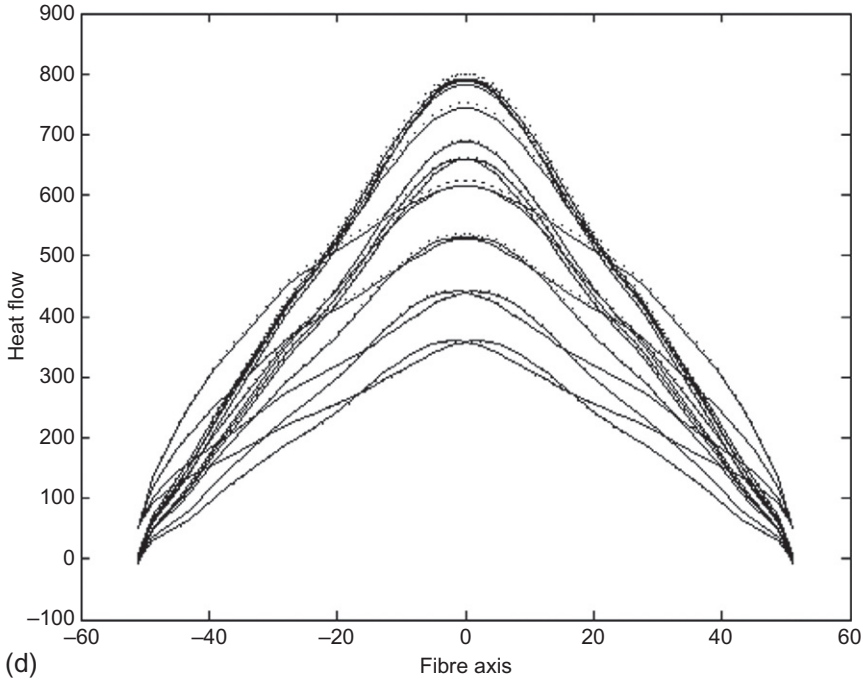

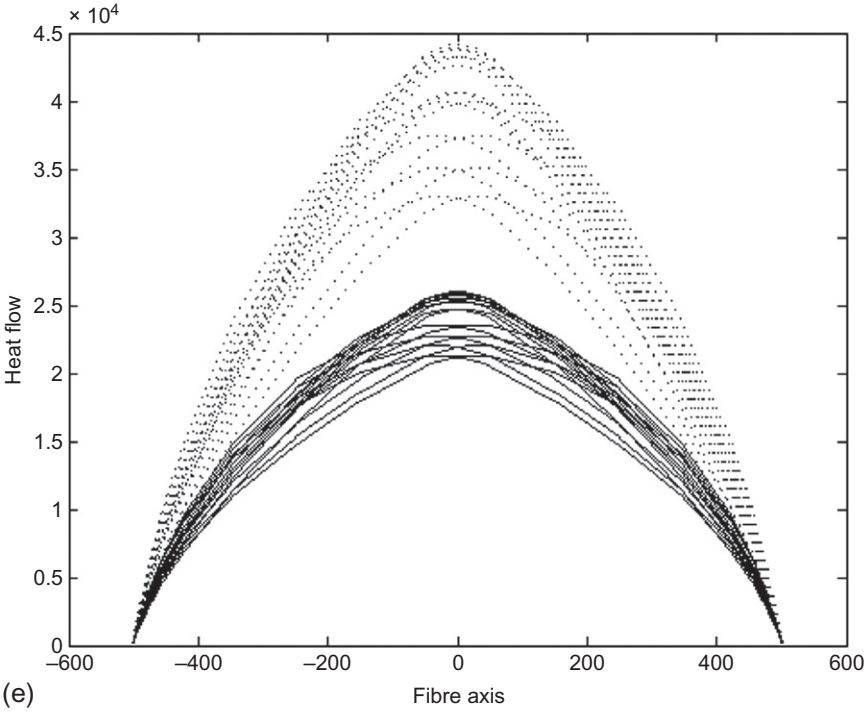

Figure 5.3. continued

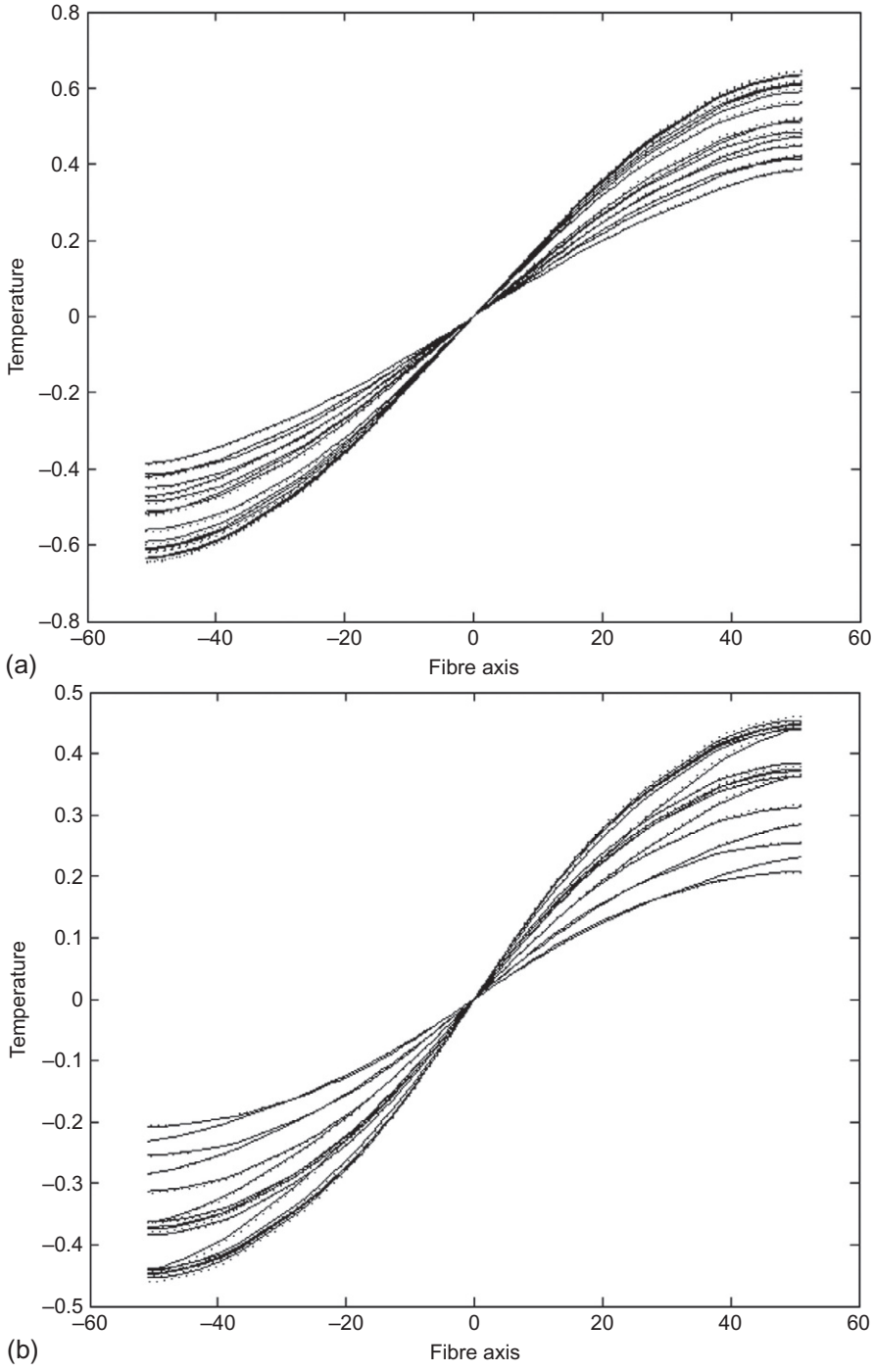

Figure 5.4 Temperature along fibers.

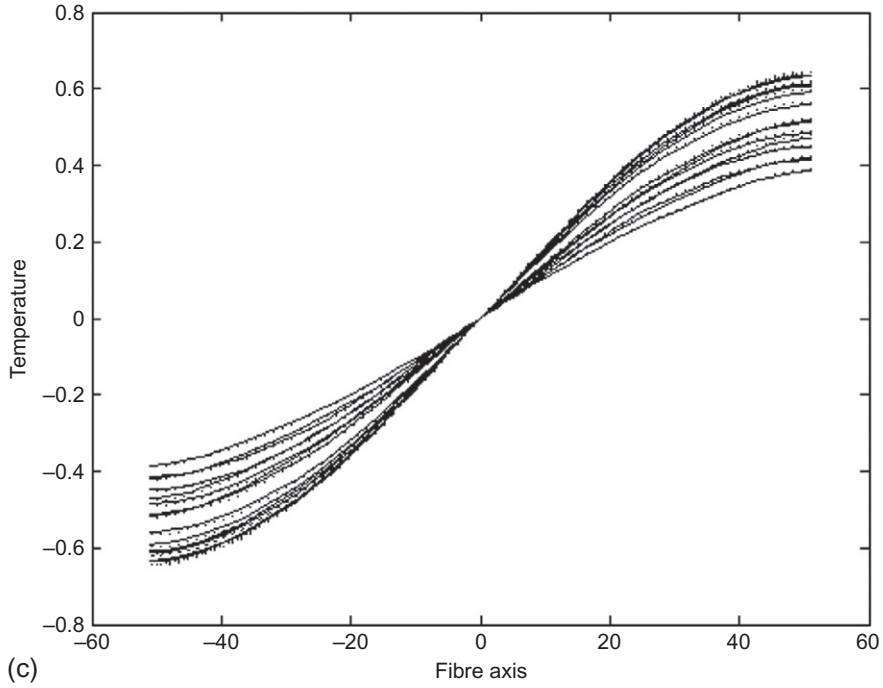

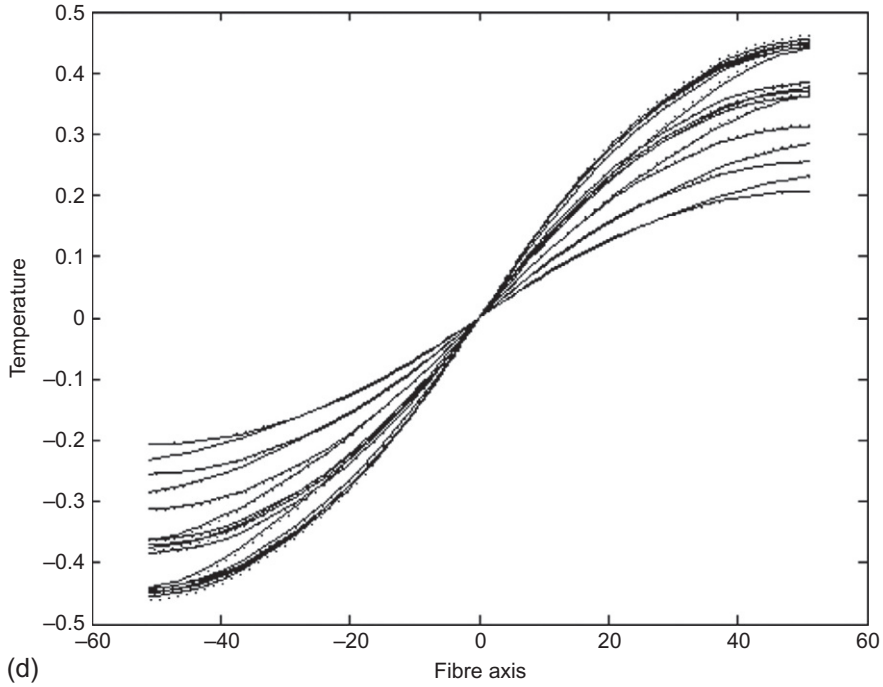

Figure 5.4. continued

(Continued)

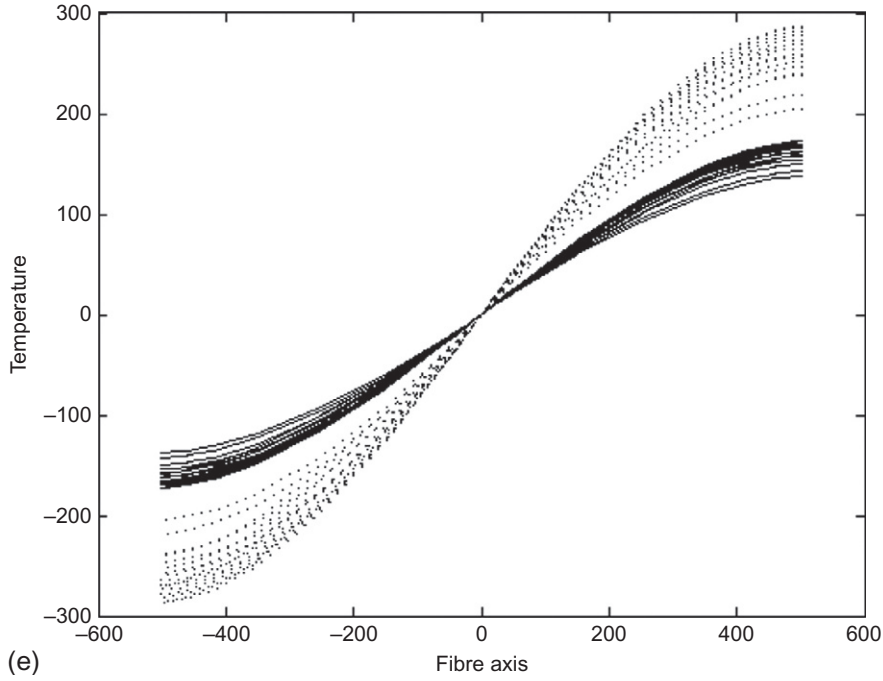

Figure 5.4. continued

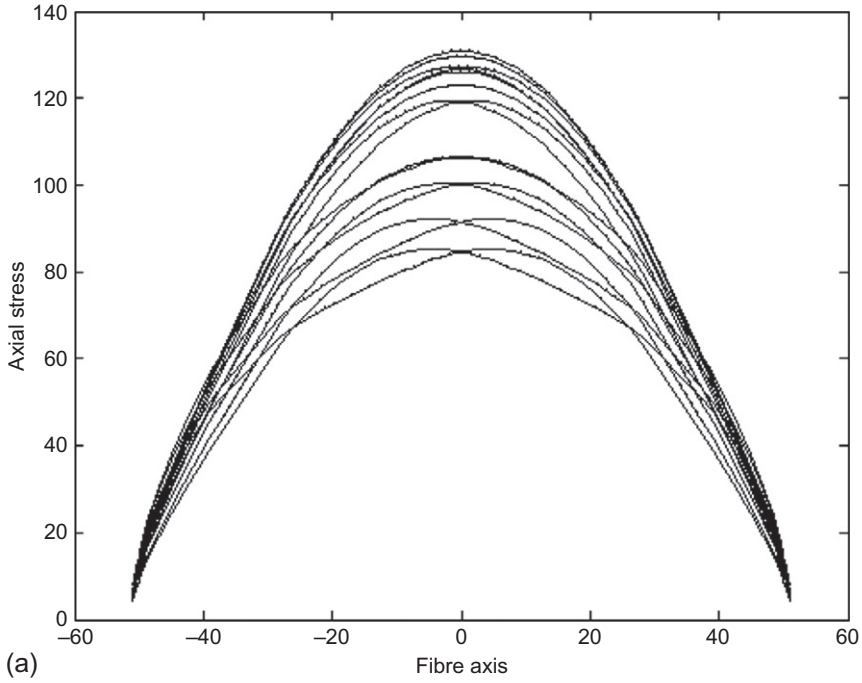

Figure 5.5 Axial stresses along fibers.

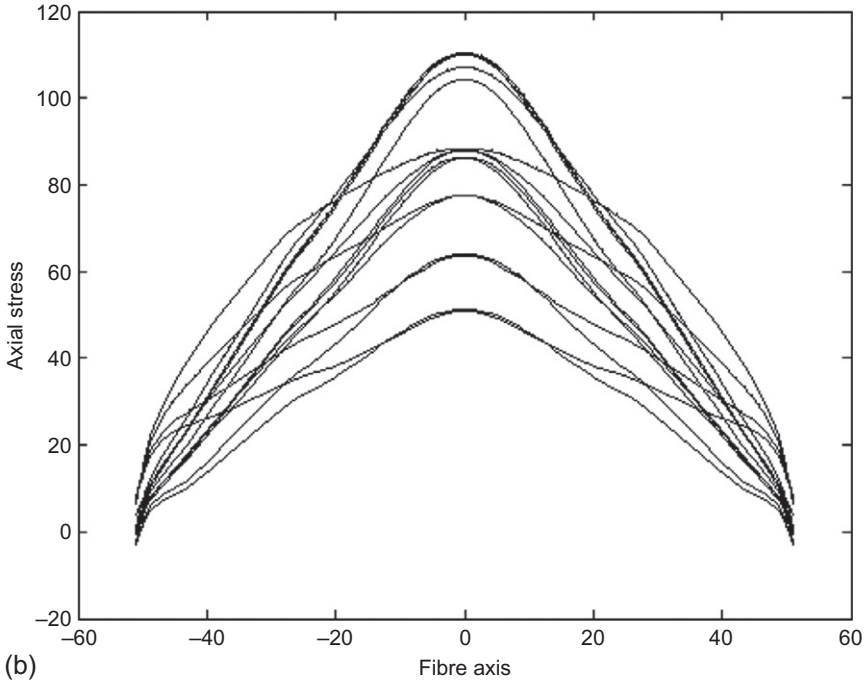

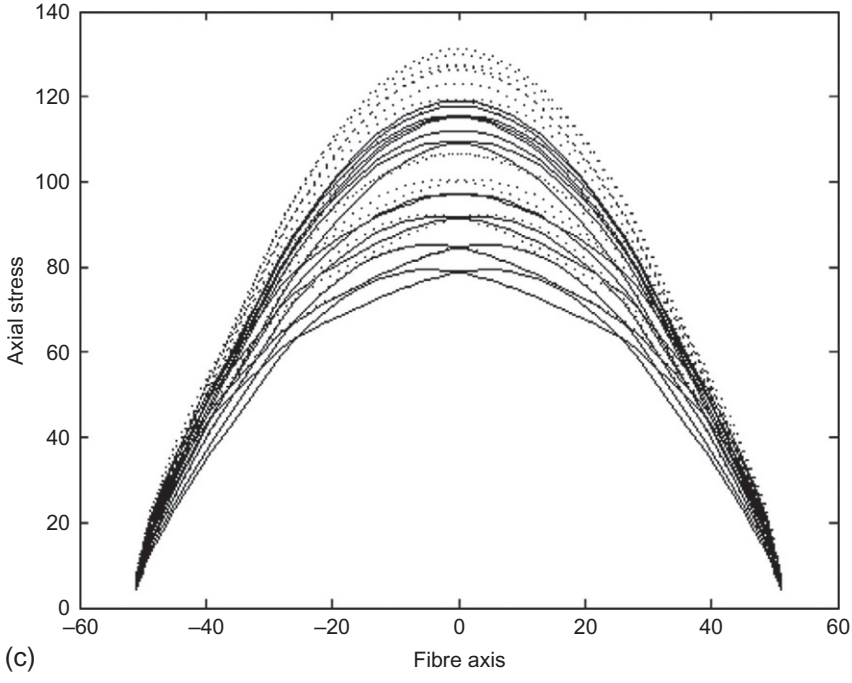

Figure 5.5. continued

(Continued)

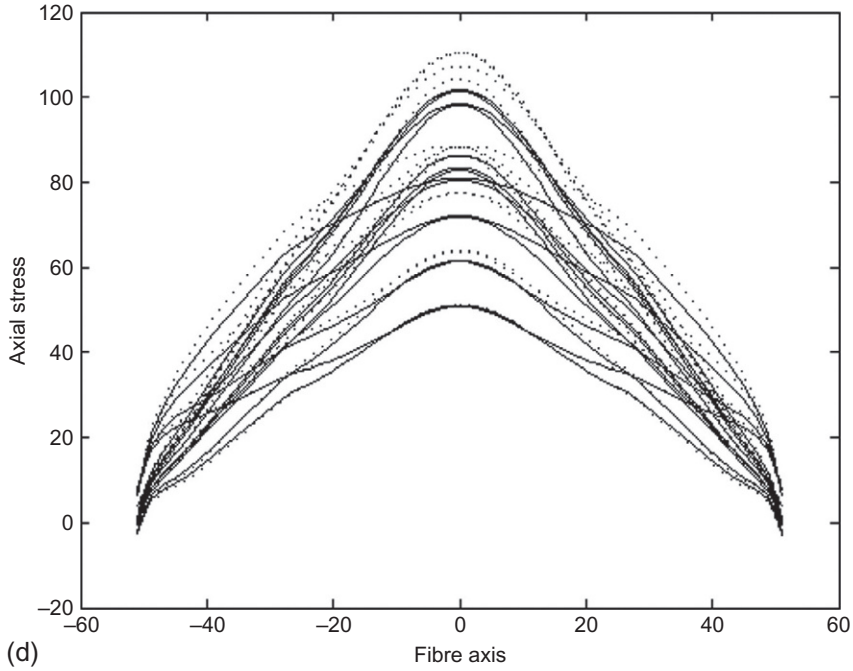

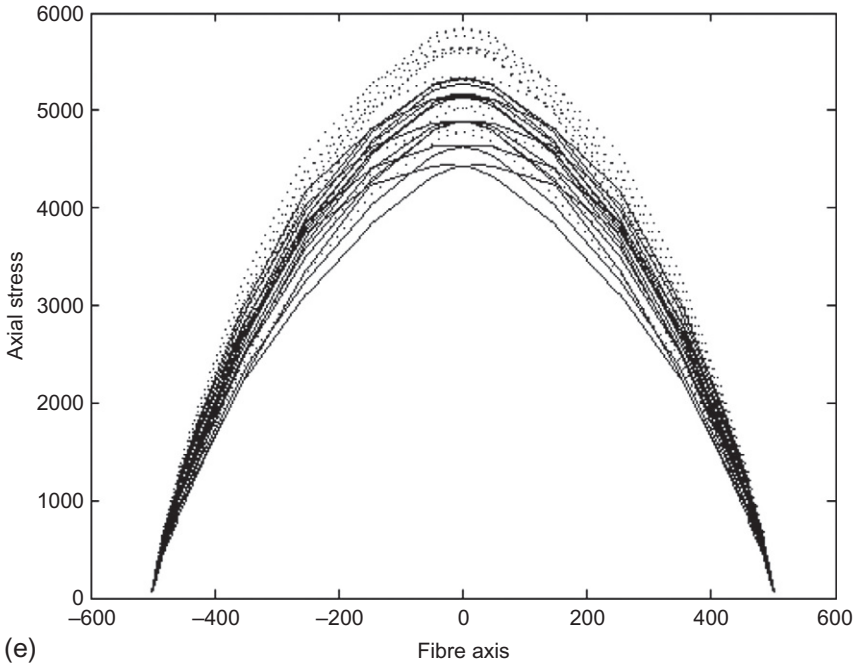

Figure 5.5. continued

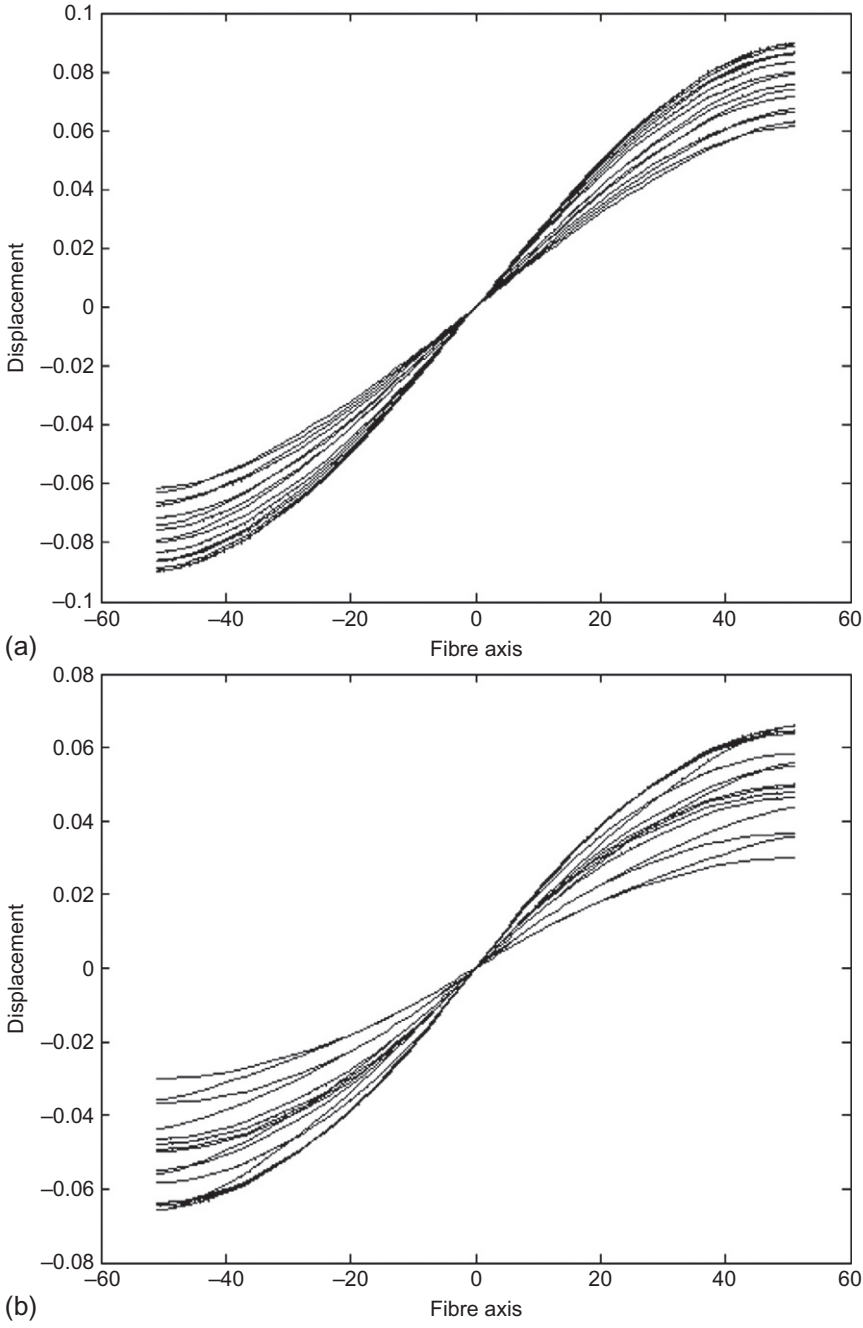

Figure 5.6 Displacement in axis direction along fibers.

(Continued)

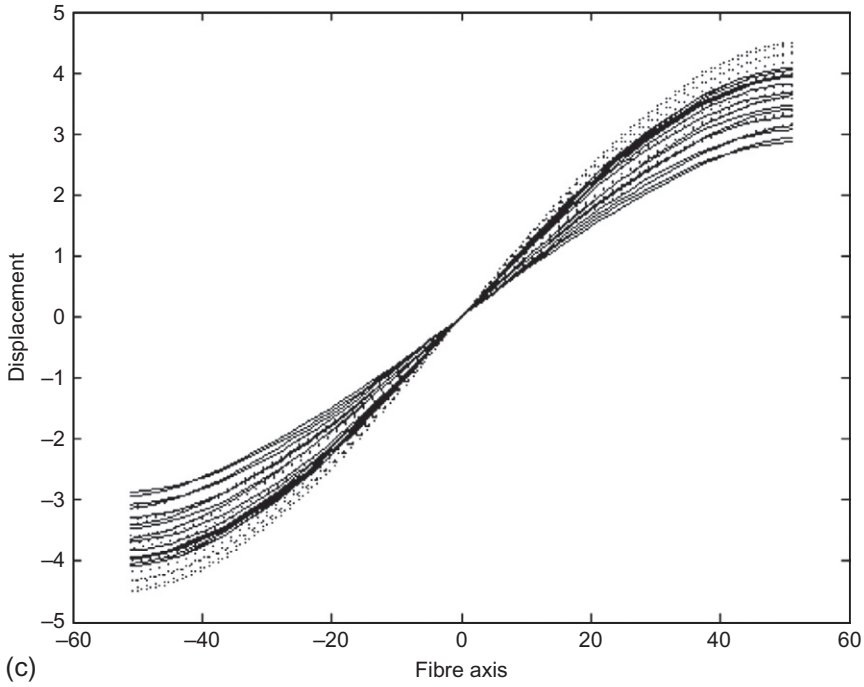

(c)

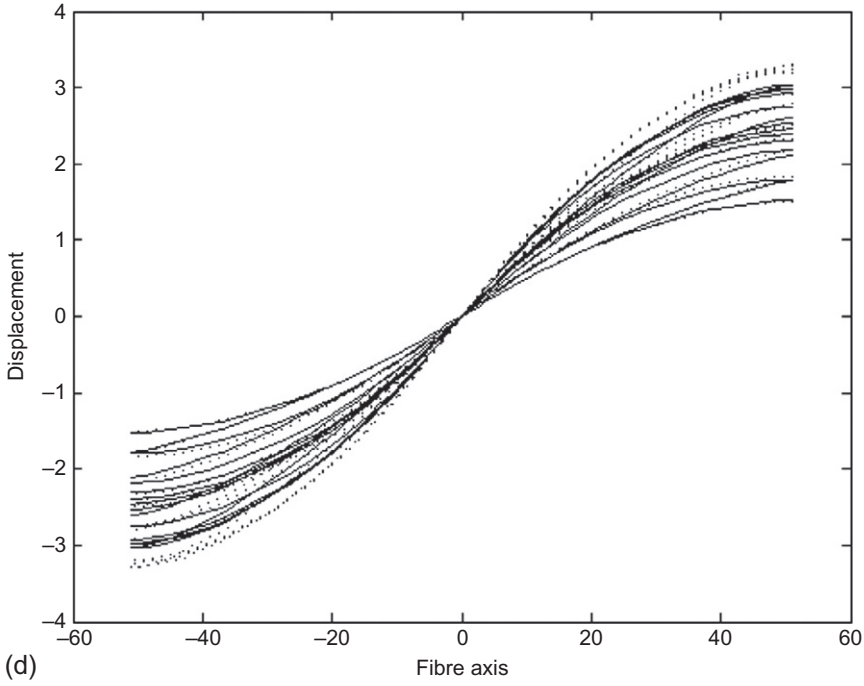

(d)

Figure 5.6. continued

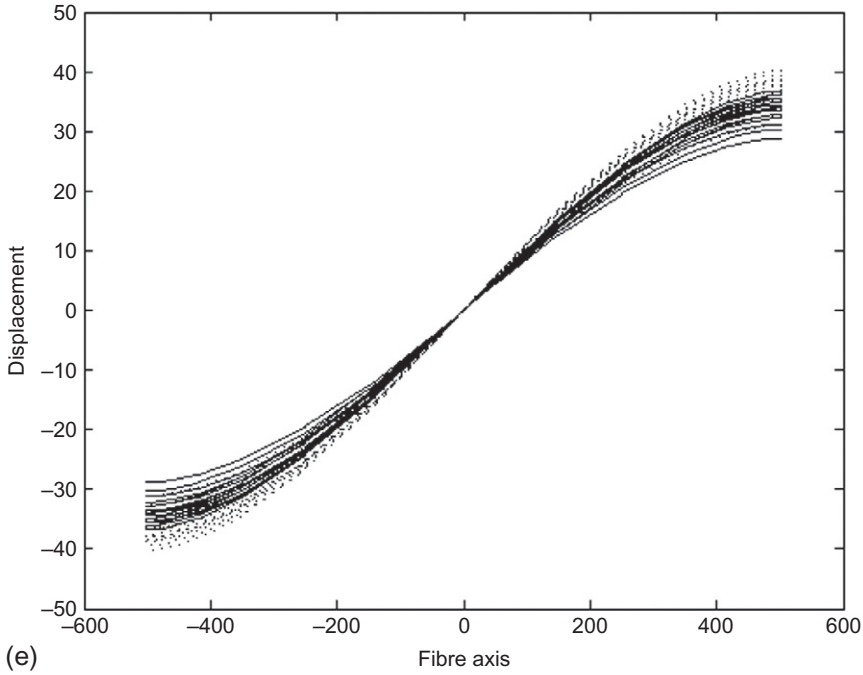

Figure 5.6. continued

Table 5.2 Maximal heat flow in fibers

Level x_1, x_2, x_3	Model No.				
	A	**B**	**C**	**D**	**E**
0, 0, 0	895	692	538	769	25,762
1, 1, 0	930	790	543	533	25,997
2, 0, 0	925	780	537	478	25,879
2, 2, 0	874	742	517	433	25,517
2, 1, 1	912	792	531	454	25,322
0, 1, 1	845	661	516	573	24,754
1, 1, 2	626	442	401	356	22,030
0, 0, 2	575	362	383	381	21,348
2, 0, 2	676	530	417	356	22,716
2, 2, 2	716	615	432	355	23,484

Table 5.3 Temperatures in the centers of fibers

Level x_1, x_2, x_3	Model No.				
	A	**B**	**C**	**D**	**E**
0, 0, 0	0	0	0	0	0
1, 1, 0	0	0	0	0	0
2, 0, 0	0	0	0	0	0
2, 2, 0	0	0	0	0	0
2, 1, 1	26.49	40.35	14.50	25.80	44.8
0, 1, 1	29.89	43.62	16.13	28.05	106.8
1, 1, 2	65.26	88.56	38.83	59.98	244.4
0, 0, 2	69.29	91.65	41.31	62.87	261.1
2, 0, 2	60.36	84.50	35.98	56.99	224.5
2, 2, 2	52.77	77.65	31.53	52.10	194.5

Table 5.4 Maximal stresses in fibers

Level x_1, x_2, x_3	Model No.				
	A	**B**	**C**	**D**	**E**
0, 0, 0	126.0	88.0	115.44	86.25	5141
1, 1, 0	130.7	104.0	119.00	97.94	5271
2, 0, 0	129.6	110.0	117.82	101.76	5319
2, 2, 0	122.9	106.9	112.03	98.31	5324
2, 1, 1	127.1	110.3	115.53	101.44	5160
0, 1, 1	119.2	86.2	109.35	83.11	4884
1, 1, 2	92.1	63.9	85.20	61.43	4642
0, 0, 2	85.2	51.0	79.36	50.89	4440
2, 0, 2	100.3	77.4	91.96	72.01	4890
2, 2, 2	106.4	88.2	97.21	80.81	3184

We especially evaluated the material properties in fiber direction, as they are decisive for estimation of the toughening mechanism by short fibers. Because of the regular distribution of fibers and symmetry, we have chosen the representative volume element to be the part of the composite containing the fiber in the middle of the patch and separated by middle planes going between the layers of fibers (the shadow part in Figure 5.2).

A homogenized increase of the conductivity in the fiber direction, respectively, toughening (increasing the modulus of elasticity) of the composite material evaluated

Table 5.5 Displacements of centers of fibers

Level x_1, x_2, x_3	Model No.				
	A	B	C	D	E
0, 0, 0	0	0	0	0	0
1, 1, 0	0	0	0	0	0
2, 0, 0	0	0	0	0	0
2, 2, 0	0	0	0	0	0
2, 1, 1	23.82	38.73	21.54	36.03	133
0, 1, 1	27.53	43.65	24.82	40.58	154
1, 1, 2	59.85	87.73	54.75	82.21	321
0, 0, 2	64.21	91.99	58.76	86.34	346
2, 0, 2	54.48	81.78	49.84	76.60	290
2, 2, 2	46.25	72.80	42.41	68.15	345

Table 5.6 Homogenized conductivity and modulus of elasticity

	Model No.				
	A	B	C	D	E
Conductivity	1.7132	4.8158	1.2942	2.0425	1.2555
Modulus of elasticity	1.6336	5.0452	1.5382	3.9225	1.4145
Infinite fibers	1571.8	157,180	10.968	197.15	1.6708

in the CVE, is given in Table 5.6. In the last row of the table are corresponding values for infinite fibers. They are equal for both conductivity and elasticity for corresponding models as the material constants and volumes of matrix to fiber are equal for both fields.

5.4 Conclusions and future trends

MCSF is a quasi-meshles method using 1D continuous distribution of source functions to simulate the mechanism of increased conductivity and toughening by short fibers in composite materials. In the present models, there is a patch of straight fibers regularly distributed in an infinite matrix. Material of the fibers is supposed to be considerably better conductor and considerably stiffer than the matrix. As the model has some inaccuracies and restrictions, it will help to understand the composite material properties from the influence of fibers, their configuration, and topology.

Comparing the computational simulations from the figures and tables in the previous section, we can note the following:

- Although the temperature and elastic fields are described by integral equations with different intensity of the singularity (stronger singularity is in elasticity problem), the behavior of both problems is similar.
- The reinforcing effect of composites reinforced by finite fibres is less than that by infinite fibres (compare results in Table 5.6). This difference is smaller, the smaller is the difference of material properties of the matrix and the fibres. One has to realize, however, that the BC in finite domain do not correspond to infinite fibers.
- As for the presented models simulating the local reinforcement of the matrix, one can observe that the fields in middle fibers and those on the boundaries of the reinforcement behave differently and the fields are not symmetric along fibers. A similar effect is to be expected on the boundaries of composite of finite dimensions.
- The ends of fibers strongly influence the fields not only in the matrix but also in neighbor fibers (Wang et al., 2005). This effect is not so clear from the presented figures. One has to imagine the configuration of fibers in the space, the overlap, and the gaps in fiber direction in order to better understand the figures.

The results document that the finite number of fibers in the infinite matrix is adequate to partial reinforcement of the matrix. This is similar to the composite inclusion in a homogeneous matrix. It is clear that other BC (the form of the finite domain, interface with part of different material properties, etc.) are also parameters influencing the resulting material properties. The models simulate straight fibers; however, the fibers in real material can be curved with random configuration. The MCSF can be used also for such cases, but further generalization of models will be necessary (changes of temperature and displacements in all directions, BC on fiber–matrix interface to local direction of fiber axis, etc.). Also, the RVE must contain larger number of fibers for a more general configuration in order to represent the material properties in macrodimension.

In present models, we solve the problem for infinite matrix with BC along fiber boundaries, and the finite material fiber properties are included iteratively. This is because the BC are not known *a priori* and the corrections are obtained by integrating results from the preliminary steps. If the material properties of fibers and matrix are too different, and fibers are not too close to each other, the solution is obtained in one or two iterations. In problems such as those presented here, the convergent results are received in not more than eight steps.

Present models do not include nonlinear effects in all material behavior of matrix and fibers, large deformations, etc. We have to realize that the microfibers will often be curved and the curvature can change with deformation; this will contribute to nonlinear behavior of composites, too.

The models were programmed in MATLAB and take into account the same length and regular distribution of fibers. The models are suitable for parallel computing; such a version of the programs was also prepared.

We would like to emphasize that the models can also be used to simulate composite materials reinforced by nanofibers. However, the nanofibers have cross-sectional dimensions in nanometers; and as such, the methods of continuum mechanics cannot be used to model such structure. If, however, the AR of the fibers is large, then the length dimensions satisfy conditions when continuum mechanics can be used for the simulation.

One can also obtain other fields from the models, especially those from elasticity, like shear stresses in the fiber–matrix interface, maximal stresses in the matrix, etc. (Kompiš et al., 2008); these are important for damage and fracture analysis of this kind of composite materials. It is expected that all kind of problems will be important for design and optimization of the composite materials. In this way, one can obtain functionally graded materials with properties suited to the form and special conditions of use of the structure.

E-mail vlado.kompis@gmail.com to request MATLAB codes for parallel and serial computations of the models and to obtain answers to any questions.

Acknowledgments

Support of DSSI, Inc. Bratislava, and APVV project, bilateral project of Slovak and Czech Republic of applied research of 7AMB12SK126 resp. SK-CZ-0008-11 "Computational Models and Applications of Composite Materials Reinforced by Short Fibres," for this research is gratefully acknowledged.

References

Agarwal, B.D., Broutman, L.J., Chandrashekhara, K., 2006. Analysis and Performance of Fiber Composites, third ed. Wiley, New York.

Brebbia, C.A., Telles, J.C.F., Wrobel, L.C., 1984. Boundary Element Technique, Theory and Applications in Engineering. Springer Verlag, New York.

Kachanov, M., Shafiro, B., Tsukrov, I., 2003. Handbook of Elasticity Solutions. Kluver Academic Publishers, Dordrecht.

Kaukič, M., 1998. Numerická analýza. In: Základné problémy a metódy (Numerical analysis, Basic problems and methods). MC Energy, Žilina.

Kompiš, V., Kompiš, M., Kaukič, M., 2007. Method of continuous dipoles for modeling of materials reinforced by short micro-fibers. Eng. Anal. Bound. Elem. 31, 416–424.

Kompiš, V., Štiavnický, M., Kompiš, M., Murčinková, Z., Qin, Q.H., 2008. Method of continuous source functions for modeling of matrix reinforced by finite fibres. In: Kompiš, V. (Ed.), Composites with Micro- and Nanostructure. Springer, Dordrecht.

Legrand, A.P., Sénémand, C., 2003. Nanostructured Silicon-Based Powders and Composites. Taylor & Francis, London.

Peters, S.T., 1998. Handbook of Composites. Chapman & Hall.

Piegl, L., Tiller, W., 1997. The NURBS Book, second ed. Springer-Verlag, New York.

Rogers, D.R., 2001. An Introduction to NURBS. Morgan Kaufmann Publishers, London.

Shonaike, G.O., Advani, S.G., 2003. Advanced Polymeric Materials. Structure Property Relations. CRC Press, London.

Tang, Z., Sheng, P., 2003. Nano Science and Technology: Novel Structures and Phenomena. Taylor & Francis, London.

Wang, H., Qin, Q.H., Kang, Y.L., 2005. A new meshless method for steady-state heat conduction in anisotropic problems and inhomogeneous media. Arch. Appl. Mech. 74, 563–579.

This page intentionally left blank

Damage-tolerant composite structures by Z-pinning

6

I.K. Partridge[1], *M. Yasaee*[1], *G. Allegri*[2], *J.K. Lander*[3]
[1]University of Bristol, Bristol, UK; [2]Imperial College London, London, UK;
[3]Rolls-Royce Plc, Derby, UK

6.1 Introduction

In the context of high-performance engineering structures made from polymer matrix composites, the technique of "Z-pinning" may have been considered in the past as the answer to a postdesign delamination problem. The aim of this chapter is to present recent progress in the understanding of the relevant mechanisms of composite toughening by crack bridging via the Z-pins, the quantification of the bridging laws, and their use in predictive structure performance models. Using the manufacturing technology with the new tools at the designer's disposal makes it possible to conceive and produce highly damage-tolerant structures (Partridge et al., 2003).

Z-pins are a specific example of a generic orthogonal "microfastener" designed for localized use in prepreg-based composites. Other examples include tufts (Dell'Anno et al., 2007) or stitches (Tong et al., 2002) best suited for reinforcement of dry fiber preforms prior to liquid resin infusion and cure. The technique of z-anchoring (Boisse, 2011) has also been applied to dry preforms, and most recently metallic pin protrusions from a metal base have been used to create strong metal-to-composite joints (Heimbs et al., 2014). All these types of microfasteners in a composite act in a similar fashion; none of them prevent actual crack initiation, but all are effective, to different extents, in reducing or even preventing delamination crack growth. The toughening concepts described below need to be appreciated in this context and in the context of damage tolerance of structures rather than the prevention of the first "failure."

The chapter starts with a description of the manufacturing processes involved in application of Z-pins, pointing out the topological causes of disturbances to initial prepreg lay-up and indicating the consequences of such inevitable "defects." The strong influence of the mesostructure on the balance of mechanical properties of Z-pinned laminates, and hence on the failure modes of locally reinforced structures, is shown. Subsequent sections concentrate on the mechanical testing of single Z-pin specimens and show how the information on the crack bridging laws can be exploited in the formulation of new modeling tools for the structures designer.

Toughening Mechanisms in Composite Materials. http://dx.doi.org/10.1016/B978-1-78242-279-2.00006-8

6.2 Manufacture of Z-pinned polymer matrix composites and effects on mesostructure

While early Z-Fiber® products included titanium pin preforms (http://www.albint.com/businesses/), and some of the early references and models relate to the mechanical properties of metallic Z-pins (Tong and Sun, 2004), this chapter describes methods and results concerning carbon fiber/bismaleimide matrix Z-pins exclusively. Figure 6.1 shows a single T300 CF/BMI Z-pin. An array of Z-pins in a double-density foam layer, known as the "preform," is the raw material supplied for the standard manufacturing process. The pins are available in either 0.28 or 0.51 mm diameters, in a range of pinning areal densities between 0.5% and 4.0%.

6.2.1 Manufacture and laminate defects

The basic principles of this through-the-thickness localized reinforcement technique have been described in detail in a number of earlier publications (Mouritz, 2007b; Partridge and Cartie, 2005; Vazquez et al., 2011). The patented method of insertion of the Z-pins into the uncured lay-up is via an ultrasonic hammer (see Figure 6.2).

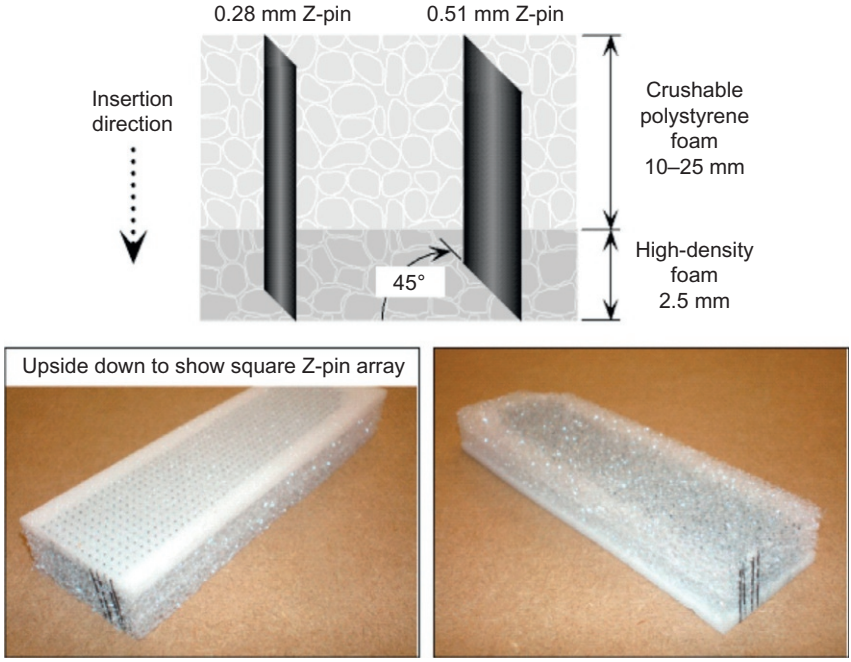

Figure 6.1 Schematic detailing chamfered Z-pin tip detail and idealized positioning within carrier foam (top) and an example of "preform," the commercial product of Albany International Corp. (bottom).

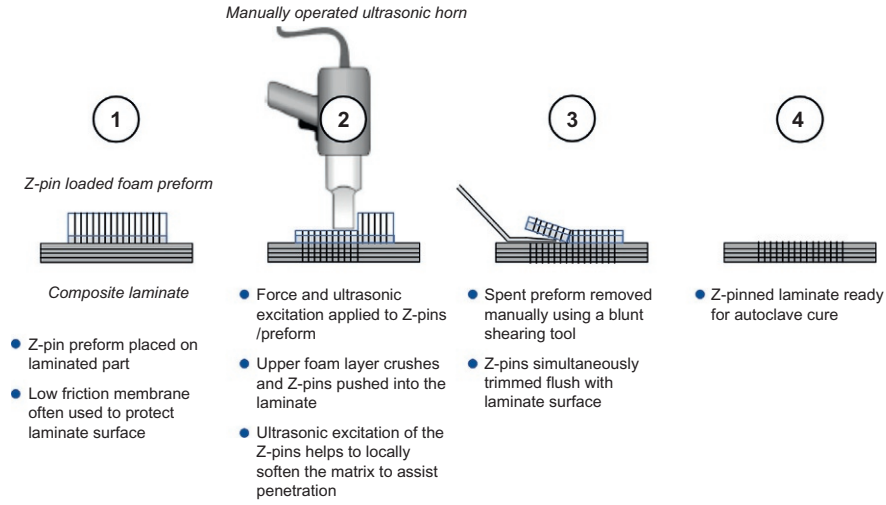

Figure 6.2 Ultrasonically assisted Z-pinning (UAZ) insertion method.

The action of the hammer assists the pins in finding their way through the tightly packed laminate fibers and the in-plane fibers to move away from the orthogonally inserted Z-pins.

This deflection of fibers in the in-plane direction is important in minimizing the potential laminate in-plane stiffness and strength reduction (Steeves and Fleck, 2006). The movement of the in-plane fibers results in a characteristic "eyelet" feature, where resin-rich pockets are formed around the orthogonal Z-pin. Deflection of fibers can become severe if the pin spacing and/or pattern promotes coalescence of the eyelets (Figure 6.3). Multidirectional stacking naturally prevents such coalescence extending through the thickness, but caution is required when Z-pinning blocked-ply or unidirectional (UD) laminates.

The insertion action also induces out-of-plane waviness in the prepreg plies and inevitably causes a significant variation in the local fiber volume fractions (Figures 6.4 and 6.5).

While all of the above-mentioned features could be considered as laminate "defects," they are an intrinsic part of the nature of through-the-thickness reinforced laminates and the reason why detailed mechanical response is very heavily governed by the mesostructure of the particular laminate, including density/pattern/insertion depth of the reinforcement and the fiber bed topology.

One potential manufacturing quality advantage of the localized reinforcement is the ability of the Z-pins to provide a route for volatiles in the laminate to escape during the early stages of cure. Remaining volatiles may become trapped around the pins (Figure 6.6), but no systematic evaluation of this effect has been reported as yet.

Some modern composite resin systems contain a variety of particulates, which also have a tendency to congregate around Z-pins and in the resin-rich eyelets (Figure 6.7); care needs to be taken in microscopy evaluation not to confuse such features with porosity.

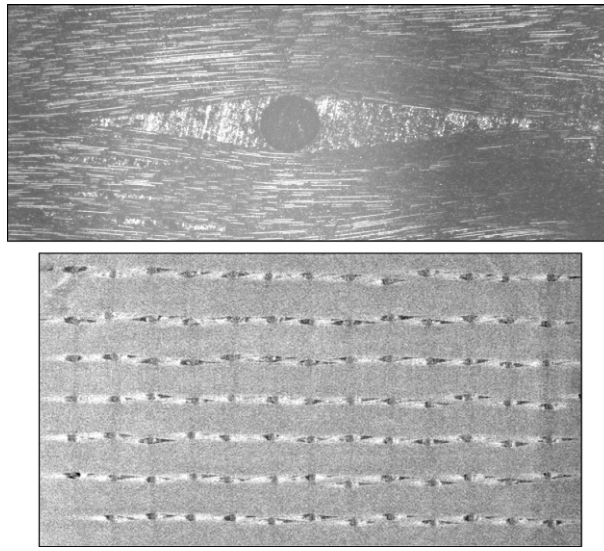

Figure 6.3 Micrograph showing the signature pin/ply eyelet feature (top) and near insertion surface CT scan slice image showing eyelet coalescence in a standard 2% areal density Z-pin array (bottom).

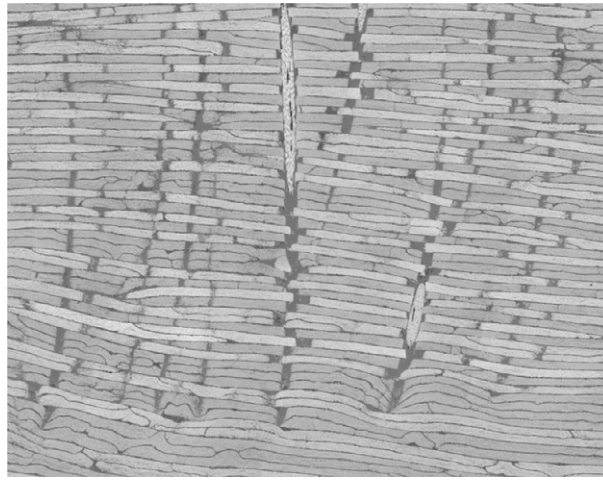

Figure 6.4 CT scan/micrograph showing deflection of laminate plies due to the through-thickness force imparted during insertion of Z-pins.

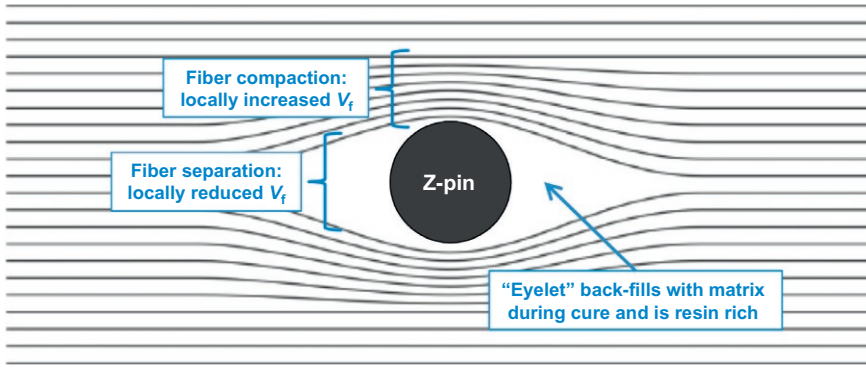

Figure 6.5 Schematic showing localized in-plane V_f increase and resin richness (V_f decrease) around an inserted Z-pin.

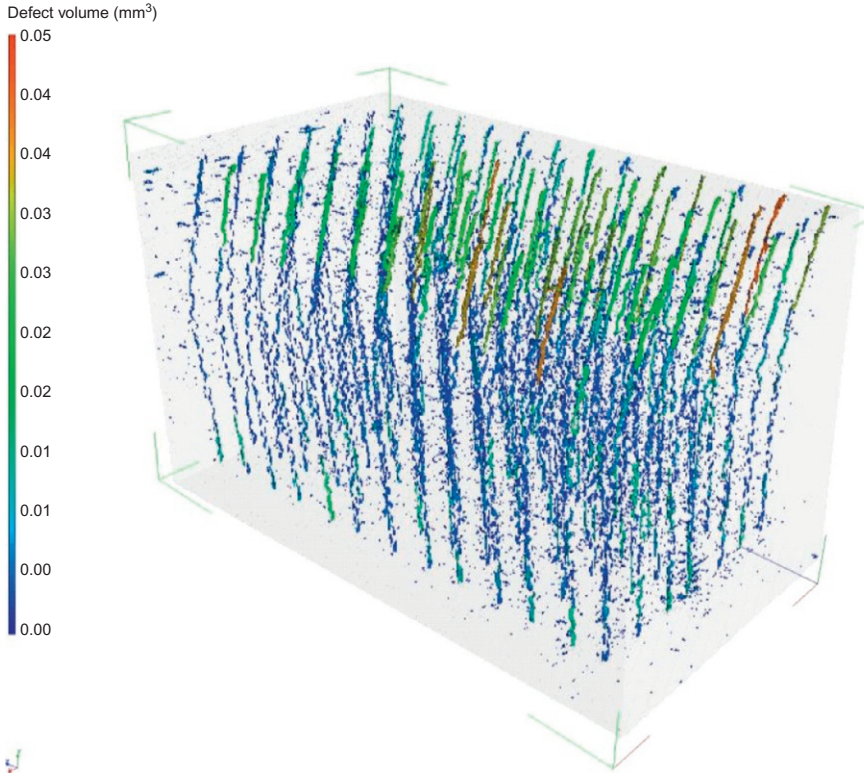

Figure 6.6 CT scan reconstruction showing porosity concentrated around the TTR pin/laminate interface in an array of pins. All solid laminate and pin material have been removed by postprocessing.

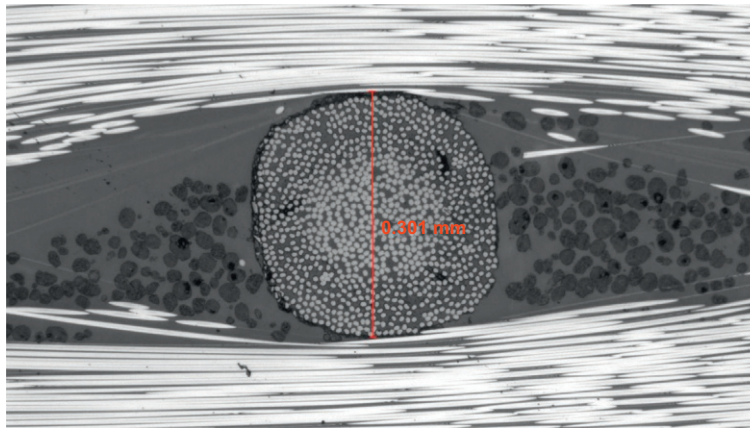

Figure 6.7 Micrograph showing modern resin system polymeric particulates in the eyelet feature around a pin.

6.2.2 Controlling Z-pin orientation

The above-described mesostructural perturbations in Z-pinned laminates can be regarded as inevitable and are defined by the choices of laminate architecture and the location and density of Z-pinning. They can all be expected to influence the in-plane mechanical properties of the laminate and, where possible, should be minimized.

Provided the in-plane property reductions are acceptable in design, it is the out-of-plane behavior of the reinforced structures that is the feature of most interest, as the resistance to interlaminar cracking can be increased by an order of magnitude (Cartie et al., 2006; Liu et al., 2007).

The basic assumption in modeling Z-pinning is that the localized reinforcement, inserted orthogonal to the laminate plane, remains orthogonal. However, this is often not the case, as seen in Figures 6.8 and 6.9, with significant consequences on the actual mechanical response and the micromechanisms of failure (see Section 6.3.1.1).

Composite Z-pins are also often damaged by traditional insertion processes (Figure 6.10). Damage often goes unnoticed because it cannot be detected using NDT methods. Luck is required if microscopy assessment is being performed (split strands can be polished through) due to pins rarely being aligned in any single plane. computer tomography (CT) scanning has allowed greater insight into the integrity of inserted Z-pins, but this is not trivial. CT scanning relies on differences in density within the sample to generate an image that presents a challenge for carbon-composite pins in carbon-composite laminates, which is "harder than finding a needle in a haystack."

6.2.3 Achieving best Z-pinned laminate quality

Porosity is an inherent feature of composites in general and not a defect specific to Z-pin insertion. The CT scan reconstruction shown in Figure 6.6 was analyzed to sum the porosity percentage within the full sample volume. For this ~100 pin sample,

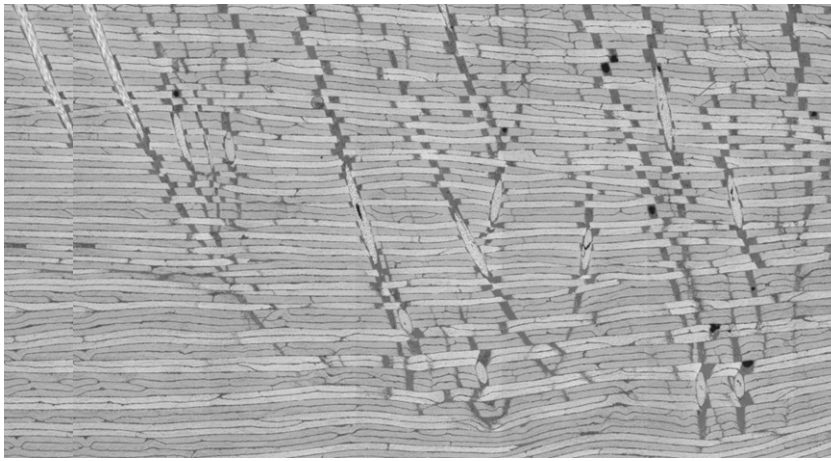

Figure 6.8 Micrograph showing misalignment of pins inserted by the Z-pinning method.

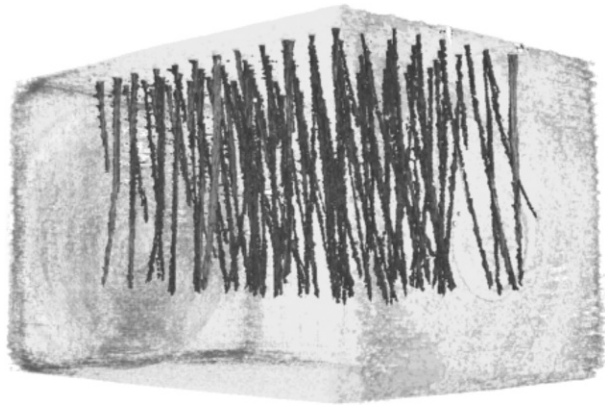

Figure 6.9 CT scan reconstruction of an array of pins inserted by the Z-pinning method. Misalignment (and other features) are visible when the scan is postprocessed to expose the pins.

the porosity percentage was increased by about 0.25% compared to the baseline non-pinned laminate porosity. A porosity level of 2% by volume is regarded as the acceptable industry standard for an aerospace grade, autoclave-cured component; however, volatiles escape can be hindered by poor Z-pin insertion practice, particularly where a design requires pins to extend through the full material/component thickness. Z-pins are stiff, well supported after insertion, and generally remain in their as-inserted position. At the typical areal Z-pinning densities of 2–4%, they will readily act against the consolidation forces imparted by a caul plate or a matched tooling set (leading to tool "stand-off") during cure. This is particularly true in cases where standard material cure cycles are used without the presence of through-the-thickness microfasteners being

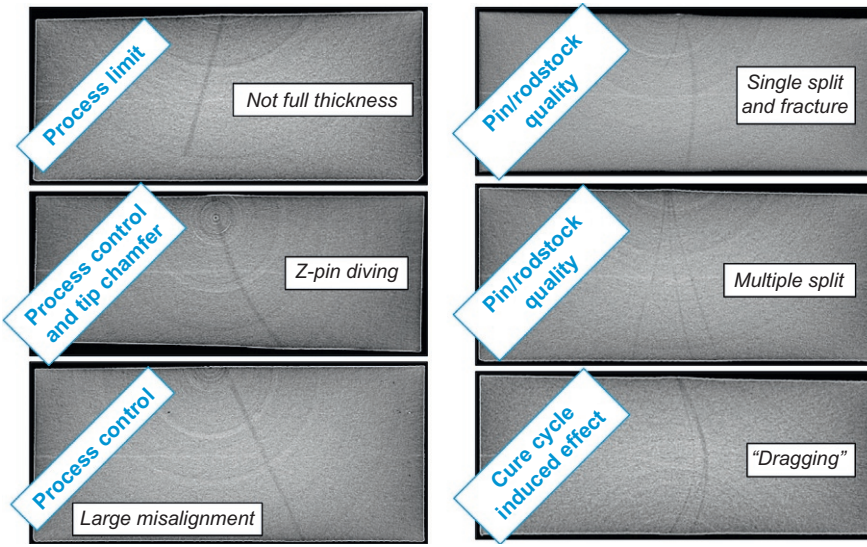

Figure 6.10 Very high-resolution CT scan images of individually inserted Z-pins showing a range of defects and their root causes.

taken into account. When Z-pins produce tool stand-off, the surrounding material does not experience the full consolidation pressure imparted by the autoclave, and remaining volatiles within the material itself are not driven out prior to gelation of the resin. Thickness variation around the pinned region in the cured component can also be expected.

The two key manufacturing practices required to ensure low porosity in a cured, Z-pinned component are debulking and insertion length control. Debulking—including heated debulking under vacuum and ideally to the cured component thickness prior to Z-pin insertion—will ensure that the lowest amount of porosity is present to begin with. Controlling the length of the inserted Z-pin and ensuring that it does not exceed the component-cured thickness will ultimately ensure that tool stand-off is prevented. Where such tight control is not possible, a penetrable layer can be included in the autoclave bagging arrangement to absorb any excess pin length while providing consolidation to the surrounding material. This option should only be considered where a nontool surface finish is acceptable. Another way around this issue is to lay additional plies after Z-pins have been inserted, to perform a similar function.

Tight control over the inserted pin length is also important for controlling the final orientation of the Z-pins in the cured part. If the Z-pin length exceeds the cured component thickness and pins are subjected to compressive forces during cure, then they can buckle or deflect laterally. Pin buckling within the material is rarely seen, as the matrix material in the Z-pins is very highly cross-linked, but lateral pin deflection is far more common. Countermeasures similar to those described for managing porosity can be deployed in this case (Figure 6.11).

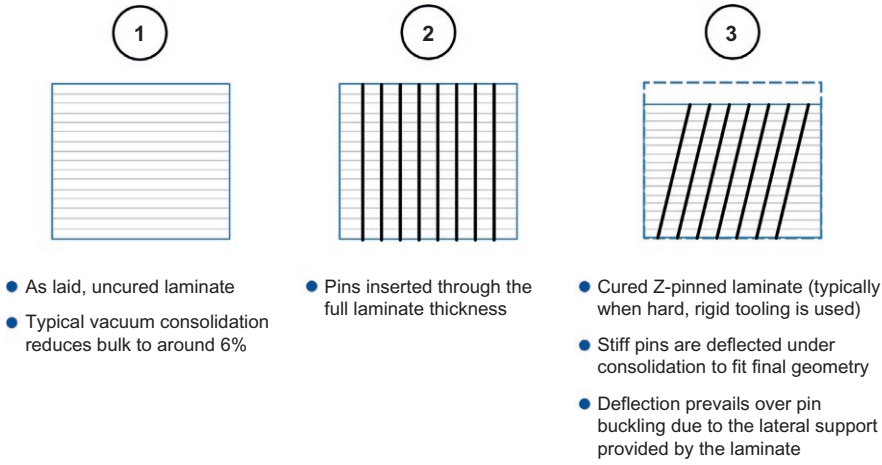

Figure 6.11 Lateral deflection of overlength Z-pins during cure.

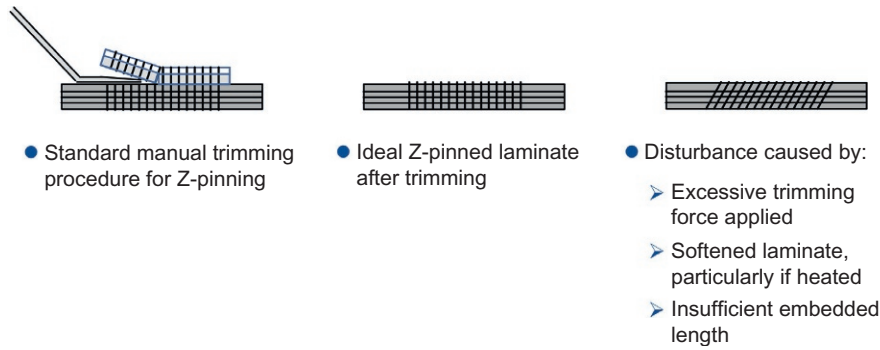

Figure 6.12 Pin disturbance due to manual trimming.

The traditional Z-pinning UAZ process uses a manual shear trimming process to leave Z-pins flush with the material/component insertion surface. The action of this shear trimming procedure can cause undesirable misalignment of the inserted Z-pins; care needs to be taken to avoid this (Figure 6.12).

6.2.3.1 *Managing Z-pin damage*

For the traditional UAZ Z-pinning method, there will always be an inherent amount of pin damage to be expected. The Z-pins are required to find/force their way through the uncured laminate/component architecture; where there is a contact, there will inevitably be damage. This is a particular concern for the composite pins where the alignment of reinforcement in the pin itself is in the direction that makes the pin prone to splitting.

The only real manufacturing controls available in this case are the applied insertion pressure and the material/component temperature. Insertion force should be minimized

to avoid buckling or fracturing pins during insertion. These issues become more pronounced if pin splitting occurs. Additionally, the material/component can be softened by heating to reduce the insertion force required for Z-pins to penetrate. Heating has the added advantage of reducing the risk of material fiber damage; however, careful consideration should be given to the temperatures and durations used to avoid undesirable matrix staging. The level of Z-pin damage will depend on a number of factors including, but not limited to, the pin material plus the laminate material, its architecture, age or degree of cure of the matrix, and level of consolidation.

It should be kept in mind that the above-mentioned "defects" of pin misalignment or pin splitting may, in fact, further contribute to the increase in the delamination resistance of the component rather than causing detrimental changes to the mechanical performance. The problematic issue is one of the quality assurance and documentation. The following sections illustrate the strong dependence of the balance of properties in Z-pinned laminates on its mesostructure under a variety of loading modes.

6.3 Structure–property relationships

The purpose of insertion of Z-pins is to limit delamination crack propagation in selected critical areas of a highly loaded composite structure. The dramatic improvement in the out-of-plane strength of the composite has to be balanced against the loss of performance in its in-plane properties. Not getting this balance right can result in undesirable/unforeseen changes in the failure mode of the structure. For example, the increase in the length of a Z-pinned overlap in an I-joint will eventually result in the joint failing in the Web (see Figure 6.13).

6.3.1 Out-of-plane properties

Published experimental out-of-plane loading studies on Z-pinned laminates have typically characterized arrays of pins through standard fracture mechanical tests (Rugg et al., 2002; Cartie et al., 2006) and bespoke pull-out and shear tests (Cartie et al., 2006; Liu et al., 2007; Mouritz and Koh, 2014). However, due to the pin-to-pin

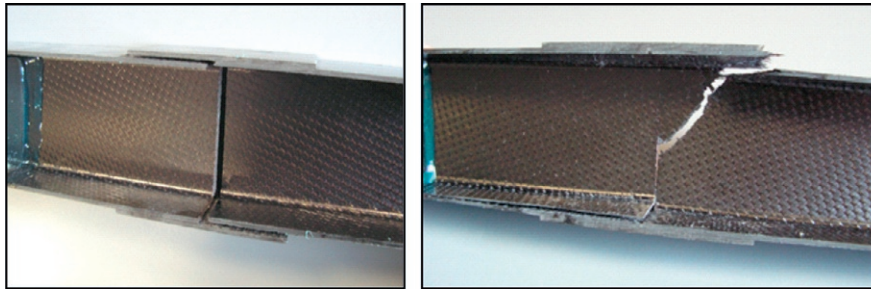

Figure 6.13 Joined composite I-section. Left: With non-Z-pinned overlap, failing in delamination. Right: With highly Z-pinned overlap, initiating failure in the Web section.

interaction and to the large variation of the inserted pin quality and misalignment angles that arise from the manufacturing process, it is difficult to extract single pin behavior from such tests, and the final orientation of individual pins relative to the loading direction will be incidental rather than desired. In order to remove ambiguity on the actual traction forces of Z-pins, tests have been carried out on single carbon Z-pin inserted through the thickness of a composite block.

6.3.1.1 Characterizing single Z-pin bridging performance

For the tests designed to accurately quantify the bridging tractions due to a single Z-pin, under different modes of mechanical loading, samples of laminates containing a single Z-pin in the center of a 20×20 mm^2 (or larger) can be cut from specially prepared cured plates, containing a centrally placed release film and strategically positioned single Z-pins (Yasaee et al., 2014a). A suitable stacking sequence for a UD sample would be $[0_{32}/10//0_{32}]$. The additional 10° ply at the mid-plane is intended to prevent the interpenetration or "nestling" of the fibers across the mid-plane, which would interlock and cause traction forces over and above those exerted by the pin, or induce opening of the specimen, especially when loaded at high proportion of shear. In the case of quasi-isotropic (QI) laminates, a stacking sequence $[(0/45/90/-45)_{-4s}//(90/-45/0/45)_{4s}]$ is designed such that there is a 0/90 interface at the center-line to avoid fiber nestling. The 16-μm thick PTFE release film in the central plane of the specimen ensures the only traction force holding the top and bottom sections of the specimen together is that of the pin. The top and bottom halves of the specimen need to be balanced and symmetric, and the asymmetry in the total specimen stacking sequence has to be sufficiently small so as not to cause any significant deformation during cure of the laminate.

The loading fixtures used are shown in Figure 6.14; the one on the left is a modified version of the Arcan fixture and can be used to apply varying degrees of mode II

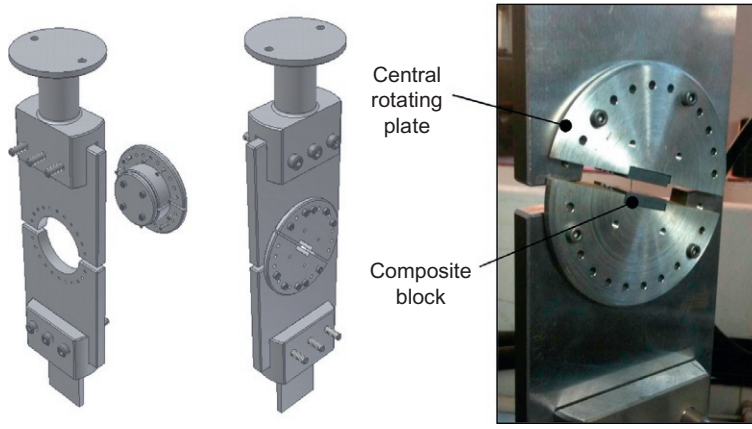

Figure 6.14 Mixed-mode I/II test fixture.

loading, from 0% to 83% mode II. It comprises a top and bottom section; each is coupled to the upper and lower crossheads of the testing machine, respectively. The central rotating plate is split into two, with a cut-out to accommodate the ($20 \times 20 \times 8$ mm^3) test specimen. To attach the individual specimen to the fixture, a small amount of cyanoacrylate superglue is applied on each corner of the specimen, taking care to ensure that the glue does not spread to contact the pin. The specimen is placed into the cut-out, with the 0° fiber direction being perpendicular to the plane of the test fixture. The plate is then rotated between 0° (mode I) and 90° (mode II) in 15° intervals to achieve the desired mixed-mode angle. The rotation (χ) of the actual specimen relative to the vertical loading direction determines the percentage of mode I/mode II load mixity applied to the specimen. Once in position, the rotating plate is secured to the top and bottom parts of the fixture with standard cap screws.

The (constrained) mode II shear testing fixture, shown in Figure 6.15, comprises two inner blocks that hold the test specimen and are designed to slide parallel to each other, shearing the top and bottom half of the specimen. The blocks fit inside a rigid outer guide, which prevents any out-of-plane opening.

For truly rigorous analysis of the data, the inspection of each specimen is recommended to identify the exact condition of the pin inside the laminate including form, the misalignment from the intended surface normal orientation, and any damage that may have occurred. X-ray CT is becoming the technique of choice for this kind of microstructural characterization.

The axis system and the label conventions of the misalignment angles used in the analysis of the mechanical response are presented in Figure 6.16. The relative offset angle from the vertical (z-axis), ζ, and the deviation from the 0° fiber direction (x-axis), Ψ, of each pin are calculated from the misalignment angles, α_{13} and α_{23}. The true loading mode mixity can then be calculated for each specimen, taking into account the pin offset angle (ζ), deviation from x-axis (ψ) and the rotation of the specimen or nominal mixed-mode angle (χ) relative to the loading direction. Full detail of the analysis can be found in Yasaee et al. (2014a).

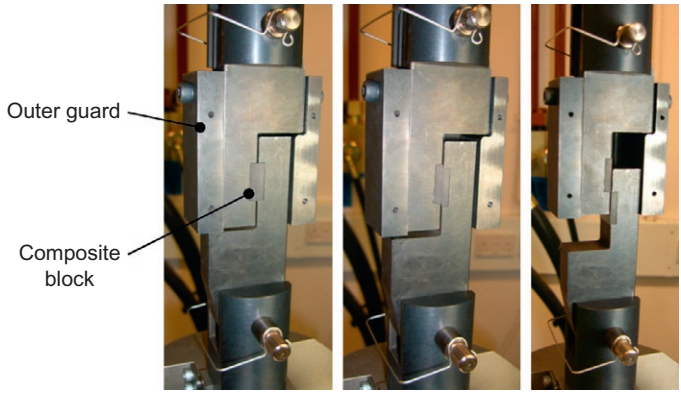

Figure 6.15 Mode II test fixture.

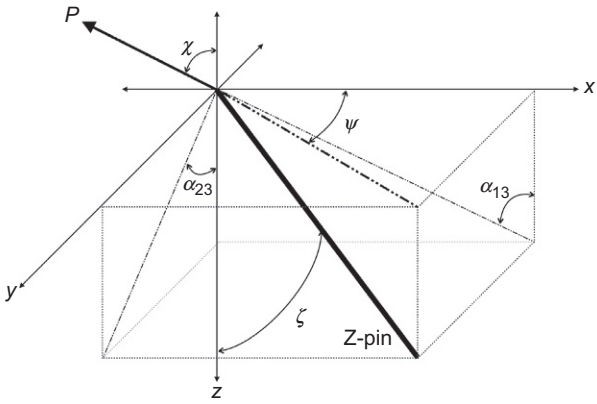

Figure 6.16 Pin alignment angle labeling convention.

The different characteristic traction displacement curve profiles from single Z-pin tests are shown in Figure 6.17. Plot (a) represents a Z-pin well bonded into its surroundings, which results in initial large debond load (P_d) followed by high frictional pull-out. The second curve (b) represents a pin loosely bonded to its surroundings, which results in a low P_d and low frictional pull-out loads. Plot (c) represents the traction curve of a predominantly mode II loaded Z-pin, which does not pull out, and thus ruptures. The total work done by the Z-pin in bridging the two composite interfaces is determined from the area under the curve.

Figures 6.18 and 6.19 show specific data obtained from measurements of single Z-pin samples, which contained a T300/BMI pin inserted in a UD and QI sample configurations. There is a clear difference in the mode I pull-out response of the pins in the UD specimens compared to the QI type. Two distinct stages of the pin pull-out response can be seen. In stage I, for the UD laminates, the maximum load required to overcome the bond between the surface of the pin and the surrounding matrix was on average 86 N, while for the QI configuration the equivalent load to overcome the pin/matrix bond strength was only about 9 N. In stage II, the response is dominated by the frictional pull-out of the pins from the laminate. Also, higher pull-out resistance is noted in the UD laminates compared to the QI laminates.

These very significant differences in response between the UD and QI type specimens can be attributed to the difference in thermal contraction of the laminate and the pins during the cooling down process following cure (Sweeting and Thomson, 2004). In the UD case, there are no off-angle plies that would inhibit the thermal contraction in the transverse direction of the laminate. Thus, the laminate will be unrestrained to contract in the transverse direction and not disbond from the pin. However, in the QI case, the presence of the multiple ply orientations inhibits the contraction of the laminate in these respective fiber directions. For this reason, the pin, when contracting during the cool down from the laminate cure temperature, will develop significant residual stresses at its boundary with the laminate, weakening the pin/matrix interface. This reduces or even eliminates stage I of the bridging mechanism for the QI case and only stage II, frictional pull-out of the pins, as seen in some of the curves.

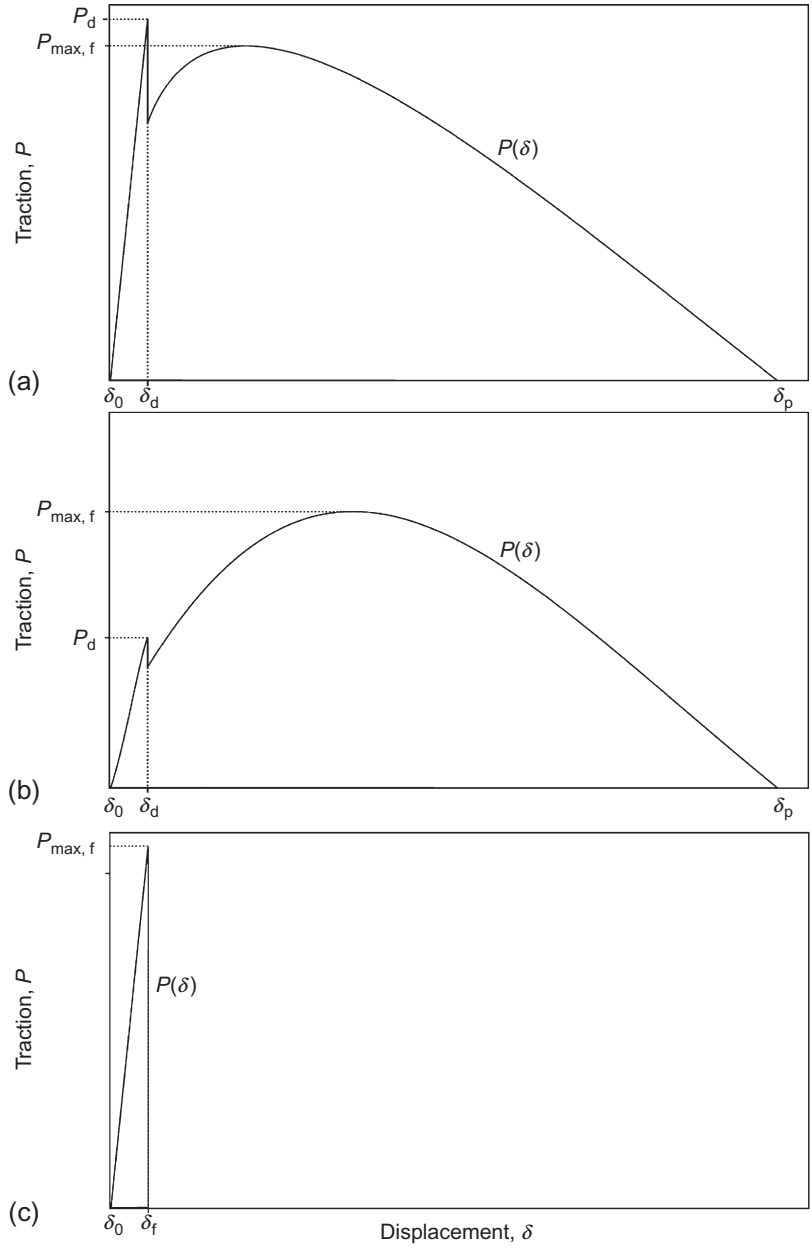

Figure 6.17 Characteristic diagrammatic traction displacement curves of a pin. (a) Well-bonded Z-pin experiencing pull-out. (b) Less strongly bonded Z-pin, and (c) Z-pin failing in rupture, with no pull-out, typically observed in mode II loading tests.

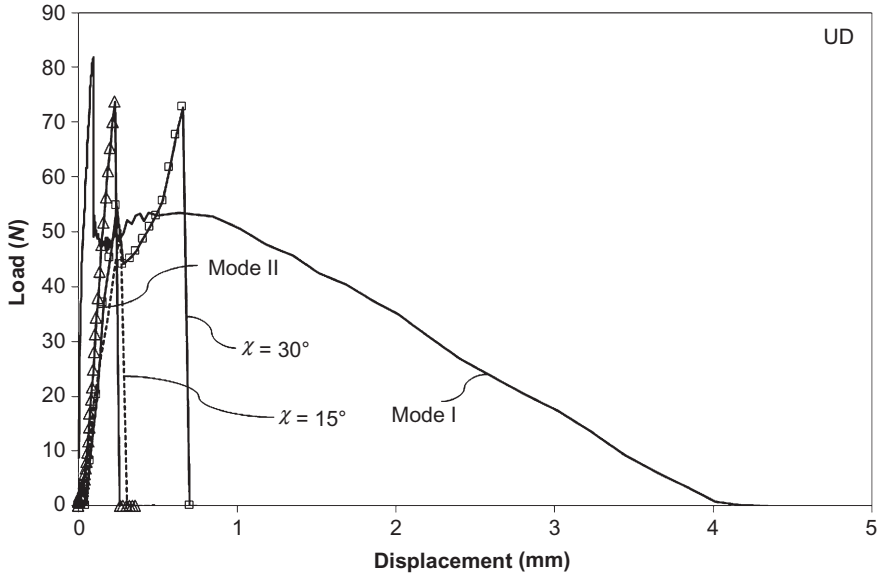

Figure 6.18 Representative UD laminate load vs. displacement results.

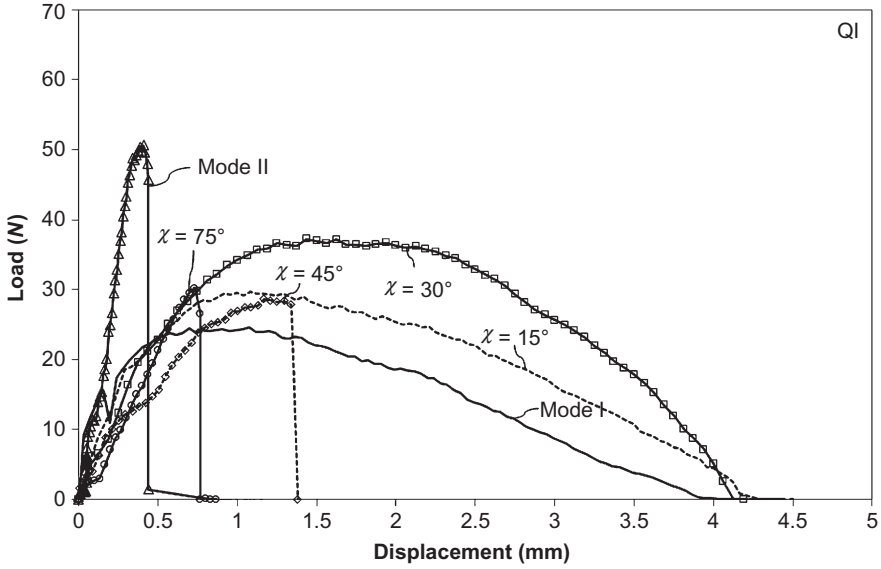

Figure 6.19 Representative QI laminate load vs. displacement results.

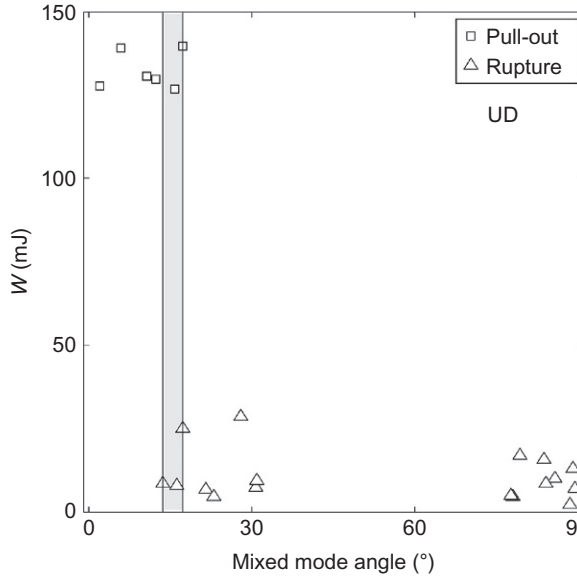

Figure 6.20 Absorbed energy vs. corrected mixed-mode angle for failure/pull-out of pins inside UD laminates.

In the UD type specimens, no pull-out was observed as soon as any significant shear component in present in the loading. It appears that the load necessary to overcome the bond strength between the pin and the matrix and the enhanced friction due to the rotated pin acting on the foundation of the composite (Cox, 2005) exceeds the (tensile) strength of the pin, resulting in a complex mode of pin rupture, with the actual strength being highly dependent on the presence and position of any flaws in the pin.

Plots of energy absorbed by pin deformation/pull-out/failure against the corrected mixed-mode angle from the loading direction are shown in Figures 6.20 and 6.21 for the UD and the QI laminates, respectively. In both cases, there is a transition region between the Z-pin pull-out and Z-pin failure (rupture), bounded by the minimum angle at which Z-pins ruptured during the test and a maximum angle at which Z-pins exhibited complete pull-out. The minimum corrected angle (mode mixity) at which Z-pins in a UD laminate rupture is relatively low; it is approximately 14° compared to 23° in the QI laminates.

This detailed quantitative analysis of single pin tests provides a useful set of data, which makes it possible to calibrate modeling parameters in subsequent analyses. It represents a significant enhancement in the understanding of the inter-relationship between "pinning quality" and the mechanical behavior outcomes in these structural systems.

6.3.1.2 Pin array resistance to delamination

Standardized fracture toughness testing is used to understand the ability of Z-pins arranged in an array to resist a propagating delamination; the major departure from the standard (ISO 15114:2014, 2014; ISO-15024:2001, 2001) is that a deliberate

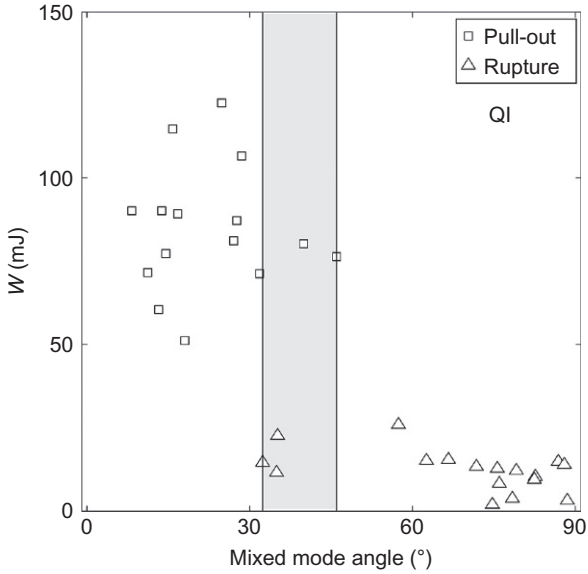

Figure 6.21 Absorbed energy vs. corrected mixed-mode angle for failure/pull-out of pins inside QI laminates.

gap is left between the edge of the crack initiation film and the first row of the pinned array. This results in the delamination propagating in a stable manner toward a Z-pin reinforced region; all data obtained thereafter therefore relate to the ability of the Z-pin array to limit delamination propagation (Partridge and Cartie, 2005; Cartie and Partridge, 2003). It is important to note that the calculations used for these tests follow the assumptions of linear elastic fracture mechanics, which may not be valid under conditions of large-scale bridging. Nevertheless, the trends in the "apparent fracture toughness" are valid for comparison purposes. The practical details of tests of Z-pinned composites under different loading modes, and the accompanying analyses, have been documented elsewhere (Yasaee et al., 2014b). Here, we use data obtained on the same materials as used for the single Z-pin tests to illustrate the differences between UD and QI laminate double cantilever beam specimens containing identical arrays of Z-pins of 2% areal pinning density. It is apparent from reviewing Figure 6.22 that the Z-pin arrays in QI specimens act more effectively than in UD specimens in terms of delamination suppression under mode I loading.

Inspection of the fractured surfaces reveals a higher proportion of Z-pins pulled out in the QI than in the UD specimens. As previously shown in single pin specimens, pins inside a UD laminate with mixed-mode angle (offset angle relative to the loading direction) greater than 14° will more likely exhibit tensile rupture than pull-out. The typical misalignment angles of the pins in the UD specimens were found to be greater than the critical 14°; this caused the pins to rupture, resulting in a lower effective fracture resistance and shorter bridging zones. The majority of the pins inside the QI specimens exhibited pull-out. In both cases, the mode I R-curves almost reach the stage of a fully developed bridging zone (stage III) (Figure 6.23), which is not the case under mixed mode or mode II loadings shown in Figures 6.24–6.26.

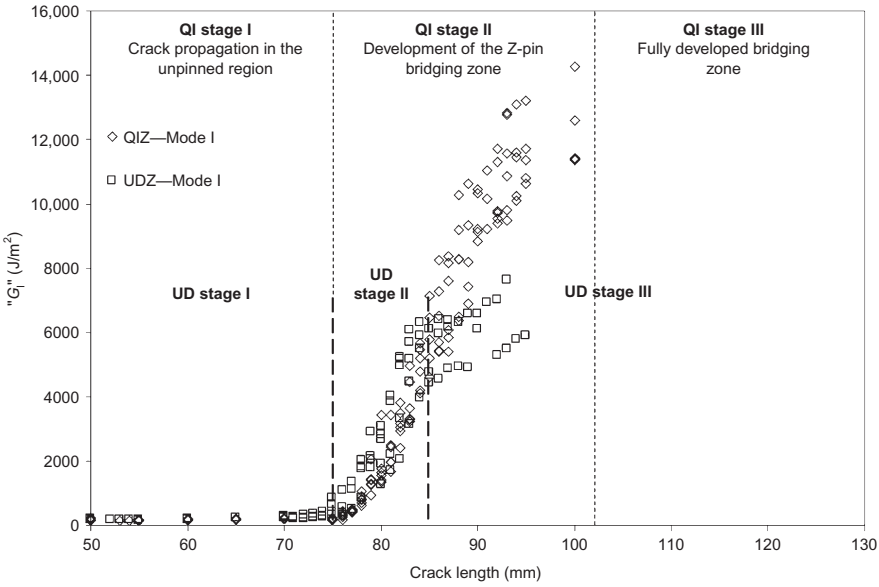

Figure 6.22 Mode I fracture resistance of Z-pinned UD and QI DCB specimens.

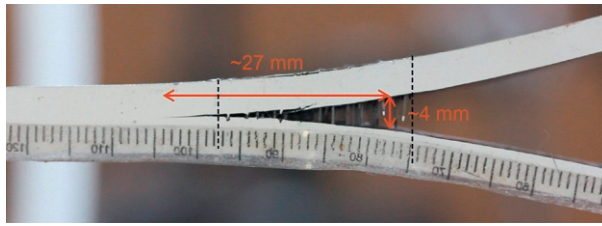

Figure 6.23 Fully developed Z-pin bridging length in the QI DCB specimens (Z-pinned region between dashed lines).

Given that delaminations with fully developed bridging zones in the Z-pinned region were not achieved, no valid direct comparison can be made of the different mode mixity tests, since the measured values are at different stages of the bridging zone development. An approach was therefore adopted that compares the effective delamination resistance values at predetermined positions within the Z-pinned region. Values of effective delamination resistance of all the specimens were collated at arbitrary delamination positions of 9 and 19 mm into the Z-pinned array, plotted as a function of the mixed-mode ratio in Figure 6.27.

The Z-pins bring about similar resistance to delamination for both UD and QI specimens at 9 mm into the array. The resistance reduces with increased proportion of shear in the loading mode mixture. When looking at 19 mm into the array, the Z-pins in the QI samples cause a significant increase in delamination resistance compared to

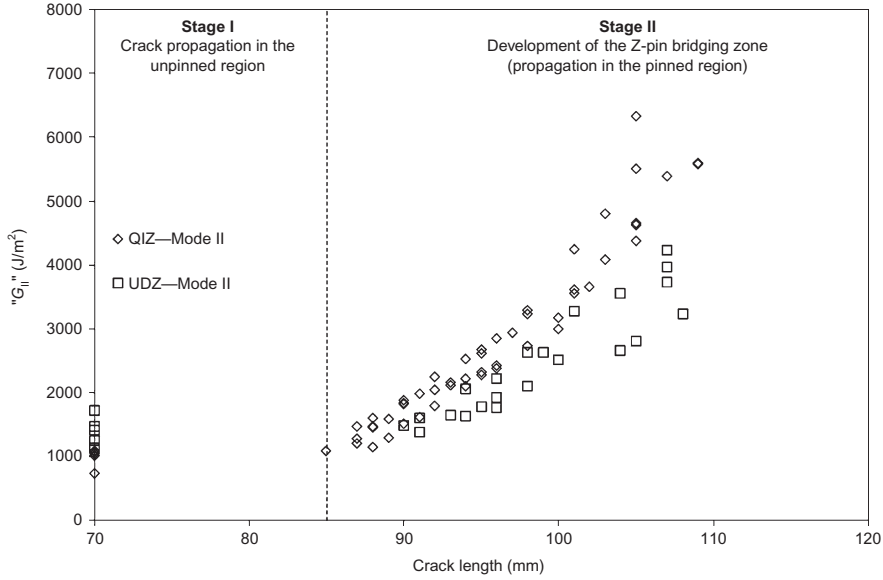

Figure 6.24 Mode II fracture resistance of Z-pinned ELS specimens.

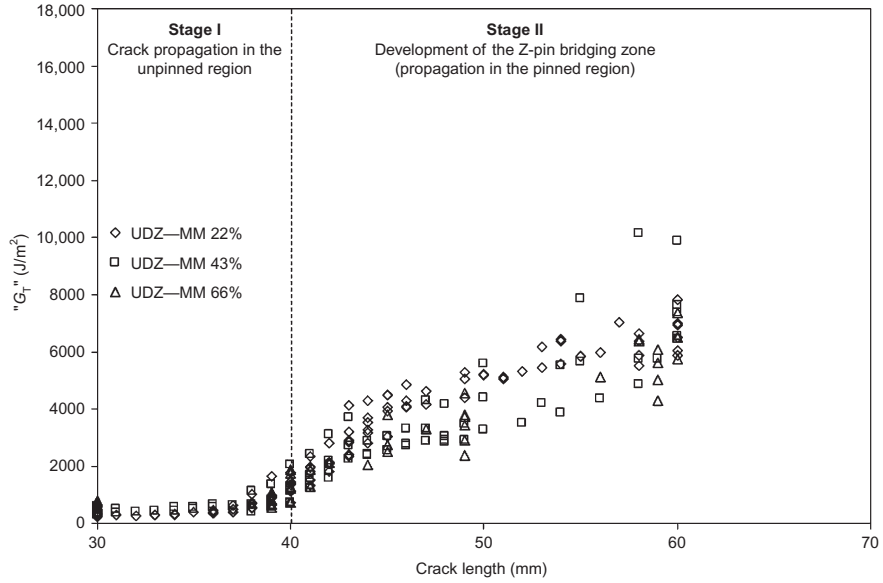

Figure 6.25 Total fracture resistance of Z-pinned UD MMB specimens at 0.22, 0.43, and 0.66 mixed-mode ratio.

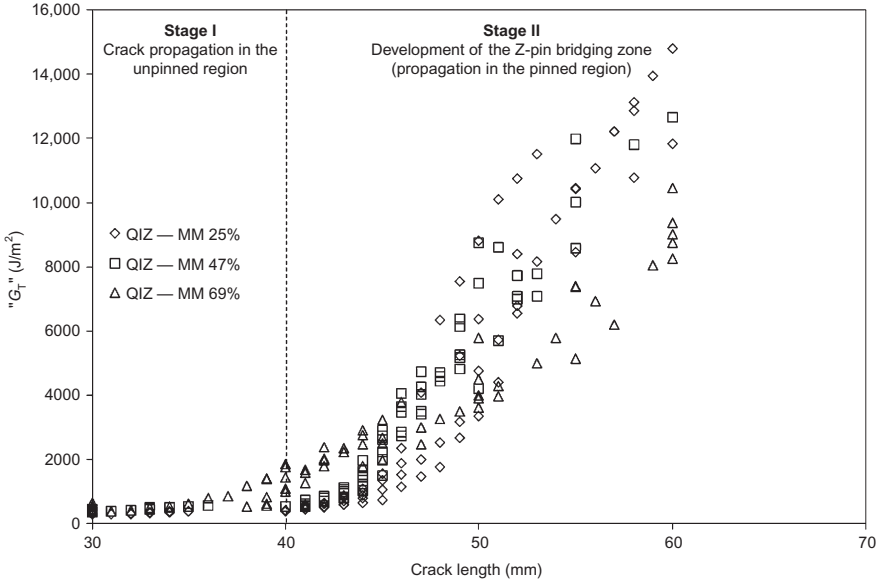

Figure 6.26 Total fracture resistance of Z-pinned QI MMB specimens at 0.22, 0.43, and 0.66 mixed-mode ratio.

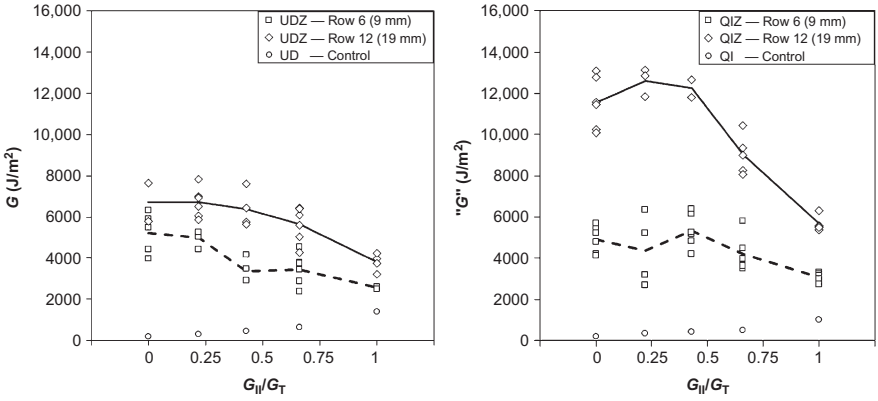

Figure 6.27 Effective delamination resistance of Z-pinned UD and QI composites at 9 and 19 mm into the pinned array.

the case of the UD specimens. This is due to the development of the bridging forces by the pins behind the crack contributing to the overall resistance. This resistance is less pronounced for the UD samples, indicating fewer pins contributing to the overall bridging forces. This is once again most likely caused by the misalignment and hence early failure of the pins inside the UD samples. The equivalent critical offset angle for a pin in a QI laminate is higher than the misalignment angles seen in the QI specimens.

This is why a majority of the pins exhibited pull-out in the QI specimens, resulting in a much larger bridging force contribution.

In all cases, the contribution by the Z-pins to the bridging forces reduces as more shear is introduced into the load mix, finally reaching the lowest value in "pure" shear loading case, as the pins rupture prematurely in a mixture of bending and shear. This coincides with observations from previous experience, where applications of Z-pinning to predominantly shear loaded structures have shown little benefit under quasistatic loading.

6.3.2 In-plane properties

Recent review by Mouritz (Mouritz and Cox, 2010) summarizes the limited available literature pertinent to evaluation of the effects of Z-pins on the in-plane properties of the laminates containing them. The main messages are that the effective in-plane moduli of the "material" are not changed significantly by the presence of the through-the-thickness reinforcement, but there are detriments to the quasistatic in-plane strengths. For a given mode of loading, these reductions depend on the areal density of reinforcement but also on the initial in-plane fiber architecture. As might be expected, the most severe drop in properties is exemplified by compressive strength reduction in UD laminates (Steeves and Fleck, 2006; Mouritz, 2007a) while QI laminate strengths are only weakly affected by the pinning. It is premature to quote specific values for such in-plane property drop offs, since the dependencies on mesostructure are complex; the best advice is to determine the strengths values for the specific material/Z-pin combination for the geometry (thickness) of the structure under consideration. Standard tests for tensile, shear, and compressive strength determinations generally give consistent results and some simple models exist for specific cases (Grassi et al., 2002).

Mouritz and coworkers have extended studies of in-plane properties of Z-pinned samples to the case of tensile–tensile fatigue, illustrating the degradation of tensile fatigue lifetime (Mouritz and Chang, 2010). Recent work has incorporated consideration of the overall balance of properties into the design of demonstrator structural elements, namely T-joints, to ensure that the desired modes of deformation and failure are obtained (Bianchi et al., 2012).

6.4 Modeling approaches for design of Z-pinned structures

Several experimental and numerical techniques have been presented in the literature to address the design of through-the-thickness reinforced composite structures. Regardless of the specific nature of the microfasteners (stitch, Z-pin, or tuft), a common "multilevel" (or multiscale) modeling strategy can be identified when considering the bulk of the existing literature: First of all, it is necessary to characterize and predict the bridging actions exerted by single Z-pins embedded into a delaminated composite. This element of the overall modeling strategy can be considered as

level-1 mesoscale analysis (meso-1). The second level of the modeling approaches requires identifying the bridging response of multiple microfasteners (array) bridging delaminations. This represents a level-2 mesoscale analysis (meso-2), whereby homogenization is introduced into the models in order to appropriately "smear" the mechanical response of multiple interacting microfasteners. Finally, it is necessary to consider full structures, i.e., macroscale models, where microfasteners are selectively applied in regions prone to delamination damage. This usually requires a further homogenization step with respect to the meso-2 level, since equivalent through-thickness properties will have to be introduced in order to reduce the computational cost of the simulations.

Depending on the overall approach taken, there may exist some overlap between the modeling levels mentioned above. Moreover, different modeling techniques may be required at the different scales. The most important point to make is that fracture mechanics are not valid for large-scale delamination bridging, so extreme care needs to be taken when trying to scale up coupon test results to full-scale (macro) structural components. However, it is in principle possible to translate the results of single microfastener testing into apparent fracture toughness or a set of mode-mixity-dependent bridging forces (meso-1), which can then be employed to predict the response of microfastener arrays (meso-2). Similarly, the macroscale structural response can be predicted by considering the interaction of multiple arrays in a component.

6.4.1 Modeling response of single Z-pins

The literature contains several semianalytical models to cover this scenario, both for the case of rigid Z-pins (Cox and Sridhar, 2002; Cox, 2005; Tong and Sun, 2007; Bianchi and Zhang, 2012) and for the more "rope-like" stitches (Plain and Tong, 2009). The equilibrium during progressive pull-out of the microfastener from the laminate is ensured by frictional forces due to thermal residual stresses between the microfastener and the laminate, but also by the phenomenon known as "snubbing." This refers to the localized increase of frictional force due to contact pressure in the neighborhood of the delamination plane. Since the laminate is assumed to be perfectly plastic under punch indentation, the through-thickness reinforcement can "plough" across the laminate. As indicated in earlier sections, in multidirectional laminates, the ply fibers surrounding the through-thickness reinforcement may prevent the in-plane ploughing of microfasteners. Since the fibers are linear elastic until failure and are much stronger than the matrix, the laminate will tend to provide an elastic foundation for the microfasteners.

As an alternative to the semianalytical models, finite element simulations at the meso-1 level have the potential of capturing the complex behavior governing the Z-pin pull-out and failure, since they can account for cohesive/frictional behavior at interfaces, internal splitting, matrix/laminate plasticity, and fiber failure (Meo et al., 2005; Cui et al., 2011). However, the computational cost incurred in the use of these models is much higher than for semianalytical approaches. There is an inevitable trade-off between physical consistency/accuracy and the computational resources available.

6.4.1.1 A new semianalytical model for mixed-mode bridging

The authors recently published details of a new semianalytical model for the bridging tractions exerted by a single Z-pin having a total length L, embedded into a composite laminate in which a delamination intersects the Z-pin at a given depth (Allegri et al., 2014). The thicknesses of the sublaminates are denoted as L^- and L^+. Upon delamination opening/sliding, the Z-pin exerts bridging forces that constrain the interlaminar crack displacements. The Z-pin pull-out displacement is denoted as W, while U is the delamination sliding displacement (see Figure 6.28a–c). The Z-pin is modeled as an

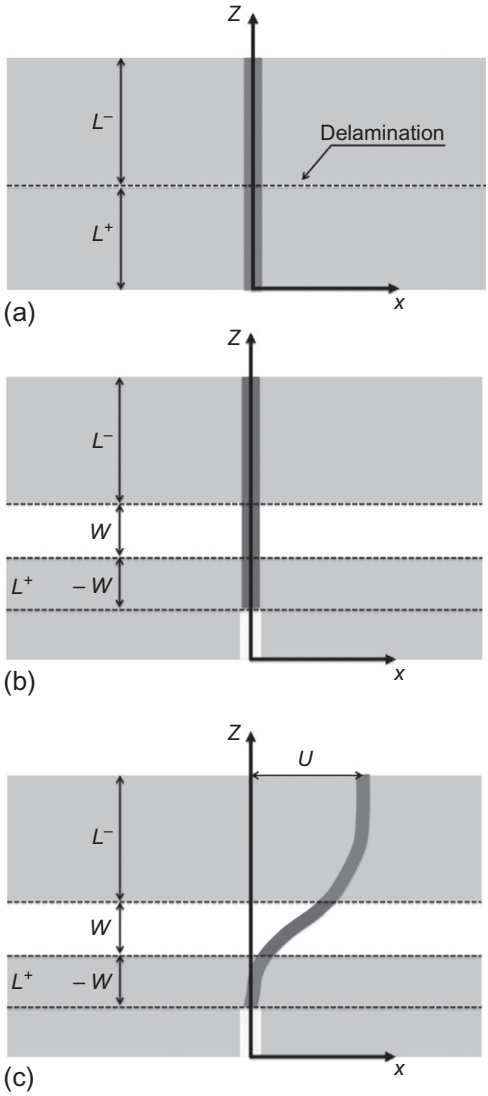

Figure 6.28 Z-pin bridging a delamination: (a) reference configuration; (b) opening mode; and (c) sliding mode.

axially inextensible Euler–Bernoulli beam embedded in a linear elastic foundation. The foundation supports the Z-pin by a distributed normal force. The frictional forces acting on the Z-pin are described as an equivalent axial load per unit length. Considering possibility of small but finite rotations of the Z-pin cross section, the following differential equations govern the transversal deformation of the microfastener:

$$\mathrm{EI}\frac{\mathrm{d}^4u}{\mathrm{d}z^4}-N\frac{\mathrm{d}^2u}{\mathrm{d}z^2}+q=0 \tag{6.1}$$

$$\frac{\mathrm{d}N}{\mathrm{d}z}=-\mathrm{EI}\frac{\mathrm{d}^3u}{\mathrm{d}z^3}\frac{\mathrm{d}^2u}{\mathrm{d}z^2}-p \tag{6.2}$$

where EI is the Z-pin bending stiffness, u the transversal displacement, N the axial force carried by the Z-pin; p and q are, respectively, the distributed tangential and normal load along the Z-pin axis.

Equations (6.1) and (6.2) are solved using an adaptive collocation procedure. The foundation forces q are assumed proportional to the local transversal displacement u. The frictional forces p comprise a residual term due to the clamping pressure exerted by the laminate on the microfastener plus a Coulomb enhancement term that accounts for the snubbing effect. The solution is obtained for incremental pull-out displacements for variable mode-mixity values. The microfastener failure is modeled employing the Weibull criterion, accounting for the size effect on the strength. The failure mode is essentially fiber dominated, as confirmed by post-test Scanning Electron Microscopy (SEM) fractography of the failed Z-pins. The model predicts that failure always occurs within the laminate, close to the delamination surfaces, in agreement with the experimental evidence. The frictional work $W(\phi)$ done by the microfastener during pull-out is computed by integrating the numerical load versus deflection curves.

As shown in Section 6.3.1.1, the mode mixity for the single Z-pin test configuration can be adjusted by changing the ratio of the sliding to opening displacements; thereafter, establishing which failure mode affects composite Z-pins is crucial for the success of any modeling attempt. However, when Z-pin arrays are considered, the mode mixity needs to be extracted from finite element simulations at meso-2 level. The cross-sectional axial and shear forces calculated at the mid-delamination plane represent the bridging tractions that the Z-pin exerts on the delamination edges. The analysis produces "bridging maps," as the loci of the bridging forces expressed as functions of the pull-out displacement and mode mixity. The energy dissipated due to bridging comprises two terms: the first represents the work done by the frictional forces, while the second represents the eventual energy spent in fracture of the Z-pin in incomplete pull-out situations.

Multiplying the energy dissipated by the Z-pin bridging by the Z-pin areal density ρ, it is straightforward to obtain the apparent fracture toughness $G(\phi)$ associated with the pull-out of Z-pin arrays taking place at constant mode mixity:

$$G(\phi)=\frac{4\rho}{\pi D^2}W(\phi) \tag{6.3}$$

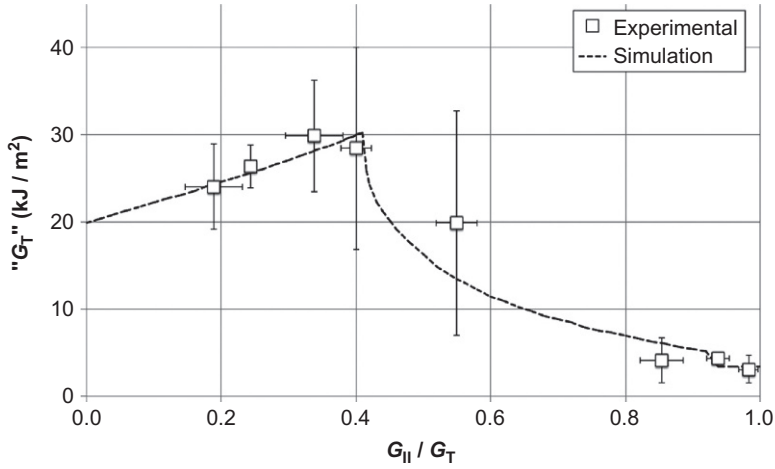

Figure 6.29 Apparent fracture toughness of single Z-pin coupons, normalized for a 2% areal density, versus mode mixity.

where $W(\phi)$ is the total bridging work performed by a microfastener during the progressive pull-out.

The value obtained from Eq. (6.3) must be regarded as "apparent fracture toughness," since it is not a material property but a structural property at the meso-1 level. The assembly of the laminate with the through-thickness reinforcement array constitutes the structure.

The model has been validated for data obtained from tests on QI laminates, with the calibration process performed by means of a multiobjective minimization of the error between the model predictions and the experimental data for the mode I/II response and the overall apparent toughness trend. The agreement between model and test data is good in loading modes dominated by one or other mode (Figure 6.29); the transition region is characterized by significant scatter of experimental data. This is because in this region there exists a multiplicity of failure mechanisms affecting the Z-pin/laminate interaction.

The deterministic model used cannot capture this random behavior, which clearly cannot be ascribed only to the Z-pin misalignment, since the latter has been included in the calculation of the actual mode mixity for each of the coupons tested. The source of this randomness is most possibly due to the effect of the residual curvature that affects the Z-pins following insertion and cure, and that can be appreciated in some of the CT scan images of the tested coupons (Figure 6.30). The residual curvature induces stresses in the through-thickness reinforcement that may lead either to premature failure or complete pull-out, depending on the relative shearing direction.

6.5 Concluding remarks

Historically, the commercial use of Z-pinning technology has preceded a full understanding of how the Z-pins act as the highly effective toughening agent they can be. At

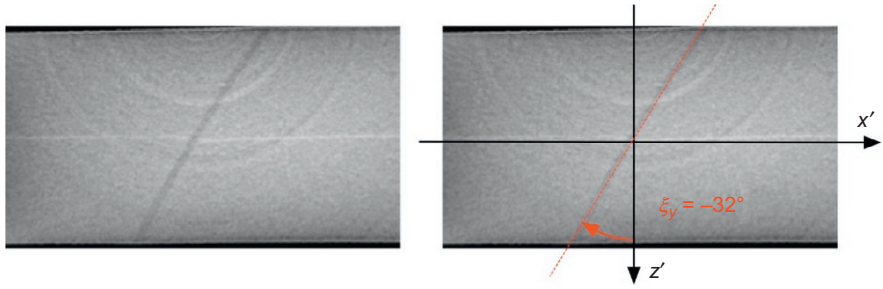

Figure 6.30 CT scan image of a Z-pin and evaluation of the associated misalignment angle; note the residual curvature of the through-the-thickness reinforcement.

the present time, there is considerable effort underway to understand, characterize, and model these toughening mechanisms, in the authors' laboratories and elsewhere. This work is prompted by a significant increase in interest in critical new application in the industry as well as developments in the use of tufting as the equivalent method of delamination control in structures made via the dry preform and liquid resin infusion routes. The requirements for validated models of the balance of mechanical properties are the same for these technologies, and the generic approaches to modeling are identical.

The present contribution has been directed to demonstrate the strong link that exists between the mesostructure of a Z-pinned laminate and its response to quasistatic mechanical loading. The bridging laws, determined from specialized tests on single microfastener specimens, are shown to depend on the environment that the Z-pin is inserted into. Thus a single Z-pin specimen test becomes the necessary "calibrating" test for any specific material+Z-pin combination. The above sections demonstrate how the bridging law obtained from the test can be used in subsequent prediction of the delamination resistance of an array of Z-pins, inserted in the specific laminate. From that information, and an assessment of the in-plane properties of the Z-pinned laminate, the designer can progress to full structural analysis through user-defined cohesive zone models inside commercial finite element (FE) packages.

It should be apparent from the preceding sections that there remains a significant amount of work to be done before a rigorous yet simple-to-use route to characterization and modeling is available. The examples given in this chapter are limited, and many questions remain. For example, the question of pin-to-pin interaction has not been addressed; at the practical level of 2% pinning density, it seems likely that the interaction is more significant in those fabrics where the proximity of the pins significantly influences the geometry of the resin-rich pockets and that the effects are probably more likely to be seen under shear loading. Similarly, there are some indications that the length of the embedded Z-pin may play a secondary role: more specifically, the depth of insertion within the laminate structure. The in-plane properties of Z-pinned laminates have so far received relatively scant attention, and there is a need for more systematic studies to complement the understanding of the crack bridging mechanisms. As in the case of the out-of-plane properties, the approach needs to

be to identify the relevant tests and models on the mesoscale, carry out parametric studies, and form the appropriate elements for larger scale FE models. Some studies of mechanical response of Z-pinned laminates under fatigue (Cartié et al., 2009; Pegorin et al., 2014a,b) and impact loadings (Zhang et al., 2006) have been reported; much more information is required and should probably be directed to address the ongoing development and validation of those meso- and macroscale models identified as appropriate in the quasistatic loading cases.

For practical applications in highly loaded critical structures, the certification requirements will be to demonstrate the presence of the microfasteners by suitable nondestructive techniques and to have validated multiscale models for design. Clearly, the level of analysis exemplified by the use of CT scans in the single Z-pin tests in Section 6.3.1.1, to correct the analysis for Z-pin inclination angle, is not a practical proposition. Instead, the issue of control of Z-pin insertion has to be tackled in the manufacturing stages; consistent placement of the pins simplifies analysis and increases the validity and hence the usefulness of the models.

References

Allegri, G., Yasaee, M., Partridge, I.K., Hallett, S.R., 2014. A novel model of delamination bridging via Z-pins in composite laminates. Int. J. Solids Struct. 51 (19–20), 3314–3332. http://dx.doi.org/10.1016/j.ijsolstr.2014.05.017.

Bianchi, F., Zhang, X., 2012. Predicting mode-II delamination suppression in z-pinned laminates. Compos. Sci. Technol. 72 (8), 924–932. http://dx.doi.org/10.1016/j.compscitech.2012.03.003, Elsevier Ltd.

Bianchi, F., Koh, T.M., Zhang, X., Partridge, I.K., Mouritz, A.P., 2012. Finite element modelling of z-pinned composite T-joints. Compos. Sci. Technol. 73, 48–56. http://dx.doi.org/10.1016/j.compscitech.2012.09.008.

Boisse, P., 2011. Composite Reinforcements for Optimum Performance. Woodhead Publishing, Cambridge. ISBN: 978-1-84569-965-9.

Cartie, D.D.R., Partridge, I.K., 2004. Suppression of delamination propagation in UD laminates by Z-fiber pinning. In: Moore, D. (Ed.), The Application of Fracture Mechanics to Polymers, Adhesives and Composites. Elsevier, Oxford. ISBN: 978-0-08-044205-6.

Cartie, D.D.R., Troulis, M., Partridge, I.K., 2006. Delamination of Z-pinned carbon fibre reinforced laminates. Compos. Sci. Technol. 66, 855–861. http://dx.doi.org/10.1016/j.compscitech.2004.12.018.

Cartié, D.D.R., Laffaille, J.-M., Partridge, I.K., Brunner, A.J., 2009. Fatigue delamination behaviour of unidirectional carbon fibre/epoxy laminates reinforced by Z-Fiber® pinning. Eng. Fract. Mech. 76 (18), 2834–2845. http://dx.doi.org/10.1016/j.engfracmech.2009.07.018.

Cox, B.N., 2005. Snubbing effects in the pullout of a fibrous rod from a laminate. Mech. Adv. Mater. Struct. 12 (2), 85–98. http://dx.doi.org/10.1080/15376490490493899.

Cox, B., Sridhar, N., 2002. A traction law for inclined fiber tows bridging mixed-mode cracks. Mech. Adv. Mater. Struct. 9, 299–331. http://dx.doi.org/10.1080/1537649029009697.

Cui, H., Li, Y., Koussios, S., Zu, L., Beukers, A., 2011. Bridging micromechanisms of Z-pin in mixed mode delamination. Compos. Struct. 93 (11), 2685–2695. http://dx.doi.org/10.1016/j.compstruct.2011.06.004.

Dell'Anno, G., Cartié, D.D., Partridge, I.K., Rezai, A., 2007. Exploring mechanical property balance in tufted carbon fabric/epoxy composites. Compos. A: Appl. Sci. Manuf. 38 (11), 2366–2373. http://dx.doi.org/10.1016/j.compositesa.2007.06.004.

Grassi, M., Zhang, X., Meo, M., 2002. Prediction of stiffness and stresses in z-fibre reinforced composite laminates. Compos. A: Appl. Sci. Manuf. 33 (12), 1653–1664. http://dx.doi.org/10.1016/S1359-835X(02)00137-9.

Heimbs, S., Nogueira, A.C., Hombergsmeier, E., May, M., Wolfrum, J., 2014. Failure behaviour of composite T-joints with novel metallic arrow-pin reinforcement. Compos. Struct. 110, 16–28. http://dx.doi.org/10.1016/j.compstruct.2013.11.022.

ISO 15114:2014, 2014. Fibre-reinforced plastic composites—determination of the mode II fracture resistance for unidirectionally reinforced materials using the calibrated end-loaded split (C-ELS) test and an effective crack length approach. International Organization for Standardization.

ISO-15024:2001, 2001. Fibre-reinforced plastic composites—determination of mode I interlaminar fracture toughness, GIC, for unidirectionally reinforced materials. International Organization for Standardization 15024.

Liu, H., Yan, W., Yu, X., Mai, Y., 2007. Experimental study on effect of loading rate on mode I delamination of z-pin reinforced laminates. Compos. Sci. Technol. 67 (7–8), 1294–1301. http://dx.doi.org/10.1016/j.compscitech.2006.10.001.

Meo, M., Achard, F., Grassi, M., 2005. Finite element modelling of bridging micro-mechanics in through-thickness reinforced composite laminates. Compos. Struct. 71 (3–4), 383–387. http://dx.doi.org/10.1016/j.compstruct.2005.09.025.

Mouritz, A.P., 2007a. Compression properties of z-pinned composite laminates. Compos. Sci. Technol. 67 (15–16), 3110–3120. http://dx.doi.org/10.1016/j.compscitech.2007.04.017.

Mouritz, A.P., 2007b. Review of z-pinned composite laminates. Compos. A: Appl. Sci. Manuf. 38 (12), 2383–2397. http://dx.doi.org/10.1016/j.compositesa.2007.08.016, Langford Lane, Kidlington, Oxford, OX5 1GB, United Kingdom: Elsevier Ltd.

Mouritz, A.P., Chang, P., 2010. Tension fatigue of fibre-dominated and matrix-dominated laminates reinforced with z-pins. Int. J. Fatigue 32 (4), 650–658. http://dx.doi.org/10.1016/j.ijfatigue.2009.09.001.

Mouritz, A.P., Cox, B.N., 2010. A mechanistic interpretation of the comparative in-plane mechanical properties of 3D woven, stitched and pinned composites. Compos. A: Appl. Sci. Manuf. 41 (6), 709–728. http://dx.doi.org/10.1016/j.compositesa.2010.02.001.

Mouritz, A.P., Koh, T.M., 2014. Re-evaluation of mode I bridging traction modelling for z-pinned laminates based on experimental analysis. Compos. Part B 56, 797–807. http://dx.doi.org/10.1016/j.compositesb.2013.09.016, Elsevier Ltd.

Partridge, I.K., Cartie, D.D.R., 2005. Delamination resistant laminates by Z-fiber pinning: part I manufacture and fracture performance. Compos. A: Appl. Sci. Manuf. 36 (1), 55–64. http://dx.doi.org/10.1016/j.compositesa.2004.06.029, Elsevier Ltd.

Partridge, I.K., Cartie, D.D.R., Bonnington, T., 2003. Manufacture and performance of Z-pinned composites. In: Advani, S., Shonaike, G.O. (Eds.), Advanced Polymeric Materials: Structure Property Relationships. CRC Press LLC, Boca Raton, FL. http://dx.doi.org/10.1201/9780203492901.ch3.

Pegorin, F., Pingkarawat, K., Daynes, S., Mouritz, A.P., 2014a. Mode II interlaminar fatigue properties of z-pinned carbon fibre reinforced epoxy composites. Compos. A: Appl. Sci. Manuf. 67, 8–15. http://dx.doi.org/10.1016/j.compositesa.2014.08.008.

Pegorin, F., Pingkarawat, K., Mouritz, A.P., 2014b. Comparative study of the mode I and mode II delamination fatigue properties of z-pinned aircraft composites. Mater. Des. 65, 139–146. http://dx.doi.org/10.1016/j.matdes.2014.08.072.

Plain, K.P., Tong, L., 2009. Traction law for inclined through-thickness reinforcement using a geometrical approach. Compos. Struct. 88 (4), 558–569. http://dx.doi.org/10.1016/j.compstruct.2008.06.002.

Rugg, K.L., Cox, B.N., Massabò, R., 2002. Mixed mode delamination of polymer composite laminates reinforced through the thickness by z-fibers. Compos. A: Appl. Sci. Manuf. 33, 177–190. http://dx.doi.org/10.1016/S1359-835X(01)00109-9.

Steeves, C.A., Fleck, N.A., 2006. In-plane properties of composite laminates with through-thickness pin reinforcement. Int. J. Solids Struct. 43 (10), 3197–3212. http://dx.doi.org/10.1016/j.ijsolstr.2005.05.017.

Sweeting, R.D., Thomson, R.S., 2004. The effect of thermal mismatch on Z-pinned laminated composite structures. Compos. Struct. 66, 189–195. http://dx.doi.org/10.1016/j.compstruct.2004.04.037.

Tong, L., Sun, X., 2004. Bending effect of through-thickness reinforcement rods on mode I delamination toughness of DCB specimen. I. Linearly elastic and rigid-perfectly plastic models. Int. J. Solids Struct. 41 (24–25), 6831–6852. http://dx.doi.org/10.1016/j.ijsolstr.2004.06.010.

Tong, L., Sun, X., 2007. Bending effect of through-thickness reinforcement rods on mode II delamination toughness of ENF specimen: elastic and rigid–perfectly plastic analyses. Compos. A: Appl. Sci. Manuf. 38 (2), 323–336. http://dx.doi.org/10.1016/j.compositesa.2006.04.001.

Tong, L., Mouritz, A.P., Bannister, M.K., 2002. 3D Fibre Reinforced Polymer Composites. Elsevier, Boston. ISBN: 978-0-08-043938-9.

Vazquez, J.T., Castanié, B., Barrau, J.-J., Swiergiel, N., 2011. Multi-level analysis of low-cost Z-pinned composite joints: part 1: single Z-pin behavior. Compos. A: Appl. Sci. Manuf. 42 (12), 2070–2081. http://dx.doi.org/10.1016/j.compositesa.2011.09.018, Elsevier Ltd.

Yasaee, M., Lander, J., Allegri, G., Hallett, S., 2014a. Experimental characterisation of mixed mode traction–displacement relationships for a single carbon composite Z-pin. Compos. Sci. Technol. 94, 123–131. http://dx.doi.org/10.1016/j.compscitech.2014.02.001.

Yasaee, M., Mohamed, G., Allegri, G., Hallett, S.R., 2014b. Delamination resistance of through thickness reinforced composites. In: 16th European Conference on Composite Materials ECCM16, Seville, Spain.

Zhang, X., Hounslow, L., Grassi, M., 2006. Improvement of low-velocity impact and compression-after-impact performance by z-fibre pinning. Compos. Sci. Technol. 66 (15), 2785–2794. http://dx.doi.org/10.1016/j.compscitech.2006.02.029.

This page intentionally left blank

Toughening mechanisms for whisker-reinforced composites

7

Y.X. Zhang, H. Tian
The University of New South Wales, Canberra, ACT, Australia

7.1 Introduction

Whisker-reinforced composites are composites reinforced with short fibers. Whisker-reinforced composites applied in various engineering fields, including mechanical engineering, aeronautical engineering, and civil engineering, have been developed over the years. Usually, in whisker-reinforced composites, the whiskers are used to cooperate with the matrix, which always exhibits the disadvantage of low tensile strength or brittleness and loses its load-carrying capacity suddenly with the occurrence of cracks. However, with the addition of the whiskers, the stress release incurred by the cracks in the matrix could be transferred to the whiskers due to the fiber-bridging effects, and as a result, the cracking progress could be restrained, and the ductility of the composite can usually be enhanced.

Great efforts have been made to develop high-performance fiber-reinforced cementitious composites, and various short fibers have been used to reinforce the cementitious composites to obtain a desired mechanical behavior. Engineered cementitious composite (ECC) is one of the high-performance fiber-reinforced cementitious composites containing up to 2% whiskers with strain-hardening capacity superior to that of the conventional concrete materials. The development and application of sustainable, green, and environmentally friendly fiber-reinforced cementitious composites is of great significance to the environment and society; they have attracted great research interest in recent decades. Industrial wastes or by-products have been used in the development of green and sustainable building and construction materials.

Fly ash is a by-product of coal-fired power stations. Usually, with the generation of electricity, thousands of tons of fly ash are produced; the disposal of this waste is a long-term problem. As a kind of pozzolana material, fly ash is often used together with cement as a component of concrete matrix and coaction with cement. Employing fly ash in this way not only uses the industrial waste efficiently but also the amount of CO_2 emissions produced during the manufacturing of cement is reduced significantly (Yang et al., 2007). In addition to the benefits to the environment, it was found that a high-performance fiber-reinforced cementitious composite containing a high-volume fraction of fly ash exhibited outstanding strain capacity in the experimental studies (Yang et al., 2007), and the use of high-volume fly ash could also improve the long-term mechanical behavior of the composite and reduce the business cost (Mehta, 2004).

Toughening Mechanisms in Composite Materials. http://dx.doi.org/10.1016/B978-1-78242-279-2.00007-X

In whisker-reinforced cementitious composites, the short fibers, which are usually distributed randomly in the composite, play an important role in tailoring the composites. The fibers distributed in the cement could be used to control plastic shrinkage cracking and improve mechanical behavior of the cementitious composites (Li, 2007). Steel fibers, glass fibers, and other synthetic fibers, such as polyvinyl alcohol fibers and polyethylene fibers, have been often employed in the development of the fiber-reinforced cementitious composites.

Natural fibers, such as coconut husk, bagasse fiber, bamboo fiber, coir fiber, jute fiber, sisal fiber, wood fiber, and vegetable fiber, which are the natural wastes or the by-products of the agricultural industry, have been used increasingly in the development of green and sustainable construction and building materials. Natural fibers are widely available around the world and cost much less than steel fibers or synthetic fibers. Furthermore, natural fibers have been demonstrated to be capable of improving the mechanical properties of the cementitious matrix, such as flexural toughness, flexural strength, compression strength, impact resistance, tensile strength, and tensile ductility (Al-Oraimi and Seibi, 1995; Ramakrishna and Sundararajan, 2005; Savastano et al., 2000, 2003).

However, due to the impact of the long-term alkali surroundings, the material characteristics of natural fibers are degraded; accordingly, the mechanical properties of natural fiber-reinforced cementitious composites also decrease with time. This is because some components of the natural fibers, such as hemicellulose, are likely to degrade in the cementitious media in the alkali environment, resulting in a decrease in the mechanical properties of the composites. In order to prevent the degradation of the material properties of the materials from the environment, natural fibers are usually modified through pyrolyzation and chemical treatment before being mixed. The fibers are treated with special chemical solutions (such as alkali, acetylation, and silane solution) in high-temperature conditions to remove the adverse components such as the hemicellulose, so as to change the structure and chemical composition of the natural fibers, therefore, improving the long-term mechanical behavior of the composites (Bledzki et al., 1996; Belgacem and Gandini, 2005; Li et al., 2007; John and Anandjiwala, 2008). After this treatment, the natural fibers could be refined into pulp material, which is a kind of microfiber with a length of only about 2 mm. This natural pulp shows lower capability of water absorption and could be used to improve the mechanical behavior of the composites (Coutts and Warden, 1992). Composites containing flax fiber, jute fiber, banana fiber, and coir fiber treated according to these procedures have been developed, and the test demonstrated that these composites exhibited comparable mechanical properties to conventional concrete (Coutts, 1983; Coutts and Waren, 1990; Zhu and Tobias, 1994). The chemical treatment of the fibers would also benefit the long-term mechanical behavior of the whisker-reinforced composites. The natural fibers that were treated chemically using these procedures were demonstrated to be able to enhance the long-term mechanical properties of the composites through long-term mechanical tests (Aggarwal, 1995).

Natural fiber-reinforced cementitious specimens were usually processed in different curing conditions, such as natural weathering condition, air condition, water-immersing condition, repeating wetting and drying cycles, and accelerating ambient

environment. Comparison of these different environmental effects on the mechanical behavior and chemical components of the composites were performed through mechanical and microenergy dispersive measurement (Coutts, 1987; Akers and Studinka, 1989; Marikunte and Soroushian, 1994; Macvicar et al., 1999). Although the other curing conditions can be applied to modify the composites, the natural weathering condition, which represents the practical condition, has been demonstrated to be the most appropriate curing condition.

A few research studies on fiber-reinforced composites with a high volume of fly ash or natural fibers have been reported. With the high-volume fraction of fly ash, the matrix gets a lower alkali degree; this may have reduced the corresponding degradation of the natural fibers, which plays an important role in improving the mechanical properties of the composite especially after long-term curing (Marikunte and Soroushian, 1994). On the other hand, natural fibers will absorb the water in the matrix and influence the water distribution, and this may have a strong effect on the hydration of matrix and interaction between cement and fly ash.

This chapter reports a green whisker-reinforced cementitious composite with high-volume fly ash and bagasse fiber recently developed by the authors; the combined influence of a high volume of fly ash and bagasse fibers on the fiber-reinforced cementitious composites are reported. The material processing and toughening methods of the new cementitious composite are introduced in this chapter. The mechanical properties such as compressive strength, modulus of elasticity, flexural strength, and tensile strength were tested, and the test method and results are presented.

7.2 A green whisker-reinforced cementitious composite

A green hybrid fiber-reinforced cementitious composite with high-volume fly ash and bagasse fibers was recently developed by the authors (Tian and Zhang, 2013, 2014). Bagasse fiber is the by-product of the sugar cane industry. It is a totally eco-friendly material and has been found to be able to change the setting behavior and improve the basic mechanical properties of the matrix (Bilba et al., 2003). Furthermore, bagasse fiber could improve the long-term durability of fiber-reinforced cementitious composites than other natural fibers when the composites specimens were cured through long-term curing conditions like weather curing, wetting, and drying cycles or water immersion (Aggarwal, 1995). In addition, low-volume steel fibers were also used for strength of the new cementitious composite. The new cementitious composite was designed according to the mix for the ECC with high-volume fly ash (Yang et al., 2007). The new green cementitious composite was composed of cement, fly ash, sand, water, and reducing agent and was reinforced with 0.5% steel fiber and 3% bagasse fiber. The mixture proportion of the composite design is shown in Table 7.1. ASTM Type I ordinary Poland cement and a low-calcium Class F fly ash were used. The high-range water-reducing agent used was Grace ADVA 142. The average size of the sand used was 150 μm, with the maximum size of 220 μm. The ratio of fly ash to cement was 1.6 and the ratio of sand to cement was 0.9.

Table 7.1 Mix design of the new cementitious composite

Cement (kg/m^3)	Fly ash (kg/m^3)	Sand (kg/m^3)	Water (kg/m^3)	Reducing agent (kg/m^3)
487.78	780.45	439	329	6.34

The steel fibers were provided by Ganzhou Daye Metallic Fibers Co., Ltd, and were coppered micro steel fibers of 13 mm in length and 0.2 mm in diameter. The tensile strength of the steel fiber was 2400 MPa. The original bagasse fibers were provided by Queensland University of Technology and were treated according to the following procedures to improve their mechanical and chemical properties before mixing. First, the bagasse fibers were sieved through a 1.18 mm screen, removing coarse fibers. Next, in order to remove degradable components, such as hemicellulose, the finer bagasse fibers were boiled in 3% NaOH solution at a temperature of 100 °C for 2 h. Then, the bagasse fibers were dried in an oven at 105° for 1 h, and coated with silane through immersion in 6% silane solution for 2 h (Bilba and Arsene, 2008). Finally, bagasse fibers were dried in the oven again for 2 h. After these modifications, the bagasse fibers had a mean length of 10.1 mm, and mean diameter of 0.39 mm.

7.3 Material processing and toughening methods

The fiber-reinforceed cementitious composites were processed according to the following procedures. The solid ingredients, including cement, sand, and fly ash were first mixed in a 40-L capacity mixer for approximately 2 min. Because the water contained in the bagasse fibers evaporates gradually out of the fibers during the final drying progress, the bagasse fibers stuck to adjacent fibers. If adhesive fibers cannot absorb water and get seperated from other fibers, it is hard for these fibers to be evenly dispersed into the matrix. Therefore, the bagasse fibers were immersed into water for about 5 min before being added into the mix to make sure they dispersed evenly in the composite. After that, 50% of the bagasse fibers and water together with the water-reducing agent were added into the mixer and blended for another 3 min. The remaining water and bagasse fibers were added into the mix when the water in the mix was fully absorbed. Once a consistent mixture was obtained, steel fibers were gradually added and the mix was blended for 10 min. The finished fresh mixture was then casted into molds for the specimens. The molds were vibrated on the vibration table for 3 min.

7.4 Mechanical properties and testing

The mechanical behavior of the new composite, including compressive strength, Young's modulus, flexural strength, and material properties under direct tensile loading at the age of 7, 14, and 28 days, was studied experimentally. The testing method,

specimens used, and test results are presented herein. All the specimens followed the same curing procedures, i.e., the finished fresh mixture, were poured into the molds, were demolded after 24 h, and placed in a curing chamber with a constant temperature of 23 °C and 100% relative humidity until the day of testing.

7.4.1 Compressive strength and Young's modulus

Cubes of 50 mm were used to test uniaxial compressive strength, and cylinders of 200 mm in length and 100 mm in diameter were used to test the Young's modulus of the new composite. The testing of compressive strength and Young's moduls followed the Australian code SAI AS, 1012.9 (1986) and SAI AS, 1012.17 (1997), respectively. Testing machine TECNOTEST, as shown in Figure 7.1, was used to test the compressive strength and the Young's modulus. Three specimens were tested to get the mean value of the compressive strength and Young's modulus. The tested compressive strength and Young's modulus of the composite at the age of 7, 14, and 28 days is shown in Table 7.2. It can be seen that the new composite has a compressive strength of 32 MPa at the age of 7 days, 41 MPa at the age of 14 days, and 49 MPa at the age of 28 days, while the Young's modulus increases from 15.24 GPa at the age of 7 days to 18.07 GPa at the age of 14 days and to 18.69 GPa at the age of 28 days. Compared to the material properties of conventional concrete (Siddique, 2004), the developed composite material shows higher compressive strength but lower Young's modulus. This phenomenon may be caused by the replacement of coarse aggregates with fine particle materials, i.e., cement and fly ash in the composite and as a result the composite is more compact with more paste available to combine the components in the matrix. Besides, as a large part of fly ash does not join in the reaction with cement and the particle size of fly ash is smaller than the cement particles and their hydration products, fly ash plays a role of filler in the space between large particles, and therefore makes the composites more compact than the conventional concrete. Accordingly, the compressive strength of the matrix was increased compared to that of the conventional concrete. Moreover, the existence of fiber also contributes to the increased value of the compressive strength of the composite. The bridging fibers, which are crossing the microcracks caused by compression, may restrain the development of cracks, and hence indirectly increase the compressive strength of the composites. The newly developed material exhibits lower Young's modulus than the conventional concrete; this is because the coarse aggregates in the conventional concrete were replaced by cements in the new composite.

7.4.2 Flexural strength and flexural behavior of the composite

Beam specimens of the dimensions of $350 \times 100 \times 100$ mm^3 were tested to determine the textural behavior of the new composite. Four-point bending testing, as shown in Figure 7.2, is conducted to study the flextural behavior and flexural strength of the composite. The flexural tests are conducted according to the American standard (ASTM C 1018-97, 1998). Two external linear variable displacement transducers were attached to the mid-span of the specimen surface to measure its corresponding

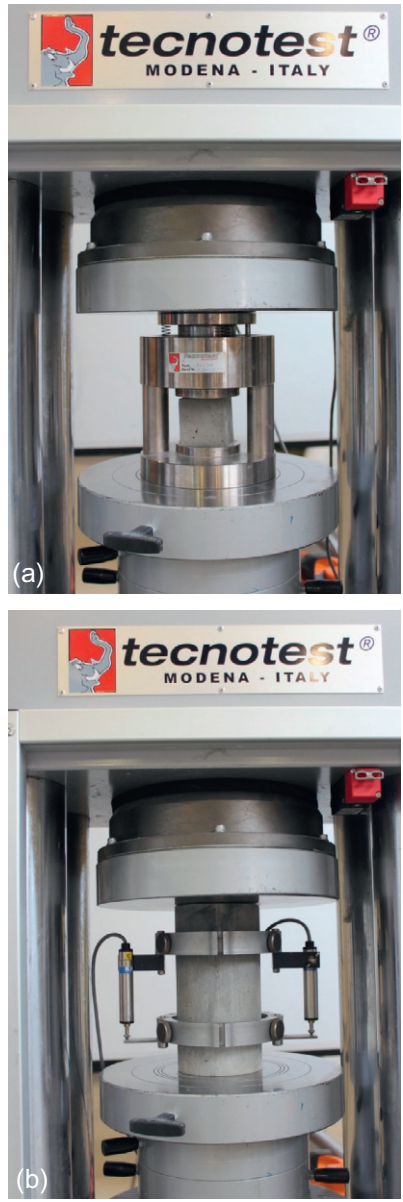

Figure 7.1 Testing setup for compressive strength (a) and Young's modulus (b).

vertical displacement of the beam. Three specimens were tested to get a mean value of the material property. The flexural (bending) strength–mid-span deflection curve of the beam tested at the age of 7, 14, and 28 days is shown in Figure 7.3.

It can be seen from the figure that the flexural strength of the composite increases gradually with curing time. The flexural strength of the composite tested at the age of

Table 7.2 Compressive strength and Young's modulus of the composite

Testing days	7 days	14 days	28 days	Conventional concrete (Siddique, 2004)
Compressive strength (MPa)	31.8	41.29	49.01	37.2
Young's modulus (GPa)	15.24	18.07	18.69	29.9

Figure 7.2 Setup of the four-point bending test.

7, 14, and 28 days is 3.93, 4.38, and 5.09 MPa, respectively. The ductility of the composite also exhibits dramatic increase with time, which could be seen from the gentle decline of the postpeak bending resistance. The flexural strength of the new material is comparable to that of the conventional concrete, which is about 5 MPa for normal concrete (Siddique, 2004).

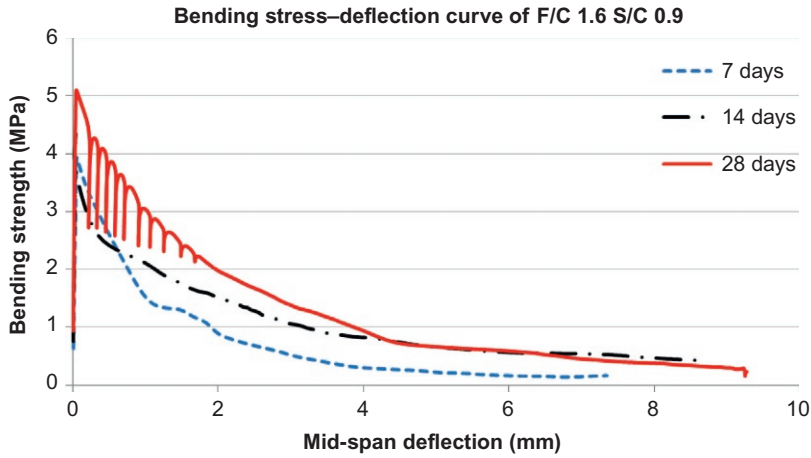

Figure 7.3 Flexural behavior of the composite at the age of 28 days.

7.4.3 Material properties under direct tension

For the direct tensile test of fiber-reinforced concrete a definite standard is usually not available. The dog bone-shaped specimens and tensile test setup (Soe et al., 2013) are utilized to test the tensile behavior of the composite. The dog bone-shaped specimens are of a gauge length of 80 mm, width of 32 mm, and thickness of about 13 mm, as shown in Figure 7.4. Direct tension test was conducted using the Shimadzu AG-X testing machine to study the tensile behavior of the composite. Non-contact extensometer

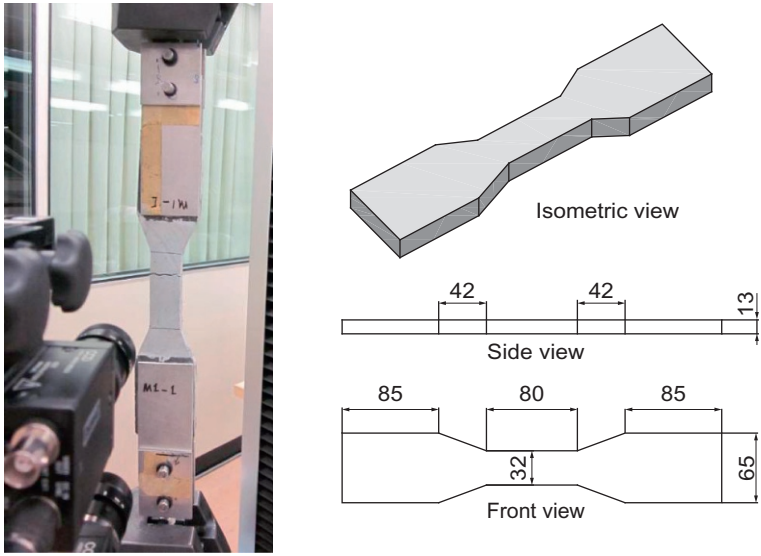

Figure 7.4 Tensile test setup and the dog bone specimen.

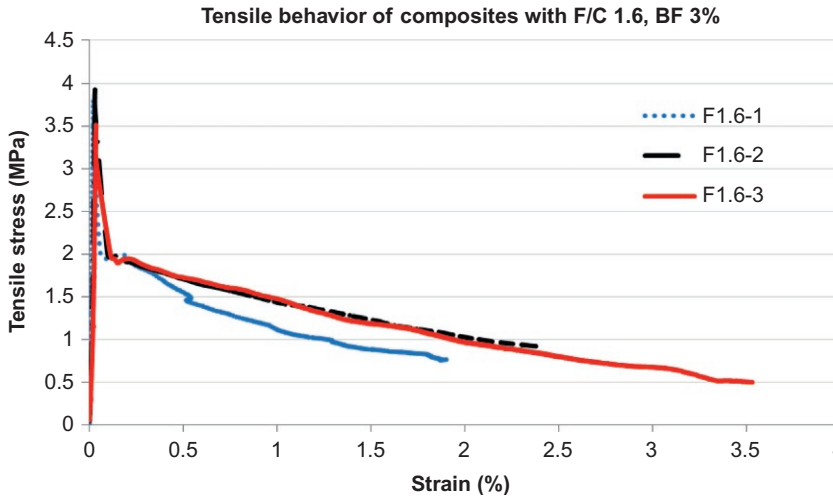

Figure 7.5 Tensile behavior of the composite at the age of 28 days.

was also used to detect the displacement of the gauge. Pin joints in the aluminium tags glued to the specimen were utilized to transmit the aligned force applied by the machine. Three specimens were tested to get a mean value of the material property. The tensile strength–strain curve of the dog bone specimens tested at the age of 28 days is shown in Figure 7.5. As can be seen from Figure 7.5, the tensile strength of the developed composite is about 3.5 MPa, which is comparable to the tensile strength of normal concrete, which is usually about 3 MPa (Phillips and Zhang, 1990). However, for conventional concrete, once the tensile stress reaches the peak value, a crack suddenly occurs across the specimen and the specimen losses its load-carrying capacity completely. This phenomenon of sudden loss of load-carrying capability in conventional concrete is avoided in the new composite due to the effects of the short fibers. It can be seen from Figure 7.5 that although the tensile resistance of the composite specimen dropped suddenly after the specimen cracks, the specimen still carries 2 MPa of tensile resistance, followed by gradual decrease till the specimen collapsed.

7.5 Effect of parameters on the mechanical properties

The mechanical properties of a composite are affected by the proportions and characteristics of its ingredients. Mechanical properties of the cementitious composite with varying fly ash to cement ratio of 1.2, 1.6, and 2.0 were tested, and the results are reported and analyzed in this session so as to understand the influence of fly ash content on the mechanical behavior of the developed new cementitious composite. The mechanical properties of the cementitious composite reinforced with 3%, 8%, and 12% bagasse fiber with fixed 0.7% steel fiber and fly ash to cement ratio of 1.6 were also tested, and the results are presented herein to study the influence of bagasse fiber

content on the mechanical properties of the composites. Material properties of the composite, including compressive strength, Young's modulus, and flexural strength, were tested at the age of 7, 14, and 28 days, and the material properties of the composite under direct tensile loading were tested at the age of 28 days.

7.5.1 Influence of fly ash content on mechanical properties

The compressive strength of the composite with varying fly ash to cement ratio tested at the age of 7, 14, and 28 days (Tian and Zhang, 2013) is shown in Table 7.3.

It can be seen that the compressive strength of the composite is comparable to that of the conventional concrete with the value at the age of 28 days reaching 42.37, 36.67, and 33.82 MPa for the composite with fly ash/cement ratio of 1.2, 1.6, and 2.0, respectively. As the fly ash to cement ratio increases from 1.2 to 1.6 and 2.0, the 28-day compressive strength of the composite is reduced. This can be explained as follows. After mixed together, chemical reaction will occur between the different ingredients of the composite. During the process of chemical reaction, only a small part of the composition of the fly ash takes part in the pozzolanic reaction with the cementitious compound, while a majority of the composition of the fly ash only plays a role to fill the space between the compounds of the matrix. Because of the high volume of fly ash in the new composite and significantly reduced amount of cement compared to that in the conventional concrete, the adhesion stress between the particles declines, since less paste is available to combine the particles contained in the matrix. Besides, the addition of fly ash can increase the air content in the matrix; this may also cause the decrease of the compressive strength of the composite. For the composite with a constant fly ash/cement ratio, the compressive strength of the composite increases from 7 to 14 days with a increase of 13.93% for the fly ash/cement ratio of 1.2, 14.16% for the fly ash/cement ratio of 1.6, and 14.27% for the fly ash/cement ratio of 2.0, respectively. But the increase in the compressive strength at 28 days from 7 days is more significant with an increase of 35.4%, 51.2%, and 55.7% for fly ash/cement ratio of 1.2, 1.6, and 2.0, respectively. This phenomenon reflects that the pozzolanic reaction between the materials is more intense in the period between 14 and 28 days than that at the earlier stage.

Table 7.3 Compressive strength of the composite with different fly ash/cement ratio

Compressive strength (MPa)			
	Days at testing		
Fly ash/cement ratio	7	14	28
$F/C = 1.2$	31.3	35.66	42.37
$F/C = 1.6$	24.24	28.24	36.67
$F/C = 2.0$	21.72	24.82	33.82

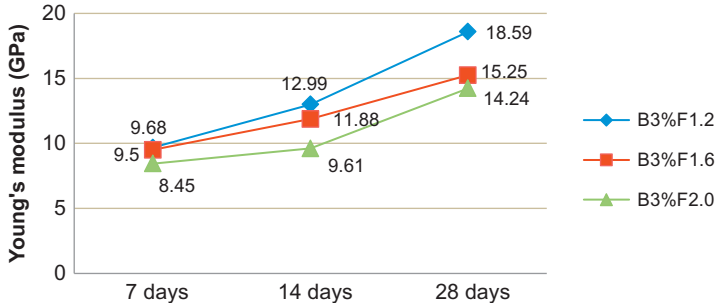

Figure 7.6 Young's modulus of the composite with different fly ash/cement ratio.

The tested Young's modulus of the composite with varying fly ash/cement ratio at the age of 7, 14, and 28 days is shown in Figure 7.6.

As can be seen from Figure 7.6, from 7 to 28 days, the Young's modulus of the composite increases by 92.05% for the fly ash/cement ratio of 1.2, 60.52% for the fly ash/cement ratio of 1.6, and 68.52% for the fly ash/cement ratio of 2.0. Moreover, the tested Young's modulus at the same curing age decreases with the increase of the fly ash/cement ratio. At the age of 28 days, the Young's modulus is 18.59 GPa for the fly ash/cement ratio of 1.2, 15.25 GPa for the fly ash/cement ratio of 1.6 (with a reduction of 17.97%), and 14.24 GPa for the fly ash/cement ratio of 2.0 (with a reduction of 6.62%). The application of high-volume fly ash to replace the cement results in less adhesion stress between the particles and more air content in the matrix; therefore, the Young's modulus of the composite is decreased accordingly.

Table 7.4 shows the flexural strength of the composite with varying fly ash/cement ratio of 1.2, 1.6, and 2.0 tested at the age of 7, 14, and 28 days. It is seen that the flexural strength of the composite decreases with the increase of the fly ash/cement ratio. At the age of 28 days, the tested flexural strength of the composite is 5.74 MPa for the fly ash/cement ratio of 1.2, 5.22 MPa (a decrease of 9.06%) and 4.67 MPa (a decrease of 18.64%) for fly ash/cement ratio of 1.6 and 2.0, respectively. The flexural strength of the composite at the age of 7 days for all three fly ash/cement ratios is over 3 MPa. Due to the hydration reaction of the cementitious material, the specimens become

Table 7.4 Flexural strength for the composite with different fly ash/cement ratio

Flexural strength (MPa)			
	Days at testing		
Fly ash/cement ratio	7	14	28
$F/C = 1.2$	4.61	4.84	5.74
$F/C = 1.6$	3.23	4.2	5.22
$F/C = 2.0$	3.01	3.79	4.67

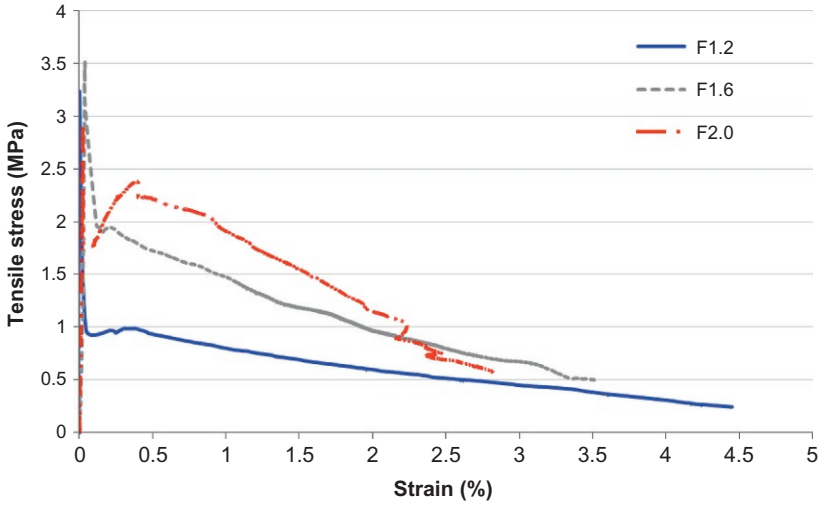

Figure 7.7 Direct tensile stress–strain curves of new developed composites under different fly ash contents.

harder and its flexural strength increases gradually with the curing time, with an increase of 24.51% for the fly ash/cement ratio of 1.2, 61.61% for the fly ash/cement ratio of 1.6, and 55.15% for the fly ash/cement ratio of 2.0, respectively from the age of 7 days to the age of 28 days.

The tested tensile strength–strain behavior of the composite with varying fly ash to cement ratio is shown in Figure 7.7.

Figure 7.7 shows that there is a slight change in the tensile strength of the composite with the fly ash to cement ratio varying from 1.2 to 2.0. In order to better interpret the mechanical behavior of the developed composite, another mechanical property, namely tensile ductility, is presented. Tensile ductility stands for the capability of energy absorption of certain material and can be calculated as the area under the curves prior to a specific strain value. It can be observed from Figure 7.7 that before strain reaches 2%, the area under the curves increases greatly with the increase of the fly ash content. This means tensile ductility of the composite increases dramatically and more energy is absorbed with the increase of the content of the fly ash. For the new composite with a fly ash to cement ratio of 1.2, the tensile strength dropped suddenly to no more than 1 MPa when cracks happened, and the tensile strength continued to decline gradually till the specimen was finally damaged. Although the tensile strength also decreased suddenly when cracks happened in the tensile specimens with a fly ash to cement ratio of 1.6, the residual tensile strength was about 2 MPa, which was nearly two times of that for its counterpart with a fly ash/cement ratio of 1.2. The increased toughness was more obviously in the cementitious composite with a fly ash/cement ratio of 2.0. For this composite, the tensile strength also exhibited a sharp decrease when the specimen cracked, but the residual tensile stress increased again with the increase of the strain with the residual tensile strength peaking at

2.41 MPa. This means the composite exhibits strain-hardening behavior, which is usually associated with excellent toughness of the materials. As shown in Figure 7.7, this strain-hardening behavior continued until the tensile strain of the specimen reached 0.4%, and then the residual tensile strength decreased gradually till the specimen was finally damaged.

The strain-hardening behavior can be explained from the micro-mechanism of the composite. At the very beginning, as tensile force was applied on the ends of the specimen, the same strain occurred to the fibers and matrix of the specimen under the application of the tensile force. With the increase of the tensile load, some micro-cracks occurred and developed in the matrix, and the fibers bridged the micro-cracks. With the progress and propagation of the micro-cracks across the fibers, debonding occurred firstly between part of the fibers and the matrix in the crack region, and then further developed along the surface between the fibers and the matrix. During this process, tensile stress in the cracked matrix was released and transferred to the bridging fibers, and the tensile stress was usually held due to the chemical bond stress and mechanical interaction between the matrix and bridging fibers in the undebonded area. The tensile strength suddenly endowed to the bridging fibers, increased the strain of the bridging fibers, and promoted the debonding process of fibers from the matrix. Despite the micro-cracks in the matrix, the tensile stress of the specimen was increased with strain due to the fiber-bridging effects. With the development of micro-cracks, the micro-cracks joined together gradually and formed a visible crack through the weakest section of the specimen. The formulation of this major crack led to the sudden drop of the tensile stress–strain curve from the peak value due to the rapidly release of tensile stress from the brittle cementitious material (Jun and Mechtcherine, 2010). Then, with the increase of the strain, the width of the major crack was enlarged and the stress was enhanced due to the strengthening role of the bridging fibers. As a result, the residual tensile stress increased again and exhibited the strain-hardening behavior until the tensile stress reached the second peak value (Zhang et al., 2000; Roth et al., 2010). After this, when more tensile load is applied to the specimen, debonding between bridging fibers and matrix progressed quickly and bridging fibers began to be pulled out from the matrix. When the fibers were totally debonded from the surrounding matrix, the adhesive stress between the fiber and the matrix due to chemical bonding effect was lost, and thus only friction stress was exhibited between the bridging fibers and the matrix. For bagasse fibers, when the fibers were pulled out, the surface of natural fibers got damaged and the fibers became coarser, and as a result the friction stress was increased. Therefore, after the tensile stress reached the second peak value, it declined gradually with the increase of strain due to the fraction stress incurred. Finally, when the fibers were completely pulled out from the matrix, the bridging action of the fibers across the major crack was lost; as a result, the specimen got fractured and lost its tensile carrying capacity completely.

The fly ash plays a role of filling the space between the hydration products, making the composite more compact, and therefore increasing the bonding behavior of bridging fibers. However, with the decreases of the fly ash content, the strain-hardening behavior became not obvious for the composite. From the tested results, it can be concluded that the increase of fly ash content in the composite could increase the

toughness of the whisker-reinforced cementitious composite but at a cost of sacrificing compressive strength and Young's modulus. The increase of fly ash content may have impaired the hydration process of cement, resulting in the decrease of compressive strength and Young's modulus of the composite. The fly ash particle could fill in the space between the hydration products, i.e., between the matrix and the fibers for the composite. As a result, the use of fly ash can compact the matrix and improve the bonding behavior of the composite, and this plays a significant role in the toughness mechanism of the composite.

7.5.2 Influence of bagasse fiber content on the mechanical behavior of the composite

Mechanical properties such as compressive strength, Young's modulus, flexural strength, tensile strength, and tensile ductility of the hybrid fiber-reinforced cementitious composite with varying bagasse fiber content (3%, 8%, and 12% by volume) were tested (Tian and Zhang, 2014). Table 7.5 shows the tested compressive strength of the composite with varying bagasse fiber content at the age of 7 days, 14 days, and 28 days.

It can be observed that with the increase of the bagasse fiber content, the early-age compressive strength of the composite reduces significantly. At the age of 7 days, the compressive strength of the composite with bagasse fiber content of 3% is 24.24 MPa, and the value drops to a much lower value of 12.54 and 10.55 MPa, respectively, for the composite with bagasse fiber content of 8% and 12% (only 51.7% and 43.52% of that for 3% bagasse fiber). However, when specimens are 28 day old, the compressive strength of the composite of a different mix does not show such a dramatic change. The compressive strength of 36.67 MPa for bagasse fiber content of 3% is reduced to 32.96 MPa (a reduction of 10.2%) for the bagasse fiber content of 8% and 25.78 MPa (a reduction of 29.7%) for bagasse fiber content of 12%. The application of bagasse fiber postpones the hydration of cementitious material, which may be caused by the chemical component of the bagasse fiber such as sugar contained, and therefore the compressive strength of the materials at the age of 7 days decreases more significantly than that at the age of 28 days. With the increase of curing age, the

Table 7.5 Compressive strength of the composite with varying bagasse fiber content

Compressive strength (MPa)			
	Days of testing		
Bagasse fiber content (%)	7	14	28
3	24.24	28.24	36.67
8	12.54	23.54	32.96
12	10.55	18.76	25.78

hydration process becomes stable, and the difference in the compressive strength of the composite with different bagasse fiber content became not so significant. In addition, the increase of the bagasse fiber content increases the specific area of fibers and the void content in the matrix and accordingly decreases the adhesive effect of the matrix, causing reduction of the compression strength of the material.

The tested Young's modulus of the composite with varying bagasse fiber content is shown in Figure 7.8. As can be seen in Figure 7.8, the Young's modulus of the composite reduces with the increase of bagasse fiber content. At the age of 28 days, the Young's modulus of the composite is 15.25 GPa with the bagasse fiber content of 3%, and this value is decreased to 13.51 and 11.76 GPa for the bagasse fiber content of 8% and 12% with a reduction of 11.41% and 22.89%, respectively. Besides, as shown in Figure 7.8, the composite containing different bagasse fiber content shows stable and consistent trend of change in the Young's modulus with the increase of the curing time.

Table 7.6 shows the flexural strength of the composite with varying bagasse fiber content of 3%, 8%, and 12% tested at the age of 7, 14, and 28 days. The composite containing 3% bagasse fiber shows the greatest value in the flexural strength of 5.22 MPa at the age of 28 days. As the fiber content increases, the flexural strength

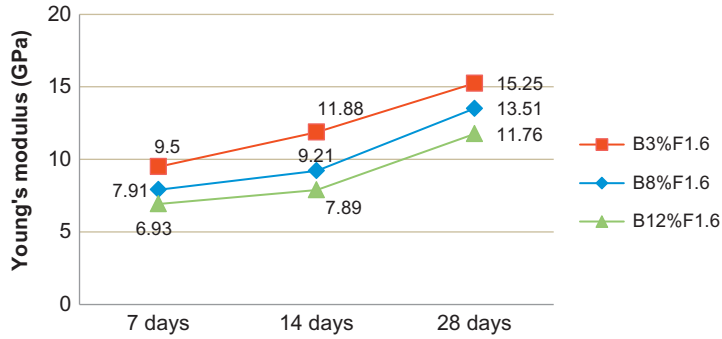

Figure 7.8 Young's modulus of the composite with different bagasse fiber contents.

Table 7.6 Flexural strength of the composite with different bagasse fiber content

Flexural strength (MPa)			
	Days at testing		
Bagasse fiber content (%)	7	14	28
3	3.23	4.2	5.22
8	2.94	4.17	5.05
12	2.57	2.68	3.89

declines gradually to 5.05 and 3.89 MPa for the composite with 8% and 12% bagasse fiber content respectively (with a reduction of 3.26% and 25.48%). At the age of 7 days, the flexural strength is only 3.23, 2.94, and 2.57 MPa for the composite containing 3%, 8%, and 12% bagasse fiber by volume respectively, and flexural strength increases gradually with the increase of the curing age. The effect of bagasse fiber on the hydration process and the void content of the matrix as described previously also applies to the flexural strength, and the flexural strength increased with the increase of the bagasse fiber content.

The tensile strength–strain behavior of the composite with various bagasse fiber content is shown in Figure 7.9.

It can be found from Figure 7.9 that both the tensile strength and the residual tensile strength of the composite decline continually with the increase of the bagasse fiber content. When cracks take place in the specimens containing 3% bagasse fiber, the tensile stress drops to 1.94 MPa, followed by a gradual decrease of the residual tensile strength. However, the residual tensile strength after the first crack is only 1.21 and 0.64 MPa for the cementitious composite containing 8% and 12% bagasse fiber (a reduction of 37.6% and 67.1% of that for the composite with 3% bagasse fiber). This might be due to the increase of the void content caused by the increase of the bagasse fiber content. With the increase of the bagasse fiber content in the composite, more air is brought into the matrix and trapped between the interfaces of the matrix and fibers. The trapped voids could decrease the compactness of the composite, and therefore cause a decrease in the compressive strength and bonding strength between cementitious matrix and fibers. Besides, as bagasse fibers will release the absorbed water from the surrounded cement hydration, the volume of the bagasse fiber decreases as shrinkage occurs; this may also play a role in decreasing the compactness and the bonding strength of the composite.

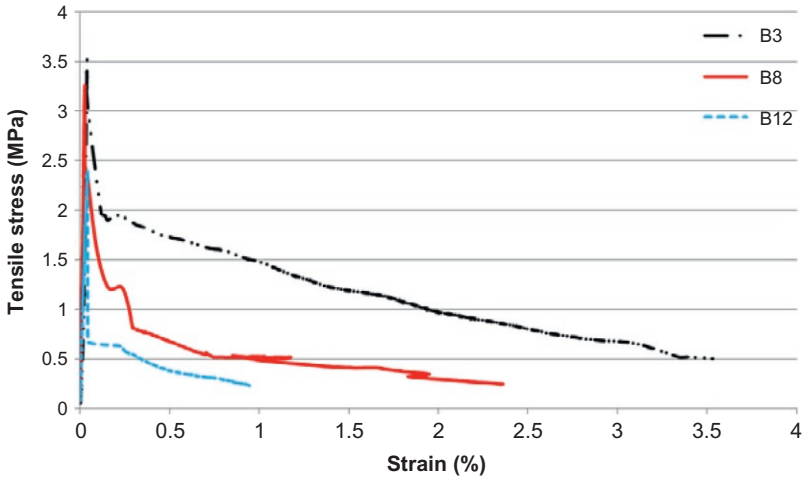

Figure 7.9 Direct tensile stress–strain curves of the new developed composite with varying bagasse fiber content.

7.6 Application and future trends

This chapter presents a green whisker-reinforced cementitious composite containing a high volume of fly ash and bagasse fibers and reports on the tested mechanical properties. From the test results, it can be seen that the composite exhibits mechanical properties comparable to the conventional concrete. These mechanical properties equip the whisker-reinforced cementitious composite strong potential to be used as a construction and building material as an alternate of the conventional concrete.

It is well known that natural fibers may degrade with time. The degradation of natural fibers will cause a decrease in its mechanical properties and, accordingly, the mechanical properties of the cementitious composite. Therefore, for the composite containing natural fibers, it is important to investigate the long-term mechanical behavior so as to evaluate the long-term effect on the mechanical properties of the composite. Thus, the long-term mechanical behavior of the newly developed composite will be investigated in further research. Since high-temperature working conditions cannot be prevented for civil structures, and natural fibers are weak in resisting high temperatures, research on material properties and structural behavior of the composite at elevated temperatures including under fire conditions should also be conducted in the future. To enhance the application of the composites, other aspects of the composite, in particular the durability of the cementitious composite, should also be investigated. In addition to the mechanical behavior of the composite, the structural behavior of typical structural components made of the natural fiber-reinforced composite should also be investigated in the future.

References

Aggarwal, L.K., 1995. Bagasse-reinforced cement composites. Cem. Concr. Compos. 17, 107–112.

Akers, S.A.S., Studinka, J.B., 1989. Aging behaviour of cellulose fibre cement composites in natural and accelerated tests. Int. J. Cem. Compos. Light. Concr. 11 (2), 93–97.

Al-Oraimi, S.K., Seibi, A.C., 1995. Mechanical characterisation and impact behaviour of concrete reinforced with natural fibres. Compos. Struct. 32, 165–171.

ASTM C 1018-97, 1998. Standard test method for flexural toughness and first crack strength of fiber-reinforced concrete (using beam with third-point loading). Am. Soc. Test. Mater. 4, 506–513.

AS 1012.17, 1997. Determination of the static chord modulus of elasticity and Poisson's ratio of concrete specimens. Australian Standards.

AS 1012.9, 1986. Determination of the compressive strength of concrete specimens. Australian Standards.

Belgacem, M.N., Gandini, A., 2005. The surface modification of cellulose fibres for use as reinforcing elements in composite materials. Compos. Interfaces 12 (1–2), 41–75.

Bilba, K., Arsene, M.A., 2008. Silane treatment of bagasse fiber for reinforcement of cementitious composites. Compos. A: Appl. Sci. Manuf. 39 (9), 1488–1495.

Bilba, K., Arsene, M.A., Ouensanga, A., 2003. Sugar cane bagasse fibre reinforced cement composites. Part I. Influence of the botanical components of bagasse on the setting of bagasse/cement composite. Cem. Concr. Compos. 25, 91–96.

Bledzki, A.K., Reihmane, S., Gassan, J., 1996. Properties and modification methods for vegetable fibers for natural fiber composites. J. Appl. Polym. Sci. 59 (8), 1329–1336.
Coutts, R.S.P., 1983. Flax fibres as a reinforcement in cement mortars. Int. J. Cem. Compos. Light. Concr. 5 (4), 257–262.
Coutts, R.S.P., 1987. Air-cured woodpulp, fibre/cement mortars. Composites 18 (4), 325–328.
Coutts, R.S.P., Warden, P.G., 1992. Sisal pulp reinforced cement mortar. Cem. Concr. Compos. 14, 17–21.
Coutts, R.S.P., Waren, P.G., 1990. Effect of compaction on the properties of air-cured wood fibre reinforced cement. Cem. Concr. Compos. 12, 151–156.
John, M.J., Anandjiwala, R.D., 2008. Recent developments in chemical modification and characterization of natural fiber-reinforced composites. Polym. Compos. 29 (2), 187–207.
Jun, P., Mechtcherine, V., 2010. Behavior of strain-hardening cement-based composites (SHCC) under monotonic and cyclic tensile loading: part 1—experimental investigations. Cem. Concr. Compos. 32, 801–809.
Li, V.C., 2007. Engineered Cementitious Composites (ECC)—Material Structural and Durability Performance. CRC Press, Boca Raton.
Li, X., Tabil, L.G., Panigrahi, S., 2007. Chemical treatments of natural fiber for use in natural fiber-reinforced composites: a review. J. Polym. Environ. 15 (1), 25–33.
MacVicar, R., Matuana, L.M., Balatinecz, J.J., 1999. Aging mechanisms in cellulose fiber reinforced cement composites. Cem. Concr. Compos. 21, 189–196.
Marikunte, S., Soroushian, P., 1994. Statistical evaluation of long-term durability characteristics of cellulose fiber-reinforced cement composites. ACI Mater. J. 91, 607–616.
Mehta, P.K., 2004. High-performance, high-volume fly ash concrete for sustainable development. In: Proceedings of the International Workshop on Sustainable Development and Concrete Technology. University of California, Berkeley, USA.
Phillips, D.V., Zhang, B., 1990. Fracture energy and brittleness of plain concrete specimens under direct tension. In: Firrao, D. (Ed.), Fracture Behaviour and Design of Materials and Structures.Proceedings of the 8th European Conference on Fracture, Torino, Italia, October, pp. 646–652.
Ramakrishna, G., Sundararajan, T., 2005. Impact strength of a few natural fibre reinforced cement mortar slabs: a comparative study. Cem. Concr. Compos. 27 (5), 547–553.
Roth, M.J., Eamon, C.D., Slawson, T.R., Dubey, A., 2010. Ultra-high-strength glass fiber-reinforced concrete: mechanical behaviour and numerical modeling. ACI Mater. J. 107 (2), 185–194.
Savastano, H., Warden, G., Coutts, R.S.P., 2000. Brazilian waste fibres as reinforcement for cement-base composites. Cem. Concr. Compos. 22, 379–384.
Savastano, H., Warden, P.G., Coutts, R.S.P., 2003. Mechanically pulped sisal as reinforcement in cementitious matrices. Cem. Concr. Compos. 25, 311–319.
Siddique, R., 2004. Performance characteristics of high-volume Class F fly ash concrete. Cem. Concr. Res. 34, 487–493.
Soe, K.T., Zhang, Y.X., Zhang, L.C., 2013. Material properties of a new hybrid fibre-reinforced engineered cementitious composite. Constr. Build. Mater. 43, 399–407.
Tian, H., Zhang, Y.X., 2013. Mechanical properties of an eco-friendly hybrid fiber reinforced cementitious composite. Appl. Mech. Mater. 438–438, 275–279.
Tian, H., Zhang, Y.X., 2014. Tensile mechanical properties of a sustainable hybrid fibre reinforced cementitious composite. In: Composite Australia and CRC-ACS 2014 Composites Conference, Newcastle, Australia, 7–9 April, 2014.

Yang, E.H., Yang, Y.Z., Li, V.C., 2007. Use of high volumes of fly ash to improve ECC mechanical properties and material greenness. ACI Mater. J. 104, 303–311.
Zhang, J., Stang, H., Li, V., 2000. Experimental study on crack bridging in FRC under uniaxial fatigue tension. J. Mater. Civ. Eng. ASCE 12 (1), 66–73.
Zhu, W.H., Tobias, B.C., 1994. Air-cured banana-fibre-reinforced cement composites. Cem. Concr. Compos. 16, 3–8.

This page intentionally left blank

Toughening mechanisms for glass fiber-reinforced polyamide composites

8

J. Njuguna[1], *Z. Mouti*[2], *K. Westwood*[2]
[1]Robert Gordon University, Aberdeen, UK; [2]Eaton, West Midlands, UK

8.1 Introduction

Polymer composites are increasingly being used in various industrial applications, such as the aerospace, automotive, and chemical industries. This is because these materials provide a high strength/weight ratio in comparison to classic materials. In addition, most classic polymer materials have limited structural applications due to their low mechanical, thermal, and impact-resistance properties. Therefore, reinforcements are often used to improve their properties.

Polyamides (PAs) are the materials of choice for auto parts (see Table 8.1 for examples) because they meet design requirements in terms of mechanical performance, stiffness and strength, chemical resistance, recyclability, and tailorability. Polyamides have been selected due to the balance of physical and chemical properties against cost, hence the cost-effectiveness of end-product components. Injection molding, using mold flow, is well suited for mass production of components with complex geometry.

As the use of thermoplastics in the automotive industry increases, the need to determine their impact responses to ensure safety and stability of designed structures is important. As such, the impact test should be ideally designed to simulate the loading conditions to which the composite component is subjected in operational service and then reproduce the failure modes and mechanisms likely to occur in real conditions. Today, various types of polyamides covering a wide range of properties are commercially available. Polyamide 6 and 66 (PA 6 and PA66) is one of the polyamides grades most widely used in the automotive industry. PA 6 and PA66 are a high-performance engineering thermoplastic used in electrical/electronics, automobile, packaging, textiles, and consumer applications. However, limitations in mechanical properties, the low heat deflection temperature, high water absorption, and dimensional instability of pure PA6 have prevented its wide range of applications in load-bearing applications, such as under-the-hood automotive applications.

Toughening Mechanisms in Composite Materials. http://dx.doi.org/10.1016/B978-1-78242-279-2.00008-1

Table 8.1 Glass fiber-reinforced polyamide grades used for automotive applications

Grades	Features	Processing method	Example of use
PA66-GF30–GF36 (polyamide 66 reinforced with 30–35 wt.% short glass fibres)	Heat stabilized, high stiffness, oil resistant, hydrolysis resistant, good heat-aging resistance, good flow	Injection molding or blow molding	Air inlet manifolds, oil pans, cylinder head covers, solenoid valve housings, cable attachments, electrical insulating parts
PA6-GF30–GF36 (polyamide 6 reinforced with 30–35 wt.% short glass fibres)	Heat stabilized, oil resistant, good heat-aging resistance, good flow	Injection molding	Manifolds, pedals, oil pans, exterior body panels, external door handle, fan

8.2 Manufacturing conditions

8.2.1 Processing by injection molding

Polyamide can be processed by a lot of techniques such as using injection molding, mono and multilayer injection, injection blow molding, rotomolding, extrusion blow molding, mono or multilayer extrusion, thermoforming, thermoretraction, and so on. However, injection molding is the most widely used process to produce automotive parts, such as the oil pan, thanks to its ease of forming complex shapes and fine details with excellent surface finish, good dimensional accuracy for high production rates, and low cost (Murphy, 1998; Platt, 2003). Most reinforced thermoplastics for under-the-hood applications are injection molded in 30–35% short glass fibre reinforced (SGFR) PA or PA66, making parts up to 50% lighter than their metal counterparts and contributing to improved engine efficiency and better emissions (Leaversuch, 2003, 2004).

The process cycle of injection molding consists of four stages: clamping, injection, cooling, and ejection. The cycle begins when the clamping unit closes the mold halves together. The materials, however, have to be predried to an undefined level identified in the material data sheets to remove moisture. Next, the granulated PA66 is melted with chopped glass fibers by heat between 280 and 300 °C (above its melt temperature of 260 °C) and pressure of about 100 bars. The molten plastic is then injected, thanks to a screw mixing at 200–300 mm/s into the mold cavity (mold temperature 80–90 °C). When the mold is filled, a holding pressure is maintained to compensate for the volumetric contraction occurring (shrinkage 0.5%) on solidification and subsequent cooling. After cooling, the part is ejected from the mold (BASF SE, 2011).

It is important to note that the processing of glass fibers in injection-molded composites leads to large reductions in the fiber length as observed by Hassan et al. (2004), Thomason (2002), and Gibson and Payne (1989). Thomason (2009) measured a reduction from the initial 4 mm fibers to less than 0.7 mm caused by the compounding and

molding process. He noted that the increase of fibers concentration above 10 wt% reduces linearly the average length of fibers. He attributed this fact by the increased probability of fiber-to-fiber and fiber-to-machine interaction and an increased apparent melt viscosity, resulting in higher bending forces on fibers during compounding and molding. This can explain why the strength-based properties show a decreasing reinforcing effect as the fiber concentration is increased.

Russell and Beaumont (1980a,b,c) inspected the structure and properties of injection-molded PA66 and recognized a morphology type skin–core. They noticed that the core was composed with spherulites of average diameter of 6 μm. They found that the skin thickness was dependent and affected with the increase in mold temperature. The increase of the mold temperature augments the crystallinity of PA66 in the skin, which increases yield strength but reduces toughness. Apichartpattanasiri et al. (2001) investigated the tribological behavior of PA66 with varying injection molding parameters. By increasing the mold temperature, they obtained different microstructures in the core with increasing average spherulite size. Paterson and White (1992, 1993) examined the effects of absorbed water on residual stresses and distortion on injection-molded PA66. For low water absorption in the normal stress distribution, they found compressive stresses at the surface and tensile stresses in the interior. For high water absorption, water causes increase of crystallization in the skin and therefore relative volume change and residual stresses between skin and core but, however, with increased toughness. Furthermore, they noticed that uneven water absorption creates distortions and changes in residual stresses.

8.2.2 Joint assembly by vibration welding

Sometimes, further processing techniques are required after injection molding. In an oil pan module, the integration of functional parts such as the pick-up oil pipe cover is required. In composite structures, assemblies can be mechanically fastened (bolts, rivets, and pins) (Wong et al., 2005), bonded with adhesive joints (Laura et al., 2003), or welded (Huang et al., 2004).

For mass volume production of automotive parts, welding is the preferred process as it is a robust method to produce cost-effective high strength and pressure tight seals with a joint strength approaching that of the parent material. Welding techniques allow a physical joining of thermoplastics to fabricate complex hollow assemblies from simpler injection-molded semifinished parts. Polyamides can be welded by all the processes normally employed for thermoplastics such as vibration, ultrasonic, laser, hot plate, or infrared welding.

Among all of the welding techniques, vibration welding offers advantages in relation to speed (2–3 s), final appearance, and, most importantly, bond strength even on complex irregular shapes. The vibration welding is based on friction welding, where the heat required to melt the plastic is generated by pressing one part against another and vibrating it through a small relative displacement or amplitude in the plane of the joint. One of the two halves is kept stationary while the other moves. Amplitudes range from 0.7 to 1.8 mm at 240 Hz (high frequency) and 2.0–4.0 mm at 100 Hz (low frequency). When vibrations stop, the parts are aligned and the weld cools down and solidifies. Hatcher (1983) pointed out in their studies that components should be

dry prior to welding since excessive moisture can reduce the strength of the bond. Variable levels of moisture in the material prior to welding cause a change in modulus and will influence the welding especially as it is performed under pressure. Moreover, vibrations and high welding pressure can cause stress and grainy weld flash, and wide seam can be observed as well. However, vibration welding has relatively short cycle times and makes high-strength bonds. Since friction welding is poor for cleanliness, laser welding could be considered for a cleaner welding process that is essential for future engine requirements.

8.2.3 Effect of rubber in toughened polyamides

Semicrystalline engineering thermoplastics such as composite polyamides are pseudoductile (Wu, 1985, 1988), which means that they have a much higher crack initiation resistance than crack propagation resistance due to the fact that they are notch-sensitive materials. In order to improve their toughness and impact strength, especially at low temperature, an elastomeric/rubbery phase is incorporated and dispersed into the matrix (Laura et al., 2003). Under impact loading, the elastomeric regions absorb additional energy and prevent brittle fracture. The role of the rubbery particles is simply to induce yielding processes in the matrix (Pegoretti and Ricco, 2006). In principle, the glass fiber-reinforced rubber-toughened polyamide formed has a good balance of stiffness, strength, and toughness.

Different types of rubbers have been successfully used for thermoplastics toughening, such as styrene ethylene/butylene styrene (SEBS), ethylene propylene diene monomer (EPDM), ethylene propylene rubber (EPR), and styrene butadiene rubber (SBR); however, most rubbers do not show necessary compatibility with polyamides and cannot correctly disperse in rubber (Dermanaki Farahani and Ramazani, 2008; Gaymans et al., 1990; González-Montiel et al., 1995; Wong and Mai, 1999).

Laura et al. (2000) studied the effect of glass fiber and maleated EPR content on tensile and impact properties of PA6. She reported that the incorporation of the rubber into PA6 reduces modulus and yield strength but can be completely reversed by the addition of glass fibers' providing stiffness and strength. The Izod impact energy of the glass fiber-reinforced rubber-toughened PA6 is improved comparatively to the material containing no rubber.

The selection of an elastomer with appropriate mechanical properties is also critical to blend performance. Dermanaki Farahani and Ramazani (2008) investigated the mechanical properties of PA66 and toughened PA66 with 20 wt% SEBS triblock copolymers grafted (g) with different levels of maleic anhydride (MA), PA66/SEBS-g-MA. Impact and tensile tests results showed that 20% rubber-toughened PA66 exhibits significantly more impact strength (15 times) and elongation at break compared to the polyamide alone. Huang et al. (2004) also investigated rubber-toughened PA6 and PA66 with SEBS-g-MA, they found that the ductile-to-brittle temperature transition decreased with increased rubber content and decreased rubber particle size.

Indeed, maleated rubbers are high interest for impact modification, Laura et al. (2003) reported that during melt processing, the MA grafted to the elastomer rapidly reacts with the amine end groups of the polyamide to give graft copolymers that simultaneously improve interfacial adhesion, reduce rubber particle size, and stabilize blend morphology. Huang et al. (2004) reported that the nature of the rubber, the

matrix, the morphology of the dispersed phase (rubber particle size and distribution), and the rubber content as well as the processing conditions play an important role in determining the level of toughening of polyamides.

8.2.4 Influence of fiber length, diameter, and concentration

The mechanical performance of glass fiber-reinforced polyamides results from a combination of the fiber and the matrix interface. The fiber content, diameter, orientation, and the interfacial strength are key factors to the final balance of properties exhibited by injection-molded thermoplastic composites. For instance, Bernasconi and Cosmi (2011) studied the fiber length distribution on PA6 with 10–20–30 wt% of glass fibers and noticed that fibers are shorter (473–354–276 μm) as the fiber content increases presumably because of fiber breaking during the injection molding process. Hassan et al. (2011) also observed the fiber length degradation. From the initial length of 3–6 mm before compounding, they found an average fiber length in the injection-molded part in the range of 0.2–0.4 mm. When compared to long glass fibers, short glass fibers have statistically more total fiber length (56%) and more total fiber surface area (33%), which is an advantage in terms of interfacial bonding to the matrix. However, the tensile strength and modulus of long glass fibers reinforced PA66 are superior (20–30%) to those of short glass-reinforced PA66, meaning that the length of the individual fiber itself is also a determining parameter of the composite properties. On the other hand, the fracture strain of long fiber composite is found 20% lower than the short fiber composite, and that is believed to be due to the existence of longer fiber that restricts the matrix movement. Curtis et al. (1978) also described this reduction of fracture strain associated with a longer fiber and higher fiber volume fraction. In terms of fracture energy and peak load, Hassan et al. (2011) found that they are increased with the increase in fiber volume ratio and fiber length.

The effect of fiber diameter and fiber diameter distribution is also an influencing parameter on the performance of glass-reinforced polyamides. Sato et al. (1998) studied the mechanical properties of injection-molded polyamides with 30 wt% of glass fiber. In the 7–13 μm diameter range, they found that the tensile and flexural strength are low dependent on fiber diameter but below 7 μm, strengths drastically fall. Thomason et al. (2010) reported a study on the 9–18 μm range on glass fiber-reinforced PA66. He found that the unnotched impact and tensile strength decreased significantly, but the tensile modulus presented no dependency over the range. The notched impact varied less but showed a maximum at 14 μm. Over the range studied, the fiber diameter is little significant on fiber orientation. Ramsteiner and Theysohn (1985) investigated the fiber diameter range of 10–24 μm and found significant dependence of unnotched Charpy impact and tensile strength on the fiber diameter but slight effect on tensile modulus and notched Charpy impact.

Thomason (2007a, 2008, 2009) conducted extensive studies on the effect of fiber content (0–40 wt% range) on short glass (4 mm length, diameter 10 μm) reinforced PA66. He noticed that the stiffness and strengths in tension and flexion increase almost linearly with increasing fiber concentration. Tensile modulus evolved from 3 to 12 GPa, tensile strength from 70 to 170 MPa, and flexural strength from 120 to 330 MPa over the full range of fiber content studied. He also noticed that the tensile elongation drops (3.8–2.9%) with increasing

fiber content in the 2–10 wt% range leading to a large reduction in the ductility of the material. From 10 to 30 wt%, the elongation was approximately constant; above 33%, it started to fall again (below 2.8%). Thomason also found that the impact behavior of PA66 is altered by the addition of fibers. On the notched Izod impact, the increase of fiber content has only beneficial effects above 10 wt%. However, it has severe effects on the unnotched Izod impact since the initial performance of the PA66 is very high and did not break. A small concentration of fibers leads to a sharp fall until 4 wt% and then above the impact resistance steadily rises.

8.3 Effect of environmental conditions

8.3.1 Effect of water absorption and hydrolysis aging

Akay (1994) investigated the moisture absorption and its influence on tensile properties of glass fiber-reinforced PA66 and found that the equilibrium amounts of moisture absorbed is proportional to the weight fraction of the polymer but also varies with sample preparation and microstructure. The moisture uptake of the injection-molded composites was found significantly different than those with machined edges. Akay (1994) and Valentin et al. (1987) observed a sharp deterioration of the tensile strength for glass fiber-reinforced PA66 and PA66 at, respectively, 1.5 and 3 wt% moisture contents. Moisture uptake resulted in increased elongation to failure for PA66 but practically no variation in the elongation behavior for the glass fiber-reinforced PA66.

More than a simple moisture diffusion, Camino et al. (1998) witnessed three different mechanisms within the material: the hydrolysis of the macromolecular chains into low molecular weight chains; the hydrophilization with matrices that swell and plasticize; and the interfacial decohesion, inducing a degradation of the composite. Bergeret et al. (2001) studied the stress–strain response of PA66 and found that this relation strongly depended on the humidity conditions. They considered PA66 as dry when the hygrometry is less than 0.2% and saturated at 7.2% and observed that the tensile strength in dry condition in glass fiber-reinforced PA66 is twice higher than when saturated. Thomason et al. (2010) observed the plasticizing effect of water on PA66, and its composites significantly reduce their performance tensile (modulus, respectively, reduced by 80–45% and strength by 45–50%) over a range of 0–40 wt% of glass fibers. The tensile elongation showed a large increase particularly at low fiber content. Thomason also assessed the hydrolysis aging effect after 200, 500, and 1000 h of water–glycol treatment at 120 °C. He found that all conditioned samples behaved similarly and showed a significant low tensile modulus and strength compared with dried samples. However, the 1000 h water–glycol treatment had a slightly higher tensile modulus and lower strength compared to the other conditioned samples. The conditioning causes a high level of plasticization of the polyamide matrix.

Figure 8.1 shows the tensile load versus the extension for materials PA66-GF35 and PA66-i-GF35 (polyamide 66 reinforced with 35 wt.% short glass fibres and toughened with elastomer) when dry as molded and after water uptake. These data are collected directly from the testing machine. PA66-GF35 tensile samples that have been subjected to water uptake have undergone a maximum tensile force of 4.8 kN and extended by 7.2 mm. Compared to PA66-GF35 in dry as molded condition, that is

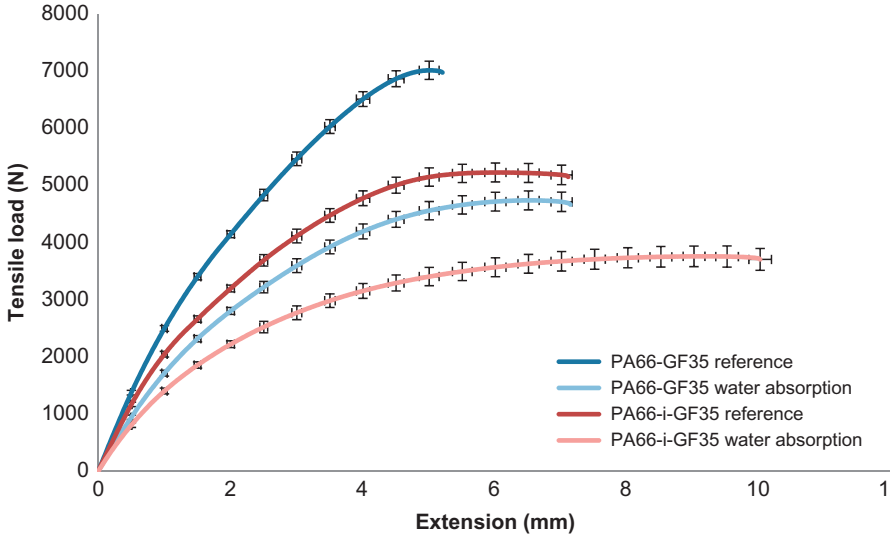

Figure 8.1 Tensile load versus extension up to breaking point in dry as molded and water uptake conditions (with standard deviation).

a loss of 46% of strength but a gain of 38% of extension. PA66-i-GF35 tensile samples that have been subjected to water uptake have undergone a maximum tensile force of 3.8 kN and extended by 10 mm. Compared to PA66-i-GF35 in dry as molded condition, that is a loss of 37% of strength but a gain of 41% of extension. In both materials, PA66-GF35 and PA66-i-GF35, the water uptake affects the strength in tension but increases the elongation. PA66-GF35 seems to be slightly more affected by the water uptake than PA66-i-GF35.

8.3.2 Effect of aqueous salt solutions

Polyamides used in under-the-hood components undergo deterioration in their mechanical properties when exposed to salt splash used on roads to melt ice during the winter (Mouti, 2012; Mouti et al., 2010, 2011).

Kim et al. (2006) and Hong et al. (2007) observed the degradation of PA66 under repeated contact with aqueous calcium chloride/ethylene glycol solutions (aq. $CaCl_2$/EG), which led to stress cracking. Hattori and Saito (1996) and Hattori et al. (1995) characterized PA66 dissolved in a mixture of calcium chloride/methanol ($CaCl_2$/Me) and observed the formation of a complex with PA66.

Wyzgoski and Novak (1987a,b,c) investigated the stress-rupture behavior, polyamide–salt interactions, and craze-growth kinetics in aqueous $CaCl_2$ treated PA66 and proposed a plasticization mechanism for the salt-induced crazing of crystalline PA66. Xiong et al. (2010) examined the complexation mechanism of PA6/$CaCl_2$ and explained the reaction between the amide group and the $CaCl_2$. They proposed that calcium cations coordinate with the oxygen atom of the carbonyl group, which weakens the hydrogen bonding between the molecular chains of PA6 and

releases the free N—H group, so that the N—H group can coordinate with chloride anions to form the hydrogen bonding. They found that there was no complexation between calcium cations and the nitrogen atom.

Dhevi et al. (2009) investigated the deterioration in mechanical properties of PA66 and glass fiber (30 wt%) reinforced PA66 by aqueous $CaCl_2$ mixture solutions. In Xiong et al. (2010) study on PA66, they noticed that aqueous $CaCl_2$ treated PA66 was not significantly degraded, and physical changes involved H-bond breakage and the coordination of calcium cations with the oxygen atom of the carbonyl group of the amide linkage. The absorbed $CaCl_2$ modified the melting and recrystallization of PA66. However, they found that the mechanical properties of aqueous $CaCl_2$ treated glass fiber-reinforced PA66 exhibited pronounced degradation, which they have associated to the interfacial failure between glass fiber and PA66 matrix.

8.3.3 Effect of temperature

The properties of thermoplastics are temperature dependent due to the fact that they are soft when heated and hard when cooled. The increase of temperature reduces the Young's modulus and tensile strength but increases the failure strain leading to a material more ductile and less stiff. Polyamides are recognized to be temperature dependent with the increase of temperature reducing both the Young's modulus and tensile strength but increasing the failure strain leading to a material more ductile and less stiff. Lhymn and Schultz (1987) and Chevali et al. (2010) noted that the temperature could increase the moisture absorption in the material. Eriksson et al. (1997) and Rudzinski et al. (2011) examined the effect of thermal aging on unreinforced and glass-reinforced polyamide (Dray et al., 2007) and reported that thermal aging causes oxidative degradation on the surface region, resulting in a decreased elongation at break and embrittlement of the material.

Mouhmid et al. (2006) studied the mechanical behavior of 0–50 wt% glass fiber-reinforced PA66 and the effect of the temperature on tensile properties. They noted that the tensile behavior was strongly dependent on the temperature. In the range of 20–80 °C studied, the increase of temperature decreases the normalized Young's modulus following a nonlinear relationship whereas the normalized tensile strength also decreases but almost linearly. They also noted that the failure strain increases as the temperature is increased in the range of 5–8% for the reinforced PA66. However, the effect of temperature on the failure strain of the unreinforced PA66 is much more pronounced (12–63%).

Figure 8.2 shows the TG of PA66-i-GF35. The mass of the sample at the start is 5.1 mg. The same comment can be used concerning the increase of mass at the beginning as a sign of oxidation. The material at 221 °C has lost 1% of its original mass. The temperature of degradation is reached at 444.3 °C after having lost, since the beginning, 33% in mass and at 467 °C it has lost 50% of its mass. Over 600 °C, the mass does not seem to stabilize but the rate of mass lost decreases after 68.3%.

De Monte et al. (2010) investigated the influence of temperature on the anisotropic properties of SGFR PA66 under tension–tension and tension–compression cyclic loading (constant load at frequency range 5–10 Hz). They noticed that the temperature

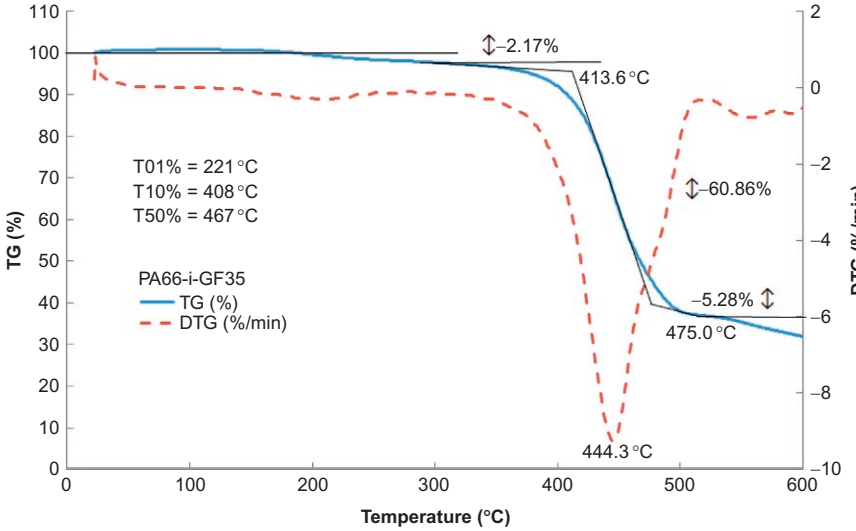

Figure 8.2 TG results of PA66-i-GF35.

affects only the ductility of the matrix and has no effect on the material anisotropy. The temperature strongly reduces the fatigue strength under cyclic loading, especially at about 130 °C. They observed the temperature distribution and discerned local overheating nearby the shoulder area of the specimen. After 6400 cycles at 10 Hz and 90 °C of a 3 mm thick specimen, the temperature differences were up to 20 °C between the central and shoulder area. Temperature shortened fatigue life and failure was of thermal rather than mechanical.

Sonsino and Moosbrugger (2008) also perceived the self-heating phenomenon while investigating fatigue design of highly loaded SGFR PA66. High temperatures reduced the fatigue strength considerably, which diminished fatigue life (80–130 °C). With the increase of temperature, the notch sensitivity of PA66 practically disappeared due to the softening of the material.

Thomason (2006, 2007a,b) assessed the elevated performance of SGFR PA66. He observed that between 0 and 10 wt% of fibers, the deflection temperature under load is raised from 75 to 245 °C. Above 10 wt% of fibers, the temperature slowly increases until it reaches the melting point of PA66 (around 265 °C). They (Thomason, 2006, 2007a,b) also investigated the impact performance of PA66 and glass fiber-reinforced PA66 in the range from −40 to 80 °C. A notched Charpy impact at 80 °C increases the performance of both materials in comparison to room temperature (23 °C) results and particularly for PA66 due to testing above its glass transition temperature (range of 50–75 °C). However, at −40 °C, both materials drop in performance; this is significantly more for PA66. The notched impact resistance of PA66 from 80 to −40 °C reduced by 80% associated to its ductile–brittle transition temperature. This clearly shows that additional energy dissipation mechanisms are activated thanks to the

addition of fibers. The loss in impact resistance across the same temperature range was reduced to only 40% for the SGFR PA66.

8.4 Impact and energy absorption properties

8.4.1 Impact performance of polyamides

In order to comprehend the impact performance of SGFR PA66, initial investigations should determine their mechanical properties over a range of stresses and assess the influence and consequences of environmental conditions. Structure-property should also be investigated using experiments and simulations so as to understand their relationship and as a final point improve material and structure on a component.

The measurement of the impact resistance of thermoplastic composites often depends on the parameters of the test as much as the structure–performance relationships of the material under test. Thomason (2009) estimates that a major discriminating factor is whether the sample under testing has been notched. From a structure–performance point of view, he found that composite impact strength appears to be influenced by all of the same parameters as tensile strength but to different levels. Notched impact data will mostly reflect the energy required to propagate an existing crack through the sample, whereas unnotched impact data will depend on both initiation and propagation energies (Mouti et al., 2011). Results from similar glass in both PP and PA showed that the PPGF matrix provided higher performance levels compared to the PAGF. This was due to the PP bending with the glass and the stiffer PA fracturing due to its low elongation and the glass fiber was pulled out of the PA matrix. Two areas assist the PA coating of the glass to increase the bond strength between glass and PA. A second improvement appears to the addition of the impact modification system that provides an improvement in elongation and therefore allows increased movement with the glass prior to the bond failure.

De Monte et al. (2010) highlighted that the specimen thickness in thermoplastics affected mechanical properties as the thinner the specimen is the higher is the degree of anisotropy. Hassan et al. (2004, 2011) reported wide discrepancies on impact properties of PA6 composites (even if the same polyamide grade was used) while assessing three testing parameters using Charpy and drop weight impact testers. They concluded that impact properties, such as fracture energy, peal load, critical strain energy, and critical stress intensity are largely dependent on the testing conditions such as specimen size/geometry, impactor tip velocity/mass.

As the use of thermoplastics in the automotive industry increases, the need to determine their impact responses to ensure safety and stability of designed structures is important. The impact test fixture should be ideally designed to simulate the loading conditions to which the composite component is subjected in operational service and then reproduce the failure modes and mechanisms likely to occur in real conditions.

Most efforts in understanding the impact performance and failure mechanisms of reinforced thermoplastics were principally concentrated on Charpy and Izod impact testing, and to a lesser extent, drop weight tower impact testing. These tests can yield information on the processes of energy absorption and dissipation within composites. Charpy and Izod

are usually destructive and therefore induce failure modes that are not necessarily observed under real conditions on operational structures. They force the specimen to fail at a predetermined area rather than along the weakest plane. The results can be skewed because of the highly anisotropic nature of reinforced thermoplastics. Consequently, these tests are only suitable for comparing impact resistance of composite materials.

A more representative test to simulate the effect of stones would be in the low velocity range with a blunt tip impactor or projectile. This can be achieved with a gas gun or to a certain extent with a low velocity drop weight tower. In a low velocity drop weight tower, the impact energy and velocity can be varied by changing the mass and height of the dropping weight to where the impactor is attached. The low velocity gas gun impact test gives a more representative test of a stone impact scenario and can be used to test large structures in different angles. It is a single-stage high-performance projector using compressed air to propel projectiles with various profiles and masses. These tests are not necessarily destructive but can often results in large-scale damage.

8.4.2 Impact failure mechanism and capability of energy absorption

In composite materials, fracture behavior is a complex mechanism. The mechanical properties of thermoplastic composites result from a combination of the fiber and matrix properties and the ability to transfer stresses across the fiber/matrix interface. Key factors such as interfacial adhesion, fiber length to diameter ratio and concentration, matrix ductility, and residual matrix stresses due to differences in thermal expansion between fibers and matrix during processing determine the composite fracture mechanisms. Therefore, all of these parameters influence the load-bearing capacity of the finished product.

In impact testing, Hassan et al. (2011) noticed that longer fibers tend to break in more brittle manner by fiber breakage mechanism and contribute less fracture energy to the composite compared to shorter fibers that tend to break in more ductile manner by fiber pull-out mechanism and contribute more fracture energy to the composite. Many studies in short fiber-reinforced composites agreed that fibers act both to initiate cracks and to inhibit crack propagation. On one hand, fiber discontinuities can be considered as structural flaws that initiate cracks, but on the other hand since cracks must often travel around fibers in the crack path, fibers act to inhibit crack propagation by increasing the volume in which energy dissipation can take place.

As previously found, composites with small diameter fibers have a large interfacial area between matrix and reinforcement. Since fibers are generally high in modulus and the matrix is low, the interfacial region is subjected to high stresses during composite deformation. Blumentritt et al. (1975) investigated and described fracture mechanisms in short fiber-reinforced thermoplastics. They noticed that if fracture occurs at the interface, fibers are pulled out of the matrix with little or no matrix material adhering and very few fibers are found fractured. Matrix failure also results in fibers pull-out, but they will be coated with the matrix material. If the matrix and interfacial strengths are high, fiber fracture becomes the predominant failure mode and only fibers with ends near the fracture surface are pulled out during fracture.

Since fibers are generally strong but brittle, and matrices are weak but tough, fiber fractures are found in high-strength composites with low toughness, and conversely fiber pull-out are found in tough composites with low strength. As a composite material, the macroscopic behavior of injection-molded SGFR thermoplastic results from interactions between the highly nonlinear thermoplastic matrix and elastic short fibers.

To simulate the macroscopic mechanical response, some authors proposed a micromodeling method to describe the fiber orientation but encounter complications to describe the overall mechanical behavior. However, Dray et al. (2007) and Vincent et al. (1997) observed in their approach the anisotropic distribution with fibers parallel to the injection flow in the composite skin and perpendicular in the composite core.

To overcome the complexity of fibers distribution, several other authors proposed to homogenize the mechanical behavior of the matrix and short fibers; Doghri and Friebel (2005), Doghri and Tinel (2005), and Mlekusch (1999) studied elasto-plastic materials; Pierard and Doghri (2006) looked into elasto-visco-plastic composites. These approaches can handle complex interactions between fibers and matrix such as damage, interfacial debonding, and so on. However, they require much data to be efficiently used.

Zhou and Mallick (2005) described a nonlinear elasto-plastic model based on the stress–strain relationship for the tensile behavior of PA66 with 33 wt% of glass fibers using the tensile modulus and a Weibull continuous probability distribution with a Weibull shape parameter, and a Weibull scale parameter as a linear logarithm function of strain rate. In the range of 0.05–5 mm/min, they noticed that the failure strain was not affected by the strain rate but only the tensile modulus and tensile strength.

Lobo et al. (2006) also proposed a stress–strain relationship to describe the nonlinear behavior and tried to implement it into LS-DYNA using MAT24 for modeling crash and drop impacts. Despite the fact that thermoplastics do not exhibit a clear yield transition, he decomposed the stress–strain curve between an initial linearity up to a chosen yield point and beyond the stress–strain curve is described as an effective stress–plastic strain curve up to the failure strain. However, the accuracy of the model on the stiffness depends on the choice of the modulus.

8.5 Polyamide clay/nanocomposites

The concept of nanostructured materials design is becoming more important in the automotive industry (Njuguna, 2013). Although the use of nanotechnology in current and future automotives will aid in solving environmental crises either directly or indirectly, it is necessary to understand both the hazards associated with nanomaterials and the levels of exposure that are likely to occur. The existing knowledge in these areas is quite limited and is required in the near future. The key issues associated with the use of nanomaterials in the automotive industry, including opportunities and environmental health challenges, have been reported in the literature (Njuguna, 2013; Njuguna et al., 2010, 2014).

Polyamide clay nanocomposites: In the early 1990s, Toyota Research group synthesized polyamide-6-based clay nanocomposites that demonstrated the first use of nanoclays as reinforcement of polymer systems (Kojima et al., 1993a,b). The most recent key research activities in polyamides nanofillers reinforcement are reported in literature

(Silva et al., 2012, 2013; Sachse et al., 2012). Introduction of nanoparticles into a polymer causes physical or chemical crosslinking and thus an additional bonding forces and residual crystallinity must be surmounted by thermal energy over the melting temperature. Typical clays used in polymer-based nanocomposites have a twofold catalytic effect on the thermal degradation of organic molecules in close contact with the clay layers (organic modifier). Carbon–carbon bond scission is accelerated by the clay while increasing the temperature in inert atmosphere (thermal degradation) which comes in competition with acceleration of carbon–hydrogen bond scission in the presence of oxygen (thermal oxidation) (Njuguna et al., 2008, 2011; Njuguna and Pielichowski, 2003).

As an example of how significant improvements in modulus are achievable in both the dry and the moisture conditioned state for PA6 nanocomposites compared to standard PA6, at any given level of glass fiber reinforcement. In particular, a small amount (3–4 wt%) of nanometer scale dispersed layered silicate are capable of replacing up to 40 wt% of a standard mineral filler or 10–15 wt% of glass fiber to give equivalent stiffness at a lower density (Akkapeddi, 2000). In addition, improved moisture resistance, permeation barrier, and fast crystallization/mold cycle time contribute to the usefulness of such composites (Vlasveld et al., 2005a,b). Additionally, a cheap low molecular weight (MW) nanocomposite can replace a high MW unfilled polyamide. The other advantage of the use of polymer nanocomposites compared to the use of different polymers is to improve the high temperature behavior of fiber composites and therefore the properties can be improved without any change in the melting temperature and processing conditions. When tailored effectively, polymers such as PA can be used as matrix material at temperatures up to 50 °C higher at the same composite strength without changes in the impregnation and forming temperature. Therefore, there is sufficient evidence that both improved PAs may be expected to enhance the matrix-dominated composite properties (Figure 8.3) such as compressive and

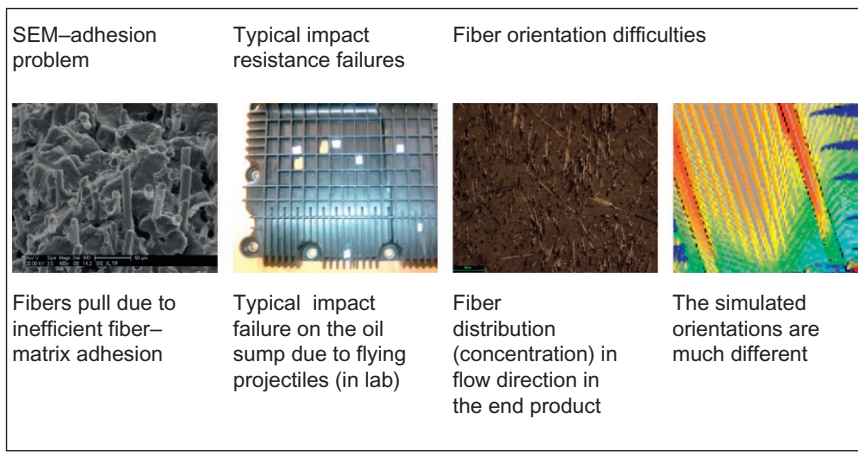

Figure 8.3 Illustration of typical material performance deficiencies (in the final product). Typical impact failure on the oil sump due to flying projectiles (in lab), fiber distribution (concentration) in flow direction in the end product, and the simulated orientations are much different.

flexural strength and impact resistance provided that a strong fiber-to-matrix interphase is obtained (Silva et al., 2014).

Figure 8.3 Illustration of typical material performance deficiencies (in the final product). Typical impact failure on the oil sump due to flying projectiles (in lab), fibers distribution (concentration) in flow direction in the end product, the simulated orientations are much different.

8.6 Applications in the automotive industry

There is a trend in the automotive industry toward more use of composite materials over metals. The automotive sector is the biggest market for polyamides. Early applications included gears, windshield wiper components, wiring clips, bearings, and switch housings. Table 8.1 shows the main automotive applications of glass fiber-reinforced polyamides. With the introduction of glass fiber-reinforced polyamides, main applications are now under-the-hood applications, such as the air intake manifold, the air and cooling systems, the throttle body housing, the cylinder head cover, the acoustic cover, the oil pump, and the oil pan and mounting elements for the air duct cover on an oil pan. Table 8.2 presents some examples of composite polyamides under-the-hood components and their principal characteristics and advantages (BASF SE, 2011; Mouti, 2012; Leaversuch, 2004; Mouti et al., 2012).

PA66 and PA6 account for most automotive applications of polyamides. The balance between PA66 and PA6 varies with the application. In under-the-hood uses, PA66 accounts for almost 80% (Helps, 2001; Drake, 1998; Platt, 2003). New components made of thermoplastics are still finding applications in under-the-hood. The substitution of metals to thermoplastics allows new design of very complex parts consisting of assemblies of many components that could not be designed using metals. The weight saving by

Table 8.2 PA6 and PA66 usage for under-the-hood applications

Under-the-hood products	PA grades	GF content (%)	Characteristics over counterparts
Engine covers	PA6	20–30	Surface finish, heat resistance, stiffness, low warpage
Air intake manifolds	PA6 PA66	30–35	Up to −30% cost production/metals, up to −50% weight/metals, parts integration
Rocker covers	PA6 PA66	30–35	Weight reduction and flexibility of design over aluminum and thermosets
Heating and cooling systems	PA66	30–35	Heat stability, high stiffness, low warpage, corrosion resistance, weight reduction over metals
Oil pan reservoir	PA6 PA66	30–35 >35	Weight and cost savings over metals, noise reduction, increased capacity, enables additional module content

Table 8.3 Properties of commercial polyamide materials for oil pan

Properties (dry)	Supplier 1 PA66-GF35	Supplier 2 PA66-GF35	Supplier 3 PA66-GF35	Supplier 2 PA6-GF60	Supplier 3 PA6-GF35
Tensile modulus (GPa)	11	10.6	11.2	18.9	10
Stress at break (MPa)	210	200	200	235	170
Strain at break (%)	3	3.1	3	2.1	3.5
Charpy impact strength +23/−30 °C (kJ/m^2)	80/80	80/70	95/75	90/90	102/113
Charpy notched impact strength +23/−30 °C (kJ/m^2)	15/10	12/10	13/12	−/−	26/18
Melting temperature (10 °C/min) (°C)	260	263	260	–	220
Water absorption (%)	5.5	5	5	5	–
Humidity absorption (%)	1.7	1.7	1.6	1.5	1.1
Density (kg/m^3)	1410	1410	1410	1570	1360

integrating several functional components in one plastic part is the driving force for a further substitution of traditional materials by thermoplastics (Leaversuch, 2004; Drake, 1998). Tables 8.3 and 8.4 present some properties of commercial polyamide materials and illustrate that within the same polyamide polymer and glass fiber content the properties differ depending on each material brand (BASF SE, 2011; Mouti, 2012; Leaversuch, 2004; BASF SE, Personal communication) and lessons learned.

Table 8.4 Summary of findings and lessons learned from previous investigations and development activities

Materials	Component	Problems to addressed	Typical solutions achieved
Polyamide	Radiator (on the market now)	Complex geometry Engine temperatures exposure (up to 160 °C)	Overcame difficulties in handling complex geometries though appropriate training, design, and usage of modeling tools Chemical additives used to improve thermal properties Thermal aging testing to optimum acceptable performance

Continued

Table 8.4 Continued

Materials	Component	Problems to addressed	Typical solutions achieved
Polyamide	Rocker arm cover (industrial vehicles—tractors, factory machinery) (on the market now)	Vibrations leading to cracks on bolt attachments to crankcase Weld lines leading to cracks Moisture uptake	Innovative solution through use of bolt, spring, double bushings combination, allowed vibration reduction at bolt assembly protecting the plastic–metal interaction/attachment points Refinement of mold flow mixture improved the weld line Use of appropriate chemical additives; though the part is not subjected to water, moisture uptake is identified due to PA oil exposure and mechanical properties effects
Polyamide	Transmissions sump and radiator tanks (cars) + oil sumps for tractors (both on the market now)	Large size + challenging manufacturing difficulties Complex shape and size of the models Impact on the sump Wrapping effect	Appropriate molds developed and samples manufactured Shape optimization performed Stiffness and strength not an issue—toughness is due to possible large (above 5 cm diameter) low velocity impact. Rigorous testing and material properties improvement for impact resistance Oil flow and position change in the component studies conducted. Chemical additives + improved geometrical designs utilized
Polyamide	Automotive—road cars and vans (on the market autumn 2009)	Determination of damage tolerances due to impact on component Airflow effects—aero drag and heat flow under engine Weld lines Engines mounting directions in the car	Equipment designed, built, and commissioned for sump impact from small projectiles (road debris) at high velocity (up to 100 m/s) and possible low velocity impact during engine transportation and installation and accidental drops Ribs added on the sump to add cushioning on impact Road testing (above 20,000 miles) on individual components at extreme conditions Ribs added, redesigned, and optimized for impact resistance and to assist in heat and air flow under the sump A streamlined design is developed Reduction of number of feed "gates" to one reduces weld lines, hence fewer cracks in propagation routes Added functionalities—a reversible sump developed such that one sump can be mounted on either engine

8.7 Conclusions

Glass fibers characteristics associated with the matrix have a significant influence on properties of the final material. The addition of glass fiber in the matrix causes a loss of ductility and a greater stiffness. Therefore, tensile strength and modulus are augmented and failure strain is reduced. Long fibers have superior mechanical properties over short fibers but break in a brittle manner. Short fibers have more interfacial bonding with the matrix and allow more ductility in the material. Fibers are crack initiators in the composite but at the same time inhibit its propagation by increasing the volume in which energy dissipation can take place. With fibers content above 10 wt% the elongation is improved constantly up to 30–40 wt%. Fiber diameter is found less significant than fiber length and fiber concentration. Composite materials in automotive industry are predominantly processed by injection molding. However, the injection molding process significantly reduces fiber length (up to 80%). Injection molding creates skin–core morphology, with fibers in the skin following the direction of the injection flow and agglomerate of spherulites in the core. Stresses are found in the skin–core morphology. Water uptake can amplify residual stresses and distortion in the structure. The temperature of the mold is also an important parameter determining the skin thickness and the crystallinity of the matrix.

Impact performance varies with specimen configurations and impact test methods. Specimen thickness in thermoplastics affects mechanical properties responses. The thinner, the higher is the degree of anisotropy. There are discrepancies on composite impact properties that largely depend on testing conditions. Notched impact data reflects the energy required to propagate an existing crack, whereas unnotched impact data depends on both initiation and propagation energies. Polyamides are notch-sensitive materials. Incorporating and dispersing an elastomeric/rubbery phase into the matrix can improve their toughness and impact strength. The rubber improves the elongation at break and impact resistance especially at low temperature. Indeed, the increase of rubber decreases the ductile-to-brittle temperature transition. However, the addition of rubber reduces tensile modulus and yield strength. Water and aqueous salt uptakes are significant affecting parameters with deterioration of strength and reduction of impact performance. Water plasticizes the matrix resulting in an increased elongation to failure. Aqueous salt can cause stress cracking and interfacial failure. The temperature is also a very significant parameter with the increase of temperature leading to more ductility and less stiffness. Thermal aging can cause oxidative degradation, resulting in a decreased elongation at break and embrittlement of the material. Impact simulation depends on the scale investigated, the structure, and the type of solicitation. At macroscopic scale, short glass fibers and polyamide matrix can be approximated as the behavior of a single material. Impact simulation of composite material can be performed if the model comprehends the nonlinear behavior of the matrix associated with the elastic behavior of the fibers. Finally, identical commercial materials (matrix and fiber content) were found with different mechanical properties meaning that manufacturing processing parameters and materials compositions are different.

References

Akay, M., 1994. Moisture absorption and its influence on the tensile properties of glass-fibre reinforced polyamide 6,6. Polym. Polym. Compos. 2 (6), 349–354.

Akkapeddi, M.K., 2000. Glass fiber reinforced polyamide-6 nanocomposites. Polym. Compos. 21 (4), 576–585.

Apichartpattanasiri, S., Hay, J.N., Kukureka, S.N., 2001. A study of the tribological behaviour of polyamide 66 with varying injection-moulding parameters. Wear 251 (1–12), 1557–1566.

BASF SE, 2011. Processing by injection molding. Available at: http://worldaccount.basf.com/wa/plasticsAP~en_GB/portal/show/common/content/products/engineering_plastics/ultramid/processing_by_injection_molding (accessed 30.04.15).

Bergeret, A., Pires, I., Foulc, M.P., Abadie, B., Ferry, L., Crespy, A., 2001. The hygrothermal behaviour of glass-fibre-reinforced thermoplastic composites: a prediction of the composite lifetime. Polym. Test. 20 (7), 753–763.

Bernasconi, A., Cosmi, F., 2011. Analysis of the dependence of the tensile behaviour of a short fibre reinforced polyamide upon fibre volume fraction, length and orientation. Procedia Eng. 10, 2129–2134.

Blumentritt, B.F., Vu, B.T., Cooper, S.L., 1975. Fracture in oriented short fibre-reinforced thermoplastics. Composites 6 (3), 105–114.

Camino, G., Polishchuk, A.Y., Luda, M.P., Revellino, M., Blancon, R., Martinez-Vega, J.J., 1998. Water ageing of SMC composite materials: a tool for material characterisation. Polym. Degrad. Stab. 61 (1), 53–63.

Chevali, V.S., Dean, D.R., Janowski, G.M., 2010. Effect of environmental weathering on flexural creep behavior of long fiber-reinforced thermoplastic composites. Polym. Degrad. Stab. 95 (12), 2628–2640.

Curtis, P.T., Bader, M.G., Bailey, J.E., 1978. The stiffness and strength of a polyamide thermoplastic reinforced with glass and carbon fibres. J. Mater. Sci. 13 (2), 377–390.

De Monte, M., Moosbrugger, E., Quaresimin, M., 2010. Influence of temperature and thickness on the off-axis behaviour of short glass fibre reinforced polyamide 6.6—cyclic loading. Compos. A: Appl. Sci. Manuf. 41 (10), 1368–1379.

Dermanaki Farahani, R., Ramazani, S.A., 2008. Melt preparation and investigation of properties of toughened polyamide 66 with SEBS-g-MA and their nanocomposites. Mater. Design 29 (1), 105–111.

Dhevi, D.M., Choi, C.W., Prabu, A.A., Kim, K.J., 2009. Deterioration in mechanical properties of glass fiber-reinforced nylon 6,6 composites by aqueous calcium chloride mixture solutions. Polym. Compos. 30 (4), 481–489.

Dijkstra, K., Wevers, H.H., Gaymans, R.J., 1994. Nylon-6/rubber blends: 7. Temperature–time effects in the impact behaviour of nylon/rubber blends. Polymer 35 (2), 323–331.

Doghri, I., Friebel, C., 2005. Effective elasto-plastic properties of inclusion-reinforced composites. Study of shape, orientation and cyclic response. Mech. Mater. 37 (1), 45–68.

Doghri, I., Tinel, L., 2005. Micromechanical modeling and computation of elasto-plastic materials reinforced with distributed-orientation fibers. Int. J. Plast. 21 (10), 1919–1940.

Drake, N. (Ed.), 1998. Thermoplastics and Thermoplastic Composites in the Automotive Industry 1997–2000. Rapra Technology Limited, Shawbury, Shrewsbury Shropshire, UK.

Dray, D., Gilormini, P., Régnier, G., 2007. Comparison of several closure approximations for evaluating the thermoelastic properties of an injection molded short-fiber composite. Compos. Sci. Technol. 67 (7–8), 1601–1610.

Eriksson, P., Boydell, P., Eriksson, K., Månson, J.-E., Albertsson, A.-C., 1997. Effect of thermal-oxidative aging on mechanical, chemical, and thermal properties of recycled polyamide 66. J. Appl. Polym. Sci. 65 (8), 1619–1630.

Estes, A.C., Frangopol, D.M., 1998. RELSYS: a computer program for structural system reliability analysis. Struct. Eng. Mech. 6 (8), 901–919.

Gaymans, R.J., Borggreve, R.J.M., Oostenbrink, A.J., 1990. Toughening behavior of polyamide-rubber blends. Makromol. Chem. Macromol. Symp. 38 (1), 125–136.

Gibson, A.G., Payne, D.J., 1989. Flexural and impact strength improvement in injection moulded SMC. Composites 20 (2), 151–158.

González-Montiel, A., Keskkula, H., Paul, D.R., 1995. Impact-modified nylon 6/polypropylene blends: 2. Effect of reactive functionality on morphology and mechanical properties. Polymer 36 (24), 4605–4620.

Hassan, A., Yahya, R., Yahaya, A.H., Tahir, A.R.M., Hornsby, P.R., 2004. Tensile, impact and fiber length properties of injection-molded short and long glass fiber-reinforced polyamide 6,6 composites. J. Reinf. Plast. Compos. 23 (9), 969–986.

Hassan, A., Hassan, A.A., Mohd Rafiq, M.I., 2011. Impact properties of injection molded glass fiber/polyamide-6 composites: effect of testing parameters. J. Reinf. Plast. Compos. 30 (10), 889–898.

Hatcher, W.J., 1983. Vibration welding of automotive thermoplastic box beam bumpers. In: Anonymous National Technical Conference—Society of Plastics Engineers, pp. 133–134.

Hattori, M., Saito, M., 1996. Thermal gelation of the nylon 6,6-calcium chloride-methanol system. Polym. J. 28, 139–144.

Hattori, M., Saito, M., Okajima, K., Kamide, K., 1995. Molecular characterization of nylon 6,6 and its dissolved state in mixture of calcium chloride and methanol. Polym. J. 27 (6), 631–644.

Helps, I.G. (Ed.), 2001. Plastics in European Cars 2000–2008Rapra Technology Limited, Shawbury, Shrewsbury Shropshire, UK.

Hong, J.H., Dhevi, D.M., Lee, J.S., Kim, K.J., 2007. Origin of deterioration in mechanical properties of glass fiber reinforced nylon 6,6 composites by aqueous ethylene glycol solution. Polym. Compos. 28 (6), 778–784.

Huang, J.J., Keskkula, H., Paul, D.R., 2004. Rubber toughening of an amorphous polyamide by functionalized SEBS copolymers: morphology and Izod impact behavior. Polymer 45 (12), 4203–4215.

Kim, K.J., Dhevi, D.M., Lee, J.S., Cho, Y.D., Choe, E.K., 2006. Mechanism of glycolysis of nylon 6,6 and its model compound by ethylene glycol. Polym. Degrad. Stab. 91 (7), 1545–1555.

Kojima, Y., Usuki, A., Kawasumi, M., Okada, A., Kurauchi, T., Kamigaito, O., 1993a. Synthesis of nylon 6-clay hybrid by montmorillonite intercalated with ε-caprolactam. J. Polym. Sci. A Polym. Chem. 31 (4), 983–986.

Kojima, Y., Usuki, A., Kawasumi, M., Okada, A., Kurauchi, T., Kamigaito, O., 1993b. Sorption of water in nylon 6-clay hybrid. J. Appl. Polym. Sci. 49 (7), 1259–1264.

Lau, K.T., Chan, W.L., Shi, S.Q., Zhou, L.M., 2002. Interfacial bonding behaviour of embedded SMA wire in smart composites: micro-scale observation. Mater. Des. 23, 265–270.

Laura, D.M., Keskkula, H., Barlow, J.W., Paul, D.R., 2000. Effect of glass fiber and maleated ethylene–propylene rubber content on tensile and impact properties of Nylon 6. Polymer 41 (19), 7165–7174.

Laura, D.M., Keskkula, H., Barlow, J.W., Paul, D.R., 2003. Effect of rubber particle size and rubber type on the mechanical properties of glass fiber reinforced, rubber-toughened nylon 6. Polymer 44 (11), 3347–3361.

Leaversuch, R.D., 2003. Strength and beauty – new nylons bring both to under-hood parts. Plast. Technol. [Online], January 2003. Available at: http://www.ptonline.com/articles/strength-and-beauty-new-nylons-bring-both-to-under-hood-parts (accessed 30.04.15).

Leaversuch, R.D., 2004. Metal replacement accelerates in under-hood parts. Plast. Technol. March 2004. See http://www.ptonline.com/articles/metal-replacement-accelerates-in-under-hood-parts (accessed 30.04.15).

Lee, J.J., Choi, S., 1999. Thermal buckling and postbuckling analysis of a laminated composite beam with embedded SMA actuators. Compos. Struct. 47, 695–703.

Lhymn, C., Schultz, J.M., 1987. Strength and toughness of fibre-reinforced thermoplastics: effect of temperature and loading rate. Composites 18 (4), 287–292.

Lobo, H., Hurtado, J., 2006. Characterization and modeling of nonlinear behavior of plastics. In: ABAQUS User Conference, Boston.

Mlekusch, B., 1999. Thermoelastic properties of short-fibre-reinforced thermoplastics. Compos. Sci. Technol. 59 (6), 911–923.

Mouhmid, B., Imad, A., Benseddiq, N., Benmedakhène, S., Maazouz, A., 2006. A study of the mechanical behaviour of a glass fibre reinforced polyamide 6,6: experimental investigation. Polym. Test. 25 (4), 544–552.

Mouti, Z., 2012. Localised low velocity impact performance of short glass fibre reinforced polyamide 66 oil pans. PhD thesis, Cranfield University, UK.

Mouti, Z., Westwood, K., Kayvantash, K., Njuguna, J., 2010. Low velocity impact behavior of glass filled fiber-reinforced thermoplastic engine components. Materials 3 (4), 2463–2473.

Mouti, Z., Westwood, K., Long, D., Njuguna, J., 2011. Finite element analysis of localised impact loading on short glass fibre-reinforced polyamide engine oil pan subjected to low velocity impact from flying projectiles. In: 8th European LS-DYNA Users Conference, Strasbourg, May 2011.

Mouti, Z., Westwood, K., Long, D., Njuguna, J., 2012. Finite element analysis of glass fiber-reinforced polyamide engine oil pan subjected to localized low velocity impact from flying projectiles. Steel Res. Int. 83 (10), 957–963.

Murphy, J. (Ed.). 1998. The Reinforced Plastics Handbook, second ed. Elsevier Advanced Technology.

Newnham, R.E., Bowen, L.J., Klicker, K.A., Cross, L.E., 1980. Composite piezoelectric transducers. Mater. Eng. 2, 93–106.

Newsom, J.R., 1979. Control law synthesis for active flutter suppression using optimal control theory. J. Guid. Control. Dyn. 2, 388–394.

Njuguna, J., 2013. Structural Nanocomposites: Perspectives for Future Applications. Springer, Berlin, Heidelberg.

Njuguna, J., Pielichowski, K., 2003. Polymer nanocomposites for aerospace applications: properties. Adv. Eng. Mater. 5 (11), 769–778.

Njuguna, J., Pielichowski, K., Desai, S., 2008. Nanofiller-reinforced polymer nanocomposites. Polym. Adv. Technol. 19 (8), 947–959.

Njuguna, J., Pena, I., Zhu, H., Rocks, S.A., Blazquez, M., Desai, S.A., 2010. Opportunities and environmental health challenges facing integration of polymer nanocomposites technologies for automotive applications. Int. J. Polym. Technol. 2, 117–126.

Njuguna, J., Silva, F., Sachse, S., 2011. Nanocomposites for vehicle structural applications. In: Lin, T. (Ed.), Nanofibers—Production, Properties and Functional Applications. InTech, Rijeka, pp. 401–434.

Njuguna, J., Pielichowski, K., Zhu, H., 2014. Health and Environmental Safety of Nanomaterials: Polymer Nancomposites and Other Materials Containing Nanoparticles. Elsevier, United Kingdom.

Paterson, M.W.A., White, J.R., 1992. Effect of water absorption on residual stresses in injection-moulded nylon 6,6. J. Mater. Sci. 27 (22), 6229–6240.

Paterson, M.W.A., White, J.R., 1993. Distortion of nylon 6,6 moldings caused by asymmetric water absorption. Polym. Eng. Sci. 33 (22), 1475–1482.

Pegoretti, A., Ricco, T., 2006. On the essential work of fracture of neat and rubber toughened polyamide-66. Eng. Fract. Mech. 73 (16), 2486–2502.

Pierard, O., Doghri, I., 2006. An enhanced affine formulation and the corresponding numerical algorithms for the mean-field homogenization of elasto-viscoplastic composites. Int. J. Plast. 22 (1), 131–157.

Platt, D. (Ed.), 2003. Engineering and High Performance Plastics. Rapra Technology Limited, Shawbury, Shrewsbury Shropshire, UK.

Ramsteiner, F., Theysohn, R., 1985. The influence of fibre diameter on the tensile behaviour of short-glass-fibre reinforced polymers. Compos. Sci. Technol. 24 (3), 231–240.

Rudzinski, S., Häussler, L., Harnisch, C., Mäder, E., Heinrich, G., 2011. Glass fibre reinforced polyamide composites: thermal behaviour of sizings. Compos. A: Appl. Sci. Manuf. 42 (2), 157–164.

Russell, D.P., Beaumont, P.W.R., 1980a. Structure and properties of injection-moulded nylon-6. Part 1. Structure and morphology of nylon-6. J. Mater. Sci. 15 (1), 197–207.

Russell, D.P., Beaumont, P.W.R., 1980b. Structure and properties of injection-moulded nylon-6. Part 2. Residual stresses in injection-moulded nylon-6. J. Mater. Sci. 15 (1), 208–215.

Russell, D.P., Beaumont, P.W.R., 1980c. Structure and properties of injection-moulded nylon-6. Part 3. Yield and fracture of injection-moulded nylon 6. J. Mater. Sci. 15 (1), 216–221.

Sachse, S., Silva, F., Irfan, A., Zhu, H., Pielichowski, K., Leszczynska, A., et al., 2012. Physical characteristics of nanoparticles emitted during drilling of silica based polyamide 6 nanocomposites. In: IOP Conference Series: Materials Science and Engineering. IOP Publishing, Bristol, p. 012012.

Sato, N., Kurauchi, T., Sato, S., Kamigaito, O., 1998. Reinforcing mechanism by small diameter fiber in short fiber composite. Composites 22, 850–873.

Silva, F., Sachse, S., Njuguna, J., 2012. Mechanical properties and impact-energy absorption of injection moulded nanocomposite structures. In: Anonymous 15th European Conference on Composite Materials (ECCM15), Venice, 24–28 June.

Silva, F., Njuguna, J., Sachse, S., Pielichowski, K., Leszczynska, A., Giacomelli, M., 2013. The influence of multiscale fillers reinforcement into impact resistance and energy absorption properties of polyamide 6 and polypropylene nanocomposite structures. Mater. Des. 50, 244–252.

Silva, F., Sachse, S., Zhu, H., Pielichowski, K., Leszczyńska, A., Njuguna, J., 2014. The effect of matrix and reinforcement material selection on the tensile properties of hybrid composites. J. Sust. Mobility 1 (1), 37–52.

Sonsino, C.M., Moosbrugger, E., 2008. Fatigue design of highly loaded short-glass-fibre reinforced polyamide parts in engine compartments. Int. J. Fatigue 30 (7), 1279–1288.

Thomason, J.L., 2002. The influence of fibre length and concentration on the properties of glass fibre-reinforced polypropylene: 5. Injection moulded long and short fibre PP. Compos. Part A: Appl. Sci. Manuf. 33, 1641–1652.

Thomason, J.L., 2006. Structure–property relationships in glass-reinforced polyamide, part 1: the effects of fiber content. Polym. Compos. 27 (5), 552–562.

Thomason, J.L., 2007a. Structure–property relationships in glass reinforced polyamide, part 2: the effects of average fiber diameter and diameter distribution. Polym. Compos. 28 (3), 331–343.

Thomason, J.L., 2007b. Structure–property relationships in glass-reinforced polyamide, part 3: effects of hydrolysis ageing on the dimensional stability and performance of short glass-fiber-reinforced polyamide 66. Polym. Compos. 28 (3), 344–354.
Thomason, J.L., 2008. The influence of fibre length, diameter and concentration on the modulus of glass fibre reinforced polyamide 6,6. Compos. A: Appl. Sci. Manuf. 39 (11), 1732–1738.
Thomason, J.L., 2009. The influence of fibre length, diameter and concentration on the impact performance of long glass-fibre reinforced polyamide 6,6. Compos. A: Appl. Sci. Manuf. 40 (2), 114–124.
Thomason, J.L., Ali, J.Z., Anderson, J., 2010. The thermo-mechanical performance of glass-fibre reinforced polyamide 66 during glycol–water hydrolysis conditioning. Compos. A: Appl. Sci. Manuf. 41 (7), 820–826.
Valentin, D., Paray, F., Guetta, B., 1987. The hygrothermal behaviour of glass fibre reinforced PA66 composites: a study of the effect of water absorption on their mechanical properties. J. Mater. Sci. 22 (1), 46–56.
Vincent, M., Devilers, E., Agassant, J., 1997. Fibre orientation calculation in injection moulding of reinforced thermoplastics. J. Non-Newtonian Fluid Mech. 73 (3), 317–326.
Vlasveld, D.P.N., Bersee, H.E.N., Picken, S.J., 2005a. Nanocomposite matrix for increased fibre composite strength. Polymer 46 (23), 10269–10278.
Vlasveld, D.P.N., Parlevliet, P.P., Bersee, H.E.N., Picken, S.J., 2005b. Fibre-matrix adhesion in glass-fibre reinforced polyamide-6 silicate nanocomposites. Compos. A: Appl. Sci. Manuf. 36 (1), 1–11.
Wong, S., Mai, Y., 1999. Essential fracture work of short fiber reinforced polymer blends. Polym. Eng. Sci. 39 (2), 356–364.
Wong, Y.M., Kang, W.P., Davidson, J.L., Choi, B.K., Kerns, D.V., Huang, J.H., 2005. Design and fabrication of single-chip carbon nanotubes vacuum field emission differential amplifier. In: Anonymous Technical Digest of the 18th International Vacuum Nanoelectronics Conference, IVNC 2005, Jul 10–14, 2005, Oxford, United Kingdom. Institute of Electrical and Electronics Engineers Computer Society, Piscataway, NJ, pp. 35–36.
Wu, S., 1985. Phase structure and adhesion in polymer blends: a criterion for rubber toughening. Polymer 26 (12), 1855–1863.
Wu, S., 1988. Generalized criterion for rubber toughening: the critical matrix ligament thickness. J. Appl. Polym. Sci. 35 (2), 549–561.
Wyzgoski, M.G., Novak, G.E., 1987a. Stress cracking of nylon polymers in aqueous salt solutions: part 2. Nylon–salt interactions. J. Mater. Sci. 22 (5), 1715–1723.
Wyzgoski, M.G., Novak, G.E., 1987b. Stress cracking of nylon polymers in aqueous salt solutions: part 1. Stress-rupture behaviour. J. Mater. Sci. 22 (5), 1707–1714.
Wyzgoski, M.G., Novak, G.E., 1987c. Stress cracking of nylon polymers in aqueous salt solutions: part 3. Craze-growth kinetics. J. Mater. Sci. 22 (7), 2615–2623.
Xiong, Z., Li, X., Jia, Q., Fu, Z., Yang, Z., 2010. Complexation mechanism of polyamide 6/calcium chloride. Acta Polym. Sin. 8, 1003–1008.
Zhao, B., Liu, C.S., Zhu XSX, K.W., 2002. Research on the vibration cutting performance of particle reinforced metallic matrix composites SiCp/Al. J. Mater. Process. Technol. 129 (1–3), 380.
Zhou, Y., Mallick, P.K., 2005. A non-linear damage model for the tensile behavior of an injection molded short E-glass fiber reinforced polyamide-6,6. Mater. Sci. Eng. A 393 (1–2), 303–309.

Part Three

Other toughening mechanisms for composite materials

This page intentionally left blank

Toughening mechanisms in Zanchor-reinforced composites

9

T. Kusaka
Ritsumeikan University, Kusatsu, Japan

9.1 Introduction

Advanced composite materials such as CFRP (carbon fiber-reinforced plastics) have been used in various industrial applications because of their favorable properties, including stiffness, strength, lightness, and chemical resistance. In particular, in recent years, increasing attention has been paid to the extensive use of advanced composite materials for the primary structures of next-generation passenger airplanes. However, the reduction in compressive strength caused by the delamination has been recognized as one of the most serious problems in structures made of composite laminates. Hence, a number of challenging works have been created to improve the interlaminar strength of composite laminates, where the development of the toughened interlayer composites is a symbolic innovation in aeronautical applications (Odagiri et al., 1991, 1996). In addition, the usability of through-thickness reinforcements, such as stitching and three-dimensional fabrics, has been actively examined in recent years (Tada and Ishikawa, 1989; Sharma and Sankar, 1997; Mouritz et al., 1997, 1999; Mouritz and Cox, 2000; Liu and Mai, 2001; Yan et al., 2003, 2004; Dai et al., 2004; Robinson and Das, 2004; Byrd and Birman, 2005; Meo et al., 2005; Chen et al., 2005; O'Brien and Krueger, 2006; Scarponi et al., 2007; Dantuluri et al., 2007; Liu et al., 2007; Mouritz, 2007). However, such through-thickness reinforcement techniques have some drawbacks in in-plane mechanical properties and manufacturing costs, in spite of their very high effectiveness against interlaminar fracture.

Zanchor, a novel through-thickness reinforcement technique, was developed by Mitsubishi Heavy Industries and Shikibo with the aim of improving the interlaminar strength and the resin permeability of composite laminates without significant increase in manufacturing costs (Abe et al., 2003). Iwahori et al. (Iwahori et al., 2004; Itabashi et al., 2007) showed that the compression after impact performance of composite materials was greatly improved by the Zanchor process without a serious reduction of in-plane properties. Our research group (Kusaka et al., 2005, 2006, 2007, 2008a,b,c, 2009, 2010, 2012, 2013; Hojo et al., 2008a,b, 2010; Watanabe et al., 2007) investigated the fracture behavior of Zanchor-reinforced composites on the basis of fracture mechanics. In these studies, the macroscopic and microscopic fracture behaviors under mode I and II loading were analyzed in detail. In addition, the toughening mechanism by the Zanchor process was studied through the comparison of experimental results between fracture toughness tests and through-thickness strength tests. The mode I and II fracture toughness and the crack growth behavior under impact loading

Toughening Mechanisms in Composite Materials. http://dx.doi.org/10.1016/B978-1-78242-279-2.00009-3

were investigated in Kusaka et al. (2006, 2008c). The mode I fracture toughness and the crack growth behavior under fatigue loading were investigated in Hojo et al. (2008b, 2010).

The main focus of this chapter is on the static fracture behavior and the toughening mechanism. DCB (double cantilever beams) and TTT (through-thickness tension) specimens were employed for mode I testing (Kusaka et al., 2012; Hojo et al., 1995). ENF (end-notched flexure) and ILS (interlaminar shear) specimens were employed for mode II testing (Kusaka et al., 2009; Tanaka et al., 1995). Microscopic observations were also conducted to study the toughening mechanism.

9.2 Zanchor process and materials

9.2.1 Zanchor process

As shown in Figure 9.1, Zanchor is a kind of needling process for dry preforms using a set of specially designed needles. Applying this process, in-plane fibers can be oriented in an out-of-plane direction, typically forming a conical shape, as shown later. In this chapter, the conical-shaped fibers are named EFB (entangled fiber bundles), and they play an important role in the improvement in interlaminar strength. It should be noted that no additional fibers are necessary in the Zanchor process, which is totally different from other reinforcement techniques, such as stitching or Z-pin. Some researchers have investigated the fundamental properties of Zanchor-reinforced composites, where the interlaminar strength and impact resistance are drastically improved by the Zanchor process, with slight reduction in in-plane stiffness and strength.

Speaking of the conclusions, the reinforcing mechanisms of Zanchor can be roughly classified into "wedge effect" and "bridging effect," as shown in Figure 9.2. The wedge effect relates to the pullout or breakage strength of EFB, as shown in Figure 9.3. The pullout mode in Figure 9.3a was mainly observed in mode I fracture, whereas the breakage mode in Figure 9.3b was mainly observed in mode II fracture. Figure 9.3a also shows the typical shape of EFB generated by the Zanchor process. The bridging effect relates to the closure force due to the fiber bridgings induced by the EFB, as shown in Figure 9.4. Fiber bridgings were commonly observed in mode I

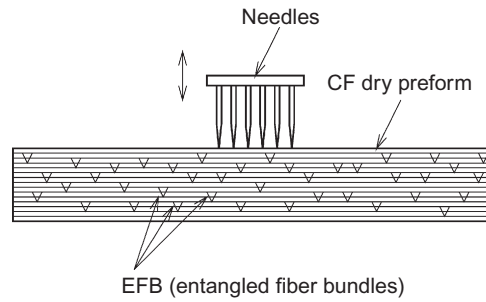

Figure 9.1 Schematic drawing of the Zanchor process.

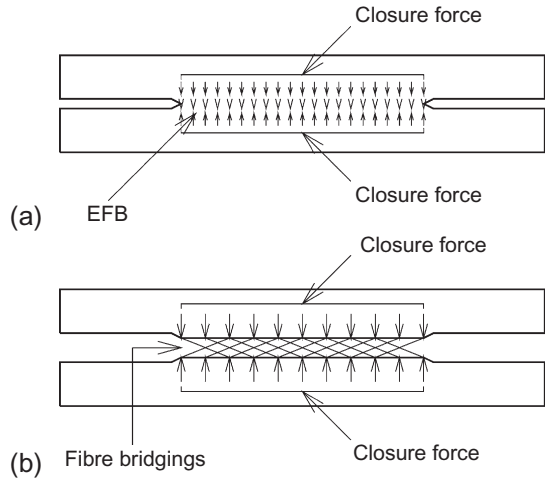

Figure 9.2 Classification of Zanchor effects. (a) Wedge effect. (b) Bridging effect.

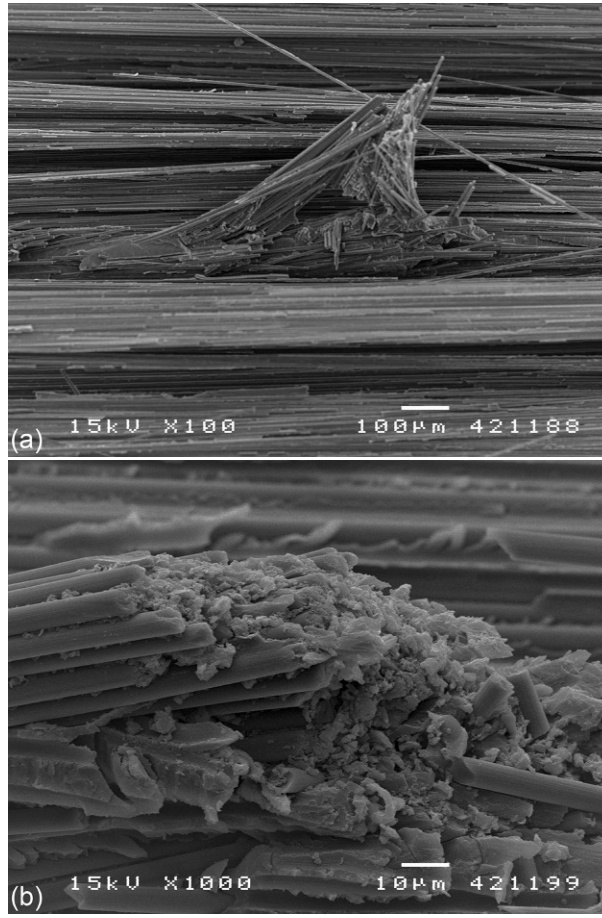

Figure 9.3 Failure modes related to EFB (crack growth: ⊗). (a) Pullout mode. (b) Breakage mode.

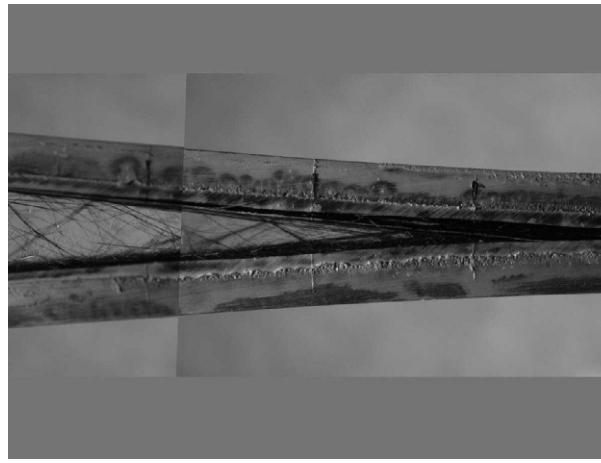

Figure 9.4 Fiber bridging in Zanchor composites (crack growth: →).

fracture but scarcely observed in mode II fracture. The difference of crack growth behavior between mode I and II fracture will be discussed in later sections.

9.2.2 Materials and specimens

CF (carbon fibers) dry preforms of [0/90/90/0]s stacking sequence were fabricated with a high-strength intermediate-modulus CF dry fabrics. The Zanchor process was applied to the dry preforms prior to the resin impregnation. Composite panels were fabricated using a modified epoxy resin with the resin film infusion process. A 50-mm thick Kapton film was inserted at the mid-plane of the panels to introduce an artificial starter slit. The Zanchor process was not applied to the region of starter slit. Hence, an inhomogeneous region in Zanchor density existed around the end of the starter slit. Three types of composite panels with different Zanchor densities (Zanchor composites), Z1, Z2, and Z4, were fabricated to study the toughening mechanism. In this chapter, the Zanchor density, Z, was defined as a nondimensional parameter proportional to the number of needling per unit area; the Zanchor density of Z4 was four times that of Z1 and twice that of Z2. A composite panel without Zanchor process (base composite), Z0, was also fabricated with the same materials for comparison. The fiber volume fractions of Z0, Z1, Z2, and Z4, were 66%, 63%, 63%, and 61%, respectively. The nominal thickness of the panels was 2.4 mm.

9.3 Fracture behavior under mode I loading

9.3.1 DCB tests

DCB specimens (Hojo et al., 1995) were employed to study the mode I fracture behavior of Zanchor composites, as shown in Figure 9.5. The width and length of the specimens were 10 and 170 mm, respectively. The initial crack length was about 40 mm.

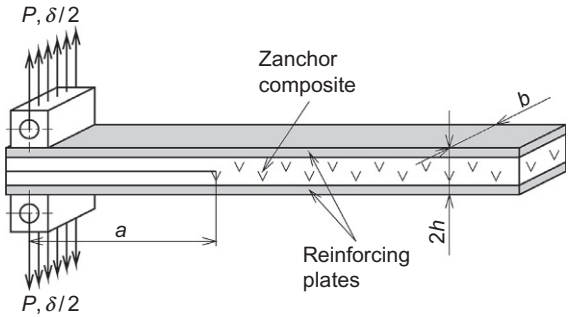

Figure 9.5 Double cantilever beams specimen.

Unidirectional CFRP plates of 2-mm thickness were bonded to both faces of the specimens to prevent the bending failure. The specimens were monotonously loaded or intermittently loaded and unloaded with measuring the crack extension, Δa, to evaluate the fracture toughness, G_{IC}, as a function of crack extension, Δa. A screw-driven testing machine was used to perform the DCB tests at a displacement rate, $d\delta/dt = 0.1$ mm/min. Precracks were not introduced to the specimens. Mode I fracture toughness can be investigated as the critical value of the energy release rate, G_I, using the following equation:

$$G_{IC} = \frac{3}{2(2h)}\left(\frac{P_C}{b}\right)^2 \frac{\sqrt[3]{(bC_C)^2}}{\alpha} \tag{9.1}$$

where b, $2h$, and C ($=\delta/P$) are the width, thickness, and loading point compliance of the specimen, respectively. P is the load applied to the specimen. δ is the displacement of the loading point. The subscript, C, indicates the critical state of crack growth. α and β, which are the coefficients depending on the material properties, can be obtained experimentally by the least square fitting using the following equation:

$$\frac{a}{2h} = \alpha\sqrt[3]{bC} + \beta \tag{9.2}$$

For unidirectional composites, the coefficients, α and β, which, respectively, relate to the bending stiffness and the end correction factor of cantilevers, are theoretically given by the following equations using the elastic modulus in longitudinal direction, E_L, the elastic modulus in transverse direction, E_T, and the shear modulus in in-plane direction, G_{LT}, of the composite panel:

$$\alpha = \frac{\sqrt[3]{E_L}}{4} \tag{9.3}$$

$$\beta = -\frac{1}{2}\sqrt{\frac{E_L}{11G_{LT}}\left\{3 - 2\left(\frac{1.18\sqrt{E_L E_T/G_{LT}}}{1 + 1.18\sqrt{E_L E_T/G_{LT}}}\right)^2\right\}} \tag{9.4}$$

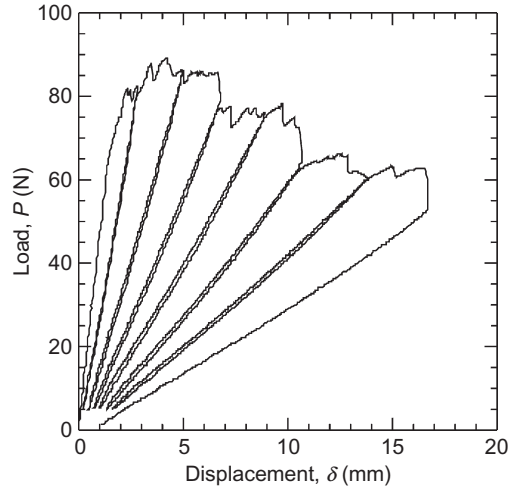

Figure 9.6 Load–displacement relations in a DCB test (material: Z1).

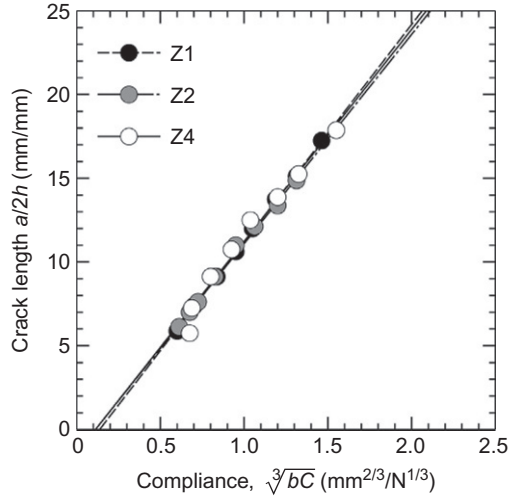

Figure 9.7 Relationship between crack length and compliance in DCB tests.

Figure 9.6 shows a typical DCB test result of the Zanchor composite, Z1. The abscissa represents the displacement of the loading point, δ. The ordinate represents the load applied to the specimen, P. Figure 9.7 shows the relationship between the third root of compliance, $(bC)^{1/3}$, and the normalized crack length, $a/2h$. The solid, shaded, and open circles represent the results of the Zanchor composites, Z1–Z4, respectively.

As shown in Figure 9.6, the load–displacement curves of the Zanchor composites, Z1–Z4, were slightly concaved, where the gradient of the curves, $dP/d\delta$, increased with increasing the applied load, P, except for the first loading cycle. This tendency was mainly due to the strained and unstrained behaviors of fiber bridgings generated on the fracture surfaces. However, the relationship between $a/2h$ and $(bC)^{1/3}$ was almost linear, as shown in Figure 9.7, where the compliance, C, was determined from

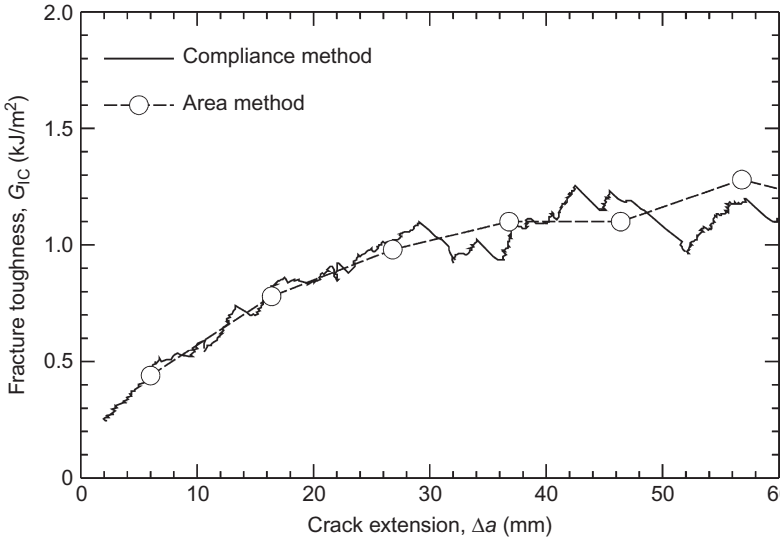

Figure 9.8 Comparison of fracture toughness in DCB tests (material: Z1).

the initial slope of the load–displacement curves. Consequently, the coefficients, α and β, could be determined, respectively, from the slope and intercept of the lines using Eq. (9.2). Fiber bridgings were observed regardless of the Zanchor density, Z, under mode I loading, as shown in Figure 9.4, but not observed under mode II loading.

Figure 9.8 shows the crack resistance curves of the Zanchor composite, Z1, obtained from the result shown in Figure 9.6. The abscissa represents the crack extension, Δa. The ordinate represents the fracture toughness, G_{IC}. The solid lines represent the results obtained by the compliance method using Eq. (9.1). The broken line represents the results obtained by the area method, which can be applied to the nonlinear fracture behavior. As shown in Figure 9.8, the results of the compliance method agreed well with those of the area method. In other words, the mode I fracture toughness, G_{IC}, and the crack length, a, can be calculated from the results of DCB tests by using the equations based on the compliance method with acceptable accuracy in spite of the nonlinear response of the load–displacement relations.

9.3.2 Mode I fracture toughness

Figure 9.9 shows typical crack resistance curves obtained by the DCB tests. The abscissa represents the crack extension, Δa, calculated by using Eq. (9.2). The ordinate represents the mode I fracture toughness, G_{IC}, calculated by using Eq. (9.1). The dotted line represents the results of the base composite, Z0. The broken, dash–dotted, and solid lines represent those of the Zanchor composites, Z1–Z4, respectively.

As shown in Figure 9.9, the fracture toughness, G_{IC}, of the Zanchor composites, Z1–Z4, was much higher than that of the base composite, Z0, where the fracture toughness, G_{IC}, increased with increasing the Zanchor density, Z. In addition, the

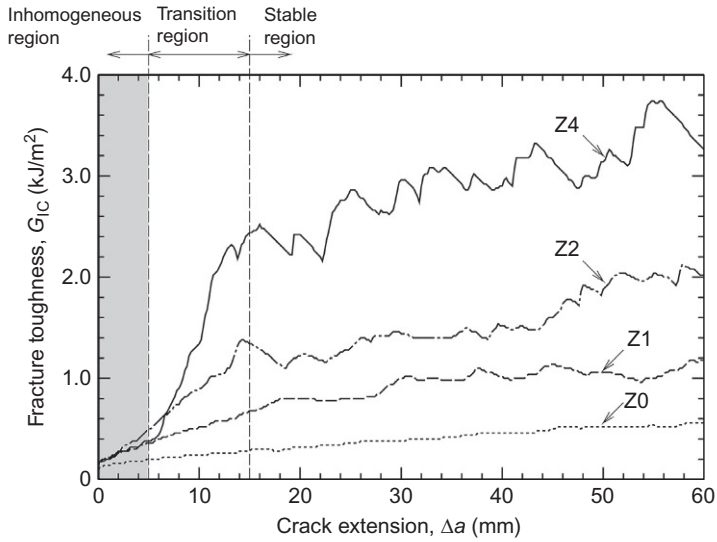

Figure 9.9 Crack resistance curves of the composites under mode I loading.

fracture toughness, G_{IC}, drastically increased with increasing the crack extension, Δa, in the region of $\Delta a = 0$–15 mm for the Zanchor composites, Z1–Z4. In the region of $\Delta a = 0$–5 mm, the increase of the fracture toughness, G_{IC}, presumably came from the inhomogeneity of Zanchor density caused by the fabrication process (inhomogeneous region). The initial values for $\Delta a = 0$ mm was nearly constant regardless of the Zanchor density, Z. On the other hand, in the region of 5–15 mm, the increase of the fracture toughness, G_{IC}, was undoubtedly caused by the fiber bridgings induced by the Zanchor process (transition region). However, in the region of $\Delta a > 15$ mm, the increase of the fracture toughness, G_{IC}, was gradually saturated due to the breakage or inactivation behavior of fiber bridgings with crack growth (stable region). This trend in the stable region under mode I loading was fundamentally different from that under mode II loading shown in the latter section.

The DCB test results are summarized in Figure 9.10, parameterizing with the crack extension, Δa. The abscissa represents the Zanchor density, Z. The ordinate represents the mode I fracture toughness, G_{IC}. The open triangles represent the initial values for $\Delta a = 0$ mm. The solid, shaded, and open circles represent the results for $\Delta a = 10$, 20, and 40 mm, respectively. All of the plots represent the average values for three specimens.

As shown in Figure 9.10, the fracture toughness, G_{IC}, increased largely and almost linearly with increasing the Zanchor density, Z, regardless of the crack extension, Δa, except for the initial values for $\Delta a = 0$ mm. A quantitative study of the results indicates that the fracture toughness, G_{IC}, of the Zanchor composite, Z4, reached more than six times of the base composite, Z0. However, it should be noted that the effect of Zanchor process on mode I fracture toughness depends on the material compositions, such as CF, matrix resin, interfacial treatment, fiber pattern, and stacking

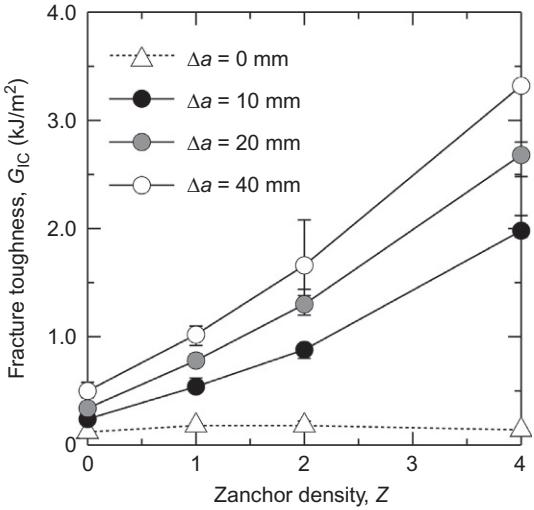

Figure 9.10 Relationship between Zanchor density and mode I fracture toughness.

sequence. Also, it should be noted that the saturation of the fracture toughness, G_{IC}, probably occurs with increasing the Zanchor density, Z. Further research will be necessary for clear understanding of this problem.

The above results demonstrated that the Zanchor process was highly effective at improving the mode I fracture toughness of composite laminates, where the fracture toughness, G_{IC}, increased almost linearly with the Zanchor density, Z. The fracture toughness, G_{IC}, of the Zanchor composites gradually increased with increasing the crack extension, Δa, under mode I loading regardless of the Zanchor density, Z.

9.4 Toughening mechanisms under mode I loading

9.4.1 TTT tests

TTT tests (Kusaka et al., 2012) were carried out to study the through-thickness tensile fracture behavior of Zanchor composites, as shown in Figure 9.11a. TTT specimens were machined from the same composite panels as the DCB specimens. Unidirectional CFRP plates of 0.6-mm thickness were bonded to both faces of the specimens. The outer dimensions of the specimens were $10 \times 10 \times 3.6$ mm^3. U-shaped notches of 0.1-mm width and 0.05-mm route radius were carefully introduced at the mid-plane of the specimens with a thin diamond saw. The size of the unnotched region was 5×5 mm^2. The specimens were bonded to the loading fixtures with a two-component epoxy adhesive, as shown in Figure 9.11b. A screw-driven testing machine was used to perform the TTT tests at a displacement rate, $d\delta/dt = 0.1$ mm/min.

Figure 9.12 shows typical TTT test results. The abscissa represents the displacement of the crosshead, δ_h. The ordinate represents the load applied to the specimen, P. Figure 9.13 shows modified load–displacement curves of the results in Figure 9.12

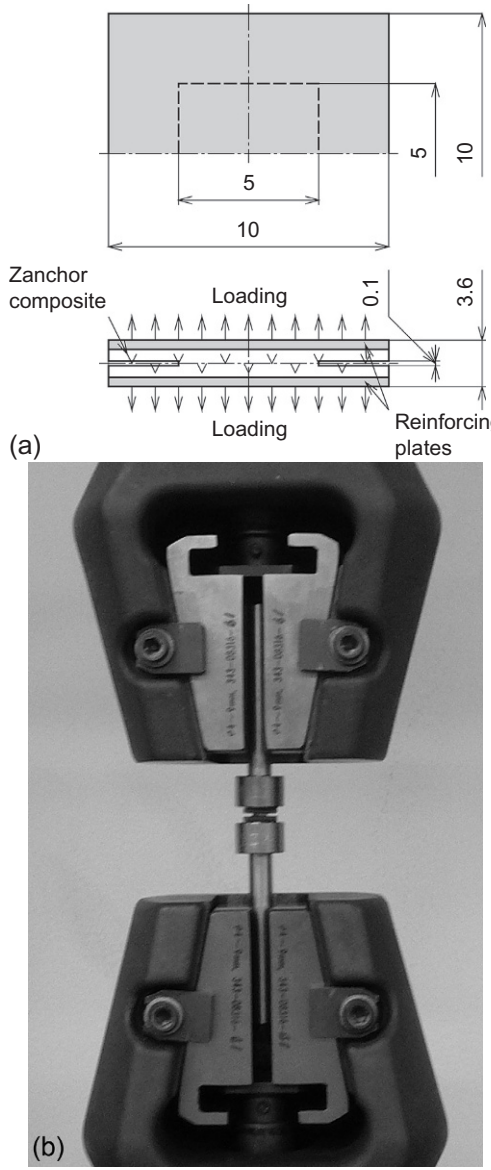

Figure 9.11 Through-thickness tension specimen. (a) Specimen. (b) Fixtures.

with canceling the deformation of loading fixtures and testing machine. The abscissa represents the elongation of the specimen, δ. The dotted line represents the results of the base composite, Z0. The broken, dash–dotted, and solid lines represent the results of the Zanchor composites, Z1–Z4, respectively. The open circles in Figure 9.12 represent the points of maximum load, $P_{\max}$. The solid circles in Figure 9.13 represent the

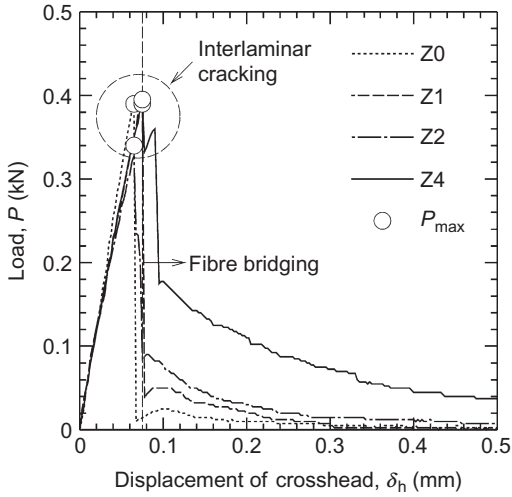

Figure 9.12 Load–displacement relations in TTT tests.

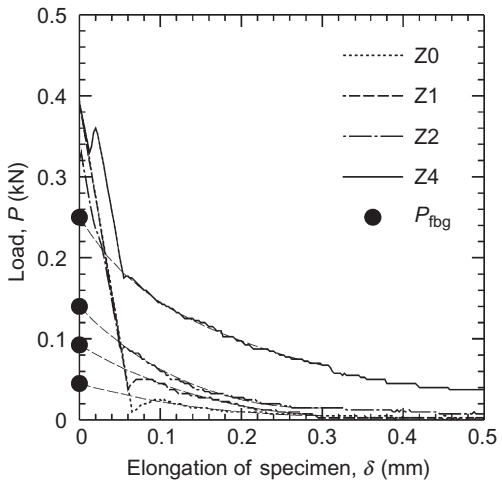

Figure 9.13 Modified load–displacement relations in TTT tests.

exponentially extrapolated points of the stable parts of load–displacement curves to the displacement of interlaminar crack onset, P_{fbg}, as indicated by the thin broken lines.

As shown in Figure 9.12, the load, P, dropped unstably at the maximum points, P_{max}, where the interlaminar cracking occurred over the unnotched parts of the specimens. However, the specimens still sustained the load by the fiber bridgings in the Zanchor composites, Z1–Z4. After the unstable fracture, the load, P, gradually decreased to zero with the pullout of fiber bridgings due to the dimensional limitation of the unnotched part. As shown in Figure 9.13, the stable parts of the load–displacement curves related to the fiber bridgings. The fracture behavior of the Zanchor composites under

mode I loading can be attributed to the cracking at interlaminar and the breakage of fiber bridgings. The Zanchor process affects the initiation of interlaminar cracking, where the EFB acts as a wedge to connect the laminas (wedge effect). The contribution of this effect can be grasped through the evaluation of the maximum load, P_{max}. The Zanchor process also affects the generation of fiber bridgings, where the EFB acts as a trigger to generate the fiber bridgings (bridging effect). The contribution of this effect can be grasped through the evaluation of the bridging load, P_{fbg}. The fracture energy absorbed after the point of P_{max}, was much larger than that absorbed before the point.

9.4.2 Toughening mechanisms under mode I loading

Figure 9.14 shows the summary of the TTT test results. The abscissa represents the Zanchor density, Z. The ordinate represents the maximum tensile strength, σ_{max}, calculated from the maximum load, P_{max}, and the bridging strength, σ_{fbg}, calculated from the bridging load, P_{fbg}. The solid and open circles represent the measured and averaged values of the maximum tensile strength, σ_{max}, respectively. The solid and open triangles represent those of the bridging strength, σ_{fbg}, respectively. As shown in Figure 9.14, the maximum tensile strength, σ_{max}, was nearly constant regardless of the Zanchor density, Z. However, the bridging strength, σ_{fbg}, drastically increased with an increase in the Zanchor density, Z. The former result indicated that the effect of the Zanchor process on the maximum tensile strength, σ_{max}, was approximately negligible compared to the interlaminar strength of base lamina. This was essentially because the microscopic fracture mode for the maximum tensile strength, σ_{max}, was not the breakage of EFB but the pullout of EFB. On the other hand, the latter result indicated that the effect of the Zanchor process on the bridging strength, σ_{fbg}, was very large under mode I loading.

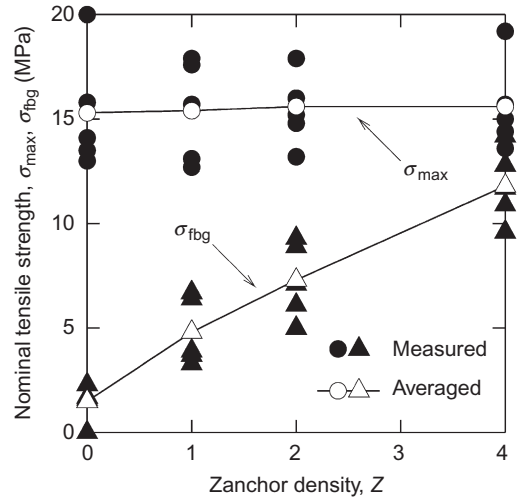

Figure 9.14 Relationship between Zanchor density and tensile strength.

On the basis of the knowledge obtained above, the mode I fracture toughness of Zanchor composites, G_{IC}, can be approximately divided into two components. One is the fracture toughness related to the strength of the base lamina, G_{IC}^{base}. The other is the fracture toughness related to the fiber bridgings, G_{IC}^{fbg}. Consequently, the following equation can be stated:

$$G_{IC} = G_{IC}^{base} + G_{IC}^{fbg} \tag{9.5}$$

Assuming that the closure force by the fiber bridgings, p_{fbg}, is acting on a part of the fracture surface of DCB specimen, as shown in Figure 9.15, the component related to the fiber bridgings, G_{IC}^{fbg}, can be given by the following equations using the bending moment, M_{fbg}, caused by the closure force of fiber bridgings, p_{fbg}, on the basis of the conventional beam theory:

$$G_{IC}^{fbg} = \frac{M_{fbg}^2}{b\mathrm{EI}} \tag{9.6}$$

$$M_{fbg} = \int_{e}^{l_{fbg}+e} p_{fbg} b\xi d\xi \tag{9.7}$$

where b and EI are the width and bending stiffness of the specimen, respectively. l_{fbg} is the equivalent length of the part where the closure force, p_{fbg}, is acting. e ($=-2h\beta$) is the correction value for the crack length, a, commonly used in the analysis of DCB specimen (Williams, 1989). ξ is the local coordinate system parallel to the crack growth direction with the equivalent crack tip at the origin.

Considering the fracture behavior during the early stage of crack growth, the breakage of fiber bridgings can be neglected. Hence, the approximation of $p_{fbg} = s_{fbg}$ and $l_{fbg} = \Delta a$ yields the predictions of R-curves shown in Figure 9.16, where the solid lines represent the experimental results of the Zanchor composites, Z1–Z4, and the broken lines represent the predictions based on Eqs. (9.5)–(9.7). Here, the component, G_{IC}^{base}, of Eq. (9.5) was approximated by the fracture toughness of the base composite, Z0.

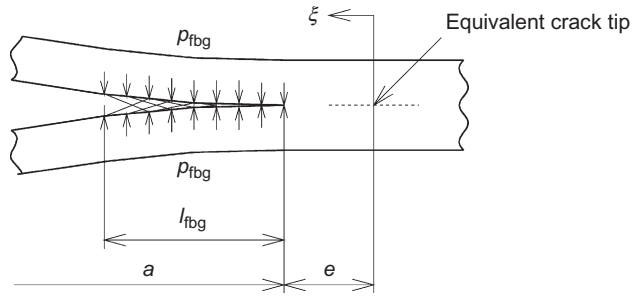

Figure 9.15 Crack closure force caused by fiber bridgings.

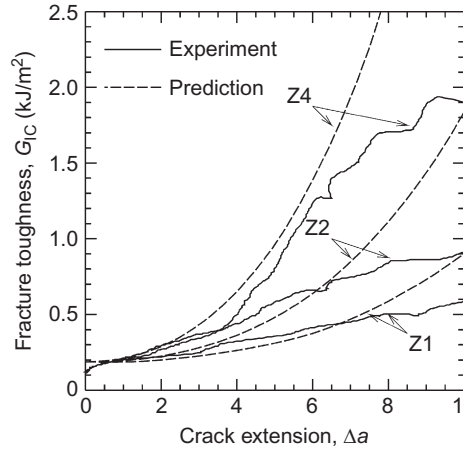

Figure 9.16 Effect of the Zanchor process on mode I fracture toughness.

As shown in Figure 9.16, the predictions showed similar tendencies to the experimental results for small values of Δa. However, the discrepancies between the predictions and experimental results became larger with increasing the crack extension due to the breakage or pullout of fiber bridgings.

The above results suggested that the Zanchor process was effective at improving the bridging strength, σ_{fbg}, but ineffective at improving the maximum strength, σ_{max}, where the increase in G_{IC} could be quantitatively predicted from the bridging strength, σ_{fbg}. Namely, the bridging effect was the dominant toughening mechanism against the mode I fracture, where the fiber bridgings played an important role.

9.4.3 Crack growth behavior under mode I loading

Figure 9.17 shows the cross sections of the DCB specimens observed by an optical microscope. The cutting planes are perpendicular to the crack growth direction and are about 10 mm from the final crack tip after the DCB tests. The whole of the central 0 layers and parts of the 90 layers can be observed in the figures. The crack growth direction is indicated by the arrow in the figure caption. As shown in Figure 9.17, the profiles of the interlaminar cracks were relatively rough and wavy in the Zanchor composites, Z1–Z4, while the profile of the interlaminar crack was relatively smooth in the base composite, Z0. The roughness of the fracture surfaces obviously increased with increasing Zanchor density, Z. In addition, a number of fiber bridgings were observed in the Zanchor composites, Z1–Z4.

Figure 9.3a shows the fracture surface of the Zanchor composite, Z1, around the EFB observed by a scanning electron microscope. The crack growth direction is indicated by the arrow in the figure caption. As shown in Figure 9.3a, typical morphology of EFB was a shelving conical shape. Hence, it was revealed that the microscopic fracture mode around the EFB was mainly the pullout of EFB under mode I loading. Such fracture behavior led to the trend in Figure 9.12, where the load, P, dropped unstably at the maximum points, and the trend in Figure 9.14, where the maximum

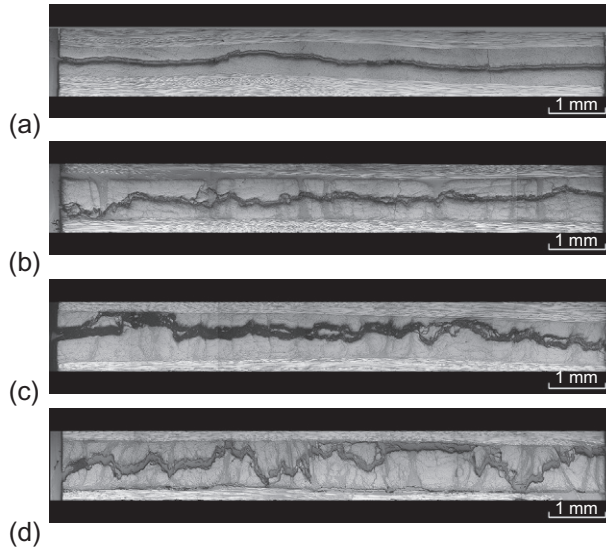

Figure 9.17 Cross sections of DCB specimens (crack growth: ⊗). (a) Base composite, Z0. (b) Zanchor composite, Z1. (c) Zanchor composite, Z2. (d) Zanchor composite, Z4.

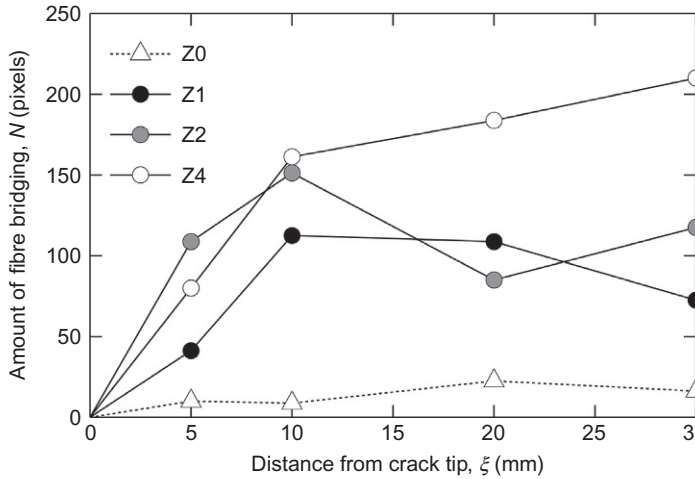

Figure 9.18 Effect of Zanchor process on fiber bridgings.

stress, σ_{max}, was not affected by the Zanchor density, Z. In other words, the EFB did not directly contribute to the increase in fracture toughness under mode I loading, because the pullout strength of EFB was considerably small.

Figure 9.18 shows the effect of the Zanchor process on the generation of fiber bridgings. The abscissa represents the distance from the final crack tip after the

DCB tests, ξ. The ordinate represents the amount of fiber bridgings, N, in the cross section. The open triangles represent the results of the base composite, Z0. The solid, shaded, and open circles represent those of the Zanchor composites, Z1–Z4, respectively. As shown in Figure 9.18, the amount of fiber bridgings, N, increased with increasing the Zanchor density, Z. In addition, the amount of fiber bridgings, N, increased mainly in the region close to the crack tip, while it was almost saturated in the region of $\xi > 10$ mm. This trend suggested that the EFB worked as a trigger to generate the fiber bridgings in the vicinity of the crack tip.

The above results demonstrated that the Zanchor process induced the fiber bridgings and increased the roughness of fracture surfaces, where the EFB played an important role in generating the fiber bridgings, resulting in the increase in mode I fracture toughness. In addition, the microscopic fracture mode around the EFB was mainly the pullout of EFB rather than the breakage of EFB.

9.5 Fracture behavior under mode II loading

9.5.1 ENF tests

ENF specimens (Tanaka et al., 1995) were employed to study the mode II fracture behavior of Zanchor composites, as shown in Figure 9.19. The width and bending span of the specimens were 10 and 80 mm, respectively. The initial crack length was about 20 mm. Unidirectional CFRP plates of 0.6-mm thickness were bonded to both faces of the specimens to prevent the bending failure. The specimens were intermittently loaded several times with sliding the loading and supporting points to evaluate the fracture toughness, G_{IIC}, as a function of crack extension, Δa. A screw-driven testing machine was used to perform the ENF tests at a displacement rate, $d\delta/dt = 1$ mm/min. Precracks were not introduced to the specimens. Mode II fracture toughness can be investigated as the critical value of the energy release rate, G_{II}, using the following equation:

$$G_{IIC} = \frac{9P_C^2 a_C^2 C_C}{2b\left(2L^3 + 3a_C^3\right)} \tag{9.8}$$

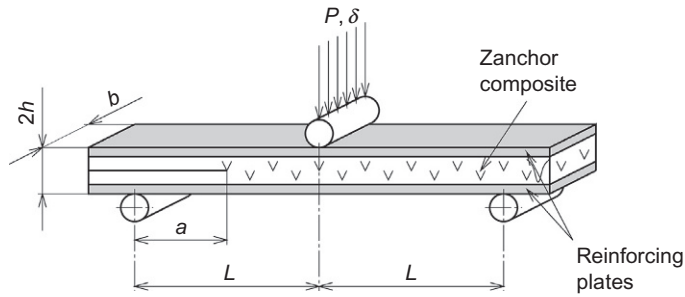

Figure 9.19 End-notched flexure specimen.

where b, $2h$, $2L$, and C ($=\delta/P$) are the width, thickness, bending span, and loading point compliance of the specimen, respectively. P is the load applied to the specimen. δ is the displacement of the loading point. The subscript, C, indicates the critical state of crack growth. The critical crack length, a_C, can be obtained from the initial crack length, a_0, initial compliance, C_0, and critical compliance, C_C, using the following equation:

$$a_C = \sqrt[3]{\frac{C_C}{C_0}a_0^3 + \frac{2}{3}\left(\frac{C_C}{C_0} - 1\right)L^3} \tag{9.9}$$

Figure 9.20 shows a typical ENF test result of the base composite, Z0. Figure 9.21 shows a typical ENF test result of the Zanchor composite, Z2. The abscissa represents the displacement of the loading point, δ. The ordinate represents the load applied to the specimen, P. The dotted lines represent the results for the first loading process, and the broken, dash–dotted, and solid lines represent those for the second, third, and fourth loading processes, respectively. The solid and open circles show the nonlinear and maximum points of the load–displacement curves. At the start of each loading process, the crack extension, Δa, which was defined as the distance from the artificial starter slit to the current crack tip, was 0, 20, 35, and 51 mm for the results in Figure 9.20, and 0, 13, 34, and 54 mm for those in Figure 9.21, respectively.

As shown in Figure 9.20, the load–displacement curves of the base composite, Z0, were almost linear up to the maximum points, suggesting that the fracture behavior of the base composite, Z0, was rather brittle. The variation of the maximum load, P_{max}, was considerably small for the base composite, Z0. As shown in Figure 9.21, the load–displacement curves of Zanchor composite, Z2, were also linear up to the maximum points. However, the maximum load, P_{max}, increased largely from the first loading process to the second loading process, while it was approximately constant after

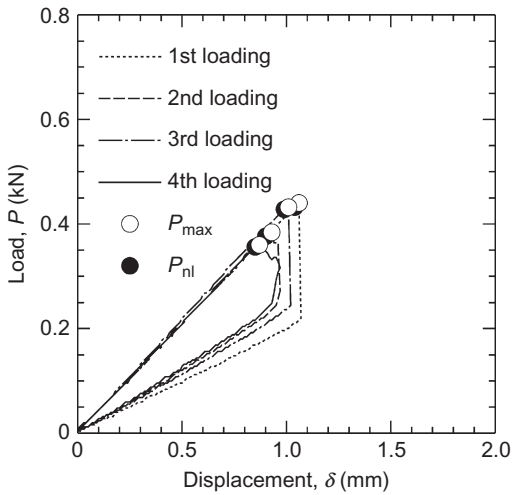

Figure 9.20 Load–displacement relations in ENF tests (material: Z0).

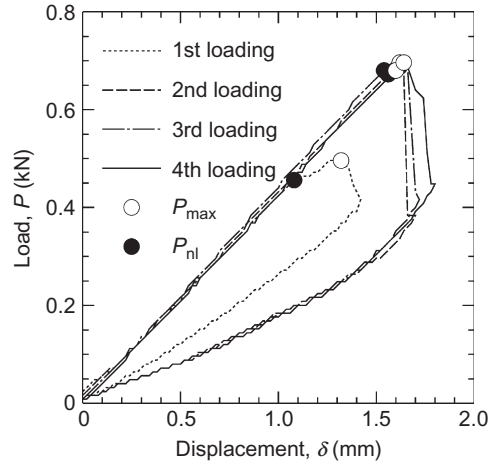

Figure 9.21 Load–displacement relations in ENF tests (material: Z2).

the second loading process. The nonlinear point, P_{nl}, in the first loading process of the Zanchor composite, Z2, was almost the same as that of the base composite, Z0, because the Zanchor process was not applied to the region of artificial starter slit. The nonlinear behavior in load–displacement curves can be considered as a sign of the subcritical crack growth behavior, such as interface debonding or matrix cracking, in the vicinity of the crack tip. The size of the crack tip process zone could be roughly estimated at 1–3 mm from the increase of the compliance, C, by using Eq. (9.9) regardless of the Zanchor density, Z.

9.5.2 Mode II fracture toughness

Figure 9.22 shows typical crack resistance curves obtained by the ENF tests. The abscissa represents the crack extension, Δa, calculated by using Eq. (9.9). The ordinate represents the mode II fracture toughness, G_{IIC}, calculated by using Eq. (9.8). The open triangles represent the results of the base composite, Z0. The solid, shaded, and open circles represent those of the Zanchor composites, Z1–Z4, respectively.

As shown in Figure 9.23, the fracture toughness, G_{IIC}, of the Zanchor composites, Z1–Z4, was much higher than that of the base composite, Z0, where the fracture toughness, G_{IIC}, increased with increasing the Zanchor density, Z. For the base composite, Z0, the fracture toughness, G_{IIC}, was almost constant regardless of the crack extension, Δa. However, for the Zanchor composites, Z1–Z4, the fracture toughness, G_{IIC}, was largely increased with increasing the crack extension, Δa, due to the inhomogeneity of Zanchor density in the region of $\Delta a = 0$–5 mm (inhomogeneous region). On the other hand, the fracture toughness, G_{IIC}, was approximately constant in the region of $\Delta a > 5$ mm (stable region). This trend in the stable region under mode II loading was fundamentally different from that under mode I loadings shown in the former section.

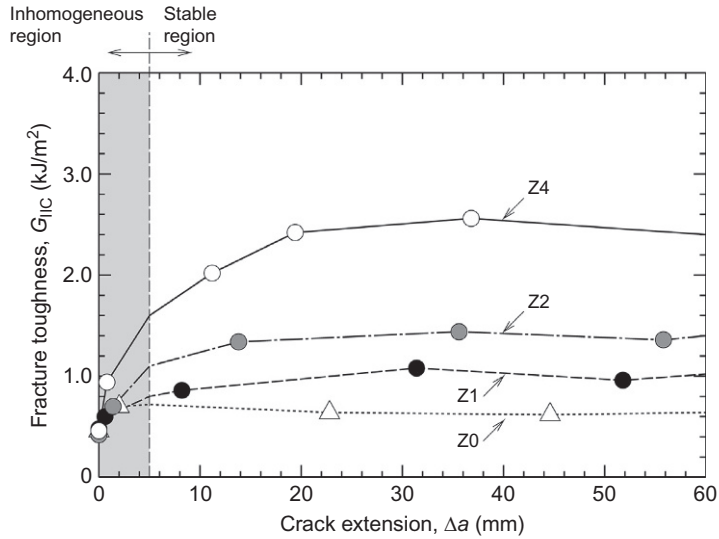

Figure 9.22 Crack resistance curves of the composites under mode II loading.

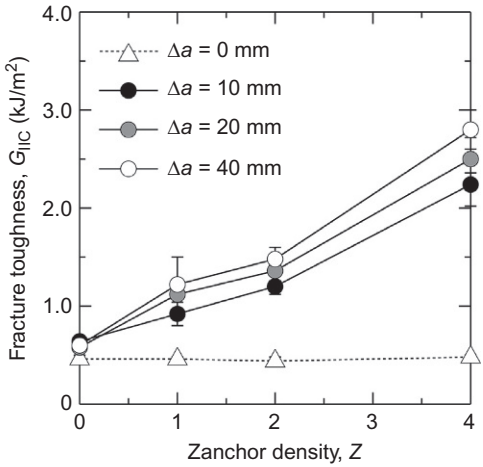

Figure 9.23 Relationship between Zanchor density and mode II fracture toughness.

The ENF test results are summarized in Figure 9.23, parameterizing with the crack extension, Δa. The abscissa represents the Zanchor density, Z. The ordinate represents the mode II fracture toughness, G_{IIC}. The open triangles represent the initial values for $\Delta a = 0$ mm. The solid, shaded, and open circles represent the results for $\Delta a = 10$, 20, and 40 mm, respectively. All of the plots are the average values for three specimens.

As shown in Figure 9.23, the fracture toughness, G_{IIC}, increased largely and almost linearly with increasing the Zanchor density, Z, regardless of the crack extension,

Δa, except for the initial values for $\Delta a = 0$ mm. On the other hand, the fracture toughness, G_{IIC}, was approximately independent of the crack extension, Δa, regardless of the Zanchor density, Z. A quantitative study of the results indicates that the fracture toughness, G_{IIC}, of the Zanchor composite, Z4, reached more than four times of the base composite, Z0. However, it should be noted that the effect of Zanchor process on mode II fracture toughness will depend on the material compositions, similar to the trend in mode I results. Also, the difference between mode I and II fracture should be clarified for further understanding of toughening mechanism in Zanchor composites.

The above results demonstrated that the Zanchor process was highly effective at improving the mode II fracture toughness of composite laminates, where the fracture toughness, G_{IIC}, increased almost linearly with the Zanchor density, Z. The fracture toughness, G_{II}, of the Zanchor composites was approximately independent of the crack extension, Δa, under mode II loading regardless of the Zanchor density, Z.

9.6 Toughening mechanisms under mode II loading

9.6.1 ILS tests

ILS tests (Kusaka et al., 2009) were carried out to study the ILS fracture behavior of Zanchor composites, as shown in Figure 9.24a. ILS specimens were machined from the same composite panels as the ENF specimens. Unidirectional CFRP plates of 0.6-mm thickness were bonded to both faces of the specimens. The outer dimensions of the specimens were $10 \times 10 \times 3.8$ mm^3. U-shaped notches of 0.1-mm width and 0.05-mm route radius were carefully introduced at the mid-plane of the specimens with a thin diamond saw. The size of the unnotched region was 5×5 mm^2. The specimens were bonded to the loading fixtures with a two-component epoxy adhesive, as shown in Figure 9.24b. A screw-driven testing machine was used to perform the ILS tests at a displacement rate, $d\delta/dt = 0.1$ mm/min.

Figure 9.25 shows typical ILS test results. The abscissa represents the displacement of the crosshead, δ_h. The ordinate represents the load applied to the specimen, P. The dotted line represents the results of the base composite, Z0. The broken, dash–dotted, and solid lines represent the results of the Zanchor composites, Z1–Z4, respectively. The open circles represent the points of maximum load, P_{max}.

As shown in Figure 9.25, the load, P, dropped unstably to zero at the maximum points, P_{max}, where the specimens were completely separated into two parts, regardless of the Zanchor density, Z. On the other hand, the maximum load, P_{max}, clearly increased with increasing the Zanchor density, Z. Fiber bridgings were not observed on the fracture surface of the specimens. This kind of brittle fracture behavior suggested that the critical fracture occurred without accompanying subcritical fracture, which was consistent with the fracture behavior of the ENF specimens. The results of ENF and ILS tests were different from those of DCB and TTT tests. The results of microscopic observation revealed that the unstable fracture at the maximum point, P_{max}, corresponded to the breakage of the EFB (wedge effect).

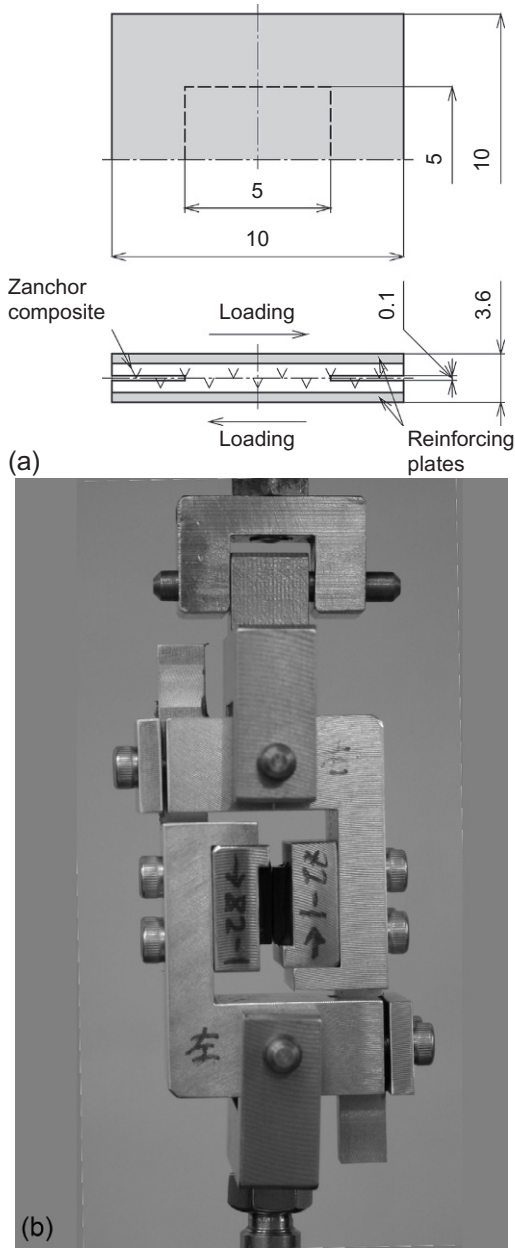

Figure 9.24 Interlaminar shear specimen. (a) Specimen. (b) Fixtures.

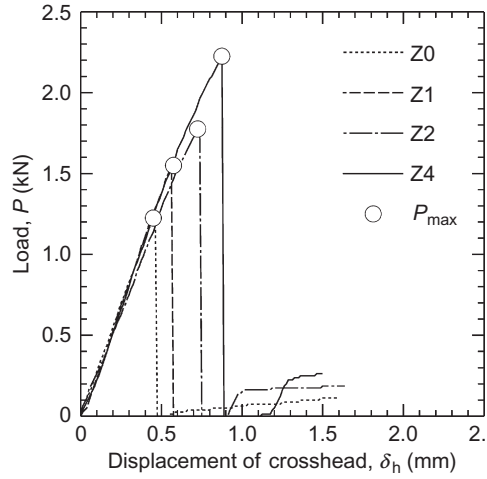

Figure 9.25 Load–displacement relations in ILS tests.

9.6.2 Toughening mechanisms under mode II loading

Figure 9.26 shows the summary of the ILS test results. The abscissa represents the Zanchor density, Z. The ordinate represents the maximum strength, τ_{max}, calculated from the maximum load, P_{max}. The solid and open circles represent the measured and averaged values of the maximum strength, τ_{max}, respectively. As shown in Figure 9.26, the maximum shear strength, τ_{max}, drastically increased with increasing the Zanchor density, Z. However, the behavior was not linear. In other words, the strength of the EFB was not directly contributed to the macroscopic strength of the composites. Considering the microscopic fracture morphology, it could be presumed that the breakage of the EFB was preceded by the fracture of the base lamina,

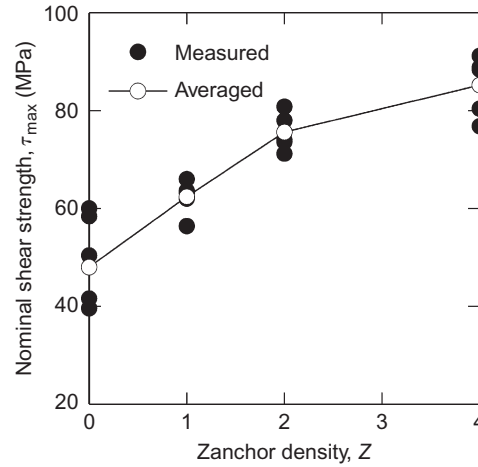

Figure 9.26 Relationship between Zanchor density and shear strength.

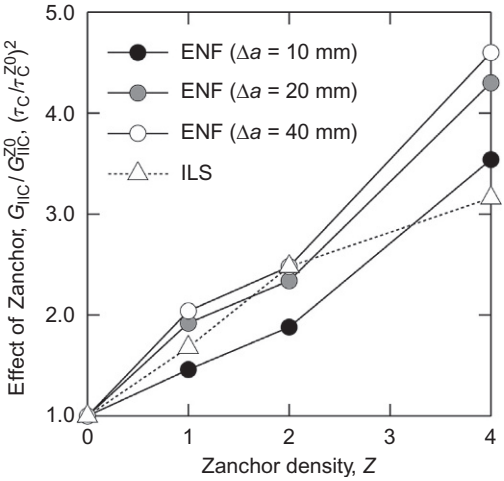

Figure 9.27 Effect of the Zanchor process on mode II fracture toughness.

and consequently the strength of the EFB was not directly added to that of the base lamina.

Figure 9.27 shows the summary of the ILS test results, comparing with the ENF test results shown in Figure 9.22. The abscissa represents the Zanchor density, Z. The ordinate represents the square of the nominal shear strength, $(\tau_{max}/\tau_{max}^{Z0})^2$, or the normalized fracture toughness, G_{IIC}/G_{IIC}^{Z0}, where τ_{max}^{Z0} and G_{IIC}^{Z0} are the nominal shear strength and fracture toughness of the base composite, Z0. The open triangles represent the results of the ILS tests. The solid, shaded, and open circles represent the results of the ENF tests for $\Delta a = 10$, 20, and 40 mm, respectively. As shown in Figure 9.27, the relationship between the square of the normalized shear strength, $(\tau_{max}/\tau_{max}^{Z0})^2$, and the Zanchor density, Z, was approximately linear in the similar manner to the relationship between the normalized fracture toughness, G_{IIC}/G_{IIC}^{Z0}, and the Zanchor density, Z. In addition, the values of $(\tau_{max}/\tau_{max}^{Z0})^2$ quantitatively agreed with those of G_{IIC}/G_{IIC}^{Z0}. These trends were theoretically consistent with the fact that the energy release rate, G_{II}, is proportional to the intensity of shear stress field, τ, in the vicinity of the crack tip. In other words, the shear strength of the EFB was directly contributed to the increase in the fracture toughness, G_{IIC}, under mode II loading.

The above results suggested that the Zanchor process was effective at improving the ILS strength, τ_{max}, of composite laminates, where the increase in τ_{max} was consistent with that in G_{IIC}. Namely, the wedge effect was the dominant toughening mechanism against the mode II fracture, where the EFB directly shared the mode II stress in the vicinity of the crack tip.

9.6.3 Crack growth behavior under mode II loading

Figure 9.28 shows the cross sections of the ENF specimens observed by an optical microscope. The cutting planes are perpendicular to the crack growth direction and

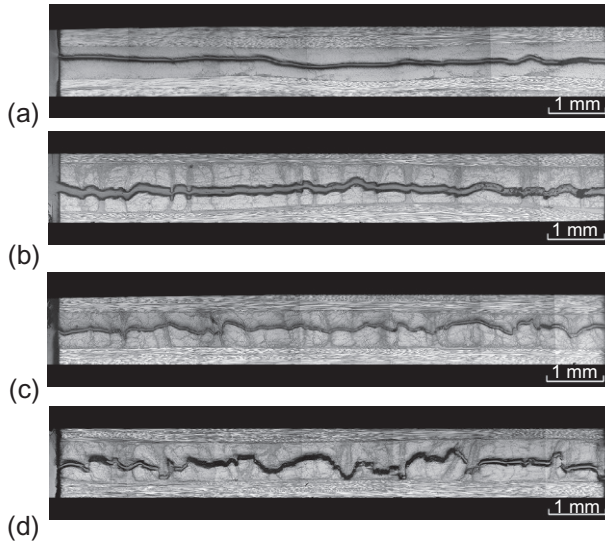

Figure 9.28 Cross sections of ENF specimens (crack growth: ⊗). (a) Base composite, Z0. (b) Zanchor composite, Z1. (c) Zanchor composite, Z2. (d) Zanchor composite, Z4.

are about 10 mm from the final crack tip after the ENF tests. The whole of the central 0 layers and parts of the 90 layers are shown in the figures. The crack growth directions are indicated by the arrow in the figure caption. As shown in Figure 9.28, the profiles of the interlaminar cracks were relatively rough and wavy in the Zanchor composites, Z1–Z4, while the profile of the interlaminar crack was relatively smooth in the base composite, Z0. The roughness of the fracture surfaces obviously increased with increasing the Zanchor density, *Z*, where the crack path partly reached the 0/90 interlaminar. However, any fiber bridgings were barely observed regardless of the Zanchor density, *Z*.

Figure 9.3b shows the fracture surfaces of the Zanchor composite, Z2, around the EFB observed by a scanning electron microscope. The crack growth direction is indicated by the arrow in the figure caption. As shown in Figure 9.3b, the conical shape of EFB was not retained under mode II loading. Hence, it was revealed that the microscopic fracture mode around the EFB was not mainly the pullout, but the breakage of EFB. In more detail, the breakage of EFB occurred under compressive stress field in the region as shown in Figure 9.3b, where the CF were broken into short pieces due to the microbuckling. On the other hand, the breakage of EFB also occurred under tensile stress field in other regions, where the CF were sharply cut off perpendicular to their longitudinal directions.

The above results demonstrated that the Zanchor process increased the roughness of fracture surface, where the EFB played an important role in increasing the roughness, resulting in the increase in mode II fracture toughness. In addition, the microscopic fracture mode around the EFB was mainly the breakage of EFB in the directions of tensile or compressive principle stress rather than the pullout of EFB.

9.7 Conclusions

Interlaminar fracture behavior and the toughening mechanism of Zanchor-reinforced composite laminates were investigated by using DCB and TTT specimens for mode I fracture and by using ENF and ILS specimens for mode II fracture. Fractographic examination was also conducted to study the microscopic fracture behavior in more detail. The results are summarized as follows:

DCB and ENF test results demonstrated that the Zanchor process was highly effective at improving the mode I and II fracture toughness of composite laminates, where the fracture toughness increased almost linearly with the Zanchor density. The fracture toughness gradually increased with crack extension under mode I loading, whereas it was approximately independent of crack extension under mode II loading.

TTT test results demonstrated that the Zanchor process was effective at improving the bridging strength but ineffective at improving the maximum strength of composite laminates under TTT loading. On the other hand, ILS test results demonstrated that the Zanchor process was effective at improving the maximum strength of composite laminates under ILS loading.

The effect of the Zanchor process could be roughly attributed to the "wedge effect" and "bridging effect." The bridging effect was the dominant toughening mechanism against the mode I fracture, where the fiber bridgings played an important role. The wedge effect was the dominant toughening mechanism against the mode II fracture, where the EFB directly shared the mode II stress around the crack tip.

Under mode I loading, the Zanchor process induced the fiber bridgings and increased the roughness of fracture surfaces, where the microscopic fracture mode around the EFB was mainly the pullout of EFB. Under mode II loading, the Zanchor process increased the roughness of fracture surface, where the microscopic fracture mode around the EFB was mainly the breakage of EFB.

References

Abe, T., Hayashi, K., Sato, T., Yamane, S., Hirokawa, T., 2003. A-VaRTM process and Z-anchor technology for primary aircraft structures. In: Proceedings of the 24th International SAMPE Europe Conference, pp. 87–94.

Byrd, L.W., Birman, V., 2005. The estimate of the effect of z-pins on the strain release rate, fracture and fatigue in a composite co-cured z-pinned double cantilever beam. Compos. Struct. 68, 53–63.

Chen, L., Sankar, B.V., Ifju, P.G., 2005. Analysis of mode I and mode II tests for composites with translaminar reinforcements. J. Compos. Mater. 39, 1311–1333.

Dai, S.C., Yan, W., Liu, H.Y., Mai, Y.W., 2004. Experimental study on z-pin bridging law by pullout test. Compos. Sci. Technol. 64, 2451–2457.

Dantuluri, V., Maiti, S., Geubelle, P.H., Patel, R., Kilic, H., 2007. Cohesive modeling of delamination in Z-pin reinforced composite laminates. Compos. Sci. Technol. 67, 616–631.

Hojo, M., Kageyama, K., Tanaka, K., 1995. Prestandardization study on mode I interlaminar fracture toughness test for CFRP in Japan. Composites 26, 243–255.

Hojo, M., Namashima, K., Kusaka, T., Tanaka, M., Adachi, T., Fukuoka, T., Ishibashi, M., 2008a. Modes I and II interlaminar fracture toughness of Zanchor-reinforced CFRP. In: Proceedings of the 17th European Conference on Fracture, EC1700280.

Hojo, M., Kusaka, T., Fukuoka, T., Ishibashi, M., 2008b. Static and fatigue delamination of Zanchor reinforced CF/epoxy laminates under modes I and II loadings. In: Proceedings of the 11th Japanese–European Symposium on Composite Materials, CD-ROM.

Hojo, M., Nakashima, K., Kusaka, T., Tanaka, M., Adachi, T., Fukuoka, T., Ishibashi, M., 2010. Mode I fatigue delamination of Zanchor reinforced CF/epoxy laminates. Int. J. Fatigue 32, 37–45.

Itabashi, T., Ishibashi, M., Takeda, F., Iwahori, Y., Ishikawa, T., Watanabe, N., 2007. Mode I interlaminar fracture mechanical properties of the CFRP laminates enhanced by Zanchor technology. In: Proceedings of the 16th International Conference on Composite Materials, FrBM1-02.

Iwahori, Y., Yamada, K., Ishibashi, M., Fukuoka, T., Ishikawa, T., Ben, G., 2004. Compression-after-impact properties of Z-anchor CFRP laminates. In: Proceedings of JSMS Composites, vol. 33, pp. 213–215 (in Japanese).

Kusaka, T., Hojo, M., Fukuoka, T., Ishibashi, M., 2005. Effect of strain rate on the interlaminar fracture toughness of Zanchor reinforced composites. In: Proceedings of the JSME/ASME International Conference on Materials and Processing, IMP-12-1-5.

Kusaka, T., Hojo, M., Fukuoka, T., Ishibashi, M., 2006. Effect of loading rate on the modes I and II fracture behaviour of Zanchor reinforced composites. J. Phys. IV 134, 1105–1111.

Kusaka, T., Yamaguchi, Y., Watanabe, K., Hojo, M., Fukuoka, T., Ishibashi, M., 2007. Mode I fracture behaviour and toughening mechanism of Zanchor reinforced composites. In: Proceedings of the 16th International Conference on Composite Materials, ThBM1-05.

Kusaka, T., Hojo, M., Watanabe, K., Fukuoka, T., Ishibashi, M., 2008a. Effect of Zanchor process on interlaminar crack growth behaviour of composite laminates under mode I loading. In: Abstracts of the 5th International Conference on Fracture of Polymers, Composites and Adhesives, O9.4.

Kusaka, T., Hojo, M., Watanabe, K., Fukuoka, T., Ishibashi, M., 2008b. Experimental characterization of mode I fracture behavior of Zanchor reinforced CF/epoxy composites. In: Progress of Composites 2008 in Asia and Australasia, pp. 176–179.

Kusaka, T., Ogawa, K., Watanabe, K., Hojo, M., Fukuoka, T., Ishibashi, M., 2008c. Experimental characterization of dynamic mode II fracture behavior of Zanchor reinforced CF/epoxy composites using SHPB technique. In: Proceedings of the 3rd JSME/ASME International Conference on Materials and Processing, MSEC_ICMP2008-72170.

Kusaka, T., Hojo, M., Watanabe, K., Fukuoka, T., Ishibashi, M., 2009. Fracture behaviour and toughening mechanism in Zanchor reinforced composites under mode II loading. Compos. Sci. Technol. 69, 2323–2330.

Kusaka, T., Mojo, M., Watanabe, K., Fukuoka, T., Ishibashi, M., 2010. Effect of Zanchor process on interlaminar crack growth behaviour of composite laminates. In: Proceedings of the 9th China–Japan Joint Conference on Composites, pp. 44–47.

Kusaka, T., Watanabe, K., Hojo, M., Fukuoka, T., Ishibashi, M., 2012. Fracture behaviour and toughening mechanism in Zanchor reinforced composites under mode I loading. Eng. Fract. Mech. 96, 433–446.

Kusaka, T., Hojo, M., Watanabe, K., Fukuoka, T., Ishibashi, M., 2013. Fracture behavior and toughening mechanism in Zanchor reinforced composites. In: Proceedings of the 13th Euro-Japanese Symposium on Composite Materials, pp. 132–135.

Liu, H.Y., Mai, Y.W., 2001. Delamination fracture mechanics of composite laminates with through-thickness pinning. In: Proceedings of the International Conference on Complexity and Frontiers in Strength and Fracture, pp. 24–27.

Liu, H.Y., Yan, W., Yu, X.Y., Mai, Y.W., 2007. Experimental study of effect of loading rate on mode I delamination of Z-pin reinforced laminates. Compos. Sci. Technol. 67, 1294–1301.

Meo, M., Achard, F., Grassi, M., 2005. Finite element modeling of bridging micro-mechanics in through-thickness reinforced composite laminates. Compos. Struct. 71, 383–387.

Mouritz, A.P., 2007. Review of z-pinned composite laminates. Compos. Part A 38, 2383–2397.

Mouritz, A.P., Cox, B.N., 2000. A mechanistic approach to the properties of stitched laminates. Compos. Part A 31, 1–27.

Mouritz, A.P., Leong, K.H., Herszberg, I., 1997. A review of the effect of stitching on the in-plane mechanical properties of fibre-reinforced polymer composites. Compos. Part A 28, 979–991.

Mouritz, A.P., Bannister, M.K., Falzon, P.J., Leong, K.H., 1999. Review of applications for advanced three-dimensional fibre textile composites. Compos. Part A 30, 1445–1461.

O'Brien, T.K., Krueger, R., 2006. Influence of compression and shear on the strength of composite laminates with Z-pinned reinforcement. Appl. Compos. Mater. 13, 173–189.

Odagiri, N., Kishi, H., Nakae, T., 1991. T800H/3900-2 toughened epoxy prepreg system: toughening concept and mechanism. In: Proceeding of the 6th Conference of the American Society for Composites, pp. 43–52.

Odagiri, N., Kishi, H., Yamashita, M., 1996. Development of TORAYCA prepreg P2302 carbon-fiber-reinforced plastic for aircraft primary structural-materials. Adv. Compos. Mater. 5, 249–254.

Robinson, P., Das, S., 2004. Mode I DCB testing of composite laminates reinforced with z-direction pins: a simple model for the investigation of data reduction strategies. Eng. Fract. Mech. 71, 345–364.

Scarponi, C., Perillo, A.M., Cutillo, L., Foglio, C., 2007. Advanced TTT composite materials for aeronautical purposes: compression after impact (CAI) behavior. Compos. Part B 38, 258–264.

Sharma, S.K., Sankar, B.V., 1997. Mode II delamination toughness of stitched graphite/epoxy textile composites. Compos. Sci. Technol. 57, 729–737.

Tada, Y., Ishikawa, T., 1989. Experimental evaluation of the effects of stitching on CFRP laminate specimens with various shapes and locations. Key Eng. Mater. 37, 305–316.

Tanaka, K., Kageyama, K., Hojo, M., 1995. Prestandardization study on mode II interlaminar fracture toughness test for CFRP in Japan. Composites 26, 257–267.

Watanabe, K., Kusaka, T., Hojo, M., Fukuoka, T., Ishibashi, M., 2007. Mode II fracture behaviour and toughening mechanism of Zanchor reinforced composites. In: Proceedings of the 16th International Conference on Composite Materials, ThBM1-06.

Williams, J.G., 1989. End corrections for orthotropic DCB specimens. Compos. Sci. Technol. 35, 367–376.

Yan, W., Liu, H.Y., Mai, Y.W., 2003. Numerical study on the mode I delamination toughness of z-pinned laminates. Compos. Sci. Technol. 63, 1481–1493.

Yan, W., Liu, H.Y., Mai, Y.W., 2004. Mode II delamination toughness of Z-pinned laminates. Compos. Sci. Technol. 64, 1937–1945.

This page intentionally left blank

Interlayer toughening mechanisms of composite materials

10

K. Bilge, M. Papila
Sabanci University, Istanbul, Turkey

10.1 Introduction: interlayer toughening methods

Tailorable specific strength and modulus (strength-to-weight and modulus-to-weight ratios, respectively) of advanced composite materials are of great advantage in design of lightweight high-performance structures. However, there are limitations yet to overcome for making use of the composites at their full potential and capacity. Interlaminar strength is arguably the weakest link for which substantial improvement may be sought by a strategy called interlayer toughening.

Among several other toughening strategies for composites, the interlayer toughening focuses basically on the interlaminar regions of laminated composites, where two subsequent plies are interfaced with each other. Theoretically speaking, the interlaminar regions are very thin resin-rich regions with relatively weak mechanical properties. In these terms, the behavior of an interlaminar region depends on the mechanical properties of the matrix phase as well as the interaction of the two subsequent plies affected by the fiber architecture, orientation, and lamination sequence (Tsotsis, 2009). Toughening of the interlaminar region may be achieved by enhanced matrix toughness itself. But also by the introduction of a crack deflection/suppression media in which more energy is required for crack growth to continue, that is, the cracks can essentially be stopped. Therefore, interlayer toughening strategies typically consider the addition of subphases such as dispersed particles, films, secondary fibrous reinforcements, or their combinations into interlaminar planes to avoid extensive crack formation (Shivakumar and Panduranga, 2013).

10.1.1 Particle/filler dispersion-based interlaminar toughening

Particle/filler-based interlaminar toughening strategies for structural composites are implemented by inserting/dispersing particles/nanotubes that have different mechanical behavior than the resin phase. The addition of thermoplastic particles effectively toughens the matrix phase by increasing Mode I, Mode II fracture toughness (Pham and Burchill, 1995; Huang and Horn, 1998; Matsuda et al., 1999) as well as specific energy absorption capacities (Sela and Ishai, 1989; Wilkinson et al., 1993). Through a well-exemplified fractography analysis, Stevanovic et al. (2003) showed how a thermoplastic particle acrylonitrile butadiene styrene (ABS) played role on plastic

Toughening Mechanisms in Composite Materials. http://dx.doi.org/10.1016/B978-1-78242-279-2.00010-X

deformation of interlaminar region and underlined the importance of particle/matrix compatibility. On an application problem, Warrior et al. (2004) investigated the effect of thermoplastic particles on the behavior of composite tubes made of continuous filament random mats and noncrimp fibers and showed the effect of fiber architecture.

Particle/filler inclusion-based interlaminar toughening of structural composites especially drew attention with the availability of very stiff nanotube structures. Numerous recent studies showing the hierarchical integration of carbon nanotubes (CNTs) into conventional composites have been comprehensively reviewed by Qian et al. (2010). Khan and Kim (2011) collected and presented specific studies that focus on the effect of carbon nanotubes (CNT) to impact and delamination characteristics of polymer composites. Among similar efforts, Garcia et al. (2008) clearly showed the CNT orientation effect on the out-of-plane properties by aligning them transversely inside the epoxy matrix. In another study, Veedu et al. (2006) increased the Mode I and Mode II interlaminar toughness of 3D composites by 348% and 54%, respectively, by growing aligned CNTs on the surface of SiC fibers. Apart from CNTs, nanoclays (Nuhiji et al., 2011) halloysite nanotubes (Ye et al., 2011) can be stated among the recently reported nanoscale fillers/additives for composite materials. The main focus in these studies was to improve the out-of-plane properties of composite materials by both toughening the matrix phase and introducing stiff crack deflection zones into the interlaminar region. However, the particle-based toughening methodology may profoundly suffer from dispersion problems associated with the nano nature of inclusion materials (Coleman, 2006). Any potential inhomogeneity due to the agglomerates of stiff nanofillers can create potential cracking spots inside the composite laminate, which will significantly decrease composite performance.

10.1.2 Film interleaving approaches

The main idea of film interleaving methods is to introduce a continuous crack deflection media into the interlaminar planes (Tsotsis, 2009). Planar addition of reinforced or nonreinforced thermoplastic/thermoset polymer films has been considered extensively since the beginning of the 1990s until the early 2000s (Ishai et al., 1988; Masters, 1989; Carlsson and Aksoy, 1991, 1992; Ozdil and Carlsson, 1992; Li et al., 1996; Duarte et al., 1999; Sohn et al., 2000; Jiang et al., 2001; Xuefeng et al., 2002). The goal of these studies was primarily to enhance out-of-plane properties such as impact, Mode I, and Mode II delamination resistances. Hojo et al. (2006) compared the behavior of Mode I delamination fatigue properties of composite materials interleaved with thermoplastic particles and ionomer based continuous resin films. Combining the emerging nanotube technologies and their advantages, Sun et al. (2010) offered the use of partially cured epoxy/SWCNT thin films as reinforcement agents for vacuum-assisted resin transfer molded (VARTM) composites. More recently, White and Sue (2012) followed this idea and noted significant increases in Mode II crack initiation and propagation onsets for composites manufactured by VARTM method. Yasaee et al. (2012a,b) considered the addition of different types of interlayers, thermoplastic film, chopped aramid fibers, pre-impregnated fiber reinforced tape, and thermosetting adhesive film, and compared their efficiencies in damage suppression specifically for Mode I and Mode II delaminations. Moreover,

Khan and Kim (2012) managed to manufacture bucky-paper interleaves out of carbon nanofibers (CNF) and showed significant improvements in interlaminar shear properties for carbon fiber reinforced polymer (CFRP) composites.

10.1.3 Nanofibrous interlayers for composite materials

Nanofibrous interlayer toughening strategy is in principal the same as of film-interleaving, but incorporates nano- to submicron fibrous interleafs with substantially high surface area instead of the continuous polymeric films. Fibrous interlayers are inserted into the laminates for their potential to increase the resistance against microcracking and ensure better bonding of the adjacent plies (Zucchelli et al., 2011). Lee et al. (2002, 2008) demonstrated the use of nonwoven mats for interlayer toughening without referring to the manufacturing technique of interest herein, so-called electrospinning, which is commonly used to produce nonwoven polymeric nanofibers (Huang et al., 2003). This relatively new concept was first introduced by Kim and Reneker (1999), Dzenis and Reneker (2001), and Dzenis (2008). Zucchelli et al. (2011) thoroughly reviewed the available studies that have followed the traces of this novel idea and demonstrated capabilities of electrospun nanofibers as interlayers in the composite materials. Table 10.1 aims to also supplement the review with very recent studies on polymeric nanofiber toughening of composite materials (Dzenis and Reneker, 2001; Dzenis, 2008; Sihn et al., 2008; Liu et al., 2006, 2008, 2014; Zucchelli et al., 2012; Magniez et al., 2011; Zhang et al., 2010, 2012; Bilge et al., 2012, 2014; Subagia et al., 2014; Li et al., 2015; Heijden et al., 2014). It is clear from the available literature that nanofiber interlayer toughening method via polymeric nanofibers is considered a promising strategy to toughen composite materials both under in-plane and out-of-plane loading conditions (Sihn et al., 2008).

The polymer choice of electrospun interleaf fibers for toughening composites should be made carefully in compliance with the polymer matrix chemistry and cure conditions (Ozden et al., 2010, 2012; Zucchelli et al., 2011; Bilge et al., 2012). Because thermal stability of the polymeric fibrous interleaf morphology, wettability, and nanofiber interfacial compatibility with the resin system have impact on the interlayer performance. On the other hand, polymer-based nanofibers may be converted into much stiffer CNF (Zussman et al., 2005; Wang et al., 2003; Gu et al., 2005a,b; Zhou et al., 2009). Chen et al. (2011) showed that the incorporation of CNF interlayers (made from electrospun PAN nanofibers) into composite laminates resulted in significant increases in both in-plane and out-of-plane plane properties. The capabilities of CNF as efficient interlayers were reported on several other studies in the literature, with special attention on the crack-bridging characteristics on Mode I (Palmeri et al., 2011; Yudin et al., 2008; Sadeghian et al., 2006; Rodriguez et al., 2011; Hossain et al., 2013).

There is a challenge and demand for interlayer materials that can work and provide improvement efficiently both under in-plane and out-of-plane loading conditions. It is also important to adapt the interlayer toughening concept into conventional manufacturing techniques and materials. In this regard, the nanofibrous interleaf/interlayer toughening arguably appears to be more promising, for which particular attention is devoted in this chapter. Therefore, the objective herein is to provide a

Table 10.1 Summary of works incorporating polymeric nanofibers as interlayer toughening agents in structural composites

References	Composite system	Nanofibrous interlayer	Experiment	Results
Dzenis and Reneker (2001) and Dzenis (2008)	Carbon/epoxy	Polibenzimidazol	DCB	G_{Ic} 15%
			ENF	G_{IIc} 130%
Liu et al. (2006)	Glass/epoxy	PA 6	T	Comparison of three nanofibers
		Epoxy 609	3 PB	
		TPU	SBS	
Sihn et al. (2008)	Carbon/epoxy	Polycarbonate	T	Microcrack initiation 8.5% Delamination 8%
Liu et al. (2008)	Glass/epoxy	Epoxy 609	ENF	G_{IIc} 9%
Zucchelli et al. (2012)	Graphite/epoxy	Nylon 6,6	DCB	G_{Ic} 5% energy absorbed 23%
			ENF	Energy absorbed 8.1% G_{IIc} 6.5%
Magniez et al. (2011)	Carbon/epoxy	poly(hydroxyether bisphenol A)	DCB	G_{Ic} 118%
Zhang et al. (2010)	Carbon/epoxy	Polyetherketone cardo	DCB	Initiation G_{Ic} 60% Propagation G_{Ic} 81%
Zhang et al. (2012)	Carbon/epoxy	poly(ε-caprolactone)	DCB	Initiation G_{Ic} 37% Propagation G_{Ic} 92%
Bilge et al. (2012)	Carbon/epoxy	P(St-co-GMA)	3 PB	Flexural strength 16%
			ENF	G_{IIc} 55%
			Impact	Absorbed energy 8%
			TT	Transverse tensile strength 17%

		P(St-co-GMA)/MWCNT	3 PB	Flexural strength 25%
			ENF	G_{IIc} 70%
			Impact	Absorbed energy 20%
			TT	Transverse tensile strength 27%
Bilge et al. (2014)	Carbon/epoxy	P(St-co-GMA)	T	Ultimate tensile strength 12%
			OHT	Open-hole tensile strength 9%
Subagia et al. (2014)	Basalt/epoxy	Polyurethane/CNT	T	Flexural strength 17%
			3 PB	Tensile strength 13%
Liu et al. (2014)	Carbon/epoxy	Polyurethane/CNT	3 PB	Tensile strength 8%
			T	Flexural strength 16%
Li et al. (2015)	Carbon/epoxy	MWCNTs-EP/PSF with different MWCNT loadings	SBS	Interlaminar shear strength 12%
			3 PB	Flexural strength 13%
			ENF	G_{IIc} 49%
Heijden et al. (2014)	Glass/epoxy	Polycaprolactane	DCB	20% G_{Ic} initiation
				12% G_{Ic} propagation
			T	Maintained
			OHT	Open-hole tensile strength 7.5%

DCB, double cantilever beam; ENF, end-notched flexure; T, tension; TT, transverse tension; OHT, open-hole tension; 3 PB, three-point bending; SBS, short beam shear.

guideline for incorporating nanofibrous interlayers effectively into laminated composites and discuss their toughening effects.

Key steps for exploring this toughening strategy are elaborated, namely polymer synthesis and characterization, electrospinning, laminate manufacturing, specimen preparation, mechanical testing strategies, and mechanical property improvements in accordance with microscopy-assisted failure analysis. Supplementary examples and case studies in Section 10.4 are also provided from our reference studies (Bilge et al., 2012, 2014).

10.2 Materials, process, and characterization

Although the nanofibrous interlayer toughening strategy is rather simple, its interdisciplinary and multiscale nature asks for a systematic work to demonstrate its potential and establish an effective implementation. A proposed roadmap herein needs to cover three major sections: materials choice/development, processing, and characterization. The materials section typically addresses polymer selection and synthesis for the base polymeric nanofiber interlayers. Processing should first discuss the preferred nanofiber manufacturing technique, the so-called electrospinning. A plan and description of how the interlayers are incorporated into conventional composite manufacturing techniques should follow next. Specimen preparation is also under this general topic. Characterization content overlaps with both materials and processing sections. Therefore, associated details are nested in respective sections. In addition, a separate section covers the ultimate assessments for toughening of the interlayered/interleaved composites via extensive mechanical testing.

10.2.1 Materials (and characterization)

10.2.1.1 Base polymeric material selection for nanofibrous interlayers

The idea of toughening by nanofibrous interlayers begins with the choice of a base polymer (see Table 10.1 for the variety of polymeric materials introduced as interlayer materials). The right choice is the initial and essential step for the success of nanofibers as a toughening interleaf, and should therefore taken into account the sequel of the processes and materials systems in the targeted composite laminate. In regard to sequence of the whole process, key factors to note are:

(i) Electrospinnability: This criterion is related to the characteristics of electrospinning a polymer solution that can enable uniform fiber spinning, preferably without any bead formations.

(ii) Matrix/resin of composite material: It is of paramount importance that the polymeric nanofiber material should enable strong bonding and interface compatibility with the hosting matrix of the composite material. For instance, epoxy compatibility is sought in the majority of practical cases.

(iii) Resin curing conditions: Posterior to the nanofiber formations via electrospinning, composites are formed following the cure cycle of the resin system of the target composite

material. Therefore, the thermal properties of the nanofibers (such as glass transition or melting temperature) should allow stability/integrity of the fibrous interlayer to be maintained in accordance with the cure cycle, which can be at an elevated temperature.

Polymer choice example: P(St-co-GMA) for highly epoxy compatible nanofibers

Considering the traditional epoxy matrix composite systems, compatibility between the polymeric nanofibrous structure and the epoxy can be incorporated into the choice. The main idea is to create surface modified/reactive nanofibers with epoxide functional groups so that the interfacial bonding with the epoxy-based polymer matrix is improved. As a consequence, the crosslinking between the epoxy and nanofibers is promoted. In the recent study (Ozden et al., 2010), choice of P(St-co-GMA), for which the chemical structure is given in Figure 10.1, has been demonstrated to be superior to polystyrene, which would be another commercially available choice. The custom choice may typically require specific synthesis procedures, as next exemplified.

10.2.1.2 Synthesis and characterization of a custom polymer

In the scope of toughening via electrospun interlayers, the polymer synthesis is a very crucial step in particular for the custom polymer choice as described in the previous section. The correct synthesis of the base polymer does not only affect the nanofiber properties but also determines the electrospinning characteristics in the nanofiber manufacturing. In parallel, another important step is to choose the right synthesis methodology among several conventional polymer synthesis methodologies (Braun et al., 2013) in order to obtain the base polymers with proper molecular weight and polydispersity characteristics required for the electrospinning process. These characteristics of the synthesized polymer must be well characterized and reported. Gel permeation chromatography (Moore, 1964) is an efficient method to determine molecular weight distribution and polydispersity index of synthesized polymers. In addition, nuclear magnetic resonance (NMR) (Hatada and Kitayama, 2004) and

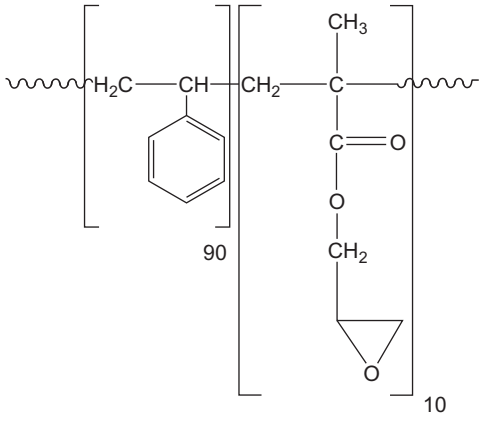

Figure 10.1 Chemical structure of in-house synthesized P(St-co-GMA) polymer with 10 wt% of GMA.

Fourier transform infrared (Koenig, 2005) analyses determine if the synthesized polymer has the targeted chemical structure.

Synthesis example: P(St-co-GMA) copolymer synthesis

Copolymer poly(St-*co*-GMA) can be synthesized by solution polymerization technique as reported in Ozden et al. (2010). Purified styrene and GMA (by weight fractions: 0.9 styrene and 0.1 GMA) are mixed in a test tube contained in ice bath. Dimethylformamide (DMF) is then added into the St-GMA monomer mix such that volume proportion is 3:2, respectively. The initiator azobisisobutyronitrile is added into the test tube flushed with nitrogen. The tube containing the dissolved monomers is then kept in the isothermal bath at 65 °C for 24 h for the polymerization reaction. Finally, the polymer solution is poured out into a beaker containing methanol, and the methanol/polymer mixture is filtered and dried in an oven at 60 °C for 2 h. The synthesized P(St-*co*-GMA) copolymer structure can be determined by ^{1}H NMR. For instance, molecular weights and polydispersities were recorded as 110,000 and 160,000 g/mol (1.35–1.45 PDI).

10.2.2 Process (and characterization)

10.2.2.1 Electrospinning of nanofibers

Electrospinning is widely used for manufacturing nanofibers for a variety of applications, including interlayer toughening. Figure 10.2 presents a typical laboratory setup for the electrospinning process, where a polymer solution in a syringe is charged by

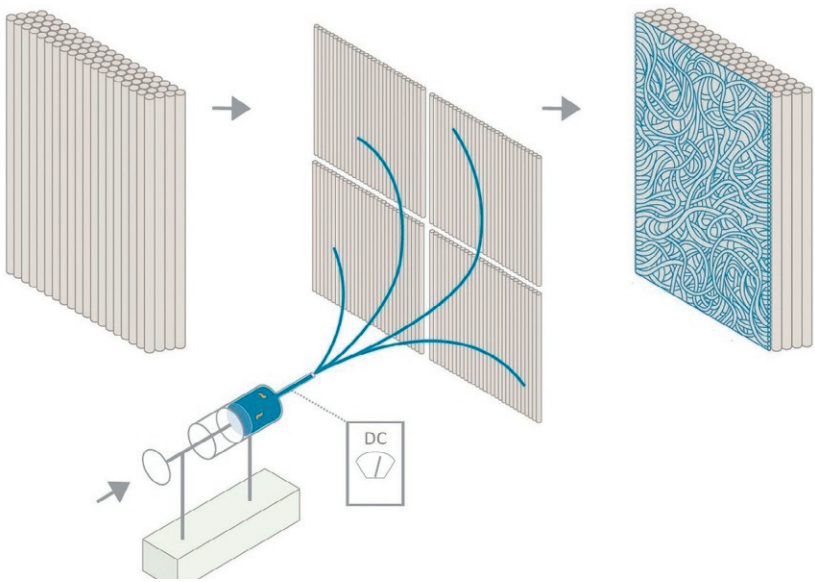

Figure 10.2 A representative electrospinning setup for nanofiber production.

high voltage and an electric field between the tip of the syringe and an electrically grounded collector is formed. When the magnitude of this electrical field overcomes the surface tension of the polymeric solution on the tip of the pipette/syringe needle, the fluid is ejected as a jet from the tip to the grounded collector. During the flight of the jet, the solvent evaporates and the base polymer solidifies, forming nanofiber mats at the grounded collector.

Although it is an efficient and easy way to manufacture nanofibers, the optimal electrospinning process is highly dependent on the correct choice of process parameters, such as tip to collector distance, voltage applied, and the flow rate of polymeric solution as well as the properties of polymeric solutions itself. In terms of electrospinning operation parameters, the applied voltage, distance between the collector and the tip, and the flow rate of the solution inside the pump may be considered as major parameters (Yordem et al., 2008). Depending on the nature of the polymeric solution and targeted morphology, these parameters must be optimized with the help of assessments on the scanning electron microscopy (SEM) images.

Apart from the electrospinning operation parameters, an important fact for nanofiber manufacturing is the need for a homogenous polymer solution. Therefore, it is vital to choose the right solvent for the base polymer to electrospin. The problem of inhomogeneity mostly shows itself during the electrospinning as an unstabilized Taylor Cone (Wendorff et al., 2012) or bead-occupied structures on the nanofiber morphologies, which are arguably undesired in the composite applications. A solution inhomogeneity problem especially occurs when the electrospinning is done in the presence of inclusions, such as CNTs, silica nanoparticles, and numerous other nano- to submicron nanoparticles (Liu et al., 2011). The inclusions can be used to alter/tailor properties of the electrospun nanofibers. However, agglomeration problems may occur which hinder the electrospinning process and cause inhomogeneous particle distribution in/on the nanofibers. Hence, in order to have a homogenous interlayer, the polymer solutions with the nanoinclusions should be well characterized, preferentially with a dynamic light scattering method (Schartl, 2007). Also, a process optimization effort may be followed to determine the optimum particle/inclusion percentage and polymer concentration, aiming to reduce the fiber diameter and typically avoid bead and/or agglomerate formation.

Example: electrospinning on carbon/epoxy prepreg plies

For this specific example, P(St-co-GMA)/DMF solutions were prepared by dissolving 30 wt% P(St-co-GMA) in DMF solution. The solution was stirred for 3 h on a magnetic stirrer. MWCNTs at 1 wt% were also loaded into another batch of the same copolymer solution to consider an additional case with composite nanofiber interlayers. Note that the amount to be added to the solution was determined by a preliminary process optimization study (Ozden et al., 2012). Solutions containing MWCNTs were further stirred for another 24 h to achieve good dispersion. Applied voltage, solution flow rate, and tip-to-ground distance were set at 15 kV, 30 μl/min, and 10 cm, respectively, during electrospinning. The polymer solution was electrospun directly onto carbon/epoxy prepreg layers such that the overall interlaminar regions will be toughened by a thin homogenous layer of nanofibers, with an additional weight as low as 0.2% of the prepreg ply weight.

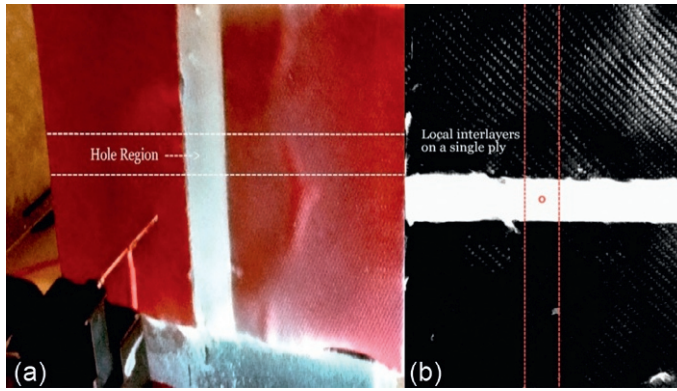

Figure 10.3 (a) Electrospinning with nonconductive mask for OHT specimen preparation. (b) Local interlayer addition over single prepreg ply.

For open-hole tension (OHT) test specimens, the electrospinning was carried out onto the prepreg layers, which were partially masked with a nonconducting and nonadherent plastic layer. As a result, the electrospun nanofibers were only collected on the targeted area of the prepreg layers that is at the intended area—the vicinity of stress raisers (see Figure 10.3a and b, the holes to be drilled after the consolidation of the source laminate for the OHT specimens); there was no weight addition.

10.2.2.2 Manufacturing of structural composites with nanofibrous interlayers

For the manufacturing of nanointerlayered structural composites, the conventional composite manufacturing strategies may be employed. Commonly used methods can be noted as vacuum-assisted transfer molding (Seyhan et al., 2008), RTM (Heijden et al., 2014), and prepreg lamination (Bilge et al., 2012, 2014). Among these manufacturing processes, the prepreg lamination strategy may be arguably classified as the most efficient and superior way to implement nanofibrous interlayers to composite structures; it avoids the possibility of unstable positioning of the interlayer between the dry reinforcing fibers and the resin flow-front pressure during the liquid-molding type productions (resin infusion/transfer), which can also have detrimental effects of the nanofibers network position and structure.

On the other hand, the prepreg lamination requires a certain speed of manufacturing in order to minimize environmental effects such as moisture on the prepreg plies. Depending on the equipment/setup used, the deposition of nanofibers onto prepreg surfaces through electrospinning may demand a considerable amount of time, which can be detrimental to the prepreg plies. Therefore, this process is preferably done in a working area of controlled temperature and humidity, as in a regular prepreg-based production.

This time constraint may be addressed with the targeted use of electrospinning to the potential stress raisers in the structure, as exemplified in Figure 10.3a. The

localized use of nanointerlayers at preferential zones is very effective in terms of time and base material consumption, provided that there are such positions highly prone to damage and/or stress raisers.

10.2.3 Characterization nanofibers and composite

10.2.3.1 Microscopy for interlayer morphology

Microscopy is an essential tool in the assessment of the nanofibrous interlayer study and its composites. The first part is on the study of morphology of the nanofibers that is relevant to both materials and processing. This is because the resultant nanofiber formation depends significantly on electrospinning process variables, the choice of polymer type, solvent, and their solutions along with the operation parameters such as applied electric field. The morphology characterization for nanofibrous materials is typically done by SEM. Fiber diameter distributions may be analyzed via SEM images. Transmission electron microscopy (TEM) or high-resolution transmission electron microscopy (HR-TEM), on the other hand, are typically needed to see nanoscaled particle inclusion if they too are incorporated in the electrospinning process.

Noting that SEM imaging is also very effective in fractography of composite materials, it is used in the fracture surface and cross-section analysis required for understanding the effect/trace of the interlayers on crack propagation and deformation paths along with optical microscopy.

Example: P(St-co-GMA) and P(St-co-GMA)/MWCNT nanofiber morphologies

A systematic study on the electrospinning of P(St-co-GMA)/MWCNT fibers was first carried out and reported by Ozden et al. (2012). Bilge et al. (2012) then implemented the process parameters and material proportion suggested for successful introduction of the MWCNTs and the morphology of the fibrous webs. Figure 10.4 presents the TEM analysis of P(St-co-GMA) electrospun nanofibers composed of 1 wt% MWCNTs and demonstrates that MWCNTs were efficiently placed in the polymeric nanofibers as supplementary pin-like reinforcing elements.

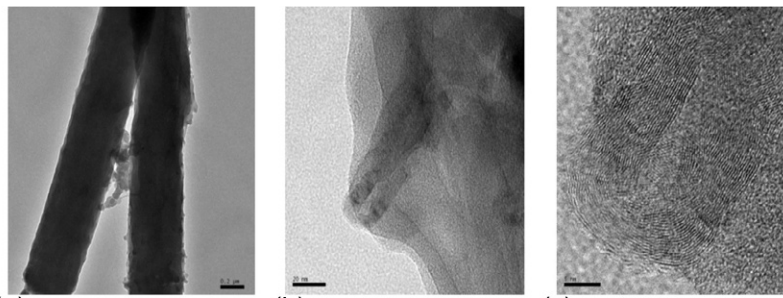

Figure 10.4 TEM images of MWCNTs on nanofiber surfaces. (a) A single fiber. (b) Slice view of a single fiber. (c) Zoomed view of MWCNTs.

10.2.3.2 Compatibility via wettability

Compatibility of interlayer toughening agents with matrix phase forms the main bridge between toughening for both in-plane and out-of-plane responses. Therefore, the interlayer addition specifically asks for a detailed compatibility analysis, which can be done interactively with SEM analysis and drop shape analysis as exemplified in the following section.

Example: epoxy compatible interlayers

Another key aspect in evaluating the properties of polymeric nanofiber morphologies is to determine their *in situ* wettability and stability once exposed to resin and associated curing conditions. High-performance resin systems typically require elevated temperature and pressure for curing. These conditions should be tested for and tailored in regard to the thermal characteristics and limits of the nanofibrous interlayers. Otherwise, the electrospun nanofiber morphologies or network of the nanofibers may not be preserved when integrated into composite laminates.

This evaluation is exemplified in Figure 10.5a–d, which were taken for the nanofibers at the prepreg surface. Figure 10.5a and b belongs to electrospun P(St-co-GMA)/MWCNT nanofibers at room temperature, whereas Figure 10.5c and d belong to the nanofiber morphology at 100 °C (i.e., the curing temperature for the prepreg system). It is clearly visible that the nonwoven fibrous morphology was transformed into a network-like structure composed of fibers covered by epoxy and micron scale epoxy-coated bead-like nodal points. This change in the microstructure suggests the presence of a good interaction and wetting between nanofibrous interlayers and epoxy matrix phase at the laminate curing temperature. Figure 10.6 shows an image of the

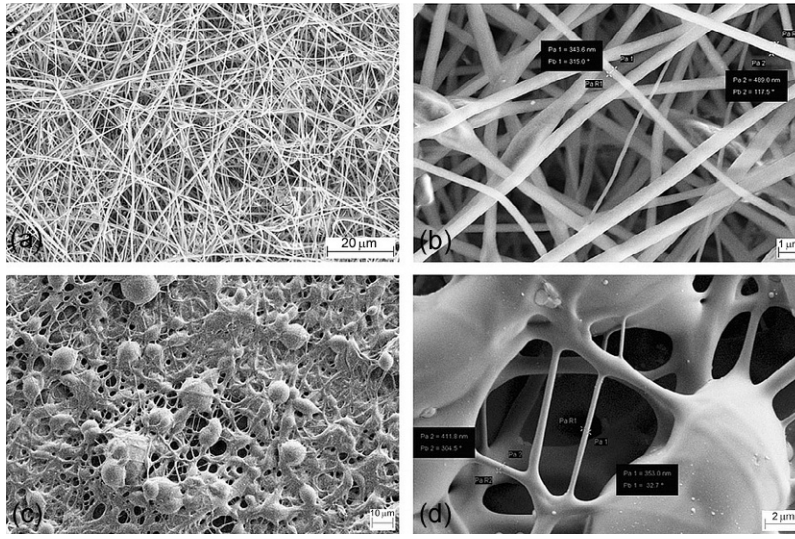

Figure 10.5 Nanofiber morphologies on the prepreg surfaces: (a and b) at room temperature and (c and d) at 100 °C.

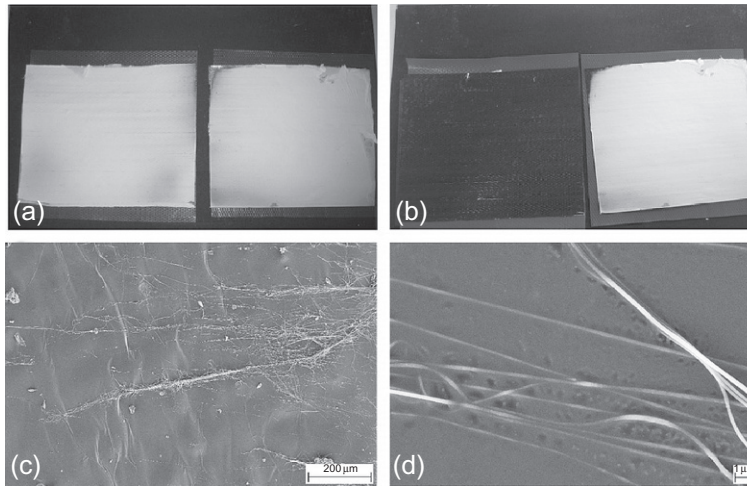

Figure 10.6 Nanofiber morphologies on the prepreg surfaces: (a and b) at room temperature and (c and d) at 100 °C.

electrospun layer-prepreg system kept at curing temperature 100 °C (left-hand side) and pristine samples at room temperature (right-hand side) for comparison. It was quite visible that when the prepreg with the electrospun fibrous layer coat was heated, the epoxy matrix penetrated into the fibrous layer and wetting of the layer was completed, even standing free with no consolidation pressure (i.e., vacuum bagging pressure) (Figure 10.6b). Recall that the zoomed-in view of the surface of unheated laminate in Figure 10.6b appeared as shown in Figure 10.5a. However, when the temperature was increased, those layers of the majority of the nanofibers were no longer visible due to what may be called as progressive self-wetting (Figure 10.6c and d).

More direct and formal investigation of the wettability was performed via contact angle measurements with epoxy/hardener mixture on the surface of the electrospun mat. When a droplet of epoxy/hardener mixture was put on the electrospun mat, it advanced and wetted the surface by leaving an average contact angle as low as 26.5 ± 6.1, as shown in Figure 10.7. This result indicated that the viscous epoxy/hardener

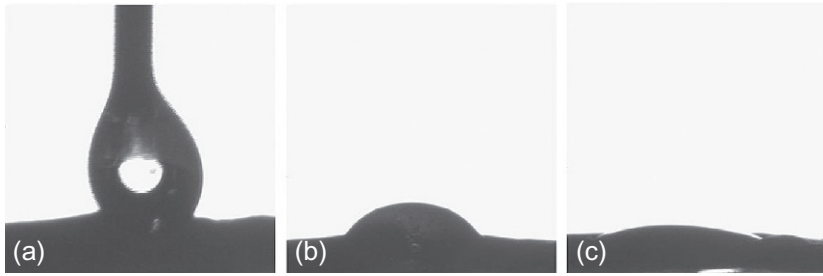

Figure 10.7 An epoxy/hardener drop on the P(St-co-GMA)/MWCNT surface.

mixture could penetrate through the pores in the fibrous surface morphology without challenging a remarkable capillary pressure due to the attractive forces (Feng and Jiang, 2006), which is another indication of the chemical compatibility between the copolymer and the epoxy system.

10.2.3.3 *Mechanical testing of nanointerlayered structural composites*

Example: mechanical testing strategy

Mechanical tests that are included as example in this chapter are summarized in Table 10.2. All of the tests were carried on both neat and P(St-co-GMA) interlayered carbon/epoxy laminates. For some cases, composite interlayers of P(St-co-GMA)/MWCNT were also considered. In addition to these tests, the resistance against delamination can also be measured by short-beam shear and four-point bending tests.

It should be noted that the choice of fiber orientations and stacking sequences of the laminates can be tailored in accordance with the test to be applied and the determination of delamination resistance and/or matrix cracking. Considering (0°) and (90°) fiber orientations in parallel and transverse, respectively, to the major axis (longer side) of rectangular test specimens made by unidirectional composite materials, the use of (0/90) lay-up variations can introduce characteristics for critical failure modes to be toughened about. For instance, the presence of (90°) plies under tension enables the facilitation of matrix cracking/interfiber failure (IFF) described by Knops (2008). Moreover, inducing the matrix cracking initiation and delamination posterior to matured transverse cracking through the 90° ply thickness can be enforced by the presence of (0/90) ply interface, which creates the anisotropic mismatch at the interlayer region maximum. A good example is (90/0/90) configuration, for which interleaved version can be represented as (90/I/0/I/90), "I" denoting the nanofibrous interleaf/interlayer. When it is subject to the three-point bending test, the bottom 90° ply is expected to fail under tension due to transverse matrix failure; an opening and/or shear mode failure with stable crack growth from 90/0 interface can progress and lead to the ultimate failure (Bilge et al., 2012).

10.3 How does the mechanism work?

Under various loading conditions, the toughening of interlaminar regions mainly works against extensive matrix cracking and delaminations, which can cause premature failure of the composite laminates. Transverse matrix cracking in the unidirectional composite materials, for instance, may arise within the individual plies or ply blocks (Johnson and Chang, 2001a,b), where the stresses transverse to their fiber orientation are critical for the given loading conditions. Interlaminar stresses at the interface of the adjacent plies due to the Poisson mismatch and mechanical anisotropy, and presence of the edge stresses or stress raisers such as joints (Shivakumar and Panduranga, 2013), are also potential reasons for mechanism failure.

Table 10.2 Followed mechanical strategy for example case

Test name	Standard	Properties	Lay-up sequence	Interlayer region	Comments on failure+
Three-point bending	ASTM D790	Flexural modulus/ flexural strength	$(0)_x$	All[a]	Both delamination and matrix cracking occur
			$(90/0/90)_x$	All[a]	90° ply tension failure is followed by delamination (more controlled failure)
Charpy impact test	ASTM D6110	Energy absorbed upon impact	$(90)_{xs}$	All[a]	Transverse matrix cracking is dominant
Double cantilever beam	D5528	G_{1c} vs. crack length	$(0)_x$	Only midplane	Opening mode delamination and interlayer bridging effect occurs
End-notched flexure	ASTM WK22949	G_{IIc}	$(0)_x$	Only midplane	Ensures crack initiation and growth from interlayered region
Longitudinal tensile test	ASTM D3039	Tensile strength Elastic modulus Poisson's ratio	$(0)_x$	All[a]	For UD carbon/epoxy composites, early matrix cracking and premature failure are observed
			$(0/90)_{xs}$	All[a]	Premature failure and edge delaminations are observed
Transverse tensile test	ASTM D3039	Transverse tensile strength	$(90)_x$	All[a]	Direct observation of matrix toughening effect
Open-hole tension test	ASTM D5766	Open-hole tensile strength	$(0/90)_{xs}$	All[a] Around hole region	Matrix cracking from the hole region and delaminations are observed
Custom matrix cracking test	ASTM D3039	Resistance to transverse matrix cracking	$(0_2/90_4)_s$	Between 90° blocks	Specific test measuring directly the transverse matrix cracking between 90° plies (Specifics are explained below)

[a]All interlaminar planes.

Depending on the lamination sequence and loading conditions, the matrix cracks inside the laminate can cause a ply-by-ply failure, can induce both internal and edge delaminations, and eventually facilitate fiber breakage by diminishing the effective load transfer between plies (Johnson and Chang, 2001a,b). In this regard, the matrix cracking is an intermediate failure mode and mostly not the direct cause of the ultimate failure. On the contrary, delamination can lead the ultimate failure by totally separating subsequent composite plies.

A custom design test by the choice of $(0_m/90_n)_s$ with the blocks of 90° plies was studied to enforce the transverse cracking in composite laminates (Praveen and Reddy, 1998). Likewise, the suppression of the matrix cracking and IFF can be assessed by the interleaved/interlayered variations of $(0_m/90_n)_s$ as proposed here. Detailed investigation through this experiment design and the effect of nanofibrous interlayers on transverse matrix cracking is used as an example case to show crack suppression achieved through electrospun nanofibrous interlayers.

Custom matrix cracking test and sound-assisted failure analysis for nanofibrous toughening mechanism

A simple and yet effective way to detect the matrix cracking is also exemplified as uniaxial tension tests of custom select laminate. The interlayer(s) are incorporated at various positions through the thickness to correlate the toughening strategy. The base or reference laminate is $(0_2/90_4)_s$. Interleaving levels or cases are selected as $(0_2/90_4/I)_s$ where only midplane is toughened $(0_2/90_2/I/90_2/I)_s$ with three interlayers between the blocks of two 90° plies and $(0_2/90/I/90/I/90/I/90/I)_s$ with seven interlayers between each 90° plies.

An efficient way of characterizing crack initiation and progression is to capture their acoustic signatures during the mechanical testing. The specimens are accompanied by a noise-reducing microphone in order to capture the occurrence of minor and major cracks inside the laminates during the loading as each discrete, mostly invisible, series of cracking events generate sounds. All of the recordings are started in sync with the loading of the mechanical test.

Figure 10.8 corresponds to the representative stress–strain curves of the neat and interlayered/interleaved $(0_2/90_4)_s$ laminates where critical matrix cracking segments are also zoomed in. Test curves and observations suggested that the visible and degrading cracks of the custom select family of laminates occur progressively in the matrix until an ultimate catastrophic failure. Zoomed-in view to the critical matrix cracking segments shows that the critical transverse major matrix cracking in the neat laminates begins earlier than the interlayered counterparts. The resistance against transverse matrix cracking clearly increases with the addition and distribution of the electrospun interlayers. The laminate with the most dispersed interlayers nearly eliminated the damage progression and resulted in the highest ultimate strength.

Supportive evidence of improved cracking and failure behavior can be sought by the assistance of captured acoustic signatures. Figure 10.9 corresponds to the sound spectra of the neat laminate recorded during the mechanical tests. In correspondence with the previous discussions, discrete sound peaks are associated with the minor

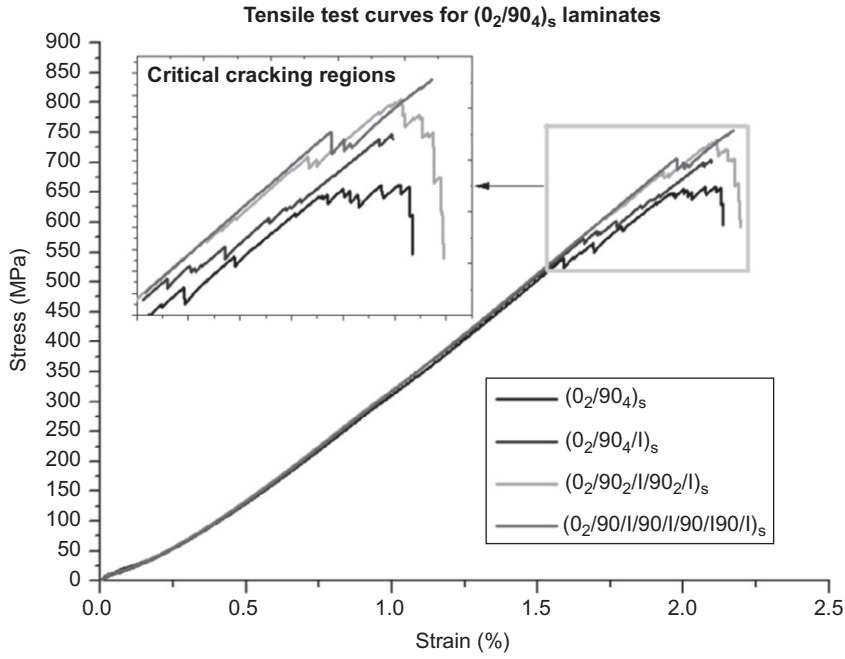

Figure 10.8 Tensile test results for custom matrix cracking test with $(0_2/90_4)_s$ laminates.

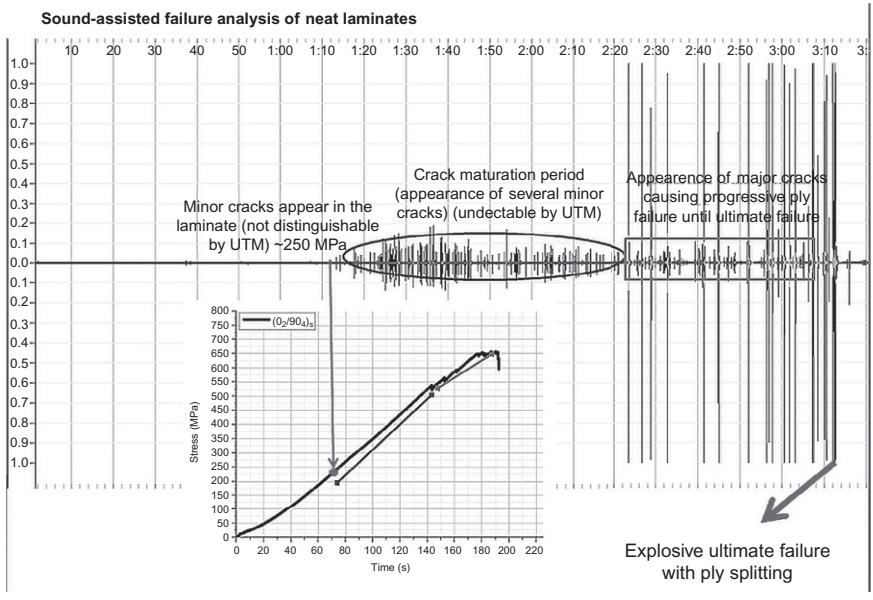

Figure 10.9 Sound spectrum corresponding to the tension test of neat $(0_2/90_4)_s$ laminates.

cracking inside the 90° ply blocks and are observed at about 250 MPa (at an early stage of the test). As the load is increased, such microcracks propagate through the 90° block thickness. Further load ramp-up induces multiple of such through-the-thickness cracks (IFF) and causes crack density to increase until the ultimate fracture is observed. Sound spectrum suggested that maturity and multiplication of internal cracks seem to continue until about 550 MPa. After this maturity period, critical or major cracks causing the failure of overall 90° blocks are correlated with higher amplitude peaks in the sound spectrum. This region exactly coincides with the observed load drops in Figure 10.8. The load drops signify that a major crack was able to move between 90° plies and caused the localized whole-block failure. After this block failure, stress is redistributed over the laminate and it can continue to carry loads until another major crack travels the whole ply blocks at another location. This process continues till the catastrophic ultimate failure, which is differentiated by bold and high amplitude peak at the end of the test.

In the case of $(0_2/90_4/I)_s$ the first sound pickup occurred at about 250 MPa, as in the neat specimen test (Figure 10.10). This is again attributed to the initiation of minor cracks in 90° plies. However, for this case, the crack maturity and multiplication phase continued until about 560 MPa, thanks to the interlayer addition in the midplane, which suppressed the critical crack formation. Both stress–strain curves and higher amplitude sound peaks also suggest an increase of 6% in the ultimate tensile strength of laminates at a lower crack density (Table 10.3).

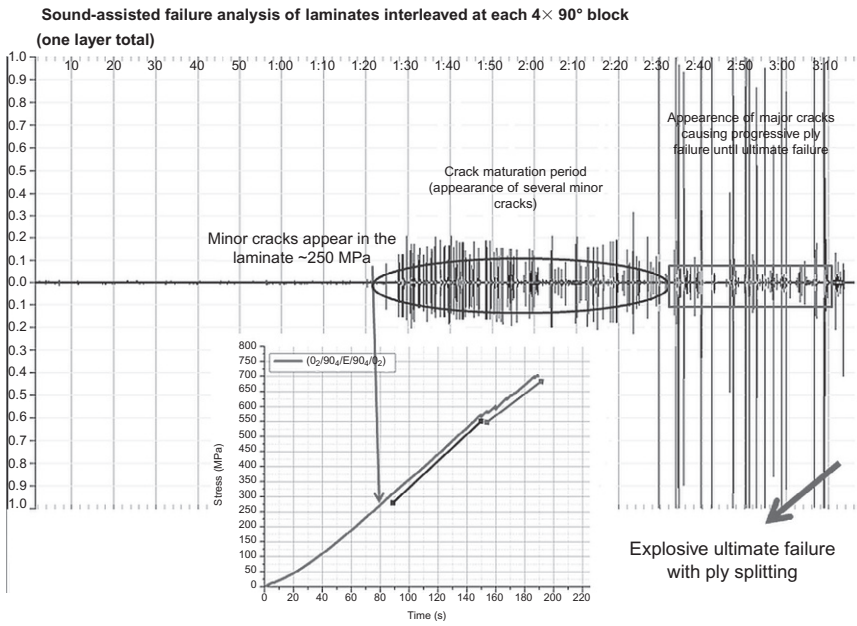

Figure 10.10 Sound spectrum corresponding to the tension test of interlayered $(0_2/90_4/I)_s$ laminates.

Table 10.3 Mechanical property improvements for nanofiber interlayered composites

Test type	Lay-up sequence	Interlayer type	Interlayered sequence	Target property	Neat	Interlayered
Custom matrix cracking	$(0_2/90_4)_s$	P(St-co-GMA)	$(0_2/90_4/I)_s$	Tensile strength (MPa)	645 ± 14	696 ± 28
			$(0_2/90_2/I/90_2/I)_s$			737 ± 5
			$(0_2/90/I/90/I/90/I)_s$			757 ± 4
Uniaxial tension	$(0/90)_{6woven}$	P(St-co-GMA)	$((0/90)_{woven}/I)_6$	Tensile strength (MPa)	493 ± 19	620 ± 11
Open-hole tension	$(0/90)_{6woven}$	P(St-co-GMA)	$((0/90)_{woven}/I)_6$ (only around hole region)	Tensile strength (MPa)	393 ± 9	427 ± 8
Uniaxial tension	$(0)_6$	P(St-co-GMA)	$(0/I)_6$	Ultimate tensile strength (MPa)	1151 ± 70	1312 ± 65
Transverse tension	$(90)_6$	P(St-co-GMA)	$(90/I)_6$	Transverse tensile strength (MPa)	26.5 ± 0.7	31.2 ± 0.6
		P(St-co-GMA)/MWCNT				33.6 ± 0.7
Three-point bending	(0/0/0)	P(St-co-GMA)	(0/I/0/I/0)	Flexural strength (MPa)	875 ± 16	965 ± 17
		P(St-co-GMA)/MWCNT				1002 ± 14
	(90/0/90)	P(St-co-GMA)	(90/I/90/I/90)		243 ± 6	282 ± 9
		P(St-co-GMA)/MWCNT				296 ± 6
End-notched flexure	$(0)_4$	P(St-co-GMA)	(0/0/I/0/0) (only ahead of crack tip on midplane)	G_{IIc} (kJ/m^2)	0.95 ± 0.03	1.47 ± 0.04
		P(St-co-GMA)/MWCNT				1.6 ± 0.1

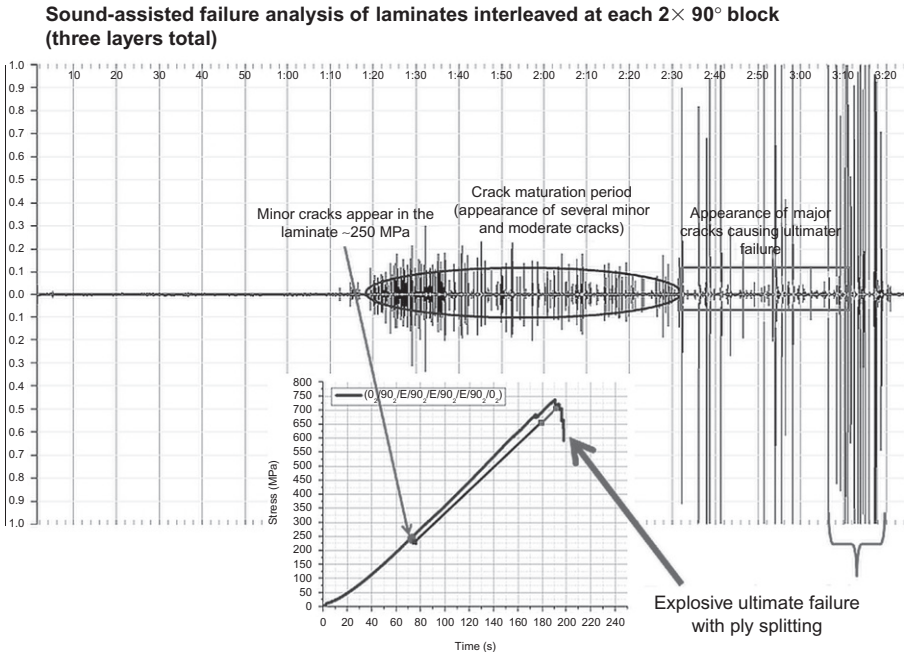

Figure 10.11 Sound spectrum corresponding to the tension test of interlayered $(0_2/90_2/I/90_2/I)_s$ laminates.

In the case of $(0_2/90_2/I/90_2/I)_s$, minor crack initiation stress did not change. However, the interlayer addition for this case significantly delayed the occurrence of the major cracks and extended the crack maturity process up to around 680 MPa. Sound spectrum (Figure 10.11) and significant load drops in the stress–strain curve suggest that the number of critical major cracks were reduced. Hence, the ultimate failure stress was about 10% higher than the neat laminate result.

In the final case of $(0_2/90/I/90/I/90/I)_s$ of seven interlayers (between each 90° ply), the minor crack initiation again began at around 250 MPa whereas the crack maturity period was the longest. Hence, critical matrix cracking was mostly avoided up until 700 MPa (Figure 10.12). In addition, the occurrence of load drops associated with the ply degradation was minimized and ultimate failure stress is up to 15% higher than the neat laminates. This set of experiments on the interlayer toughening by the electrospun nanofibrous interleafs and the sound pickup-assisted failure analysis suggest the following:

- The presence of the nanofibrous interlayers does not seem to affect the initiation of minor crack formations inside the 90° plies.
- Their main role is to suppress microcracks, i.e., delay/avoid the growth and crossing through the interlaminar planes that can cause the ply block transverse failure (degradation). Hence, their presence constrains the occurrence or growth of the major/critical cracks inside the laminates.
- The evaluation of crack progress inside a laminate can easily be spotted and recognized through a simple synchronous sound recording and its postprocessing.

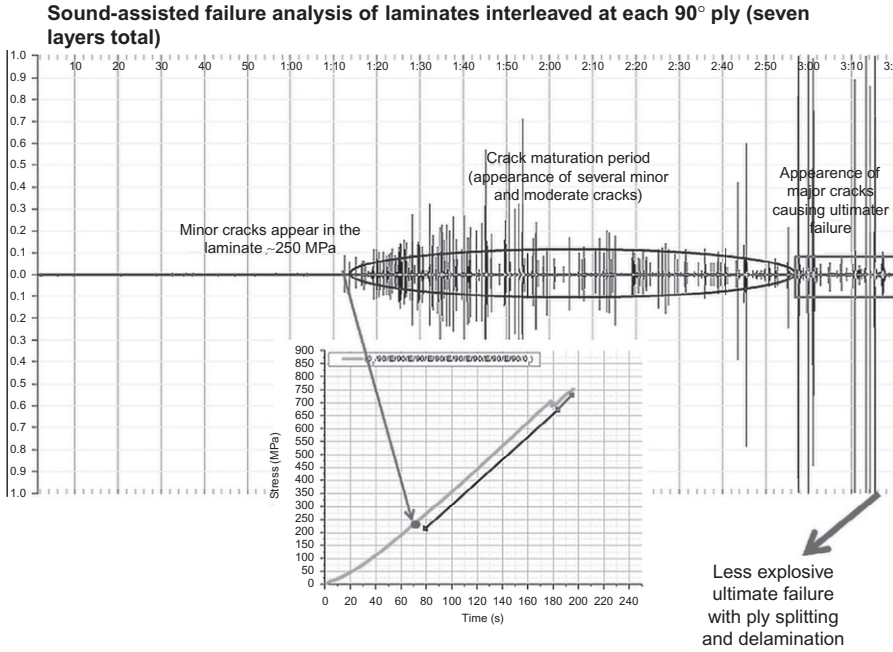

Figure 10.12 Sound spectrum corresponding to the tension test of interlayered $(0_2/90/I/90/I/90/I/90/I)_s$ laminates.

10.4 Changes in mechanical behavior

This section aims to provide supporting evidence for the toughening and mechanical behavior enhancement in the presence of nanofibrous interlayers/interleaves. For consistency with the earlier examples of materials and synthesis, processing and manufacturing sections, the mechanical property improvements achieved through the application of P(St-co-GMA) nanofibers are discussed. The resistance against transverse matrix cracking and delamination are explored as the primary interlayer toughening issues subject to in-plane and out-of-plane loading conditions. For the tests of out-of-plane loading conditions, the addition of 1 wt% of MWCNTs and case study of P(St-co-GMA)/MWCNT composite nanofibers are also provided.

10.4.1 Improvements under in-plane loading

10.4.1.1 Unnotched and OHT tests of woven fabric composites

The free-edge stresses appear to be an extra matrix crack-inducing factor (Shivakumar and Panduranga, 2013). The incorporation of free-edge stresses to the failure analysis is especially critical for damage-based composite design processes in the presence of potential stress raisers. This section explores the mechanical property improvements achieved through the incorporation of global and local (around stress raisers)

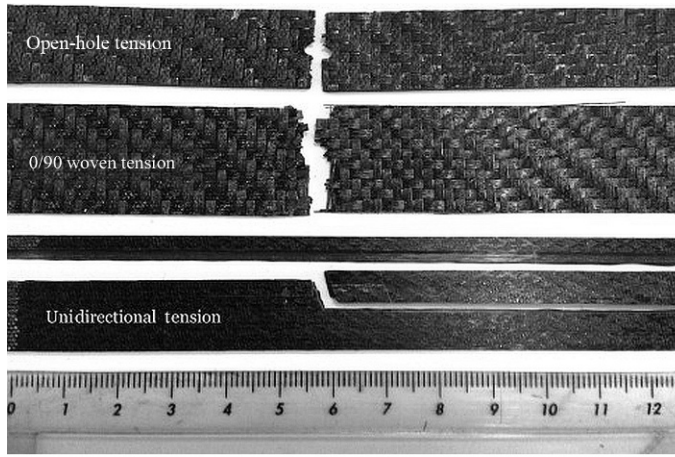

Figure 10.13 Fractured $(0/90)_{6woven}$ OHT (top), unnotched $(0/90)_{6woven}$ tensile (middle), and $(0)_6$ tensile (bottom) specimens.

P(St-co-GMA) nanofibrous interlayers into unnotched and open-hole (0/90) woven fabric/epoxy laminates, respectively. For OHT laminates, the interlayers were placed only in the vicinity around hole region, as shown in Figure 10.6.

For $(0/90)_{6woven}$ fabric carbon/epoxy laminates, the fracture was initiated by matrix cracks from the edges and finalized by fiber failure (Figure 10.13). The failure mode of the neat and interlayered laminates was similar. The early matrix cracking was again characterized by discrete instant cracking noises. The ultimate failure load of $(0/90)_{6woven}$ laminates with P(St-co-GMA) interlayers, however, were 18% higher than the neat ones (Table 10.3). Moreover, the OHT tests done with $(0/90)_{6woven}$ laminates showed a performance increase of 9% (see Table 10.3). For OHT specimens, the failure was mostly dominated by a major crack formation from the periphery of the hole. This observation suggests the following: (i) the in-plane strength increase is attributed to the presence of interlayers since the crack moved through toughened region and (ii) the increase, however, was not as high as it was on the case of unnotched tensile test specimens. It is noteworthy that the amount of interlayer material to cover the near hole region was smaller, and the localization procedure provides efficiency in both the use of time and material compared to the interlayer application on the whole-ply surfaces.

Together with transverse matrix cracking tests, these results suggest that incorporation of nanofibrous interlayers to structural composites is also effective when woven cross-ply fabrics are used. OHT results underlined the fact that the interlayer incorporation may also be limited to stress raising points, which both decreases the electrospinning time and polymer consumption during nanofiber manufacturing.

10.4.1.2 Longitudinal and transverse tension tests of UD laminates

Regardless of the presence of cross-ply interface mismatches or a stress raiser in the structure, IFF, or cracking may be a problematic issue in general for the UD-based composite laminates. For instance, it can also occur during the coupon testing of

$(90)_n$ and $(0)_n$ laminates due to the relatively weak nature of the matrix phase when subject to in-plane loads or the presence of strong, free-edge effects. In both scenarios, initiation of the cracking and IFF decrease the performance of UD laminates and may cause premature failure. In support of toughening by the nanofibrous interleafs/interlayers, P(St-co-GMA) nanofibers can also be incorporated as $(0/I)_6$ and $(90/I)_6$ laminates.

A summary of the test results of laminates with and without interlayers is presented in Table 10.3. The results of longitudinal tensile tests on $(0)_6$ UD specimens indicates that the presence of P(St-co-GMA) interlayers on the interlaminar planes increased the tensile strength of UD composite laminates by 12%. The fracture is thought to be initiated by cracking from the free edges, as suggested by the discrete instant cracking noises throughout the test and the overall failure that occurred due to ply splitting as expected for the tensile tests of UD carbon/epoxy specimens (Figure 10.13).

As for the $(90/I)_6$ laminates subject to transverse tension, integration of P(St-co-GMA) and P(St-co-GMA)/MWCNTs interlayers resulted in a 17% and 27% increase, respectively, in transverse tensile strength (Table 10.3), with negligible weight penalty. The ultimate fracture of the UD transverse tension specimens was in the matrix cracking mode, as expected. The cross-sectional analysis of failed specimens further revealed the difference in ply-to-ply resin structure at the interlaminar plane, which was differentiated by the space between two subsequent carbon fibers. Figure 10.14a corresponds to the cross-sectional view of a laminate of neat epoxy interlayer, where the damage marks occurred due to the resin fracture are clearly visible and the between-ply and in-ply resin fracture patterns are consistent. On the contrary, the resin morphology between the plies (ply-to-ply interface) and inside the plies were different on the cross-sectional fracture surface of the P(St-co-GMA)/MWCNTs interlayered specimens, as can be seen in Figure 10.14b.

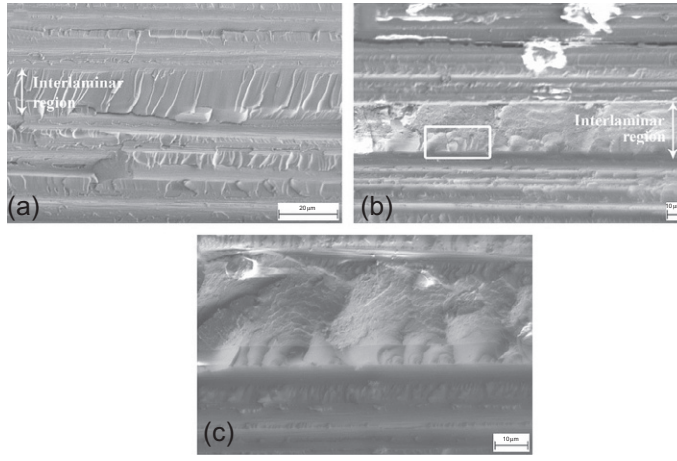

Figure 10.14 Cross-sectional view of a fractured transverse tensile UD test specimen (a) neat epoxy ply-to-ply interface and (b) P(St-co-GMA)/MWCNT interlayered. (c) Zoomed-in view of encircled area in (b).

10.4.2 Improvements under out-of-plane loading

10.4.2.1 Three-point bending tests

Comparison of three-point bending tests on laminates with and without fibrous interlayers showed that their addition led to increase in both flexural strength and modulus of the samples. The nanofibrous interlayers (denoted by I) within the laminates (0/I/0/I/0) resulted in 10% increase in the flexural strength (Table 10.3). Introduction of the nanotubes by 1% weight to the copolymer fibers led to a further improvement, adding up to 15% increase in flexural strength compared to results without nanocomposite interlayers incorporated. Comparing (90/0/90) versus (90/I/0/I/90) laminates, P(St-co-GMA) nanofibrous interlayers increased both the flexural strength of the samples by 16%. The increase in these values was 22% with P(St-co-GMA)/MWCNT interlayers. Postfailure SEM analyses on a cross section of the specimens revealed that the lamination sequence was a factor in the fracture mode. Two distinct active failure mechanisms, transverse matrix cracking and/or delamination, were observed in (0/0/0) laminates (Figures 10.15 and 10.16). Coexistence of the two failure mechanisms on the samples is attributed to the inability of the three-point bending test to create pure shear conditions.

An example is shown in the SEM image of a (0/0) interface represented in Figure 10.17a, where the two corresponding mechanisms were indicated with arrows (1: transverse matrix cracking and 2: delamination). Oblique intra-ply damage (Knops, 2008) initiated at the end of delamination growth occurred due to the presence of high-stress regions at the contact of the loading tip. The flexural strength and

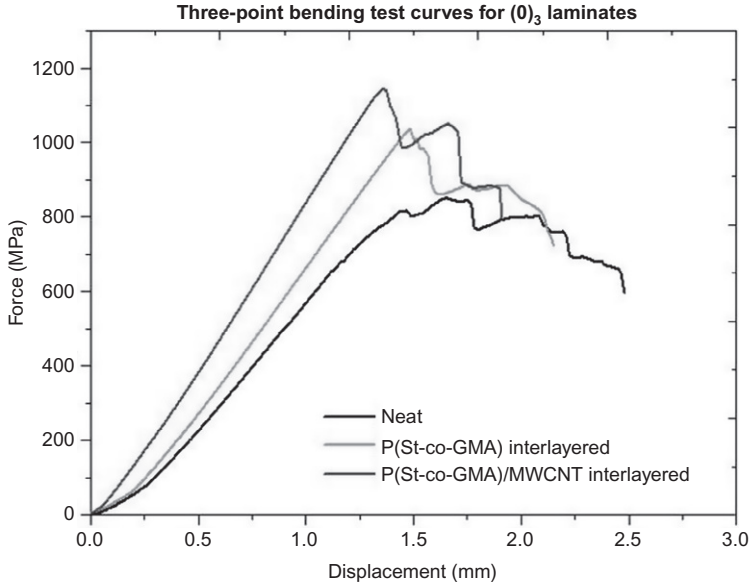

Figure 10.15 Representative three-point bending curves for (0/0/0) laminates.

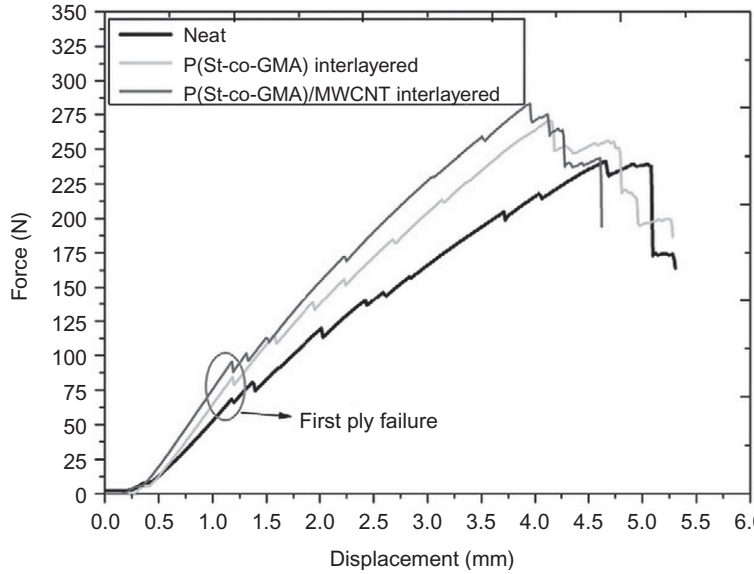

Figure 10.16 Representative three-point bending curves for (90/0/90) laminates.

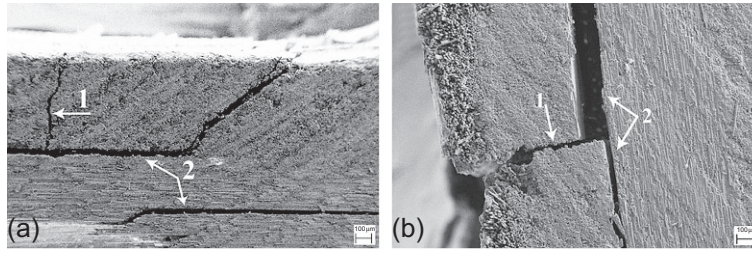

Figure 10.17 Cross-sectional view of fractured three-point specimens. (a) (0/0/0) and (b) (90/0/90).

modulus increase reported by the three-point bending tests characterized both delamination resistance and matrix toughening introduced by the addition of the interlayer. This double effect of the interlayer was also studied and introduced by Sihn et al. (2008).

With (90/0/90) lamination sequence, fracture mechanism was driven by 90° plies. The presence of 90° plies at the outer surface ensured the interlaminar stresses at 90/0 interface due to the stiffness mismatch. In addition, the inherent weak links of 90° plies to tensile loads triggered a matrix crack-induced failure on the bottom ply during bending loading (Figure 10.17). Figure 10.16 shows the representative flexural force–displacement curves of the specimens with and without nanofibrous interlayers/interleafs. The initial load drop corresponds to the first ply failure due to the critical matrix cracking on the bottom 90° ply subjected to tension. Note that the local matrix failure did not cause the ultimate failure. Instead, a stable crack growth characterized

by the load drops was observed, and the final fracture occurred when 90 (degraded)/0 interface progressed to delamination. Hence, the overall flexural performance was governed by two major failure mechanisms.

The increased resistance against initial matrix cracking may be noted by comparing the first ply failure loads, whereas the delamination resistance of laminates may be compared by the ultimate load values. It is clearly visible from Figure 10.16 that the interlayer addition worked well for both mechanisms, as it was suggested for (0/0/0) laminates.

10.4.2.2 End-notched flexure tests

P(St-co-GMA) interlayer presence at the precrack tip increased G_{IIc} by 55% (Table 10.3). Further increase up to 70% in G_{IIc} by P(St-co-GMA)/MWCNTs interlayers suggests that the toughening is also correlated with the incorporation of the MWCNTs on electrospun fiber surfaces.

Failure of ENF specimens was observed as dominated by unstable crack growth parallel to the interlaminar plane with a sudden load drop (Figure 10.18). Formation of an unstable crack growth can be considered as an inherent characteristic in the testing of UD laminates under ENF test configurations with a constant displacement rate (Stevanovic et al., 2003). Further analysis of the fracture surfaces also suggested that the increase observed in G_{IIc} was directly associated with the active role of interlayers on the fracture resistance. Common hackle patterns typically due to the microcrack coalescence (Seyhan et al., 2008) all along the crack pathway are clearly visible on

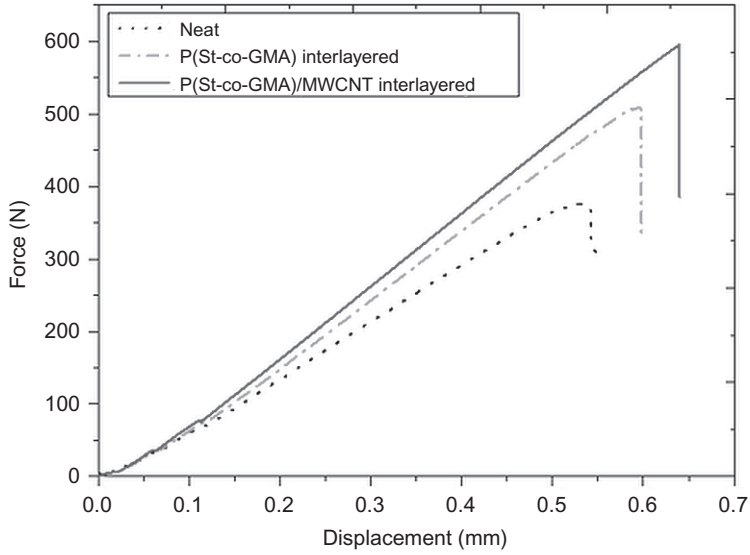

Figure 10.18 Representative end-notched flexure test for (0/0/0/0) laminates with interlayers located midplane ahead of the crack tip on the midplane.

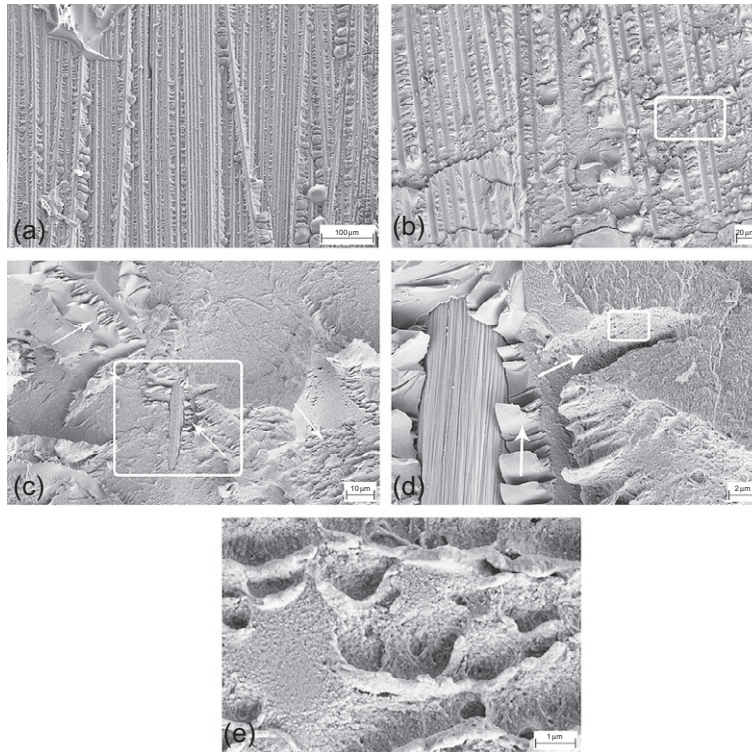

Figure 10.19 Fracture surfaces of (a) neat epoxy ply-to-ply interface and (b) P(St-co-GMA)/MWCNT interlayered interface. Zoomed-in views for (c) encircled area in (b). Arrows: the distinguishable damage marks (d) encircled area in (c), arrows: two distinct failure regions (carbon fiber interface and through interlayer/epoxy complex). (e) Encircled area in (d). Damage marks on interlayer/epoxy complex.

specimens without the nanocomposite interlayers (Figure 10.19a), whereas the hackle patterns for the interlayered specimens are either locally altered and replaced by a more complex structure or enlarged in size (Figure 10.19b). A different fracture mode was noted as the capillary-like damage marks indicated in Figure 10.19c. These damage marks were observed both in the areas consisting of epoxy–interlayer complex (left and right arrows) and around carbon fibers (center arrow) surrounded by an epoxy–interlayer complex (Figure 10.19d). Close examination of the fracture pattern seen in Figure 10.19d revealed the presence of microcrack formation through the interlayer–epoxy complex. This observation can be further supported by the cut-like damage marks inside the interlayer–epoxy complex, for which a zoomed-in image is shown in Figure 10.19e. Furthermore, the epoxy matrix and interlayers were not separated with a distinct interface, which was consistent with the structure shown in Figure 10.6c (image taken on the ply).

10.5 Applications and future trends

Nanofibrous interlayers may find extensive use in nearly all lightweight structural applications where advanced composites are necessary, such as in aerospace, automotive, and energy industries. They can be easily incorporated into existing manufacturing processes and provide substantially enhanced properties, while the weight and thickness increases associated with interleaving is nearly negligible. Additionally, as also exemplified here, with the possibilities for combining the right selection of particles/fillers, the toughening performance can be further enhanced for both in-plane and out-of-plane loading conditions. Moreover, their full potential is even higher with multifunctional possibilities, such as the tuning of mechanical, thermal, and electrical properties by the right choices of nanofiber and filler combinations and proportions. With a complete understanding of the impact on properties by using the nanofibrous interlayers, the opportunities are plentiful for developing characterization and scaled-up production capabilities and integration of the nanofibrous materials into conventional composite engineering design frameworks.

In regard to the high potential of nanofibrous interlayer strategy, some key issues to address and intriguing research fronts to pursue may be noted as follows:

- Scaling up production capabilities incorporating emerging effective, safe-to-use nanotechnology.
- Establishing the value-chain and materials supply for the industrial scale use.
- Ability to tailor nanostructures and nanofiber morphology along with the nanofiller interactions for optimal benefits and multifunctionality.
- New and direct characterization strategies for the nanofiber/filler properties and their interface with the hosting matrix material.
- Fractographic analysis and better understanding of the governing failure mechanisms of the nano–macroscale interaction in composite applications.
- Multiscale modeling strategies correlating well with the experimental development.

Acknowledgment

TUBITAK grant numbers 109 M651, 213 M542, and European Commission under the Marie Curie International Outgoing Fellowship Programme, Grant FP7-PEOPLE-2010-IOF-274737.

References

Bilge, K., Ozden-Yenigun, E., Menceloglu, Y.Z., Papila, M., 2012. Structural composites hybridized with epoxy compatible polymer/MWCNT nanofibrous interlayers. Compos. Sci. Technol. 72, 1639–1645.

Bilge, K., Venkataraman, S., Menceloglu, Y.Z., Papila, M., 2014. Global and local nanofibrous interlayer toughened composites for higher in-plane strength. Compos. Part A 58, 73–76.

Braun, D., Cherdon, H., Rehahn, M., Ritter, H., Voit, B., 2013. Polymer Synthesis, Theory and Practice, fifth ed. Springer, Berlin, Heidelberg.

Carlsson, A., Aksoy, A., 1991. Analysis of interleaved end-notched flexure specimen for measuring mode II fracture toughness. Int. J. Fract. 52 (1), 67–77.
Carlsson, A., Aksoy, A., 1992. Interlaminar shear fracture of interleaved graphite/epoxy composites. Compos. Sci. Technol. 43 (1), 55–69.
Chen, Q., Zhang, L., Rahman, A., Zhou, Z., Wu, X.F., Fong, H., 2011. Hybrid multi-scale epoxy composite made of conventional carbon fiber fabrics with interlaminar regions containing electrospun carbon nanofiber mats. Compos. Part A 42 (12), 2036–2042.
Coleman, J.N.N., 2006. Small but strong, a review of the mechanical properties of carbon nanotube–polymer composites. Carbon 44, 1624–1652.
Duarte, A., Hersxbewrg, I., Paton, R., 1999. Impact resistance and tolerance of interleaved tape laminates. Compos. Struct. 47 (1–4), 753–758.
Dzenis, Y., 2008. Structural nanocomposites. Science 319 (5862), 419–420.
Dzenis, Y., Reneker, D.H., 2001. Delamination resistant composites prepared by small diameter fiber reinforcement at ply interfaces. US Patent 626533.
Feng, X.J., Jiang, L., 2006. Design and creation of super wetting/anti wetting surfaces. Adv. Mater. 18 (23), 3063–3078.
Garcia, E.J., Wardle, B.L., Hart, A.J., 2008. Joining prepreg composite interfaces with aligned carbon nanotubes. Compos. Part A 39, 1065–1070.
Gu, S.Y., Ren, J., Vansco, G.J., 2005a. Process optimization and empirical modeling for electrospun polyacrylonitrile (PAN) nanofiber precursor of carbon nanofibers. Eur. Polym. J. 41 (11), 2559–2568.
Gu, S.Y., Ren, J., Wu, Q.L., 2005b. Preparation and structures of electrospun PAN nanofibers as a precursor of carbon nanofibers. Synth. Met. 155 (1), 157–161.
Hatada, K., Kitayama, T., 2004. NMR Spectroscopy of Polymers, seventh ed. Springer Laboratory, New York.
Heijden, S.V.D., Daelemans, L., Schoenmaker, B.D., Baere, I.D., Rahier, H., Paepegem, W.V., Clerck, K.D., 2014. Interlaminar toughening of resin transfer moulded glass fibre epoxy laminates by polycaprolactone electrospun nanofibres. Compos. Sci. Technol. 10, 66–73.
Hojo, M., Matsuda, S., Tanaka, M., Ochiai, S., Murakami, A., 2006. Mode I delamination fatigue properties of interlayer toughened CF/epoxy laminates. Compos. Sci. Technol. 66 (5), 665–675.
Hossain, M.K., Hossain, M.E., Dewan, M.W., Hosur, M., Jeelani, S., 2013. Effects of carbon nanofibers (CNFs) on thermal and interlaminar shear responses of E-glass/polyester composites. Compos. Part B 44 (1), 313–320.
Huang, Y., Horn, J., 1998. Effects of thermoplastic additives on mechanical properties and glass transition temperatures for styrene-crosslinked low-shrink polyester matrices. Polymer 39 (16), 3683–3695.
Huang, Z.M., Zhang, Y.Z., Kotaki, M., Ramakrishna, S., 2003. A review on polymer nanofibers by electrospinning and their applications in nanocomposites. Compos. Sci. Technol. 63, 2223–2253.
Ishai, O., Rosenthal, H., Sela, N., Drukker, E., 1988. Effect of selective adhesive interleaving on interlaminar fracture of graphite/epoxy laminates. Composites 19 (1), 49–54.
Jiang, W., Tjon, S.C., Chu, P.K., Li, R.K.Y., 2001. Interlaminar fracture properties of carbon fibre/epoxy matrix composites interleaved with polyethylene terephthalate (PET) films. Polym. Polym. Compos. 9 (2), 141–145.
Johnson, P., Chang, F.-K., 2001a. Characterization of matrix crack-induced laminate failure—part I: experiments. J. Compos. Mater. 35, 2009–2035.
Johnson, P., Chang, F.-K., 2001b. Characterization of matrix crack-induced laminate failure—part II: analysis and verifications. J. Compos. Mater. 35, 2037–2074.

Khan, S.U., Kim, J.K., 2011. Impact and delamination failure of multiscale carbon nanotube-fiber reinforced polymer composites: a review. Int. J. Aeronaut. Space Sci. 12 (2), 115–133.
Khan, S.U., Kim, J.K., 2012. Improved interlaminar shear properties of multiscale carbon fiber composites with bucky paper interleaves made from carbon nanofibers. Carbon 50 (14), 5265–5277.
Kim, J.S., Reneker, D.H., 1999. Mechanical properties of composites using ultra fine electrospun fibers. Polym. Compos. 20 (1), 124–131.
Knops, M., 2008. Analysis of Failure in Fiber Polymer Laminates. Springer, Berlin, Heidelberg.
Koenig, J.L., 2005. Spectroscopy, NMR, fluorescence, FT-IR. Adv. Polym. Sci. 54 (1984), 87–154.
Lee, S.H., Noguchi, H., Kim, Y.B., Cheong, S.K., 2002. Effect of interleaved non woven carbon tissue on interlaminar fracture toughness of laminated composites: part 1, mode II. J. Compos. Mater. 36 (18), 2153–2168.
Lee, S.H., Lee, J.H., Cheong, S.K., Noguchi, H., 2008. A toughening and strengthening technique of hybrid composites with non-woven tissue. J. Mater. Process. Technol. 207 (1–3), 21–29.
Li, L., Lee-Sullivan, P., Liew, K.M., 1996. The influence of thermoplastic film interleaving on the interlaminar shear strength and mode I fracture of laminated composites. J. Eng. Mater. Technol. 118 (3), 302–309.
Li, P., Liu, D., Zhu, B., Li, B., Xiaolong, J., Wang, L., Li, G., Yang, X., 2015. Synchronous effects of multiscale reinforced and toughened CFRP composites by MWNTs-EP/PSF hybrid nanofibers with preferred orientation. Compos. Part A 68, 72–80.
Liu, L., Huang, Z.M., He, C., Han, X., 2006. Mechanical performance of laminated composites incorporated with nanofibrous membranes. Mater. Sci. Eng. 435–436, 309–317.
Liu, L., Huang, Z.M., Xu, G.Y., Liang, Y.M., Dong, G.H., 2008. Mode II interlaminar delamination of composite laminates incorporating with polymer ultra thin fibers. Polym. Composite 29 (3), 285–292.
Liu, J., Gao, Y., Cao, D., Zhang, L., Guo, Z., 2011. Nanoparticle dispersion and aggregation in polymer nanocomposites: insights from molecular dynamics simulation. Langmuir 27 (12), 7926–7933.
Liu, L., Zhang, H., Zhou, Y., 2014. Quasi-static mechanical response and corresponding analytical model of laminates incorporating with nanoweb interlayers. Compos. Struct. 11, 436–445.
Magniez, K., Chaffraix, T., Fox, B., 2011. Toughening of a carbon-fibre composite using electrospun poly(hydroxyether of bisphenol A) nanofibrous membranes through inverse phase separation and inter-domain etherification. Materials 4, 1967–1984.
Masters, J.E., 1989. Improved impact and delamination resistance through interleafing. Key Eng. Mater. 37, 317.
Matsuda, S., Hojo, M., Ochiai, S., Murakami, A., Akimoto, H., Ando, M., 1999. Effect of ionomer thickness on mode I interlaminar fracture toughness for ionomer toughened CFRP. Compos. Part A 30, 1311–1319.
Moore, J.C., 1964. Gel permeation chromatography. I. A new method for molecular weight distribution of high polymers. J. Polym. Sci., Part A: Gen. Pap. 2 (2), 835–843.
Nuhiji, B., Attard, D., Thorogood, G., Hanley, T., Magniez, K., Fox, B., 2011. The effect of alternate heating rates during cure on the structure–property relationships of epoxy/MMT clay nanocomposites. Compos. Sci. Technol. 71 (15), 1761–1768.
Ozden, E., Menceloglu, Y.Z., Papila, M., 2010. Engineering chemistry of electrospun nanofibers and interfaces in nanocomposites for superior mechanical properties. ACS Appl. Mater. Interfaces 2, 1788–1793.

Ozden, E., Menceloglu, Y.Z., Papila, M., 2012. MWCNTs/P(St-co-GMA) composite nanofibers of engineered interface chemistry for epoxy matrix nanocomposites. ACS Appl. Mater. Interfaces 4 (2), 777–784.

Ozdil, F., Carlsson, A., 1992. Mode I interlaminar fracture of interleaved graphite/epoxy. J. Compos. Mater. 26 (3), 432–459.

Palmeri, M.J., Putz, K.W., Ramanathan, T., Brinson, L.C., 2011. Multi-scale reinforcement of CFRPs using carbon nanofibers. Compos. Sci. Technol. 71 (2), 79–86.

Pham, S., Burchill, P., 1995. Toughening of vinyl ester resins with modified polybutadienes. Polymer 36 (17), 3279–3285.

Praveen, G.N., Reddy, J.N., 1998. Transverse matrix cracks in cross-ply laminates: stress transfer, stiffness reduction, crack opening profiles. Acta Mech. 130, 227–248.

Qian, H., Greenhalgh, E.S., Shaffer, M.S.P., Bismarck, A., 2010. Carbon nanotube-based hierarchical composites: a review. J. Mater. Chem. 20 (23), 4751–4762.

Rodriguez, A.J., Guzman, M.E., Lim, C.S., Minaie, B., 2011. Mechanical properties of carbon nanofiber/fiber-reinforced hierarchical polymer composites manufactured with multiscale-reinforcement fabrics. Carbon 49 (3), 937–948.

Sadeghian, R., Gangireddy, S., Minaie, B., Hsiaio, K., 2006. Manufacturing carbon nanofibers toughened polyester/glass fiber composites using vacuum assisted resin transfer molding for enhancing the mode-I delamination resistance. Compos. Part A 37 (10), 1787–1795.

Schartl, W., 2007. Light Scattering Polymer Solutions and Nanoparticle Dispersions. Springer Laboratory, New York.

Sela, N., Ishai, O., 1989. Interlaminar fracture toughness and toughening of laminated composite materials: a review. Composites 20 (5), 423–435.

Seyhan, A.T., Tanoglu, M., Schulte, K., 2008. Mode I and mode II fracture toughness of E-glass non-crimp fabric/carbon nanotube (CNT) modified polymer based composites. Eng. Fract. Mech. 75 (18), 5151–5162.

Shivakumar, K., Panduranga, R., 2013. Interleaved polymer matrix composites: a review. In: 54th AIAA/ASME/ASCE/AHS/ASC Structures, Structural Dynamics, and Materials Conference, April 8–11, Boston, Massachusetts.

Sihn, S., Kim, R.Y., Huh, W., Lee, K.H., Roy, A.K., 2008. Improvement of damage resistance in laminated composites with electrospun nano-interlayers. Compos. Sci. Technol. 68 (3–4), 673–683.

Sohn, M.S., Hu, X.Z., Kim, J.K., Walker, L., 2000. Impact damage characterisation of carbon/fibre epoxy composites with multi-layer reinforcement. Compos. Part B 31 (8), 681–691.

Stevanovic, D., Kalyanasundaram, S., Lowe, A., Jar, P.Y., 2003. Mode I and mode II delamination properties of glass/vinyl-ester composite toughened by particulate modified interlayers. Compos. Sci. Technol. 63 (13), 1949–1964.

Subagia, I.D.G., Jiang, Z., Tijing, L.D., Kim, Y., Kim, C.S., Lim, J.K., 2014. Hybrid multi-scale basalt fiber-epoxy composite laminate reinforced with electrospun polyurethane nanofibers containing carbon nanotubes. Fibers Polym. 15 (6), 1295–1302.

Sun, L., Warren, G.L., Sue, H.J., 2010. Partially cured epoxy/SWCNT thin films for the reinforcement of vacuum-assisted resin-transfer-molded composites. Carbon 48 (8), 2364–2367.

Tsotsis, T.K., 2009. Interlayer toughening of composite materials. Polym. Compos. 30 (1), 70–86.

Veedu, V.P., Cao, A., Li, X., Ma, K., Soldano, C., Kar, S., Ajayan, P.M., Ghasemi-Nejhad, M.N., 2006. Multifunctional composites using reinforced laminae with carbon-nanotube forests. Nat. Mater. 5, 457–462.

Wang, Y., Serrano, S., Santiago-Avilles, J.J., 2003. Raman characterization of carbon nanofibers prepared using electrospinning. Synth. Met. 138 (3), 423–427.

Warrior, N.A., Turner, T.A., Robitaille, F., Rudd, C.D., 2004. The effect of interlaminar toughening strategies on the energy absorption of composite tubes. Compos. Part A 35, 431–437.

Wendorff, J.H., Agarwal, S., Greiner, A., 2012. Electrospinning, Materials, Processing, and Applications. Wiley, Weinheim.

White, K.L., Sue, H.J., 2012. Delamination toughness of fiber-reinforced composites containing a carbon nanotube/polymamide-12 epoxy thin film interlayer. Polymer 53 (1), 37–42.

Wilkinson, S.P., Ward, T.C., McGrath, J.E., 1993. Effect of thermoplastic modifier variables on toughening a bismaleimide matrix resin for high-performance composite materials. Polymer 34 (4), 870–884.

Xuefeng, A.N., Shuangying, J.I., Bangming, T., Zilong, Z., Xiao-Su, Y., 2002. Toughness improvement of carbon laminates by periodic interleaving thin thermoplastic films. J. Mater. Sci. Lett. 21 (22), 1763–1765.

Yasaee, M., Bond, I.P., Trask, R.S., Greenhalgh, E.S., 2012a. Mode I interfacial toughening through discontinuous interleaves for damage suspension and control. Compos. Part A 43 (1), 198–207.

Yasaee, M., Bond, I.P., Trask, R.S., Greenhalgh, E.S., 2012b. Mode II interfacial toughening through discontinuous interleaves for damage suspension and control. Compos. Part A 43 (1), 121–128.

Ye, Y., Chen, H., Wu, J., Chan, C.M., 2011. Interlaminar properties of carbon fiber composites with halloysite nanotube-toughened epoxy matrix. Compos. Sci. Technol. 71, 717–723.

Yordem, O.S., Papila, M., Menceloglu, Y.Z., 2008. Effects of electrospinning parameters on polyacrylonitrile nanofiber diameter: an investigation by response surface methodology. Mater. Des. 29 (1), 34–44.

Yudin, V.E., Svetlichnyi, V.M., Shumakov, A.N., Schechter, R., Harel, H., Marom, G., 2008. Morphology and mechanical properties of carbon fiber reinforced composites based on semicrystalline polyimides modified by carbon nanofibers. Compos. Part A 39 (1), 85–90.

Zhang, J., Lin, T., Wang, X., 2010. Electrospun nanofibre toughened carbon/epoxy composites: effects of polyetherketone cardo (PEK-C) nanofibre diameter and interlayer thickness. Compos. Sci. Technol. 70, 1660–1666.

Zhang, J., Yang, T., Lin, C., Wang, C.H., 2012. Phase morphology of nanofibre interlayers: critical factor for toughening carbon/epoxy composites. Compos. Sci. Technol. 72, 256–262.

Zhou, Z., Lai, C., Zhang, L., Qian, Y., Hou, H., Reneker, D.H., Fong, H., 2009. Development of carbon nanofibers from aligned electrospun polyacrylonitrile nanofiber bundles and characterization of their microstructural, electrical, and mechanical properties. Polymer 50 (13), 2999–3006.

Zucchelli, A., Focarete, M.L., Gualandi, C., Ramakrishna, S., 2011. Electrospun nanofibers for enhancing structural performance of composite materials. Polym. Adv. Technol. 22 (3), 339–349.

Zucchelli, A., Gualandi, C., Focarete, M.L., Donati, L., Minak, G., Ramakrishna, S., 2012. Influence of electrospun Nylon 6,6 nanofibrous mats on the interlaminar properties of Gr–epoxy composite laminates. Compos. Struct. 94 (2), 571–579.

Zussman, E., Chen, X., Ding, W., Calabri, L., Dikin, D.A., Quintana, J.P., Ruoff, R.S., 2005. Mechanical and structural characterization of electrospun PAN-derived carbon nanofibers. Carbon 43 (10), 2175–2185.

Toughening mechanisms of nanoparticle-reinforced polymers

11

M.M. Shokrieh, S.M. Ghoreishi, M. Esmkhani
Iran University of Science and Technology, Tehran, Iran

11.1 Introduction

Thermosetting polymeric systems have become considerably useful as the matrix for polymeric composite materials. The highly cross-linked molecular chains give these materials excellent mechanical properties and chemical resistance. However, the brittleness of these materials is a major drawback for load-bearing applications. Considering the brittle fracture behavior of these systems, especially those with preexisting cracks and defects, which are created most often during the process of manufacturing or preparation, many scientific investigations have been performed with the aim of improving the toughness of these materials. One of the earliest methods used to manipulate the toughness of brittle materials is the incorporation of second-phase particles. This chapter provides an overview of the most recognized toughening methods in particulate composite polymers. The latest research on this subject is presented, and some important remarks on choosing the reinforcing agents are discussed.

11.2 Toughening concepts

In general, the toughness of a material is the amount of absorbed energy per unit volume before final fracture. It can be determined by integrating the true stress–strain curve of material. Therefore, tough materials are expected to have sufficiently high strength as well as large strain against failure. Several factors can affect material toughness; the most important are temperature, strain rate, and the existence of flows or cracks. For example, for most materials, a dynamic loading condition or temperature reduction decreases the toughness. In fracture mechanics, the resistance of a material against unstable propagation of a preexisting crack is defined as the fracture toughness. There are two common parameters to characterize the fracture toughness, which are briefly presented in the following sections.

Toughening Mechanisms in Composite Materials. http://dx.doi.org/10.1016/B978-1-78242-279-2.00011-1

11.2.1 Fracture toughness K_{IC}

A parameter called the stress intensity factor (K) is used to describe the stress field near the crack tip (Irwin, 1957). The value of K increases as the applied stress is increased, and finally, at a certain value, unstable crack growth occurs. For a certain material, this critical value strongly depends on the loading condition and stress state. The lowest critical value of K before fracture can be obtained in a plane strain condition when applied stress is perpendicular to crack faces (mode I loading). As a result, mode I critical stress intensity factor in a plane strain condition is considered to be the fracture toughness of the material. For most real cases, when the crack is loaded in tension, the material elements near the crack tip develop a plastic strained region. For brittle materials such as ceramics and glassy polymers, the plastic zone size is small enough so that linear elastic fracture mechanics can effectively characterize the toughness behavior with the stress intensity approach. The plastic zone diameter $2r_y$ can be calculated using the Irwin (1960) model:

$$2r_y = \frac{1}{\pi}\left(\frac{K_{IC}}{\sigma_y}\right)^2 \quad \text{for plane stress condition} \tag{11.1}$$

$$2r_y = \frac{1}{3\pi}\left(\frac{K_{IC}}{\sigma_y}\right)^2 \quad \text{for plane strain condition} \tag{11.2}$$

where K_{IC} is the critical stress intensity factor and σ_y is the tensile yield stress of the material. The plastic zone shape is illustrated in Figure 11.1.

11.2.2 Toughness G_C

The second parameter (G_C) to describe the crack growth is based on Griffith's (1920) energy approach. Griffith's theory is a simple application of the thermodynamic energy conservation law. It assumes that during the fracture, new surfaces are created

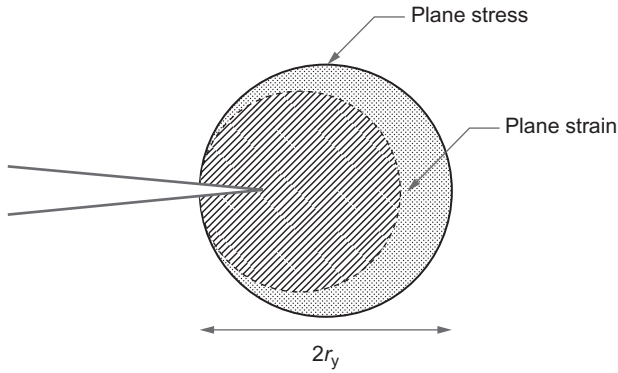

Figure 11.1 Relative size of a plastic zone under plane strain and plane stress conditions (Irwin, 1960).

to release the stored elastic strain energy. Under static loading condition, the work required to extend the crack by the unit length is equal to the dissipated elastic energy:

$$G_C = \frac{dU}{da} = \frac{dW}{da} \tag{11.3}$$

G_C is the critical strain energy release rate, which is a measure of fracture energy and is alternatively called the toughness or fracture toughness. Although in isotropic material G_C is simply related to the critical stress intensity factor (K_C), their relationship is much more complicated for orthotropic materials. Whenever the plastic deformation at the crack tip is not small or the plane strain condition does not exist, which is the case in many structural components, other fracture parameters, such as the J-integral or crack opening displacement, can be used to study the fracture behavior.

Further details on toughness or fracture toughness are available on appropriate fracture mechanics textbooks, but from the overview presented in this section, it can be concluded that almost any method that increases the toughness of a cracked body either decreases the stress intensity at the crack tip or increases the absorbed energy during the fracture process.

11.3 Toughening in polymers

The toughness of brittle polymers can be influenced by many factors. For instance, the curing process and the resultant cross-link density are considered as the most important intrinsic sources of the toughening. On the other hand, any microstructural inhomogeneity, which locally resists the crack propagation, is an extrinsic source of the toughness. Ritchie (1988) classified extrinsic toughening mechanisms as zone shielding and contact shielding. Zone-shielding mechanisms are those operating at the tip of a crack, but contact-shielding mechanisms are those related to crack wake processes.

11.3.1 Particulate toughened polymers

Modifying the polymer matrix with micro- and nanoscale particles is the most common technique to activate the extrinsic toughening mechanisms. Based on the available experimental researches, three types of fillers are used as matrix toughener: (i) rubbery or elastomeric particles; (ii) rigid inorganic particles; and (iii) carbon nanostructures.

Fracture toughness of a thermoset system can substantially improve by incorporation of rubber or thermoplastic particles (Kinloch et al., 1983; Sultan and McGarry, 1973). The major drawback is that these additives undesirably reduce the composite modulus and its thermal properties. On the other hand, microglass spheres and clay platelets can successfully improve both the elastic modulus and fracture toughness (Kinloch and Taylor, 2003; Lee and Yee, 2000a, 2001). Recently, the use of nanometer-sized inorganic stiff fillers such as nanosilica, alumina, rutile (TiO_2), and nanoclay provide the advantage of toughening without notable influence of

precured mixture viscosity, which is an important factor in mass-automated production (Johnsen et al., 2007; Liu et al., 2004; Wetzel et al., 2006).

The third types of particle-modified polymers are those reinforced with carbon nanostructures. Serious attempts to manufacture advanced materials with carbonic nanostructures started from early 2000s (Chen et al., 2003; Gojny et al., 2004; Thostenson and Chou, 2003). Carbon nanotubes (CNTs), carbon nanofibers, and graphene nanoplatelets (GPLs) are among the most frequent choices. Many studies concerning the effects of these rigid carbonic fillers on mechanical and fracture behavior of thermosetting polymers had reported a notable change in fracture resistance with lower filler contents in comparison with inorganic nanoparticles (Rafiee et al., 2009; Zhou et al., 2007, 2008; Shokrieh et al., 2014b). Figure 11.2 represents the increase in fracture toughness and fracture energy of an epoxy matrix with incorporation of GPLs (Shokrieh et al., 2014b). It shows that the fracture toughness of nanocomposites is generally increased by the addition of low contents of GPLs. It also indicates an optimum filler fraction.

Although the most reliable method to study the toughness of particulate polymers is by macroscopic experiment, understanding the fundamental aspects of toughening micromechanics can reduce the burden of checking several factors to achieve an optimized material.

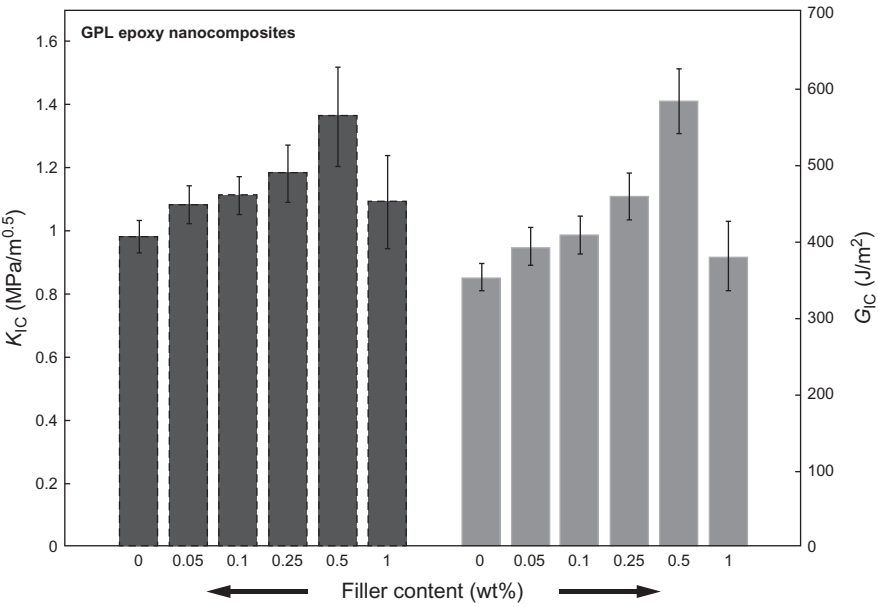

Figure 11.2 Effect of different GPL contents on the fracture toughness and the fracture energy of an epoxy matrix (Shokrieh et al., 2014b).

11.4 Toughening micromechanisms

11.4.1 Crack tip pinning

The theory of crack tip pinning was first expressed by Lange (1970) for the toughness of brittle matrices enhanced by using microsize glass particles. The theory is based on an idea that facing an array of impenetrable obstacles, the propagating crack front is pinned and forced to bow out. By forming local semicircular crack, the interparticle crack length increases until the crack front breaks away at a critical state. Using the concept of "line energy," Lange claimed more energy will be dissipated by increasing the crack length (Eq. 11.4). The crack pinning, which is also referred to as crack trapping or crack front bowing, is represented in Figure 11.3, schematically

$$G_C = G_0 + 2\frac{T}{d} \tag{11.4}$$

where T is the line energy per unit length and d is the interparticle spacing as shown in Figure 11.3.

Evans (1972) extended Lange's model by calculating the stress required to propagate the secondary semicircular cracks and further modified the expressions for the case of semielliptical cracks. His proposed stress analysis showed the required crack stress to extend the fracture surface depends on the ratio of the obstacle dimension to the obstacle spacing. Figure 11.4 shows the predicted fracture energy calculated from Evans's model in case of spherical impenetrable particles. It is noteworthy that the maximum points in the experimental curves were not predictable with the theoretical model. Evans suggested that reversing the rising trend can be attributed to the possibility of the particle penetration.

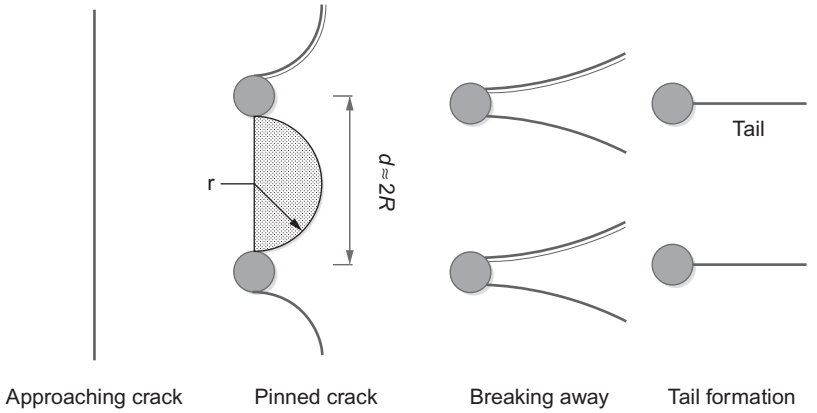

Figure 11.3 Formation of semicircular secondary cracks at the pinning stage and subsequent tail formation (Lange, 1970).

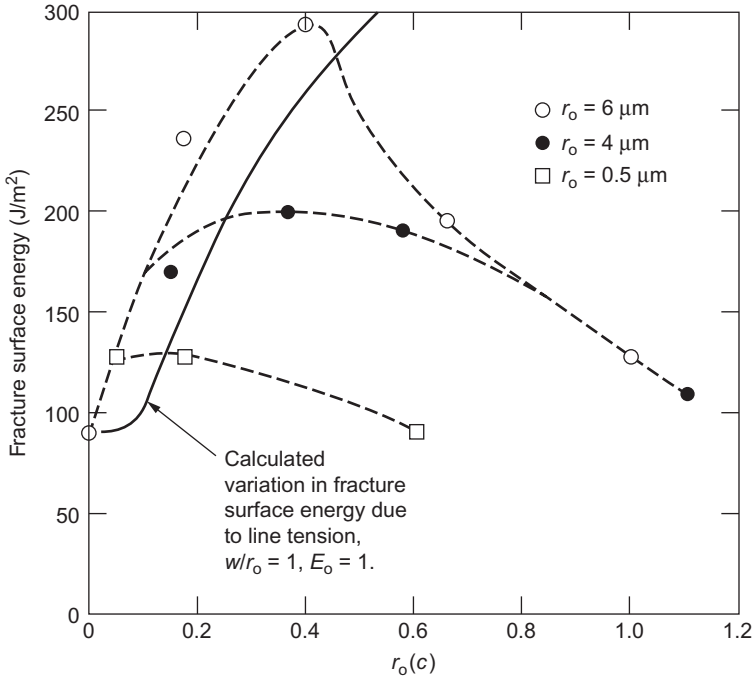

Figure 11.4 The fracture energy predictions for spherical, impenetrable particles compared with Lange and Radford experimental results (Evans and Faber, 1983b).

Rose (1987a) considered that the inclusions behave as separated spring and suggested that both the bridging and pinning are likely to affect the fracture process. The variation of the fracture toughness is as in the following expression:

$$\frac{k^c}{k^\circ} = \frac{\left\{\left(\frac{2S}{\lambda}\right) + \left(\frac{2r}{\lambda}\right)\left(\frac{k_L}{k^\circ}\right)^2\right\}^{1/2}}{F_1(kl)} \tag{11.5}$$

where λ is the interparticle distance and r is the inclusions radius, k_L denotes the second-phase critical stress intensity factor, which determines the possibility of cutting through $(k_L < k^\circ)$ or circumventing the particles $(k_L > k^\circ)$. Moreover, F_1 is an interpolation function. Compared to Lange and Radford (1971) experimental results, Rose's model successfully predicted maximum condition in a relative toughness. Bower and Ortiz (1978) investigated different possible types of interactions between the crack front and inclusions. For the case of cracks penetrating the obstacles, the toughening due to the trapping, neglecting the bridging formation, is calculated using the following equation:

$$k^\infty = \left\{\left(k_c^o\right)^2 + \frac{2R}{L}\left[\left(k_c^p\right)^2 - \left(k_c^o\right)^2\right]\right\}^{1/2} \tag{11.6}$$

where k_c^p is the fracture toughness of reinforcing particles and k_c° is the fracture toughness of unmodified matrix. Moreover, R is particle radius and L is distance between neighboring particles. In case of highly tough and impenetrable particles, both crack bridging and crack pinning occur $\left(k_c^p > 7k_c^\circ\right)$. Bower's and Ortiz's calculations for $R/L < 0.25$ can be accomplished in the following approximated expression:

$$\frac{k^c}{k^\circ} = 3.08\ R\Big/L\ \frac{k_c^p}{k_c^\circ} \tag{11.7}$$

where k^c and k° are stress intensity factor of modified and neat matrix, respectively.

In Lang's model, the influence of particle size indirectly affects the particle spaces. So, for a certain volume fraction, the predicted pinning energy will significantly increase in case of using nanoscale particles. Further studies (Evans, 1972; Green and Nicholson, 1979) also concluded that crack-pinning contribution decreases with the growth of particle size.

In experimental studies, evidence of crack-pinning mechanism in the fracture surface of epoxy reinforced with micron-sized glass particles has been observed (Kinloch et al., 1985). After breaking away, interception of adjacent bowed cracks creates tails behind the particles (Figure 11.3). Pinning sites in the fracture surface of a GPL/epoxy specimen is shown in Figure 11.5. It shows that the crack pinning takes place, if the size of GPL clusters reaches a certain value. Johnsen et al. (2007) indicated that the crack pinning is unlikely to happen in case of reinforcement with nanosilica due to their relatively small dimensions. They proposed an empirical limit for the crack-pinning mechanism, which will require the dimensions of reinforcing particle to be

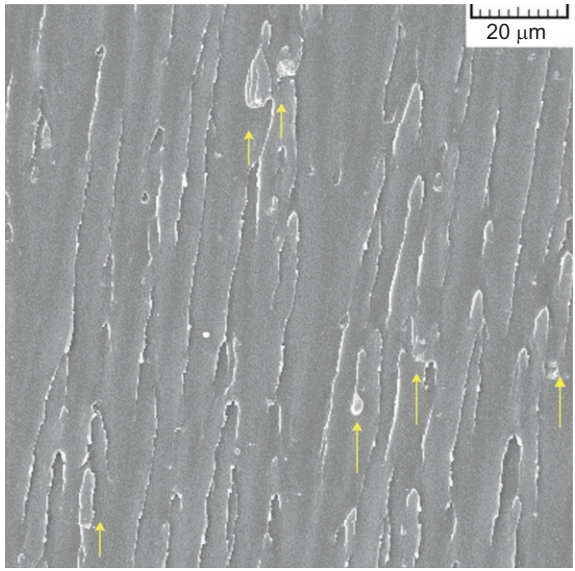

Figure 11.5 Fracture surface of GPL/epoxy composites. Evidence of the crack tip pinning is indicated by arrows (Shokrieh et al., 2014b).

comparable with the crack tip opening displacement (CTOD). CTOD can be approximated by the following equation (Kinloch and Young, 1983):

$$\mathrm{CTOD} = \frac{k_c^2}{E\sigma_y}\left(1-v^2\right) = \frac{G_c}{\sigma_y} \tag{11.8}$$

where σ_y, E, and v are the yield stress, Young's modulus, and Poisson's ratios of unmodified matrix. Accordingly, for particles with all dimensions in nanoscale, crack pinning is not expected.

11.4.2 Crack deflection

Evans and Faber (1983a,b) developed a fracture mechanics approach to express the toughening due to the crack path deflection process in particulate composites. In the deflection theory, the second phase inclusion deviates the crack out of its initial plane and produces a nonplanar propagating crack. The local behavior of the crack tip consists of an initial tilting and a subsequent twisting (Figure 11.6). The tilted crack tip causes a mixed-mode I/II (opening/sliding) stress state, while the twisted crack encounters a mixed-mode I/III (opening/tearing) condition. This mode mixity increases the total energy required for the fracture process, which results in a fracture toughness improvement. The mixed-mode fracture energy during the deflection process can be described using Eq. (11.9) in terms of local stress intensity factors:

$$EG = K_I^2\left(1-v^2\right) + K_{II}^2\left(1-v^2\right) + K_{III}^2\left(1-v^2\right) \tag{11.9}$$

The local stress intensity factors for tilted and twisted cracks can be computed from applied stress intensity factors (Cotterell and Rice, 1980). For a crack tilted by an

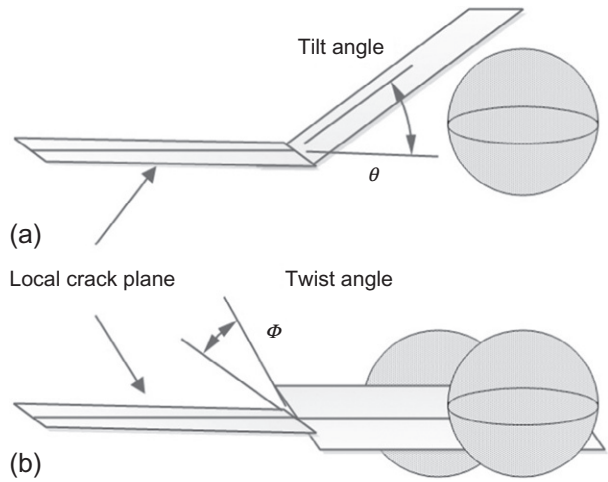

Figure 11.6 Schematic representation of crack tip tilting and twisting (Evans and Faber, 1983a,b).

angle of θ, the local stress intensity factors are given by Eq. (11.10). The corresponding expression for a crack twisted at angle ϕ is presented in Eq. (11.11):

$$\begin{aligned} k_{\mathrm{I}}^{t} &= C_{11}(\theta)K_{\mathrm{I}} + C_{12}(\theta)K_{\mathrm{II}} \\ k_{\mathrm{II}}^{t} &= C_{21}(\theta)K_{\mathrm{I}} + C_{22}(\theta)K_{\mathrm{II}} \end{aligned} \tag{11.10}$$

$$\begin{aligned} k_{\mathrm{I}}^{T} &= D_{11}(\phi)k_{\mathrm{I}}^{t} + D_{12}(\phi)k_{\mathrm{II}}^{t} \\ k_{\mathrm{III}}^{T} &= D_{31}(\phi)k_{\mathrm{I}}^{t} + D_{32}(\phi)k_{\mathrm{II}}^{t} \end{aligned} \tag{11.11}$$

where $C_{ij}(\theta)$ and $D_{ij}(\phi)$ are given angular functions. Faber and Evans derived the toughening increment for three different morphologies of spherical-, rod-, and disc-shaped particles, assuming it depends only on filler's shape and volume fraction. They expressed that maximum toughening arises for rod-shaped particles in the crack deflection theory. Moreover, the experimental results for a glass matrix with second-phase ceramics verified the independence of the crack deflection model from the particle size (Evans and Faber, 1983b). Experimental evaluation of the crack deflection theory for a polymeric matrix modified with inorganic fillers can be assessed in the study of Kinloch and Taylor (2002). They compared the experimental results with the predictions of the crack deflection theory (Evans and Faber, 1983a), assuming a uniform spacing distribution. For hollow glass spheres and disc-like mica flakes with an approximate size of 10 μm, a good qualitative agreement was observed. However, the relative fracture energy for rod-shaped Wollastonite ($CaSiO_3$) and larger mica particles (>40 μm) stayed far below the predictions, indicating a contrary to the assumption of particle size independence in Faber and Evans's crack deflection model. In fact, the crack deflection is strongly influenced by particle size, so that for particles smaller than the CTOD, tilting the crack tip is not possible (Johnsen et al., 2007).

Continuous local deflection of the crack front increases the roughness of the fracture surface. Although measuring the exact surface area increase is not easily feasible due to the intricate morphology of the visible surface or microcracks generated slightly below the surface, Faber and Evans approximated the surface area increase by modeling the deflection-induced roughness as a row of cones and formulated a lower bound for normalized fracture energy. The normalized toughness increment for spherical particles as a function of center-to-center particle spacing Δ and particle radius r is shown in the following equation:

$$\frac{G_{\mathrm{c}}^{\mathrm{s}}}{G_{\mathrm{c}}^{\mathrm{m}}} = \frac{1}{2}\left(1 + \frac{\sqrt{\left(\Delta/2\right)^2 + r^2}}{\Delta/2}\right) \tag{11.12}$$

where $G_{\mathrm{c}}^{\mathrm{m}}$ is the energy release rate for un-deflected crack.

Kitey and Tippur (2005a,b) investigated the effect of glass particle size and filler–matrix adhesion strength on the fracture toughness of epoxy matrix. Spherical particles of diameter 7–200 μm were used at a constant volume fraction of 10%. Trying to establish a correlation between the surface roughness and the fracture toughness, they defined the surface profile Ra as a combination of the particle-related roughness Ra_{p}

and roughness due to fracture process Ra_f, which is named as the "fracture induced roughness." By excluding effects of the particle size and volume fraction, it was concluded that the toughness increment depends on overall surface roughness, and Ra_f is the only proportional parameter:

$$\Delta K_I = \beta \frac{\sigma_c^f - \sigma_c^m}{\sqrt{D}} Ra_f \tag{11.13}$$

where σ_c^f and σ_c^m are the critical far-field stresses required for the fracture of composites and the neat epoxy, D is the particle diameter, and β is the proportionality constant. Kitey and Tippur related the toughness increase for a strong filler–matrix interface to the crack deflection behavior; while in the case of weakly bounded interfaces, a combination of twisting the filler and subsequent blunting due to complete debonding happens. A locally blunted crack requires additional energy to reinitiate the crack and causes greater impact on toughness increment than the prescribed tilting and twisting. According to Eq. (11.13), the fracture toughness of particulate composites could not be invariant with the particle size if the volume fraction remains untouched.

The increase in the surface roughness, which is generally recognized as an important indicator of crack deflection mechanism, has been widely observed in SEM micrographs of modified composites fracture surfaces (Kinloch and Taylor, 2006; Rafiee et al., 2010; Wang et al., 2011). Although in most cases, a linear relationship between the surface roughness and the fracture energy is reported, increasing the fracture energy is not completely explainable with the fracture surface increase (Wetzel et al., 2006).

11.4.3 Microcracks

In particle-reinforced glassy polymers, microcracks occur in the form of debonding at weakly bonded particle matrix interface (Evans et al., 1985). The interaction of microcracks with a maincrack is studied by several authors. It is stated that the microcrack zone in some cases results in a lower crack resistance at the macrocrack tip and promotes the crack advance and in other cases increases the crack resistance and can be considered as a toughening mechanism. Influence of microcracks on the fracture propagation can be studied in two different ways: (i) energy dissipation due to the nucleation of micro-cracks (Evans and Faber, 1983c; Evans and Fu, 1985) and (ii) change in local stress intensity factor by modeling the interaction of one or several microcracks with the main crack (Dolgopolsky et al., 1989; Kachanov and Montagut, 1986; Rose, 1986; Rubinstein and Choi, 1988).

In the first category (Evans and Faber, 1983c; Evans and Fu, 1985), the effects of microcracks on R-curve behavior of materials are predicted. They classified the microcrack toughening as the frontal process zone and crack wake process zone. They concluded that the damage produced by the process zone countervails the shielding effect of frontal process zone so that toughness change is relatively weak. On the other hand, unloading in the wake zone provides an additional contribution to the crack shielding in the form of energy dissipation so that crack resistance in a microcracked zone continuously increases with the main crack growth.

Rose (1986) utilized a point-source representation for microcracks to determine the stress perturbation near a main crack surrounded by microcracks. Rose's calculations for symmetrical microcracks introduced the shielding function. A special case of microcrack parallel to the main crack variation of shielding function indicates that $\theta \approx 70$ is the neutral-shielding angle in which the antishielding effect turns to the shielding effect. Kachanov et al. (1990) statistically analyzed the interaction of microcrack arrays with the main crack. Their analysis for different 2D and 3D microcrack configurations showed that the microcrack toughening in the form of influence on the crack tip stress intensity is insignificant.

11.4.4 Crack bridging

Crack bridging takes place at a wake behind the crack front where the bridging ligaments connect the crack faces. By adding extra pressure during the crack opening, these bridging elements decrease the stress intensity near the crack tip and thus toughen the brittle material. In general, crack bridging can be simulated as a series of distributed springs that are connected to crack faces in both ends and insert closure force (Krstic, 1983; Rose, 1987b; Figure 11.7a). For a small scale bridging (the length of the bridging zone is very small compared to specimen dimensions), which is the case for toughening with micron-sized particles, the toughening ratio for spherical particles with linear elastic response is expressed as (Budiansky et al., 1988)

$$\frac{K_c}{K_m} = \sqrt{\frac{E_c\left(1-v_m^2\right)}{E_m\left(1-v_c^2\right)}(1-c)}\left\{1+{}^{\pi}/_{2}\frac{\sigma_u^2 ac(1-\sqrt{c})}{K_m^2}\right\}^{0.5} \tag{11.14}$$

where c and m subscripts denote the elastic and fracture properties of composite and matrix, respectively. Moreover, σ_u is the particle strength at failure, a is the average particle radius, and c is the second phase concentration factor (Figure 11.7b).

The spring approach for studying the bridging mechanism in brittle metal or ceramic matrices toughened by ductile metallic phase is conventional. However, the application of these types of particles for brittle polymers is rare. On the other hand, it has been shown that rubber additives can bridge the crack faces in a brittle polymer matrix (Kunz-Douglass et al., 1980; Huang and Kinloch, 1992a; Pearson and Yee, 1991). Kunz et al. related the toughness increment of a rubber-modified epoxy to the elastic energy, which stores in bridged rubber and dissipates during the particle failure. They showed that instead of rubber strength, particle tearing limits the maximum energy storage so that variation of the fracture energy for a dispersion of rubber particles of volume V_p can be determined using the following equation:

$$\Delta G_{IC} = 4\Gamma_t\left(1-\frac{6}{\lambda_t^2+\lambda_t+4}\right)V_p \tag{11.15}$$

In which Γ_t is the tear energy of the rubber and λ_t is its extension prior to failure. According to this model, rubber bridging has a linear dependence on volume the

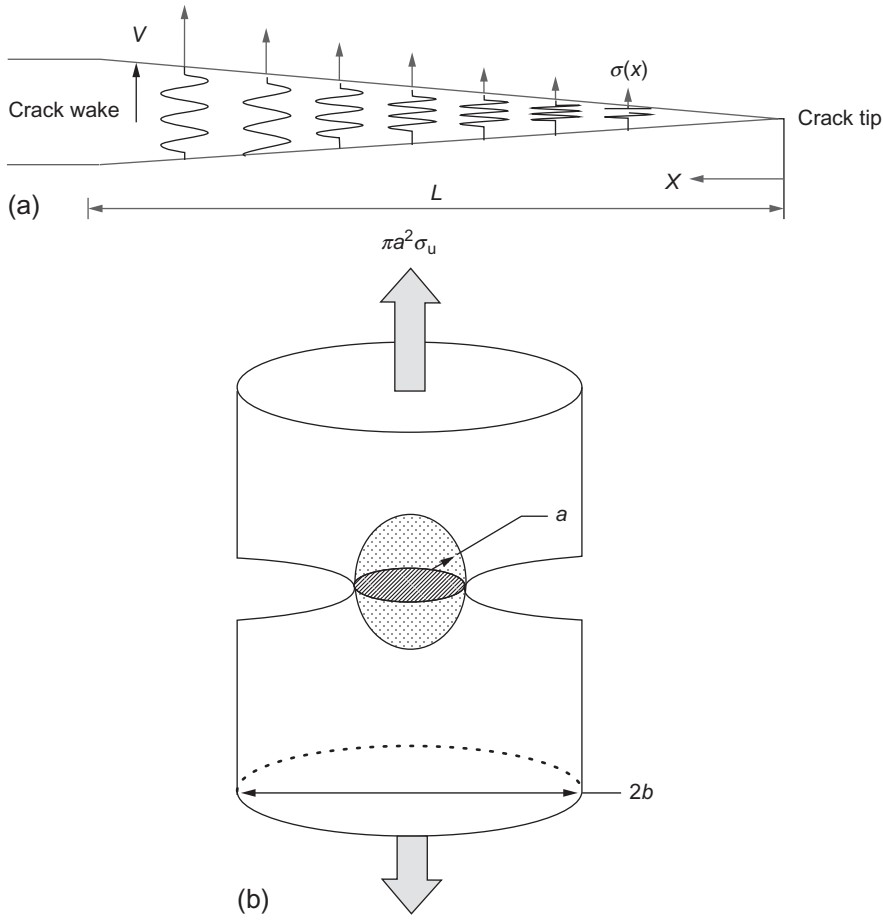

Figure 11.7 (a) Crack bridging by springs and (b) determining the effective spring constant for spherical particles with concentration factor $c = \left(\frac{a}{b}\right)^2$ (Budiansky et al., 1988).

fraction of particles. Their experimental results for particles with diameter range from 0.2 to 40 μm shows that although tearing strain of smaller particles is higher than that of large ones, the fracture energy does not change significantly with the incorporation of smaller particles. In contrast, Pearson and Yee (1991) related the major contribution of the toughening with small particles to void formation and shear banding. They suggested that only the rubber particles that are larger than the matrix plastic zone can bridge the crack faces (Pearson and Yee, 1991). Their observations indicate that the rubber bridging has a moderate toughening effect. Later in 1992, Huang and Kinloch utilized a quantitative approach to determine the dominant toughening mechanisms in rubber-modified epoxy composites. They calculated the toughening increment for the rubber bridging, shear banding, and plastic void growth. It was concluded

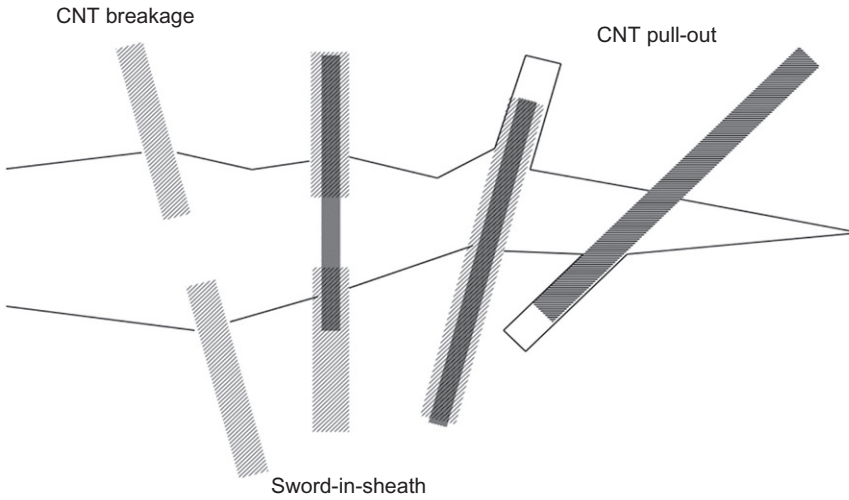

Figure 11.8 Schematic representation of CNT breakage, CNT pull-out, and sword-in-sheath mechanism.

that the effect of particle bridging in such composites is negligible. Meanwhile, in low temperatures, where the absence of matrix yielding diminishes the plastic void formation, rubber bridging can have a considerable proportional contribution. Increase in toughness with rubbery particles is further discussed in the next sections; however, here, we focus on the crack bridging in polymers by stiff brittle reinforcements (Figure 11.8).

For bridging by brittle short fibers, interfacial shear forces increase until the particles either brake or debond from the matrix. The interfacial debonding followed by the subsequent frictional pulling-out process greatly influence the material toughness. The fracture energy associated by fibers pull-out is expressed by Hull and Clyne (1996) as

$$\Delta G_{\text{pull-out}} = \int_0^l \frac{N\pi r x^2 \tau_i}{l} \mathrm{d}x = \frac{V_f l^2 \tau_i}{3r} \tag{11.16}$$

where τ_i is the interfacial shear strength, r is the fiber radius, l is the pull-out length, and N is the number of fibers per unit area.

CNTs are commonly known for having the potential for bridging the crack in polymeric composites (Fiedler et al., 2006). Total lengths of these carbonic structures are typically large enough (>10 μm) so that a small bridge zone in the wake of crack appears. For multiwalled carbon nanotubes (MWCNTs) apart from the pulling-out mechanism, another sword-in-sheath mechanism is observed (Yu et al., 2000). The outer layer of MWCNT is strongly bonded to the matrix and most shear traction is transferred through this layer. In sword-in-sheath mechanism the outer CNT layer is assumed to break before complete pull-out of the inner section. Note that according

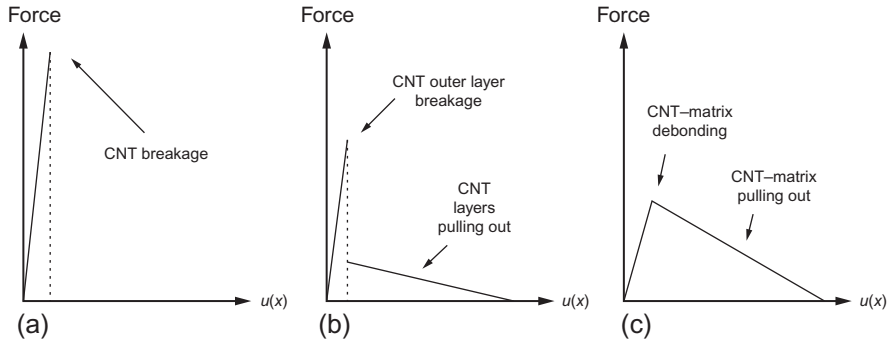

Figure 11.9 Force–displacement modeling of CNT-bridging laws. (a) CNT total breakage; (b) CNT sword-in-sheath mechanism; and (c) CNT pull-out mechanism (Blanco et al., 2009; Tong et al., 2008).

to experimental data for force–displacement relationship for a MWCNT being pulled-out from the matrix, the energy dissipation during debonding or outer layer breakage is much lower than the part for the frictional pulling process (Figure 11.9). As a result, ignoring the initial part is an acceptable assumption for the modeling of a mathematical bridging behavior. The effect of perfectly aligned MWCNTs bridging on interlaminar toughness of polymeric composites is studied experimentally (Garcia et al., 2008) and later theoretically (Blanco et al., 2009; Tong et al., 2008). Equation (11.17) describes the interlaminar fracture energy considering the closure effect by MWCNTs:

$$G_R = G_c + \frac{dU_{CNT}}{da} \tag{11.17}$$

where G_c is the required fracture energy for growing fracture surface by da, and U is obtained from force–displacement curve of nanotubes (Figure 11.9). Mirjalili and Hubert (2010) also proposed a bridging model for calculating the fracture toughness of a CNT modified polymer. In this model, a critical embedded length is considered, which determines whether CNT pulling-out or CNT breakage occurs

$$\frac{l_c}{r} = \frac{\sigma_u}{\tau} \tag{11.18}$$

where r is the CNT radius, σ_u is the CNT ultimate strength, and τ is the interfacial shear stress. They also counted the effect of randomly oriented nanotubes and showed that only 23% of nanotubes effectively contribute to bridging process for such conditions.

11.4.5 Plastic deformation

Matrix inelastic deformation is known as the major inherent source of the toughness in polymers. The inelastic response originates from the matrix microcracking, crazing, or plastic deformation (Evans et al., 1985; Kinloch et al., 1983; Sultan and McGarry,

1973). In glassy polymers, stress concentrations around the rigid or elastomeric particles changes the uniaxial stress state to triaxial stress state, which facilitates the matrix shear yielding (Guild and Young, 1989a,b). In a cracked media under uniform tensile stress, prior to the initial propagation of the crack tip, a frontal process zone develops and material elements within the near crack process zone undergo monotonic postyield strain. Since the 1970s, there has been extensive study over the main energy absorption processes in the fracture process zone. Yee and Pearson (1986) discounted crazing as an influential parameter in an epoxy modified with carboxyl-terminated butadiene-nitrile rubber and related the main toughening contribution to the shear band formation and the plastic void growth. Evidence of the matrix shear banding and plastic void growth initiated by either elastomeric cavitation or rigid particle debonding has been reported by several other authors (Kinloch et al., 1983, 1985; Guild and Young, 1989a,b; Kawaguchi and Pearson, 2003; Lee and Yee, 2000a; Sue, 1991; Sultan and McGarry, 1973). These two mechanisms are represented schematically in Figure 11.10. The shear banding mechanism is introduced in the current section and void formation will be discussed in the subsequent section. The shear banding is a result of inhomogeneous plastic deformation when all shear plastic strain is concentrated in narrow regions while the rest of the material remains in elastic domain. Figure 11.11 is a reflection optical micrograph taken from a fracture surface

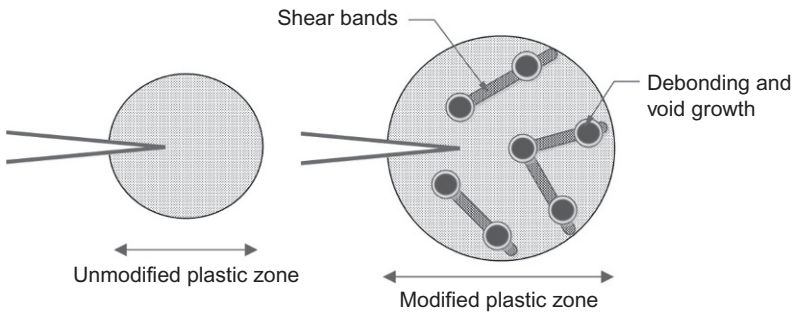

Figure 11.10 A schematic representation of the shear banding and plastic void growth (Dittanet and Pearson, 2013).

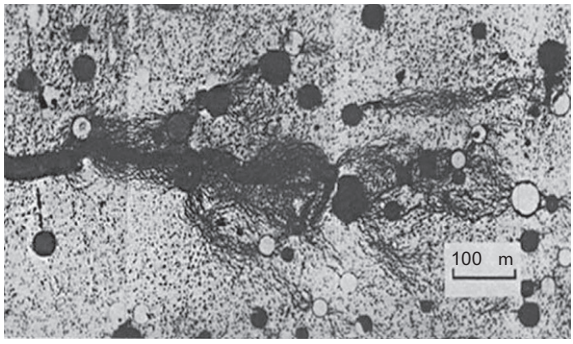

Figure 11.11 Shear band formation in an optical reflection micrograph of the fracture surface in a hybrid-particulate composites (Kinloch et al., 1985).

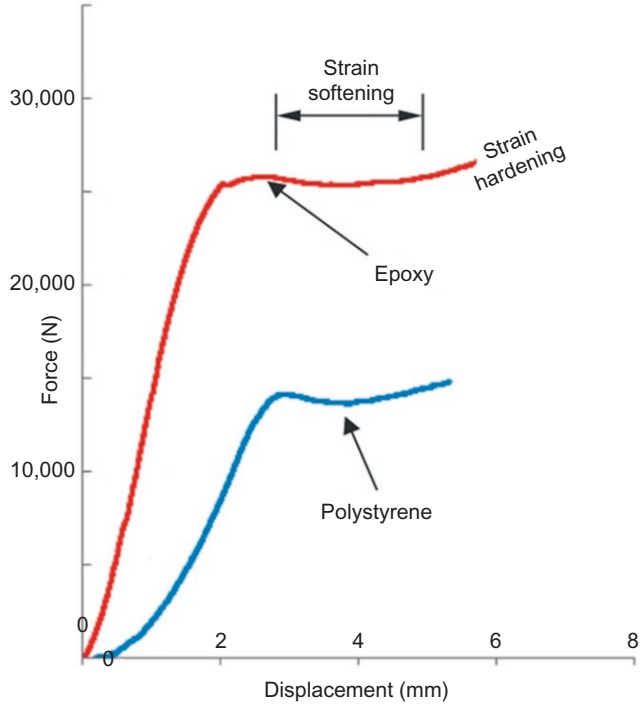

Figure 11.12 Stress–strain curve derived from a plane strain compression test of two different thermoset systems showing strain softening and strain hardening stages.

of a hybrid-particulate composite (Kinloch et al., 1985). The black lines indicate shear bands that are oriented at an angle of about 45° relative to the maximum principal tensile stress. Localized plastic strain is induced by instability of a uniform deformation. This requires macroscopic strain softening in postyield behavior of a true stress–strain curve, which can be stabilized by strain hardening in a compression test. The true stress–strain curve was obtained from a plane strain compression test (Bowden, 1973). A postyield strain softening followed by a strain hardening is generally understood as an essential condition for the shear band formation (Figure 11.12). Lee and Yee (2000b) reported that shear bands disappear when the specimen is heated near the glass transition temperature of the respective matrix. The double-notch four-point-bend (DN-4 PB) test method is a useful technique in probing the process zone mechanisms (Pearson and Yee, 1991; Sue, 1991; Sue and Yee, 1993). This test method consists of a four-point bending geometry with two identical cracks, which are closely positioned in the same edge (Figure 11.13). Since the two cracks are not exactly identical, applied bending moment generates slightly different stress fields. Consequently, only one crack propagates and the other one remains with a nearly critical process zone. Then, the birefringence behavior of the plastically deformed material can be used to measure the size of this process zone (or plastic zone) by a transmitted optical microscopy (TOM). The measured size of

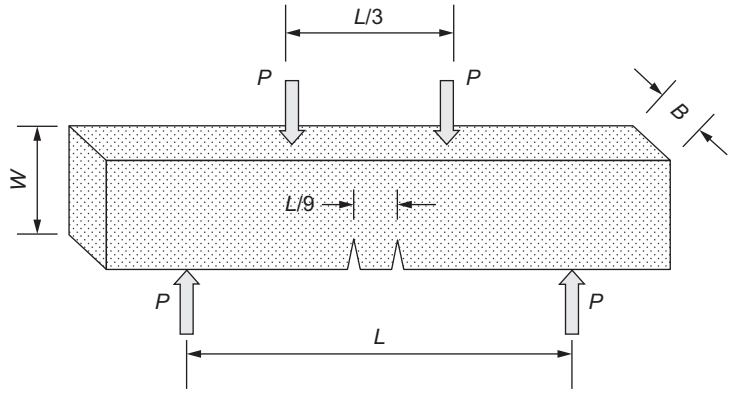

Figure 11.13 Schematic representation of a double-notch four-point bending test (Pearson, 1991; Sue, 1991).

the plastic zone can be compared to the theoretical prediction using Eqs. (11.1) and (11.2). Several authors compared the plastic zone size of TOM micrographs for both pure and particle-filled polymers with calculated values from Irwin's formula and found a reasonable agreement between predictions and observations (Hsieh et al., 2010; Lee and Yee, 2000b; Wetzel et al., 2006).

Evans et al. (1986) provided a theoretical approach to investigate toughness change in rubber-modified polymers. They modeled toughness change as a synergistic influence of rubber stretching, matrix shear banding and matrix dilation "analogous to void growth." Later, Huang and Kinloch (1992a,b) also predicted the toughness increase in the presence of a rubbery phase as a combination of the three pre-mentioned mechanisms. Assuming that $U_s(r)$ is the dissipated strain-energy density due to shear band formation, then the contribution of the shear banding over the entire process zone can be calculated using Huang and Kinloch's model.

$$\Delta G_s = 2\int_0^{r_y} U_s(r)\mathrm{d}r = 0.5V_f\sigma_{yc}\gamma_f\acute{F}\left(r_y\right) \tag{11.19}$$

where V_f is volume fraction of particles, σ_{yc} and γ_f are the plane strain compressive yield stress and fracture strain, respectively, which are obtained from the plane strain compression test of an unmodified matrix. Also, $\acute{F}\left(r_y\right)$ is a function based on the spatial position of spherical particles, assuming that each particle has generated four shear bands (Hsieh et al., 2010, 2011b,c).

$$\acute{F}\left(r_y\right) = r_y\left[\left(\frac{4\pi}{3V_f}\right)^{1/3}\left(1-\frac{r_p}{r_y}\right)^3 - \left(\frac{8}{5}\right)\left(1-\frac{r_p}{r_y}\right)\left(\frac{r_p}{r_y}\right)^{5/2} - \left(\frac{16}{35}\right)\left(\frac{r_p}{r_y}\right)^{7/2} - 2\left(1-\frac{r_p}{r_y}\right)^2 + \left(\frac{16}{35}\right)\right] \tag{11.20}$$

where r_p is the radius of particles or voids and r_y is the radius of the plane strain plastic zone at the crack tip of the particle modified composites which is given by the following equation:

$$r_y = K_{vm}^2\left(1+\mu_m/3^{1/2}\right)^2 r_{yu} \tag{11.21}$$

where K_{vm} is the maximum von Mises stress concentration around stiff (Guild and Young, 1989a) or rubber particles (Huang and Kinloch, 1992b). Also, r_{yu} is the radius of the plastic zone at the crack tip of the neat polymer, which is obtained from Eq. (11.2).

The results of toughness enhancement predicted from the shear band theoretical model with experimental measurements are presented by many research studies (Chen et al., 2013; Dittanet and Pearson, 2013; Hsieh et al., 2011a,b). Consequently, although the shear band formation is inevitable whether the matrix is modified with rubbery particles or inorganic particles, it is concluded that the effect of the shear banding in overall toughness is more significant in case of rubber toughened polymers.

11.4.6 Plastic void growth

As it was mentioned in the previous section, the matrix plastic void growth is commonly understood as a major toughening mechanism within the process zone. The plastic void growth initiates from rubber cavitations (Sultan and McGarry, 1973) or rigid particle debonding (Lee and Yee, 2000a; Shokrieh et al., 2014b; Figures 11.10 and 11.14). Indeed, there have been different interpretations of whether cavitations (or debonding) do individually influence the material toughness or are just

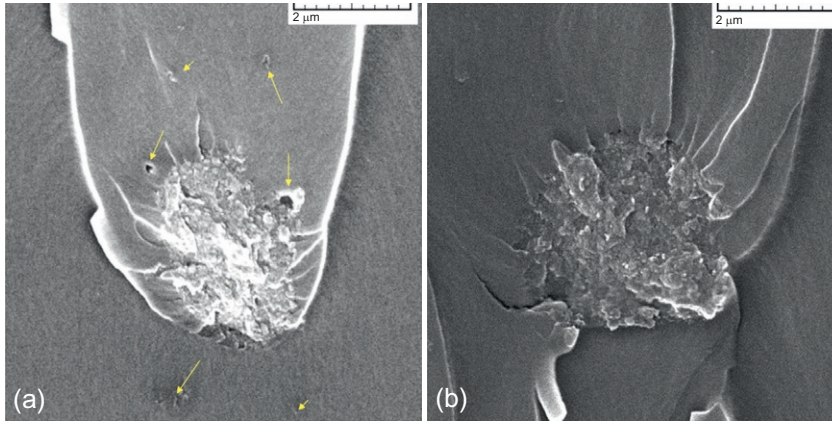

Figure 11.14 A close view at surface texture near small GPL clusters at 20,000 × SEM MAG. Penetration of polymer through agglomerate causes extensive local yielding and debonding during the fracture process (Shokrieh et al., 2014b).

a prerequisite that triggers the shear banding. For example, Guild and Young (1989b) obtained the stress distribution near a rubber particle and a similar void from an axisymmetric finite element model, which showed the stress contour for either cases are almost the same and the cavitations thus do not greatly influence the matrix plastic yielding.

Evans et al. (1985) proposed a model for rigid particle debonding assuming that all tensile strain is accommodated in the polymer. With the crack propagation, the debonded matrix between closely spaced particles experience full stress–strain hysteresis from the crack tip process zone to the crack wake. Hence, the initial toughness decreases due to the loss of section f:

$$G_c = G_0(1-f) \tag{11.22}$$

But with subsequent crack growth, additional toughening term inserted in Eq. (11.22):

$$G_c = G_0(1-f+0.8\ln[h/R]) \tag{11.23}$$

where R is particles radius, h is the process zone width, and n is the strain hardening coefficient in the stress–strain curve. It is noteworthy that Evan's model does not specify whether the source of nonlinear behavior is the debonding or microcracking and considers that both affect the toughness similarly.

As was discussed in the previous section, the combined effects of plastic void growth, shear banding, and rubber bridging were quantitatively studied by Evans et al. (1986) and later by Huang and Kinloch in 1992. Let V_{fr} be the rubber particles volume fraction, which is grown to V_{fv}; then, the increase in toughness can be calculated from the following equation (Huang and Kinloch, 1992a):

$$\Delta G_v = (V_{fv} - V_{fr})\sigma_y r_y \tag{11.24}$$

where σ_y is the tensile yield stress and r_y can be obtained from Eq. (11.21). Note that if the specimen fractures prior to yielding, the value of σ_y must derives from the compression yield stress, as is depicted in the following equation (Huang and Kinloch, 1992a):

$$\sigma_y = \sigma_{yc}\frac{(\sqrt{3}-\mu_m)}{(\sqrt{3}+\mu_m)} \tag{11.25}$$

where μ_m is a material constant that defines the proportionality of the polymer shear yield stress to hydrostatic pressure and has a value between 0.1 and 0.25 (Bowden, 1973).

Johnson et al. (2007) studied the effect of silica nanoparticles on the fracture toughness of an epoxy matrix. Their AFM micrographs revealed that the plastic void formation is the main toughening source in silica/epoxy composites. Their experimental results were compared with theoretical predictions from Eq. (11.24) given in the

Huang and Kinloch model. The calculations of Johnson et al. showed that in lower silica volume fractions, the void growth theory slightly underestimated the experiments while significantly higher values were predicted for volume fractions over 10%. They believed that the assumption of void growth for all particles within the process zone is the main source of the discrepancy between predicted and measured toughness values.

Similar comprehensive studies over silica/epoxy composites were conducted by Liang and Pearson (2009) and later by Hsieh et al. (2010). Liang and Pearson provided visual evidence of shear banding and void growth from TOM micrographs. They predicted the fracture energy considering the contribution from both shear banding and plastic void growth mechanisms.

$$G_c = G_0 + \Delta G_s + \Delta G_v \tag{11.26}$$

where ΔG_s and ΔG_v are described in Eqs. (11.19) and (11.24), respectively.

11.5 Changes in mechanical properties and performances

The mechanical properties of polymers are generally supposed to be improved with the addition of stiff modifiers and can be decreased by applying soft particles. There are several micromechanics models for the prediction of the elastic properties of nanocomposite materials, based on the geometry, orientation of the filler, and elastic properties of the filler and matrix, such as the Halpin–Tsai model, Nielsen model, Mori–Tanaka model, and Eshelby model, etc. In the case of adding 2D nanoparticles into polymers, the Halpin–Tsai and Mori–Tanaka models are sufficient to predict the stiffness of nanocomposites. The Halpin–Tsai model is a mathematical model based on the self-consistent field method. This model can be used to predict the modulus of composite materials (Halpin, 1969; Halpin and Kardos, 1976; Hsieh et al., 2010). The Mori–Tanaka (MT) method (Benveniste, 1987; Qu and Cherkaoui, 2006; Mori and Tanaka, 1973) is an effective field theory based on Eshelby's elasticity method for inhomogeneity in an infinite medium. The MT method calculates the average internal stress in the matrix of a material containing inclusions with transformation of the strain. Average elastic energy is also considered by taking into account the effects of the interaction among the inclusions and of the presence of the free boundary (Mori and Tanaka, 1973). In this method, to predict the modulus of nanocomposites, three-dimensional elastic parameters of both polymer matrix and nanofiller are needed. To simplify the mathematical manipulations of MT model, Hill's elastic moduli are implemented. For the GPLs, the modulus parameters for multilayered GPLs were obtained from MT and HT models to calculate the stiffness of nanocomposites. Then, results of the models are compared with experimental results (Figure 11.15; Shokrieh et al., 2014a).

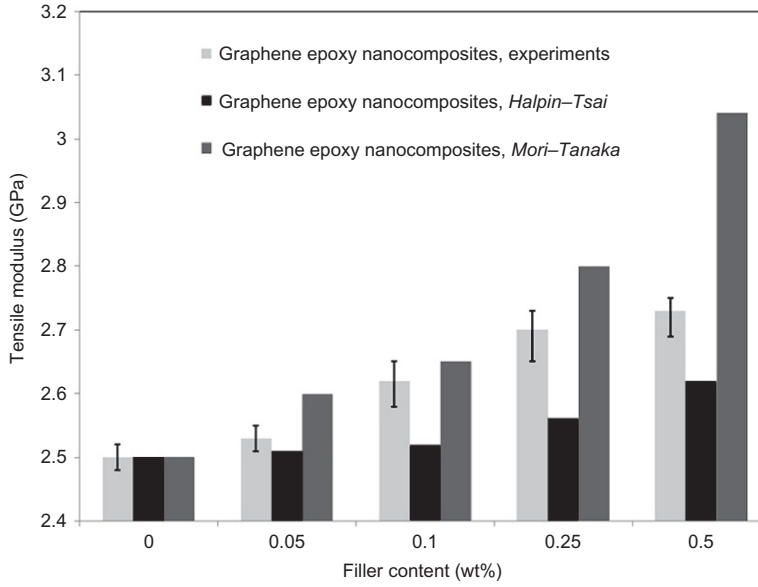

Figure 11.15 Tensile modulus of nanocomposites versus filler content, Mori–Tanaka and Halpin–Tsai models and experimental observations (Shokrieh et al., 2014a).

11.6 Future trends

Although available models have been developed, due to their assumptions and simplifications, various challenges still exist. In practice, an ideal uniform dispersion during fabrication is difficult to achieve when nanoparticles with complicated geometries or strong interparticle attraction are applied. Moreover, investigations of the fracture surface morphology of epoxy modified with clay or graphene platelets represent that a combination of all above-mentioned toughening mechanisms participate specially in the presence of agglomerates.

To clarify how the local plastic deformations can be affected by modifier geometry, particle matrix adhesion, orientation and interparticle interactions, and finite element method simulations are becoming prevalent. Meanwhile, main efforts will be remain focused on the experimental development of nanocomposite fabrication and processes.

11.7 Concluding remarks

In this chapter, the latest research studies on particle toughened thermoset matrices are reviewed. Firstly, stress intensity factor and energy release rate were presented as the fundamental parameters of toughness characterization. Next, conventional modifiers were introduced and classified as rubber particles, stiff inorganic particles, and rigid

carbonic nanostructures. In the main section, well-known toughening mechanisms are described, and some of the most relevant modeling studies are discussed. Although there has been much dispute regarding the influence of particles nature, size, geometrical shape, and interface strength on toughening behavior, some important remarks can be outlined.

The crack tip pinning, crack deflection, and crack bridging are three mechanisms that have been observed at crack faces. Their limiting factor is the particle size. In other words, at least one of the particle dimensions has to be greater than CTOD for these three mechanisms to possibly occur. The first two mentioned mechanisms exist only for rigid modifiers. The crack bridging with elastomers can modestly enhance the fracture energy. However, when using high aspect ratio stiff nanostructures like CNTs or carbon nanofibers, remarkable closure effects generate from bridging of ligaments.

The matrix plastic deformation in the forms of shear banding or void growth occurs at the crack process zone and is not limited to the fracture surface. The shear band formation and the plastic void growth are not dependent on the particle size and are the main energy dissipaters when using nanorubber or inorganic rigid nanoparticles.

References

Benveniste, Y., 1987. A new approach to the application of Mori–Tanaka's theory in composite materials. Mech. Mater. 6 (2), 147–157. http://dx.doi.org/10.1016/0167-6636(87)90005-6.

Blanco, J., Garcia, E.J., Guzman de Villoria, R., Wardle, B.L., 2009. Limiting mechanisms of mode I interlaminar toughening of composites reinforced with aligned carbon nanotubes. J. Compos. Mater. 43 (8), 825–841. http://dx.doi.org/10.1177/0021998309102398.

Bowden, P., 1973. The Yield Behaviour of Glassy Polymers. Springer, Netherlands, pp. 307–313.

Bower, A.F., Ortiz, M., 1978. A three-dimensional analysis of crack trapping and bridging by tough particles. J. Mech. Phys. Solid. 39 (6), 815–858. http://dx.doi.org/10.1016/0022-5096(91)90026-K.

Budiansky, B., Amazicki, J.C., Evans, A., 1988. Small-scale crack bridging and the fracture toughness of particulated-reinforced ceramics. J. Mech. Phys. Solids 36 (2), 167–187. http://dx.doi.org/10.1016/S0022-5096(98)90003-5.

Chen, G., Wu, C., Weng, W., Wu, D., Yan, W., 2003. Preparation of polystyrene/graphite nanosheet composite. Polymer 44 (6), 1781–1784. http://dx.doi.org/10.1016/S0032-3861(03)00050-8.

Chen, J., Kinloch, A.J., Sprenger, S., Taylor, A.C., 2013. The mechanical properties and toughening mechanisms of an epoxy polymer modified with polysiloxane-based core–shell particles. Polymer 54 (16), 4276–4289. http://dx.doi.org/10.1016/j.polymer.2013.06.009.

Cotterell, B., Rice, J., 1980. Slightly curved or kinked cracks. Int. J. Fract. 16 (2), 155–169. http://dx.doi.org/10.1007/BF00012619.

Dittanet, P., Pearson, R.A., 2013. Effect of bimodal particle size distributions on the toughening mechanisms in silica nanoparticle filled epoxy resin. Polymer 54 (7), 1832–1845. http://dx.doi.org/10.1016/j.polymer.2012.12.059.

Dolgopolsky, A., Karbhari, V., Kwak, S.S., 1989. Microcrack induced toughening—an interaction model. Acta Metall. 37 (5), 1349–1354. http://dx.doi.org/10.1016/0001-6160(89)90165-X.

Evans, A., 1972. The strength of brittle materials containing second phase dispersions. Philos. Mag. 26 (6), 1327–1344. http://dx.doi.org/10.1080/14786437208220346.

Evans, A.G., Faber, K., 1983a. Crack deflection processes—I. Theory. Acta Metall. 31 (4), 565–576. http://dx.doi.org/10.1016/0001-6160(83)90046-9.

Evans, A.G., Faber, K., 1983b. Crack deflection processes—II. Experiment. Acta Metall. 31 (4), 577–584. http://dx.doi.org/10.1016/0001-6160(83)90047-0.

Evans, A.G., Faber, K., 1983c. Crack-growth resistance of microcracking brittle materials. J. Am. Ceram. Soc. 67 (4), 255–260. http://dx.doi.org/10.1111/j.1151-2916.1984.tb18842.x.

Evans, A., Fu, Y., 1985. Some effects of microcracks on the mechanical properties of brittle silids—II. Microcrack toughening. Acta Metall. http://dx.doi.org/10.1016/0001-6160(85)90053-7.

Evans, A.G., Williams, S., Beaumont, P.W.R., 1985. On the toughness of particulate filled polymers. J. Mater. Sci. 20 (3), 3668–3674. http://dx.doi.org/10.1007/BF01113774.

Evans, A.G., Ahmad, Z.B., Gilbert, D.G., Beaumont, P., 1986. Mechanisms of toughening in rubber toughened polymers. Acta Metall. 34 (1), 79–87. http://dx.doi.org/10.1016/0001-6160(86)90234-8.

Fiedler, B., Gojny, F.H., Wichmann, M.H.G., Nolte, M.C.M., Schulte, K., 2006. Fundamental aspects of nano-reinforced composites. Compos. Sci. Technol. 66 (16), 3115–3125. http://dx.doi.org/10.1016/j.compscitech.2005.01.014.

Garcia, E.J., Wardle, B.L., Hart, A.J., 2008. Joining prepreg composite interfaces with aligned carbon nanotubes. Compos. A 39, 1065–1070. http://dx.doi.org/10.1016/j.compositesa.2008.03.011.

Gojny, F.H., Wichmann, M.H.G., Köpke, U., Fiedler, B., Schulte, K., 2004. Carbon nanotube-reinforced epoxy-composites: enhanced stiffness and fracture toughness at low nanotube content. Compos. Sci. Technol. 64 (15), 2363–2371. http://dx.doi.org/10.1016/j.compscitech.2004.04.002.

Green, D.J., Nicholson, P.E.J., 1979. Fracture of a brittle particulate composite. Part 2: theoretical aspects. J. Mater. Sci. 14, 1413–1420. http://dx.doi.org/10.1007/BF00569287.

Griffith, A., 1920. The phenomena of rupture and flow in solids. Philos. Trans. Roy. Soc. Lond. Ser. A 221, 163–197. http://dx.doi.org/10.1098/rsta.1921.0006.

Guild, F.J., Young, R.J., 1989a. A predictive model for particulate-filled composite materials. Part 1: hard particles. J. Mater. Sci. 24, 298–306. http://dx.doi.org/10.1007/BF00660971.

Guild, F.J., Young, R.J., 1989b. A predictive model for particulate filled composite materials. Part 2: soft particles. J. Mater. Sci. 24, 2454–2460. http://dx.doi.org/10.1007/BF01174511.

Halpin, J.C., 1969. Stiffness and expansion estimates for oriented short fiber composites. J. Compos. Mater. 3 (4), 732–734. http://dx.doi.org/10.1177/002199836900300419.

Halpin, J.C., Kardos, J.L., 1976. The Halpin–Tsai equations: a review. Polym. Eng. Sci. 16, 344–352. http://dx.doi.org/10.1002/pen.760160512.

Hsieh, T.H., Kinloch, A.J., Masania, K., Taylor, A.C., Sprenger, S., 2010. The mechanisms and mechanics of the toughening of epoxy polymers modified with silica nanoparticles. Polymer 51 (26), 6284–6294. http://dx.doi.org/10.1016/j.polymer.2010.10.048.

Hsieh, T.H., Kinloch, A.J., Taylor, A.C., Kinloch, I.A., 2011a. The effect of carbon nanotubes on the fracture toughness and fatigue performance of a thermosetting epoxy polymer. J. Mater. Sci. 46, 7525–7535. http://dx.doi.org/10.1007/s10853-011-5724-0.

Hsieh, T.H., Kinloch, A.J., Masania, K., Sohn Lee, J., Taylor, A.C., Sprenger, S., 2011b. Erratum to: the toughness of epoxy polymers and fibre composites modified with rubber microparticles and silica nanoparticles. J. Mater. Sci. 46 (11), 4092. http://dx.doi.org/10.1007/s10853-011-5420-0.

Hsieh, T.H., Kinloch, A.J., Masania, K., Sohn Lee, J., Taylor, A.C., Sprenger, S., 2011c. The toughness of epoxy polymers and fibre composites modified with rubber microparticles and silica nanoparticles. J. Mater. Sci. 45, 1193–1210. http://dx.doi.org/10.1007/s10853-009-4064-9.

Huang, Y., Kinloch, A., 1992a. Modelling of the toughening mechanisms in rubber-modified epoxy polymers, Part II: a quantitative description of the microstructure–fracture property relationships. J. Mater. Sci. 27, 2763–2769. http://dx.doi.org/10.1007/BF00540703.

Huang, Y., Kinloch, A., 1992b. Modelling of the toughening mechanisms in rubber-modified epoxy polymers, Part I: finite element analysis studies. J. Mater. Sci. 27, 2753–2762. http://dx.doi.org/10.1007/BF00540702.

Hull, D., Clyne, T.W., 1996. An Introduction to Composite Materials. Cambridge Solid State Science Series, second ed. Cambridge University Press, Cambridge.

Irwin, G., 1957. Analysis of stresses and strains near the end of cracking traversing a plate. J. Appl. Mech. 24, 361–364.

Irwin, G., 1960. Plastic zone near a crack and fracture toughness. In: Proceedings of the 7th Sagamore Ordnance Materials Conference, pp. 463–478.

Johnsen, B.B., Kinloch, A.J., Mohammed, R.D., Taylor, A.C., Sprenger, S., 2007. Toughening mechanisms of nanoparticle-modified epoxy polymers. Polymer 48, 530–541. http://dx.doi.org/10.1016/j.polymer.2006.11.038.

Kachanov, M., Montagut, E., 1986. Interaction of a crack with certain microcrack arrays. Eng. Fract. Mech. 25, 625–636. http://dx.doi.org/10.1016/0013-7944(86)90028-7.

Kachanov, M., Montagut, E.L., Laures, J.P., 1990. Mechanics of crack—microcrack interactions. Mech. Mater. 10 (1–2), 59–71. http://dx.doi.org/10.1016/0167-6636(90)90017-A.

Kawaguchi, T., Pearson, R.A., 2003. The effect of particle–matrix adhesion on the mechanical behavior of glass filled epoxies. Part 2. A study on fracture toughness. Polymer 44 (15), 4239–4247. http://dx.doi.org/10.1016/S0032-3861(03)00372-0.

Kinloch, A.J., Taylor, A.C., 2002. The toughening of cyanate-ester polymers. Part I: physical modification using particles, fibres and woven-mats. J. Mater. Sci. 37, 433–460. http://dx.doi.org/10.1023/A:1013735103120.

Kinloch, A.J., Taylor, A.C., 2003. Mechanical and fracture properties of epoxy/inorganic micro- and nano-composites. J. Mater. Sci. Lett. 22, 1439–1441. http://dx.doi.org/10.1023/A:1025719715808.

Kinloch, A.J., Taylor, A.C., 2006. The mechanical properties and fracture behaviour of epoxy-inorganic micro- and nano-composites. J. Mater. Sci. 41, 3271–3297. http://dx.doi.org/10.1007/s10853-005-5472-0.

Kinloch, A.J., Young, R., 1983. Fracture Behaviour of Polymers. Applied Science Publishers, London. http://dx.doi.org/10.1007/978-94-017-1594-2.

Kinloch, A.J., Shaw, S.J., Hunston, D., 1983. Deformation and fracture behaviour of a rubber-toughened epoxy: 1. Microstructure and fracture studies. Polymer 24, 1341–1354. http://dx.doi.org/10.1016/0032-3861(83)90070-8.

Kinloch, A.J., Maxwell, D., Young, R., 1985. Micromechanisms of crack propagation in hybrid-particulate composites. J. Mater. Sci. Lett. 4 (10), 1276–1279. http://dx.doi.org/10.1007/BF00723480.

Kitey, R., Tippur, H.V., 2005a. Role of particle size and filler–matrix adhesion on dynamic fracture of glass-filled epoxy. I. Macromeasurements. Acta Mater. 53 (4), 1153–1165. http://dx.doi.org/10.1016/j.actamat.2004.11.012.

Kitey, R., Tippur, H.V., 2005b. Role of particle size and filler–matrix adhesion on dynamic fracture of glass-filled epoxy. II. Linkage between macro- and micro-measurements. Acta Mater. 53 (4), 1167–1178. http://dx.doi.org/10.1016/j.actamat.2004.11.011.

Krstic, V.D., 1983. On the fracture of brittle-matrix/ductile-particle composites. Philos. Mag. A 48 (5), 695–708. http://dx.doi.org/10.1080/01418618308236538.

Kunz-Douglass, S., Beaumont, P.W.R., Ashby, M.F., 1980. A model for the toughness of epoxy-rubber particulate composites. J. Mater. Sci. 15 (5), 1109–1123. http://dx.doi.org/10.1007/BF00551799.

Lange, F., 1970. The interaction of a crack front with a second-phase dispersion. Philos. Mag. 22 (179), 983–992. http://dx.doi.org/10.1080/14786437008221068.

Lange, F., Radford, K., 1971. Fracture energy of an epoxy composite system. J. Mater. Sci. 6 (9), 1197–1203. http://dx.doi.org/10.1007/BF00550091.

Lee, J., Yee, A.F., 2000a. Fracture of glass bead/epoxy composites: on micro-mechanical deformations. Polymer 41, 8363–8373. http://dx.doi.org/10.1016/S0032-3861(00)00187-7.

Lee, J., Yee, A.F., 2000b. Role of inherent matrix toughness on fracture of glass bead filled epoxies. Polymer 41, 8375–8385. http://dx.doi.org/10.1016/S0032-3861(00)00186-5.

Lee, J., Yee, A.F., 2001. Inorganic particle toughening II: toughening mechanisms of glass bead filled epoxies. Polymer 42 (2), 589–597. http://dx.doi.org/10.1016/S0032-3861(00)00398-0.

Liang, Y.L., Pearson, R.A., 2009. Toughening mechanisms in epoxy–silica nanocomposites (ESNs). Polymer 50 (20), 4895–4905. http://dx.doi.org/10.1016/j.polymer.2009.08.014.

Liu, T., Tjiu, W.C., Tong, Y., He, C., Goh, S.S., Chung, T., 2004. Morphology and fracture behavior of intercalated epoxy/clay nanocomposites. J. Appl. Polym. Sci. 94 (3), 1236–1244. http://dx.doi.org/10.1002/app.21033.

Mirjalili, V., Hubert, P., 2010. Modelling of the carbon nanotube bridging effect on the toughening of polymers and experimental verification. Compos. Sci. Technol. 70 (10), 1537–1543. http://dx.doi.org/10.1016/j.compscitech.2010.05.016.

Mori, T., Tanaka, K., 1973. Average stress in matrix and average elastic energy of materials with misfitting inclusions. Acta Metall. 21 (5), 571–574. http://dx.doi.org/10.1016/0001-6160(73)90064-3.

Pearson, R.A., Yee, A., 1991. Influence of particle size and particle size distribution on toughening mechanisms in rubber-modified epoxies. J. Mater. Sci. 26, 3828–3844. http://dx.doi.org/10.1007/BF01184979.

Qu, J., Cherkaoui, M., 2006. Fundamentals of Micromechanics of Solids. John Wiley & Sons, Hoboken, NJ. http://dx.doi.org/10.1002/9780470117835.

Rafiee, M.A., Rafiee, J., Wang, Z., Song, H., Yu, Z., Koratkar, N., 2009. Enhanced mechanical properties of nanocomposites at low graphene content. ACS Nano 3 (12), 3884–3890. http://dx.doi.org/10.1021/nn9010472.

Rafiee, M.A., Rafiee, J., Srivastava, I., Wang, Z., Song, H., Yu, Z.-Z., Koratkar, N., 2010. Fracture and fatigue in graphene nanocomposites. Small 6 (2), 179–183. http://dx.doi.org/10.1002/smll.200901480.

Ritchie, R., 1988. Mechanisms of fatigue crack propagation in metals, ceramics and composites: role of crack tip shielding. Mater. Sci. Eng. A 103, 15–28. http://dx.doi.org/10.1016/0025-5416(88)90547-2.

Rose, L., 1986. Microcrack interaction with a main crack. Int. J. Fract. 31 (3), 233–242. http://dx.doi.org/10.1007/BF00018929.

Rose, L., 1987a. Toughening due to crack-front interaction with a second-phase dispersion. Mech. Mater. 6, 11–15. http://dx.doi.org/10.1016/0167-6636(87)90018-4.

Rose, L., 1987b. Crack reinforcement by distributed springs. J. Mech. Phys. Solids 35 (4), 383–405. http://dx.doi.org/10.1016/0022-5096(87)90044-5.

Rubinstein, A.A., Choi, H., 1988. Macrocrack interaction with transverse array of microcracks. Int. J. Fract. 36, 15–26. http://dx.doi.org/10.1007/BF00034814.

Shokrieh, M.M., Esmkhani, M., Shokrieh, Z., Zhao, Z., 2014a. Stiffness prediction of graphene nanoplatelet/epoxy nanocomposites by a combined molecular dynamics-micromechanics method. Comput. Mater. Sci. 92, 444–450.

Shokrieh, M.M., Ghoreishi, S.M., Esmkhani, M., Zhao, Z., 2014b. Effects of graphene nanoplatelets and graphene nanosheets on fracture toughness of epoxy nanocomposites. Fatig. Fract. Eng. Mater. Struct. 37 (10), 1116–1123. http://dx.doi.org/10.1111/ffe.12191.

Sue, H., 1991. Study of rubber-modified brittle epoxy systems. Part II: toughening mechanisms under model fracture. Polym. Eng. Sci. 31 (4), 275–288. http://dx.doi.org/10.1002/pen.760310411.

Sue, H.-J., Yee, A.F., 1993. Study of fracture mechanisms of multiphase polymers using the double-notch four-point-bending method. J. Mater. Sci. 28 (11), 2975–2980. http://dx.doi.org/10.1088/0022-3727/36/5/323.

Sultan, J.N., McGarry, F., 1973. Effect of rubber particle size on deformation mechanisms in glassy epoxy. Polym. Eng. Sci. 13 (1), 29–34. http://dx.doi.org/10.1002/pen.760130105.

Thostenson, E.T., Chou, T.-W., 2003. On the elastic properties of carbon nanotube-based composites: modelling and characterization. J. Phys. D: Appl. Phys. 36 (5), 573–582. http://dx.doi.org/10.1088/0022-3727/36/5/323.

Tong, L., Sun, X., Tan, P., 2008. Effect of long multi-walled carbon nanotubes on delamination toughness of laminated composites. J. Compos. Mater. http://dx.doi.org/10.1177/0021998307086186.

Wang, Y., Zhang, B., Ye, J., 2011. Microstructures and toughening mechanisms of organoclay/polyethersulphone/epoxy hybrid nanocomposites. Mater. Sci. Eng. A 528 (27), 7999–8005. http://dx.doi.org/10.1016/j.msea.2011.07.009.

Wetzel, B., Rosso, P., Haupert, F., Friedrich, K., 2006. Epoxy nanocomposites—fracture and toughening mechanisms. Eng. Fract. Mech. 73, 2375–2398. http://dx.doi.org/10.1016/j.engfracmech.2006.05.018.

Yee, A.F., Pearson, R., 1986. Toughening mechanisms in elastomer-modified epoxies, part 1: mechanical studies. J. Mater. Sci. 21, 2462–2474. http://dx.doi.org/10.1007/BF01114293.

Yu, M.F., Yakobson, B.I., Ruoff, R., 2000. Controlled sliding and pullout of nested shells in individual multiwalled carbon nanotubes. J. Phys. Chem. B 104 (37), 8764–8767. http://dx.doi.org/10.1021/jp002828d.

Zhou, Y., Pervin, F., Jeelani, S., 2007. Effect vapor grown carbon nanofiber on thermal and mechanical properties of epoxy. J. Mater. Sci. 42 (17), 7544–7553. http://dx.doi.org/10.1007/s10853-007-1618-6.

Zhou, Y., Pervin, F., Lewis, L., Jeelani, S., 2008. Fabrication and characterization of carbon/epoxy composites mixed with multi-walled carbon nanotubes. Mater. Sci. Eng. A 475 (1–2), 157–165. http://dx.doi.org/10.1016/j.msea.2007.04.043.

Toughening mechanisms in dental composites

12

C.B. Emrullahoglu Abi
Afyon Kocatepe University, Afyonkarahisar, Turkey

12.1 Introduction

Developments in routine dental practice, including prosthodontic treatments, are often driven by the introduction of new dental materials and processing technologies. Dental prostheses such as crowns, fixed dental prostheses (FDPs), and removable dental prostheses are fabricated from a variety of dental materials using a range of dental laboratory processes. Because of the popularity of osseo-integrated implants, the application of fixed prostheses has expanded, even in an edentulous situation (Miyazaki et al., 2013).

The development of both casting gold alloys and precision dental casting technologies has contributed to the application of metallic prostheses. However, because of the recent demand from patients for esthetics and biosafety, there has been a call for metal-free prostheses (Miyazaki et al., 2013).

Ceramic composite materials can successfully replicate the esthetic qualities of natural teeth (Webber et al., 2003) and have low thermal conductivity (Tinschert et al., 2001). However, despite their strength under compression, they are brittle materials with limited tensile strength, and they do not exhibit plastic deformation before failure (Probster and Diehl, 1992; Piconi et al., 1998; Lawn et al., 2001). Ceramic materials are also subject to time-dependent stress failure (Yoshinari and Derand, 1994). Microscopic flaws generate microcracks that can propagate in response to relatively low stress values. In addition, the humidity of the oral environment has the potential to weaken ceramic dental restorations as a result of stress corrosion (Vult von Steyern et al., 2001).

In 1989, Sadoun introduced to the dental community a new ceramic system (In-Ceram Alumina; Vita Zahnfabrik, Bad Sackingen, Germany) based on slip casting of an alumina (Al_2O_3) core with its subsequent glass infusion (Suarez et al., 2004). The flexural strength of this material has been measured at 446 MPa (Seghi and Sorensen, 1995), a strength that exceeds maximal occlusal loads recorded intraorally on anterior teeth (Suarez et al., 2004; Kern et al., 1991). The evolution of In-Ceram technology continued with the introduction of a zirconia-based system (In-Ceram Zirconia; Vita Zahnfabrik), which uses a mixture of 35% partially stabilized zirconia (ZrO_2), plus alumina to form a porous substructure, stabilized by 16% CeO_2 (Suarez et al., 2004). The interpenetrating phase structure provides improved resistance to crack propagation, combined with the high strength of the zirconia material (McLaren and White, 2000).

Toughening Mechanisms in Composite Materials. http://dx.doi.org/10.1016/B978-1-78242-279-2.00012-3

12.2 Development of dental composites

Restorative dentistry is still developing to mimic natural tooth structures, keeping their functional and esthetic properties (Höland et al., 2009).

Metal–ceramic restorations are still the most reliable method in dental prosthetics, especially when a good adhesion of the ceramic to the metal substrate is achieved (Anusavice, 2006).

The increased popularity of all-ceramic materials as an alternative to metal–ceramic restorations is attributable to their excellent esthetics, chemical stability, and biocompatibility (Craig and Powers, 2002; Van Noort, 2002). However, the brittleness and low tensile strength of conventional glass-ceramics limits their long-term clinical application in restorations (Craig and Powers, 2002; Van Noort, 2002). Recently, the development of advanced dental ceramic composites has led to the application of partially stabilized zirconia (PSZ) in restorative dentistry that can be produced from a computer-assisted design/computer-assisted manufacturing (CAD/CAM) system. The use of zirconia-based ceramics for dental restorations has risen in popularity due to their superior fracture strength (Tinschert et al., 2000, 2001; Guazzato et al., 2005) and toughness compared with other dental ceramic systems (Guazzato et al., 2005; Tinschert et al., 2000; Porter and Heuer, 1977).

12.2.1 Metal–ceramic composites

Dental ceramics at various compositions for metal–ceramic composites were introduced in 1962 (Weinsten et al., 1962). Since then, most of these ceramics have been composed of leucite crystals dispersed in a glassy matrix (Kontonasaki et al., 2008). Leucite has a high coefficient of thermal expansion (CTE) and raises the overall thermal expansion of the bulk porcelain, leading to thermal compatibility with metal frameworks (Anusavice and Gray, 1989; Cesar et al., 2005). The amount of leucite and the amount and composition of glass determine decisively the CTE of the final product (Kontonasaki et al., 2008). Leucite structure relies on a framework of SiO_4 tetrahedra that form rings (Wyckoff, 1963). At room temperature, leucite crystals are of tetragonal symmetry. When heated, the SiO_4 structure expands slowly by untilting and untwisting the tetragonal rings until the symmetry changes to cubic at 625 °C (Mackert et al., 1986; Faust, 1963). The phase transformation of leucite from cubic to tetragonal when cooled, in combination with the greater contraction of the leucite crystals compared to the glassy matrix due to their large thermal contraction mismatch, cause tangential compressive stresses around leucite crystals (Mackert et al., 1986). These stresses may act either as crack deflectors or crack initiators influencing the mechanical performance of the ceramic (Lee et al., 1997; Mackert and Williams, 1996).

The leucite content in dental ceramics is critical also due to its contribution to the flexural strength of feldspathic porcelains (Kontonasaki et al., 2008). It has been reported that an increase in leucite content from 10% to 30% increased the flexural strength from 34.1 to 64.8 MPa (Kadimisetty and Rosenblum, 1998), while studies

on fracture toughness (K_{IC}) showed a direct relation of the leucite content to K_{IC} (Quinn et al., 2003; Piché et al., 1994). Moreover, Cesar et al. (2005) proved evidence that ceramic compositions with higher leucite content presented higher incidence of crack deflection. Commercial leucite dental ceramic compositions contain 17–45% of tetragonal leucite (Mackert and Russell, 1996; Mackert and Evans, 1991), although leucite volume fraction may be altered due to repeated firings or different cooling rates (Cesar et al., 2005; Mackert and Evans, 1991).

Glass–ceramics that can be sintered to conventional or fine metal frameworks have been introduced in clinical practice. They are polycrystalline solids prepared by the controlled crystallization of glasses (McMillan, 1979) and have been reported to present improved optical, physicochemical, or mechanical properties (Sinmazişik and Öveçoğlu, 2006; Höland et al., 2000). Glass–ceramics are made by forming special base glasses, mostly by melting, and then using controlled heat treatment (ceraming) to nucleate and precipitate crystals in the glassy matrix (Höland et al., 2003). The number of crystals, their growth rate, and thus their size are regulated by the time and temperature of the ceraming process. The chemical composition and microstructure of the glass–ceramic determine its properties and main applications, while to ensure high mechanical performance it is important that the crystals are numerous and uniformly distributed throughout the glassy phase (Höland et al., 2003). Recently, combined leucite-fluorapatite or fluorapatite glass-ceramics have been introduced in the dental market, as fluorapatite crystals present increased chemical durability compared to that of natural teeth (hydroxyapatite), and closely resemble the crystals in natural teeth optimizing the optical properties of the material (Sinmazişik and Öveçoğlu, 2006). Major recent changes in dental ceramic formulations for metal–ceramic restorations comprise low fusing ceramics with about 200 °C lower fusion temperature compared to conventional dental ceramics. The reduction of fusion temperatures initially occurred in order to eliminate the problems of bonding between titanium and its alloys and dental ceramics. The exposure of the Ti alloy to temperatures that exceed 800 °C leads to the absorption of oxygen and nitrogen, providing the formation of a thick superficial layer of Ti oxide that may attain a thickness up to 1 mm and harms the bonding of ceramic to substrate (Kimura et al., 1990; Togaya et al., 1983). In compliance with these criteria, additional clinical interest for these low fusing compositions arises from their significant advantages, as the reduction of the fusion temperature allows for increased opalescence, highly polished surface, and considerably less potential for abrading any materials against which they occlude (Leinfelder, 2000).

Modern dentistry is said to have its beginnings during the year 1728, when Fauchard published a treatise describing many types of dental restorations, including a method for the construction of artificial dentures from ivory. The year 1792 is important as the date when de Chamant patented a process for the construction of porcelain teeth; this was followed early in the next century by the introduction of the porcelain inlay (Anusavice, 2003). However, since Taggart introduced the technique of cast inlay restorations in 1907, metals have been accepted as the most reliable dental restorations because of higher mechanical strength and easier preparation than ceramics. Sixty years later, reinforcement of the jacket crown with aluminum oxide was

achieved as a result of the work of McLean and Hughes. Further materials developments were based on increasing the crystalline content, for example leucite (Empress), mica (Dicor), hydroxyapatite (Cerapearl), or mixed glass oxides (In-Ceram). Pure crystalline oxide ceramics (e.g., Procera AllCeram) have only been used for about 15 years. Casting (Dicor), pressing (Empress), and grinding techniques (CEREC) are all used to create morphology. The idea of using CAD/CAM techniques for the fabrication of tooth restorations originated with Duret in the 1970s. Ten years later, Mörmann developed the CEREC-system, first marketed by Siemens (now Sirona); this technology enabled the first chairside fabrication of restorations (Ban, 2008).

Because of the need for an alternative technique for an esthetic custom implant abutment, especially in patients with high parafunctional stresses and high esthetic demands, a strong esthetic abutment that would survive under heavy occlusal load conditions is of importance. The development of a pressable metal ceramic custom implant abutment provides an alternative esthetic solution for patients with heavy occlusal and functional load conditions (Protopapadaki et al., 2013).

An early attempt to fabricate a pressable metal ceramic custom implant (PR) abutment was reported by Kim et al. (2009) for Regular Platform (RP) Nobel Biocare internal connection implants. Fracture resistance was compared to that of a duplicate zirconia abutment, and the results revealed that the mean (SD) fracture load was significantly higher in the experimental group than in the zirconia group (Kim et al., 2009). However, the performance of the PR abutment for narrow platform implants is unknown (Protopapadaki et al., 2013).

In a study, the standard lost-wax technique (Taggart, 1907) was used and adapted for the fabrication of a pressable metal ceramic abutment. This was an efficient and predictable method for the fabrication of esthetic restorations, but so far it has been applied only to conventional FDPs and crowns. Protopapadaki et al. concluded that the application of the hot pressing technique to implant abutments appears promising, but research is needed with regard to the mechanical properties and design of such an application (Protopapadaki et al., 2013).

12.2.2 Metal-free ceramic composites

Over the past 30 years, clinical applications of all-ceramic materials in dentistry have expanded from single unit anterior restorations to multi-unit posterior restorations, dental abutments and, more recently, dental implants (Denry, 2013).

Ceramic systems with high crystalline content were introduced in dentistry with the objective of replacing the metal frameworks used for metal–ceramic crowns and fixed partial dentures (FPDs). All-ceramic structures are more translucent than the metallic ones, resulting in a natural-looking restoration (Heffernan et al., 2002a,b). The finish line of the prepared tooth can be placed at the free gingival margin without compromising the esthetic appearance and avoiding the violation of the biological width, which reduces the risk of iatrogenic periodontal disease (Raigrodski and Chiche, 2001).

Also, ceramic materials have low thermal conductivity and are highly biocompatible (Raigrodski and Chiche, 2001; Della Bona, 2009).

However, these materials, when placed in load-bearing applications, often display an inability to resist stress-induced crack propagation (Barsoum et al., 2003; Sakaguchi et al., 1992; Wiederhorn, 1984).

A noticeable improvement in the mechanical properties of all-ceramic restorations was offered by the so-called "glass infiltrated high-strength ceramic core systems," developed for the first time in the late 1980s with In-Ceram Alumina (IA), followed, after some years, by In-Ceram Spinell and In-Ceram Zirconia (IZ) (VITA Zahnfabrik, Germany) (Xiao-Ping et al., 2002). IZ is a glass infiltrated zirconia-toughened alumina (ZTA), in which, for the first time, zirconium oxide was used in a dental ceramic, thanks to its metastable nature, zirconia is a high performance ceramic material (Ruff and Ebert, 1929).

12.2.2.1 Development of advanced dental material technologies

In dentistry, ceramic restorations are used cautiously, since they show susceptibility to fracture when they face high compression conditions in the interoclusal impact areas (Linkevicius et al., 2008). Currently, the development of advanced Dent Material technologies has recently led to the application of zirconia-based ceramics (Guazzato et al., 2004).

Zirconia

Zirconia is one of the most promising restorative materials, because it yields very favorable mechanical properties and a reasonable esthetic (Zarone et al., 2011). Zirconia stabilized with Y_2O_3 has the best properties for these applications. When a stress occurs on a ZrO_2 surface, a crystalline modification opposes the propagation of cracks. Compression resistance of ZrO_2 is about 2000 MPa (Manicone et al., 2007).

Zirconia cores for FPD on anterior and posterior teeth and on implants are now available. Clinical evaluation of abutments and periodontal tissue must be performed prior to their use. Zirconia opacity is very useful in adverse clinical situations, for example, for masking of dischromic abutment teeth. Radiopacity can aid evaluation during radiographic controls. Zirconia frameworks are realized by using CAD/CAM technology. Cementation of Zr-ceramic restorations can be performed with adhesive luting. Mechanical properties of zirconium oxide FPDs have proved superior to those of other metal-free restorations. Clinical evaluations, which have been ongoing for 3 years, indicate a good success rate for zirconia FPDs. Zirconia implant abutments can also be used to improve the esthetic outcome of implant-supported rehabilitations. Newly proposed zirconia implants seem to have good biological and mechanical properties; further studies are needed to validate their application (Manicone et al., 2007).

Toughening mechanisms of zirconia

Zirconia is often used as a prosthetic material due to its excellent mechanical properties and considerable amount of research work has been carried out since the discovery of the transformation toughening of zirconia in 1970s by Garvie et al. (1975).

Zirconia is a well-known polymorph that occurs in three forms: monoclinic, tetragonal, and cubic. Pure zirconia is monoclinic at the room temperature. This phase is

stable up to 1170 °C. Above this temperature, it transforms into tetragonal and then into cubic phase at 2370 °C. During cooling, a tetragonal-monoclinic transformation takes place in a temperature range of about 100 °C below 1070 °C. The addition of stabilizing oxide like CaO and MgO to pure zirconia allows to generate multiphase materials known as PSZ which consists of cubic zirconia as the major phase at room temperature, with monoclinic and tetragonal zirconia precipitates as the minor phase (Ban, 2008). Garvie et al. (1975) called PSZ as "Ceramic Steel" and showed how to make the best of tetragonal-monoclinic transformation in PSZ improving mechanical strength and toughness of zirconia. They observed that tetragonal metastable precipitates finely dispersed within the cubic matrix were able to be transformed into the monoclinic phase when the constraint exerted on them by the matrix was relieved, i.e., by a crack advancing in the material. In that case, the stress field associated with expansion due to the phase transformation acts in opposition to the stress fields that promotes the propagation of the crack. An enhancement in toughness is obtained, because the energy associated with crack propagation is dissipated both in the tetragonal-monoclinic transformation and in overcoming the compression stresses due to the volume expansion (Piconi and Maccauro, 1999). Figure 12.1 shows a schematic illustration of this phenomenon (Ban, 2008).

Development of zirconia-based dental composites

Depending on the material surrounding the zirconia grains susceptible to the *t–m* transformation, different types of materials can be obtained; the most important ones are the following (the acronyms in brackets are the most widely used in the scientific literature):

(i) Partially stabilized zirconia (PSZ)—a matrix of cubic zirconia embedding transformable *t*-zirconia grains.

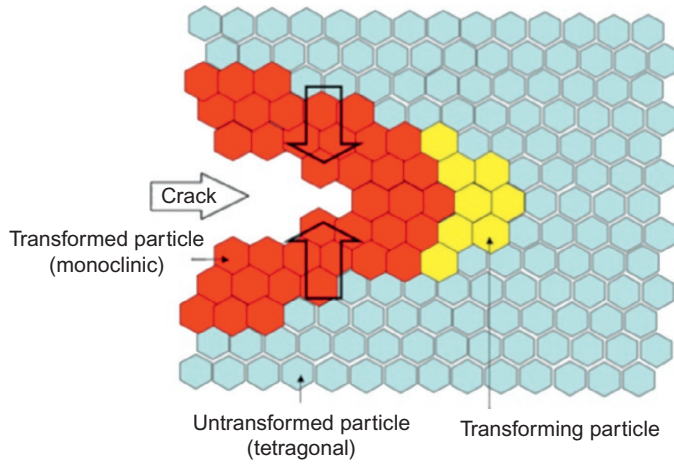

Figure 12.1 Inhibition of crack propagation by stress-induced phase transformation (Ban, 2008).

(ii) Zirconia-toughened composites (ZTC)—a matrix with high elastic modulus embedding transformable *t*-zirconia grains. The most used matrix, with relevant biomedical application in prostheses, is alumina, and the material is known as zirconia-toughened alumina (Piconi et al., 2005).

(iii) Tetragonal zirconia polycrystals (TZP)—the whole material is constituted by transformable *t*-zirconia grains.

Differently from the two previous cases, which are two phase materials, TZP is single phase (Lughi and Sergo, 2010).

The addition of unstabilized zirconia to alumina increases the fracture toughness of a material. Claussen first discovered this phenomenon in 1976. The fracture toughness of alumina increases due to interaction between the crack front and the second phase (crack blunting, crack deviation) and interactions between the crack front and pre-existing microcracks, which are formed during the tetragonal-monoclinic transformation of zirconia (Claussen, 1976). Upon cooling from sintering, fine tetragonal zirconia grains dispersed in a matrix can be constrained from transforming by the surrounding matrix, allowing the material to retain the metastable tetragonal phase. Alternatively, an approaching crack front can act as a catalyst, and trigger the transformation, compressing the zone ahead of the crack tip (Barsoum, 2003).

In alumina–zirconia composites, high tensile stresses are developed in the alumina matrix. However, the volume expansion due to zirconia transformation is approximately 3–4%, which greatly exceeds matrix stresses. Thus, small particles can induce cracks in composite materials. By retaining tetragonal grains in the metastable state, the potential for transformation toughening is maximized.

Toughening can be achieved with PSZ, and the addition of oxides (typically MgO, CaO, or Y_2O_3) leads to a tetragonal phase in a cubic zirconia matrix. However, the size of tetragonal precipitates must be minimized so that they do not spontaneously transform within the cubic zirconia matrix. Namely, tetragonal precipitates must only transform due to stress (Rafferty et al., 2009). Microcracks and induced stress promote toughening in alumina–zirconia systems. The production of microcracks, which dissipate the energy of propagating cracks, is dependent on the difference between the thermal expansion of the alumina matrix and that of zirconia particles. For instance, a 3–5% volume expansion of zirconia particles can generate microcracks in the matrix. In contrast, induced stress is dependent on the tetragonal to monoclinic transformation of ZrO_2 at temperatures less than 1200 °C. Transformation-toughened alumina (TTA) can retain a metastable, high-temperature tetragonal phase because the alumina matrix provides a compressive force. Stress energies from propagating cracks induce the martensitic transition of the metastable tetragonal phase to stable monoclinic zirconia. The energy used by this transformation (multiplied by the number of transformations) is sufficient to slow or stop the propagation of cracks. Stress theories based on both microcrack formation and induced stress may be applicable, and TTA can be formed by dry pressing and slip casting. The majority of characterization studies have been conducted on dry-pressed and sintered samples, and slip casted-TTA is a relatively new material. Single-phase beta-Al_2O_3 and beta-Al_2O_3/ZrO_2 composites fabricated via slip casting have sintering temperatures of 1480 and 1535 °C,

respectively, which are lower than those of dry-pressed bodies with identical compositions. A typical Al_2O_3/ZrO_2 composite contains 8–15 vol.% ZrO_2 (Anon, 2011). A noticeable improvement in the mechanical properties of all-ceramic restorations was offered by the so-called "glass infiltrated high-strength ceramic core systems," developed for the first time in the late 80s with IA, followed, after some years, by In-Ceram Spinell and IZ (VITA Zahnfabrik, Germany) (Xiao-Ping et al., 2002). IZ is a glass infiltrated ZTA, in which, for the first time, zirconium oxide was used in a dental ceramic; as reported below, thanks to its metastable nature, zirconia is a high performance ceramic material (Ruff and Ebert, 1929). High strength cores are composed of 67 wt% of aluminum oxide 33% of 12 mol% cerium-partially stabilized zirconium oxide (Raigrodski, 2004), so that zirconia crystals (grain size <1 μm) are embedded in an alumina matrix (larger grains <2–6 μm, high elastic modulus) in such a composition that yields the highest tenacity and flexure strength inside this class of ceramics (400–800 MPa): microcracks may trigger the so-called "transformation toughening" of zirconia, so that a crack tip is more often seen to propagate through the alumina matrix surrounding the transformed crystals (Heuer et al., 1986; Denry and Kelly, 2008). ZTA can be manufactured according to two different processes: soft machining or slip casting. The latter presents the advantage of a more limited shrinkage but, at the same time, higher porosity and poorer mechanical properties than yttrium partially stabilized tetragonal zirconia polycrystal (3Y-TZP) (Denry and Kelly, 2008; Guazzato et al., 2003, 2004, 2005), the strongest and most commonly used zirconia-based ceramic.

Finally, industrial dense polycrystalline ceramics such as alumina, zirconia, and alumina–zirconia composites are currently available for use with CAD/CAM technology via a networked machining center. In particular, yttrium partially stabilized tetragonal zirconia polycrystalline (Y-TZP) shows better mechanical properties and superior resistance to fracture (Miyazaki et al., 2013). Y-TZP has a high fracture toughness, from 5 to 10 MPa $m^{1/2}$, and a flexural strength of 900–1400 MPa (Christel et al., 1989; Guazzato et al., 2004). Ceria-stabilized tetragonal zirconia polycrystals (Ce-TZP) showed much higher fracture toughness of 19 MPa $m^{1/2}$ but lower flexural strength and hardness than Y-TZP. Ce-TZP/alumina nanocomposites (Ce-TZP/A) were developed to improve Ce-TZP (Nawa et al., 1998). Ce-TZP/A consists of nanometer-sized Al_2O_3 particles that are dispersed within the Ce-TZP grains and grain boundries, and nanometer-sized Ce-TZP particles that are dispersed within the alumina grains and grain boundaries. This homogeneous dispersion of alumina in the Ce-TZP matrix suppresses grain growth and increases hardness, flexural strength, and hydrothermal stability of tetragonal zirconia while preserving its toughness (Nawa et al., 1998). Ce-TZP/A is the toughest dental ceramic material available, with a fracture toughness of 19 MPa $m^{1/2}$, and a flexural strength of 1400 MPa (Tanaka et al., 2002).

Processing

Among the many ceramic processing techniques used to improve physical and chemical properties of zirconia-based composite materials, the synthesis of nanocrystalline powders has been considered extremely important (Lazar et al., 2008). As an

alternative to the traditional mechanical mixing procedure, chemical methods can be used to synthesize different doped zirconia ceramic powders with higher reactivity, allowing better sintering without the application of pressure (Lee and Rainforth, 1994). Some examples of these powder preparation techniques are sol–gel synthesis (Livage et al., 1998), polymeric precursor route (Quinelato et al., 2000), combustion synthesis (Juarez et al., 2000), hydrothermal treatment (Dell'Agli and Mascolo, 2000), and coprecipitation from metal aqueous solutions (Duran et al., 1996; Segal, 1998; Lazar et al., 2002). From a commercial standpoint, however, coprecipitation is the most common route adopted due to the great chemical and physical homogeneity of the products, cost effectiveness and simplicity (Duran et al., 1996; Segal, 1998; Lazar et al., 2002). The coprecipitation route consists of preparing an aqueous solution with the metal ions (i.e., YCl_3 and $ZrOCl_2$), with the desirable composition and slowly mixing them with aqueous base (i.e., NH_4OH), causing precipitation. The use of organic liquids to dehydrate the precipitate and wet milling to control the state of powder agglomeration have to be employed (Lazar et al., 2002).

The advantages of the colloidal processing route are a very fine and very homogeneous microstructure, with minimal aggregates of zirconia. By using a colloidal processing route (zirconium precursor), narrower ZrO_2 grain size distributions (in the region of 200 nm) are expected (Rafferty et al., 2009). According to Schehl et al., this route may avoid the need for any stabilizing oxide (Schehl et al., 2002). This is due to the fact that all ZrO_2 grains have practically the same size and can be kept below the critical size for spontaneous transformation. These particles are also greater than the critical size needed for transformation during crack growth. Schehl et al. (2002) used X-ray diffraction to investigate a colloidally processed (95 wt% Al_2O_3; 5 wt% ZrO_2) sample and found that during sintering only 9.07 vol% of the particles reacted the critical size at which they will spontaneously transform to monoclinic zirconia (m-ZrO_2) during cooling, the vast majority of particles (90.93 vol%) were retained below the critical size as tetragonal zirconia (t-ZrO_2) particles. A fracture toughness of 7.5 MPa $m^{1/2}$ was recorded. Deville et al. (2003) also highlight the difficulties associated with trying to avoid aggregate formation when using classical powder mixing. They claim that by using a colloidal route, it should be possible to increase the zirconia content but avoid aging phenomena related to the presence of aggregates. In addition, the starting monoclinic phase fraction could be much lower. Significantly, aging studies revealed that colloidally processed samples (using unstabilized zirconia) showed no evidence of aging and were thus preferred over yttria-stabilized materials (Deville et al., 2003).

In a study, Moraes et al. (2004) investigated alumina composites with yttria-tetragonal zirconia polycrystal (Y-TZP) additions ranging from 5 to 80 wt% prepared by conventional powder processing method. They concluded that the addition of Y-TZP promoted composites with higher densities, higher flexural strength, and higher fracture toughness. An inverse dependence of K_{IC} on hardness was revealed. Improvement in flexural strength as high as 93% and improvement in fracture toughness of 29% were obtained compared to pure alumina samples (Moraes et al., 2004).

Ipek et al. (2011) used the precipitation method to synthesis alumina and alumina-zirconia composite powders and those nanopowders were then used to form dense

compacts to study their microstructure and mechanical properties. They concluded that nanosize powders were successively synthesized by precipitation method. The size of the powders ranged from 100 to 300 nm.

In another study, Abi et al. (2013) investigated the production of t-ZrO_2 powder by heat treating m-ZrO_2 containing 10 wt% MgO. Alumina and alumina-zirconia composite powders containing various types and amounts of m-ZrO_2 and t-ZrO_2 were prepared (0–20 wt%) and shaped by slip casting technique. They reported that t-ZrO_2 was produced by mechanical mixing of m-ZrO_2 and MgO powders and sintering the homogenized powder mixtures at 1400 °C.

Chan et al. (2013) investigated the toughening mechanisms of yttria-stabilized zirconia (YSZ) thin film coatings as a viable method for improving fracture toughness of all-ceramic dental restorations. They showed that surface modification of dental ceramics with YSZ thin film coatings is a viable method for improved reliability of dental ceramic materials.

Changes in mechanical properties and performance

Because of the brittle properties of ceramic materials, the indication spectrum for dental ceramics was considerably limited in the past (Ban, 2008). However, a supercritical loading that results in the immediate brittle fracture of a ceramic restoration is rarely observed *in vivo*, e.g., in case of trauma or extreme para function. In contrast, the subcritical stresses are of greater clinical importance. For instance, such stress occurs during cyclic masticatory loading and also when very small manufacturing-related structural flaws are exposed to the corrosive oral environment. This can lead to crack initiation and further propagation. If the external loading continues, the initial subcritical crack growth may reach a critical crack length and cause an unstable spread of cracks, ultimately followed by the failure of the ceramic restoration (Tinschert et al., 2007).

Various studies have already used fracture mechanics to measure the subcritical crack extension and provide information on the susceptibility of zirconia to subcritical crack growth and thus a characterization of its long-term behavior (Sundh et al., 2005; von Steyern et al., 2006; Curtis et al., 2006; Studart et al., 2007a,b; Teixeira et al., 2007; Pittayachawan et al., 2007). Teixeira et al. (2007) reported that the lifetime predictions after 10 years indicate a reduction of 50%, 36%, and 29% in strength for porcelain, alumina, and Y-TZP, respectively. On the other hand, Studart et al. (2007a,b) demonstrated that posterior bridges with zirconia frameworks can exhibit lifetimes longer than 20 years if the diameter of the bridge connector is properly designed. Each prediction of the lifetime depends on each assumption of many factors such as design, dimension, environment, initial strength, etc. Although the conclusion of the lifetime of zirconia is still not consistent, it is commonly concluded that the lifetime of zirconia bridge is longer than those of alumina and others, and comparable to metal-based restorations (Ban, 2008).

The main drawback of Y-TZP zirconia ceramics is their sensitivity to low-temperature degradation (LTD)—aging that leads to exaggerated $t \rightarrow m$ transformation and a degradation that starts on the surface and propagates into the depth of the material, diminishing its mechanical properties (Kobayashi et al., 1981;

Li and Watanabe, 1996; Chevalier et al., 1999). This is of particular interest for dental zirconia ceramics, as their degradation in the oral environment due to the exposure to oral fluids and mechanical stress over prolonged periods of time cannot be overlooked. Although minimally exposed to the oral environment, the margins of zirconia restorations allow a continuous contact of zirconia core with saliva or other fluids that may start and progressively lead to the degradation of the material. Furthermore, there is growing popularity of monolithic zirconia restorations where much larger areas of zirconia are in contact with the oral environment (Vatali et al., 2014). The majority of the models proposed to explain the spontaneous $t \rightarrow m$ transformation taking place during LTD-aging, are either based on the formation of zirconium hydroxides (Zr-OH) (Sato and Shimada, 1985; Yoshimura et al., 1987) or yttrium hydroxides ($Y(OH)_3$) or (Y(O)OH) (Lange et al., 1986) due to the diffusion of water through the material, promoting phase transition with local stress concentration or variation of the yttrium/zirconium ratio. According to the most recent proposed model (Chevalier et al., 2009), oxygen anions are responsible for the transformation nucleation and therefore for the LTD. Due to volume changes, the transformed grains cause microcracks, and the material becomes degraded (Chevalier et al., 2009).

Several studies on alumina–zirconia composites have remarked on the positive effect of alumina on the hydrothermal stability of tetragonal zirconia phase (Tsukuma and Shimada, 1985; Tsubakino et al., 1991). This is mainly due to the elastic modulus of alumina, almost twice the one of Y-TZP. Namely, the introduction of alumina increases the matrix stiffness, then the constraint that the matrix exerts on zirconia particles maintains them in the metastable tetragonal state (Gutknecht et al., 2007), thus acting as "mechanical stabilizer." ATZ materials show improved aging resistance versus Y-TZP; nevertheless, these composites still exhibit a certain degree of aging (Douillard et al., 2012), whereas ZTA materials can exhibit much better aging resistance than monolithic Y-TZP (Douillard et al., 2012; Deville et al., 2003).

Applications

Individual restorations such as inlays, onlays, veneers, crowns, crown copings, and FPD frameworks can be machined easily from ceramic blocks by using CAD/CAM technology with the system (Cerec; Sirona, Charlotte, NC) developed by Apholt (Apholt et al., 2001).

Y-TZP ceramic is available as (1) fully sintered blocks fabricated by a process known as hot isostatic pressing (HIP) or (2) partially sintered prefabricated blocks, which are used to produce enlarged restorations to compensate the final sintering shrinkage. The milling of fully sintered blocks may produce more accurate fitting restorations but is associated with high wear rates of the milling burs and is time-consuming (Borba et al., 2011). Conversely, the increased milling efficiency obtained using partially sintered blocks has the disadvantage of a potentially lower precision of fit due to the sintering shrinkage (Della Bona, 2009; Tinschert et al., 2004; Beuer et al., 2009). IZ is a ceramic core material used for CAD/CAM restorations. It consists of an alumina-based porous structure with addition of about 33% ceria PSZ infiltrated with

a lanthanum oxide-based glass (Della Bona et al., 2007). The system is available as dry-pressed blocks that can be milled into the final dimension and subsequently glass infiltrated (Della Bona, 2009; Reich et al., 2005).

12.3 Future trends

All-ceramic composite restorations made by zirconia have the potential to withstand physiological occlusal forces in the posterior region. In the future, the improved characteristics of zirconia composite materials are expected to expand the clinical application of dental ceramics to other fields, such as the implant bodies, abutment of implants, and removable denture bases and parts.

References

Abi, C.B., Emrullahoğlu, O.F., Said, G., 2013. Microstructure and mechanical properties of MgO-stabilized ZrO_2–Al_2O_3 dental composites. J. Mech. Behav. Biomed. Mater. 18, 123–131.

Anon, 2011. Materials Handbook. Ceramic Industry, p. 22.

Anusavice, K.J., 2003. Dental ceramics. In: Anusavice, K.J. (Ed.), Phillips' Science of Dental Materials, 12th ed. Saunders, Philadelphia, pp. 655–719.

Anusavice, K.J., 2006. Phillips' Science of Dental Materials, 11th ed. W.B. Saunders, Philadelphia, pp. 621–654.

Anusavice, K.J., Gray, A., 1989. Influence of framework design, contraction mismatch, and thermal history on porcelain checking in fixed partial dentures. Dent. Mater. 5, 58–63.

Apholt, W., Bindl, A., Luthy, H., Mormann, W.H., 2001. Flexural strength of Cerec 2 machined and jointed InCeram-Alumina and InCeram-Zirconia bars. Dent. Mater. 17, 260–267.

Ban, S., 2008. Reliability and properties of core materials for all-ceramic dental restorations. Jpn. Dent. Sci. Rev. 44, 3–21.

Barsoum, M.W., 2003. Fundamentals of Ceramics. Institute of Physics Publishing, Bristol.

Barsoum, M.W., Cantor, B., Goringe, M.J. (Eds.), 2003. Fund Ceram. Taylor & Francis Group, New York, NY, pp. 356–399.

Beuer, F., Naumann, M., Gernet, W., Sorensen, J.A., 2009. Precision of fit: zirconia three-unit fixed dental prostheses. Clin. Oral Investig. 13 (3), 343–349.

Borba, M., Cesar, P.F., Griggs, J.A., Bona, A.D., 2011. Adaptation of all-ceramic fixed partial dentures. Dent. Mater. 27, 1119–1126.

Cesar, P., Yoshimura, H., Miranda Júnior, W., Okada, C., 2005. Correlation between fracture toughness and leucite content in dental porcelains. J. Dent. 33, 721–729.

Chan, R.N., Stoner, B.R., Thompson, J.Y., Scattergood, R.O., Piascik, J.R., 2013. Fracture toughness improvements of dental ceramic through use of yttria-stabilized zirconia (YSZ) thin-film coatings. Dent. Mater. 29, 881–887.

Chevalier, J., Cales, B., Drouet, J.M., 1999. Low temperature aging of Y-TZP ceramics. J. Am. Ceram. Soc. 82, 2150–2154.

Chevalier, J., Gremillard, L., Virkar, A.V., Clarke, D.R., 2009. The tetragonal-monoclinic transformation in zirconia: lessons learned and future trends. J. Am. Ceram. Soc. 92, 1901–1920.

Christel, P., Meunier, A., Heller, M., Torre, J.P., Peill, C.N., 1989. Mechanical properties and short-term in-vivo evaluation of yttrium-oxide partially-stabilized zirconia. J. Biomed. Mater. Res. 23, 45–61.

Claussen, N., 1976. Fracture toughness of Al_2O_3 with an unstabilized ZrO_2 dispersed phase. J. Am. Ceram. Soc. 59 (1–2), 49–51.

Craig, R.G., Powers, J.M., 2002. Restorative Dental Materials, 11th ed. Mosby Inc., St. Louis.

Curtis, A.R., Wright, A.J., Fleming, G.J.P., 2006. The influence of simulated masticatory loading regimes on the bi-axial flexure strength and reliability of a Y-TZP dental ceramic. J. Dent. 34, 317–325.

Dell'Agli, G., Mascolo, G., 2000. Hydrothermal synthesis of ZrO_2–Y_2O_3 solid solution at low temperature. J. Eur. Ceram. Soc. 20, 139–145.

Della Bona, A., 2009. Bonding to Ceramics: Scientific Evidences for Clinical Dentistry, first ed. Camara Brasileira do Livro, SP, Brazil, p. 254.

Della Bona, A., Donassollo, T.A., Demarco, F.F., Barrett, A.A., Mecholsky Jr., J.J., 2007. Characterization and surface treatment effects on topography of a glass-infiltrated alumina/zirconia-reinforced ceramic. Dent. Mater. 23 (6), 769–775.

Denry, I., 2013. How and when does fabrication damage adversely affect the clinical performance of ceramic restorations? Dent. Mater. 29, 85–96.

Denry, I., Kelly, J.R., 2008. State of the art of zirconia for dental applications. Dent. Mater. 24, 299–307.

Deville, S., Chevalier, J., Fantozzi, G., Bartolome, J.F., Requena, J., Moya, J.S., Torrecillas, R., Diaz, L.A., 2003. Low-temperature aging of zirconia-toughened alumina ceramics and its implication in biomedical implants. J. Eur. Ceram. Soc. 23, 2975.

Douillard, T., Chevalier, J., Descamps-Mandine, A., Warner, I., Galais, Y., Whitaker, P., et al., 2012. Comparative ageing behaviour of commercial, unworn and worn 3Y-TZP and zirconia-toughened alumina hip joint heads. J. Eur. Ceram. Soc. 32, 1529–1540.

Duran, P., Villegas, M., Capel, F., Recio, P., Moure, C., 1996. Low temperature sintering and microstructural development of nanocrystalline Y-TZP powders. J. Eur. Ceram. Soc. 16, 945–952.

Faust, G.T., 1963. Phase transition in synthetic and natural leucite. Schweiz. Mineral. Petrogr. Mitt. 43, 165–195.

Garvie, R.C., Haaink, R.H., Pascoe, R.T., 1975. Ceramic steel? Nature 258, 703–704.

Guazzato, M., Albakry, M., Swain, M.V., Ringer, S.P., 2003. Microstructure of alumina- and alumina/zirconia-glass infiltrated dental ceramics. Bioceramics 15, 879–882.

Guazzato, M., Proos, K., Quach, L., Swain, M.V., 2004. Strength, reliability and mode of fracture of bilayered porcelain/zirconia (Y-TZP) dental ceramics. Biomaterials 25, 5045–5052.

Guazzato, M., Albakry, M., Ringer, S.P., Swain, M.V., 2005. Strength, fracture toughness and microstructure of a selection of all-ceramic materials. Part II. Zirconia-based dental ceramics. Dent. Mater. 20, 449–456.

Gutknecht, D., Chevalier, J., Garnier, V., Fantozzi, G., 2007. Key role of processing to avoid low temperature ageing in alümina zirconia composites for orthopaedic application. J. Eur. Ceram. Soc. 27, 1547–1552.

Heffernan, M.J., Aquilino, S.A., Diaz-Arnold, A.M., Haselton, D.R., Stanford, C.M., Vargas, M.A., 2002a. Relative translucency of six all-ceramic systems. Part II: core and veneer materials. J. Prosthet. Dent. 88 (1), 10–15.

Heffernan, M.J., Aquilino, S.A., Diaz-Arnold, A.M., Haselton, D.R., Stanford, C.M., Vargas, M.A., 2002b. Relative translucency of six all-ceramic systems. Part I: core materials. J. Prosthet. Dent. 88 (1), 4–9.

Heuer, A.H., Lange, F.F., Swain, M.V., Evans, A.G., 1986. Transformation toughening: an overview. J. Am. Ceram. Soc. 69, 1–4.

Höland, W., Schweiger, M., Frank, M., Rheinberger, V., 2000. A comparison of the microstructure and properties of the IPS empressT2 and the IPS empressT glass–ceramics. J. Biomed. Mater. Res. B Appl. Biomater. 53, 297–303.

Höland, W., Rheinberger, V., Schweiger, M., 2003. Control of nucleation in glass ceramics. Philos. Trans. R. Soc. Lond. A 361, 575–579.

Höland, W., Rheinberger, V., Apel, E., Ritzberger, C., Rothbrust, F., Kappert, H., Krumeich, F., Nesper, R., 2009. Future perspectives of biomaterials for dental restoration. J. Eur. Ceram. Soc. 29, 1291–1297.

Ipek, M., Zeytin, S., Bindal, C., 2011. An evaluation of Al_2O_3–ZrO_2 composites produced by coprecipitation method. J. Alloys Compd. 509, 486–489.

Juarez, R.E., Lamas, D.G., Lascalea, G.E., Walsöe de Reca, N.E., 2000. Synthesis of nanocrystalline zirconia powders for TZP ceramics by a nitrate–citrate combustion route. J. Eur. Ceram. Soc. 20, 133–138.

Kadimisetty, S., Rosenblum, M., 1998. Flexural strength of feldspathic porcelain as a function of leucite content. J. Dent. Res. 77, 171, Abstr. no. 523.

Kern, M., Knode, H., Strubb, J.R., 1991. The all-porcelain, resin-bonded bridge. Quintessence Int. 22, 257–262.

Kim, S., Kim, H.I., Brewer, J.D., Monaco Jr., E.A., 2009. Comparison of fracture resistance of pressable metal ceramic custom implant abutments with CAD/CAM commercially fabricated zirconia implant abutments. J. Prosthet. Dent. 101, 226–230.

Kimura, H., Horning, C.J., Okazak, M.I., Takahahi, J., 1990. Oxidation effect on porcelain titanium interface reaction and bond strength. Dent. Mater. J. 9, 91–99.

Kobayashi, K., Kuwajima, H., Masak, T., 1981. Phase change andmechanical properties of ZrO_2-Y_2O_3 solid electrolyte afteraging. Solid State Ion. 3–4, 489–493.

Kontonasaki, E., Kantiranis, N., Papadopoulou, L., Chatzistavrou, X., Kavouras, P., Zorba, T., Sivropoulou, A., Chrissafis, K., Paraskevopoulos, K.M., Koidis, P.T., 2008. Microstructural characterization and comparative evaluation of physical, mechanical and biological properties of three ceramics for metal–ceramic restorations. Dent. Mater. 24, 1362–1373.

Lange, F.F., Dunlop, G.L., Davis, B.I., 1986. Degradation during aging oftransformation-toughened ZrO_2–Y_2O_3 materials at 250°C. J. Am. Ceram. Soc. 69 (4), 237–240.

Lawn, B.R., Deng, Y., Thompson, V.P., 2001. Use of contact testing in the characterization and design of all-ceramic crownlike layer structures: a review. J. Prosthet. Dent. 86, 495–510.

Lazar, D.R.R., Menezes, C.A.B., Ussui, V., Bressiani, A.H.A., Paschoal, J.O.A., 2002. The influence of sulphur on the processing of zirconia based ceramics. J. Eur. Ceram. Soc. 22, 2813–2820.

Lazar, D.R.R., Bottino, M.C., Ozcan, M., Valandro, L.F., Amaral, R., Ussui, V., Bressiani, A.H.A., 2008. Y-TZP ceramic processing from coprecipitated powders: a comparative study with three commercial dental ceramics. Dent. Mater. 24, 1676–1685.

Lee, W.E., Rainforth, W.M., 1994. Ceramic Microstructures—Property Control by Processing. Chapman & Hall, London.

Lee, H.H., Kon, M., Asaoka, K., 1997. Influence of modification of Na_2O in a glassy matrix on the strength of leucite containing porcelains. Dent. Mater. J. 16, 134–143.

Leinfelder, K.F., 2000. Porcelain esthetics for the 21st century. J. Am. Dent. Assoc. 131, 47S–51S.

Li, J., Watanabe, R., 1996. X-ray photoelectron spectroscopyinvestigation on the low-temperature degradation of 2 mol% ZrO_2–Y_2O_3 ceramics. J. Am. Ceram. Soc. 79, 109–112.

Linkevicius, T., Vladimirovas, E., Grybauskas, S., Puisys, A., Rutkunas, V., 2008. Venner fracture in implant-supported metal–ceramic restorations: part I: overall success rate and impact of occlusal guidance. Stomatologija, Baltic Den. Maxillofac. J. 10, 133–139.
Livage, J., Beteille, F., Rouse, C., Chatry, M., Davidson, P., 1998. Sol–gel synthesis of oxide materials. Acta Mater. 46, 743–750.
Lughi, V., Sergo, V., 2010. Low temperature degradation -aging- of zirconia: a critical review of the relevant aspects in dentistry. Dent. Mater. 26, 807–820.
Mackert Jr., J.R., Evans, A.L., 1991. Effect of cooling rate on leucite volume fraction in dental porcelains. J. Dent. Res. 70, 137–139.
Mackert Jr., J.R., Russell, C.M., 1996. Leucite crystallization during processing of a heat pressed dental ceramic. Int. J. Prosthodont. 9, 261–265.
Mackert, J.R., Williams, A.L., 1996. Microcracks in dental porcelain and their behaviour during multiple firing. J. Dent. Res. 75, 1484–1490.
Mackert, J.R., Butts, M.B., Morena, R., Fairhurst, C.W., 1986. The effect of the leucite transformation on dental porcelain expansion. Dent. Mater. 2, 32–36.
Manicone, P.F., Iommetti, P.R., Raffaelli, L., 2007. An overview of zirconia ceramics: basic properties and clinical applications. J. Dent. 35, 819–826.
McLaren, E.A., White, S.N., 2000. Survival of In-Ceram crowns in a private practice: a prospective clinical trial. J. Prosthet. Dent. 83, 216–222.
McMillan, P.W., 1979. Glass–Ceramics, second ed. Academic Press, London, pp. 1–12.
Miyazaki, T., Nakamura, T., Matsumura, H., Ban, S., Kobayashi, T., 2013. Current status of zirconia restoration. J. Prosthodont. Res. 57, 236–261.
Moraes, D.B.M., Carlos, N.E., Jamil, D.F., Leandra, G.O., 2004. Mechanical properties of alumina-zirconia composites for ceramic abutments. Mater. Res. 7, 643.
Nawa, M., Nakamoto, S., Sekino, T., Niihara, K., 1998. Tough and strong Ce-TZP/alumina nanocomposites doped with titania. Ceram. Int. 24, 497–506.
Piché, P.W., Obrian, W.J., Groh, C.L., Boenke, K.M., 1994. Leucite content of selected porcelains. J. Biomed. Mater. Res. 28, 603–609.
Piconi, C., Maccauro, G., 1999. Zirconia as a ceramic biomaterial. Biomaterials 20, 1–25.
Piconi, C., Burger, W., Richter, G.H., Cittadini, A., Maccauro, G., Covacci, V., et al., 1998. Y-TZP ceramics for artificial joint replacements. Biomaterials 19, 1489–1494.
Piconi, C., Maccauro, G., Muratori, F., 2005. Alumina matrix composites in arthroplasty. Key Eng. Mater. 284–286, 979–982.
Pittayachawan, P., McDonald, A., Petrie, A., Knowles, J.C., 2007. The biaxial flexural strength and fatigue property of Lava Y-TZPTM dental ceramic. Dent. Mater. 23, 1018–1029.
Porter, D.L., Heuer, A.H., 1977. Mechanisms of toughening partially stabilized zirconia (PSZ). J. Am. Ceram. Soc. 60, 183–184.
Probster, L., Diehl, J., 1992. Slip-casting alumina ceramics for crown and bridge restorations. Quintessence Int. 23, 25–31.
Protopapadaki, M., Edward, A., Monaco, J., Kim, H., Davis, E.L., 2013. Comparison of fracture resistance of pressable metal ceramic custom implant abutment with a commercially fabricated CAD/CAM zirconia implant abutment. J. Prosthet. Dent. 110, 389–396.
Quinelato, A.L., Longo, E., Perazolli, L.A., Varela, J.A., 2000. Effect of ceria content on the sintering of ZrO_2 based ceramics synthesized from a polymeric precursor. J. Eur. Ceram. Soc. 20, 1077–1084.
Quinn, J.B., Sundar, V., Lloyd, K., 2003. Influence of microstructure and chemistry on the fracture toughness of dental ceramics. Dent. Mater. 19, 603–611.

Rafferty, A., Alsebaie, A.M., Olabi, A.G., Prescott, T., 2009. Properties of zirconia-toughened-alumina prepared via powder processing and colloidal processing routes. J. Colloid Interface Sci. 329, 310–315.
Raigrodski, A.J., 2004. Contemporary materials and technologies for all-ceramic fixed partial dentures: a review of the literature. J. Prosthet. Dent. 92, 557–562.
Raigrodski, A.J., Chiche, G.J., 2001. The safety and efficacy of anterior ceramic fixed partial dentures: a review of the literature. J. Prosthet. Dent. 86 (5), 520–525.
Reich, S., Wichmann, M., Nkenke, E., Proeschel, P., 2005. Clinical fit of all-ceramic three-unit fixed partial dentures, generated with three different CAD/CAM systems. Eur. J. Oral Sci. 113 (2), 174–179.
Ruff, O., Ebert, F., 1929. Refractory ceramics: I. The forms of zirconium dioxide. Z. Anorg. Allg. Chem. 180, 19–41.
Sakaguchi, R.L., Cross, M., Douglas, W.H., 1992. A simple model of crack propagation in dental materials. Dent. Mater. 8, 131.
Sato, T., Shimada, M., 1985. Transformation of yttria-doped tetragonal ZrO_2 polycrystal by annealing in water. J. Am. Ceram. Soc. 68 (6), 356–359.
Schehl, M., Diaz, L.A., Torrecillas, R., 2002. Acta Mater. 50, 1125.
Segal, D., 1998. Soft chemistry routes to zirconia ceramics. Key Eng. Mater. 153 (154), 241–250.
Seghi, R.R., Sorensen, J.A., 1995. Relative flexural strength of six new ceramic materials. Int. J. Prosthodont. 8, 239–246.
Sinmazişik, G., Öveçoğlu, M.L., 2006. Physical properties and microstructural characterization of dental porcelains mixed with distilled water and modeling liquid. Dent. Mater. 22, 735–745.
Studart, A.R., Filser, F., Kocher, P., Gauckler, L.J., 2007a. Fatigue of zirconia under cyclic loading in water and its implications for the design of dental bridges. Dent. Mater. 23, 106–114.
Studart, A.R., Filser, F., Kocher, P., Gauckler, L.J., 2007b. In vitro lifetime of dental ceramics under cyclic loading in water. Biomaterials 28, 2695–2705.
Suarez, M.J., Lozano, J.F.L., Paz Salido, M.P., Martinez, F., 2004. Three-year clinical evaluation of In-Ceram Zirconia posterior FPDs. Int. J. Prosthodont. 17, 35–38.
Sundh, A., Molin, M., Sjögren, G., 2005. Fracture resistance of yttrium oxide partially stabilized zirconia all-ceramic bridges after veneering and mechanical fatigue testing. Dent. Mater. 21, 476–482.
Taggart, W.H., 1907. A new and accurate method of making gold inlays. Dent. Cosmos 49, 117–121.
Tanaka, K., Tamura, J., Kawanabe, K., Nawa, M., Oka, M., Uchida, M., et al., 2002. Ce-TZP/ASl_2O_3 nanocomposites as a bearing material in total joint replacement. J. Biomed. Mater. Res. 63, 262–270.
Teixeira, E.C., Piascik, J.R., Stoner, B.R., Thompson, J.Y., 2007. Dynamic fatigue and strength characterization of three ceramic materials. J. Mater. Sci. Mater. Med. 18, 1219–1224.
Tinschert, J., Zwez, D., Marx, R., Anusavice, K.J., 2000. Structural reliability of alumina-, feldspar-, leucite-, mica- and zirconia-based ceramics. J. Dent. 28, 529–535.
Tinschert, J., Natt, G., Mautsch, W., Augthum, M., Spiekermann, H., 2001. Fracture resistance of lithium disilicate-, alumina-, and zirconia-based three-unit fixed partial dentures: a laboratory study. Int. J. Prosthodont. 14, 231–238.
Tinschert, J., Natt, G., Hassenpflug, S., Spiekermann, H., 2004. Status of current CAD/CAM technology in dental medicine. Int. J. Comput. Dent. 7 (1), 25–45.

Tinschert, J., Natt, G., Mohbotter, N., Spiekermann, H., Schulze, K.A., 2007. Lifetime of alumina and zirconia ceramics used for crown and bridge restorations. J. Biomed. Mater. Res. B Appl. Biomater. 80B, 317–321.

Togaya, T., Suzuki, M., Tsutsumi, S., Ida, K., 1983. An application of pure titanium to the metal porcelain system. Dent. Mater. 2, 210–219.

Tsubakino, H., Nozato, R., Hamamoto, M., 1991. Effect of alumina addition on the tetragonal-to-monoclinic phase transformation in ziconia–3% mol yttria. J. Am. Ceram. Soc. 74, 440–443.

Tsukuma, K., Shimada, M., 1985. Thermal stability of Y_2O_3-partially stabilized (Y-PSZ) and Y-PSZ/Al_2O_3 composites. J. Mater. Sci. Lett. 4, 857–861.

Van Noort, R., 2002. Introduction to Dental Materials, second ed. Mosby, London.

Vatali, A., Kontonasaki, E., Kavouras, P., Kantiranis, N., Papadopoulou, L., Paraskevopoulos, K.K.M., Koidis, P., 2014. Effect of heat treatment and in vitro aging on the microstructure and mechanical properties of cold isostatic-pressed zirconia ceramics for dental restorations. Dent. Mater. 30, e272–e282.

Von Steyern, P.V., Ebbesson, S., Holmgren, J., Haag, P., Nilner, K., 2006. Fracture strength of two oxide ceramic crown systems after cyclic pre-loading and thermocycling. J. Oral Rehabil. 33, 682–689.

Vult von Steyern, P., Jonsson, O., Nilner, K., 2001. Five-year evaluation of posterior all-ceramic three-unit (In-Ceram) FPDs. Int. J. Prosthodont. 14, 379–384.

Webber, B., McDonald, A., Knowles, J., 2003. An in vitro study of the compressive load at fracture of Procera AllCeram crowns with varying thickness of veneer porcelain. J. Prosthet. Dent. 89, 154–160.

Weinsten, M., Katz, S., Weinstein, A.B., 1962. Fused porcelain-to-metal teeth. US Patent 3,052,982.

Wiederhorn, S.M., 1984. Brittle fracture and toughening mechanisms in ceramics. Annu. Rev. Mater. Sci. 14, 373.

Wyckoff, R.W.G., 1963. Crystal Structures, second ed. Interscience Publishers, New York.

Xiao-Ping, L., Jie-Mo, T., Yun-Long, Z., Ling, W., 2002. Strength and fracture toughness of MgO-modified glass infiltrated alumina for CAD/CAM. Dent. Mater. 1 (8), 216–220.

Yoshimura, M., Noma, T., Kawabata, K., Somiya, S., 1987. Role of H_2O on the degradation process of Y-TZP. J. Mater. Sci. Lett. 6 (4), 465–467.

Yoshinari, M., Derand, T., 1994. Fracture strength of all-ceramic crowns. Int. J. Prosthodont. 7, 329–338.

Zarone, F., Russo, S., Sorrentino, R., 2011. From porcelain-fusedto-metal to zirconia: clinical and experimental considerations. Dent. Mater. 27, 83–96.

This page intentionally left blank

Mechanical behavior of extra-strong CNT fibers and their composites

13

Q.-S. Yang, X. Liu
Beijing University of Technology, Beijing, China

13.1 Introduction

Carbon nanotubes (CNTs) were discovered in the early 1990s. As a novel nano-structure material, CNTs have attracted extensive attention since their discovery (Baughman et al., 2002; Li et al., 2008). As a one-dimensional nanomaterial, CNTs typically have a layered hollow structure and are lightweight, thereby giving rise to their excellent mechanical, electrical, thermal, and chemical performances (Yang and Yang, 2008; Yu et al., 2000; Lourie and Wagner, 1998). In particular, an individual CNT possesses a high Young's modulus of up to 1 TPa and a high strength of over 60 GPa (Krasheninnikov et al., 2004). A primary application of CNTs is therefore reinforcement of composites, in which process-isolated CNTs dispersed in a solvent are mixed with a polymer solution. However, the mechanical performance of the composites is not as good as expected due to weak interfacial adhesion between CNTs and the polymer (Frankland and Harik, 2003; Coleman et al., 2006; Manchado et al., 2005; Song and Youn, 2005). Therefore, great efforts have been made to improve the bonding strength of the CNT/polymer interface as well as the content of CNT in polymer. Covalent functionalization and non covalent functionalization of CNTs are commonly used methods to create a stronger interface between CNTs and polymer in such composites (Xie et al., 2005; Daniel et al., 2007; Meng et al., 2009). Covalent functionalization methods allow specific carbon atoms for the sidewall modification of CNTs by hybridizing the functional group or a particular atom, such as the hydrogen atom. Non covalent functionalization is mainly based on supramolecular complexation using various adsorption forces (Khan et al., 2010). However, some research has also indicated that the functionalization of CNTs will lead to the degradation of some of their properties, depending on the chirality and functionalization configuration (Garg and Sinnott, 1998; Buffa et al., 2007; Xin et al., 2007; Yang et al., 2014; Kuang et al., 2009; Kuang and He, 2009; He et al., 2009).

Consequently, to be used in practical applications, CNTs need to be formed into macroscale assemblies rather than dispersed in solvent. In the past few years, considerable attention has been paid to macroscale assemblies of CNTs, e.g., covalent structures and non covalent structures, depending on their preparation techniques. In terms of covalent networks, two or more CNTs are connected covalently through non hexagonal rings in different types of junction. Shortly after the discovery of CNTs, theoretical and experimental research showed that covalent CNT junctions can be formed by electron

Toughening Mechanisms in Composite Materials. http://dx.doi.org/10.1016/B978-1-78242-279-2.00013-5

irradiation at high temperatures (Banhart et al., 2002) or atomic welders (e.g., B atoms) during heat treatment (Endo et al., 2005). Thereafter, many research groups began to study macroscale covalent networks of CNTs, aiming to produce larger, stronger, and tougher macrostructures (Snow et al., 2003, 2004; Gruner, 2007; Hall et al., 2008; Liang et al., 2013). On the other hand, CNTs can be assembled to non covalent macroscale structures, which consist of a variety of materials such as CNT films, CNT fibers, CNT sponge, CNT foam, and so on. Because of outstanding properties of CNTs, macroscale CNT structures present a fascinating research opportunity with significant technological implications (Liu et al., 2011a; Jiang et al., 2011).

13.2 Mechanical performance of CNT composites

Despite the exceptional properties of CNTs, there are two main limitations that hinder their use in composites. First, their surface energy is significantly different from that of the surrounding matrix, thus the dispersion of CNTs into matrix is a big obstacle in practice. Moreover, the physical interaction between CNTs and matrix is very weak (Bosea et al., 2010; Gibson et al., 2007).

13.2.1 Mechanical properties of functionalized CNT

To resolve the problems mentioned above, several methods have been developed to modify the surface properties of CNTs. These approaches can be simply divided into covalent (chemical) and non covalent (physical) functionalizations. In covalent functionalization, functional groups are introduced onto the surface of CNTs to enhance their cohesion with polymer and break the cohesion of aggregated CNTs (Liu and Yang, 2009). However, functionalized CNT might have mechanical properties that are different from those of the original CNT. Garg and Sinnott (1998) indicated that the functionalization of CNTs decreases their maximum buckling load by about 15%, regardless of tubule helical structure or radius. Buffa et al. (2007) also stated that surface defects induced by functionalization can lead to the loss of tensile strength of the CNTs. Molecular dynamics (MD) simulation results by Xin et al. (2007) indicated that the buckling behavior of single-walled CNTs (SWNTs) is greatly affected by vacancy defects caused in chemical functionalization process. Molecular mechanics (MM) investigations by Kuang et al. (2009); Kuang and He (2009), and He et al. (2009) revealed a reduction in Young's modulus of up to 37% after functionalization when the functional group is densely distributed. What's more, functionalization may also weaken the fracture strain and tensile strength (Zhang et al., 2008) and the torsion behavior of CNTs (Jeong et al., 2007).

In addition, the functionalization configuration at the atomic level influences the mechanical properties of functionalized CNTs and their composites. Figure 13.1 illustrates the cross section of CNT functionalized by the H atoms. The functionalized length is half the total length of the CNT, thus the functionalization density is 12.5%. Different functionalization configurations are adopted. The H atoms in the models are divided into one, two, three, and six separate segments along the CNT axial direction, which are named as F-CNT-1, F-CNT-2, F-CNT-3, and F-CNT-4, as shown in Figure 13.2. The simulation details can be found in Yang et al. (2014).

Figure 13.1 Cross section of CNT functionalized by H atoms.

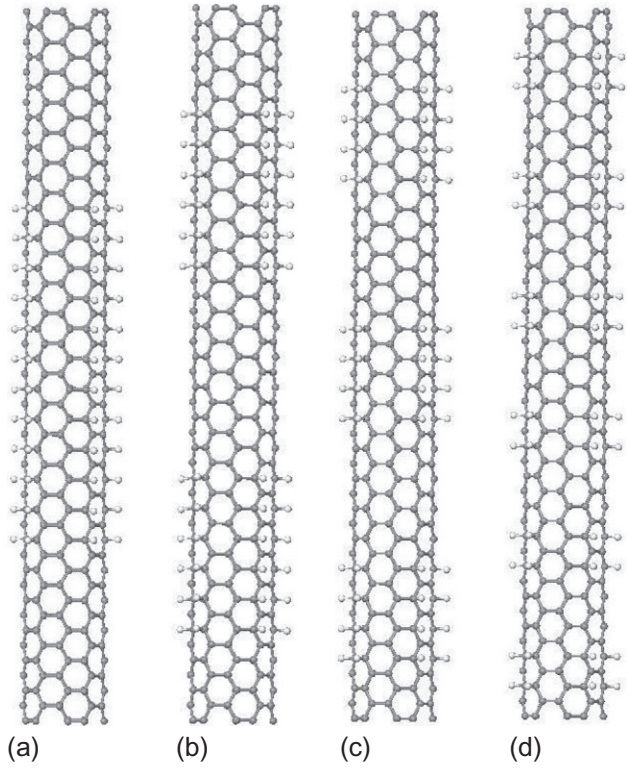

Figure 13.2 Functionalized CNT models: (a) F-CNT-1, (b) F-CNT-2, (c) F-CNT-3, and (d) F-CNT-4.

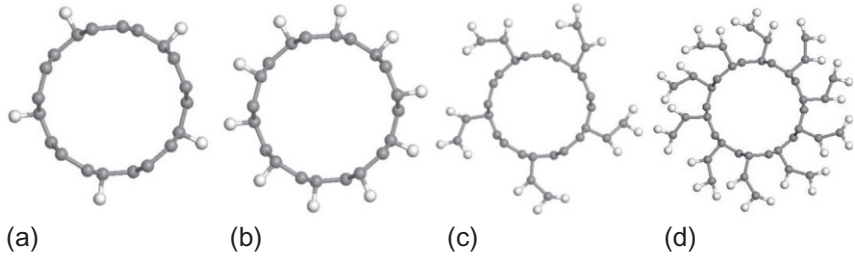

Figure 13.3 MD models of H- and C_2H_2-functionalized CNTs with different densities.

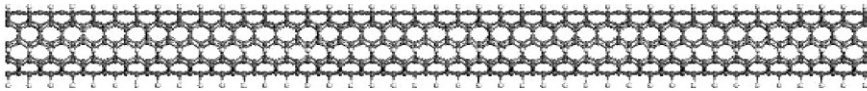

Figure 13.4 MD model of H-functionalized CNT.

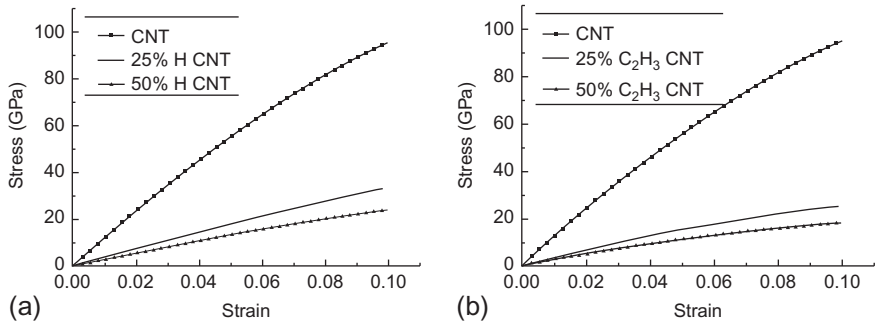

Figure 13.5 Variation of stress with applied strain of CNTs functionalized by (a) H atoms and (b) C_2H_3 molecules.

As shown in Figure 13.3, a (5,5) SWNT is functionalized with H atoms and C_2H_2 molecules. Figure 13.4 shows the full functionalization of CNT along the whole tube (length of 10 nm).

The tensile stretch of CNT is performed by applying loads on one end while the other end is fixed. Figure 13.5 illustrates the variation of tensile stress with applied strain of H- and C_2H_3-functionalized CNT with different density. The Young's modulus of CNT is derived from the slope of elastic stage of the stress–strain curves and listed in Table 13.1. The Young's modulus of CNT is reduced in a large proportion after functionalization with both H atoms and C_2H_3 molecules. In addition, the degree of reduction is increased with the increasing functionalization density.

On the other hand, the tensile compression of pure CNT and functionalized CNTs were performed to study their buckling behaviors. As shown in Figure 13.6, it is clear

Table 13.1 Young's modulus of pure CNT and functionalized CNTs with different densities

Pure CNT	25% H	50% H
1.11 TPa	0.368 TPa 25% C_2H_3 0.304 TPa	0.269 TPa 50% C_2H_3 0.224 TPa

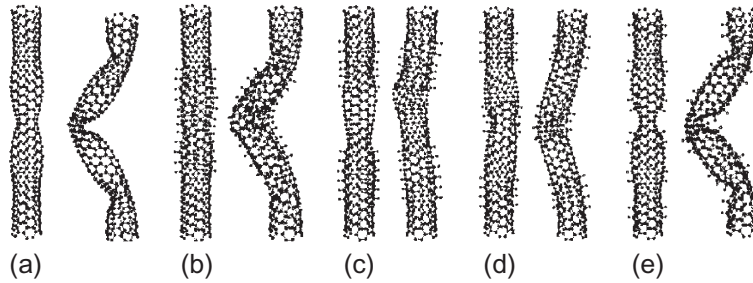

Figure 13.6 Buckling deformation of CNTs with different functionalization configurations: (a) pristine CNT, (b) F-CNT-1, (c) F-CNT-2, (d) F-CNT-3, and (e) F-CNT-4.

that the functionalization type plays a remarkable role in the buckling deformation of CNTs. The buckling is prone to take place at regions where the CNT is functionalized, owing to the defect at the surface.

13.2.2 Interfacial properties of CNT/polymer composite

Since Ajayan et al. (1994) mixed CNTs as inorganic filler into polymer matrix and prepared polymer composites, a lot of work has been done to make CNT composites by nano composite technology. It has been revealed from experimental results that interfacial properties between CNT and polymer play an important role in overall mechanical properties of their composites. Cooper et al. (2001) performed a pull-out experiment on a single carbon nanotube, which crossed the hole of matrix by atomic force microscope and directly found that the interface strength between multi wall carbon nanotube and epoxy resin was 35–376 MPa. For better understanding of the interfacial behavior of CNT/polymer composite, the pull-out test can be simulated by using MD method and MM method (Zheng et al., 2009; Liu and Yang, 2009).

As shown in Figure 13.7, a model of CNT/polyethylene composite is built for the pull-out simulation by using the MD method.

Figure 13.8 illustrates the deformation of the composite. We can see that some polyethylene chains move along with CNT, but those polyethylene chains far from CNT will keep their position when the displacement of CNT is small enough.

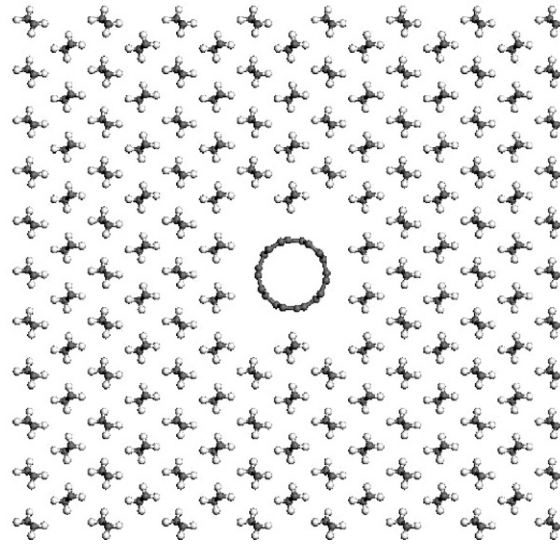

Figure 13.7 MD model of CNT/polyethylene composite.

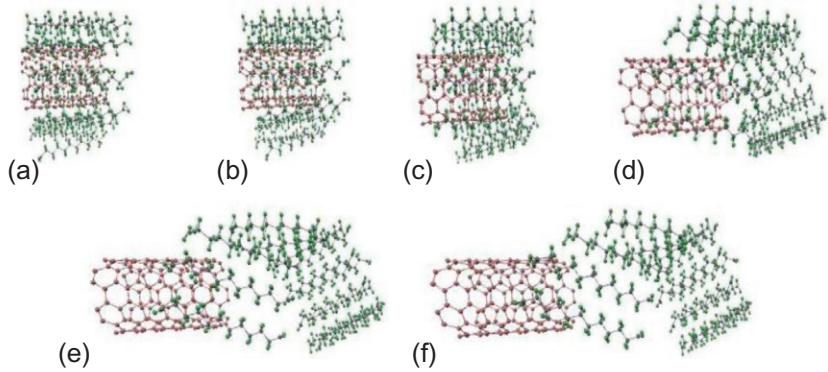

Figure 13.8 Interfacial failure process of CNT/polymer composite: (a) $z = 0.35$ nm, (b) $z = 0.6$ nm, (c) $z = 1$ nm, (d) $z = 2.5$ nm, (e) $z = 3.5$ nm, and (f) $z = 4$ nm.

Polyethylene chains will move slowly because of the increase of the displacement of the CNT and the function of the immovable polyethylene chains. At last, CNT divorces from the polyethylene.

13.3 Mechanical performance of covalent CNT assemblies

To date, a great effort has been made to manufacture covalent CNT assemblies, e.g., 1D, 2D, and 3D networks (Ting and Chang, 2002; Ma et al., 2009; Teng et al., 2011; Fu et al., 2012; Lalwani et al., 2013; Hashim et al., 2012). With the development of a

preparation technique, theoretical models of these assemblies have also been developed (Romo-Herrera et al., 2006; Coluci et al., 2007; Yin and Yin, 2006). Representative CNT networks are super square (SS), super graphene (SG), super cubic (SC), and super CNT. Among these assemblies, the SG is constructed by replacing carbon–carbon bonds of a graphene layer by CNTs, which are covalently connected by many non hexagonal rings. The SS is constructed in a similar manner, but the SWCNTs are linked by four-terminal X-like junctions. In a process analogous to the one used to generate a SWNT, super CNT can be generated from the SG. Having described these 2D and 3D SWCNT networks, the design of optimized super structures and characterization of their mechanical behavior are important issues.

13.3.1 Mechanical properties of CNT plane network

The effects of CNT chirality and size of the junctions on mechanical properties, deformation patterns, and failure mode of CNT plane networks are discussed in this section. Model construction and simulation details can be found in the literature (Liu et al., 2011b).

Typical deformation patterns and the failure mode of the junction in the CNT plane network formed by three (6,6) CNTs subjected to horizontal tensile loads are shown in Figure 13.9. Elastic deformation of the Y junction starts at the beginning of loading and finishes when the load of the Y junction reaches its peak at point *A*. Then a sudden drop in load, caused by the breakage of the carbon–carbon bonds at the top corner of the junction, brings the junction into the second stage at point *B*. In the rupture stage, several "saw-tooth" steps are reduced. This is due to the successional breakage of

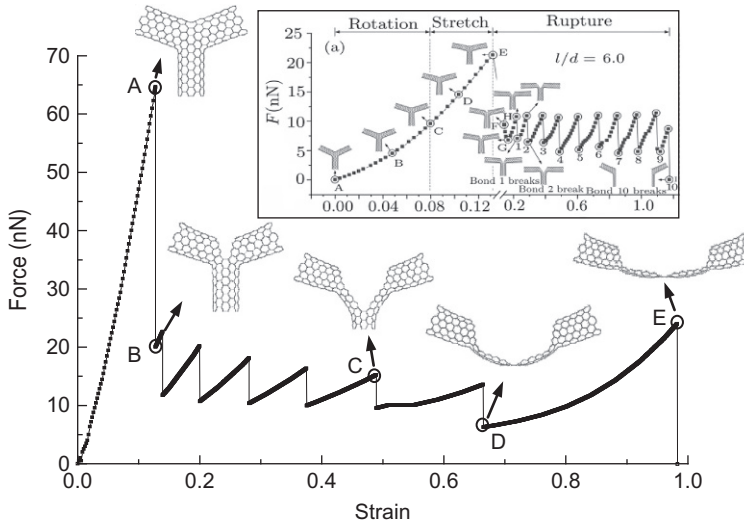

Figure 13.9 Typical deformation patterns and failure mode of a super graphene under horizontal loads; the inset is the result from Chen et al. (2008).

carbon–carbon bonds in the center CNT with the increase of tensile strain, as shown in the deformed states of C and D in Figure 13.9.

Therefore, geometrical parameters of SWCNTs can influence the mechanical properties of the junctions. Their maximum force and corresponding strain as well as failure strain are controlled by both the longitudinal and circumferential sizes of the SWNTs.

13.3.2 Mechanical properties of super CNT

Atomistic, quasi-continuum, and continuum simulations have been adopted in previous studies to study the mechanical properties of super CNT. Nicola (2006) has found the optimum structure for super CNTs with a number of ~2 hierarchical levels, which are similar to the natural optimization in nacre by repeating the procedure used to generate a super CNT. Yin et al. (2008) have also revealed the geometric conditions for designing fractal super CNTs with strict self-similarities and explained the fractal dimensions of zigzag and armchair topologies of the fractal super CNT. What's more, Liu et al. (2012) calculated the size- and shape-dependence of the Young's modulus and Poisson's ratio of the super CNTs (Figure 13.10).

The construction of a super CNT is quite similar to a single SWNT in which the SG is initially built by connecting SWNTs through Y junctions, and then the super CNT is generated by wrapping the SG. Analogous to (n, m) SWNTs, (N, M) super CNTs with different chiralities can be constructed. Hence, super CNT is a quasi-1D fiber with high porosity.

The structure of a super CNT is denoted by $[N, M]$ @ (n, m), where $[N, M]$ represent chirality of super CNT formed by (n, m) SWNTs. Radius R $[N, M]$ of a $[N, M]$ @ (n, m) super CNT can be calculated by

$$R[N, M] = l\sqrt{3(N^2 + NM + M^2)}/2\pi \tag{13.1}$$

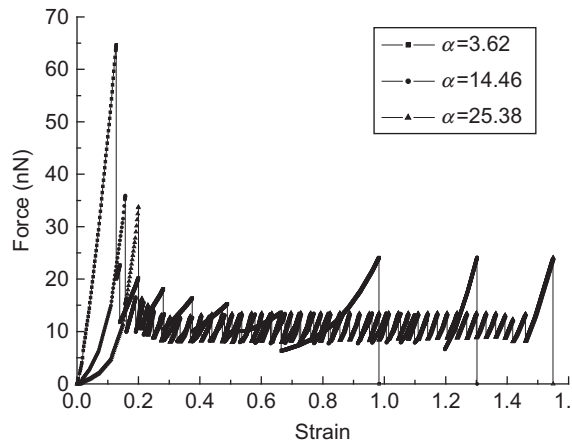

Figure 13.10 Force–strain curves of SS@(6,6) with different aspect ratios of nanotube arm under loads in armchair direction.

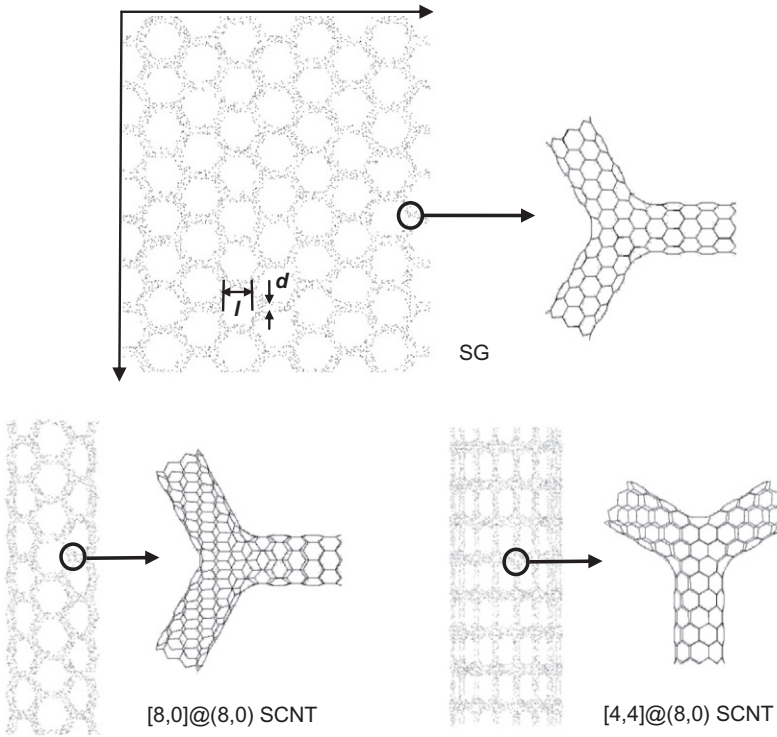

Figure 13.11 Structural representations of a SG and a super CNT.

where l is the length of SWNTs used to generate the SCNT. Particularly, $R[N,N] = 3\,l\,N/2\pi$ for an armchair SCNT and $R[N,0] = \sqrt{3}\,l\,N/2\pi$ for a zigzag SCNT. According to Eq. (13.1), radius of the SCNT explicitly depends on the length of SWCNT and the number of junctions along the circumferential direction.

As shown in Figure 13.11, an SG with eight junctions in both directions is wrapped along the vertical direction to a zigzag [8,0]@(8,0) SCNT and along horizontal direction to an armchair [4,4]@(8,0) SCNT. Details of their representative Y junctions are also given in Figure 13.11.

Figure 13.12 shows the behavior of the tensile force during tensile testing of different Y junctions of armchair and zigzag super CNTs. We can see that the forces used to produce the same tensile strain for different Y junctions depend on their shapes and sizes. Therefore, since the loaded areas are the same, it is noted that the strength of these Y junctions depends on their shapes and sizes. For example, in case of junctions of the zigzag super CNT, the force needed to apply a 10% tensile strain at the junction is increased with increase of the junction angle but is decreased with increase of the SWCNT length (curves a–c in Figure 13.12). The same variation is found in junctions of the armchair super CNT; however, the forces are smaller than of junctions of zigzag super CNTs with the same size.

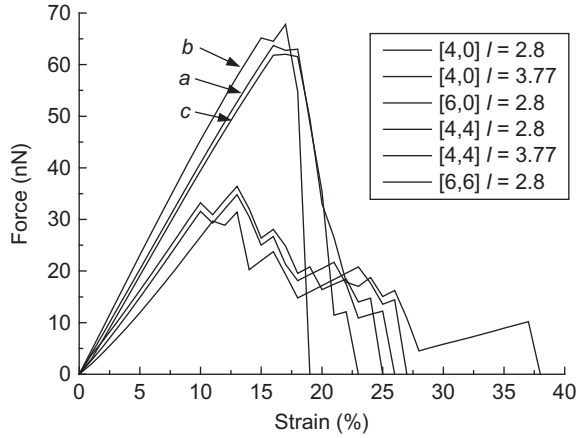

Figure 13.12 Tensile behavior of different junctions of SCNTs.

To show further shape and size dependence of effective properties of super CNTs, simulations of tensile tests on super CNTs were carried out by stretching the super CNTs extremities along the axial directions with a total force F. Since the super CNT can be considered as a cylindrical shell, we may define the normal stress of the super CNT as $\sigma = F/A_0$ and the normal strain as $\varepsilon = \Delta L/L_0$. Therefore, the Young's modulus of the super CNT is the ratio of the normal stress to the normal strain in an axial tension test,

$$Y = \frac{\sigma}{\varepsilon} = \frac{F/A_0}{\Delta L/L_0}, \tag{13.2}$$

where A_0 is the cross-sectional area of the super CNT, L_0 is the initial length of the super CNT, and ΔL is its elongation. For zigzag super CNTs $A_0\,[N, 0] = Na_0$ and for the armchair SCNTs $A_0\,[N, 0] = 2Na_0$, where $a_0 = 2\pi rt$ ($r = 0.313$ nm for (8,0) SWNT and $r = 0.543$ nm for (8,8) SWNT, $t = 0.34$ nm) is the cross-sectional area of the interior SWNTs.

The effective Poisson's ratio v is defined as the ratio of radial shrinkage strain ε' to the normal strain ε,

$$v = -\frac{\varepsilon'}{\varepsilon} = -\frac{\Delta R/R_0}{\Delta L/L_0} \tag{13.3}$$

where R_0 is the initial radius value of the super CNT and ΔR is the radial shrinkage at the free end of the super CNT.

Figure 13.13 presents the computed Young's modulus of both zigzag and armchair super CNTs, changing with their radii, which increase with junction numbers N in the circumferential direction. For fixed values of l, we can see that the Young's modulus of both zigzag and armchair super CNTs increases with their radii R, which is increased by N, and their limits are the same as the Young's modulus of the original SGs. This behavior can be expressed by the relation

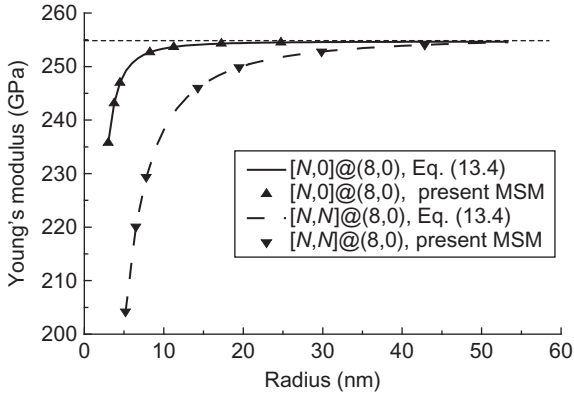

Figure 13.13 Variation of Young's modulus of SCNT with their radii increased by junctions' number.

Table 13.2 Fitted values of parameters in Eq. (13.4)

Type	E_0 (GPa)	R_0 (nm)	α	β	γ
[*N*,0]@(8,0)	235.75	3.09	−18.93	−2.22	18.93
[*N*,*N*]@(8,0)	204.2	5.19	−51.42	−1.66	51.42

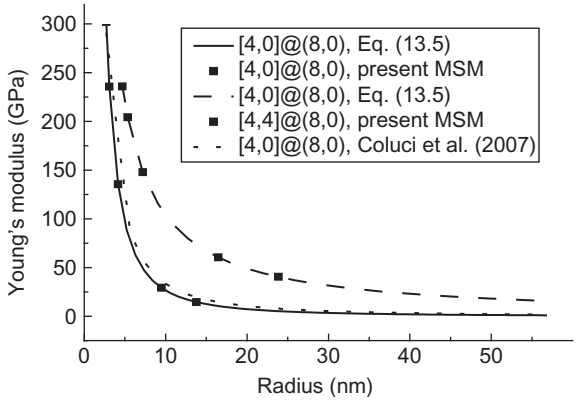

Figure 13.14 Variation of Young's modulus of SCNT with their radii increased by length of SWCNTs.

$$E = E_0 + \alpha(N/N_0)^{\beta} + \gamma \tag{13.4}$$

which can reasonably fit the results with high accuracy. We have chosen $R_0 = 3.09$ nm as the radius of a given zigzag SCNT and $R_0 = 5.19$ nm as the radius of a given armchair super CNT. E_0 is the Young's modulus (calculated by using the modified MSM method) of the smallest super CNTs, α, β, and γ are the parameters. The values of these parameters are listed in Table 13.2.

Figure 13.14 illustrates the computed Young's modulus of both zigzag and armchair super CNTs, changing with their radii, which increase with SWNT length l.

It is seen that for fixed values of N, Young's modulus of both zigzag and armchair super CNTs decrease rapidly with increase of SCNT radius R, which is increased by l, and move toward values that are very close to zero. This Young's modulus can be exactly approximated by the relation

$$E = E_0(l/l_0)^{\beta} \tag{13.5}$$

where $R_0 = 3.09$ nm is radius of a given zigzag SCNT, $R_0 = 5.19$ nm is radius of a given armchair SCNT, E_0 is the Young's modulus of the smallest super CNTs, calculated by using the modified MSM method, and β is the parameter. Values of these parameters are listed in Table 13.3.

These results indicate that Young's modulus of super CNTs depends on their shapes and sizes. On the one hand, stiffness of both armchair and zigzag super CNTs can be improved by increasing the junctions number (N for zigzag super CNTs and $2N$ for armchair super CNTs) and the limits of their values are the same as those of their original SG. On the other hand, their stiffness can be reduced rapidly to zero by increasing length l of the constituent SWNTs.

Figures 13.15 and 13.16 show Poisson's ratio of zigzag and armchair super CNTs. We can see that Poisson's ratios of super CNTs are very large, which means remarkable radial shrinkage may occur when super CNTs are axially stretched. At the same time, they are also shape and size dependent. This Poisson's ratio can be expressed by the relation

Table 13.3 Fitted values of parameters in Eq. (13.5)

Type	E_0 (GPa)	R_0 (nm)	β
[4,0]@(8,0)	235.75	3.09	−1.86
[4,4]@(8,0)	204.2	5.19	−1.08

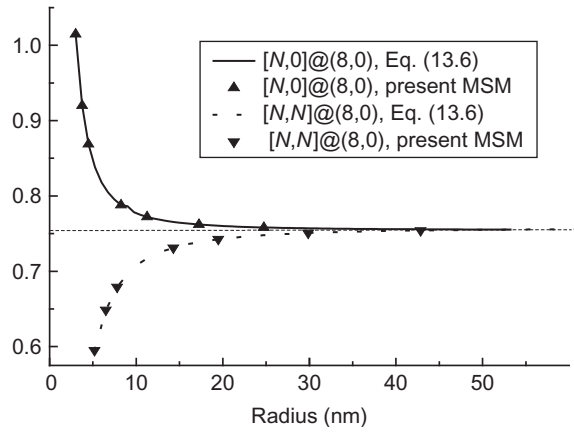

Figure 13.15 Variation of Poisson's ratio of super CNTs with their radii increased by junctions' number.

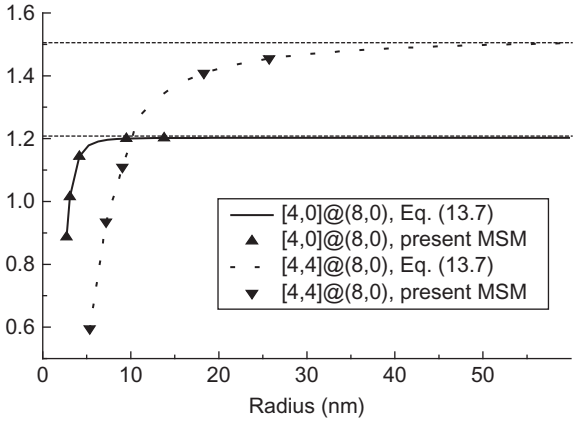

Figure 13.16 Variation of Poisson's ratio of super CNTs with their radii increased by length of SWNTs.

Table 13.4 Fitted values of parameters in Eq. (13.6)

	ν_0	R_0 (nm)	α	β	γ
[*N*,0]@(8,0)	1.01	3.09	0.26	−2.03	−0.26
[*N*,*N*]@(8,0)	0.594997	5.19	−0.16	−1.79	0.16

Table 13.5 Fitted values of parameters in Eq. (13.7)

	ν_0	R_0 (nm)	α	β	γ
[4,0]@(8,0)	0.89	3.09	−0.32	−3.90	0.32
[4,4]@(8,0)	0.59	5.19	−0.93	−1.54	0.93

$$v = v_0 + \alpha(N/N_0)^{\beta} + \gamma \quad \text{for fixed } l \tag{13.6}$$

$$v = v_0 + \alpha(l/l_0)^{\beta} + \gamma \quad \text{for fixed } N \tag{13.7}$$

where $R_0 = 3.09$ nm is the radius of a given zigzag super CNT and $R_0 = 5.19$ nm is the radius of a given armchair super CNT. v_0 is the Poisson's ratio of the smallest SCNTs, and α, β, and γ are parameters. Values of these parameters are listed in Tables 13.4 and 13.5.

For fixed SWNT length l, Poisson's ratio of armchair super CNTs is increasing from 0.6 to 0.75 with increase of the *N* value; however, on the contrary, Poisson's ratio of zigzag super CNTs is decreasing from 1.1 to 0.75 with increase of the *N* value. Hence, the limit values of zigzag and armchair super CNTs wrapped with similar original SGs are quite the same. On the other hand, for fixed junctions number N_0, Poisson's ratio of armchair super CNTs increases from 0.59 to 1.5 with increase of

the l value, and Poisson's ratio of zigzag super CNTs increases from 0.88 to 1.2 with an increase of the l value. It is revealed that the high-bending flexibility of these long SWNTs is transferred to the radial flexibility of their super CNTs. What's more, armchair super CNTs are more sensitive to increase of the l value.

Therefore, both zigzag and armchair super CNTs have upper and lower bounds of Young's modulus and Poisson's ratio. The shape and size of super CNT can be determined by choosing junctions number and SWNT length. In addition, the axial Young's modulus of zigzag and armchair super CNTs can be improved by increasing the junction number but is weakened greatly by increase of SWNT length. What's more, super CNT's chirality, particularly armchair and zigzag, has notable effects on Poisson's ratio. Poisson's ratios of zigzag super CNTs decrease with the increase of junctions' number but increase with increase of radius. On the contrary, Poisson's ratios of armchair super CNTs increase with increase of radius, which depends on the junctions' number or length of SWNTs.

13.3.3 Mechanical properties of covalent CNT network composites

Composites reinforced by covalent CNT network can be considered as an orthotropic composite. Therefore, to learn mechanical properties of the composite, we need to calculate the stiffness coefficients: $\overline{D}_{11}$, $\overline{D}_{12}$, $\overline{D}_{22}$, and $\overline{D}_{66}$, where the 11-direction follows the growth direction of the branches of a CNT at a joint. Figure 13.17 illustrates the variations of stiffness coefficients versus the length ratio for different junction angles. All of the stiffness coefficients increase with the length ratio of the *R*-CNT. However, the change in magnitude of the stiffness coefficients differs depending on the junction angle. The longitudinal stiffness $\overline{D}_{11}$ increases remarkably with the length ratio, and a larger junction angle leads to a lower stress level. When $\alpha = 5°$, the effective stiffness coefficient is close to the value derived from the simple mixtures rule for continuous fiber composites, as shown in Figure 13.17a. Larger junction angles improve stiffness coefficients $\overline{D}_{12}$ and $\overline{D}_{22}$, which are not sensitive to the length ratio of the *R*-CNT (see Figure 13.17b and c). In contrast, when $\alpha = 75°$, $\overline{D}_{66}$ increases smoothly with the length ratio and a higher shear property is obtained.

13.4 Mechanical performance of non covalent CNT assemblies

The high-performance macroscale non covalent assemblies comprise CNT arrays, films, fibers, sponges, foams, etc. (Zhou et al., 2012; Lu et al., 2012). Their superior mechanical properties, such as tensile strength and flexibility, result not only from the outstanding properties of individual CNTs but also from the additional properties attributed to the tube–tube junctions and interactions. Addition of these CNT macrostructures into the in-brittle matrix can significantly improve the flexibility of the matrix material.

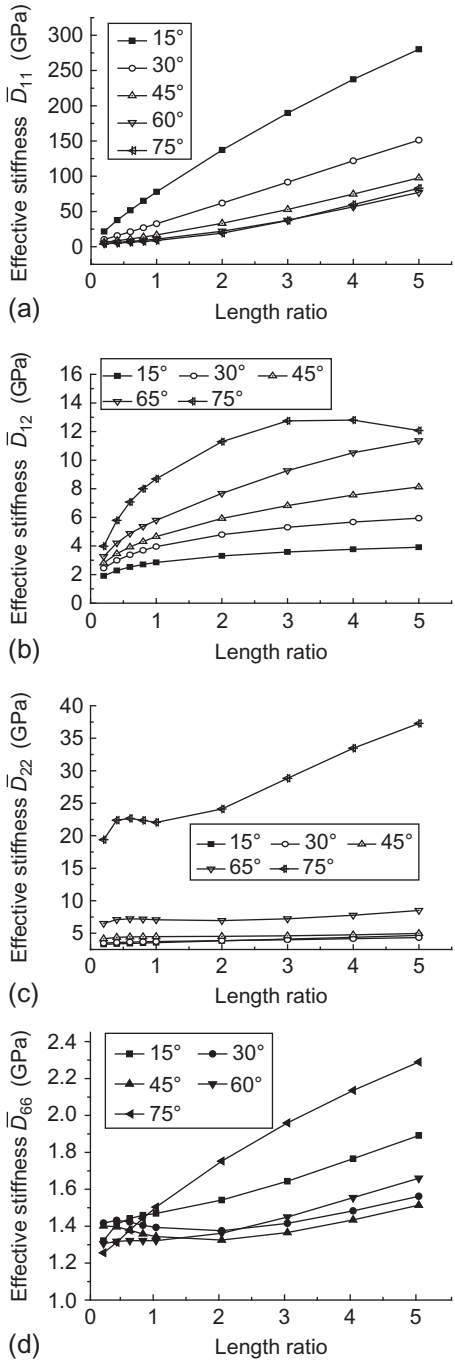

Figure 13.17 Variations of stiffness coefficients with length ratio.

The processing of CNT fibers based on CNTs offers a unique demonstration of the evolution of CNT structures at the various length scales as well as the opportunity to identify key contributing factors driving fiber performance (Lu et al., 2012; Koziol et al., 2007). In 2002, Jiang et al. (2002) first spun a 30-cm long CNT fiber from a free-standing vertical-aligned CNT array. It was claimed that the processability of the continuous fiber was attributed to the high quality and regular structure of the super-aligned CNT array (Zhang et al., 2006). Zhang et al. (2006) considered that the Van der Waals (VdW) forces play a prominent role in CNT fiber spinning and proposed a schematic mechanistic model of the process. In addition, Zhang et al. (2007a) affirmed that the pure bundles without amorphous carbon are more important for CNT web drawing. However, some researchers proposed that CNT junctions might play a pivotal role in the formation of films and influence their morphological and mechanical properties. Using an optical microscope, Kuang and He (2009) validated the presence of these end-to-end junctions from in situ recording of the CNT film forming process. Fallah Gilvaei et al. (2011) identified two factors involved in the bundle drawing process: end knots, entanglement in the middle of the CNT array.

CNT fibers are characterized by multi level structures including macroscopic fiber, mesoscopic bundle networks, and microscopic nanotubes, as shown in Figure 13.18. So far, experiments have indicated that the tensile strength of CNT fibers spun from CNT forests varies from hundreds of MPa to about 4 GPa (Zhang et al., 2004, 2007a,b; Deng et al., 2011; Zu et al., 2012; Li et al., 2006). Hence, the mechanical performance of the fibers produced so far has fallen far behind that of their constituent CNTs.

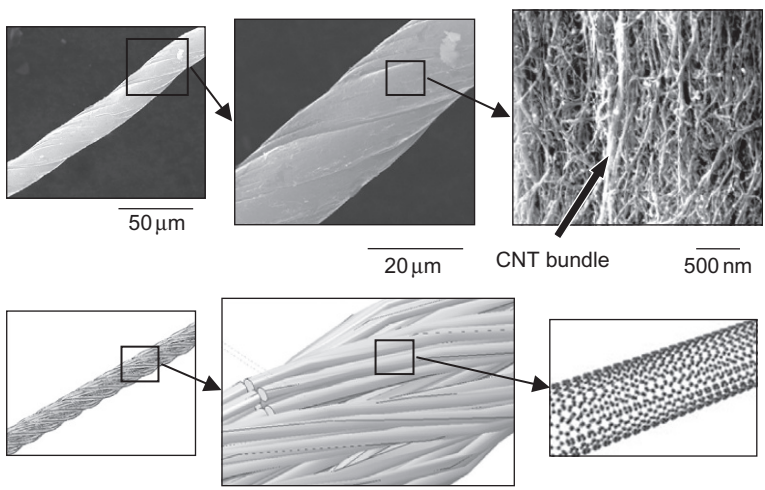

Figure 13.18 SEM photos of the CNT fiber: the overall view (top left) with enlarged view (top middle) showing macroscopic feature of the fiber. The second level of the fiber is CNT bundles (top right), consisting of CNTs as the third level. The bottom row presents a schematic diagram of the fiber hierarchical structure, sequentially magnified from left to right.

In mesoscale, two main failure modes are deemed to limit the bundle strength, i.e., (i) CNT intrinsic fracture or (ii) CNT sliding. Therefore, in macroscale, CNT bundle fracture and CNT bundle sliding may follow on to block the fiber strength.

In theory, a few mechanics models have been put forward to quantitatively investigate the effects of constituents in two different scales on the mechanical properties of CNT fibers (Li et al., 2012; Liu et al., 2013; Rong et al., 2012; Sun et al., 2012). Liu et al. (2013) use coarse-grained MD (CGMD) simulation to illustrate the structural evolution mechanisms of CNT fibers under tension and study the effect of intertube interactions on the CNT fibers. What's more, Li et al. (2012) summarized that interfacial contact and load transfer in the fiber occur between both the mesoscopic bundles/threads and the microscopic nanotubes by combining multiscale experiments and two-level simulations.

In this paper, the multiscale modeling approach covers classical MD simulations and mesoscale MD simulations as well as macroscale FE simulations to further explore the limitations of the hierarchy structures and the relations of mechanical behavior at different scales.

13.4.1 Mechanical properties of dry-spun CNT fibers

The main mechanism contributing to a significant toughening of fiber is energy-dissipating sliding of the bundles or tubes at micrometer scale, while nano-order mechanisms are, however, important in controlling the bundle sliding behavior. Here, the mechanisms are classified according to the components involved and the dimensions at which the mechanism operates. CNT-fiber-based composites are expected to play a super-stiffening, strengthening, and toughening role in the next generation of composites.

The stress–strain curves of CNT fibers at different strain rates are shown in Figure 13.19, which can be divided into three stages. In the first stage, the stress

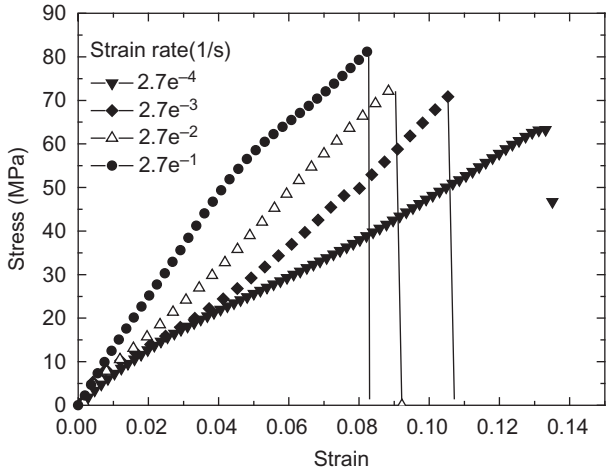

Figure 13.19 The tensile stress–strain curves of CNT fibers at different strain rates.

linearly increases with the strain. As the fiber further extends, the CNTs in bundles bear the main load initially and then the CNTs in the thread become straight. As a result, the plastic deformation of the fiber generates. Then, the CNT fiber breaks due to slipping and sliding of more and more CNTs in bundles and threads. The elastic modulus of CNT fiber is about 1–1.5 GPa, which is in the range of reported dry-spun CNT fibers (Deng et al., 2011; Zu et al., 2012). The modulus of the CNT fiber depends on the loading rate significantly. At the lower strain rate, the CNT fiber exhibits a well ductility, and the fracture strain can be reached to 0.14. In contrast, the strength of CNT fiber is enhanced with the increase of the strain rate. A reasonable explanation is that for the lower tensile rate, the CNTs in bundles can be adequately redistributed and the stress be released by the tube sliding, which results in a lower tensile modulus and yield strength. As the inter connections between CNTs in bundles are partly destroyed, the strain of the CNT fiber is well redistributed through the slipping of CNTs in bundles as well as unfolding and stretching of CNTs in threads, leading to a high fracture strain. At the higher strain rate, the failure mechanism of the CNT fiber belongs to the rapid damage of the CNTs in bundles, leading to a small fracture strain.

In order to illustrate the fact that the redistribution of the CNTs can improve the ductility of CNT fiber, the cyclic tensile testing is carried out under strain rate 2.7×10^{-3}/ps. The loop stress–strain curve is shown in Figure 13.20. At first cycling, the stress increases with the tensile strain. Then, the unloading starts at the strain about 8–9%. It can be seen that the averaged plastic strain is about 5%. For each cycling, the peak stress is up to a higher value than in previous cycling due to the obvious strain hardening. For a CNT fiber, the lower-rate loading leads to enough relaxation and recovery of the CNTs in a loading–unloading cycling. Moreover, CNTs in thread and bundles are elongated or redistributed in the fiber. Consequently, more and more CNTs take part in the bearing of the load. Thus, the maximum stress at fiber breakage is about 100 MPa undergoing six loading–unloading cycles, which is much higher than the strength of 70 MPa of fiber under single-tensile testing at the same strain rate

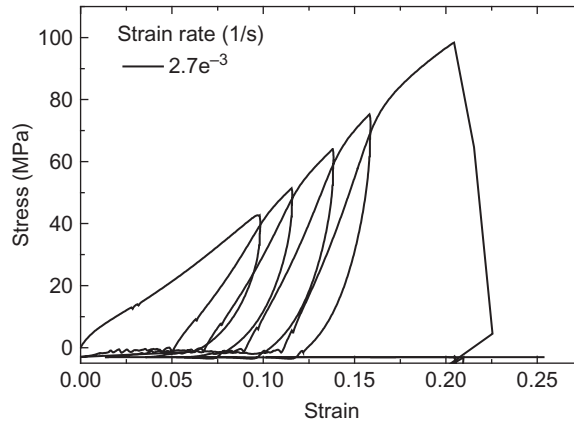

Figure 13.20 Stress–strain curve of a single fiber under cyclic tensile testing with strain rate 2.7×10^{-3}/ps.

2.7×10^{-3}/ps. Therefore, a deformation and failure mechanism of CNT fiber can be described by the fact that more and more CNTs in bundles and threads take part in bearing of the load in the loading–unloading cycling, which leads to a higher strength of the fiber in cyclic test.

To investigate microstructural evolution of the CNT fiber, MD models of two types of CNT films are developed, in one of which CNTs are randomly stacked, while in another CNTs are regular stacked. Figure 13.21 depicts the initial CNT film segment of these two types; each of them is 500 nm in length. The size of the CNT film is $1 \times 36 \times 2$ nm^3, where the CNTs are initially parallel aligned along the length of the film with spacing of 2 nm.

During each simulation, random velocities are first assigned to each bead of the CNT film to attain a desired initial temperature of 300 K. Afterward, simulations of the twisting process from the equilibrated CNT films to fibers are conducted by applying torsion to the film ends in opposite directions with a rate of 360° per 100,000 fs. Afterward, during the simulation of fiber tension, a uniform axial strain rate of 0.0001 per 500,000 fs is applied to one end of the fiber while keeping another end fixed.

Twisting simulations are carried out on the above-mentioned equilibrated CNT films. Configurations of CNT fibers twisted from CNT films with random and regular end stacking are described in Figure 13.22. In both fibers, CNTs are curled up under the external twist loading and bundled by the intertube VdW forces. However, a remarkable difference in crisscross and winding patterns can be found in these two types of fibers. In the fiber obtained from a CNT film with random CNT stacking, CNTs in different layers bundle into a uniform cylinder under the coupling effect of twisting and VdW interactions, as shown in Figure 13.22a. However, the fiber obtained from a CNT film with regular CNT stacking displays a significantly different morphology: the CNTs form a distinct, uniform crisscross pattern in some regions; however, this pattern unravels at the overlapped regions of the fiber due to insufficient VdW interactions, as shown in Figure 13.22b. Thus, the fiber diameter at these

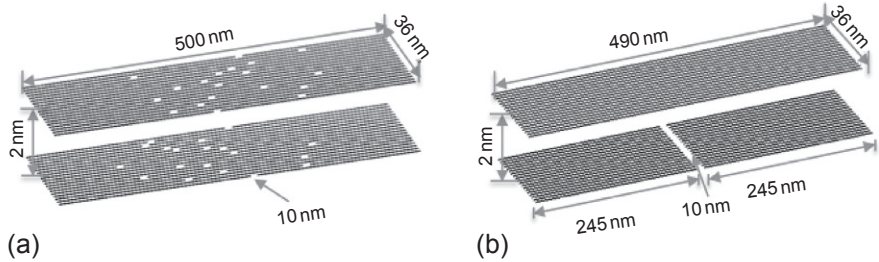

Figure 13.21 Initial coarse-grained models of CNT films with (a) random stacking and (b) regular stacking. The red and blue lines represent CNTs on top and bottom layers of the film, respectively. The spacing among CNTs at the same layer as well as the distance between two layers are enlarged for better distinction.

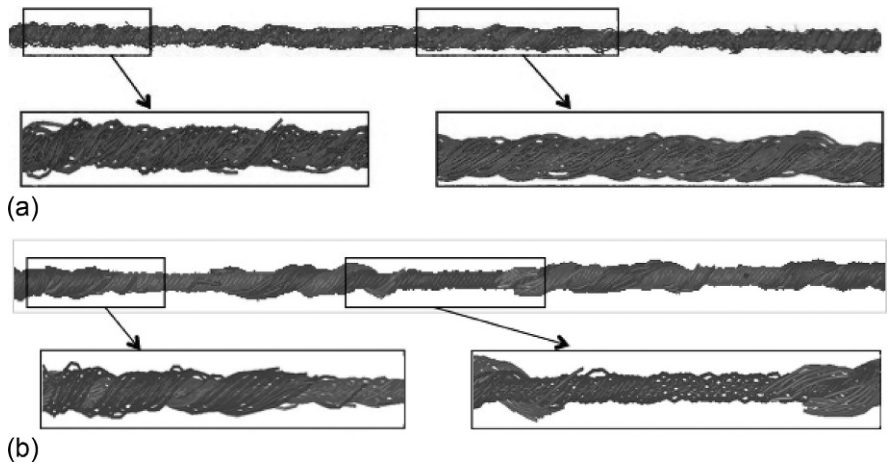

Figure 13.22 Structural reorganization of (a) fiber with random CNT stacking and (b) fiber with regular CNT stacking after twisting. Enlarged drawings show different morphologies at different sections of the fibers.

overlapped areas is larger than that at the other area. The morphology also shows that the CNT ends in the fiber with regular stacking are concentrated and form weak cross sections while the ends in the fiber with random stacking are scattered after twisting.

In a CNT fiber, the inevitable tube ends signify the discontinuities in CNT load-carrying capability when the fiber is under tension. To gain insight into the relationship between microstructural characteristics and macroscopic mechanical behavior, tensile simulations are conducted on both regular and random CNT fibers. Variations of tensile strength of these two types of CNT fibers (both are 1 μm in length) with increasing twist are illustrated in Figure 13.23a. These simulations demonstrate that

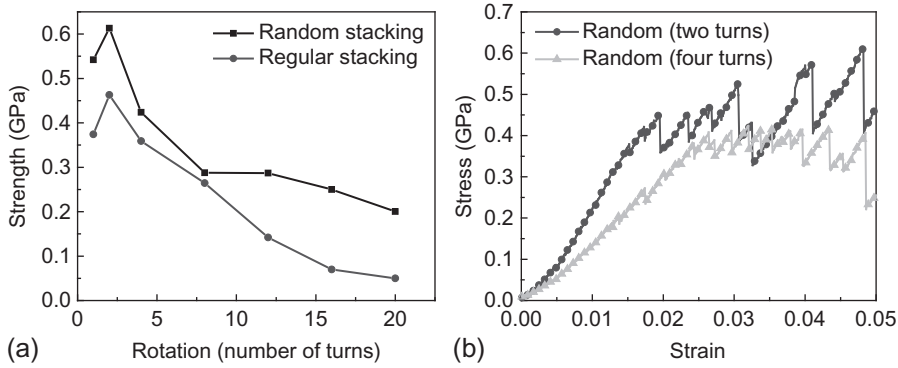

Figure 13.23 Computed results of random CNT fiber and regular CNT fiber: (a) comparison of strength of twisted CNT fibers with random end stacking and regular end stacking under different rotation turns and (b) typical stress–strain curves for CNT fibers with random end stacking.

the highest tensile strength is 0.62 and 0.57 GPa for random and regular CNT stacking fibers, respectively. The difference shown in their tensile response clearly demonstrates the benefits of random CNT stacking along the fiber length. In addition, it is interesting to note that the fiber tensile strength is initially enhanced with increasing twist. The highest fiber strength is reached after two full turns of rotation while the strength drops subsequently with further twisting. The effect of twisting on the fiber strength obtained here is consistent with that concluded from experimental characterizations. The strength increase at low rotation angle may be attributed to an enhancement in VdW interactions between CNTs, while the strength reduction after optimal rotation can be attributed to the large off-axis angle of the CNTs induced by fiber twisting. The trade-off between tightening the nanotubes (higher VdW interaction and better load transfer) and nanotube axial load-carrying capability (better alignment) needs to be taken into account in the optimal design of fiber strength. Furthermore, typical tensile stress–strain relations of the random fiber with small twisting angles are given in Figure 13.23b. Each of these curves has two stages. In the first stage, the fiber stress increases nearly linearly with strain because of the CNT stretching; in the second stage, the fiber stress oscillates due to continuing bond stretching and intertube sliding.

To further identify the contributions to the axial tensile stress in the CNT fiber, the axial stress is decomposed into three categories, which are attributed to bond stretching, bond angle bending, and VdW interactions. The same decomposition has been employed to identify the relation between microstructural characteristics and macroscopic mechanical behavior of CNT networks. As shown in Figure 13.24, the bond stretching term plays the dominant role, while the bond angle term and the VdW interaction term are much smaller. This fact has also been noticed during the deformation of films with randomly distributed CNTs. Thus, to obtain a CNT fiber with better mechanical performance, higher individual CNT stretching is needed. In other words, more CNTs along the axial direction are needed to bear tensile loads after the densification via twisting. Moreover, by tracking the length change of the CNT bonds in the

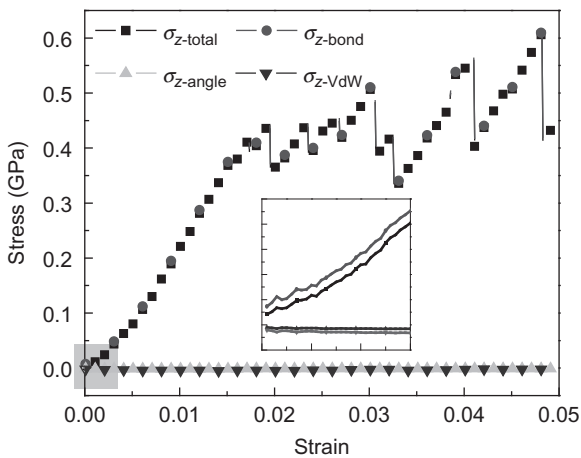

Figure 13.24 The relationship between total fiber tensile stress and strain, with decomposition of $\sigma_{z\text{-total}}$ into contributions from bond stretching, $\sigma_{z\text{-bond}}$, bond angle bending, $\sigma_{z\text{-angle}}$, and intertube VdW interactions, $\sigma_{z\text{-VdW}}$.

two CNT fibers during the whole tension process, it is revealed that all the tensile strains of CNTs in the fiber are under 2%, which is significantly lower than their failure strain of about 16%. Consequently, if only intertube VdW forces are responsible for the stress transference among the CNTs within the fibers, the superior mechanical properties of the individual CNTs are hardly brought into full play.

A schematic diagram in Figure 13.25 illustrates a CNT fiber assembled from collapsed DWNTs, where the white cylinders indicate mesoscale bundles of CNTs. A schematic sketch of eight close-packed collapsed DWNTs in a bundle is plotted in Figure 13.25b. A full-atom model of an elementary collapsed DWNT is enlarged and drawn in Figure 13.25c.

The CG models of the CNT fibers for simulations were constructed with the CNT bundles aligned along the fiber axis direction (Figure 13.26). In the present fiber models, the length of each bundle is considered as 100 nm with a constant gap size of 40 nm. The gap size is in the same order of magnitude to make volume density of the CNT fiber

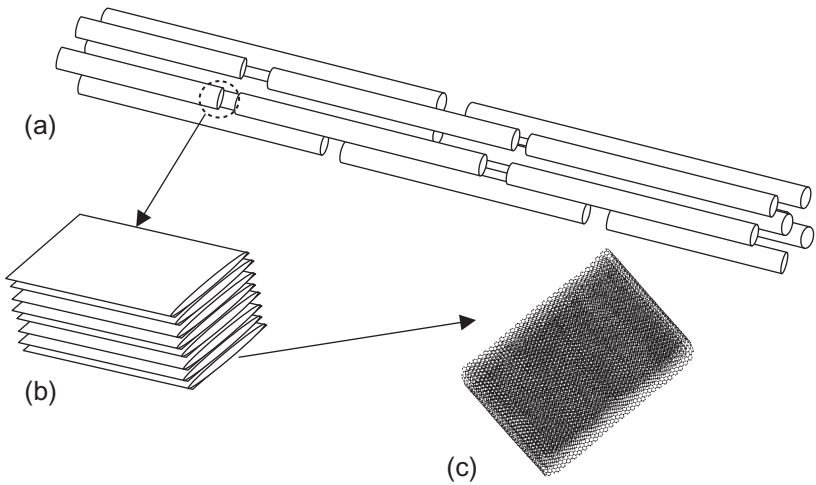

Figure 13.25 Schematic diagram of hierarchical structural of CNT fiber: (a) macroscopic fiber, (b) mesoscopic bundle, and (c) microscopic flattened SWNTs.

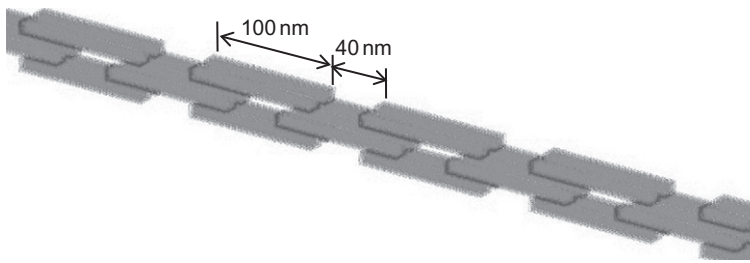

Figure 13.26 CG model of pure CNT fiber composed of aligned DWNT bundles.

model close to measured value. The system is under periodic boundary conditions in dimensions perpendicular to fiber direction, and the system size in the x–y plane is large enough to prevent any interaction across the boundary for atoms in the fiber.

Static tensile tests were performed using the same CNT fiber model at different strain rates, ranging from $1e^{-4}$ to $8e^{-4}$/ps. During the tensile tests, a constant velocity is applied on one end of CNT fiber model while the other end is clamped. The force on the mobile CNT fiber end is recorded, and the stress is calculated as the average force per unit area.

The stress–strain curves of the CNT fibers under different strain rates are plotted in Figure 13.27a. All the curves can be divided into three stages: an elastic stage with initial slope, a hardening stage with reduced slope, and a failure stage. The slope of the stress–strain curve in the linear stage increases significantly with the strain rate (see inset for its enlarged drawing), resulting in significantly increase of tensile modulus with strain rate. The dependence of bond energy and pair energy on strain of the CNT fibers at different strain rates are deducted and illustrated in Figure 13.27b and c.

However, the tensile strength of CNT fibers to the strain rate is involved in two regimes: the tensile strength increases monotonically with the strain rate before $4e^{-4}$/ps and then reaches a saturated value that is determined by CNT bundle characteristics. Therefore, in this model, $4e^{-4}$/ps can be considered as a critical strain rate, from which the deformation mechanism changes. Specifically, when the strain rate is less than the critical value, the deformation and failure of CNT fiber is owning to interbundle sliding, as revealed in Figure 13.28a. A SEM image showing sliding-induced fracture of CNT fiber under low strain rate is also given in Figure 13.28a. The elongation degree of DWNT bundle in the fiber under loading at low strain rates is less, which can also be demonstrated by bond energy–strain curves in Figure 13.27b. Therefore, the strength of CNT fiber is determined by interfacial properties between DWNT bundles when the strain rate is small. The sliding between DWNT bundles and pull-out of CNTs result in significant plastic deformation of CNT fiber. The SEM image of failure morphology of CNT fiber shows that a large number of CNTs is pulled out, as shown in Figure 13.28b, which is consistent with the simulation of CG model. What's more, the failure strain is increased accordingly, due to an increase of elongation of CNT bundles. In the other regime, when the strain rate rises up to the critical value, fiber breakage occurs where consternation stress reaches the ultimate stress of the CNTs, as revealed in Figure 13.28b and c. The SEM photo showing a fracture surface of CNT fiber under high strain rate is also given in Figure 13.28c where a brittle-like failure of the CNT fiber can be found.

Beyond the critical strain rate, the plastic deformation process of CNT fiber is shortened and all the CNT fiber failure is caused by CNT bundle breakage, although the elongation degree of bundles is varied with the strain rate (see Figure 13.29a–f). Therefore, the tensile strength keeps the saturated value that depends on the mechanical properties of CNT bundles used in the present model. In addition, a higher strain rate leads to an earlier breakage of the CNT bundle and then a decreased failure strain and brittle breakage of the CNT fiber. The dependence of modulus, strength, and failure strain are plotted in Figure 13.30a–c. The simulation results also prove that the

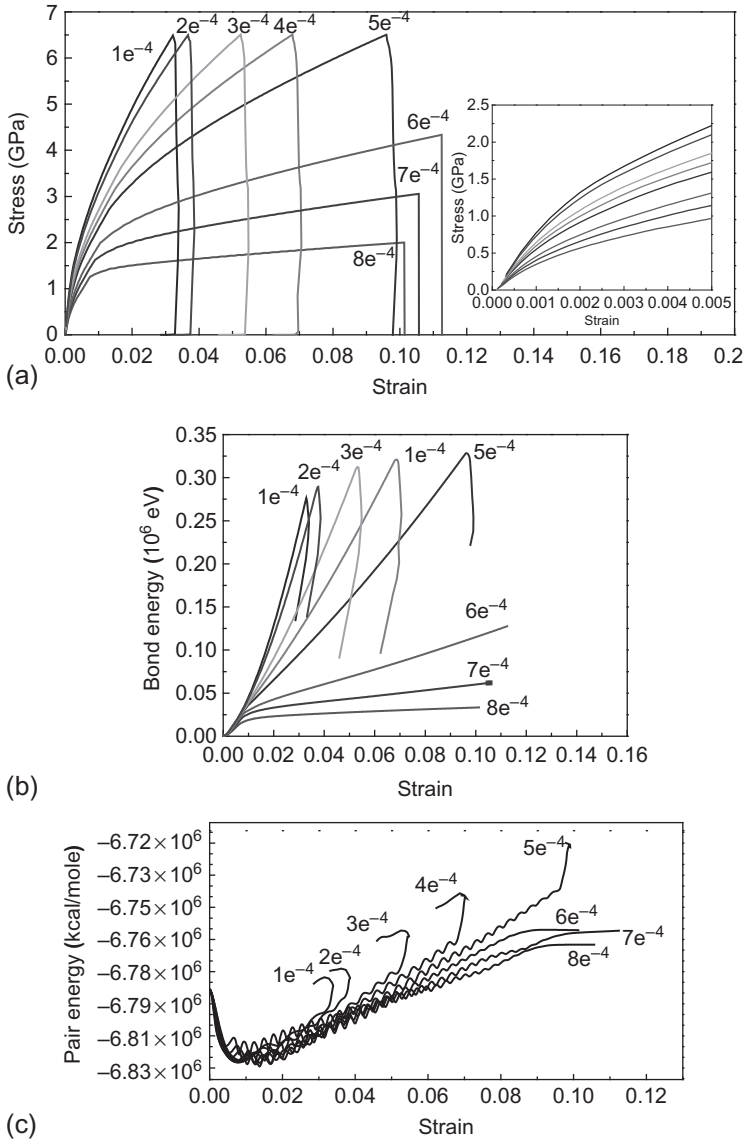

Figure 13.27 Variation of tensile properties of CDWNT fiber with strain under static stretching at different strain rates: (a) stress–strain curve, (b) bond energy, and (c) VdW energy.

interface between DWNT bundles is weaker in the fiber, so slipping beyond a critical load will firstly occur at the inter-bundle interfaces.

To further study the plasticity of the CNT fibers, cyclic loading/unloading tension at low strain rates was performed. In these tests, the CNT fibers experienced loading and unloading in each cycle, and a higher peak force (add 1000 nN) than that in the

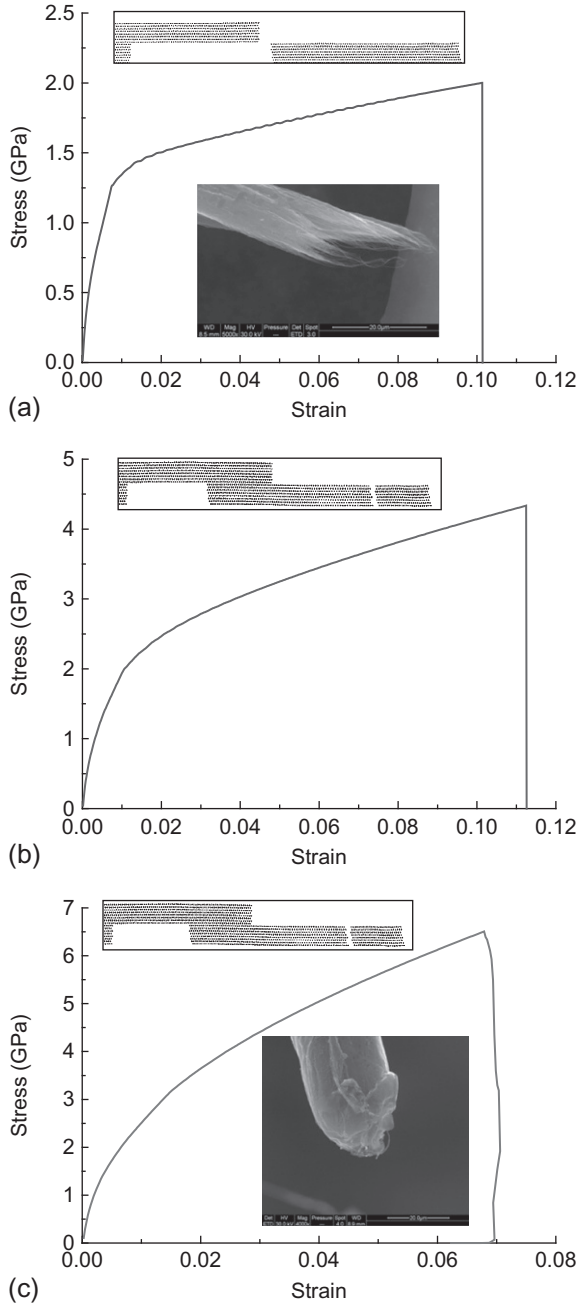

Figure 13.28 Failure modes of CNT fibers under stretching at different strain rates: (a) $1e^{-4}$/ps, (b) $3e^{-4}$/ps, and (c) $5e^{-4}$/ps.

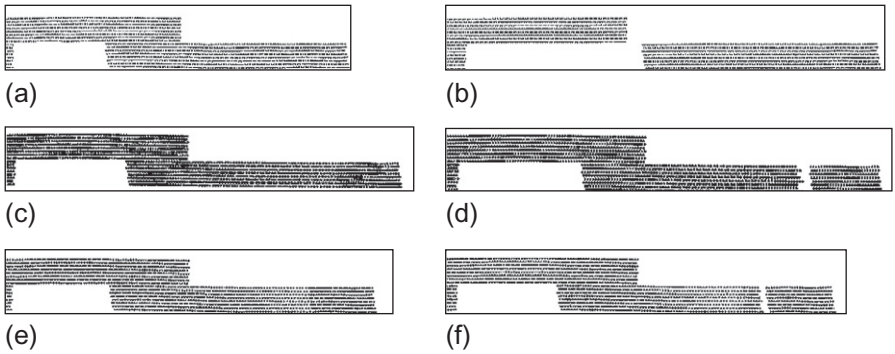

Figure 13.29 Plastic deformation process and failure of DWNT bundles at different strain rates: (a) plastic deformation; (b) failure at strain rate of $1e^{-4}$/ps; (c) plastic deformation; (d) failure at strain rate of $3e^{-4}$/ps; (e) plastic deformation; and (f) failure at strain rate of $5e^{-4}$/ps.

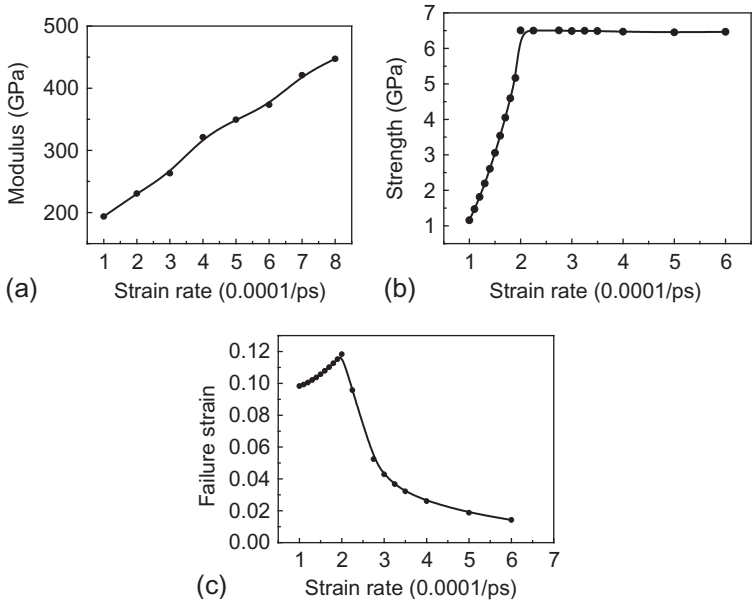

Figure 13.30 Dependence of properties on strain rate of the CNT fiber: (a) tensile modulus, (b) tensile strength, and (c) fracture strain.

previous cycle was applied under each reloading period. Figure 13.31 shows the stress–strain curves of a CNT fiber under the cyclic loading/unloading at strain rates of $2e^{-4}$ and $3e^{-4}$/ps, respectively. The CNT fibers exhibit excellent plastic deformation. Progressive permanent strain of the CNT fibers was calculated and is illustrated

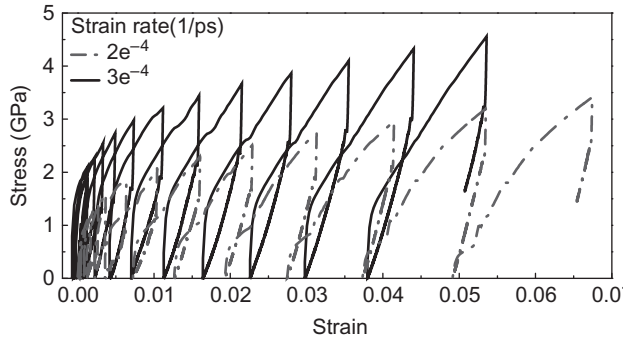

Figure 13.31 Stress–strain behavior of CNT fibers during incremental cyclic loading at different strain rates.

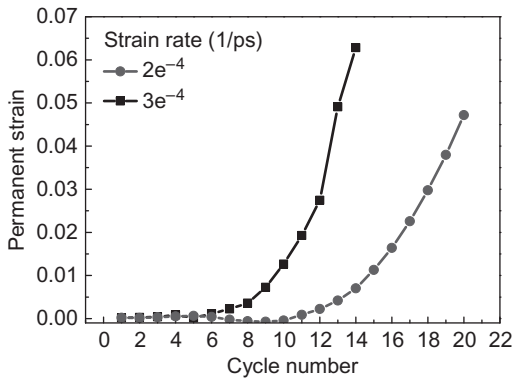

Figure 13.32 Permanent strain of CNT fibers after cyclic loading at different strain rates.

in Figure 13.32. It is found that the plastic deformation emerges after a few cycles and increases more and more rapidly with cycle number.

13.4.2 Interfacial shear strength of CNT fiber/polymer

The composite interfacial shear strength, which reflects the load transfer efficiency between the fiber and the resin, plays a significant role in determining the mechanical properties of the composite. The micro mechanical techniques available for the measurement of single fiber interfacial shear strength include a fragmentation test (Godara et al., 2010), single fiber pull-out (Nova et al., 2013), single fiber push-out test (Sharma et al., 2012), and microdroplet test (Kang et al., 2009). For the microdroplet test, the magnitude of force applied to the microdroplet during the test can be accurately measured.

As shown in Figure 13.33, a CNT fiber with a diameter of 20 μm was utilized as a single fiber for a microdroplet test. Droplets were made from three types of polymers,

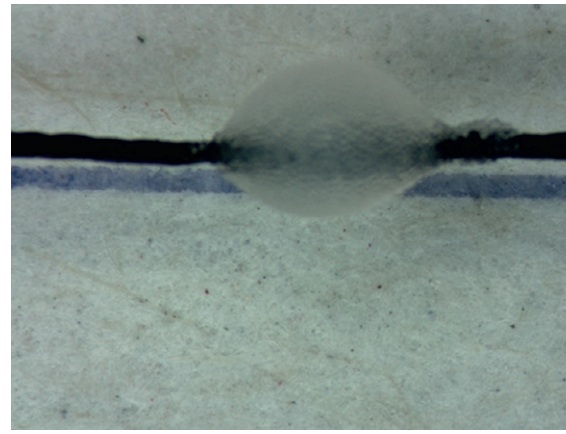

Figure 13.33 CNT fiber microdroplet test.

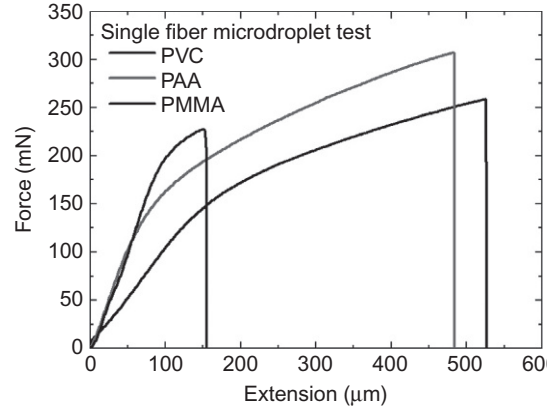

Figure 13.34 Force–extension curves for different CNT/polymer microdroplet test.

including PVC, PAA, and PMMA. Figure 13.34 shows the typical behavior of load versus extension measured from the microdroplet test for an embedded length of 500 μm. The load non linearly increased up to the maximum load (F_d) and then abruptly dropped to zero. Just after the maximum load, the interfacial fracture between fiber and epoxy occurred.

The interfacial shear strength between fiber and epoxy may be calculated from the following expression:

$$\tau_{max} = \frac{F_d}{\pi D_f L_e} \tag{13.8}$$

where τ_{max} is the interfacial shear strength, F_d is the maximum load, D_f is the fiber diameter, and L_e is the embedded length. This equation assumes a uniform shear lag model of a cylindrical single fiber with a surrounding matrix where shear stresses

are uniformly distributed along the fiber–matrix interface. From the force–extension curves illustrated in Figure 13.34, the interfacial shear strength of CNT composites is 3.75, 4.17, and 5 MPa for PMMA, PVC, and PAA as matrix, respectively.

13.5 Concluding remarks

Novel carbon nanotube-based macrostructures, including covalent networks and self-assembled films, are expected to attain the superb mechanical properties of CNTs at macroscale. The successful fabrication of these macrostructures will contribute to development of high-performance composites and multi functional devices. Based on geometric configuration and construction pattern, carbon nanotube-based macrostructures can be divided into 1D carbon nanotube fibers and super carbon nanotube networks, 2D carbon nanotube covalent networks and carbon nanotube films, and 3D carbon nanotube sponges, carbon nanotube arrays, etc. To date, preparation techniques and experimental research have been well developed. However, carbon nanotube-based macrostructures have not been fully investigated theoretically.

In this paper, the mechanical behavior of typical 2D and 3D carbon nanotube-based macrostructures is emphasized. The three main objectives of the research are tensile modulus and load capacity of the macrostructures; macrostructural deformation and failure behavior and correlated microstructural evolution of the macrostructures; and effective mechanical properties of macrostructure composites. The present research is of important academic and practical significance in understanding macro- and micro mechanical behavior of carbon nanotube-based macrostructures as well as their reinforcement mechanism in composites. The following points are addressed.

(1) A generalized molecular structural mechanics method is proposed to study non linear deformation and failure behavior of carbon nanotube-based covalent macrostructures, i.e., SG, SS, and super carbon nanotube. Based on the energy equivalence of strain energies caused by the beam deformation and steric potential energies caused by bond changing, the macrostructural parameters for non linear beam are obtained. Thereafter, the deformation and failure behavior of the covalent macrostructures are investigated within quasi static approximation. The load capacity, Poisson's ratio, and tensile modulus of the covalent macrostructures are examined as well.

(2) 2D and 3D finite element models are built based on the configuration characteristic of the composites prepared by infiltrating polymer into the covalent carbon nanotube-based macrostructures. The effective stiffness coefficients of the composite are predicted by using two-scale expansion method. The effect of geometric parameters, i.e., tube length and junction angle, are evaluated. For further discussion of interfacial bonding performances between covalent macrostructures and polymer, a cohesive model for interface between SG/super carbon nanotube and polymer is established based on non bonded VdW forces between the interface atoms.

(3) The coarse-grained molecular dynamic models of circular single-walled carbon nanotube and collapsed double-walled carbon nanotube (CDWNT) are established to reproduce atomistic molecular dynamic results effectively. Dry-spun carbon nanotube films and carbon nanotube fibers are hierarchical macrostructures of CNTs assembled through VdW

forces. High-performance carbon nanotube films and fibers are usually composed of well-aligned SWNTs and double-walled CNTs, which are in forms of thick bundles at meso-scale. Some of double-walled CNTs are collapsed owning to radial pressure in the carbon nanotube films and fibers. The hierarchical molecular dynamic models of carbon nanotube films and fibers are then constructed. Microstructural evolution and energy change under various loading conditions, such as twisting, monotonic stretching, and cyclic stretching, are investigated to explicate contributions of strength of carbon nanotube fibers. The effect of the stacking pattern of CNTs along axial direction, alignment, and entanglements on tensile strength, tensile modulus, and failure mode are investigated as well.

Acknowledgment

This work is supported by the National Natural Science Foundation of China under grant Nos. 10872011 and 11172012, which are gratefully acknowledged.

References

Ajayan, P.M., Stephan, O., Collies, C., Trauth, D., 1994. Aligned carbon nanotube arrays formed by cutting a polymer resin–nanotube composite. Science 265, 1212–1214.

Banhart, F., Grobert, N., Charlier, J.C., Terrones, H., Ajayan, P.M., Terrones, M., 2002. Molecular junctions by joining single-walled carbon nanotubes. Phys. Rev. Lett. 89 (7), 75505.

Baughman, R.H., Zakhidov, A.A., de Heer, W.A., 2002. Carbon nanotubes—the route toward applications. Science 297 (5582), 787–792.

Bosea, S., Khareb, R.A., Moldenaersa, P., 2010. Assessing the strengths and weaknesses of various types of pre-treatments of carbon nanotubes on the properties of polymer/carbon nanotubes composites: a critical review. Polymer 51 (5), 975–993.

Buffa, F., Abraham, G.A., Grady, B.P., Resasco, D., 2007. Effect of nanotube functionalization on the properties of single-walled carbon nanotube/polyurethane composites. J. Polym. Sci. B 45 (4), 490–501.

Chen, Y.L., Liu, B., Yin, Y.J., Huang, Y.G., Hwuang, K.C., 2008. Nonlinear deformation processes and damage modes of super carbon nanotubes with armchair–armchair topology. Chin. Phys. Lett. 25 (7), 2577–2580.

Coleman, J.N., Khan, U., Blau, W.J., Gun'ko, Y.K., 2006. Small but strong: a review of the mechanical properties of carbon nanotube–polymer composites. Carbon 44 (9), 1624–1652.

Coluci, V.R., Dantas, S.O., Jorio, A., Galvão, D.S., 2007. Mechanical properties of carbon nanotube networks by molecular mechanics and impact molecular dynamics calculations. Phys. Rev. B 7 (75), 75414.

Cooper, C.A., Young, R.J., Halsall, M., 2001. Investigation into the deformation of carbon nanotubes and their composites through the use of Raman spectroscopy. Compos. Part A 3–4 (32), 401–411.

Daniel, S., Rao, T.P., Rao, K.S., Rani, S.U., Naidu, G.R.K., Lee, H., Kawai, T., 2007. A review of DNA functionalized/grafted carbon nanotubes and their characterization. Sens. Actuators B 122 (2), 672–682.

Deng, F., Lu, W., Zhao, H., Zhu, Y., Kim, B., Chou, T., 2011. The properties of dry-spun carbon nanotube fibers and their interfacial shear strength in an epoxy composite. Carbon 49 (5), 1752–1757.

Endo, M., Muramatsu, H., Hayashi, T., Kim, Y.A., Lier, G.V., Charlier, J.C., Terrones, H., Terrones, M., Dresselhaus, M.S., 2005. Atomic nanotube welders: boron interstitials triggering connections in double-walled carbon nanotubes. Nano Lett. 5 (6), 1099–1105.

Fallah Gilvaei, A., Hirahara, K., Nakayama, Y., 2011. In-situ study of the carbon nanotube yarn drawing process. Carbon 49 (14), 4928–4935.

Frankland, S., Harik, V., 2003. Analysis of carbon nanotube pull-out from a polymer matrix. Surf. Sci. 525 (1–3), L103–L108.

Fu, Y.F., Carlberg, B., Lindahl, N., Lindvall, N., Bielecki, J., Matic, A., Song, Y.X., Hu, Z.L., Lai, Z.H., Ye, L.L., Sun, J., Zhang, Y.H., Zhang, Y., Liu, J.H., 2012. Templated growth of covalently bonded three-dimensional carbon nanotube networks originated from graphene. Adv. Mater. 24 (12), 1576–1581.

Garg, A., Sinnott, S.B., 1998. Effect of chemical functionalization on the mechanical properties of carbon nanotubes. Chem. Phys. Lett. 295 (4), 273–278.

Gibson, R.F., Ayorinde, E.O., Feng, W.Y., 2007. Vibrations of carbon nanotubes and their composites: a review. Compos. Sci. Technol. 67 (1), 1–28.

Godara, A., Gorbatikh, L., Kalinka, G., Warrier, A., Rochez, O., Mezzo, L., Luizi, F., van Vuure, A.W., Lomov, S.V., Verpoest, I., 2010. Interfacial shear strength of a glass fiber/epoxy bonding in composites modified with carbon nanotubes. Compos. Sci. Technol. 70 (9), 1346–1352.

Gruner, G., 2007. Carbon nanonets spark new electronics. Sci. Am. 296 (5), 76–83.

Hall, L.J., Coluci, V.R., Galvão, D.S., Kozlov, M.E., Zhang, M., Dantas, S.O., Baughman, R.H., 2008. Sign change of Poisson's ratio for carbon nanotube sheets. Science 320 (5875), 504–507.

Hashim, D.P., Narayanan, N.T., Romo-Herrera, J.M., Cullen, D.A., Hahm, M.G., Lezzi, P., Suttle, J.R., Kelkhoff, D., Munoz-Sandoval, E., Ganguli, S., Roy, A.K., Smith, D.J., Vajtai, R., Sumpter, B.G., Meunier, V., Terrones, H., Terrones, M., Ajayan, P.M., 2012. Covalently bonded three-dimensional carbon nanotube solids via boron induced nanojunctions. Sci. Rep. 2, 1–8.

He, X.Q., Kuang, Y.D., Chen, C.Y., Li, G.Q., 2009. Enhanced mechanical properties of single-walled carbon nanotubes due to chemical functionalization. J. Phys. Condens. Matter 21 (21), 215301.

Jeong, B.W., Lim, J.K., Sinnott, S.B., 2007. Elastic torsional responses of carbon nanotube systems. J. Appl. Phys. 101, 84309.

Jiang, K.L., Li, Q.Q., Fan, S.S., 2002. Nanotechnology: spinning continuous carbon nanotube yarns—carbon nanotubes weave their way into a range of imaginative macroscopic applications. Nature 419 (6909), 801.

Jiang, K., Wang, J., Li, Q., Liu, L., Liu, C., Fan, S., 2011. Superaligned carbon nanotube arrays, films, and yarns: a road to applications. Adv. Mater. 23 (9), 1154–1161.

Kang, S., Lee, D., Choi, N., 2009. Fiber/epoxy interfacial shear strength measured by the microdroplet test. Compos. Sci. Technol. 69 (2), 245–251.

Khan, M.U., Gomes, V.G., Altarawneh, I.S., 2010. Synthesizing polystyrene/carbon nanotube composites by emulsion polymerization with non-covalent and covalent functionalization. Carbon 48 (10), 2925–2933.

Koziol, K., Vilatela, J., Moisala, A., Motta, M., Cunniff, P., Sennett, M., Windle, A.H., 2007. High-performance carbon nanotube fiber. Science 318 (5858), 1892–1895.

Krasheninnikov, A., Kuronen, A., Nordlund, K., Kaski, K., Sammalkorpi, M., 2004. Mechanical properties of carbon nanotubes with vacancies and related defects. Phys. Rev. B 70 (24), 245416.

Kuang, Y.D., He, X.Q., 2009. Young's moduli of functionalized single-wall carbon nanotubes under tensile loading. Compos. Sci. Technol. 69 (2), 169–175.
Kuang, Y.D., He, X.Q., Chen, C.Y., Li, G.Q., 2009. Buckling of functionalized single-walled nanotubes under axial compression. Carbon 47 (1), 279–285.
Lalwani, G., Kwaczala, A.T., Kanakia, S., Patel, S.C., Judex, S., Sitharaman, B., 2013. Fabrication and characterization of three-dimensional macroscopic all-carbon scaffolds. Carbon 53, 90–100.
Li, Q.W., Zhang, X.F., Depaula, R.F., Zheng, L.X., Zhao, Y.H., Stan, L., Holesinger, T.G., Arendt, P.N., Peterson, D.E., Zhu, Y.T., 2006. Sustained growth of ultralong carbon nanotube arrays for fiber spinning. Adv. Mater. 18 (23), 3160–3163.
Li, C., Thostenson, E.T., Chou, T., 2008. Sensors and actuators based on carbon nanotubes and their composites: a review. Compos. Sci. Technol. 68 (6), 1227–1249.
Li, Q., Wang, J.S., Kang, Y.L., Li, Y.L., Qin, Q.H., Wang, Z.L., Zhong, X.H., 2012. Multi-scale study of the strength and toughness of carbon nanotube fiber materials. Mater. Sci. Eng. A 549, 118–122.
Liang, H.W., Liu, J.W., Qian, H.S., Yu, S.H., 2013. Multiplex templating process in one-dimensional nanoscale: controllable synthesis, macroscopic assemblies, and applications. Acc. Chem. Res. 46 (7), 1450–1461.
Liu, J., Yang, Q.S., 2009. Molecular dynamics simulation for mechanical properties of CNT/polyethylene composites. J. Phys. Conf. Ser. 188, 12052.
Liu, L.Q., Ma, W.J., Zhang, Z., 2011a. Macroscopic carbon nanotube assemblies: preparation, properties, and potential applications. Small 11 (7), 1501–1520.
Liu, X., Yang, Q.S., He, X.Q., Mai, Y.W., 2011b. Molecular mechanics modeling of deformation and failure of super carbon nanotube networks. Nanotechnology 22, 457501.
Liu, X., Yang, Q.S., He, X.Q., Liew, K.M., 2012. Size- and shape-dependent effective properties of single-walled super carbon nanotubes via a generalized molecular structure mechanics method. Comput. Mater. Sci. 61, 27–33.
Liu, X., Lu, W., Ayala, O.M., Wang, L., Karlsson, A.M., Yang, Q., Chou, T., 2013. Microstructural evolution of carbon nanotube fibers: deformation and strength mechanism. Nanoscale 5, 2002–2008.
Lourie, O., Wagner, H.D., 1998. Evaluation of Young's modulus of carbon nanotubes by micro-Raman spectroscopy. J. Mater. Res. 13 (9), 2418–2422.
Lu, W.B., Zu, M., Byun, J.H., Kim, B.S., Chou, T.W., 2012. State of the art of carbon nanotube fibers: opportunities and challenges. Adv. Mater. 24 (14), 1805–1833.
Ma, P., Chen, Y., Bian, Y., Jiang, J., 2009. Morphology controlled surface-assisted self-assembled microtube junctions and dendrites of metal free porphyrin-based semiconductor. Langmuir 26 (5), 3678–3684.
Manchado, M.A.L., Valentini, L., Biagiotti, J., Kenny, J.M., 2005. Thermal and mechanical properties of single-walled carbon nanotubes—polypropylene composites prepared by melt processing. Carbon 43 (7), 1499–1505.
Meng, L.J., Fu, C.L., Lu, Q.H., 2009. Advanced technology for functionalization of carbon nanotubes. Prog. Nat. Sci. 19 (7), 801–810.
Nicola, M.P., 2006. Mimicking nacre with super-nanotubes for producing optimized supercomposites. Nanotechnology 17 (21), 5480.
Nova, V., Karygianni, L., Altenburger, M.J., Wolkewitz, M., Kielbassa, A.M., Wrbas, K., 2013. Pull-out bond strength of a fibre-reinforced composite post system luted with self-adhesive resin cements. J. Dent. 41 (11), 1020–1026.
Romo-Herrera, J.M., Terrones, M., Terrones, H., Dag, S., Meunier, V., 2006. Covalent 2D and 3D networks from 1D nanostructures: designing new materials. Nano Lett. 7 (3), 570–576.

Rong, Q., Wang, J., Kang, Y., Li, Y., Qin, Q., 2012. A damage mechanics model for twisted carbon nanotube fibers. Acta Mech. Solida Sin. 25 (4), 342–347.
Sharma, R., Mahajan, P., Mittal, R.K., 2012. Fiber bundle push-out test and image-based finite element simulation for 3D carbon/carbon composites. Carbon 50 (8), 2717–2725.
Snow, E.S., Novak, J.P., Campbell, M.P., Park, D., 2003. Random networks of carbon nanotubes as an electronic material. Appl. Phys. Lett. 12 (13), 2145–2147.
Snow, E.S., Novak, J.P., Lay, M.D., House, E.H., Perkins, F.K., Campbell, P.M., 2004. Carbon nanotube networks: nanomaterial for macroelectronic applications. J. Vac. Sci. Technol., B: Microelectron. Nanometer Struct. 22 (4), 1990–1994.
Song, Y.S., Youn, J.R., 2005. Influence of dispersion states of carbon nanotubes on physical properties of epoxy nanocomposites. Carbon 43 (7), 1378–1385.
Sun, G., Pang, J.H.L., Zhou, J., Zhang, Y., Zhan, Z., Zheng, L., 2012. A modified Weibull model for tensile strength distribution of carbon nanotube fibers with strain rate and size effects. Appl. Phys. Lett. 101, 131904–131905.
Teng, I.J., Chen, K.L., Hsu, H.L., Jian, S.R., Wang, L.C., Chen, J.H., Wang, W.H., Kuo, C.T., 2011. Highly graphitized laterally interconnected SWCNT network synthesis via a sandwich-grown method. J. Phys. D. Appl. Phys. 44 (14), 145401.
Ting, J.M., Chang, C.C., 2002. Multijunction carbon nanotube network. Appl. Phys. Lett. 80 (2), 324–325.
Xie, X., Mai, Y., Zhou, X., 2005. Dispersion and alignment of carbon nanotubes in polymer matrix: a review. Mater. Sci. Eng. R. Rep. 49 (4), 89–112.
Xin, H., Han, Q., Yao, X.H., 2007. Buckling and axially compressive properties of perfect and defective single-walled carbon nanotubes. Carbon 45 (13), 2486–2495.
Yang, H., Yang, Q.S., 2008. A molecular structural model for static and dynamical buckling of single-walled carbon nanotubes. J. Beijing Univ. Technol. 36 (10), 1312–1316.
Yang, Q.S., Li, B.Q., He, X.Q., Mai, Y.W., 2014. Modeling the mechanical properties of functionalized carbon nanotubes and their composites: design at the atomic level. Adv. Condens. Matter Phys. 2014, 482056.
Yin, Y.J., Yin, J., 2006. Geometric conservation laws for perfect Y-branched carbon nanotubes. Nanotechnology 17 (19), 4941–4945.
Yin, Y., Zhang, T., Yang, F., Qiu, X., 2008. Geometric conditions for fractal super carbon nanotubes with strict self-similarities. Chaos, Solitons Fractals 37 (5), 1257–1266.
Yu, M.F., Files, B., Arepalli, S., Ruoff, R., 2000. Tensile loading of ropes of single wall carbon nanotubes and their mechanical properties. Phys. Rev. Lett. 84 (24), 5552–5555.
Zhang, M., Atkinson, K.R., Baughman, R.H., 2004. Multifunctional carbon nanotube yarns by downsizing an ancient technology. Science 306 (5700), 1358–1361.
Zhang, X.B., Jiang, K.L., Chen, F., Liu, P., Zhang, L.N., Kong, J., Zhang, T.H., Li, Q.Q., Fan, S. S., 2006. Spinning and processing continuous yarns from 4-inch wafer scale super-aligned carbon nanotube arrays. Adv. Mater. 18 (12), 1505–1510.
Zhang, X.F., Li, Q.W., Tu, Y., Li, Y., Coulter, J.Y., Zheng, L.X., Zhao, Y.H., Jia, Q.X., Peterson, D.E., Zhu, Y.T., 2007a. Strong carbon-nanotube fibers spun from long carbon-nanotube arrays. Small 3 (2), 244–248.
Zhang, X.F., Li, Q.W., Holesinger, T.G., Arendt, P.N., Huang, J.Y., Kirven, P.D., Clapp, T.G., Depaula, R.F., Liao, X.Z., Zhao, Y.H., Zheng, L.X., Peterson, D.E., Zhu, Y.T., 2007b. Ultrastrong, stiff, and lightweight carbon-nanotube fibers. Adv. Mater. 19 (23), 4198–4201.
Zhang, Z.Q., Liu, B., Chen, Y.L., Jiang, H., Hwang, K.C., Huang, Y., 2008. Mechanical properties of functionalized carbon nanotubes. Nanotechnology 19 (39), 395702.
Zheng, Q.B., Xia, D., Xue, Q.Z., Yan, K.Y., Gao, X.L., Li, Q., 2009. Computational analysis of effect of modification on the interfacial characteristics of a carbon nanotube/ polyethylene composite system. Science 255, 3534–3543.

Zhou, W.Y., Ma, W.J., Niu, Z.Q., Song, L., Xie, S.S., 2012. Freestanding single-walled carbon nanotube bundle networks: fabrication, properties and composites. Chin. Sci. Bull. 57 (2–3), 205–224.

Zu, M., Li, Q., Zhu, Y., Dey, M., Wang, G., Lu, W., Deitzel, J.M., Gillespie Jr., J.W., Byun, J., Chou, T., 2012. The effective interfacial shear strength of carbon nanotube fibers in an epoxy matrix characterized by a microdroplet test. Carbon 50 (3), 1271–1279.

Toughening mechanisms for fiber-reinforced polymer-reinforced concrete beams

14

Y.X. Zhang, X. Lin
University of New South Wales, Canberra, ACT, Australia

14.1 Introduction

Corrosion of steel-reinforcing rebars in concrete structures is a common problem encountered in the civil construction sector due to the porosity of concrete. Fiber-reinforced polymers (FRPs), which generally consist of synthetic or organic high-strength fibers in a resin matrix, have been widely used in the construction of concrete structures as substitutes for traditional steel reinforcements due to their superior material properties, such as excellent electrochemical corrosion resistance, high ratio of strength to mass density, excellent fatigue resistance, and reduced cost of fabrication. FRP-reinforcing rebars have been used in bridges, industrial roof decks, highway barriers, chemical and wastewater treatment plants, sea walls, floating docks, and many other seafront structures since the 1980s (Brown and Bartholomew, 1993; Bakis et al., 2002; Rizkalla et al., 2003).

The toughening mechanism between FRP-reinforcing rebars and concrete is one of the most critical aspects affecting the structural behavior of the concrete structures. The bond between reinforcing bars and the surrounding concrete plays an important role in transferring the stress from the reinforcing bars to the concrete. However, a poorer bond is usually found between FRP-reinforcing bars and the surrounding concrete than that between steel rebars and concrete. Therefore, it is very important to investigate the bond mechanism for FRP-reinforced concrete structures.

A beam is one of the most basic structural elements as well as an indispensable part in most civil construction, including bridges, industrial construction, buildings, and other structures. Nowadays, FRP-reinforced concrete beams are being increasingly used in these civil construction projects instead of traditional steel-reinforced concrete beams. In FRP-reinforced concrete beams, bond characteristics affect the anchorage of rebars, strength of lap splices, and required concrete cover (Davalos et al., 2008). And the performance of reinforced concrete beams depends not only on the material properties of concrete and reinforcement but also on the bond behavior between the two components. The resisting mechanisms under bending, shear, and torsion are related to the development of an adequate bond both at the serviceability state and at the ultimate state (Cosenza et al., 1997). A proper design against

Toughening Mechanisms in Composite Materials. http://dx.doi.org/10.1016/B978-1-78242-279-2.00014-7

debonding failure thus becomes a matter of concern for concrete beams reinforced with FRP rebars.

Various factors may influence the bond characteristics of FRP reinforcement in concrete, such as the type of FRPs, the diameter of the FRP rebars, the shape of the outer surface of the FRP rebars, the surface conditions, concrete compressive strength, position of the rebars in the structures, embedment length, and other environmental conditions (Cosenza et al., 1997). Among these, the types of FRPs and the surface conditions may be the most dominant factors that affect the bond behavior between FRP rebars and concrete. Three types of FRPs, i.e., carbon fiber-reinforced polymer (CFRP), aramid fiber-reinforced polymer (AFRP), and glass fiber-reinforced polymer (GFRP), are most commonly used for civil engineering applications (Benmokrane et al., 1996). In recent years, basalt fiber-reinforced polymer (BFRP) has been developed, and its advantages in mechanical, chemical, and economic aspects have been proven. Rebars of different surface conditions, such as smooth, ribbed, indented, braided and grain-covered surfaces, have been commercialized, and the bond behavior was enhanced by deforming the outer surface of the rebars and treating the surface (Cosenza et al., 1997).

Recently, the authors investigated the bond behavior between FRP rebars and concrete for FRP-reinforced concrete beams experimentally (Lin and Zhang, 2013a) and numerically (Lin and Zhang, 2013b). In this chapter, the results are presented and the toughening mechanism between FRP rebars and concrete is analyzed.

14.2 Experimental study of the bond mechanism between FRP and concrete

So far, the pull-out test is the most common method used to examine the bond slip between the FRP rebars and the concrete. However, a pull-out test does not reflect the actual condition of reinforcements in reinforced concrete members under bending (Cosenza et al., 1997). It is generally believed that a beam-bending test can realistically report the bond performance of reinforcing bars in concrete. In a beam-bending test, the concrete surrounding the reinforcing rebars is under tension, which is in contrast with the situation in the pull-out test, thus the cracking of concrete may take place under a lower stress level, resulting in the reduction of the bond strength. Nevertheless, very few experimental studies on the bond–slip behavior of FRP rebars in concrete through beam test have been reported so far.

To investigate the actual bond–slip behavior of FRP rebars in concrete beams, four-point-bending tests on FRP-reinforced concrete beams were conducted by the authors (Lin and Zhang, 2013a). Three types of FRP rebars, such as CFRP, GFRP, and BFRP, with different rebar surfaces (smooth and wrapped surfaces) were tested to investigate the effects of types and surface conditions of FRP rebars on the bond–slip behavior of reinforced concrete beams. The design of the beams, the preparation of the specimens, the test method, and tested results are introduced in this section.

14.2.1 Design of FRP-reinforced concrete beams

Three concrete beams reinforced with three different types of reinforcements, i.e., CFRP rebars for beam BC1, GFRP rebars for beam BG1, and BFRP rebars for beam BB1, were tested by the authors. FRP rebars used in the experiment are shown in Figure 14.1. The CFRP and GFRP rebars had smooth surfaces, and the BFRP rebars were spirally wrapped by strands around the outside diameter, producing a spiral indentation. Material properties of the reinforcing bars provided by the manufacturer are shown in Table 14.1.

Identical designs of cross-section and longitudinal section were applied to all the beams. Each beam was 1060-mm long with a rectangular cross-section of 100 mm×200 mm, and 25 mm concrete cover was used all around the beam. The concrete was designed to achieve a compressive strength of 40 MPa. As FRP rebars show linear behavior up to failure and do not have yielding stage as steel bars, the flexural failure of FRP-reinforced concrete beams is caused either by the concrete crushing or by FRP rupture, and the concrete becomes the ductile component. In order to achieve concrete failure first, control deflection and cracking, and satisfy the serviceability

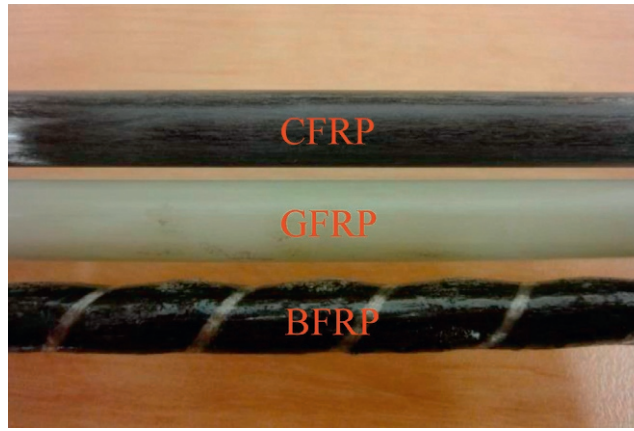

Figure 14.1 CFRP, GFRP, and BFRP rebars.

Table 14.1 Material properties of reinforcing bars

Rebar type	Diameter d (mm)	Elastic modulus E (GPa)	Ultimate strength f_u (MPa)	Elongation (%)
CFRP	10	140	2000	1.6
GFRP	10	30	500	2.0
BFRP	8	40	800	2.0
Steel	6	200	400	0.2

Table 14.2 Reinforcement ratios for FRP-reinforced concrete beams

Beam	ρ_f (%)	ρ_b (%)
BC1	1.18	0.20
BG1	1.18	0.67
BB1	0.75	0.42

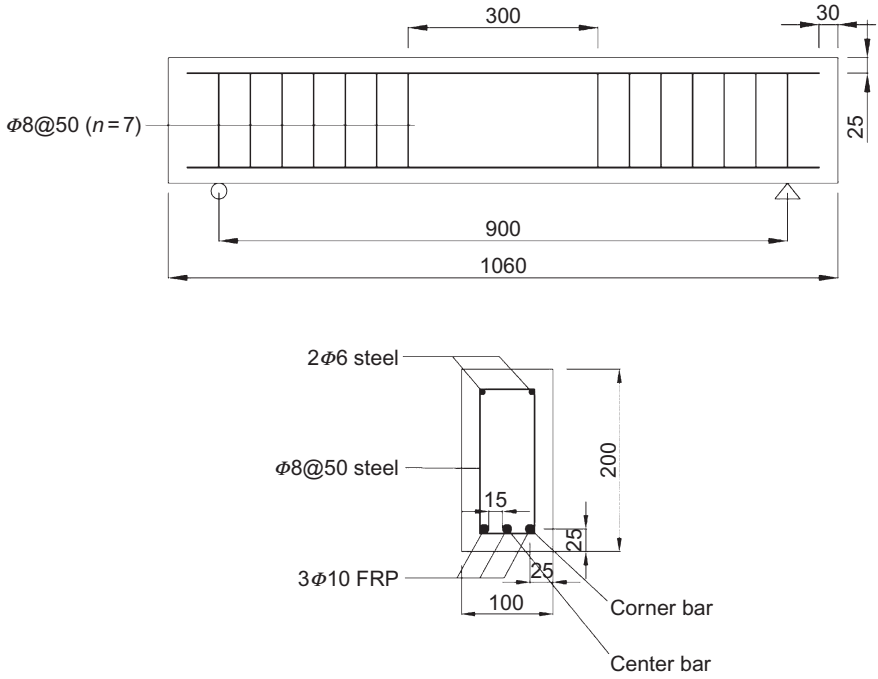

Figure 14.2 Design of FRP-reinforced concrete beams (unit: mm).

limit state, FRP-reinforced concrete beams were designed as over-reinforced. The calculated balanced reinforcement ratio ρ_b and the actual FRP reinforcement ratio ρ_f for each FRP-reinforced concrete beam are given in Table 14.2. Each beam was reinforced with three FRP bars in the tension zone, i.e., two corner bars and one center bar as shown in Figure 14.2, and two steel bars in the compression region. In order to resist the shear failure, 8-mm diameter stirrups were used throughout the shear span at a space of 50-mm center-to-center. Details of the longitudinal section and cross-section of the beams are shown in Figure 14.2.

14.2.2 Preparation of specimens

The concrete was mixed in a concrete mixer, and the cylinders were vibrated on a vibrating table. Concrete beams were cast in a wood mold. In order to separate the ends of the rebars from concrete, PVC tubes were placed at the ends of center rebar and one of the corner rebars on both ends of the beam, as shown in Figure 14.3. As such, linear variable differential transformers (LVDTs) could be inserted into the embedded PVC tubes and touch the ends of the reinforcing bars so as to measure the bond slip between the rebars and the concrete. In order to test the compressive strength and modulus of elasticity, six 100 mm×200 mm concrete cylinders were also cast for each beam with three for the testing of the concrete compressive strength and the modulus of elasticity, respectively. All beams and cylinders were placed in a water-curing chamber with constant temperature and humidity before testing.

14.2.3 Test and results

14.2.3.1 Basic material properties of the concrete

The concrete compressive strength f_c and the modulus of elasticity E_c were tested according to the Australian Standards AS 1012.9 (1999) and AS 1012.17 (1997), respectively, using a servo-hydraulic testing machine with a range of 3000 kN. In order to obtain more accurate experimental data, the concrete compressive strength and modulus of elasticity were tested on the day of the beam test instead of day 28.

Figure 14.3 Wood mold and reinforcement cage for test beams.

Table 14.3 Properties of concrete of each beam

Beam	f_c (MPa)	E_c (GPa)	Age (days)
BC1	48.24	32.54	126
BG1	51.75	33.49	110
BB1	53.84	32.54	107

The average values of the tested concrete compressive strength and modulus of elasticity and the age of testing are shown in Table 14.3.

14.2.3.2 Four-point bending test of FRP-reinforced concrete beams

Four-point bending tests were conducted on the FRP-reinforced concrete beams to study the bond–slip behavior between the FRP rebars and the concrete. The FRP-reinforced concrete beams were tested as simply supported beams over a span of 900 mm under a four-point static bending load. The loads were 300 mm apart, giving a shear span of 300 mm. The test beams were placed on the steel roller supports, which were spaced at a distance equal to the span of the beam. A universal testing machine with range of 20–1000 kN was used for loading, and a stiff spreader beam was used to transfer the applied load to the specified points on the test beam. Steel plates were placed under each roller on the top of the beam and in between the bottom of the beam and its supports in order to avoid stress concentration and local crushing. The load was applied under displacement control at a rate of 0.4 mm/min until concrete failure occurred. The setup of the beam test is shown in Figure 14.4.

Figure 14.4 Setup of beam-bending test.

Figure 14.5 Arrangement of LVDTs for bending test.

Instrumentation was set up to measure the slippage between the reinforcing bars and the surrounding concrete. Four horizontal LVDTs were inserted into the embedded PVC tubes and touched the ends of the reinforcing bars (LVDT2 and LVDT4 for one of the corner rebars, and LVDT1 and LVDT3 for the center rebar). The arrangement of LVDTs is shown in Figure 14.5. A computer data acquisition system was used to record load, deflection, and slip continuously.

As the bond stress distribution is not constant along the FRP-reinforcing rebars, it is improper to indicate the bond stress over the reinforcing bar using the mean value, as is done for steel rebars. Therefore, in this study, the horizontal LVDTs were used in direct contact with the ends of FRP rebars to measure the relative displacements between the reinforcing bars and the concrete, and the relationship between the applied load and the slippage is used to characterize the bond behavior.

14.2.3.3 Bending test results and bond mechanism

The load–slip relationships for the center and one of the corner rebars in BC1, BG1, and BB1 are shown in Figure 14.6. As can be seen, in general, the load versus slip relationship is characterized by a small slippage at the initial loading stage followed by a rapid increase once the applied load reaches the maximum bearing load.

Similar bond–slip behaviors are obtained for beam BC1 and BG1. Good bonding performances are observed at the initial loading stages in these two beams, and their

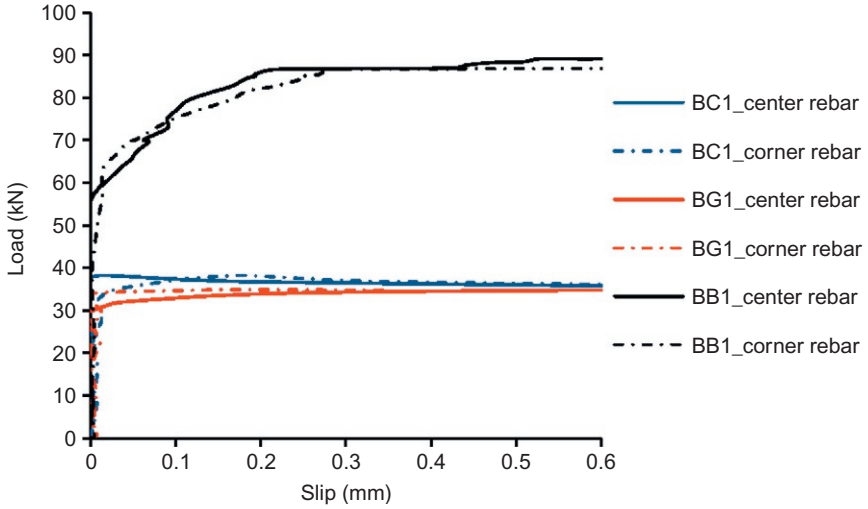

Figure 14.6 Load–slip curves for center and corner rebars in BC1, BG1, and BB1.

load–slip curves are almost linear. At this stage, chemical adhesion between the concrete and reinforcements governs the bond mechanism, and slippage is avoided. After chemical bond is lost, the friction between the concrete and reinforcements takes effect. With an increase in load, bond–slip between the rebars and concrete develops, friction diminishes, and the contact surface is damaged, and when the applied load reaches the maximum bearing load, a sudden decay is recorded. As the material properties of the CFRP rebars used in the test are much higher than those of the GFRP rebars, beam BC1 is supposed to have a much better bearing capacity than beam BG1. However, due to the smooth surfaces of the CFRP and GFRP rebars in beam BC1 and BG1, the bond between the concrete and FRP rebars is poor for both beams. Consequently, the peak loads for both beam BC1 and BG1 are attained quickly and at comparatively low slip values, and their maximum bearing loads are 38.2 and 34.8 kN, respectively.

A rebar's surface condition is very important to the bond–slip behavior between the rebar and the surrounding concrete. In beam BB1, as BFRP rebars are indented by strands, a large bearing resistance develops when chemical adhesion is lost and then, up to the maximum applied load, the bond between the concrete and BFRP rebars is dominated by mechanical interlock. Decay in the load–slip curve for beam BB1 is also found after its peak although it is not as abrupt as in the load–slip curves for beam BC1 and BG1. At this stage, the contribution of mechanical interlock is reduced, and friction through the wedging of the deformation of the BFRP rebars becomes the dominant bond mechanism. A maximum bearing load of 89.2 kN is obtained for beam BB1, which is much larger than those acquired for beam BC1 (38.2 kN) and BG1 (34.8 kN). The experimental results, including the maximum bearing loads P_{max} and slips of the center and one of the corner rebars in beams BC1, BG1, and BB1 at the peak loads, are given in Table 14.4.

Table 14.4 Slips of center and corner rebars in beam BC1, BG1, and BB1 at peak loads

Specimen	h_3 (kN)	Center rebar (mm)	Corner rebar (mm)
BC1	38.2	0.012	0.174
BG1	34.8	0.219	0.143
BB1	89.2	0.607	1.017

14.3 Numerical study of bond mechanism between FRP and concrete

14.3.1 A one-dimensional (1D) layered composite beam element with bond slip (Lin and Zhang, 2013b)

A 1D layered composite beam element has been recently developed by the authors (Lin and Zhang, 2013b) and has been demonstrated to be accurate and effective for analysis and modeling of the structural behavior, including the bond–slip behavior of FRP-reinforced concrete beams. The developed finite element model is used to model the bond–slip behavior of the tested beams so as to obtain an insightful understanding of the bonding mechanism and slippage development.

The newly developed layered composite beam element is a simple displacement-based 1D element with only two nodes and four degrees of freedom (DOF) per node, with two typical DOFs at each node (transverse displacement and rotation) as well as two additional DOFs to represent the axial displacements of the equivalent tensile and compressive reinforcing layers. The layered method is used not only to model the material nonlinearity, but also to take into account the bond slip between the reinforcing bars and the concrete. Timoshenko's composite beam functions (Lin and Zhang, 2013b) are employed to construct the displacement shape functions for transverse displacement and rotation. By doing so, the element provides a unified formulation for analyses of both slender and moderately deep beams with the notorious shear-locking problem naturally avoided. The shape function for defining the linear displacement variation along the axis of a typical bar element is used to represent the axial displacements of the reinforcements. Figure 14.7 shows the 1D layered composite beam element. The element consists of two parts: a 1D two-node beam element as shown in Figure 14.7b for analyzing the concrete and two 1D two-node bar elements as shown in Figure 14.7a and c for modeling the reinforcements in the tension zone and compression zone, respectively.

The cross-section of the layered composite beam element is divided into a number of concrete layers, and the reinforcing bars are represented by equivalent smeared reinforcing layers with equivalent thicknesses t given by $t = A_{\text{bar}}/b$, as shown in Figure 14.7e. The bending stiffness D_{bb} and transverse shear stiffness D_{ss} of the beam element are obtained by algebraically summing the contribution from each layer as:

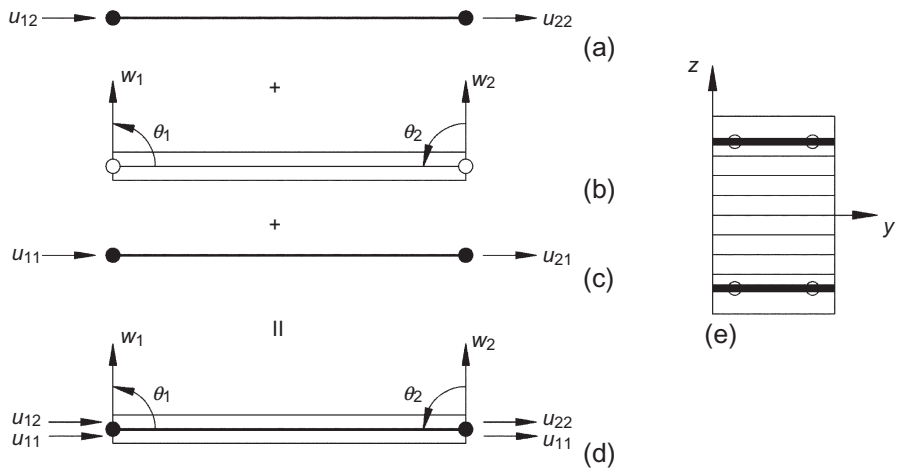

Figure 14.7 A 1D two-node composite beam element and its cross-section.

$$D_{\mathrm{bb}} = b\sum_{i=1}^{c} E_{ci} t_{ci} Y_i^2 \tag{14.1}$$

$$D_{\mathrm{ss}} = \delta b \sum_{i=1}^{c} G_{ci}(z_{i+1} - z_i) \tag{14.2}$$

In order to model the bond–slip effect between the reinforcing bars and surrounding concrete, the equivalent smeared reinforcing layers in both the tension and compression zones are represented by 1D two-node bar elements, which can slip with respect to the concrete. The bar elements are then merged into the 1D two-node layered beam element for modeling the concrete to form a new composite beam element. The nodal DOF for the reinforcing layers are separated from those for the concrete beam to permit slip, and the reinforcing layer is regarded as a system consisting of two parts: reinforcing bars and the interface between reinforcing bars and the concrete. Thus, slip is the relative displacement between the reinforcing layer and the concrete. The element has been validated and demonstrated to be accurate and computationally efficient (Lin and Zhang, 2013b).

14.3.1.1 Basic finite element formulations

The displacement field of the concrete beam is given by the following equations:

$$u_{\mathrm{c}}(x, Y) = -Y\theta(x) \tag{14.3}$$

$$w(x, Y) = w_0(x) \tag{14.4}$$

where u_{c} is the longitudinal displacement of a point in the cross-section at a distance Y from the neutral axis.

The strain–displacement relationships of the composite concrete beam are given in the following equations:

$$\varepsilon_x = \frac{\partial u}{\partial x} = -Y\frac{\mathrm{d}\theta}{\mathrm{d}x} \tag{14.5}$$

$$\varepsilon_\mathrm{b} = -\frac{\mathrm{d}\theta}{\mathrm{d}x} \tag{14.6}$$

$$\gamma = \frac{\partial u}{\partial Y} + \frac{\partial w}{\partial x} = \frac{\partial w}{\partial x} - \theta \tag{14.7}$$

where ε_x is the longitudinal strain of a point in the cross-section at distance Y from the neutral axis, ε_b is the bending strain, γ is the transverse shear strain, and $\partial w/\partial x$ is the slope of the neutral axis.

When perfect bonding between the concrete and reinforcements is assumed, the concrete and reinforcing layers located at the same depth are of the same strain, i.e.,

$$\varepsilon_\mathrm{s} = \varepsilon_\mathrm{c} = \varepsilon_x \tag{14.8}$$

where ε_s is the strain of the reinforcing layer, and ε_c is the strain of the concrete layer.

With the bond–slip effect taken into account, it is assumed that the deformation of the reinforcing layer is due partly to the bar elongation and partly to the slip between the reinforcing bar and the surrounding concrete (Monti and Spacone, 2000). Thus, the following compatibility relation between the concrete and reinforcing layer should be satisfied.

$$\varepsilon_\mathrm{bond} = \varepsilon_\mathrm{s} - \varepsilon_\mathrm{c} \tag{14.9}$$

in which $\varepsilon_\mathrm{bond}$ is the strain due to slip. The strain–displacement relationship of the reinforcing layer is given by

$$\varepsilon_\mathrm{s} = \frac{\mathrm{d}u_\mathrm{s}}{\mathrm{d}x} \tag{14.10}$$

where u_s is the axial displacement of the reinforcing layer with bond slip.

The locking-free Timoshenko's beam functions are utilized to represent the transverse displacement and rotation at any point along the longitudinal direction of the present beam element. The formulas for the deflection w and rotation θ of the composite beam element with length L, width b, and height h are given by the following equations:

$$\begin{aligned} w = {} & (L_1 + \mu_\mathrm{e}L_1L_2(L_1 - L_2))w_1 + (L_1L_2 + \mu_\mathrm{e}L_1L_2(L_1 - L_2))L/2\theta_1 \\ & + (L_2\mu_\mathrm{e}L_1L_2(L_2 - L_1))w_2 + (-L_1L_2 + \mu_\mathrm{e}L_1L_2(L_1 - L_2))L/2\theta_2 \end{aligned} \tag{14.11a}$$

$$\theta = -\left(\frac{6L_1L_2}{L}\right)\mu_\mathrm{e}w_1 + L_1(1 - 3\mu_\mathrm{e}L_2)\theta_1 + \left(\frac{6L_1L_2}{L}\right)\mu_\mathrm{e}w_2 + L_2(1 - 3\mu_\mathrm{e}L_1)\theta_2 \tag{14.11b}$$

where

$$L_1 = 1 - \frac{x}{L} \tag{14.12a}$$

$$L_2 = \frac{x}{L} \tag{14.12b}$$

$$\mu_e = \frac{1}{1 + 12\lambda_e} \tag{14.12c}$$

$$\lambda_e = \frac{D_{bb}}{D_{ss}L^2} \tag{14.12d}$$

in which x is the coordinate along the beam element.

The axial displacements of the bar elements representing the reinforcing layers with bond slip are given as

$$\text{For tensile reinforcement: } u_s = \left(1 - \frac{x}{L}\right)u_{11} + \frac{x}{L}u_{21} \tag{14.13a}$$

$$\text{For compressive reinforcement: } u_s = \left(1 - \frac{x}{L}\right)u_{12} + \frac{x}{L}u_{22} \tag{14.13b}$$

14.3.1.2 Strain and strain matrix

The element bending strain, shear strain, and the strain of the reinforcing layers with bond slip can be expressed as

$$\varepsilon_b = [B_b]\left\{q^{(e)}\right\} \tag{14.14}$$

$$\gamma = [B_s]\left\{q^{(e)}\right\} \tag{14.15}$$

$$\varepsilon_s = [B_{bar}]\left\{q^{(e)}\right\} \tag{14.16}$$

in which

$$[B_b] = \begin{bmatrix} \frac{6\mu_e}{L}\left(\frac{1}{L} - \frac{2x}{L^2}\right) & \frac{3\mu_e + 1}{L} - 6\mu_e\frac{x}{L^2} & -\frac{6\mu_e}{L}\left(\frac{1}{L} - \frac{2x}{L^2}\right) \\ -\frac{1 - 3\mu_e}{L} - 6\mu_e\frac{x}{L^2} & 0 & 0 & 0 & 0 \end{bmatrix} \tag{14.17a}$$

$$[B_s] = \begin{bmatrix} -\frac{1}{L} + \frac{\mu_e}{L} & \frac{\mu_e}{2} - \frac{1}{2} & \frac{1}{L} - \frac{\mu_e}{L} & -\frac{1}{2} + \frac{\mu_e}{L} & 0 & 0 & 0 & 0 \end{bmatrix} \tag{14.17b}$$

$$\text{For tensile reinforcement: } [B_{bar}] = \begin{bmatrix} 0 & 0 & 0 & 0 & -\frac{1}{L} & \frac{1}{L} & 0 & 0 \end{bmatrix} \tag{14.17c}$$

$$\text{For compressive reinforcement: } [B_{\text{bar}}] = \begin{bmatrix} 0 & 0 & 0 & 0 & 0 & 0 & -\dfrac{1}{L} & \dfrac{1}{L} \end{bmatrix} \tag{14.17d}$$

where $[B_b]$ is the curvature–displacement matrix of the concrete beam, $[B_s]$ is the shear strain–displacement matrix of the concrete beam, $[B_{\text{bar}}]$ is the axial strain–displacement matrix of the reinforcing layers with bond slip, and $\{q^{(e)}\}$ is the element nodal displacement vector, which can be expressed as

$$\left\{q^{(e)}\right\} = \begin{Bmatrix} q_1 \\ q_2 \end{Bmatrix} \quad \text{with} \quad \{q_i\} = \begin{Bmatrix} w_i \\ \theta_i \\ u_{i1} \\ u_{i2} \end{Bmatrix} \quad (i = 1,2) \tag{14.18}$$

where u_{i1} and u_{i2} are the axial displacements for each of the reinforcing layers with bond slip.

14.3.1.3 Material models

For concrete in compression, a nonlinear constitutive model, as shown in Figure 14.8, is employed. It is composed of two parts, an ascending quadratic curve and a descending linear branch. The relationship between the compressive stress σ and compressive strain ε is given in the following equations:

$$\frac{\sigma}{\sigma_{\text{cu}}} = \frac{\varepsilon}{\varepsilon_0}\left(2 - \frac{\varepsilon}{\varepsilon_0}\right) \quad \text{for } 0 \le \varepsilon \le \varepsilon_0 \tag{14.19a}$$

$$\frac{\sigma}{\sigma_{\text{cu}}} = 1 - 0.15\left(\frac{\varepsilon - \varepsilon_0}{\varepsilon_{\text{cu}} - \varepsilon_0}\right) \quad \text{for } \varepsilon_0 \le \varepsilon \le \varepsilon_{\text{cu}} \tag{14.19b}$$

where ε_{cu} is the ultimate compressive strain of the concrete and σ_{cu} is the ultimate compressive stress, given as $0.85 f_c'$, in which f_c' is the concrete compressive strength,

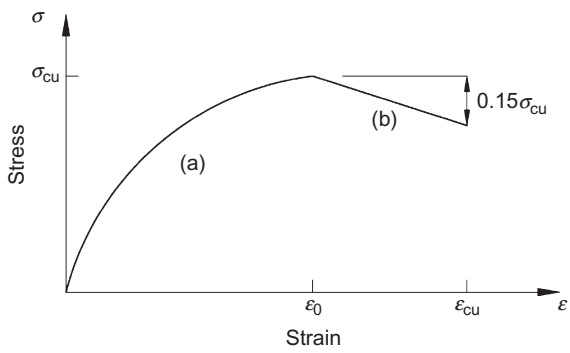

Figure 14.8 Stress–strain relationship of concrete in compression (Nitereka and Neale, 1999).

and $\varepsilon_0 = 1.71\left(f_c'/E_c\right)$ corresponds to the compressive strain at σ_{cu}, where E_c is Young's modulus of concrete (Coronado and Lopez, 2006).

Concrete in tension is assumed to be isotropic and linear elastic before cracking. Once the maximum principal strain reaches the concrete ultimate tensile strain, crack occurs, and the concrete becomes orthotropic. The concrete between the cracks carries a certain amount of tensile force normal to the cracked plane. The concrete adheres to the reinforcing bars and contributes to the overall stiffness of the structure (Owen and Figueiras, 1984). For steel or FRP-reinforced concrete beams, the tension-stiffening effect should be considered when describing the interaction between concrete and reinforcing bars after concrete cracking. A refined constitutive model allowing for the tension-stiffening effect, presented by Nour et al. (2007) and shown in Figure 14.9, is utilized in the current composite beam element, in which the effects from different reinforcements are accounted for. The stress–strain relationship described in Figure 14.9 is given by the following equations:

$$\sigma = E_c \varepsilon \quad \text{for } 0 \le \varepsilon \le \varepsilon_e \tag{14.20a}$$

$$\sigma = f_t \left[1 - (1-\beta)\frac{\varepsilon}{\varepsilon_1}\right] \quad \text{for } \varepsilon_e < \varepsilon \le \varepsilon_1 \tag{14.20b}$$

$$\sigma = \beta f_t \quad \text{for } \varepsilon_1 < \varepsilon \le \varepsilon_2 \tag{14.20c}$$

$$\sigma = \beta f_t \left(\frac{\varepsilon_{bar,y} - \varepsilon}{\varepsilon_{bar,y} - \varepsilon_2}\right) \quad \text{for } \varepsilon_2 < \varepsilon \le \varepsilon_{bar,y} \tag{14.20d}$$

in which σ and ε are the tensile stress and tensile strain, respectively, f_t is the tensile strength of concrete, ε_e is the concrete strain at f_t, and $\varepsilon_{bar,y}$ is the yield strain for steel reinforcements, or the ultimate strain for FRP bars.

β is the tension-stiffening factor given by the following equation (Bischoff and Paixao, 2004):

$$\beta = \exp\left[-1100(\varepsilon - \varepsilon_e)\left(\frac{\sum E_{bar} A_{bar}}{200 \sum A_{bar}}\right)\right] \tag{14.21}$$

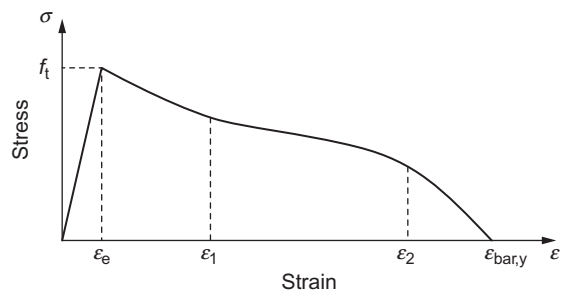

Figure 14.9 Stress–strain relationship of concrete in tension (Nour et al., 2007).

where E_{bar} is the elastic moduli of different reinforcing bars, and A_{bar} is the areas of different reinforcing bars. ε_1 and ε_2 are expressed as (Nour et al., 2007)

$$\varepsilon_1 = (1.3-\beta)f_t\left(\frac{1}{E_{bar}\rho_{eff}}+\frac{1}{E_c}\right) \tag{14.22a}$$

$$\varepsilon_2 = \varepsilon_{bar,y}-\beta f_t\left(\frac{1}{E_{bar}\rho_{eff}}+\frac{1}{E_c}\right) \tag{14.22b}$$

where ρ_{eff} is the effective reinforcement ratio, given as $\rho_{eff}=A_{bar}/A_{c,eff}$, in which $A_{c,eff}$ is the concrete area involved in the stiffening and suggested by CEB-FIP Model Code 1990 (1993) as

$$A_{c,eff}=2.5b(h-d_e)<\frac{b(h-d_n)}{3} \tag{14.23}$$

where h is the depth of the beam, d_e is the effective depth, and d_n is the depth of the neutral axis.

After cracking, shear stress is transferred across the rough surfaces of the cracked concrete through the mechanism of aggregate interlock, and the dowel action of the reinforcing bars crossing the shear cracks also contributes to the shear stiffness. In order to account for the effects of aggregate interlock and dowel action, an approach presented in reference (Owen and Figueiras, 1984), in which the cracked shear modulus is assumed to be a function of the current tensile strain, is adopted in this study as

$$G_c'=\begin{cases}0.25G_c\left(1-\dfrac{\varepsilon}{0.004}\right) & \varepsilon<0.004\\ 0 & \varepsilon\geq 0.004\end{cases} \tag{14.24}$$

where G_c is the uncracked concrete shear modulus, and G_c' is the concrete shear modulus after cracking.

The reinforcing steel bars are modeled to be elastic-perfectly plastic in both tension and compression. FRPs are assumed to be linear elastic until the tension stress reaches the material ultimate strength, causing brittle rupture. After that, the stress within FRP reduces to zero immediately.

14.3.1.4 Bond stress–slip model

In order to model local deformation accurately, bond stress–slip model is included in the finite element model. In the full bonded range, the bond stress–slip model described by the following equation (Kullaa, 1996) is used in the present finite element model:

$$\tau=\frac{2G_c}{d\ln\left(\overline{R}/r\right)}s \tag{14.25}$$

where τ is the shear stress at the interface between the rebar and concrete, s is the slip between the rebar and concrete, $G_c = E_c/2(1+\upsilon)$, υ is Poisson's ratio of the concrete, d is the rebar diameter, r is the rebar radius, $\overline{R}$ is the effective radius of the axial stress-carrying area, and $\ln(\overline{R}/r)$ is given as

$$\ln(\overline{R}/r) = \frac{-2\ln V_f - V_m(3 - V_f)}{4V_m^2} \tag{14.26}$$

in which V_f is the rebar volume fraction, and $V_m = 1 - V_f$ is the concrete volume fraction. Hence, in the elastic region, the bond modulus κ (Naaman et al., 1991) can be expressed as

$$\kappa = \frac{\tau}{s} = \frac{2G}{d\ln(\overline{R}/r)} = \frac{E}{d(1+\upsilon)\ln(\overline{R}/r)} \tag{14.27}$$

As the load increases, debonding starts and the following bond stress–slip models, which account for the bond–slip effect of steel and FRP reinforcements on the structural behavior of the concrete beams, are employed.

For steel reinforcement, the bond stress–slip model between concrete and reinforcing steel bars under monotonic loading suggested in CEB-FIP Model Code 1990 (1993) (Figure 14.10), is employed. For FRP rebars, very little work has been done to determine the bond stress–slip constitutive law for FRP rebars so far. The BPE-modified model proposed by Cosenza et al. (1997) as shown in Figure 14.11 is one of the scarce bond stress–slip models for FRP rebars and is employed in the current finite element model.

In order to apply bond stress–slip model to the proposed composite beam element, the bond stress–slip response needs to be expressed in terms of the bond stress–strain curve, and the method used in Monti and Spacone's (2000) study is employed to obtain the bond stress–strain relationship. In the current model, six Gaussian points are used in the Gaussian integration scheme. These Gaussian points divide the beam

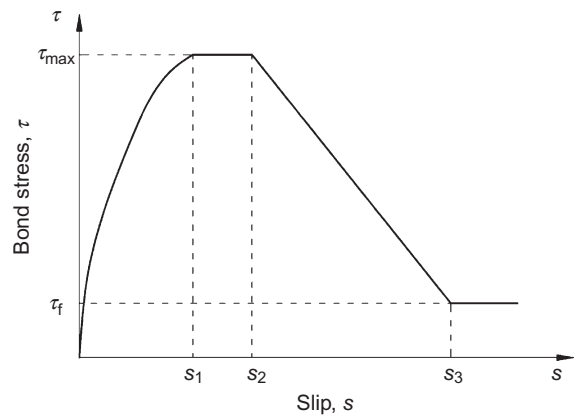

Figure 14.10 Bond stress–slip relationship of steel (CEB-FIP Model Code, 1990).

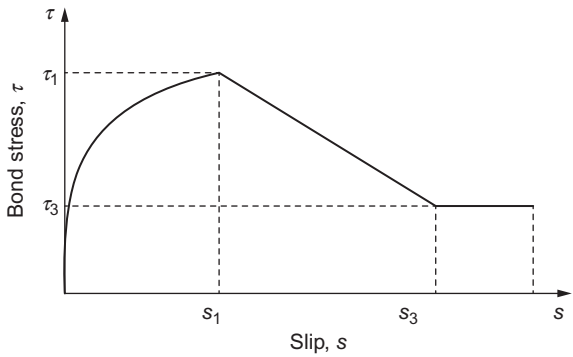

Figure 14.11 BPE-modified model (Cosenza et al., 1997).

element into several slices; thus, if the length of a beam element is L, the length of each slice can be expressed as $L_{GP} = w_{GP}L$, where w_{GP} is the weight of the Gaussian point. Then the slip at each Gaussian point can be expressed as

$$s = \varepsilon_{bond} L_{GP} \tag{14.28}$$

Thus, the bond strain is given by

$$\varepsilon_{bond} = \frac{s}{L_{GP}} \tag{14.29}$$

Then the bond stress–slip relationship described in Figures 14.10 and 14.11 can be transferred into the relationship between bond stress and bond strain. And the modulus of the bond E_{bond} is given by

$$E_{bond} = \kappa L_{GP} \tag{14.30}$$

where κ is given by Eq. (14.27).

14.3.2 Numerical modeling of bond slip between FRP and concrete for the tested FRP-reinforced concrete beams

Beams BC1, BG1, and BB1 are modeled, and the numerical results are presented herein. For BC1 and BG1, parameters for rebars with smooth surface are chosen for the bond stress–slip model, while for BB1, parameters for braided rebar surface are used in the finite element model with bond–slip effect. The test specimens are modeled by six of the proposed composite beam elements with equal length. It should be noted that the relative displacements between the reinforcing bars and the surrounding concrete were measured at the two ends of the center and one of the corner rebars, while in the current finite element model, the bond slip is calculated based on each Gaussian point and for the smeared reinforcing layer. Therefore, in order to compare the calculated bond slip with the test data, an equivalent load–slip curve is

obtained from the test results to represent the slippage of all reinforcing bars. The equivalent value of slippage is the summation of the slippages of the center and corner reinforcing bars multiplied by their respective factors. The factor for the center rebar is 0.333, and that for the corner rebar is 0.667.

14.3.2.1 Numerical results of beam BC1

The equivalent load–slip curve for beam BC1 is compared with that obtained from the finite element model in Figure 14.12. As can be seen, the computed results agree well with the equivalent load–slip values.

14.3.2.2 Numerical results of beam BG1

Figure 14.13 compares the equivalent load–slip curve for beam BG1 with the load–slip curve calculated using the finite element model with bond–slip effect. In general, the predicted results have a fairish agreement with the test data, and the trend of the curve obtained from the current finite element model is in accord with the curve acquired from experimental test.

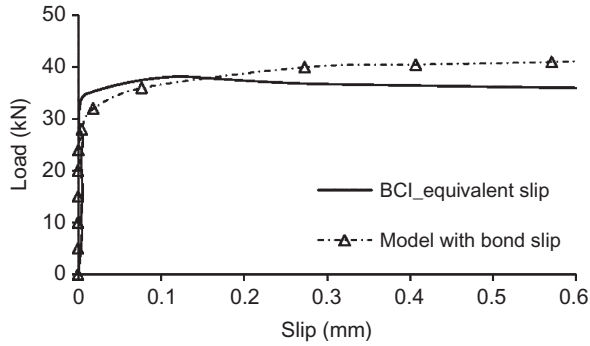

Figure 14.12 Load–slip relationship of beam BC1.

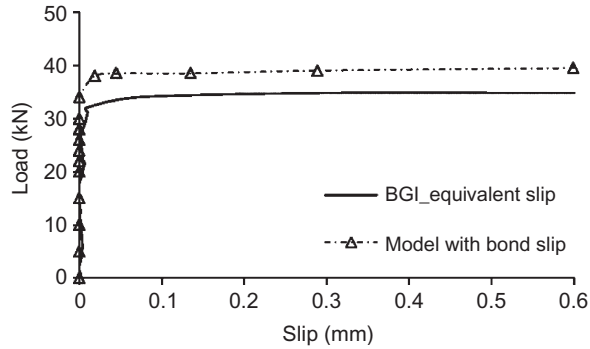

Figure 14.13 Load–slip relationship of beam BG1.

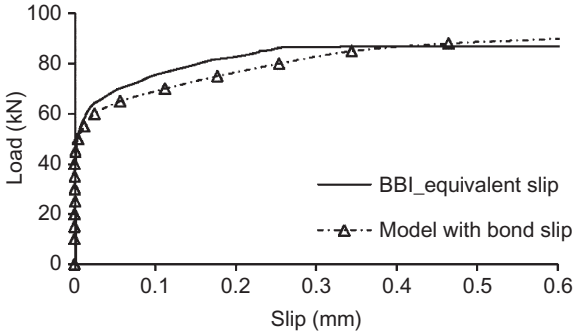

Figure 14.14 Load–slip relationship of beam BB1.

14.3.2.3 Numerical results of beam BB1

The load–slip relation curve calculated using the current finite element model with bond–slip effect is shown in Figure 14.14, and compared with the equivalent load–slip curve from the test data. In general, the current results agree well with the test data, and both the calculated curve and the test curve have same trend when a large amount of slippage starts taking place in beam BB1.

14.4 Summary and conclusion

The bond–slip behavior between FRP rebars and concrete in FRP-reinforced concrete beams was investigated experimentally and numerically in this chapter. Concrete beams reinforced with three types of FRP rebars, i.e., CFRP, GFRP, and BFRP rebars, were studied in which CFRP and GFRP rebars had smooth surfaces and BFRP rebars were wrapped by strands around the outside diameter. For the experimental study, a four-point beam-bending test was conducted to study the bond–slip behavior of FRP rebars, and equivalent load–slip curves were obtained. For the numerical analysis, a recently developed layered composite beam element was used to model the bond–slip behavior of the tested FRP-reinforced concrete beams. From the studies, the following findings are obtained:

- All beams failed by concrete crushing, which was the intended failure mode in their design.
- Bond–slip has been proved to have great influence on the structural behavior of FRP-reinforced concrete beams in addition to the material properties of reinforcing bars. BFRP rebars with proper surface preparation appear to be a promising alternative to conventional steel reinforcements.
- BFRP-reinforced concrete beams with wrapped rebar surfaces showed a good and consistent bond with concrete. No evidence of large slippage of basalt fiber rebars was noticed until the load approaching the maximum bearing capacity, whereas, due to the poor bonding conditions, large amount of slips were measured in CFRP- and GFRP-reinforced concrete beams even at a much lower load level.
- The bond–slip behavior of the tested beams obtained from experimental study and numerical study agrees very well with each other. This, on one hand, demonstrates the effectiveness of the experimental programs, and on the other hand, provides further validation to the finite element model.

References

Australian Standard (AS 1012.17–1997), 1997. Methods of testing concrete—determination of the static chord modulus of elasticity and Poisson's ratio of concrete specimens. SAI Global.

Australian Standard (AS 1012.9–1999), 1999. Methods of testing concrete—determination of the compressive strength of concrete specimens. SAI Global.

Bakis, C.E., Bank, L.C., Brown, V.L., Cosenza, E., Davalos, J.F., Lesko, J.J., Machida, A., Rizkalla, S.H., Triantafillou, T.C., 2002. Fiber-reinforced polymer composites for construction—state-of-the-art review. J. Compos. Constr. 6 (2), 73–87.

Benmokrane, B., Chaallal, O., Masmoudi, R., 1996. Flexural response of concrete beams reinforced with FRP reinforcing bars. ACI Struct. J. 93 (1), 46–55.

Bischoff, P.H., Paixao, R., 2004. Tension stiffening and cracking of concrete reinforced with glass fiber reinforced polymer (GFRP) bars. Can. J. Civ. Eng. 31 (4), 579–588.

Brown, V.L., Bartholomew, C.L., 1993. FRP reinforcing bars in reinforced concrete Members. ACI Mater. J. 90 (1), 34–39.

CEB-FIP Model Code 1990. Thomas Telford Services Ltd. London.

Coronado, C.A., Lopez, M.M., 2006. Sensitivity analysis of reinforced concrete beams strengthened with FRP laminates. Cem. Concr. Compos. 28 (1), 102–114.

Cosenza, E., Manfredi, G., Realfonzo, R., 1997. Behavior and modeling of bond of FRP rebars to concrete. J. Compos. Constr. 1 (2), 40–51.

Davalos, J.F., Chen, Y., Ray, I., 2008. Effect of FRP bar degradation on interface bond with high strength concrete. Cem. Concr. Compos. 30 (8), 722–730.

Kullaa, J., 1996. Dimensional analysis of bond modulus in fiber pullout. J. Struct. Eng. 122 (7), 783–787.

Lin, X., Zhang, Y.X., 2013a. Bond-slip behaviour of FRP-reinforced concrete beams. Constr. Build. Mater. 44, 110–117.

Lin, X., Zhang, Y.X., 2013b. A novel composite beam element with bond-slip for onlinear finite element analyses of steel/FRP-reinforced concrete beams. J. Struct. Eng. 139 (12), 06013003-1–06013003-6.

Monti, G., Spacone, E., 2000. Reinforced concrete fiber beam element with bond-slip. J. Struct. Eng. 126 (6), 654–661.

Naaman, A.E., Namur, G.G., Alwan, J.M., Najm, H.S., 1991. Fiber pullout and bond slip. I: analytical study. J. Struct. Eng. 117 (9), 2769–2790.

Nitereka, C., Neale, K.W., 1999. Analysis of reinforced concrete beams strengthened in flexure with composite laminates. Can. J. Civ. Eng. 26, 646–654.

Nour, A., Massicotte, B., Yildiz, E., Koval, V., 2007. Finite element modeling of concrete structures reinforced with internal and external fibre-reinforced polymers. Can. J. Civ. Eng. 34 (3), 340–354.

Owen, D.R.J., Figueiras, J.A., 1984. Ultimate load analysis of reinforced concrete plates and shells including geometric nonlinear effects. In: Hinton, E., Owen, D.R.J. (Eds.), Finite Element Software for Plates and Shells. Pineridge Press, Swansea, UK.

Rizkalla, S., Hassan, T., Hassan, N., 2003. Design recommendations for the use of FRP for reinforcement and strengthening of concrete structures. Prog. Struct. Eng. Mater. 5 (1), 16–28.

Index

Note: Page numbers followed by *f* indicate figures and *t* indicate tables.

Q

R

S